RILEM State-of-the-Art Reports

Eduardo M. R. Fairbairn
Miguel Azenha *Editors*

Thermal Cracking of Massive Concrete Structures

State of the Art Report of the RILEM Technical Committee 254-CMS

RILEM State-of-the-Art Reports

RILEM STATE-OF-THE-ART REPORTS

Volume 27

RILEM, The International Union of Laboratories and Experts in Construction Materials, Systems and Structures, founded in 1947, is a non-governmental scientific association whose goal is to contribute to progress in the construction sciences, techniques and industries, essentially by means of the communication it fosters between research and practice. RILEM's focus is on construction materials and their use in building and civil engineering structures, covering all phases of the building process from manufacture to use and recycling of materials. More information on RILEM and its previous publications can be found on www.RILEM.net.

The RILEM State-of-the-Art Reports (STAR) are produced by the Technical Committees. They represent one of the most important outputs that RILEM generates—high level scientific and engineering reports that provide cutting edge knowledge in a given field. The work of the TCs is one of RILEM's key functions.

Members of a TC are experts in their field and give their time freely to share their expertise. As a result, the broader scientific community benefits greatly from RILEM's activities.

RILEM's stated objective is to disseminate this information as widely as possible to the scientific community. RILEM therefore considers the STAR reports of its TCs as of highest importance, and encourages their publication whenever possible.

The information in this and similar reports is mostly pre-normative in the sense that it provides the underlying scientific fundamentals on which standards and codes of practice are based. Without such a solid scientific basis, construction practice will be less than efficient or economical.

It is RILEM's hope that this information will be of wide use to the scientific community.

More information about this series at http://www.springer.com/series/8780

Eduardo M. R. Fairbairn
Miguel Azenha
Editors

Thermal Cracking of Massive Concrete Structures

State of the Art Report of the RILEM Technical Committee 254-CMS

Springer

Editors
Eduardo M. R. Fairbairn
Department of Civil Engineering
COPPE/UFRJ
Rio de Janeiro
Brazil

Miguel Azenha
ISISE - Department of Civil Engineering
University of Minho
Guimarães
Portugal

ISSN 2213-204X ISSN 2213-2031 (electronic)
RILEM State-of-the-Art Reports
ISBN 978-3-319-76616-4 ISBN 978-3-319-76617-1 (eBook)
https://doi.org/10.1007/978-3-319-76617-1

Library of Congress Control Number: 2018933481

© RILEM 2019
No part of this work may be reproduced, stored in a retrieval system, or transmitted in any form or by any means, electronic, mechanical, photocopying, microfilming, recording or otherwise, without written permission from the Publisher, with the exception of any material supplied specifically for the purpose of being entered and executed on a computer system, for exclusive use by the purchaser of the work. Permission for use must always be obtained from the owner of the copyright: RILEM.

Printed on acid-free paper

This Springer imprint is published by the registered company Springer International Publishing AG part of Springer Nature
The registered company address is: Gewerbestrasse 11, 6330 Cham, Switzerland

Preface

This book results from the coordinated efforts of the members of RILEM TC 254-CMS 'Thermal Cracking of Massive Concrete Structures', which was proposed by Eduardo M. R. Fairbairn (Chair of the TC) in 2013. The subject matter of this TC was initially centred in establishing a state-of-the-art report (STAR) on principles, criteria, methods and technologies applied worldwide to control thermal cracking in mass concrete, such as concrete dams, nuclear power plants, massive foundations and massive members of concrete structures (including those in which cracking risk does not arise from large volumes of concrete). The TC also targets the establishment of guidelines on how to analyse and to control the risk of thermal cracks in mass concrete.

The efforts that made this book possible involved much voluntary work of all co-authors, particularly through a regular attendance to 14 TC meetings (six of which were personal meetings, where the others were made through online platforms). A truly collaborative experience was felt among all participants, resulting in an up-to-date critical review of the latest knowledge on this relevant topic for construction.

Rio de Janeiro, Brazil — Eduardo M. R. Fairbairn
Guimarães, Portugal — Miguel Azenha

Acknowledgements

The work performed by RILEM TC 254-CMS has been significantly assisted by the networking activities of COST Action TU1404 ‘Towards the next generation of standards for service life of cement-based materials and structures’.

COST (European Cooperation in Science and Technology) is a pan-European intergovernmental framework.

Its mission is to enable breakthrough scientific and technological developments leading to new concepts and products and thereby contribute to strengthening Europe’s research and innovation capacities. It allows researchers, engineers and scholars to jointly develop their own ideas and take new initiatives across all fields of science and technology, while promoting multi- and interdisciplinary approaches. COST aims at fostering a better integration of less research-intensive countries in the knowledge hubs of the European Research Area. The COST Association, an international not-for-profit association under Belgian law, integrates all management, governing and administrative functions necessary for the operation of the framework. The COST Association currently has 36 Member Countries. www.cost.eu.

TC 254-CMS Members

Chairman

Eduardo M. R. Fairbairn, Federal University of Rio de Janeiro, Brazil

Secretary

Miguel Azenha, ISISE, University of Minho, Guimarães, Portugal

TC Members (Co-authors of chapters in this book)

Shingo Asamoto, Saitama University, Japan
Yunus Ballim, University of the Witwatersrand, Johannesburg, South Africa
Farid Benboudjema, ENS-Cachan, Université Paris Saclay, France
Matthieu Briffaut, University Grenoble Alpes, CNRS, Grenoble, France
Jérôme Carette, Université Libre de Bruxelles, Brussels, Belgium
Brice Delsaute, Université Libre de Bruxelles, Brussels, Belgium
Luis Ebensperger, Construtechnik Ltda., Santiago, Chile
Túlio Honório De Faria, CEA, DEN, DPC, SECR, Gif-sur-Yvette, France
Fragkoulis Kanavaris, Queen's University of Belfast, UK
Agnieszka Knoppik, Silesian University of Technology, Gliwice, Poland
Eduardus Koenders, Technische Universität Darmstadt, Germany
Selmo Kuperman, Desek Ltda, Brazil
Laurie Lacarrière, Université de Toulouse, UPS, INSA, LMDC, France
Rodrigo Lameiras, University of Brasília (UnB), Brazil
Wilson Leal Da Silva, Danish Technological Institute, Taastrup, Denmark
Pietro Lura, EMPA/ETH, Switzerland
Anne Neiry de Mendonça Lopes, FURNAS, Brazil
Francesco Pesavento, University of Padova, Padova, Italy
Pierre Rossi, IFSTTAR, Paris, France
Dirk Schlicke, Technical University of Graz, Austria
Ioannis Sfikas, Mott MacDonald Ltd., UK
Vit Šmilauer, Czech Technical University, Prague, Czech Republic
Stéphanie Staquet, Université Libre de Bruxelles, Brussels, Belgium

Roberto Torrent, Materials Advanced Services Ltd., Buenos Aires, Argentina
Jean Michel Torrenti, University of Paris-Est, IFSTTAR, France
Neven Ukrainczyk, Technische Universität Darmstadt, Germany
Mateusz Wyrzykowski, Empa, Switzerland

RILEM Publications

The following list is presenting the global offer of RILEM Publications, sorted by series. Each publication is available in printed version and/or in online version.

RILEM Proceedings (PRO)

PRO 1: Durability of High Performance Concrete (ISBN: 2-912143-03-9; e-ISBN: 2-351580-12-5; e-ISBN: 2351580125); *Ed. H. Sommer*

PRO 2: Chloride Penetration into Concrete (ISBN: 2-912143-00-04; e-ISBN: 2912143454); *Eds. L.-O. Nilsson and J.-P. Ollivier*

PRO 3: Evaluation and Strengthening of Existing Masonry Structures (ISBN: 2-912143-02-0; e-ISBN: 2351580141); *Eds. L. Binda and C. Modena*

PRO 4: Concrete: From Material to Structure (ISBN: 2-912143-04-7; e-ISBN: 2351580206); *Eds. J.-P. Bournazel and Y. Malier*

PRO 5: The Role of Admixtures in High Performance Concrete (ISBN: 2-912143-05-5; e-ISBN: 2351580214); *Eds. J. G. Cabrera and R. Rivera-Villarreal*

PRO 6: High Performance Fiber Reinforced Cement Composites—HPFRCC 3 (ISBN: 2-912143-06-3; e-ISBN: 2351580222); *Eds. H. W. Reinhardt and A. E. Naaman*

PRO 7: 1st International RILEM Symposium on Self-Compacting Concrete (ISBN: 2-912143-09-8; e-ISBN: 2912143721); *Eds. Å. Skarendahl and Ö. Petersson*

PRO 8: International RILEM Symposium on Timber Engineering (ISBN: 2-912143-10-1; e-ISBN: 2351580230); *Ed. L. Boström*

PRO 9: 2nd International RILEM Symposium on Adhesion between Polymers and Concrete ISAP '99 (ISBN: 2-912143-11-X; e-ISBN: 2351580249); *Eds. Y. Ohama and M. Puterman*

PRO 10: 3rd International RILEM Symposium on Durability of Building and Construction Sealants (ISBN: 2-912143-13-6; e-ISBN: 2351580257); *Eds. A. T. Wolf*

PRO 11: 4th International RILEM Conference on Reflective Cracking in Pavements (ISBN: 2-912143-14-4; e-ISBN: 2351580265); *Eds. A. O. Abd El Halim, D. A. Taylor and El H. H. Mohamed*

PRO 12: International RILEM Workshop on Historic Mortars: Characteristics and Tests (ISBN: 2-912143-15-2; e-ISBN: 2351580273); *Eds. P. Bartos, C. Groot and J. J. Hughes*

PRO 13: 2nd International RILEM Symposium on Hydration and Setting (ISBN: 2-912143-16-0; e-ISBN: 2351580281); *Ed. A. Nonat*

PRO 14: Integrated Life-Cycle Design of Materials and Structures—ILCDES 2000 (ISBN: 951-758-408-3; e-ISBN: 235158029X); (ISSN: 0356-9403); *Ed. S. Sarja*

PRO 15: Fifth RILEM Symposium on Fibre-Reinforced Concretes (FRC)—BEFIB'2000 (ISBN: 2-912143-18-7; e-ISBN: 291214373X); *Eds. P. Rossi and G. Chanvillard*

PRO 16: Life Prediction and Management of Concrete Structures (ISBN: 2-912143-19-5; e-ISBN: 2351580303); *Ed. D. Naus*

PRO 17: Shrinkage of Concrete—Shrinkage 2000 (ISBN: 2-912143-20-9; e-ISBN: 2351580311); *Eds. V. Baroghel-Bouny and P.-C. Aïtcin*

PRO 18: Measurement and Interpretation of the On-Site Corrosion Rate (ISBN: 2-912143-21-7; e-ISBN: 235158032X); *Eds. C. Andrade, C. Alonso, J. Fullea, J. Polimon and J. Rodriguez*

PRO 19: Testing and Modelling the Chloride Ingress into Concrete (ISBN: 2-912143-22-5; e-ISBN: 2351580338); *Eds. C. Andrade and J. Kropp*

PRO 20: 1st International RILEM Workshop on Microbial Impacts on Building Materials (CD 02) (e-ISBN 978-2-35158-013-4); *Ed. M. Ribas Silva*

PRO 21: International RILEM Symposium on Connections between Steel and Concrete (ISBN: 2-912143-25-X; e-ISBN: 2351580346); *Ed. R. Eligehausen*

PRO 22: International RILEM Symposium on Joints in Timber Structures (ISBN: 2-912143-28-4; e-ISBN: 2351580354); *Eds. S. Aicher and H.-W. Reinhardt*

PRO 23: International RILEM Conference on Early Age Cracking in Cementitious Systems (ISBN: 2-912143-29-2; e-ISBN: 2351580362); *Eds. K. Kovler and A. Bentur*

PRO 24: 2nd International RILEM Workshop on Frost Resistance of Concrete (ISBN: 2-912143-30-6; e-ISBN: 2351580370); *Eds. M. J. Setzer, R. Auberg and H.-J. Keck*

PRO 25: International RILEM Workshop on Frost Damage in Concrete (ISBN: 2-912143-31-4; e-ISBN: 2351580389); *Eds. D. J. Janssen, M. J. Setzer and M. B. Snyder*

PRO 26: International RILEM Workshop on On-Site Control and Evaluation of Masonry Structures (ISBN: 2-912143-34-9; e-ISBN: 2351580141); *Eds. L. Binda and R. C. de Vekey*

PRO 27: International RILEM Symposium on Building Joint Sealants (CD03; e-ISBN: 235158015X); *Ed. A. T. Wolf*

PRO 28: 6th International RILEM Symposium on Performance Testing and Evaluation of Bituminous Materials—PTEBM'03 (ISBN: 2-912143-35-7; e-ISBN: 978-2-912143-77-8); *Ed. M. N. Partl*

PRO 29: 2nd International RILEM Workshop on Life Prediction and Ageing Management of Concrete Structures (ISBN: 2-912143-36-5; e-ISBN: 2912143780); *Ed. D. J. Naus*

PRO 30: 4th International RILEM Workshop on High Performance Fiber Reinforced Cement Composites—HPFRCC 4 (ISBN: 2-912143-37-3; e-ISBN: 2912143799); *Eds. A. E. Naaman and H. W. Reinhardt*

PRO 31: International RILEM Workshop on Test and Design Methods for Steel Fibre Reinforced Concrete: Background and Experiences (ISBN: 2-912143-38-1; e-ISBN: 2351580168); *Eds. B. Schnütgen and L. Vandewalle*

PRO 32: International Conference on Advances in Concrete and Structures 2 vol. (ISBN (set): 2-912143-41-1; e-ISBN: 2351580176); *Eds. Ying-shu Yuan, Surendra P. Shah and Heng-lin Lü*

PRO 33: 3rd International Symposium on Self-Compacting Concrete (ISBN: 2-912143-42-X; e-ISBN: 2912143713); *Eds. Ó. Wallevik and I. Níelsson*

PRO 34: International RILEM Conference on Microbial Impact on Building Materials (ISBN: 2-912143-43-8; e-ISBN: 2351580184); *Ed. M. Ribas Silva*

PRO 35: International RILEM TC 186-ISA on Internal Sulfate Attack and Delayed Ettringite Formation (ISBN: 2-912143-44-6; e-ISBN: 2912143802); *Eds. K. Scrivener and J. Skalny*

PRO 36: International RILEM Symposium on Concrete Science and Engineering—A Tribute to Arnon Bentur (ISBN: 2-912143-46-2; e-ISBN: 2912143586); *Eds. K. Kovler, J. Marchand, S. Mindess and J. Weiss*

PRO 37: 5th International RILEM Conference on Cracking in Pavements—Mitigation, Risk Assessment and Prevention (ISBN: 2-912143-47-0; e-ISBN: 2912143764); *Eds. C. Petit, I. Al-Qadi and A. Millien*

PRO 38: 3rd International RILEM Workshop on Testing and Modelling the Chloride Ingress into Concrete (ISBN: 2-912143-48-9; e-ISBN: 2912143578); *Eds. C. Andrade and J. Kropp*

PRO 39: 6th International RILEM Symposium on Fibre-Reinforced Concretes—BEFIB 2004 (ISBN: 2-912143-51-9; e-ISBN: 2912143748); *Eds. M. Di Prisco, R. Felicetti and G. A. Plizzari*

PRO 40: International RILEM Conference on the Use of Recycled Materials in Buildings and Structures (ISBN: 2-912143-52-7; e-ISBN: 2912143756); *Eds. E. Vázquez, Ch. F. Hendriks and G. M. T. Janssen*

PRO 41: RILEM International Symposium on Environment-Conscious Materials and Systems for Sustainable Development (ISBN: 2-912143-55-1; e-ISBN: 2912143640); *Eds. N. Kashino and Y. Ohama*

PRO 42: SCC'2005—China: 1st International Symposium on Design, Performance and Use of Self-Consolidating Concrete (ISBN: 2-912143-61-6; e-ISBN: 2912143624); *Eds. Zhiwu Yu, Caijun Shi, Kamal Henri Khayat and Youjun Xie*

PRO 43: International RILEM Workshop on Bonded Concrete Overlays (e-ISBN: 2-912143-83-7); *Eds. J. L. Granju and J. Silfwerbrand*

PRO 44: 2nd International RILEM Workshop on Microbial Impacts on Building Materials (CD11) (e-ISBN: 2-912143-84-5); *Ed. M. Ribas Silva*

PRO 45: 2nd International Symposium on Nanotechnology in Construction, Bilbao (ISBN: 2-912143-87-X; e-ISBN: 2912143888); *Eds. Peter J. M. Bartos, Yolanda de Miguel and Antonio Porro*

PRO 46: Concrete Life'06—International RILEM-JCI Seminar on Concrete Durability and Service Life Planning: Curing, Crack Control, Performance in Harsh Environments (ISBN: 2-912143-89-6; e-ISBN: 291214390X); *Ed. K. Kovler*

PRO 47: International RILEM Workshop on Performance Based Evaluation and Indicators for Concrete Durability (ISBN: 978-2-912143-95-2; e-ISBN: 9782912143969); *Eds. V. Baroghel-Bouny, C. Andrade, R. Torrent and K. Scrivener*

PRO 48: 1st International RILEM Symposium on Advances in Concrete through Science and Engineering (e-ISBN: 2-912143-92-6); *Eds. J. Weiss, K. Kovler, J. Marchand, and S. Mindess*

PRO 49: International RILEM Workshop on High Performance Fiber Reinforced Cementitious Composites in Structural Applications (ISBN: 2-912143-93-4; e-ISBN: 2912143942); *Eds. G. Fischer and V.C. Li*

PRO 50: 1st International RILEM Symposium on Textile Reinforced Concrete (ISBN: 2-912143-97-7; e-ISBN: 2351580087); *Eds. Josef Hegger, Wolfgang Brameshuber and Norbert Will*

PRO 51: 2nd International Symposium on Advances in Concrete through Science and Engineering (ISBN: 2-35158-003-6; e-ISBN: 2-35158-002-8); *Eds. J. Marchand, B. Bissonnette, R. Gagné, M. Jolin and F. Paradis*

PRO 52: Volume Changes of Hardening Concrete: Testing and Mitigation (ISBN: 2-35158-004-4; e-ISBN: 2-35158-005-2); *Eds. O. M. Jensen, P. Lura and K. Kovler*

PRO 53: High Performance Fiber Reinforced Cement Composites—HPFRCC5 (ISBN: 978-2-35158-046-2; e-ISBN: 978-2-35158-089-9); *Eds. H. W. Reinhardt and A. E. Naaman*

PRO 54: 5th International RILEM Symposium on Self-Compacting Concrete (ISBN: 978-2-35158-047-9; e-ISBN: 978-2-35158-088-2); *Eds. G. De Schutter and V. Boel*

PRO 55: International RILEM Symposium Photocatalysis, Environment and Construction Materials (ISBN: 978-2-35158-056-1; e-ISBN: 978-2-35158-057-8); *Eds. P. Baglioni and L. Cassar*

PRO 56: International RILEM Workshop on Integral Service Life Modelling of Concrete Structures (ISBN 978-2-35158-058-5; e-ISBN: 978-2-35158-090-5); *Eds. R. M. Ferreira, J. Gulikers and C. Andrade*

PRO 57: RILEM Workshop on Performance of cement-based materials in aggressive aqueous environments (e-ISBN: 978-2-35158-059-2); *Ed. N. De Belie*

PRO 58: International RILEM Symposium on Concrete Modelling—CONMOD'08 (ISBN: 978-2-35158-060-8; e-ISBN: 978-2-35158-076-9); *Eds. E. Schlangen and G. De Schutter*

PRO 59: International RILEM Conference on On Site Assessment of Concrete, Masonry and Timber Structures—SACoMaTiS 2008 (ISBN set: 978-2-35158-061-5; e-ISBN: 978-2-35158-075-2); *Eds. L. Binda, M. di Prisco and R. Felicetti*

PRO 60: Seventh RILEM International Symposium on Fibre Reinforced Concrete: Design and Applications—BEFIB 2008 (ISBN: 978-2-35158-064-6; e-ISBN: 978-2-35158-086-8); *Ed. R. Gettu*

PRO 61: 1st International Conference on Microstructure Related Durability of Cementitious Composites 2 vol., (ISBN: 978-2-35158-065-3; e-ISBN: 978-2-35158-084-4); *Eds. W. Sun, K. van Breugel, C. Miao, G. Ye and H. Chen*

PRO 62: NSF/ RILEM Workshop: In-situ Evaluation of Historic Wood and Masonry Structures (e-ISBN: 978-2-35158-068-4); *Eds. B. Kasal, R. Anthony and M. Drdácký*

PRO 63: Concrete in Aggressive Aqueous Environments: Performance, Testing and Modelling, 2 vol., (ISBN: 978-2-35158-071-4; e-ISBN: 978-2-35158-082-0); *Eds. M. G. Alexander and A. Bertron*

PRO 64: Long Term Performance of Cementitious Barriers and Reinforced Concrete in Nuclear Power Plants and Waste Management—NUCPERF 2009 (ISBN: 978-2-35158-072-1; e-ISBN: 978-2-35158-087-5); *Eds. V. L'Hostis, R. Gens, C. Gallé*

PRO 65: Design Performance and Use of Self-consolidating Concrete—SCC'2009 (ISBN: 978-2-35158-073-8; e-ISBN: 978-2-35158-093-6); *Eds. C. Shi, Z. Yu, K. H. Khayat and P. Yan*

PRO 66: 2nd International RILEM Workshop on Concrete Durability and Service Life Planning—ConcreteLife'09 (ISBN: 978-2-35158-074-5; ISBN: 978-2-35158-074-5); *Ed. K. Kovler*

PRO 67: Repairs Mortars for Historic Masonry (e-ISBN: 978-2-35158-083-7); *Ed. C. Groot*

PRO 68: Proceedings of the 3rd International RILEM Symposium on 'Rheology of Cement Suspensions such as Fresh Concrete (ISBN 978-2-35158-091-2; e-ISBN: 978-2-35158-092-9); *Eds. O. H. Wallevik, S. Kubens and S. Oesterheld*

PRO 69: 3rd International PhD Student Workshop on 'Modelling the Durability of Reinforced Concrete (ISBN: 978-2-35158-095-0); *Eds. R. M. Ferreira, J. Gulikers and C. Andrade*

PRO 70: 2nd International Conference on 'Service Life Design for Infrastructure' (ISBN set: 978-2-35158-096-7, e-ISBN: 978-2-35158-097-4); *Ed. K. van Breugel, G. Ye and Y. Yuan*

PRO 71: Advances in Civil Engineering Materials—The 50-year Teaching Anniversary of Prof. Sun Wei' (ISBN: 978-2-35158-098-1; e-ISBN: 978-2-35158-099-8); *Eds. C. Miao, G. Ye, and H. Chen*

PRO 72: First International Conference on 'Advances in Chemically-Activated Materials—CAM'2010' (2010), 264 pp, ISBN: 978-2-35158-101-8; e-ISBN: 978-2-35158-115-5, *Eds. Caijun Shi and Xiaodong Shen*

PRO 73: 2nd International Conference on 'Waste Engineering and Management —ICWEM 2010' (2010), 894 pp, ISBN: 978-2-35158-102-5; e-ISBN: 978-2-35158-103-2, *Eds. J. Zh. Xiao, Y. Zhang, M. S. Cheung and R. Chu*

PRO 74: International RILEM Conference on 'Use of Superabsorsorbent Polymers and Other New Addditives in Concrete' (2010) 374 pp., ISBN: 978-2-35158-104-9; e-ISBN: 978-2-35158-105-6; *Eds. O.M. Jensen, M.T. Hasholt, and S. Laustsen*

PRO 75: International Conference on 'Material Science—2nd ICTRC—Textile Reinforced Concrete—Theme 1' (2010) 436 pp., ISBN: 978-2-35158-106-3; e-ISBN: 978-2-35158-107-0; *Ed. W. Brameshuber*

PRO 76: International Conference on 'Material Science—HetMat—Modelling of Heterogeneous Materials—Theme 2' (2010) 255 pp., ISBN: 978-2-35158-108-7; e-ISBN: 978-2-35158-109-4; *Ed. W. Brameshuber*

PRO 77: International Conference on 'Material Science—AdIPoC—Additions Improving Properties of Concrete—Theme 3' (2010) 459 pp., ISBN: 978-2-35158-110-0; e-ISBN: 978-2-35158-111-7; *Ed. W. Brameshuber*

PRO 78: 2nd Historic Mortars Conference and RILEM TC 203-RHM Final Workshop—HMC2010 (2010) 1416 pp., e-ISBN: 978-2-35158-112-4; *Eds. J. Válek, C. Groot, and J. J. Hughes*

PRO 79: International RILEM Conference on Advances in Construction Materials Through Science and Engineering (2011) 213 pp., ISBN: 978-2-35158-116-2, e-ISBN: 978-2-35158-117-9; *Eds. Christopher Leung and K.T. Wan*

PRO 80: 2nd International RILEM Conference on Concrete Spalling due to Fire Exposure (2011) 453 pp., ISBN: 978-2-35158-118-6, e-ISBN: 978-2-35158-119-3; *Eds. E.A.B. Koenders and F. Dehn*

PRO 81: 2nd International RILEM Conference on Strain Hardening Cementitious Composites (SHCC2-Rio) (2011) 451 pp., ISBN: 978-2-35158-120-9, e-ISBN: 978-2-35158-121-6; *Eds. R.D. Toledo Filho, F.A. Silva, E.A.B. Koenders and E.M.R. Fairbairn*

PRO 82: 2nd International RILEM Conference on Progress of Recycling in the Built Environment (2011) 507 pp., e-ISBN: 978-2-35158-122-3; *Eds. V.M. John, E. Vazquez, S.C. Angulo and C. Ulsen*

PRO 83: 2nd International Conference on Microstructural-related Durability of Cementitious Composites (2012) 250 pp., ISBN: 978-2-35158-129-2; e-ISBN: 978-2-35158-123-0; *Eds. G. Ye, K. van Breugel, W. Sun and C. Miao*

PRO 84: CONSEC13—Seventh International Conference on Concrete under Severe Conditions—Environment and Loading (2013) 1930 pp., ISBN: 978-2-35158-124-7; e-ISBN: 978-2- 35158-134-6; *Eds Z.J. Li, W. Sun, C.W. Miao, K. Sakai, O.E. Gjorv & N. Banthia*

PRO 85: RILEM-JCI International Workshop on Crack Control of Mass Concrete and Related issues concerning Early-Age of Concrete Structures—

ConCrack 3—Control of Cracking in Concrete Structures 3 (2012) 237 pp., ISBN: 978-2-35158-125-4; e-ISBN: 978-2-35158-126-1; *Eds F. Toutlemonde and J.-M. Torrenti*

PRO 86: International Symposium on Life Cycle Assessment and Construction (2012) 414 pp., ISBN: 978-2-35158-127-8, e-ISBN: 978-2-35158-128-5; *Eds A. Ventura and C. de la Roche*

PRO 87: UHPFRC 2013—RILEM-fib-AFGC International Symposium on Ultra-High Performance Fibre-Reinforced Concrete (2013), ISBN: 978-2-35158-130-8, e-ISBN: 978-2-35158-131-5; *Eds F. Toutlemonde*

PRO 88: 8th RILEM International Symposium on Fibre Reinforced Concrete (2012) 344 pp., ISBN: 978-2-35158-132-2, e-ISBN: 978-2-35158-133-9; *Eds Joaquim A.O. Barros*

PRO 89: RILEM International workshop on performance-based specification and control of concrete durability (2014) 678 pp, ISBN: 978-2-35158-135-3, e-ISBN: 978-2-35158-136-0; *Eds. D. Bjegović, H. Beushausen and M. Serdar*

PRO 90: 7th RILEM International Conference on Self-Compacting Concrete and of the 1st RILEM International Conference on Rheology and Processing of Construction Materials (2013) 396 pp, ISBN: 978-2-35158-137-7, e-ISBN: 978-2-35158-138-4; *Eds. Nicolas Roussel and Hela Bessaies-Bey*

PRO 91: CONMOD 2014—RILEM International Symposium on Concrete Modelling (2014), ISBN: 978-2-35158-139-1; e-ISBN: 978-2-35158-140-7; *Eds. Kefei Li, Peiyu Yan and Rongwei Yang*

PRO 92: CAM 2014—2nd International Conference on advances in chemically-activated materials (2014) 392 pp., ISBN: 978-2-35158-141-4; e-ISBN: 978-2-35158-142-1; *Eds. Caijun Shi and Xiadong Shen*

PRO 93: SCC 2014—3rd International Symposium on Design, Performance and Use of Self-Consolidating Concrete (2014) 438 pp., ISBN: 978-2-35158-143-8; e-ISBN: 978-2-35158-144-5; *Eds. Caijun Shi, Zhihua Ou, Kamal H. Khayat*

PRO 94 (online version): HPFRCC-7—7th RILEM conference on High performance fiber reinforced cement composites (2015), e-ISBN: 978-2-35158-146-9; *Eds. H.W. Reinhardt, G.J. Parra-Montesinos, H. Garrecht*

PRO 95: International RILEM Conference on Application of superabsorbent polymers and other new admixtures in concrete construction (2014), ISBN: 978-2-35158-147-6; e-ISBN: 978-2-35158-148-3; *Eds. Viktor Mechtcherine, Christof Schroefl*

PRO 96 (online version): XIII DBMC: XIII International Conference on Durability of Building Materials and Components(2015), e-ISBN: 978-2-35158-149-0; *Eds. M. Quattrone, V.M. John*

PRO 97: SHCC3—3rd International RILEM Conference on Strain Hardening Cementitious Composites (2014), ISBN: 978-2-35158-150-6; e-ISBN: 978-2-35158-151-3; *Eds. E. Schlangen, M.G. Sierra Beltran, M. Lukovic, G. Ye*

PRO 98: FERRO-11—11th International Symposium on Ferrocement and 3rd ICTRC—International Conference on Textile Reinforced Concrete (2015), ISBN: 978-2-35158-152-0; e-ISBN: 978-2-35158-153-7; *Ed. W. Brameshuber*

PRO 99 (online version): ICBBM 2015—1st International Conference on Bio-Based Building Materials (2015), e-ISBN: 978-2-35158-154-4; *Eds. S. Amziane, M. Sonebi*

PRO 100: SCC16—RILEM Self-Consolidating Concrete Conference (2016), ISBN: 978-2-35158-156-8; e-ISBN: 978-2-35158-157-5; *Ed. Kamal H. Kayat*

PRO 101 (online version): III Progress of Recycling in the Built Environment (2015), e-ISBN: 978-2-35158-158-2; *Eds I. Martins, C. Ulsen and S. C. Angulo*

PRO 102 (online version): RILEM Conference on Microorganisms-Cementitious Materials Interactions (2016), e-ISBN: 978-2-35158-160-5; *Eds. Alexandra Bertron, Henk Jonkers, Virginie Wiktor*

PRO 103 (online version): ACESC'16—Advances in Civil Engineering and Sustainable Construction (2016), e-ISBN: 978-2-35158-161-2; *Eds. T.Ch. Madhavi, G. Prabhakar, Santhosh Ram and P.M. Rameshwaran*

PRO 104 (online version): SSCS'2015—Numerical Modeling—Strategies for Sustainable Concrete Structures (2015), e-ISBN: 978-2-35158-162-9

PRO 105: 1st International Conference on UHPC Materials and Structures (2016), ISBN: 978-2-35158-164-3, e-ISBN: 978-2-35158-165-0

PRO 106: AFGC-ACI-fib-RILEM International Conference on Ultra-High-Performance Fibre-Reinforced Concrete—UHPFRC 2017 (2017), ISBN: 978-2-35158-166-7, e-ISBN: 978-2-35158-167-4; *Eds. François Toutlemonde & Jacques Resplendino*

PRO 107 (online version): XIV DBMC—14th International Conference on Durability of Building Materials and Components (2017), e-ISBN: 978-2-35158-159-9; *Eds. Geert De Schutter, Nele De Belie, Arnold Janssens, Nathan Van Den Bossche*

PRO 108: MSSCE 2016—Innovation of Teaching in Materials and Structures (2016), ISBN: 978-2-35158-178-0, e-ISBN: 978-2-35158-179-7; *Ed. Per Goltermann*

PRO 109 (2 volumes): MSSCE 2016—Service Life of Cement-Based Materials and Structures (2016), ISBN Vol. 1: 978-2-35158-170-4, Vol. 2: 978-2-35158-171-4, Set Vol. 1&2: 978-2-35158-172-8, e-ISBN : 978-2-35158-173-5; *Eds. Miguel Azenha, Ivan Gabrijel, Dirk Schlicke, Terje Kanstad and Ole Mejlhede Jensen*

PRO 110: MSSCE 2016—Historical Masonry (2016), ISBN: 978-2-35158-178-0, e-ISBN: 978-2-35158-179-7; *Eds. Inge Rörig-Dalgaard and Ioannis Ioannou*

PRO 111: MSSCE 2016—Electrochemistry in Civil Engineering (2016), ISBN: 978-2-35158-176-6, e-ISBN: 978-2-35158-177-3; *Ed. Lisbeth M. Ottosen*

PRO 112: MSSCE 2016—Moisture in Materials and Structures (2016), ISBN: 978-2-35158-178-0, e-ISBN: 978-2-35158-179-7; *Eds. Kurt Kielsgaard Hansen, Carsten Rode and Lars-Olof Nilsson*

PRO 113: MSSCE 2016—Concrete with Supplementary Cementitious Materials (2016), ISBN: 978-2-35158-178-0, e-ISBN: 978-2-35158-179-7; *Eds. Ole Mejlhede Jensen, Konstantin Kovler and Nele De Belie*

PRO 114: MSSCE 2016—Frost Action in Concrete (2016), ISBN: 978-2-35158-182-7, e-ISBN: 978-2-35158-183-4; *Eds. Marianne Tange Hasholt, Katja Fridh and R. Doug Hooton*

PRO 115: MSSCE 2016—Fresh Concrete (2016), ISBN: 978-2-35158-184-1, e-ISBN: 978-2-35158-185-8; *Eds. Lars N. Thrane, Claus Pade, Oldrich Svec and Nicolas Roussel*

PRO 116: BEFIB 2016—9th RILEM International Symposium on Fiber Reinforced Concrete (2016), ISBN: 978-2-35158-187-2, e-ISBN: 978-2-35158-186-5; *Eds. N. Banthia, M. di Prisco and S. Soleimani-Dashtaki*

PRO 117: 3rd International RILEM Conference on Microstructure Related Durability of Cementitious Composites (2016), ISBN: 978-2-35158-188-9, e-ISBN: 978-2-35158-189-6; *Eds. Changwen Miao, Wei Sun, Jiaping Liu, Huisu Chen, Guang Ye and Klaas van Breugel*

PRO 118 (4 volumes): International Conference on Advances in Construction Materials and Systems (2017), ISBN Set: 978-2-35158-190-2, Vol. 1: 978-2-35158-193-3, Vol. 2: 978-2-35158-194-0, Vol. 3: ISBN:978-2-35158-195-7, Vol. 4: ISBN:978-2-35158-196-4, e-ISBN: 978-2-35158-191-9; *Ed. Manu Santhanam*

PRO 119 (online version): ICBBM 2017—Second International RILEM Conference on Bio-based Building Materials, (2017), e-ISBN: 978-2-35158-192-6; *Ed. Sofiane Amziane*

PRO 120: 2nd International RILEM/COST Conference on Early Age Cracking and Serviceability in Cement-based Materials and Structures (EAC-02), 2017, ISBN: 978-2-35158-197-1, e-ISBN: 978-2-35158-198-8; *Eds. Dimitrios Aggelis and Stéphanie Staquet*

PRO 121: SynerCrete18, Interdisciplinary Approaches for Cement-based Materials and Structural Concrete: Synergizing Expertise and Bridging Scales of Space and Time, (2018), ISBN: 978-2-35158-202-2, e-ISBN: 978-2-35158-203-9; *Eds. Miguel Azenha, Dirk Schlicke, Farid Benboudjema, Agnieszka Knoppik*

RILEM Reports (REP)

Report 19: Considerations for Use in Managing the Aging of Nuclear Power Plant Concrete Structures (ISBN: 2-912143-07-1); *Ed. D. J. Naus*

Report 20: Engineering and Transport Properties of the Interfacial Transition Zone in Cementitious Composites (ISBN: 2-912143-08-X); *Eds. M. G. Alexander, G. Arliguie, G. Ballivy, A. Bentur and J. Marchand*

Report 21: Durability of Building Sealants (ISBN: 2-912143-12-8); *Ed. A. T. Wolf*

Report 22: Sustainable Raw Materials—Construction and Demolition Waste (ISBN: 2-912143-17-9); *Eds. C. F. Hendriks and H. S. Pietersen*

Report 23: Self-Compacting Concrete state-of-the-art report (ISBN: 2-912143-23-3); *Eds. Å. Skarendahl and Ö. Petersson*

Report 24: Workability and Rheology of Fresh Concrete: Compendium of Tests (ISBN: 2-912143-32-2); *Eds. P. J. M. Bartos, M. Sonebi and A. K. Tamimi*

Report 25: Early Age Cracking in Cementitious Systems (ISBN: 2-912143-33-0); *Ed. A. Bentur*

Report 26: Towards Sustainable Roofing (Joint Committee CIB/RILEM) (CD 07) (e-ISBN 978-2-912143-65-5); *Eds. Thomas W. Hutchinson and Keith Roberts*

Report 27: Condition Assessment of Roofs (Joint Committee CIB/RILEM) (CD 08) (e-ISBN 978-2-912143-66-2); *Ed. CIB W 83/RILEM TC166-RMS*

Report 28: Final report of RILEM TC 167-COM 'Characterisation of Old Mortars with Respect to Their Repair (ISBN: 978-2-912143-56-3); *Eds. C. Groot, G. Ashall and J. Hughes*

Report 29: Pavement Performance Prediction and Evaluation (PPPE): Interlaboratory Tests (e-ISBN: 2-912143-68-3); *Eds. M. Partl and H. Piber*

Report 30: Final Report of RILEM TC 198-URM 'Use of Recycled Materials' (ISBN: 2-912143-82-9; e-ISBN: 2-912143-69-1); *Eds. Ch. F. Hendriks, G. M. T. Janssen and E. Vázquez*

Report 31: Final Report of RILEM TC 185-ATC 'Advanced testing of cement-based materials during setting and hardening' (ISBN: 2-912143-81-0; e-ISBN: 2-912143-70-5); *Eds. H. W. Reinhardt and C. U. Grosse*

Report 32: Probabilistic Assessment of Existing Structures. A JCSS publication (ISBN 2-912143-24-1); *Ed. D. Diamantidis*

Report 33: State-of-the-Art Report of RILEM Technical Committee TC 184-IFE 'Industrial Floors' (ISBN 2-35158-006-0); *Ed. P. Seidler*

Report 34: Report of RILEM Technical Committee TC 147-FMB 'Fracture mechanics applications to anchorage and bond' Tension of Reinforced Concrete Prisms—Round Robin Analysis and Tests on Bond (e-ISBN 2-912143-91-8); *Eds. L. Elfgren and K. Noghabai*

Report 35: Final Report of RILEM Technical Committee TC 188-CSC 'Casting of Self Compacting Concrete' (ISBN 2-35158-001-X; e-ISBN: 2-912143-98-5); *Eds. Å. Skarendahl and P. Billberg*

Report 36: State-of-the-Art Report of RILEM Technical Committee TC 201-TRC 'Textile Reinforced Concrete' (ISBN 2-912143-99-3); *Ed. W. Brameshuber*

Report 37: State-of-the-Art Report of RILEM Technical Committee TC 192-ECM 'Environment-conscious construction materials and systems' (ISBN: 978-2-35158-053-0); *Eds. N. Kashino, D. Van Gemert and K. Imamoto*

Report 38: State-of-the-Art Report of RILEM Technical Committee TC 205-DSC 'Durability of Self-Compacting Concrete' (ISBN: 978-2-35158-048-6); *Eds. G. De Schutter and K. Audenaert*

Report 39: Final Report of RILEM Technical Committee TC 187-SOC 'Experimental determination of the stress-crack opening curve for concrete in tension' (ISBN 978-2-35158-049-3); *Ed. J. Planas*

Report 40: State-of-the-Art Report of RILEM Technical Committee TC 189-NEC 'Non-Destructive Evaluation of the Penetrability and Thickness of the Concrete Cover' (ISBN 978-2-35158-054-7); *Eds. R. Torrent and L. Fernández Luco*

Report 41: State-of-the-Art Report of RILEM Technical Committee TC 196-ICC 'Internal Curing of Concrete' (ISBN 978-2-35158-009-7); *Eds. K. Kovler and O. M. Jensen*

Report 42: 'Acoustic Emission and Related Non-destructive Evaluation Techniques for Crack Detection and Damage Evaluation in Concrete'—Final Report of RILEM Technical Committee 212-ACD (e-ISBN: 978-2-35158-100-1); *Ed. M. Ohtsu*

Report 45: Repair Mortars for Historic Masonry—State-of-the-Art Report of RILEM Technical Committee TC 203-RHM (e-ISBN: 978-2-35158-163-6); *Eds. Paul Maurenbrecher and Caspar Groot*

Report 46: *S*urface delamination of concrete industrial floors and other durability related aspects guide—Report of RILEM Technical Committee TC 268-SIF (e-ISBN: 978-2-35158-201-5); *Ed. Valerie Pollet*

Terminology, Symbols and Acronyms

Terminology

Cement Chemist Notation (CCN)

The Cement chemist notation (CCN) is used throughout this STAR. The following tables give the main symbols of the CCN.

Oxides

C Calcium oxide—Lime (CaO)
S Silicon dioxide—Silica (SiO_2)
A Aluminium oxide—Alumina (Al_2O_3)
F Iron oxide (Fe_2O_3)
T Titanium dioxide (TiO_2)
M Magnesium oxide—Periclase (MgO)
K Potassium oxide (K_2O)
N Sodium oxide (Na_2O)
H Water (H_2O)
$\bar{S}$ Sulphur trioxide (SO_3)

Main Phases of Non-hydrated Portland Cement

C_3S Tricalcium silicate—Alite ($3CaO.SiO_2$)
C_2S Dicalcium silicate—Belite ($2CaO.SiO_2$)
C_3A Tricalcium aluminate—Aluminate ($3\ CaO.Al_2O_3$)
C_4AF Tetracalcium alumino ferrite—Ferrite ($4\ CaO.Al_2O_3.Fe_2O_3$)
$C\bar{S}H_2$ Gypsum ($CaSO_4.2H_2O$)

Main Compounds of Hydrated Cement Pastes

C–S–H Calcium silicate hydrate (undefined stoichiometry)
CH Calcium dioxide; Portlandite ($Ca(OH)_2$)

AFt	Ettringite ($C_6A\bar{S}_3H_{32}$)
AFm	Monosulfoaluminate ($3C_4A\bar{S}H_{12}$)

Symbols

A	Chemical affinity; area
b_H	Biot coefficient
B_1, B_2	Coefficients for affinity hydration model
B_i	Sole porosity distribution parameter
Blaine	Specific surface area of cement
C	Specific heat capacity; content of cementitious material
C_h	Concrete moisture capacity
CTE	Coefficient of thermal expansion
CTD	Coefficient of thermal dilation
D	Damage variable
$\mathbf{D}$	Diffusion tensor
D_t	Thermal diffusivity
dS_c	Capillary surface area
e	Emissivity of concrete
E	Young's modulus
E_a	Activation energy
$\mathbf{f}$	Vector of applied forces per unit volume
f	Weight fraction of cementitious material
f_c	Compressive strength
f_{cc}	Biaxial compressive strength
f_t	Tensile strength
f_y	Yield strength of reinforcement
FA	Content of fly ash
g	Gravitational acceleration
g_f	Fracture energy of an element
G	Gibbs free energy
G_f	Fracture energy
H	Total enthalpy
h	Relative humidity; heat exchange coefficient
h_v	Evaporation enthalpy of water
I	Moment of inertia of area of concrete cross section
$\mathbf{I}$	Second-order unit tensor
I_{cr}	Cracking index
J	Diffusion flux
$\mathbf{k}$	Intrinsic permeability
K_R	Structural shape restraint coefficient
K_F	Foundation restraint coefficient
l	Characteristic length
m	Mass fraction

M	Molar mass
M_R	Bending moment
N_R	Axial force
p	Pressure
P_f	Probability of failure
$Q(t)$	Cumulative heat released up to a certain time t
$q(t)$	Heat rate at time t
$r_{\min}$	Minimum pore radius
R	Universal gas constant; thermal resistance
R_N	External restraint coefficient for the degree of axial deformation restraint
R_M	External restraint coefficient for the degree of flexural deformation restraint
R_0	Plane-section restraint coefficient
R_i	Internal restraint factor
s_r	Crack spacing
S	Saturation degree
$Slag$	Content of slag
t'	Age where load/stress is applied
t	Time; superficial tension at the gas–liquid interface
t_e	Equivalent age
t_w	Interlayer thickness
T^{ad}	Adiabatic temperature
T_{∞}^{ad}	Adiabatic temperature at the end of the test
T	Temperature
T_{ref}	Constant reference temperature
u	Displacement
υ_f	Fluid kinematic viscosity
V	Volume
V_{ef}	Volume of the finite element
w/b	Water-to-binder ratio
w/c	Water-to-cement ratio
w	Crack width; moisture content by mass
w_s	Water source
w_n	Non-evaporable water flux density
W	Water content
W_p	Weight of powder materials per unit paste volume
z	Content of supplementary cementitious materials
α	Degree of hydration
β_h	Humidity transfer coefficient
γ	Safety factor; contact angle between liquid phase and solid matrix
γ_c	Weight of concrete
δ_{ij}	Kroenecker delta
δ_p	Water vapour permeability
ε	Total strain

ε_0	Thermal–shrinkage strain distribution curve
ε_{au}	Autogenous strain
ε_{bc}	Basic creep strain
ε_{chem}	Chemical strain
ε_{cm}	Mean tensile strain of concrete
ε_{cr}	Creep strain
ε_{ctu}	Strain capacity
$\varepsilon_{d,sh}$	Drying shrinkage strain
ε_e	Elastic strain
ε_f	Fracture strain
$\varepsilon_{\text{free}}$	Free strain in a given measuring point
$\varepsilon_{\text{meas}}$	Recorded strain in a given measuring point
ε_{int}	Restrained strain due to internal restraint
ε_M	Mechanical strain
ε_p	Plastic strain
ε_{sh}	Shrinkage strain
ε_{sm}	Mean tensile strain of reinforcement
ε_T	Thermal strain
ε_{ttc}	Transient thermal creep strain
λ	Thermal conductivity
μ	Dynamic viscosity
v	Poisson's ratio; wind speed
ϕ	Porosity
φ	Creep coefficient
ρ	Density
ρ_{eff}	Reinforcement ratio
σ	Stress (apparent); surface tension of water
$\tilde{\sigma}$	Effective stress
τ_{sm}	Bond stress between reinforcement and concrete
χ	Curvature of the meniscus.
ψ	Relaxation function

Acronyms

ACI	American Concrete Institute
AR	Alkali resistant
CIRIA	Construction Industry Research and Information Association
CPM	Compensation plane method
ECP	European Concrete Platform
EDF	Électricité de France
ETS	Emission Trading System
EU	European Union
FA	Fly ash
FBG	Fibre Bragg grating

FCC	Fibre cementitious composite
FDOT	Florida Department of Transportation
FEA	Finite element analysis
FIB	Fédération Internationale du Béton (International Federation for Structural Concrete)
FOSM	First-order second-moment method
FRP	Fibre-reinforced polymer
GGBS	Ground-granulated blast-furnace slag
hcp	Hydrated cement paste
HCWA	High calcium wood ash
HDPE	High-density polyethylene
HPC	High-performance concrete
ICOLD	International Commission on Large Dams
ITZ	Interfacial transition zone
JCI	Japan Concrete Institute
JSCE	Japan Society of Civil Engineers
LCA	Life-cycle analysis
LN	Liquid nitrogen
MK	Metakaolin
NA	Natural aggregates
NAC	Natural aggregate concrete
NTC	Negative temperature coefficient (thermistors)
OC	Conventional concrete
OPC	Ordinary Portland cement
PAN	Polyacrylonitrile
PC	Portland cement
PCM	Phase change materials
PE	Polyethylene
PP	Polypropylene
PSD	Particle size distribution
PVA	Polyvinyl Alcohol
QCS	Qatar Construction Specifications
RA	Recycled aggregates
RAC	Recycled aggregate Concrete
RCPT	Rapid chloride permeability
REV	Representative elementary volume
RHA	Rice husk ash
RILEM	International Union of Laboratories and Experts in Construction Materials, Systems and Structures (from the name in French Réunion Internationale des Laboratoires et Experts des Matériaux, systèmes de construction et ouvrage)
RRT	Resistance temperature detector
SCBA	Sugar-cane bagasse ash
SCM	Supplementary cementitious materials
SF	Silica fume

UC	Unit cell
VeRCoRs	Vérification réaliste du confinement des réacteurs (Realistic verification of reactor sealing), a research project from Électricité de France
Voxel	Volume element
WFD	Waste Framework Directive
XPS	Extruded polystyrene

Contents

Chapter 1
Introduction

Eduardo M. R. Fairbairn and Miguel Azenha

Abstract This chapter provides an introduction to the State of the Art Report (STAR) produced by RILEM Technical Committee 254-CMS 'Thermal Cracking of Massive Concrete Structures'. Several recent developments related to the old problem of understanding/predicting stresses originated from the evolution of the hydration of the concrete are at the origin of the creation of this technical committee. Having identified that there was a lack in the organization of up-to-date scientific and technological knowledge about cracking induced by hydration heat effects, it was decided to establish this STAR. It aims to provide both practitioners and scientists with a deep integrated overview of consolidated knowledge, together with recent developments on this subject.

1.1 General Introductory Remarks

Massive concrete structures are structures for which the effects of hydration of the cementitious materials at the early ages, such as heat generation and autogenous shrinkage, can lead to cracking. Considering the percolation threshold as the very moment when concrete becomes a solid, early-age concrete can be defined as the period after this threshold when the properties of the material are rapidly changing under the influence of hydration.

Thermal cracking of massive concrete structures is an important phenomenon, which is mostly originated and induced by matters related to the hydration reaction of the cementitious binder present in the concrete mixture.

As the hydration reaction is exothermic, and the thermal conductivity of concrete is relatively low, it normally endures temperature rises that have special relevance in massive concrete structures. Two types of relevant thermal gradients can be

E. M. R. Fairbairn (✉)
Federal University of Rio de Janeiro, Rio de Janeiro, Brazil
e-mail: eduardo@coc.ufrj.br

M. Azenha
ISISE, University of Minho, Guimarães, Portugal

© RILEM 2019

E. M. R. Fairbairn and M. Azenha (eds.), *Thermal Cracking of Massive Concrete Structures*, RILEM State-of-the-Art Reports 27,
https://doi.org/10.1007/978-3-319-76617-1_1

identified in mass concrete: (i) one is relative to time, i.e. a given point of the structure has its temperature varying throughout time; (ii) another is a spatial gradient that corresponds to the temperature difference, at a given instant, between two different points of the structure. Taking into account the thermal dilation of concrete, and structural restraints to free deformations, both the above-mentioned gradients can be responsible for the generation and evolution of strains and stresses in concrete elements. If such strains/stresses reach a certain limit, undesirable thermal cracks can occur.

Furthermore, since there is volume unbalance between reactants and products of reaction, autogenous shrinkage also imposes additional strains to concrete that may cause the cracking tendency to increase.

The heat generation and consequent temperature rise of the concrete bulk are very important, not only because it can generate thermal gradients in space and in time, but also because deleterious phenomena such as the Delayed Ettringite Formation (DEF) have been proved to be associated with the existence of thermal fields at the early ages that reach temperatures of the order of 65 °C. The set of aforementioned matters adequately back the claim that the temperature rise due to hydration is a very important issue in what concerns the durability of the structure.

In the past, cracking risks at the early ages were commonly faced in large structures in which hydration heat dissipation is normally slow, and therefore, high temperature rises were observed (quasi-adiabatic conditions). The types of concretes used in such types of structures had relatively high w/c ratios and therefore did not endure significant additional strains caused by autogenous shrinkage.

With the advent of high-performance concretes, cracking at the early ages is no longer a peculiarity of massive structures. Higher contents of cementitious materials associated with lower w/c ratios result, respectively, in higher heat of hydration and microstructures with finer pores, thus potentiating greater amplitudes of thermal gradients and autogenous shrinkage. In this way, in the present STAR, the term ‘massive concrete’ is used in a broad sense, comprising all types of concrete elements for which the effects of cement hydration can lead to thermal cracking risks.

In practice, it happens that several massive concrete structures such as hydroelectric and nuclear power plants, thick foundations, bridge pier columns and caps, thick walls, and tetrapods breakwaters may experience cracking induced by the hydration reaction (see Fig. 1.1).

Some examples can be taken from the literature. One very significant case was reported by Betioli et al. (1997) and concerns the Itaipú hydroelectric power plant. Itaipú, built in 1975, is the second largest power plant in the world for installed capacity (14,000 MW) and the first one for annual generation (2.3×10^9 MWh) (see Fig. 1.2).

During the construction of the buttress dam, thermal cracks have been observed, most of them vertical in the bulk of the block, and a few were located in the head of the buttress (see Fig. 1.3).

At that time, the analyses indicated that such cracking was induced by the heat of hydration observed in the field, which was considerably higher than the one assumed during the design of the dam (Rosso and Piazentin 1997). It was also

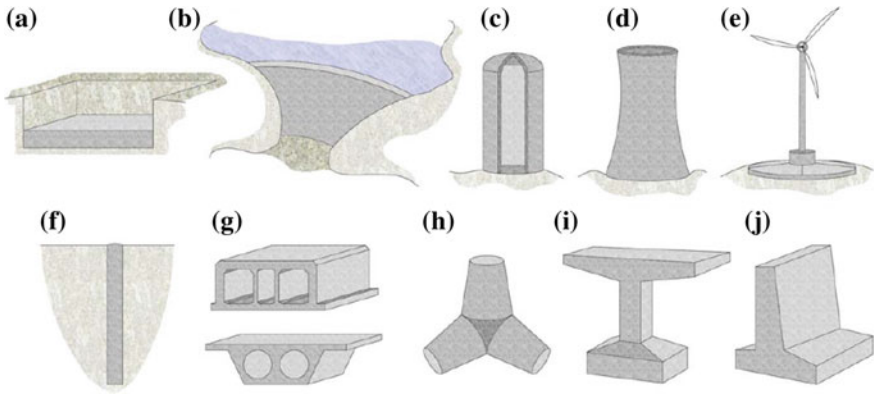

Fig. 1.1 Examples of concrete structures that can benefit from thermal simulation: **a** ground slabs; **b** concrete dams; **c** silos/containment structures; **d** cooling towers; **e** wind turbine foundations; **f** piles; **g** precast segments (top: immersed tunnel, bottom: bridge deck); **h** tetrapods units; **i** bridge piers; and **j** retaining walls. (From Sifkas et al. 2017)

found that the models used to simulate the early-age behaviour of massive concrete were very simplified and did not take into account stress concentrations induced by the geometry. Besides limiting the placing temperature of the concrete to 7 °C, several additional measures have been undertaken such as (i) introducing a contraction joint parallel to the upstream face; (ii) changing the concrete mix design, reducing the heat of hydration and Young´s modulus for the five first lifts above the foundation; (iii) changing the height of the first three lifts from 0.7 m, 1.5 m, 1.75 m to 0.75 m, 0.75 m, 1.00 m, respectively; (iv) introducing additional reinforcement in some regions.

The existing cracks were injected with epoxy resin, and the correspondent structures have been surveyed by an intense monitoring programme. After several years of observation, it was verified that the behaviour of the cracked blocks was similar to that of the sound blocks, showing that the measures taken were sufficient to ensure the stability and safety of the dam.

Another example of cracking in massive concrete has been reported by Funahashi and Kuperman (2010) in the spillway of a small hydropower plant (see Fig. 1.4). In this case, the cracks developed in the 35 m × 15 m × 7.5 m spillway block were found to have been caused by heat of hydration-induced effects.

The analysis carried out by the authors aimed to prove that the cracks were caused by the thermal gradients originated by the heat of hydration of the cementitious material. The authors did not have detailed information about the thermo-chemical-mechanical properties of the materials, such as adiabatic temperature rise, a fact that is still relatively common in dams with lower concrete volume. However, a three-dimensional finite element analysis was performed, using estimated values based on information from materials similar to those used in the construction. This analysis considered the construction of the lifts C1 to C5 built

(a) General view of the concrete dam

(b) View of the intake

Fig. 1.2 Itaipú hydroelectric power plant. (Photographs by E. M. R. Fairbairn)

every 3 days with a placing temperature of 32 °C. The construction scheme and the finite element mesh are shown in Fig. 1.5.

Temperatures of about 61 °C were computed by the thermal analysis, and stress calculations indicated the appearance of principal tensile stresses that reached the tensile strength in the regions where the cracks were actually observed in the field. The authors concluded that the cracks could be avoided by changing the concrete mix design by reducing the cement content and consequently the heat of hydration,

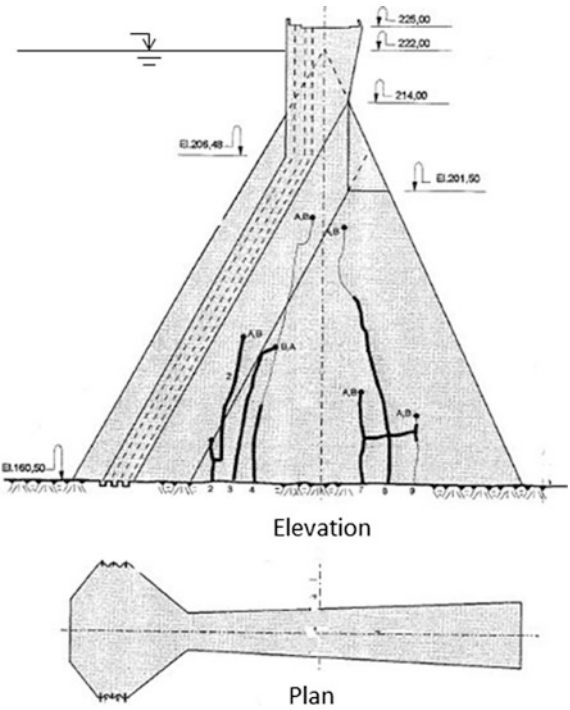

Fig. 1.3 Vertical cracks in the buttress of Itaipú Dam. (Adapted from Betioli et al 1997)

Fig. 1.4 Spillway of small hydropower plant and thermal cracking (Funahashi and Kuperman 2010)

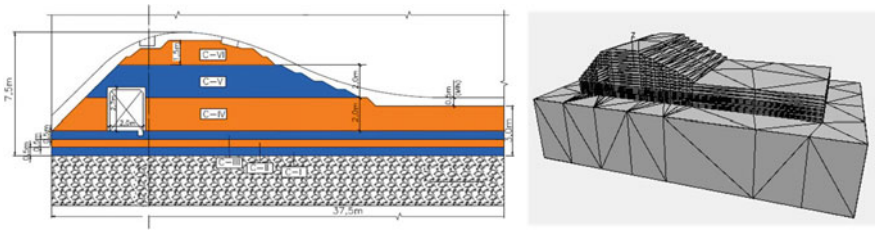

Fig. 1.5 Construction scheme and finite element mesh (Funahashi and Kuperman 2010)

and reducing the placing temperature of concrete. The authors remarked that the amount of cement could have been reduced even further if the concrete strength was not limited by minimum values at 28 days according to standards. If standards had allowed minimum compressive strength to be verified at later ages (e.g. 90 days), significant reductions of cement consumption might have been attained.

Therefore, the construction phase and the period that follows it should be accurately analysed. If cracking tendency is detected, many actions can be adopted to minimize early-age stresses, such as slowing the construction speed allowing higher heat dispersion; reducing the placement temperature of concrete; decreasing the concrete temperature by circulating water or air on pipes embedded in the bulk (post-cooling systems); and choosing a material composition that gives lower rates of hydration.

Due to the high costs and safety requirements of building and infrastructure works, thermal cracking of early-age concrete has been a concern of the engineering community since the first applications of massive concrete. The evolution of knowledge on the subject has led to the development of theories that consider the hydration reaction as exothermic and thermally activated. This means that, concerning the specific heat generation, there is a second-order effect, since the rate of heat generated by a unit mass, at a given point and at a given time, depends on the extension of the reaction, which varies as a function of the thermal history at the considered point. Also, the properties of the material and phenomena related to hydration evolution, such as strength, Young's modulus, autogenous shrinkage and creep, will vary according to the extension of the reaction.

Such theories led to sophisticated numerical models that, together with the evolution of computer hardware and software, allowed the development of very complex simulation models that successively get closer to reality both in terms of geometry and phenomenological models considered (Fairbairn et al 2012) (see Fig. 1.6).

The evolution of theory and modelling has naturally been accompanied by advances in the experimental methods related to the early-age phenomena in massive concrete. As an example, the mechanical analyses should initiate at the very moment when concrete can bear structurally relevant stresses, and the properties of the material must be known since then. Therefore, it has been worthy to

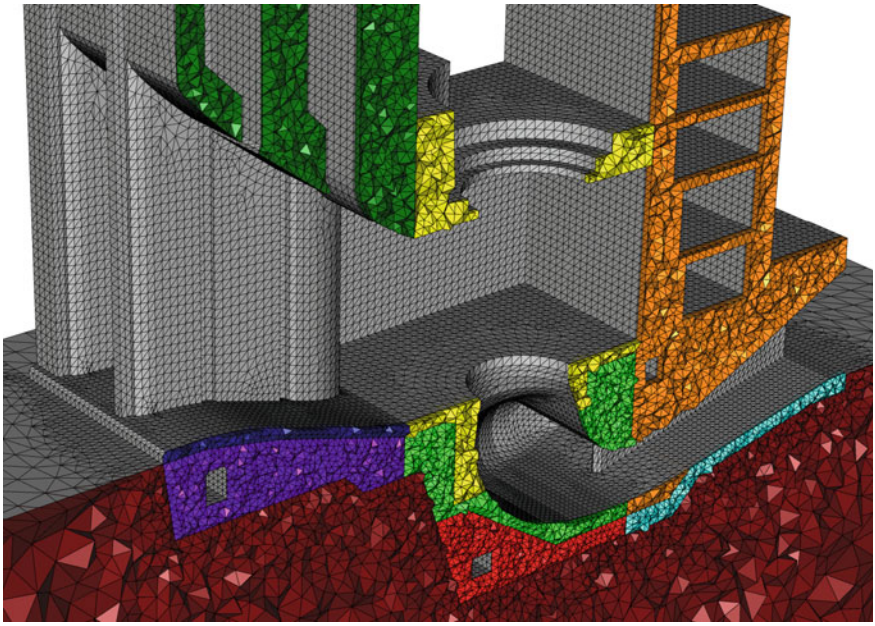

Fig. 1.6 Finite element mesh for the 3D model for the phased construction of the powerhouse of Tocoma Dam (approximately 5,000,000 elements)

develop new experimental methodologies that are dedicated to determine thermo-mechanical characteristics since the very early ages. Examples of such experimental tests can be seen in Boulay et al (2010) from where Fig. 1.7 was taken, representing a sophisticated apparatus for characterizing the early development of E-modulus of concrete (BTJASPE method).

Several other scientific and technological advances have been verified in other areas related to the control of concrete cracking in massive structures. In such context, it is relevant to mention: new techniques for temperature control and on-site monitoring; new advanced models for mix design and methods that allow the mixture proportioning optimization using computer codes; new requirements of sustainability introducing the use of a new category of green materials and practices that can contribute to the reduction of greenhouse gases emissions.

All these recent developments related to the old problem of the stresses originated from the evolution of the hydration of the concrete are at the origin of the creation of RILEM Technical Committee 254-CMS 'Thermal Cracking of Massive Concrete Structures'. Having identified that there was a lack in the systematization of recent scientific and technological knowledge about thermal cracking of massive concrete, RILEM has created this committee to provide both practitioners and scientists with a deep overview of the recent developments on this subject.

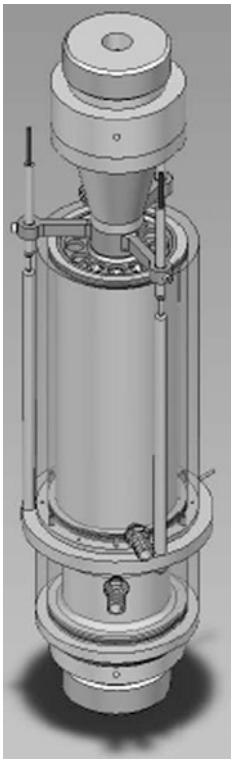

Fig. 1.7 Sketch of BTJASPE, a new testing device was designed at IFSTTAR aimed at measuring automatically the evolution of the stiffness of a concrete cylinder in compression at early age (since the setting time up to a couple of days) (Boulay et al 2012)

1.2 Presentation of STAR

The development of the hydration reaction of the cementitious materials is the main phenomenon that commands the thermal cracking of concrete at early ages. This physical–chemical phenomenon is presented in Chap. 2. In this chapter, the velocity of the reaction, and consequently the heat generation, are shown to be strongly influenced by thermal activation. This can be regarded as a second-order effect since the heat released by the reaction activates the reaction itself.

One of the main problems to simulate the evolution of the temperature fields and to compute stresses and strains is that several thermo-chemo-mechanical properties are dependent on the state of the hydration. Chapter 2 presents a survey of the main chemical properties in relation to the evolution of the hydration, the affinity and the activation energy. It also presents several types of models that are dedicated to predict the hydration evolution of a given concrete mix, and forecast the heat release and the consequent temperature rise.

In order to better understand and predict the thermal behaviour of massive concrete structures, a sound fundamental knowledge is necessary in regard to the thermal properties of concrete. The thermal properties described in Chap. 3 are

grouped into properties responsible for transport of heat and corresponding temperature changes (effective thermal conductivity and heat capacity, heat exchange parameters), and thermal expansion coefficient, which allows relating the temperature changes to thermal deformations of concrete. A special focus is given to the most recent developments that have been recently achieved in the characterization of all thermal properties at very early ages.

Chapter 4 gives a description of the main mechanical properties that will govern cracking due to the restraint of imposed deformations in massive concrete structures, taking into account both thermal and shrinkage deformations. This chapter is structured into three main subsections:

- 'Quasi-static behaviour of concrete and steel/concrete bond', covering a review on relevant properties such as compressive strength, tensile strength, Young's modulus, Poisson's ratio, strain capacity, fracture energy, steel/concrete bond and the effects of multi-axial stress states.
- 'Shrinkage', covering topics of plastic shrinkage, autogenous shrinkage and drying shrinkage.
- 'Creep', focusing on the viscoelastic features that concrete endures since its early ages, with particular focus on the elevated creep strains that are expectable in the very first hours after setting. Discussions are held about the underlying creep mechanisms, with emphasis on the distinction between basic and drying creep. A final note is given to the effects of temperature on creep behaviour, normally referred as 'transient thermal creep'.

In Chap. 5, the nature, the physical–chemical properties and the contents of the concrete constituents are discussed for the understanding of the way of making an optimized concrete mix-design for massive structures, where the temperature rise must be minimized. The chapter initially makes a systematic review of materials and their relation to crack avoidance, covering aggregates, water, admixtures, cement, supplementary cementitious materials and fibres. It also incorporates two specific sections of practical issues related to mix design for conventional mass concrete and mix design for roller compacted concrete.

Temperature rises are definitely one of the most important driving forces for thermal cracking in mass concrete, together with the restraint to deformation. Therefore, amongst the most widespread measures that can be taken to minimize the risks of thermal cracking, the temperature control of concrete since its production and throughout construction is of utmost significance. Following Chap. 5 where temperature control of concrete by limiting the heat generation potential of the binder in the mixture has already addressed, Chap. 6 is dedicated to a review on measures that can be taken to control concrete temperature at several levels, mainly focused on limiting temperature rises due to cement hydration heat: (i) pre-cooling of mix constituents; (ii) cooling concrete during the mixing procedures; (iii) controlling temperature during transport and placement; (iv) selecting and designing suitable surface measures for temperature control; (v) scheduling of construction stages; (vi) post-cooling with water or air (Fig. 1.8).

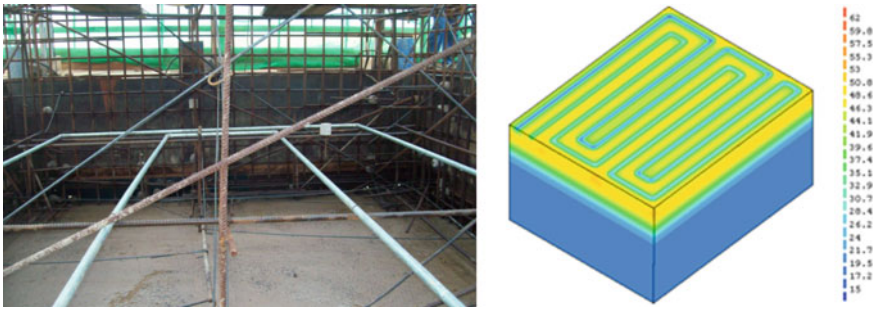

(a) In the field (photograph of W. P. Andrade) **(b)** Numerical simulation (T in ºC)

Fig. 1.8 Temperatures are reduced by post-cooling system

Chapter 7 deals with the problem of modelling the behaviour of massive concrete structures. In the last decades, the developments in the field of computational mechanics were very significant, so nowadays several numerical techniques are available for this goal, depending not only on the scale level considered but also on which phenomena/processes are taken into account. In this chapter, we limit the description to approaches/models that can be implemented using the Finite Element Method, which is still the most used numerical technique worldwide in the context of simulations for structural concrete. The chapter presents two distinct groups of models: in the first, some 'deterministic' models are described starting from the simplest ones, which consider simply the thermo-chemo-mechanical behaviour of the material, to more sophisticated approaches which consider also the fluid phases; i.e. they consider concrete as a multiphase porous material. In this first part, a specific section is dedicated to mechanical behaviour modelling considering damage of the material, plasticity, etc.

The second group of the models taken into consideration have a 'stochastic' nature. These models are formulated specifically for giving detailed information about crack spacing and opening in concrete structures in service life conditions.

Chapter 8 is focused on the cracking risk at early ages. After general considerations about cracking, the cracking risk prediction is discussed. Two main ways to assess this risk are considered: through an evaluation of the tensile stresses and through an evaluation of the strains. Finally, the evaluation of crack opening at early ages and the reinforcement design in regulations are presented. Special focus is given to a broad coverage of the aspects by which each regulation is specifically distinctive.

Chapter 9 is devoted to display the benefits of on-site monitoring of mass concrete. An important outcome is the assurance that adequate conditions for the evolution of the desired concrete properties were maintained. This refers mainly to the monitoring of the concrete temperature in the phases of warming and cooling down, but it is also possible to obtain mechanical parameters for further considerations. Besides, the measurement results provide important data to verify the

calculation models and assumptions applied for crack assessment of the considered structure as well as to improve these calculation models and assumptions for future projects. Next to very general information on monitoring affairs, this chapter presents different levels of measures with regard to the purpose and expected insights of each level, available instruments and least requirements on practical application as well as possibilities for result verification. This focuses on both established techniques with comprehensive experiences in many applications, as well as comparably new techniques available on the market.

Finally, the presented techniques and approaches were exemplified on three different application examples with regard to different measurement systems as well as types of structures.

The last chapter, Chap. 10, addresses potential alternatives for base raw materials as well as potential solutions for sustainability in mass concrete. Issues like material selection and environment, material properties and mix design, durability, carbon footprint and life-cycle analysis (LCA) of mass concretes are reviewed. The focus is put on recycling. Beside the use of conventional SCMs, non-conventional biomass pozzolans, based on combustion of renewable source of energy, like woody ashes, sugarcane bagasse ash and rice husk ash are covered. The synergic use of several mineral SCMs as a partial substituent of Portland cement is addressed. Furthermore, reuse of aggregates from construction and demolition waste, as well as natural fibre alternatives to steel and synthetic reinforcements is discussed in detail.

Material selections and the consequence of it on the properties that affect the mix design and material properties, specifically related to durability, are summarized.

An introduction on life-cycle assessment (LCA) is given with its pros and cons, followed by its review on different mass concrete mixtures, separately addressing LCA of binders, aggregates, concretes and reinforced concrete structures with placement technologies. Limitations and further research directions are highlighted.

References

Boulay, C., Crespini, M., Delsaute, B., & Staquet, S. (2012). Monitoring of the creep and the relaxation behavior of concrete since setting time, part 1: compression. In: *SSCS 2012*, *Aix-en-Provence*.

Betioli, I., Sá, S. N., & Fiorini, A. S. (1997). Criteria for control and survey of the cracking of the buttress dam of Itaipu. In *XXII Simpósio Nacional de Grandes Barragens, CDBD (Brazilian Committee on Dams) São Paulo, in Portuguese*.

Fairbairn, E. M. R., Silvoso, M. M., Koenders, E. A. B., Ribeiro, F. L. B., & Toledo-Filho, R. D. (2012). Thermo-chemo-mechanical cracking assessment for early-age mass concrete structures. *Concrete International, 34,* 30–35.

Funahashi, E. I. Jr., & Kuperman, S. C. (2010). Study of thermal cracking in the spillway of a small hydropower plant. In *VII Simpósio sobre Pequenas e Médias Centrais Hidrelétricas, CBDB (Brazilian Committee on Dams)*, *São Paulo, in Portuguese*.

Rosso, J. A., & Piasentin, C. (1997). Studies on the cracking of the buttress dam of Itaipu. In *XXII Simpósio Nacional de Grandes Barragens, CBDB (Brazilian Committee on Dams) São Paulo, in Portuguese*.

Sfikas, I., Ingham, J., & Baber, J. (2017). *Using finite-element analysis to assess the thermal behaviour of concrete structures, The Concrete Society: Concrete Magazine, February, 50–52*.

Chapter 2
Hydration and Heat Development

Laurie Lacarrière, Agnieszka Knoppik, Wilson Ricardo Leal da Silva, Tulio Honorio, Vit Šmilauer, Shingo Asamoto and Eduardo M. R. Fairbairn

Abstract The driving process of early-age cracking in massive element is the hydration and reactions of the binder that composes the concrete. Indeed, these reactions are highly exothermic and lead to heat generation in the structure. It is thus of primary importance to be able to characterise and predict the heat generation of binders in order to assess the early-age cracking risk of a concrete structure. The first section of this chapter presents the main physical phenomena responsible for this heat generation. It must be kept in mind that only the general phenomena of hydration are presented. The aim is only to present how the chemical reactions lead to heat development and water consumption (which are of interest for our purpose). The reactivity of binder is a large scientific subject, and more detailed review can be

L. Lacarrière (✉)
LMDC (Laboratoire Matériaux et Durabilité des Constructions),
Université de Toulouse, UPS, INSA, 135, avenue de Rangueil,
31 077 Toulouse Cedex 04, France
e-mail: laurie.lacarriere@insa-toulouse.fr

A. Knoppik
Faculty of Civil Engineering, Department of Structural Engineering,
Silesian University of Technology, Akademicka 5, 44-100 Gliwice, Poland

W. R. Leal da Silva
Danish Technological Institute, Gregersensvej 4, 2630 Taastrup, Denmark

T. Honorio
CEA, DEN, DPC, SECR, Laboratoire d'Etude du Comportement des Bétons et des Argiles,
91191 Gif-sur-Yvette, France

V. Šmilauer
Faculty of Civil Engineering, Czech Technical University, Thákurova 7,
166 29 Prague 6, Czech Republic

S. Asamoto
Department of Civil and Environmental Engineering, Saitama University, Saitama 338-8570,
Japan

E. M. R. Fairbairn
Department of Civil Engineering, COPPE/Universidade Federal do Rio de Janeiro,
P.O. Box 68506, 21945-970 Rio de Janeiro, RJ, Brazil

© RILEM 2019

E. M. R. Fairbairn and M. Azenha (eds.), *Thermal Cracking of Massive Concrete Structures*, RILEM State-of-the-Art Reports 27,
https://doi.org/10.1007/978-3-319-76617-1_2

found on this subject in other RILEM TCs (for instance, 238-SCM). The second (and main) section of the chapter is dedicated to the modelling of the heat development induced by cement hydration. Several approaches are presented: affinity-based models (that can be easily implemented in finite element codes), microstructural models (even if they are less adapted to the massive structure modelling), data mining, or inverse analysis.

2.1 Physical Phenomena

2.1.1 Hydration Reactions

Portland cement is mainly composed of clinker. In mineralogical composition of clinker, we distinguish four main phases which are reported in Table 2.1 and several minor species such as sulphate, alkaline, and free lime. When crushed, clinker is also mixed with gypsum in order to stabilise hydration process (C_3A reactions).

Several researchers (mainly reported in Lea 1970) proposed stoichiometric equations to represent the reactions of the four phases of clinker when mixed with water (when reactions are stabilised):

$$\begin{aligned} &C_3S + (3 - C/S + H/S)H \rightarrow C_{C/S}S\,H_{H/S} + (3 - C/S)CH \\ &C_2S + (2 - C/S + H/S)H \rightarrow C_{C/S}S\,H_{H/S} + (2 - C/S)CH \\ &C_3A + C_4AF + C_2\bar{S} + xH \rightarrow C_4(A+F)\bar{S}H_{12} + \left| \begin{matrix} C_3(A,F)H_6 \\ C_6(A,F)\bar{S}_3H_{32} \end{matrix} \right. \end{aligned} \tag{2.1}$$

In these simplified stoichiometry equations, Fe is supposed to be able to substitute to Al in every aluminium phases. The choice between formations of ettringite or tri-calcium aluminate phase (after the first stages of the reactions) depends on the initial quantity of oxides.

It is noted in these equations that the consumption of water will be dependent on the stoichiometry of the formed hydrates. The stoichiometry of crystallised hydrates such as portlandite and aluminates is well known and fixed. But stoichiometry of C–S–H is more complex to define. Indeed, calcium to silicate (C/S) depends on the chemical composition of the interstitial solution (Taylor 1990). But for Portland cement this ratio is usually between 1.5 and 2 (Richardson 2000). The water fixed

Table 2.1 Clinker constituents' proportions

Notation	% in clinker (g/g)
C_3S	60–65
C_2S	10–20
C_3A	4–12
C_4AF	4–10

in the C–S–H created by clinker hydration can be evaluated using, for instance, (Brouwers 2004) work according to the C/S ratio (H/S = C/S + 0.8).

As explained in the introduction, to limit the temperature increase in massive concrete structures, binders composed of clinker and mineral additions are more and more used (CEM II to CEM V or other blended cements).

When fly ash or silica fume are used, the reactions are due to silica and alumina content in the mineral additions. As this kind of mineral addition does not contain calcium, the additions are going to react with the calcium hydroxide produced by the reaction of clinker. Silica reacts with the portlandite to create C–S–H with lower C/S ratio than the one produced by the reaction of C_3S and C_2S (around 1.1/1.2 (Justness 1992). Alumina reacts with the portlandite to create aluminates (C–A–H hydrates) which are similar to the one created by clinker additions. Alumina can also react with portlandite and silica to create hydrogarnet (Dinelsa et al. 2014) or be incorporated in C–S–H layers (Richardson 1999). For this kind of additions (pozzolanic ones), the reaction kinetics are thus delayed.

When slag is used, due to its composition similar to the clinker's one (C, S, $\bar{S}$, A), the reactions can be less delayed because it can react by itself if it is activated. When it is mixed with clinker, it creates C–S–H, aluminates hydrates but also hydrotalcite due to the presence of magnesium. Due to the high content of alumina, a part of them are going to be fixed in the C–S–H layers (Richardson 1999). The specificity of slag is that the C–S–H created by its reaction can be enriched by calcium taken from the portlandite produced by clinker hydration (Kolani et al. 2012).

A more exhaustive review concerning the reaction of cement and mineral additions can be found in the works of RILEM TC 238-SCM in which numerous mineral additions are studied in terms of reactivity, stoichiometry of created hydrates, and thermodynamic modelling of the behaviour of these specific blended cements.

2.1.2 Definitions

The degree of hydration, α, is a variable commonly used to quantify the extent of the reactions between cementitious materials with water. It is defined as the ratio between the quantity of hydrated, $m(t)$, and the initial quantity, m_i, of the cementitious material (Schutter and Taerwe 1995; Lackner and Mang 2004; Schindler and Folliard 2005). For pure cement, it can be expressed as a ratio between the water bound in the process of cement hydration, $w(t)$, and the total amount of water needed for complete hydration, w_{tot}. Assuming that the quantity of the hydrated products is proportional to the relative heat of hydration, the degree of hydration can also be expressed as a ratio between the cumulative heat, $Q(t)$, released up to a certain time, t, and the theoretical heat that can be released by a complete hydration

of the binder, Q_{pot}, expected at the completion of the cement hydration reaction (Breugel 1991):

$$\alpha = \frac{Q(t)}{Q_{pot}} \tag{2.2}$$

The degree of hydration is a function of time and increases from 0% at the beginning of hydration to 100% when hydration is fully completed. In reality, not the whole cementitious material hydrates and 100% degree of hydration may never be reached (Schindler and Folliard 2005). The final value of the degree of hydration depends on many factors, mainly the water availability (water-to-binder ratio) and size of grains. For blended cements with an addition of supplementary cementitious materials (fly ash or slag), hydration reactions are related to cement but also the mineral additions. Several degrees of hydration could thus be used (one for cement and one for each addition) (Schutter and Taerwe 1995; Waller 1999; Buffo-Lacarrière et al. 2007; Kolani et al. 2012). The use of several variables allows reproducing the interaction between anhydrous phases (especially the dependence of addition reactions to the portlandite content).

A unique variable could also be used, and the degree of hydration can, for instance, be replaced with the degree of heat development, α_Q, which depends on the test conditions (Schutter and Taerwe 1995):

$$\alpha_Q = \frac{Q(t)}{Q_{max}} \tag{2.3}$$

where Q_{max} is the total heat of hydration corresponding to the end of the hydration tests.

For Portland cement, hydration can stop if there is no space available for new hydrates (no empty porosity), or if there is no sufficient water to hydrate residual anhydrous grains. One of the main parameters to quantify the ultimate degree of hydration that could be reached seems to be the water content (and thus the initial *w/c* ratio in autogenous conditions). Waller (1999) reports several studies on old CEM I (stored in autogenous conditions) which present the final degree of hydration of these pastes according to the initial *w/c* ratio (Fig. 2.1).

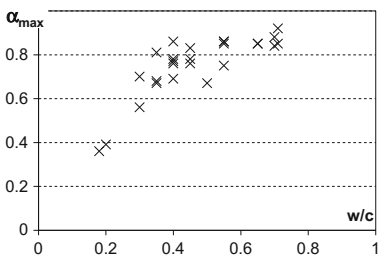

Fig. 2.1 Maximal degree of hydration for Portland cement pastes with different *w/c* ratios (experimental data reported in Waller 1999)

Table 2.2 Models for final degree of hydration for Portland cement

	α_{max}
Powers and Brownyard (1947)	$\min\left(1; \frac{w/c}{0.42}\right)$
Mills (1966)	$\frac{1.031 w/c}{0.194 + w/c}$
Schindler and Folliard (2005)	$\frac{1.031 \mathrm{W/C}}{0.194 + \mathrm{W/C}} + 0.3\mathrm{Slag} + 0.5\mathrm{FA}$

Based on the results presented in Fig. 2.1, several authors proposed empirical equations to determine "a priori" the final degree of hydration that could be reached for Portland cements (Table 2.2).

In these models, *w/c* is the water-to-cement ratio and Slag and FA are the content of slag and fly ash in the blended cement.

2.1.3 Heat Generation

Cement hydration is a highly exothermic process and large amounts of heat are produced during hydration, which leads to a significant temperature increase inside massive concrete structures. Cement hydration initiates as soon as cement grains come into contact with water, and heat is being released from that very moment until the hydration is complete.

According to the development of heat of hydration (see Fig. 2.2), in the first stage after mixing (stage 1) a rapid increase of heat production is observed, which is connected with wetting of cement grains. Then, the rate of heat production decelerates almost completely (stage 2); this phase is called a dormant period (Neville 1997).

Setting of concrete initiates a few (1–3) hours after mixing. When setting begins, the rate of heat of hydration development increases (stage 3), but with a slower rate than in the stage 1; C–S–H gel is produced in that phase. As soon as the setting of the concrete mix is terminated, concrete can be regarded as a solid material, characterised by elastic, plastic, and also strong viscous properties; this phase is called early-age concrete. Then, the hydration process decelerates again (stage 4). In

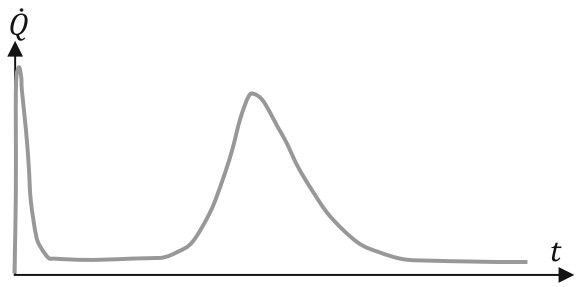

Fig. 2.2 Process of cement hydration (adapted from Neville 1997)

some types of cements, second peak in the rate of heat of hydration development might be observed (Neville 1997).

Heat of hydration rate decelerates as less and less cement is available for hydration until the hydration is complete (stage 5). At this stage, the concrete strength reaches its final, steady value; such concrete is referred to as hardened (or mature) concrete.

In reality, the hydration process is never complete—heat production and strength gain continue in mature concrete—and 100% hydration can never be achieved. That is why two measures are used to represent the total amount of heat of hydration: practical and theoretical.

Some selected values of the enthalpies of reaction involving main clinker components are shown in Table 2.3 (Gartner et al. 2002). These enthalpies are the energetic differences between the energies involved in breaking chemical bonds and in formation of new bonds. Such values could be used to determine the heat evolution at any given time provided the mineralogical composition of the system. However, since some hydration processes together with the intermediary steps are not fully known, determination of the exact enthalpies is not trivial. The proposal of using averaged heat of hydration by clinker mineral seems then more justified for early-age analysis. A comprehensive collection of enthalpies of formation of different hydration products and clinker minerals is presented in Lothenbach et al. (2008).

In the theoretical approach, it is assumed that the whole available cement hydrates and the total heat of hydration can be calculated from the enthalpies of dissolution–precipitation reactions. A simplified estimation can be done using an empirical formulation expressed according to the chemical composition. For pure Portland cement, the total amount of heat Q_{pot} is proposed to be calculated after (Bogue 1947):

Table 2.3 Total amount of heat of hydration produced by cement components Q_{pot} [J/g]

	Lea (1970)	Bogue (1947)	Schindler and Folliard (2005)	Waller (1999)	Kishi and Maekawa (1994)	Bensted (1981)	Neville (1997)
C_3S	517	500					568
C_2S	262	260					259
C_3A	1144	866					836
C_4AF	418	420					125
Free CaO		1186					
SO_3		642					
MgO		850					
Slag			461		461	355–440	
FA			1800	560 ± 50			
SF				660 ± 30			

$$Q_{\text{pot}} = 500 \cdot C_3S + 260 \cdot C_2S + 866 \cdot C_3A + 420 \cdot C_4AF + 642 \cdot SO_3 + 1186 \cdot FreeCaO + 850 \cdot MgO \quad (2.4)$$

while the total heat Q'_{pot} accounting for supplementary cementitious materials in blended cements (fly ash—FA, and slag—Slag) is proposed by Schindler and Folliard (2005) to be calculated as follows (where CaO_{FA} is the proportion of CaO in fly ash, and FA and Slag are the proportion of fly ash and slag in the binder):

$$Q'_{\text{pot}} = Q_{\text{pot}} + 1800 \cdot FA \cdot CaO_{FA} + 461 \cdot Slag \quad (2.5)$$

It should be noted that the values of the heat of hydration of the subsequent compounds obtained by other authors differ (see Table 2.3). The difference is most substantial in assessment of the heat of hydration of C_3A and C_4AF—the components in which hydration depends on the amount of gypsum in the mix (Kiernożycki 2003).

In the practical approach, for Portland cement, the total amount of heat of hydration relates to the potential heat of hydration (Q_{pot}) which is understood as the total released heat of a finely ground binder after roughly 3 years under saturated conditions. Hence, it is assumed that hydration of cement is almost complete after 3 years ($\alpha(3y) = 1$) and suggested values of Q_{pot} are listed in Table 2.4.

In practical applications, when heat of hydration development of specific cement needs to be known, the measurements are usually made for much shorter period. The final value of the total heat of hydration relates in this case not to the end of hydration but merely to the end of the laboratory test. In that sense, it does not refer to the degree of hydration but the degree of heat development (see 2.1.2). The total amount of heat $Q_{\max}$ relates to $\alpha = \alpha_{max}$ and to the $\alpha_Q = 1$ and is conventionally determined for the age of 28 days, although for blended cements longer periods are advised (56 or even 91 days).

The factors that influence the total heat of hydration and its development are:

1. **Mineral composition of clinker**. It can be noticed in Bogue's formulation that the total amount of heat is proportional to the amount of the cement constituents.
2. **Type and amount of hydraulic and pozzolanic additions** (fly ash, slag, etc.). Total heat of hydration is generally the highest in pure Portland cements and decreases with the increase in mineral addition in composed binders. A retarding effect can be observed in blended cements: initial rate of hydration is lower, and

Table 2.4 Potential heats of hydration for various cement types

Cement type	Q_{pot} (J/g of binder)
Ordinary Portland cement	375–525
Blast furnace slag cement	355–440
Sulphate-resistant cement	350–440
Pozzolanic cement	315–420
High alumina cement	545–585

the exothermic peak occurs later in these cements. Also, the values of the peak rates decrease with the amount of additions. This effect is especially visible in cements with fly ash additions and becomes more pronounced as the amount of fly ash increases (Klemczak and Batog 2015). Limestone fillers accelerate hydration at the first stages; an impact on the heat flow is observed (Berodier and Scrivener 2014). Flocculation of the cement particle may also affect the kinetics (Scherer et al. 2012).

3. **Specific surface and particle size distribution**. The size of cement particles has an important influence on the hydration rate. The smallest grains (up to 3 μm) hydrate in the first hours after coming into contact with water; larger grains (with diameter between 15 and 20 μm) hydrate completely in 14 days. The coarsest grains never undergo complete hydration.
4. **Water-to-binder ratio**. Higher w/b ratio gives higher degree of hydration, which is classically admitted (as shown in Sect. 2.2.2). But for Portland cement and before 15 h slight hydration, kinetic increase is observed for decreasing w/b ratios (Mounanga 2003). It can be explained by the fact that at very early age the hydration kinetic is driven by the supersaturation of the solution (Taylor 1990) and this supersaturation will be increased by a lower w/b ratio.
5. **Temperature**. Increased hardening temperature accelerates hydration, which is a thermally activated process. The influence of the elevated temperature is especially visible in blended cements which are characterised with higher activation energies (Klemczak and Batog 2015).

2.2 Modelling of Hydration Development

2.2.1 Thermal Activation of Hydration Development

As any chemical reaction, the reactions of hydration of cement and mineral additions are highly influenced by the temperature of the paste. This sensitivity to temperature can be modelled using an Arrhenius law (Arrhenius 1915). The activation energy in the Arrhenius formulation depends on the type and class of cement, water-to-binder ratio, additions, and admixtures.

The activation energy can be experimentally determined using mechanical or physical tests performed at different curing temperatures (compressive strength measurements, isothermal calorimetry, etc.). It can also be estimated using formulas based on the chemical composition of the cement. Jonasson (1994) introduced the following formula for the activation energy:

$$E_a = E_{a,\mathrm{ref}} \left(\frac{30}{T + 10} \right)^a \tag{2.6}$$

where T is the temperature, $E_{a,\mathrm{ref}}$ and a are material parameters dependent on the cement. Schindler (2004) proposed the formula to calculate the activation energy based on the chemical cement composition:

$$E_a = 22100 \cdot f_E \cdot C_3A^{0.30} \cdot C_4AF^{0.25} \cdot Blaine \tag{2.7}$$

where C_3A, C_4AF, FA, $Slag$, and CaO are weight ratio of C_3A, C_4AF, fly ash, slag, and CaO content in fly ash with respect to the total cement content, $Blaine$ is specific surface area of cement [m^2/kg], and f_E is the activation energy modification to account for supplementary cementitious materials which is defined as:

$$f_E = 1 - 1.05 \cdot FA\left(1 - \frac{CaO_{FA}}{0.40}\right) + 0.40 \cdot Slag \tag{2.8}$$

A similar empirical approach was proposed by Poole (2007) and Riding et al. (2011) who additionally took into consideration the effect of admixtures in the concrete mix. Simplified proposals given by standards and recommendations can be used. Hansen and Pedersen (1977) suggest the value of E_a/R = 4030 K^{-1} close to the value proposed in RILEM TC 119-TCE (1997) when the temperature of concrete T is at least 20 °C. Model Code (2010) suggests that the value of E_a/R = 3670 K^{-1} can be assumed. Nevertheless, it must be emphasised that these values are determined for concrete mixes with predominant Portland cement content; for concrete mixes in which large amounts of pozzolans are used as a replacement of cement, activation energy should be determined experimentally because the proposed values are no longer valid (Model Code 2010).

For mineral additions, the data available in the literature are not that many. Some values are proposed for the most usual additions (fly ash, slag, and silica fume) (see Table 2.5), but the results can be rather scattered for fly ash, for instance.

2.2.2 Methods Based on the Equivalent Time

There are some direct proposals for definition of the heat of hydration development, $Q(t)$, functions in which the effect of temperature is taken into account by introduction of the equivalent age instead of real age of concrete. This modelling approach can be used not only for pure Portland cements but also for blended

Table 2.5 Activation energy for and addition (E_a/R [1/K])

	Kishi and Maekawa (1994)	Biernacki et al. (2001)	Waller (1999)	Fernandez-Jimenez and Puertas (1997)	Kolani et al. (2012)
Slag				6000–7100	7000
FA	5000	4400–8300	12,000		
SF			11,400		

cements—single value of the activation energy is determined for a composed binder, and coefficients are calibrated based on the test data obtained for the binder.

The concept of the equivalent age as an alternative to the maturity was introduced by Rastrup (1954). The equivalent age was defined as the time during which the concrete would have to be cured at a constant reference temperature, T_{ref}, to achieve the same maturity as the concrete undergoing the actual curing history, that can be assessed, as proposed by Hansen and Pedersen (1977), using the Arrhenius law:

$$t_e(t,T) = \int_0^t \exp\left[-\frac{E_a}{R}\left(\frac{1}{T}-\frac{1}{T_{\text{ref}}}\right)\right]\mathrm{d}t \tag{2.9}$$

It has been proven by many authors, e.g. (Chengju 1989) or (Ballim and Graham 2003), that the formulation governing the Arrhenius law gives the most accurate results.

Using the equivalent age approach, a number of functions were proposed to depict development of heat of hydration in time. Schutter and Vuylsteke (2004) proposed a rational function of the equivalent age:

$$Q(t,T) = Q_{\text{pot}}\frac{a_1 t_e}{1+a_1 t_e} \tag{2.10}$$

A similar function was proposed by Faria et al. (2006):

$$Q(t,T) = Q_{\text{pot}}\frac{t_e^{a_3}}{a_2^{a_3}+t_e^{a_3}} \tag{2.11}$$

Alternatively, the exponentially decaying function of time was adopted by many authors (Wang and Dilger 1994; Yuan and Wan 2002; Bofang 2003; Xiang et al. 2005; JCI Guideline 2008). The following formulations for the heat of hydration development were proposed:

$$Q(t,T) = Q_{\text{pot}}\exp[-a_4 t_e] \tag{2.12}$$

$$Q(t,T) = Q_{\text{pot}}(1-\exp[-a_5 t_e]) \tag{2.13}$$

A refined exponential function was also adopted by Knoppik-Wróbel (2012) and Klemczak and Knoppik-Wróbel (2014) after Reinhard et al. (1982):

$$Q(t,T) = Q_{\text{pot}}\exp\left[-a_6 t_e^{a_7}\right] \tag{2.14}$$

In these equations, coefficients a_i depend on the type of cement (see Table 2.6).

In case of blended cement, Schindler (2002, 2004), Schindler and Folliard (2005) proposed to adapt this exponential formulation to take account of the global effect of slag and fly ash. They proposed the following heat of hydration rate function:

Table 2.6 Coefficients in equations of heat evolution for different binders proposed by Knoppik-Wróbel (2012)

	CEM I 42.5R	CEM II/B-S 42.5R	CEM III/A 42.5N	CEM V/A 32.5R
Q_{pot} [J/g]	508	466	469	396
a_6	513.62	480.51	475.70	473.72
a_7	−0.17	−0.115	−0.093	−0.091

$$q(t,T) = Q_{\text{pot}}\left(\frac{\tau}{t_e}\right)^{\beta}\left(\frac{\beta}{t_e}\right)\alpha(t_e)\exp\left[\frac{E_a}{R}\left(\frac{1}{T_{\text{ref}}}-\frac{1}{T}\right)\right] \tag{2.15}$$

where $\alpha(t_e)$ is the degree of hydration at equivalent age given as:

$$\alpha(t_e) = \alpha_{\max}\exp\left[-\left(\frac{\tau}{t_e}\right)^{\beta}\right] \tag{2.16}$$

τ and β are hydration time and shape parameters:

$$\tau = 66.78 \cdot C_3A^{-0.145} \cdot C_3S^{-0.401} \cdot Blaine^{-0.804} \cdot SO_3^{-0.758} \cdot \exp[2.187 \cdot Slag + 9.50 \cdot FA \cdot CaO_{FA}] \tag{2.17}$$

$$\beta = 181.4 \cdot C_3A^{0.146} \cdot C_3S^{0.227} \cdot Blaine^{-0.535} \cdot \mathrm{SO}_3^{0.558} \cdot \exp[-0.647 \cdot Slag] \tag{2.18}$$

$\alpha_{\max}$ is the maximal degree of hydration (in autogenous conditions) which can be evaluated, for instance, using one of the equations presented in Table 2.2, and E_a is the activation energy, calculated according to Eq. 2.7.

2.2.3 *Models Based on Affinity Laws*

2.2.3.1 Thermodynamical Definition of Chemical Affinity

The affinity is the driving force of the chemical reaction and is defined in terms of Gibbs free energy G and the degree of hydration (α) by:

$$A = -\left[\frac{G}{\alpha}\right]_{P,T} \tag{2.19}$$

at constant pressure and temperature. The affinity is negative in spontaneous reactions.

Ulm and Coussy (1998) state that at early-age the affinity may be interpreted as the difference between the chemical potentials of the free water and the water combined in the solid phase, and is the driving force of the micro-diffusion process.

In its dimensionless form, the affinity is related to the overall degree of hydration by Ulm and Coussy (1998). It is usually expressed according to a reference temperature (used for fitting of the affinity law), and the hydration kinetic can be defined as follows:

$$\dot{\alpha} = \tilde{A}_{T_{ref}}(\alpha) \cdot \exp\left(-\frac{Ea}{R}\left(\frac{1}{T} - \frac{1}{T_{ref}}\right)\right) \tag{2.20}$$

2.2.3.2 Experimental Determination of Affinity

With the previously mentioned definition, the affinity is an intrinsic material parameter, which is independent of the boundary conditions or any particular field within the domain of consideration. However, the tracking of the evolution of both α and affinity can only be indirectly assessed through the effects entailed by hydration. In this sense, Ulm and Coussy (1998) propose to experimentally obtain the affinity by means of adiabatic calorimetry and isothermal strength evolution experiments.

The affinity can be obtained experimentally from adiabatic calorimetric tests and isothermal strength evolution (Ulm and Coussy 1998). An example of the affinity law obtained for a Portland cement is given by Cervera et al. (2002) and plotted in Fig. 2.3.

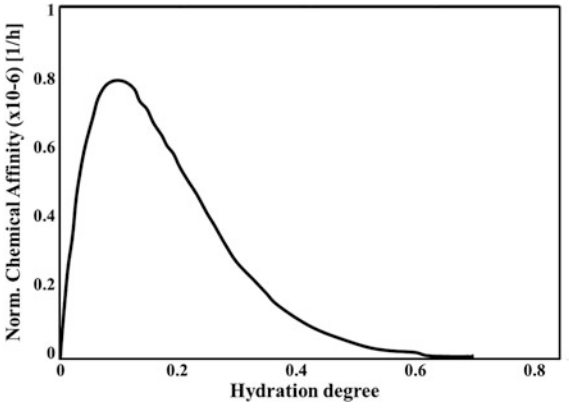

Fig. 2.3 Illustration of an affinity law (Cervera et al. 2002)

2.2.3.3 Empirical Laws for "Commercial Cements" Based on Bogue Composition

The affinity hydration models provide a framework for accommodating all stages of cement hydration. It considers hydrating cement under isothermal temperature of 25 °C. The rate of hydration can be expressed by the chemical affinity $\tilde{A}_{25}(\alpha)$ [time^{-1}]. The affinity for isothermal temperature can be obtained experimentally; in particular, the isothermal calorimetry measures a heat flow $q(t)$, which gives the heat of hydration $Q(t)$ after integration.

Cervera et al. (1999) proposed an analytical form of the normalised affinity, which was further refined by Gawin et al. (2006). A slightly modified formulation is proposed:

$$\tilde{A}_{T_{ref}}(\alpha) = B_1\left(\frac{B_2}{\alpha_{\max}} + \alpha\right)(\alpha_{\max} - \alpha)\exp\left(-\eta\frac{\alpha}{\alpha_{\max}}\right) \tag{2.21}$$

where B_1 and B_2 are coefficients to be adjusted and represent the micro-diffusion of free water through formed hydrates ($\alpha_{\max}$ could be defined using one of the empirical formulas proposed in Table 2.2 in autogenous conditions).

Using some hypotheses concerning the activation energy, the affinity hydration from Eq. 2.21 performs well on all OPC-derived binders. Supposing that the ultimate degree of hydration is the same for all binders (which is not the case for composed binders or if the w/c ratio is modified as explained in Sect. 2.1.3), Leal da Silva et al. (2015) present the determination of fitting parameters of this affinity law for several cements for a reference temperature equal to 25 °C. Table 2.7 summarises some of the parameters of the affinity model, whereas Fig. 2.4 illustrates them graphically against the isothermal calorimetry data or CEMHYD3D simulation (Bentz 1997).

Alternatively to experimental fitting, empirical laws for microstructure-property link have been proposed by Leal da Silva and Šmilauer (2015) for OPC only; in particular, the parameters B_1, B_2, and η in Eq. 2.21 can be estimated by:

Table 2.7 Parameters of affinity hydration model for different cement types for T_{ref} = 25 °C (Leal da Silva et al. 2015)

Binder	B_1 [s^{-1}]	B_2 [–]	$\alpha_{\max}$ [–]	η [–]	Q_{pot} [J/g]	E_a [J/mol]
CEM I 32.5R	1.62E–04	1.40E–03	0.85	7.0	471.15	38,300
CEM I 42.5R Mokra	3.52E–04	8.00E–06	0.85	7.4	495.33	38,300
CEM I 42.5R Prachovice	2.71E–04	7.00E–04	0.85	6.7	509.21	38,300
CEM I 52.5R ENCI	3.79E–04	6.00E–05	0.85	5.8	517.60	38,300
CEM I 52.5	3.79E–04	6.00E–05	0.85	5.8	505.90	38,300
CEM II/A-S 42.5 Mokra	2.71E–04	7.00E–04	0.85	6.7	420.00	38,300
CEM II/B-S 32.5R Mokra	2.71E–04	7.00E–04	0.85	6.7	370.00	38,300

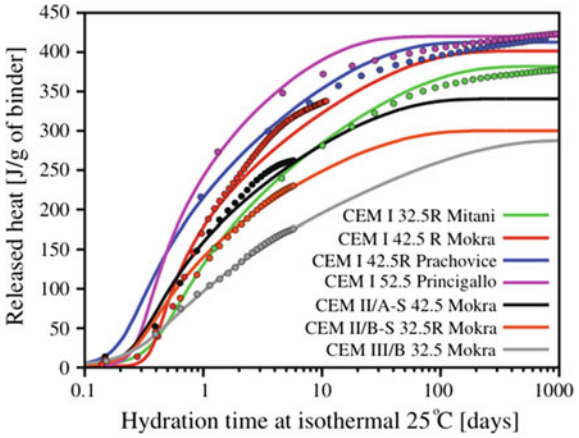

Fig. 2.4 Illustration of affinity hydration model on OPC-based cements (Leal da Silva et al. 2015)

$$B_1 = 0.738 \cdot C_3S^{-0.206} \cdot C_2S^{-0.128} \cdot C_3A^{0.161} \tag{2.22}$$

$$B_2 = (-0.0767 \cdot C_4AF + 0.0184)\frac{B_f}{350 \cdot B_1} \tag{2.23}$$

$$\eta = 10.95 \cdot C_3S + 11.25 \cdot C_2S - 4.10 \cdot C_3A - 0.892 \tag{2.24}$$

where B_f is the cement fineness (m^2/kg) and C_3S, C_2S, C_3A, and C_4AF are the mass percentages of each mineral.

Equations (2.21–2.24) were validated on OPC with different mineral compositions in Leal da Silva and Šmilauer (2015); see an example in Fig. 2.5a. The scatter plot of experimental versus predicted results as well as the corresponding coefficient

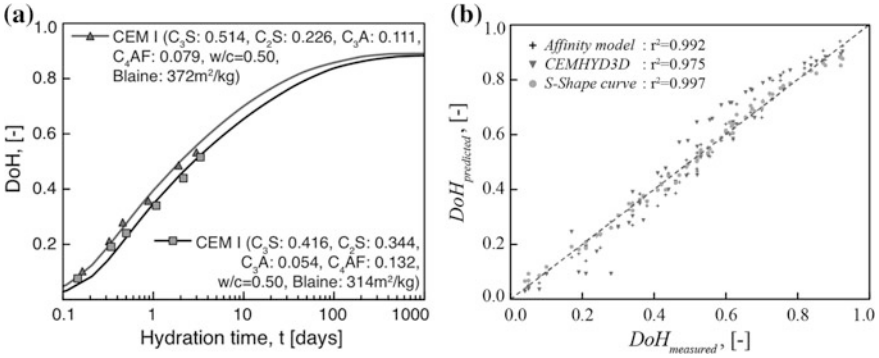

Fig. 2.5 Affinity hydration model: **a** validation based on microstructure-property link from Eq. 2.21 and **b** scatter plot of measured versus predicted α (Leal da Silva and Šmilauer 2015)

of determination (r^2) for the affinity hydration model, CEMHYD3D, and s-shape curve model proposed by Pane and Hansen (2002) are shown in Fig. 2.5b.

2.2.3.4 Effect of Water Content on Affinity

Most of affinity laws available in the literature take account of the effect of initial w/c ratio on the hydration (by the fitted parameters for the kinetic and by a limitation of degree of hydration to a maximal value as explained in Sect. 2.2.2).

When the hydration kinetic laws are solved in the same time than water mass balance equation (see Chap. 7), it is also possible to introduce in the affinity law the dependence on the water content at each calculation time.

Dependence on the internal relative humidity in the affinity law by a unique empirical function was introduced for each kind of cement or binder (Bazant and Najjar 1972):

$$\begin{cases} \tilde{A}(\alpha) = \tilde{A}(\alpha, h = 1) \cdot \beta(h) \\ \beta(h) = \frac{1}{1 + (5 - 5h)^4} \end{cases} \tag{2.25}$$

Oh and Cha (2003) proposed a similar approach, but the function to affect the kinetic according to the water content is based on the pore volume filled by water and consequently depends on the water retention curve (identified for several degrees of hydration using among others the quantity of C–S–H).

Another approach suggests to not distinguish the effect of water content on the maximal degree of hydration and on the kinetic by using a phenomenological kinetic approach able to reproduce both effects without explicit limitation of the maximal degree of hydration. The affinity law proposed is based on the two physical phenomena driving the kinetic of reaction (at constant temperature): chemical activation and water accessibility to anhydrous (Buffo-Lacarrière et al. 2007). In the first stages of hydration, when the concrete can be considered as a diluted medium, reactions are accelerated by supersaturation of interstitial solution. Then, during hydration, reaction kinetics are decreased due to the difficulty of contact between water and anhydrous caused by the progressive formation of hydrated products (Fig. 2.6). As this notion of water accessibility to anhydrous is

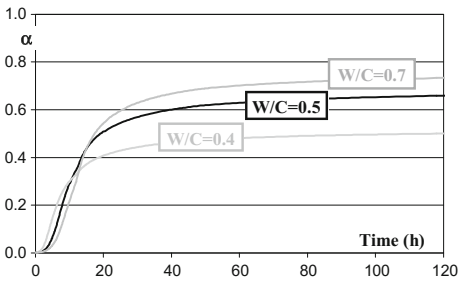

Fig. 2.6 Illustration of the effect of w/c ratio on the hydration development (using Buffo-Lacarrière et al. (2007) model)

linked to numerous physical parameters (porosity structure, water content, hydrate layer thickness, anhydrous content, etc.), the authors chose to simplify its modelling by using a unique variable merging all these parameters (Eq. 2.26).

$$\tilde{A}_{T_{ref}}(\alpha) = K \cdot \frac{\alpha \cdot C_{c0}}{W} \cdot \exp\left(-\frac{1}{n} \cdot \left(\frac{1}{r_k} \cdot \frac{\alpha}{(1-\alpha)} \cdot \frac{R_{Vh/a}}{W \cdot \phi}\right)^n\right) \tag{2.26}$$

where

K is a global kinetic constant; n and r_k are fitting parameters
W is the water content in the paste (m^3/m^3)
ϕ is the porosity of paste (m^3/m^3)
C_{c0} is the initial cement content in paste (m^3/m^3)
$R_{Vh/a}$ represents the volume of hydrates produced by the hydration of 1 m^3 of anhydrous cement (m^3 hydrates/m^3 anhydrous cement reacting). It can be evaluated using stoichiometry calculation and is around 1.83 for Portland cement (Buffo-Lacarrière et al. 2007).

2.2.3.5 Affinity Laws for Reactions of Mineral Additions

The reactions of blended cement can be predicted using a separate variable for Portland cement (or clinker) and mineral additions. In these cases, the degree of hydration of the additions can be predicted using a specific affinity law $\tilde{A}_{T_{ref\,Z}}$.

$$\begin{aligned}\dot{\alpha}_C &= \tilde{A}_{T_{ref\,C}}(\alpha_C, \alpha_Z) \cdot \exp\left(-\frac{Ea_C}{R}\left(\frac{1}{T} - \frac{1}{T_{ref}}\right)\right) \\ \dot{\alpha}_Z &= \tilde{A}_{T_{ref\,Z}}(\alpha_C, \alpha_Z) \cdot \exp\left(-\frac{Ea_Z}{R}\left(\frac{1}{T} - \frac{1}{T_{ref}}\right)\right)\end{aligned} \tag{2.27}$$

where subscript C is for cement and Z for the mineral addition (silica fume, fly ash, slag, etc.)

Empirical Laws for Blended Cements

Waller proposed, for fly ash and silica fume reaction when blended with clinker, the following empirical affinity law with the values specified in Table 2.8 (Waller 1999).

Table 2.8 Parameters of affinity hydration model for pozzolanic additions (Waller 1999)

	n_Z	τ_Z [h]
Silica fume	0.9	250
Fly ash	1	770

$$\tilde{A}_{T_{ref\,Z}}(\alpha_Z) = \frac{n_Z}{\tau_Z} \cdot \alpha_Z^{(1-1/n_Z)}(1-\alpha_Z)^{(1+1/n_Z)} \tag{2.28}$$

In the same spirit, De Schutter proposed affinity law for the reaction kinetic of slag blended with cement (De Schutter 1999).

$$\tilde{A}_{T_{ref\,slag}}(\alpha_s) = \left[\sin\left(\pi \cdot \alpha_{slag}\right)\right]^{a_s} \tag{2.29}$$

These proposed laws are easy to implement but, as the interaction with clinker hydration kinetic, they need an experimental fitting for each substitution rate.

For both pozzolanic additions and slag, the affinity laws defined here are used to evaluate the development of hydration degree of the addition and a classical affinity is used for the development of clinker hydration (two separate degrees of hydration are used as shown in Eq. 2.22).

Phenomenological Coupled Laws for Blended Cements

A phenomenological approach can be adopted to propose an affinity law adapted for blended cement in order to consider the interaction of the reaction of pozzolanic additions with the hydration of clinker. For instance, Buffo-Lacarrière et al. (2007) and Kolani et al. (2012) proposed to introduce a delay function S to introduce the dependence of the reaction of fly ash, silica fume, and slag to the calcium hydroxide content:

$$\tilde{A}_{T_{ref\,z}}(\alpha_z) = K_z \underbrace{\frac{\alpha_c \cdot C_{c0}}{W}}_{g} \cdot \underbrace{\exp\left(-\frac{1}{n_z} \cdot \left(\frac{1}{r_{kz}} \cdot \frac{\sum Hyd_z}{W \cdot \phi \cdot C_{z0}}\right)^{n_z}\right)}_{\pi} \cdot S_z(CH, CaO) \tag{2.30}$$

where

K_z	is a global kinetic constant; n_z and r_{kz} are fitting parameters
C_{c0} and C_{z0}	are the initial content of cement and mineral addition in paste (m^3/m^3)
$\sum Hyd_z$	represent the total volume of hydrates produced by the reaction of mineral addition for the "hydration" degree α_z.

In this affinity law, g is the chemical activation term, π accounts for the water accessibility to anhydrous phases, and S describes the interaction between portlandite and mineral additions. Indeed, the dissolution of slag when blended with clinker is activated by the alkalis released by clinker dissolution in the interstitial solution. In the model, the amount of clinker dissolved during hydration reactions is used as the main indicator of the alkalis available for the activation of slag dissolution. Thus, it is proposed to describe the activation of the dissolution by the expression g in Eq. 2.30, whatever the mineral addition considered.

The hydration of mineral additions is chemically activated by the CH produced by clinker in blended cements. In the case of pozzolanic additions, the kinetics of secondary reactions is linked to the quantity of CH available. In addition to the amount of CH available in blended cements, the hydration reactions of slag are also activated by the calcium content in the anhydrous slag. Thus, the hydration kinetics of slag must be linked to the quantity of CH available and to the quantity of the calcium remaining in the anhydrous slag. To take this chemical activation of mineral additions into account, which also describes the main interaction with clinker, the following expression is used:

$$S_i = \begin{cases} 1 & \text{if } i = \text{clinker} \\ C_{P_{CH}} & \text{if } i = \text{pozzolan} \\ C_{P_{CH}} + C_{P_{CaO}} & \text{if } i = \text{slag} \end{cases} \tag{2.31}$$

where $C_{P_{CH}}$ and $C_{P_{CaO}}$ are, respectively, the volumetric concentration of available CH and the remaining volumetric concentration of CaO from anhydrous slag (available through stoichiometry calculation (Kolani et al. 2012).

2.2.4 Microstructural Models

2.2.4.1 CEMHYD3D

CEMHYD3D is contemporarily one of the most advanced open-source hydration models. Developed at NIST, the CEMHYD3D model is based on observing the development of a two-dimensional cement microstructure under the electron microscope (Bentz 2000). The cement microstructure is split into voxels (abbreviation for volume elements), with a typical size of 1 × 1 × 1 μm. A voxel should be considered as a collector of a specific chemical phase from its neighbourhood, neglecting details below the voxel resolution. The voxel size must be small enough to capture important undergoing processes, i.e. dissolution, transport, diffusion, and nucleation mechanisms. Voxel size is a compromise between computational feasibility and resolution of experimental devices used for microstructure description.

CEMHYD3D operates on a three-dimensional voxelised microstructure, forming the so-called unit cell (UC). Each voxel represents a chemical phase. The rules on how to handle individual voxels are based on cellular automata, which define how voxels dissolve, move, and what happens on their collision. The cellular automata are combined with probabilistic functions that were found effective in the description within the model (Garboczi and Bentz 2001).

The initial three-dimensional UC is reconstructed from digital spherical particles, containing one of four clinker minerals, calcium sulphate's derivatives, silica fume, or other input phases. Autocorrelation functions distribute chemical phases within the particles. The UC size may be arbitrary and limit the maximum cement grain

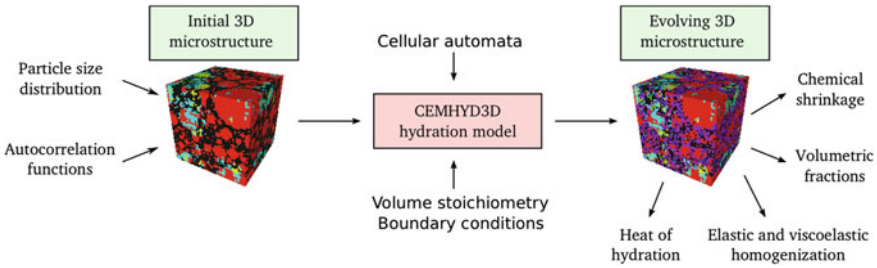

Fig. 2.7 A flowchart of the CEMHYD3D model with possible consecutive outputs

that may be accommodated within. The UC remains periodic during the simulation. A flowchart of the CEMHYD3D model is illustrated in Fig. 2.7.

Due to the CEMHYD3D discrete formulation, several precautions are necessary. The limited resolution implies that very fine cement particles under 1 μm cannot be captured with a correct surface area. The increasing dissolution bias of these fine particles, such as silica fume, can be emulated by assigning a high reactive surface (Bentz 2005). The model is unable to capture the distribution of capillary pores smaller than 1 μm.

Dissolution probabilities play a fundamental role in cement kinetics. In early stages, the kinetics is modelled by adjusting the initial dissolution probabilities of the four clinker minerals. A quadratic dependence on the normalised amount of formed C–S–H is adopted; i.e. the volume of formed C–S–H divided by the volume of the initial cement amount enters the dissolution functions. In case of fine fillers, the dissolution probability is corrected by the fraction of the surface area of the initial binder to the initial cement raised again to the second power (Bentz 2005). The dissolution rates are further scaled by temperature according to Arrhenius equation. The rates assumed for the chemical phases are found in the documentation (Bentz 2005). Numerical simulations revealed that digital resolution plays a significant role in percolation characteristics and in transport issues such as diffusivity or permeability (Garboczi and Bentz 2001). The proper voxel size probably lies between 0.125 and 1 μm/voxel; such value was determined using an assumption of a continuous C–S–H phase and a dissolution rate of larger cement grains (Garboczi and Bentz 2001).

The progress of the reaction front towards a grain is also influenced by the dissolution length, which is fixed here to be one voxel. Refining the voxel size causes an inability of the larger grains to hydrate completely; they are wrapped in the layer of hydration products, and the reaction front remains too shallow. Diffusing species originate from the dissolution and travel in the water-filled porosity. They have to be included in the reaction stoichiometry. The error in the volumetric content disregarding diffusing species is up to a few per cent, especially pronounced in the early hydration stages.

The chemical reactions are modelled on the basis of cellular automata rules, describing the process of dissolution, transport, nucleation, and reaction. Liberated

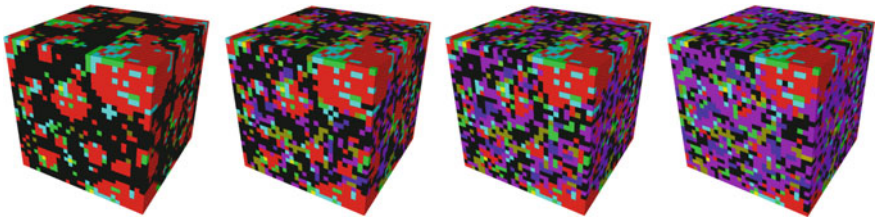

Fig. 2.8 Evolving CEMHYD3D microstructure for w/c = 0.40 and α = 0.00, 0.20, 0.40, 0.60. Black = porosity, red = C_3S, blue = CH, violet = C–S–H

heat is calculated directly from evolving microstructure assigning enthalpy to each chemical reaction (Bentz et al. 1998). For example, the hydration of the most common mineral C_3S of Portland cement yields 517 J/g of dissolved C_3S:

$$C_3S + 5.3H \rightarrow C_{1.7}SH_4 + 1.3CH \tag{2.32}$$

Saturated or sealed curing conditions are considered for microstructure evolution. Sealed conditions lead to a lack of water within a microstructure while stopping all dissolution. Temperature effect on hydration kinetics is determined from Arrhenius equations simultaneously for all implemented reactions. Example of UC 30 × 30 × 30 μm for w/c = 0.4 is showed in Fig. 2.8.

Cellular automata in CEMHYD3D model operate in cycles. Linear mapping to time showed considerable disagreement with experiments (Bentz 2000). Instead, parabolic mapping, based on Knudsen's parabolic dispersion model, was found appropriate under different curing conditions and cement types (Bentz 1995). Knudsen's model (Knudsen 1984) assumes that the diffusion of ions takes the control over the hydration rate and mapping on real time follows

$$t = t_0 + \beta \cdot \text{cycle}^2 \tag{2.33}$$

where the parameter β is usually found in the interval $1 \times 10^{-4} \leq \beta \leq 1.1\ 10^{-3}$ h/cycle^2 (Bentz 1995; Bentz et al. 1999), and t_0 represents extra dormant time. Both parameters contain the influence of admixtures, alkalis, cement impurities, etc. A standard induction period of Portland cement is included directly in the hydration modelling and sets t_0 = 0 h.

The size of UC plays a fundamental role in the calculations (Kanit et al. 2003). For the cement hydration, one has to consider at least the effect of truncated particle size distribution (PSD), cement fineness, and w/c ratio. The maximum accommodated particle diameter must be truncated to approximately half of the representative elementary volume edge to allow finer grain placement (i.e. to maximum diameter 5 μm at 10 × 10 × 10 μm, 25 μm at 50 × 50 × 50 μm, and 50 μm at 100 × 100 × 100 μm). The effect of RVE size is demonstrated in Fig. 2.9, which displays the evolution of degree of hydration. Hydration at 20 °C shows that 10 × 10 × 10 μm proceeds faster due to truncated large particles than a reference

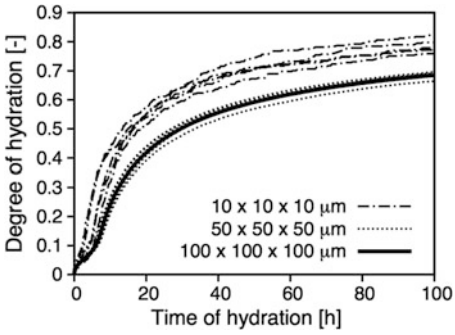

Fig. 2.9 Effect of RVE sizes on degree of hydration with Blaine fineness 250 m^2/kg and w/c = 0.5 (Šmilauer and Krejčí 2009)

at 100 × 100 × 100 µm. The reasonable selection is 50 × 50 × 50 µm for the scatter and computational speed.

Isothermal calorimetry is a standard and conventional procedure to validate hydration models. Liquid cement paste is normally poured inside a vial and inserted into a temperature-stabilised cell. The input parameters of the investigated cements are listed in Table 2.9, Fig. 2.10 then validates the CEMHYD3D model in terms of released heat. For additional details on CEMHYD3D implementation as well as validation results, see (Šmilauer 2014).

2.2.4.2 µic

µic is an open-source modelling platform developed to model the evolution of volume fractions of cement phases and hydration products based on microstructural information. This modelling platform was developed following the earlier model developed by Navi and Pignat (1996). Differently to other microstructural platforms that use as input the hydration kinetics (obtained, for instance, by calorimetry curve), µic uses assumption on the mechanics driving hydration in order to determine the kinetics (Scrivener et al. 2015). In this sense, different kinetics were studied with the platform, e.g. boundary nucleation and growth, space-filling, and diffusion-controlled growth (Bishnoi and Scrivener 2009a). The vectorial approach was employed so information about the position, orientation, and size of individual features is considered independently of their relative sizes, without imposing a resolution limit on the information (Bishnoi and Scrivener 2009b).

The main plug-ins in µic, and their respective functions, are (Bishnoi 2008):

- Particle Proportion Initialisers control the proportions of different materials in particles,
- Reaction Kinetics control reaction rates,
- Reaction Triggers control the activity of reactions,
- Densification Profiles control variation in density of materials,
- Nuclei Generators generate new nuclei for products growing in pores,
- Material Distribution Profiles control redistribution of products over particles,

Table 2.9 Input CEMHYD3D parameters for the validation of experimental data on OPC (Šmilauer 2014)

Paste name	C_3S [wt%]	C_2S [wt%]	C_3A [wt%]	C_4AF [wt%]	Gypsum [vol. %]	Fineness [m^2/kg]	T [°C]	E_a [kJ/mol]	Q_{pot} [J/g_{cem}]	t_0 [h]	β [h/cycle^2]
BAM	54.91	22.39	7.68	7.12	3.31	350	22.0	40.0	481.94	0.0	3.0×10^{-4}
Princigallo et al. (2003)	66.88	11.31	6.16	9.89	5.1	530	20.0	40.0	517.60	4.0	3.0×10^{-4}
Aalborg	66.60	23.80	3.40	0.40	3.6	390	20.0	40.0	448.70	5.0	3.0×10^{-4}
Mokra	64.35	11.81	3.99	11.87	5.0	306	25.0	38.3	495.33	6.0	3.0×10^{-4}

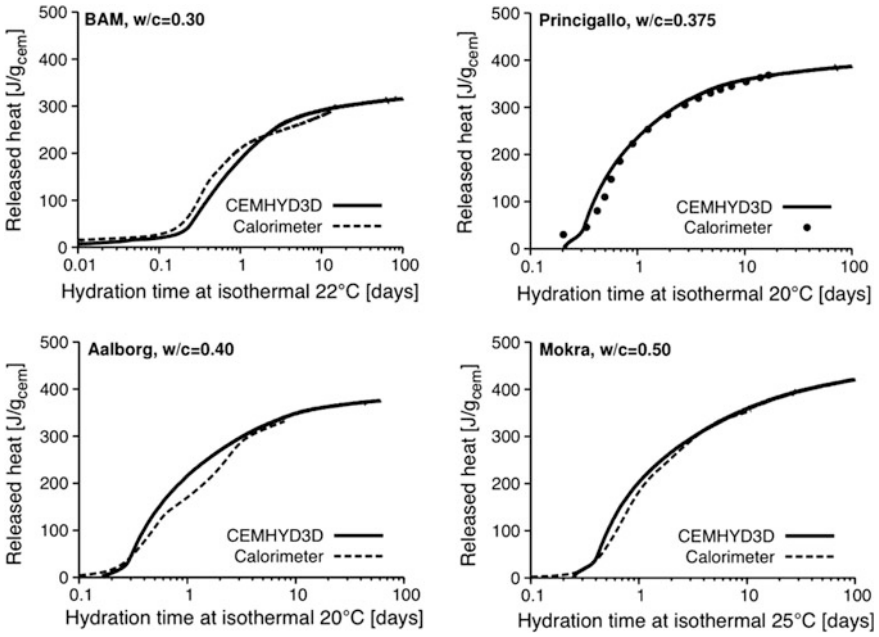

Fig. 2.10 Validation for isothermal calorimetry in terms of released heat (Šmilauer 2014)

- Particle Group Choosers control groups of particles that affect reactions of each other,
- Particle Distribution Profiles control the distribution of available space in particles to different materials, and
- Recalculators can be used to make changes to properties of reactions, etc., before each step of simulation.

μic does not directly account for solution phase chemistry or transport phenomena. The developers propose, though, that additional plug-ins can be devised either to model the overall effect of these phenomena on individual particles. Other possibility is to enable external programs such as HydratiCA (Bullard et al. 2010) or GEMS (Karpov et al. 1997) to provide μic with the necessary thermochemical information.

Simulation on μic uses the definition of the present phases and the stoichiometry of the reactions as input data for the numerical simulations. For instance, in Bishnoi and Scrivener (2009b) the employed stoichiometry of alite hydration assumes no additional entrapped water in C–S–H as in Tennis and Jennis (2000). Different morphologies of phases can be studied as well as the initial particle size distribution and the phase composition of the powders, as defined by the user (Thomas et al. 2011). Simulations on μic with a few million particles are reported to take a few hours on single-processor desktop computers (Thomas et al. 2011).

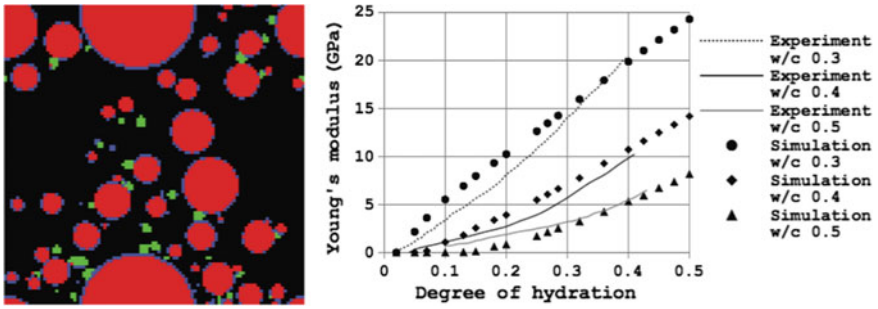

Fig. 2.11 Example of post-processed (with a burning algorithm in order to eliminate artificially connect voxels) microstructure obtained with μic to be used in FEM simulations (left) and estimation of Young's modulus obtained by the combination of μic and FEM (right)

The platform was used to study alite hydration at different stages (Bishnoi and Scrivener 2009a; Kumar et al. 2012).

Combined with FEM simulations, estimations of elastic and viscoelastic properties of cement-based materials were reported (Chamrova 2010; Do 2013) (Fig. 2.11). This combination allowed to study, for example, the effects of flocculation of fines and space-filling in the development of elastic and viscoelastic properties (Chamrova 2010; Do 2013).

2.2.4.3 DuCOM

Durability Models of Concrete (DuCOM) is a thermodynamics-oriented computational framework to simulate various chemo-physical information of ageing cement-based material using a finite element method, which has been developed by Prof. Maekawa and Prof. Ishida's research group at The University of Tokyo. According to DuCOM, hydration reaction of each clinker, pore structure formation, moisture transport/equilibrium, pore humidity, ion transfer, and others is evaluated from the casting to the end of service life. Here, the microstructure development model is summarised below based on their books (Maekawa et al. 1999, 2008).

In the microstructure model, there are three classifications of pores in the concrete: capillary pores, gel pores, and interlayer pores. The capillary pores are located in the large interparticle spaces between the powder particles; they act as free space for the precipitation of hydrated products. The interlayer pores are located between the layer structures of the C–S–H gel grains; the layer thickness is defined as 2.8 Å. The gel pores are defined as the interstitial spaces of gel product or more specifically C–S–H grains, and the intrinsic porosity at room temperature is assumed to be 0.28 based on the research by Powers (1964). The temperature-dependent model of gel porosity is also developed recently Maekawa et al. (2008)

The volume V_s of gel products in a unit volume of the paste can be obtained as:

$$V_s = \frac{\alpha W_p}{1 - \phi_{ch}} \left(\frac{1}{\rho_p} + \frac{\beta}{\rho_w} \right) \tag{2.34}$$

where α is an average degree of hydration, W_p is weight of powder materials per unit paste volume [kg/m^3], ρ_p is density of the powder [kg/m^3], β is the amount of chemically obtained water per unit weight of hydrated powder material [kg/kg], ρ_w is density of chemically obtained water (= 1.25 × 10^3 [kg/m^3]), and ϕ_{ch} is intrinsic porosity of the hydrates that has a temperature dependency.

The porosity of gel and interlayer pores can be calculated as:

$$\phi_l = \frac{t_w s_l \rho_g}{2} V_s, \phi_g = \phi_{ch} V_s - \phi_l \tag{2.35}$$

where ϕ_l and ϕ_g are, respectively, the porosity of interlayer pores and the porosity of the gel product, t_w is interlayer thickness (= 2.8 Å), s_l is specific surface area of the interlayer [m^2/kg], and ρ_g is dry density of gel products [kg/m^3].

The specific surface area of the interlayer s_l can be obtained as:

$$s_l = 510 f_{pc} + 1500 f_{sg} + 3100 f_{fa} \tag{2.36}$$

where f_{pc}, f_{sg}, and f_{fa} denote the weight fractions of Portland cement, blast furnace slag, and fly ash in the mix, respectively. Finally, from the overall volume balance of the paste, the porosity of capillary pores can be obtained as:

$$\phi_c = 1 - V_s - (1 - \alpha) \frac{W_p}{\rho_p} \tag{2.37}$$

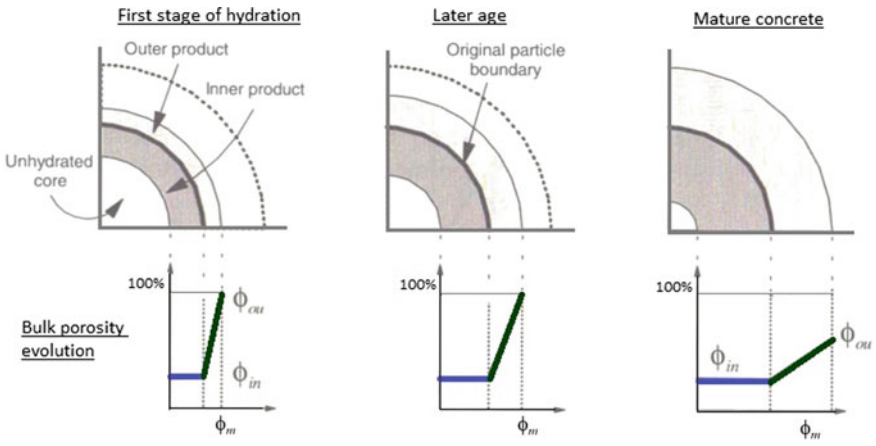

Fig. 2.12 Bulk porosity function of outer product and cluster expansion model (Maekawa et al. 1999)

The bulk porosity of the product is assumed to be increasingly distributed from intrinsic porosity of inner product, ϕ_{in}, to the porosity at the outermost boundary of the expanding cluster, ϕ_{ou}, as given in Fig. 2.12.

The bulk porosity in the outer product at distance δ from the surface of original powder particle is modelled as:

$$\phi_\delta = (\phi_{ou} - \phi_{in})\left(\frac{\delta}{\delta_m}\right)^n + \phi_{in} \tag{2.38}$$

where ϕ_m is cluster thickness at the instant of hydration, n is a power function parameter to take into account a generic pattern of deposition of products around the particle ($n = 1$ is adapted currently as shown in Fig. 2.12).

The density at distance δ in the cluster is given depending on the gel weight and bulk porosity ϕ_δ:

$$\rho_\delta = \frac{(1+\beta)(1-\phi_\delta)}{(1/\rho_p + \beta/\rho_u)} \tag{2.39}$$

The computation of specific surface area is explained as follows. The capillary surface area dS_c encompassed by region dr can be expressed as:

$$dS_c = \frac{dS_c}{dV_g} dV_g = \frac{4\pi r^2}{\varsigma}\left(\frac{1-\phi_r}{1-\phi_{in}}\right) dr \tag{2.40}$$

where ϕ_r is bulk porosity of the expanding cluster at r and ζ is the ratio of volume to external surface area of a typical grain [nm^3/nm^2]. S_c can be obtained by integrating Eq. 2.40 over cluster thickness. ζ can be obtained by the following empirical expression for blended powder:

$$\zeta = 19.0 f_{pc} + 1.5 f_{sg} + 1.0 f_{fa} \tag{2.41}$$

The surface area of gel, S_g [m^2/m^3], is simply obtained as a product of the mass of gel products to the specific surface area of gel mass. This gives:

$$S_g = W_g \cdot s_g \tag{2.42}$$

where s_g is specific surface area of hydrates (= 3.0 × 104 [m^2/kg]) and W_g is gel density [kg/m^3].

Finally, a porosity distribution model is introduced. In this model, the entire micro-pore structure is idealised as:

$$\phi(r) = \phi_c V_c(r) + \phi_g V_g(r) + \phi_l \tag{2.43}$$

where V_c is fractional capillary pore volume of the distribution up to pore radius r and V_g is fractional gel pore volume of the distribution up to pore radius r. These functions are represented by a simplistic Raleigh-Ritz function:

$$V_i(r) = 1 - \exp(-B_i \cdot r) \tag{2.44}$$

$$dV_i(r) = B_i \cdot r \cdot \exp(-B_i \cdot r) \cdot d \ln r \tag{2.45}$$

where i is c or g and B_i is sole porosity distribution parameter, which in fact represents the peak of the porosity distribution on a logarithmic scale [1/m]. If the pores are assumed to be cylindrical in shape, parameter B_i can be obtained from the equation:

$$S_i = 2\phi_i \int_{r_{\min}}^{\infty} B_i \cdot r \cdot \exp(-B_i \cdot r) d \ln r \tag{2.46}$$

where $r_{\min}$ is a minimum pore radius [m]. This expression cannot be evaluated analytically as a closed-form solution. Thus, the explicit relationship between B_i and S_i/ϕ_i obtained by fitting accurate numerical evaluations of the above integral to a large number of data sets is used for computation.

2.2.5 Data Mining Approach

A data mining approach for modelling the adiabatic temperature rise during concrete hydration was presented by Fairbairn et al. (2006). The model is based on experimental data obtained since the 1970s for several mass concrete constructions in Brazil, including some of the hugest hydroelectric power plants in operation in the world. Data obtained from 260 adiabatic tests carried out by the Technical Control Department of FURNAS (company that generates and transmits electricity for south-eastern Brazil) (Andrade 1997) was used to organise a consistent database (Faria 2004; Fonseca 2008).

The early data mining models for predicting heat of hydration were based on artificial neural networks (ANNs) (Faria 2004). An ANN is a computational structure that is inspired by the processes observed in natural networks of biological neurons in the brain. It consists of simple computational units, called neurons, which are highly interconnected and generally arranged in an input layer, hidden layers and an output layer.

The use of ANNs comprises two phases: a training phase and an exploitation phase. In the training phase, the weights of the given interconnections are adjusted according to some learning algorithm that operates on a data set generating a model

that maps the input neurons to the output neurons. Once trained, the ANN can be exploited; i.e. it is able to process a new input set resulting in a predicted output set.

For the problem at hand, the following variables were chosen as input set:

- x(1) = CaO content
- x(2) = SiO_2 content
- x(3) = Al_2O_3 content
- x(4) = Fe_2O_3 content
- x(5) = SO_3 content
- x(6) = Cement consumption
- x(7) = Blaine fineness
- x(8) = Natural pozzolan content
- x(9) = Slag content
- x(10) = Fly ash content
- x(11) = Water content
- x(12) = Chemical additive content
- x(13) = Aggregates content
- x(14) = Placing temperature

The output set is composed of three parameters that determine a function which is capable to describe the adiabatic temperature rise during concrete hydration. The following function, called the Hill function (similar to Eq. 2.12), was found to be a reasonable approximation of the adiabatic temperature rise curves:

$$\Delta T^{ad}(t) = \Delta T^{ad}_{\infty} \frac{(t/c)^n}{(\tau_0)^n + (t/c)^n} \tag{2.47}$$

where n and τ_0 are dimensionless constants and c is a constant equal to 1 with the same unit as t.

The general structure of the artificial neural network is shown in Fig. 2.13.

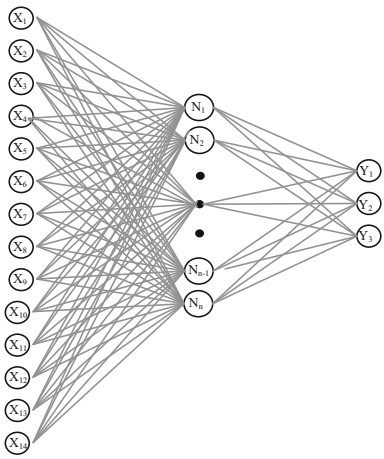

Fig. 2.13 General structure of the ANN

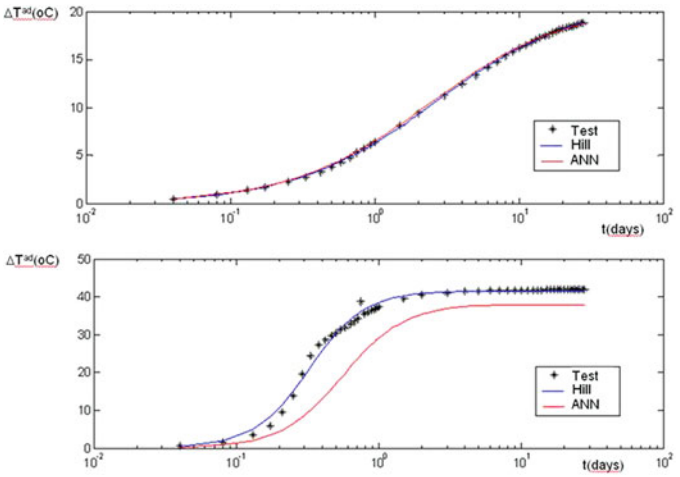

Fig. 2.14 Best and worst fits of the ANN model

As it was demonstrated by the several examples and error calculations presented in Faria (2004), the ANN approach constituted an useful tool for the prediction of the adiabatic temperature rise. To illustrate this approach, Fig. 2.14 displays the best and the worst fittings showing the evolution of ΔT^{ad} (experimental, Hill function, and ANN) with time in a semi-log graph.

An evolution of the data mining model was developed by Evsukoff et al. (2006). Here, an integrated hybrid model identification approach that combines fuzzy cluster analysis, radial basis function neural network, and genetic algorithms is presented. The input variables were divided into two subsets according to their meaning. The first subset is the five oxide concentrations, and the second subset corresponds to the other nine variables. A number of data mining techniques were used, encompassing: data-driven model identification techniques; fuzzy cluster analysis; radial basis function neural network; neuro-fuzzy modelling, and genetic algorithm variables selection. The numerical results obtained agreed with the experiments indicating that the model is ready to be used for the design of massive concrete structures. In this way, it was shown that the modern engineer can put together classical domain knowledge and up-to-date data analysis tools to develop precise models, which can be directly used by the practitioner.

2.2.6 Inverse Analysis Approach

If the history of temperatures has been measured for a specific part of a structure, accompanied by environmental temperature measurements, it is possible to have a fairly good estimate of the adiabatic temperature curve of the material using an

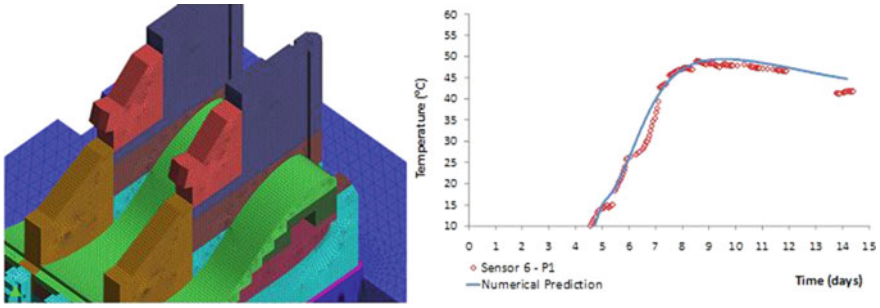

Fig. 2.15 FEM model of the spillway and comparison between temperature history measured in the bulk of the pier and obtained by using the adiabatic rise curve determined by inverse analysis

inverse analysis technique. When such an analysis is required, it is very common that many material parameters and boundary conditions may not have been precisely determined by laboratory tests or recorded in the field. Such is the case of the activation energy, and climate conditions such as wind intensity and direction, rainfall. Although the lack of this information could compromise the accuracy of the results, this source of uncertainty can be minimised if the simplifying assumptions are used within an acceptable margin of error.

A detailed description of this technique was recently presented in Fairbairn et al. (2015) where the actual case of the construction of a hydroelectric plant is analysed. Here, the temperatures measured during the phased construction of a spillway gate pier were used to determine the adiabatic temperature rise of the concrete used during the construction. A genetic algorithm was used to minimise the differences between the temperature evolution measured in the field and the one obtained by numerical analysis. The results (an extract can be seen in Fig. 2.15) demonstrated the feasibility of the method that can be of great utility in the solution of engineering problems.

References

Andrade, W. P. (1997). *Concretes: mass, structural, shotcrete and roller compacted—Tests and properties*. Sao Paulo Editora PINI.

Arrhenius, S. (1915). *Quantitative laws in biological chemistry*. London: G. Bell and Sons.

Ballim, Y., & Graham, P. C. (2003). A maturity approach to the rate of heat evolution in concrete. *Magazine of Concrete Research, 55*(3), 249–256.

Bažant, Z. P., & Najjar, L. J. (1972). Nonlinear water diffusion in nonsaturated concrete. *Materials and Structures, 5*(25), 3–20.

Bensted, J. (1981). Hydration of Portland cement. In S. N. Ghosh (Ed.), *Advances in cement technology* (pp. 307–347). New York: Pergamon Press.

Bentz, D. (1995). A three-dimensional cement hydration and microstructure program. I. Hydration rate, heat of hydration, and chemical shrinkage. Technical Report, NIST Building and Fire Research Laboratory, Gaithersburg, MD.

Bentz, D. (1997). Three-dimensional computer simulation of Portland cement hydration and microstructure development. *Journal of the American Ceramic Society, 80*(1), 3–21.

Bentz, D. (2000). CEMHYD3D: A three-dimensional cement hydration and microstructure development modeling package. Version 2.0., Technical report, NIST Building and Fire Research Laboratory, Gaithersburg, Maryland.

Bentz, D. (2005). CEMHYD3D: A three-dimensional cement hydration and microstructure development modeling package. Version 3.0., Technical report, NIST Building and Fire Research Laboratory, Gaithersburg, Maryland.

Bentz, D. P., Waller, V., & de Larrard, F. (1998). Prediction of adiabatic temperature rise in conventional and high-performance concretes using a 3-D microstructural model. *Cement and Concrete Research, 28*(2), 285–297.

Bentz, D. P., Garboczi, E., Haecker, C., & Jensen, O. (1999). Effect of cement particle size distribution on performance properties of Portland cement-based materials. *Cement and Concrete Research, 29,* 1663–1671.

Biernacki, J. J., Williams, P. J., & Stutzman, P. E. (2001). Nonlinear analysis of temperature and moisture distributions in early-age concrete structures based on degree of hydration. *ACI Material Journal, 98*(4), 340–349.

Bishnoi, S. (2008). Vector modelling of hydrating cement microstructure and kinetics. Ph.D. thesis, EPFL.

Berodier, E., & Scrivener, K. (2014). Understanding the filler effect on the nucleation and growth of C-S-H. *Journal of the American Ceramic Society, 92*(12), 1–10.

Bishnoi, S., & Scrivener, K. (2009a). Studying nucleation and growth kinetics of alite hydration using μic.pdf. *Cement and Concrete Research, 39,* 849–860.

Bishnoi, S., & Scrivener, K. L. (2009b). μic: A new platform for modelling the hydration of cements. *Cement and Concrete Research, 39,* 266–274. https://doi.org/10.1016/j.cemconres.2008.12.002.

Bofang, Z. (2003). *Thermal stresses and temperature control of mass concrete*. Beijing, People's Republic of China: China Electric Power Press.

Bogue, J. H. (1947). *The chemistry of Portland cement*. New York, USA: Reinhold Publishing Corporation.

van Breugel, K. (1991). Simulation of hydration and formation of structure in hardening cement based materials. Ph.D. thesis, Delft University of Technology, Delft, Netherlands.

Brouwers, H. J. H. (2004). The work of Powers and Brownyard revisited: Part 1. *Cement and Concrete Research, 34,* 1697–1716.

Buffo-Lacarrière, L., Sellier, A., Escadeillas, G., & Turatsinze, A. (2007). Multiphasic finite element modelling of concrete hydration. *Cement and Concrete Research, 37*(2), 131–138.

Bullard, J. W., Enjolras, E., George, W. L., Satterfield, S. G., & Terrill, J. E. (2010). A parallel reaction-transport model applied to cement hydration and microstructure development. *Modelling and Simulation in Materials Science and Engineering, 18,* 025007. https://doi.org/10.1088/0965-0393/18/2/025007.

CEB-FIP fib Model Code 2010, 2013.

Cervera, M., Oliver, J., & Prato, T. (1999). Thermo-chemo-mechanical model for concrete. I: Hydration and aging. *Journal of Engineering Mechanics ASCE, 125*(9), 1018–1027.

Cervera, M., Faria, R., Olivier, J., & Prato, T. (2002). Numerical modelling of concrete curing, regarding hydration and temperature phenomena. *Computers & Structures, 80,* 1511–1521.

Chamrova, R. (2010). Modelling and measurement of elastic properties of hydrating cement paste. Ph.D. thesis, EPFL.

Chengju, G. (1989). Maturity of concrete: Method for predicting early-age strength. *ACI Materials Journal, 86*(4), 341–353.

Dilnesa, B. Z., Lothenbach, B., Renaudin, G., Wichser, A., & Kulik, D. (2014). Synthesis and characterization of hydrogarnet $Ca_3(Al_xFe_1 - x)_2(SiO_4)_y(OH)_4(3 - y)$. *Cement and Concrete Research, 59,* 96–111. https://doi.org/10.1016/j.cemconres.2014.02.001.

Do, Q. H. (2013). Modelling properties of cement paste from microstructure: Porosity, mechanical properties, creep and shrinkage. EPFL.

Evsukof, A., Fairbairn, E. M. R., Faria, E. F., Silvoso, M. M., & Toledo Filho, R. D. (2006). Modeling adiabatic temperature rise during concrete hydration: A data mining approach. *Computers & Structures, 84,* 2351–2362.

Fairbairn, E. M. R., Toledo Filho, R. D., Silvoso, M. M., Ribeiro, F. L. B., Evsukof, A., Ferreira, I. A., et al. (2006). A new comprehensive framework for the analysis of mass concrete: Thermo-chemo-mechanical, experimental, numerical and data modeling. In L. Berga, J. M. Buil, E. Bofill, J. C. De Cea, J. A. Garcia Perez, G. Mañueco, J. Polimon, A. Soriano, & J. Yagüe (Eds.), *Dams and reservoirs, societies and environment in the 21st century* (pp. 901–910). London: Taylor & Francis Group.

Fairbairn, E. M. R., Silvoso, M. M., Ribeiro, F. L. B., & Toledo Filho, R. D. (2015). Determining the adiabatic temperature rise of concrete by inverse analysis: Case study of a spillway gate pier. *European Journal of Environmental and Civil Engineering*, pub. on-line, 1–17.

Faria, E. F. (2004). Prediction of the exothermicity of concrete hydration by thermo-chemical and data modelling. M.Sc. thesis, COPPE/UFRJ, Civil Engineering Department (in Portuguese).

Faria, R., Azenha, M., & Figueiras, J. A. (2006). Modelling of concrete at early ages: Application to an externally restrained slab. *Cement and Concrete Composites, 28*(6), 572–585.

Fernandez-Jimenez, A., & Puertas, F. (1997). Alkali-activated slag cements: Kinetic studies. *Cement and Concrete Research, 27,* 359–368.

Fonseca, D. (2008). Predicting concrete adiabatic temperature rise through models based on data. M.Sc. thesis, COPPE/UFRJ, Civil Engineering Department (in Portuguese).

Gawin, D., Pesavento, F., & Schrefler, B. A. (2006). Hygro-thermo-chemo-mechanical modelling of concrete at early ages and beyond. Part I: Hydration and hygro-thermal phenomena. *International Journal for Numerical Methods in Engineering, 67*(3), 299–331.

Garboczi, E. J., & Bentz, D. P. (2001). The effect of statistical fluctuation, finite size error, and digital resolution on the phase percolation and transport properties of the NIST cement hydration model. *Cement and Concrete Research, 31*(10), 1501–1514.

Gartner, E., Young, J., Damidot, D., & Jawed, I. (2002). Hydration of Portland cement. In *Structure and performance of cements* (Vol. 13), 978-0.

Hansen, P. F., & Pedersen, J. (1977). Maturity computer for controlled curing and hardening of concrete. *Nordisk Betong, 21,* 19–34.

JCI Japanese Concrete Institute. (2008). *Guidelines for control of cracking of mass concrete*.

Jonasson, J.-E. (1994). Modelling of temperature, moisture and stress in young concrete. Ph.D. thesis, Luleå University of Technology, Luleå, Sweden.

Justnes, H. (1992). Hydraulic binders based on condensed silica fume and slake lime. In *9th International Congress on the Chemistry of Cement*, New Delhi (Vol. III, pp. 284–290).

Kanit, T., Forest, S., Galliet, I., Mounoury, V., & Jeulin, D. (2003). Determination of the size of the representative volume element for random composites: Statistical and numerical approach. *International Journal of Solids and Structures, 40,* 3647–3679.

Karpov, I. K., Chudnenko, K. V., & Kulik, D. A. (1997). Modeling chemical mass transfer in geochemical processes; Thermodynamic relations, conditions of equilibria and numerical algorithms. *American Journal of Science, 297,* 767–806. https://doi.org/10.2475/ajs.297.8.767.

Kiernożycki, W. (2003). *Betonowe konstrukcje masywne (Massive concrete structures)*. Cracow, Poland: Polski Cement.

Kishi, T., & Maekawa, K. (1994). Thermal and mechanical modelling of young concrete based on hydration process of multi-component cement materials. In *Thermal cracking in concrete at early age, Rilem Proceeding 25* (pp. 11–19). ISBN 0-419-18710-3.

Klemczak, B., & Batog, M. (2015). Heat of hydration of low-clinker cements. Part 1, Semi-adiabatic and isothermal tests at different temperature. *Journal of Thermal Analysis and Calorimetry*.

Klemczak, B., & Knoppik-Wróbel, A. (2014). Analysis of early-age thermal and shrinkage stresses in reinforced concrete walls. *ACI Structural Journal, 111*(2), 313–322.

Knoppik-Wróbel, A. (2012). Cracking risk in early-age RC walls. In *fib Ph.D. Symposium*, Karlsruhe, Germany.

Knudsen, T. (1984). The dispersion model for hydration of Portland cement: I. General concepts. *Cement and Concrete Research, 14,* 622–630.

Kolani, B., Buffo-Lacarrière, L., Sellier, A., Escadeillas, G., Boutillon, L., & Linger, L. (2012). Hydration of slag blended cements. *Cement & Concrete Composites, 34*(9), 1009–1018.

Kumar, A., Bishnoi, S., & Scrivener, K. L. (2012). Modelling early age hydration kinetics of alite. *Cement and Concrete Research, 42,* 903–918. https://doi.org/10.1016/j.cemconres.2012.03.003.

Lackner, R., & Mang, H. A. (2004). Chemoplastic material model for the simulation of early-age cracking: From the constitutive law to numerical analyses of massive concrete structures. *Cement & Concrete Composites, 26,* 551–562.

Lea, F. M. (1970). *The chemistry of cement and concrete* (p. 727). London: Edward Arnold Ltd. ISBN 7131-2277-3.

Leal da Silva, W. R., & Šmilauer, V. (2015). Fuzzy affinity hydration model. *Journal of Intelligent and Fuzzy Systems., 28*(1), 127–139.

Leal da Silva, W. R., Šmilauer, V., & Štemberk, P. (2015). Upscaling semi-adiabatic measurements for simulating temperature evolution of mass concrete structures. *Materials and Structures, 48*(4), 1031–1041.

Lothenbach, B., Matschei, T., Möschner, G., & Glasser, F. P. (2008). Thermodynamic modelling of the effect of temperature on the hydration and porosity of Portland cement. *Cement and Concrete Research, 38,* 1–18. https://doi.org/10.1016/j.cemconres.2007.08.017.

Maekawa, K., Chaube, R. P., & Kishi, T. (1999). *Modeling of concrete performance*. London: E & FN Spon.

Maekawa, K., Ishida, T., & Kishi, T. (2008), *Multi-scale modeling of structural concrete*, Taylor and Francis.

Mills, R. H. (1966). Factors influencing cessation of hydration in water-cured cement pastes. Special report No. 90. Washington, D.C.: Highway Research Board.

Mounanga, P. (2003). Comportement des matrices cimentaires au jeune âge: relation entre évolution chimique et déformations chimique et endogène. XXIEMES Rencontres Universitaires de Génie Civil.

Navi, P., & Pignat, C. (1996). Simulation of cement hydration and the connectivity of the capillary pore space. *Advanced Cement Based Materials, 4,* 58–67.

Neville, A. (1997). M. properties of concrete. Hoboken, NJ: Wiley.

Oh, B. H., & Cha, S. W. (2003). Nonlinear analysis of temperature and moisture distributions in early-age concrete structures based on degree of hydration. *ACI Material Journal, 100*(5), 361–370.

Pane, I., & Hansen, W. (2002). Concrete hydration and mechanical properties under nonisothermal conditions. *ACI Materials Journal, 99*(6), 422–534.

Poole, J. L. (2007). Modeling temperature sensitivity and heat evolution of concrete. Ph.D. thesis, University of Texas at Austin, Austin, USA.

Powers, T. C. (1964). *The physical structure of Portland cement paste, the chemistry of cement* (H. F. Taylor Ed.) (pp. 391–416). Academic Press.

Powers, T. C., & Brownyard, T. L. (1947). Studies of the physical properties of hardened Portland cement paste, Part 9. *ACI Journal, 18*(8).

Principallo, A., Lura, P., van Breugel, K., & Levita, G. (2003). Early development of properties in a cement paste: A numerical and experimental study. *Cement and Concrete Research, 33*(7), 1013–1020.

Rastrup, E. (1954). Heat of hydration in concrete. *Magazine of Concrete Research, 6*(17), 79–92.

Reinhardt, H., Blaauwendraad, J., & Jongedijk, J. (1982). Temperature development in concrete structures taking account of state dependent properties. In *Proceedings of RILEM International Conference on Concrete at Early Ages*, Paris, France (pp. 211–218).

Richardson, I. G. (1999). The nature of C-S-H in hardened cements. *Cement and Concrete Research, 29,* 1131–1147.

Richardson, I. G. (2000). The nature of the hydration products in hardened cement pastes. *Cement & Concrete Composites, 22,* 97–113.

Riding, K. A., Poole, J. L., Folliard, K. J., Juenger, M. C. G., & Schindler, A. K. (2011). New method for estimating apparent activation energy of cementitious systems. *ACI Materials Journal, 108*(5), 550–557.

RILEM TC 119-TCE. (1997). Avoidance of thermal cracking in concrete at early ages. *Materials and Structures, 30*, 451–464.

Scherer, G. W., Zhang, J., & Thomas, J. J. (2012). Nucleation and growth models for hydration of cement. *Cement and Concrete Research*, 982–993.

Schindler, A. K. (2002). Concrete hydration, temperature development, and setting at early ages. Ph.D. thesis, University of Texas at Austin, Austin, USA.

Schindler, A. K. (2004). Effect of temperature on hydration of cementitious materials. *ACI Materials Journal, 101*(1), 72–81.

Schindler, A. K., & Folliard, K. J. (2005). Heat of hydration models for cementitious materials. *ACI Materials Journal, 102*(1), 24–33.

de Schutter, G. (1999). Hydration and temperature development of concrete made with blast-furnace slag cement. *Cement and Concrete Research, 29*(1), 143–149.

de Schutter, G., & Taerwe, L. (1995). General hydration model for Portland cement and blast furnace slag cement. *Cement and Concrete Research, 25*(3), 593–604.

de Schutter, G., & Vuylsteke, M. (2004). Minimisation of early age thermal cracking in a J-shaped non-reinforced massive concrete quay wall. *Engineering Structures, 26,* 801–808.

Scrivener, K. L., Juilland, P., & Monteiro, P. J. M. (2015). Advances in understanding hydration of Portland cement. In *Cement and Concrete Research, Keynote Papers from 14th International Congress on the Chemistry of Cement (ICCC 2015)* (Vol. 78, Part A, pp. 38–56). https://doi.org/10.1016/j.cemconres.2015.05.025.

Šmilauer, V. (2014). *Multiscale hierarchical modeling of hydrating concrete*. Saxe-Coburg Publications.

Šmilauer, V., & Krejčí, T. (2009). Multiscale model for temperature distribution in hydrating concrete. *International Journal for Multiscale Computational Engineering, 7*(2), 135–151.

Taylor, H. F. W. (1990). *Cement chemistry*. New York: Academic Press.

Tennis, P. D., & Jennings, H. M. (2000). A model for two types of calcium silicate hydrate in the microstructure of Portland cement pastes. *Cement and Concrete Research, 30,* 855–863.

Thomas, J. J., Biernacki, J. J., Bullard, J. W., Bishnoi, S., Dolado, J. S., Scherer, G. W., et al. (2011). Modeling and simulation of cement hydration kinetics and microstructure development. *Cement and Concrete Research, 41,* 1257–1278.

Ulm, F.-J., & Coussy, O. (1998). Couplings in early-age concrete: From material modeling to structural design. *International Journal of Solids and Structures, 35*(31–32), 4295–4311.

Waller, V. (1999). Relations entre composition des bétons, exothermie en cours de prise et résistance en compression. Thèse de Doctorat, Ecole Nationale des Ponts et Chaussées, Paris.

Wang, C., & Dilger, W. H. (1994). Prediction of temperature distribution in hardening concrete. In *Proceedings of the International RILEM Conference on Thermal Cracking in Concrete at Early Ages*, London, UK (pp. 21–28).

Xiang, Y., Zhang, Z., He, S., & Dong, G. (2005). Thermal–mechanical analysis of a newly cast concrete wall of a subway structure. *Tunnelling and Underground Space Technology, 20,* 442–451.

Yuan, Y., & Wan, Z. L. (2002). Prediction of cracking within early-age concrete due to thermal, drying and creep behavior. *Cement and Concrete Research, 32,* 1053–1059.

Chapter 3
Thermal Properties

Mateusz Wyrzykowski, Agnieszka Knoppik, Wilson R. Leal da Silva, Pietro Lura, Tulio Honorio, Yunus Ballim, Brice Delsaute, Stéphanie Staquet and Miguel Azenha

Abstract This chapter is dedicated to relevant thermal properties in the scope of massive concrete structures. The initial part of the chapter (Sect. 3.1) pertains to properties that affect internal temperature developments in concrete, namely the thermal conductivity, the heat capacity and the heat exchanges between concrete and the surrounding media. The final part of the chapter (Sect. 3.2) is devoted to the thermal expansion coefficient, which is of fundamental importance to understand and predict the actual volume changes that take place in massive structures due to temperature variations.

M. Wyrzykowski (✉) · P. Lura
Empa, Swiss Federal Laboratories for Materials Science and Technology, Dübendorf, Switzerland
e-mail: mateusz.wyrzykowski@empa.ch

A. Knoppik
Silesian University of Technology, Gliwice, Poland

W. R. Leal da Silva
Danish Technological Institute, Gregersensvej 4, 2630 Taastrup, Denmark

P. Lura
Institute for Building Materials, ETH Zurich, Zürich, Switzerland

T. Honorio
Laboratoire d'Etude du Comportement des Bétons et des Argiles, CEA, DEN, DPC, SECR, 91191 Gif-sur-Yvette, France

Y. Ballim
University of the Witwatersrand, Johannesburg, South Africa

B. Delsaute · S. Staquet
BATir, LGC, Université Libre de Bruxelles, Brussels, Belgium

M. Azenha
ISISE, University of Minho, Guimarães, Portugal

© RILEM 2019

E. M. R. Fairbairn and M. Azenha (eds.), *Thermal Cracking of Massive Concrete Structures*, RILEM State-of-the-Art Reports 27,
https://doi.org/10.1007/978-3-319-76617-1_3

3.1 Heat Transport and Temperature Change

In this section, properties governing the transfer of heat and the corresponding changes of temperature in concrete are discussed. In order to analyse these properties, a brief discussion of the mechanisms of heat transport is necessary, together with a commonly applied description of heat transport. Temperature evolution and heat transport in hydrating concrete can be described at the macroscale level by means of the following equation, e.g. Coussy (2005); Ulm and Coussy (2001); Klemczak (2011); Gawin et al. (2006); Azenha et al. (2011):

$$\rho C_p \frac{\partial T}{\partial t} = div(\lambda_{eff} grad\, T) + \frac{\partial Q}{\partial t} \tag{3.1}$$

where ρ is the concrete density, C_p is the specific heat capacity (ρC_p is the volumetric heat capacity), T is the temperature, t is the time, λ_{eff} is the effective thermal conductivity and Q is the volumetric heat produced due to hydration of binder (see Chap. 2). C_p, ρ and λ_{eff} are dependent on degree of hydration, moisture content and temperature. In some cases, due to anisotropy of the material, λ_{eff} may be expressed as a tensor instead of a scalar (Eq. (3.1) remains valid in this case). The boundary conditions for Eq. 3.1 are described in Sect. 3.1.3, while the initial conditions refer to fresh concrete temperature corresponding to the start of the analysis.

After simple transformations of Eq. 3.1, the temperature change in time is described with the following equation:

$$\frac{\partial T}{\partial t} = \frac{1}{\rho C_p} div(\lambda_{eff} grad\, T) + \frac{\partial \alpha}{\partial t} \frac{Q_\infty}{\rho C_p} \tag{3.2}$$

where α is the degree of hydration (see Chap. 2) and Q_∞ is the total volumetric heat of hydration, with $\partial Q/\partial t = \partial \alpha/\partial t \cdot Q_\infty$ (see Eq. 3.2). The last term in Eq. 3.2 represents the adiabatic temperature rise in concrete, and it is often used as a reasonable and safe estimation of the maximum temperature rise that might be expected in a massive structure, as shown, e.g., by Ulm and Coussy (2001). After assuming that the thermal conductivity does not depend on temperature for the temperatures normally encountered in massive structures (see Sect. 3.1.1) (Gawin et al. 1999), the problem becomes linear, and the term $\lambda_{eff}/(\rho C_p)$ can be conveniently used as thermal diffusion coefficient, e.g. Klemczak (2011); Ulm and Coussy (2001).

Equation 3.2 demonstrates that the most basic description of temperature changes due to heat transfer in concrete requires two parameters: effective heat conductivity and heat capacity. It needs to be mentioned here that such description is necessarily simplified since it does not take into account the heat transport related to migration of water in early-age concrete. In this case, migration of water in the pores towards the drying surfaces (or, from the wetted surfaces to the self-desiccated bulk) and the possible phase changes of water will cause associated

heat transport. In order to describe this process, the heat transport equation needs to be coupled with an appropriate mass balance equation of water, e.g. Gawin et al. (2006); Azenha et al. (2011). Optionally, an additional transport term may be added to Eq. 3.1 or Eq. 3.2 due to water transport, with a thermohygral thermal diffusion coefficient, see, e.g., Klemczak (2011). It can be expected that the thermohygral heat transport is more important for the surface temperature (in particular at the removal of formworks and evaporative cooling) than for the temperature evolution in the bulk (McCarter and Ben-Saleh 2001). Kovler (1995) reported about an experimental programme on the shock of evaporative cooling of concrete in hot dry climate. The importance of evaporative cooling in thin specimens was later confirmed in experiments and simulations by Azenha (2009).

The thermal properties of concrete depend strongly on the thermal properties of its components. Initially, this is reflected as a dependence upon mix composition. Further, hardening of concrete is related to, and accompanied by, various phenomena of chemo-physical nature that are due to the ongoing reaction of the cement and to interactions of the concrete with the environment. These processes cause an evolution of thermal properties of mainly the cement paste, and as a consequence, of the concrete (as evidenced, e.g., based on measurements of thermal expansion coefficient in Wyrzykowski and Lura (2013a). The thermal properties of concrete change during hardening due to (a) changes of moisture state (water content in pores) resulting from hydration (as water is consumed in the reaction) and interaction with the environment (drying/wetting), and (b) degree of hydration since cement hydration leads also to changes in volumes of unhydrated cement, hydrates and porosity in addition to changes of moisture state. As it will be shown later in the chapter, the first-order effect is due to changes of moisture state, while hydration can be in many cases neglected.

3.1.1 Thermal Conductivity

Effective thermal conductivity of concrete, λ_{eff}, describes the ability of concrete to conduct heat at the macroscopic level. In Eq. 3.1, heat flux is conveniently described at the macroscopic level as heat conduction with Fourier's law, whereby heat fluxes, q, perpendicular to a given surface (with unit area) can be described by: $q = -\lambda_{eff} gradT$. It needs to be noted that such description corresponds in fact to an effective conductivity that accounts for the coupled effect of different heat transfer mechanisms occurring at the microstructural scale due to convection and radiation in the desaturated pores in addition to conduction within different concrete components (i.e. hydration products, aggregates, cement, water) (Litovsky and Shapiro 1992).

Thermal conductivity can be determined for concrete using a variety of methods that are generally based on the principle of generating a temperature gradient in a

sample and measuring the corresponding temperature distribution either after establishing equilibrium conditions and a constant temperature gradient (steady-state methods) or in a relatively short time during or following heating (transient methods). Depending on the technique, the temperature gradient can be obtained by heating the sample at one point and/or cooling the sample at a distant point, while measuring the temperature at a given point of the sample or directly on the heating/cooling element (Campbell-Allen and Thorne 1963; Mounanga et al. 2004). One of the commonly used standard methods based on heating and measuring the temperature at the same point in a sample is the so-called transient hot wire method (ASTM 1113), where a wire is placed in the sample and heated by means of electrical current. The wire works as a resistive thermometer at the same time—the rate at which the temperature of the wire increases can be then correlated with the heat transfer (heat conductivity) within the sample. Other commonly used methods are based on placing a planar sample between a heated and a cooled plate (e.g. the so-called guarded hot plate method) (Hammerschmidt 2002) or placing a heater and a thermometer in distant holes in the sample (e.g. two-linear-parallel-probe method) (Morabito 1989).

The most relevant factors affecting thermal conductivity of concrete are aggregate volume fraction, air content and moisture state of concrete, e.g. Kim et al. (2003). Furthermore, it was also found that the age itself has a negligible net effect on the thermal conductivity of concrete, except for very early ages, i.e. below about 2 days (Kim et al. 2003, Bentz 2008, Gibbon and Ballim 1998). According to Bentz (2008) this is because the thermal conductivity of cement paste components (water: 0.604 W/(mK) and cement: 1.55 W/(mK)) and hydrated cement paste are close enough so that the percolation of solids or depercolation of porosity can have only a limited impact on this property (about ±10%). The thermal conductivity of the main hydration products, i.e. C–S–H and CH, has been reported as 0.978 W/(mK) and 1.32 W(mK), respectively (Abdolhosseini Qomi et al. 2015), see also Table 3.1. The thermal conductivity of cement paste is consequently around 1.0 W/(mK). From this point of view, admixtures can have only negligible effect on the thermal conductivity.

Moist concrete has higher thermal conductivity than dry concrete since water contained in pores is more conductive than air. Consequently, ordinary concretes have conductivity about 1.0 W/(mK) higher in moist condition compared to dry condition (Tatro 2006), see Table 3.2. Guo et al. (2011) determined thermal conductivity of concrete mixtures at 20 °C with aggregate volume ratio of 70% as equal to 1.96 and 2.47 W/(mK) for dry conditions and wet conditions, respectively.

With increasing air content, the thermal conductivity of concrete decreases. This is especially pronounced for insulating concrete, where high air content is obtained by means of aerating or using lightweight aggregates. Values below 0.3 W/(mK) for aerated concrete were reported in Tatro (2006).

A comprehensive list of thermal conductivity values for concrete mixtures produced with different types of aggregates measured at various temperatures is available in ACI 207.1 (2005). The presented values range from 1.84 to 3.70 W/(mK).

Table 3.1 Thermal properties: results for temperatures ranging from 10 to 30 °C (adapted from Honorio 2015; Honorio et al. 2018)

Compound		Specific heat [J/(gK)]	Thermal conductivity [W/(mK)]
(Free) Water		4.183 (Holman 2009)	0.608 (Vargaftik 1993)
Clinker, clinker phases, gypsum	Clinker	0.750 (Bentz 2007)	1.55 (Bentz 2007)
	C_3S	0.745 (Lothenbach et al. 2008) 0.710 (Abdolhosseini Qomi et al. 2015)[a] 0.710 (Matschei et al. 2007) 0.750 (Todd 1951)	3.35 (Abdolhosseini Qomi et al. 2015)[a]
	C_2S	0.741 (Lothenbach et al. 2008) 0.720 (Abdolhosseini Qomi et al. 2015)[a] 0.720 (Matschei et al. 2007) 0.750 (Todd 1951)	3.45 (Abdolhosseini Qomi et al. 2015)[a]
	C_3A	0.768 (Lothenbach et al. 2008)	–
	C_4AF	0.813 (Lothenbach et al. 2008) 20 °C	–
	Gypsum	1.080 (Bentz and Prasad 2007)	0.66 (Cerny and Rovnanikova 2002) 1.26 (Côté and Konrad 2005)
Hydration products	C–S–H	0.950 (Cerny and Rovnanikova 2002) 722 (Lothenbach et al. 2008)	0.978 (Abdolhosseini Qomi et al. 2015)[a]
	CH	1.140 (Abdolhosseini Qomi et al. 2015)[a] 1.150 (Matschei et al. 2007)	1.32 (Abdolhosseini Qomi et al. 2015)[a]
	AFt	1.502 (Lothenbach et al. 2008)	–
	AFm	0.888–1.115 (Baquerizo et al. 2015)	–
	Hydrogarnet	0.666–1.121 (Matschei et al. 2007)	–
Cement-based composite materials	Cement paste	1.100–1.800 (Bentz 2007)	0.53–1.16 (Bentz 2007)
	Mortar	0.642 (Xu and Chung 2000)	0.9–1.5 (Cerny and Rovnanikova 2002) 1.37–2.65 (Khan 2002)
	Concrete	1.109–1.590	1.2–2.0 (Cerny and Rovnanikova 2002) 1.60–4.18 (Khan 2002)

(continued)

Table 3.1 (continued)

Compound		Specific heat [J/(gK)]	Thermal conductivity [W/(mK)]
Aggregates	Limestone aggregates	0.845 (Marshall 1972)	3.15–3.23 (Cerny and Rovnanikova 2002) 3.22 (Marshall 1972) 2.65–3.22 (Kim et al. 2003)
	Siliceous aggregates	–	2.90–5.18 (Cerny and Rovnanikova 2002) 5.16 (Kim et al. 2003)
	Basalt	0.766 (Marshall 1972)	4.03–4.30 (Khan 2002) 2.86 (Kim et al. 2003) 1.70 (Marshall 1972)

[a]Molecular simulations

Table 3.2 Effect of different aggregates and moisture conditions on thermal conductivity of concrete (Tatro 2006)

Aggregate type	Thermal conductivity —wet state [W/mK]	Thermal conductivity —50% RH [W/mK]	Thermal conductivity —dry state [W/mK]
Limestone	2.2	1.7	1.4
Sandstone	2.9	2.2	1.4
Quartz	3.3	2.7	2.3
Basalt	1.9–2.0	–	1.7
Expanded shale	0.85	0.79	0.62

Considering that the conductivity of concrete depends strongly on the type and amount of aggregates, and it is further affected by the air content, it can be considered as dependent on the concrete density.

Although the unit mass and moisture conditions of concrete, which are considered a key factor affecting conductivity (Neville 1997; Mehta and Monteiro 2005), are not reported in ACI 207.1 (2005), the range of values is also within the limits presented in Neville (1997). Another comprehensive list is presented in Tatro (2006).

Table 3.1 summarizes thermal conductivities of concrete components and exemplary concretes, while Table 3.2 summarizes the effect of aggregate types and moisture conditions on thermal conductivity.

Different authors proposed numerous analytical approaches for simulating the development of the thermal conductivity. The simplest approach consists of lumping the overall effect of concrete microstructure development and pores desaturation and describing the temperature evolution as a linear function of degree of hydration, e.g., Reinhardt et al. (1982); de Borst and van den Boogaard (1994); Ruiz et al. (2001):

$$\lambda_{eff} = \lambda_0(a_1 - a_2 \cdot \alpha(t)) \tag{3.3}$$

where λ_0 represents the final value of thermal conductivity and a_1, a_2 are empirical constants. For example, Ruiz et al. 2001 proposed $a_1 = 1.33$ and $a_2 = 0.33$. It needs to be noted, however, that many authors obtained good numerical predictions by neglecting the change of the values of thermal conductivity and using average values based only on mix composition (de Schutter 2002; Faria et al. 2006; Craeye et al. 2009; Zreiki et al. 2010; Briffaut et al. 2012). It was shown by Azenha (2009) and Briffaut et al. (2012) that the assumption of constant values of thermal parameters of concrete yields conservative predictions (expected temperatures are overestimated).

More complex approaches allow to account for different effects influencing the development of thermal conductivity. An empirical equation obtained based on a comprehensive experimental study developed by Kim et al. (2003) reads:

$$\begin{aligned}\lambda_{eff} = \lambda_{ref}(0.293 + 1.01A_R)(0.2RH + 0.8(1.62 - 1.54w/c)) \\ \times\ (1.05 - 0.0025T)(0.86 + 0.0036F_R)\end{aligned} \tag{3.4}$$

where A_R and F_R correspond to the total and fine aggregate volumetric ratios, respectively, w/c is the water-to-cement ratio, RH is the relative humidity and λ_{ref} is the reference value of thermal conductivity. The latter is obtained from experimental measurements of reference concrete with $A_R = 0.70$, $w/c = 0.40$, $T = 20$ °C and $RH = 100\%$.

Another approach to account for the moisture content has been applied by Gawin et al. (2006):

$$\lambda_{eff} = \lambda_{dry}\left(1 + \frac{4 \cdot \Phi \cdot \rho_w \cdot S_w}{(1 - \Phi)\rho_s}\right) \tag{3.5}$$

where λ_{dry} is thermal conductivity of dry concrete, Φ is porosity (incorporating the effect of changes due to ongoing hydration), ρ_w and ρ_s are the densities of water and solid skeleton (dry concrete), respectively, and S_w is the saturation degree of pores with water.

The thermal conductivity of concrete based on its composition can be predicted using Mori-Tanaka scheme (Bohm and Nogales 2008) by homogenizing the thermal conductivities of the components: cement paste and aggregates, assuming the latter all have the same thermal conductivity:

$$\lambda_{eff} = \lambda_{paste} + \frac{3f_{agg}\lambda_{paste}(\lambda_{agg} - \lambda_{paste})}{3\lambda_{paste} + f_{paste}(\lambda_{agg} - \lambda_{paste})} \tag{3.6}$$

where f is the volumetric fraction. In particular, the Mori-Tanaka scheme in this form assumes concrete as a macro-isotropic composite material that is composed of a continuous morphologically prevailing matrix (cement paste) and reinforced by

isotropic spherical inclusions distributed homogeneously in the matrix. These inclusions correspond to, e.g., aggregates. It should be considered that the defects, e.g. microcracks or regions of increased porosity, are not accounted for; they may play an important role in the thermal conductivity of solids (e.g. Litovsky and Shapiro (1992); Honorio et al. (2018)). Moreover, specific transfer effects in pores (namely, fluid conductivity, thermal radiation, convection and surface heterogeneous phenomena (Litovsky and Shapiro 1992)) are in general neglected in multiscale estimation of thermal conductivity.

A further, simpler approximation can be obtained by mass averaging of thermal conductivities of concrete components (Zreiki et al. 2010; Jendele et al. 2014):

$$\lambda_{eff} = \sum\nolimits_i m_i \cdot \lambda_i \tag{3.7}$$

where m_i is the weight ratio of subsequent components. Such formulation is only a very rough approximation, since it assumes that the constituents are arranged in parallel.

Thermal conductivities of concrete mix components are listed in Table 3.1.

Gawin et al. (1999) stated that the dependence of the thermal conductivity upon temperature can be neglected for the temperature ranges encountered in hardening concrete. For example, an empirical relation used by Gawin et al. (1999) for their simulations of concrete at fire assumes a change of λ of +0.0005 W/(mK) per +1 K of temperature change. The effect of temperature in the range 21–54 °C on the thermal conductivity was also neglected by van Breugel (1980).

In simulations of concrete structures, Briffaut et al. (2012) observed that the computed stresses were only slightly affected by temperature and age dependence of thermal conductivity.

3.1.2 Heat Capacity

Specific heat capacity C_p is the amount of energy in [J], necessary to raise 1 unit mass, [g], of a given material by a unit of temperature, [K].

Experimental measurements of heat capacity in concrete involve the same principle as the measurements of thermal conductivity, see Sect. 3.1.1, with dynamic thermal (transient) measurements, e.g. Pomianowski et al. (2014), or a combination of transient and steady-state measurements, where the heat capacity is calculated based on the thermal diffusion coefficient (obtained from the transient method) and the heat conductivity (obtained from the steady-state method), e.g. Luca and Mrawira (2005).

Similarly to thermal conductivity, the heat capacity of concrete depends strongly on thermal capacities of the different components i. Its value can be estimated through the rule of mixtures (Bentz 2007) based on mass fractions of the

components, m_i, as long as the specific heat capacity of each independent phase, C_i, is known. This way, the specific heat capacity of concrete is computed as follows:

$$C_p = \sum_i m_i \cdot C_i \tag{3.8}$$

The heat capacity of the aggregates depends on their mineralogical characteristics. Reference values of specific heat capacity for different aggregates are reported in Choktaweekarn and Tangtermsirikul (2010), Hamzah et al. (2010), Honorio (2015) and collected in Table 3.1.

The evolution of heat capacity during hardening is driven, similarly to the thermal conductivity, mainly by changes in water content and microstructural evolution due to hydration. The specific heat capacity of cement powder is typically equal to about 0.75 J/(gK) (Bentz 2008; Bentz et al. 2011), while the specific heat capacity of water is equal to 4.18 J/(gK). Nonetheless, as water becomes incorporated into hydration products, its effective heat capacity is considerably reduced to 2.20 J/(gK), as suggested by (Bentz 2007). Molecular simulations confirm that the heat capacity of confined water in C–S–H is reduced with respect to bulk (or free) water (Abdolhosseini Qomi et al. 2015). Since volume (or mass) and energy are extensive thermodynamic quantities, upscaling heat capacity can be done by the rule of mixtures (assuming that surface effects are negligible). As shown by Bentz (2007, 2008), the heat capacity of cement paste can be also approximated as a function of its degree of hydration α. In particular, Eq. 3.9 is suggested to compute the evolution of heat capacity in sealed conditions (Bentz 2007):

$$C_p(\alpha) = C_p(\alpha_0) \cdot [1.0 - 0.26 \cdot (1 - e^{-2.9\alpha})] \tag{3.9}$$

where $C_p(\alpha_0) = C_w(\alpha_0) \cdot m_w(\alpha_0) + C_c(\alpha_0) \cdot m_c(\alpha_0)$ is the heat capacity of cement paste at initial degree of hydration α_0, calculated as a weighted average (with m being mass fractions of constituents w and c). The subscripts w and c correspond to water and cement. Based on the C_w and C_c values recommended by Bentz et al. (2011), C_p at α_0 reads:

$$C_p(\alpha_0) = 4.18 m_w(\alpha_0) + 0.75(\alpha_0) \tag{3.10}$$

As an example, Eqs. 3.8–3.10 were used by Lura and van Breugel (2001) to estimate values of concrete heat capacity for concrete mixtures containing 47% of granite and 34% of quartz sand by mass of dry materials. The heat capacity of sand and coarse aggregates was set at 0.80 and 0.61 J/(gK) (Choktaweekarn and Tangtermsirikul 2010; Hamzah et al. 2010). The results from this example are shown in Fig. 3.1.

The values in Fig. 3.1 are within the common range of heat capacity for ordinary concrete, i.e. from 0.84 to 1.17 J/(gK) (Neville 1997). The variable aspect of heat capacity is reported to impact significantly the mechanical response of concrete structures at early age. Lura and van Breugel (2001) found that a given percentage

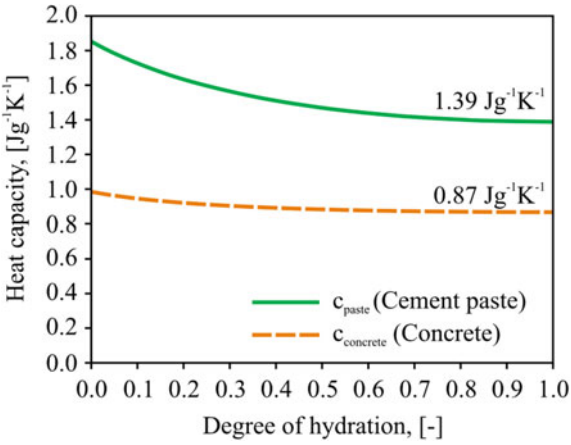

Fig. 3.1 Heat capacity for cement paste and concrete predicted by the rule of mixtures (C_{fg} = 0.80 J/(gK), C_{cg} = 0.61 J/(gK), C_c = 0.75 J/(gK), and C_w = 4.18 J/(gK))

of variation of the heat capacity may lead to a percentage of variation in the same order of magnitude in the computed stresses. Briffaut et al. (2012), in simulations with varying heat capacity, found stresses roughly 20% inferior to the stresses computed in a scenario with constant heat capacity.

The specific heat increases with temperature. In Tatro (2006), specific heat values of 0.92 and 1.04 J/(gK) were reported for temperatures of 10 °C and 66 °C, respectively.

3.1.3 Exchange of Heat with the Environment

Heat transport in concrete and the resulting temperature evolution are affected by heat exchange with the environment at the boundaries. For describing this process, boundary conditions of the III type (a linear combination of the value of a variable, i.e. temperature, and of its derivative at the boundary, i.e. heat transfer coefficient) are usually applied, e.g. Gawin et al. (2006). A heat transfer coefficient (also referred to as the heat exchange coefficient) is in general dependent upon both the characteristics of the concrete surface and the environment. Comprehensive studies on heat exchange of concrete with the environment have been presented, e.g., in Jonasson (1994) or Wojcik (2001); Wojcik et al. (2003).

Heat exchange at the open boundaries of concrete can take place due to thermal radiation and convection (Kusuda 1977). Thermal radiation occurs as energy is emitted in the form of electromagnetic waves. In convection, heat is exchanged due to movement (natural or forced) of fluids, in this case, of air in contact with the concrete surface. The heat exchange due to convection is approximately proportional to the temperature difference ($T - T_\infty$) between the concrete surface T and the surroundings T_∞ according to Newton's law of cooling, while heat exchange due to radiation is proportional to differences of temperatures in absolute scale to

the power of four, i.e. ($T^4 - T_\infty^4$) according to the Stefan–Boltzmann law (Modest 2013).

Usually, the two phenomena are considered together by means of one coefficient that accounts for both convection, h_p, and radiation, h_r (Faria et al. 2006):

$$h_{pr} = h_p + h_r \tag{3.11}$$

The coefficient of heat exchange by radiation, h_r, can be approximated by simplifying the 4th power radiative heat exchange law, for a given ambient temperature, $T_a > 5$ °C, and the emissivity of concrete, e, as follows (Branco et al. 1992):

$$h_r = \mathrm{e}[4.8 + 0.075(T_a - 5)] \tag{3.12}$$

In addition to radiative heating of concrete surfaces by the sun, radiative heat exchange can be especially important for mass concrete with regard to the night cooling effect, leading to significant daily temperature amplitudes. As estimated by Michell and Biggs (1979), a black body exposed to the clear sky at night may be cooled even 10–12 °C below ambient temperature. No indications for concrete are known, but a similar temperature difference of 10 °C has been measured for metal roof on a clear night by Hollick (2012).

The convective heat exchange coefficient at the concrete surface is influenced by geometric and aerodynamic parameters (Kim et al. 2003; Bentz 2008; Lee et al. 2009). The coefficient of heat exchange by free convection for concrete can be assumed as equal to h_p = 6.0 W/(m^{2}K) in stagnant air conditions (Branco et al. 1992). The heat exchange coefficient varies with the wind speed (Kwak et al. 2006; Briffaut et al. 2012). To account for forced convection due to wind action, the heat exchange coefficient is defined as a function of wind speed, v [m/s], according to different authors as follows:

- Branco et al. (1992):

$$h_p = 3.7v \tag{3.13}$$

- Jonasson (1994):

$$h_p = 5.6 + 3.95v \quad \text{if } v < 5\frac{m}{s}$$

$$h_p = 7.6v^{0.78} \text{ if } v > 5\frac{m}{s} \tag{3.14}$$

- Briffaut et al. (2012), as a function of the wind speed, dimensions of the structure, ambient temperature:

$$h_p = 0.13\left(\frac{g\,\alpha_{T,flu} l_{c,Cr}}{\upsilon_f D_t}(T_1 - T_a)\right)^{1/3}\left(\frac{\lambda_{flu}}{l_{c,Cr}}\right) \quad \text{for natural convection}$$
$$h_p = 0.664\left(\frac{v\,l_{c,\mathrm{Re}}}{\upsilon_f}\right)^{1/2}\left(\frac{\upsilon_f}{D_t}\right)^{1/3}\left(\frac{\lambda_{flu}}{l_{c,\mathrm{Re}}}\right) \quad \text{for forced convection} \tag{3.15}$$

where g gravitational acceleration, $\alpha_{T,flu}$ coefficient of thermal expansion (CTE) of the fluid, $l_{c,Cr}$ characteristic length of the natural convection [m], D_t thermal diffusivity; υ_f fluid kinematic viscosity; $l_{c,Re}$ characteristic length of the forced convective flux, v wind velocity; and λ_{flu} thermal conductivity of the fluid.

Lee et al. (2009) reported convective heat transfer coefficient of concrete exposed to air from 9.0 to 13.0 W/(m^{2}K) for wind velocities ranging from 2.0 to 3.0 m/s.

When concrete surface is covered with layers of other materials (arranged in series), such as formwork, insulation sheets or ground, the heat transfer coefficient due to the additional layers is expressed as follows:

$$\sum_{i=1}^{n}\frac{1}{h_i} = \frac{t_1}{\lambda_1} + \frac{t_2}{\lambda_2} + \cdots + \frac{t_i}{\lambda_i} \tag{3.16}$$

where h_i is the heat exchange coefficient of each layer, with t_i as the thickness of a layer, and λ_i is the corresponding thermal conductivity. A list of thermal conductivities of commonly used insulating materials can be found, e.g., in Jonasson (1994).

For the cases in which the boundary element is thick, or the concrete is merely in contact with soil, an older foundation or adjacent elements, significant heat can be accumulated in such an adjoining element. Therefore, the assumption at the basis of Eq. 3.16 ceases to be valid and such boundary or adjacent elements need to be explicitly considered in the models. When the adjacent member has well-determined geometry/size (e.g. a thick formwork with insulation panel), it can be modelled in full. When such element is geometrically indeterminate, such as a foundation terrain, it is necessary to introduce simplifications. Normally, the underlying terrain may be modelled to such an extent that temperature variations due to the environmental changes and the self-heating concrete cannot significantly affect the initial temperature of the most distant points of the underlying terrain included in the model (Azenha 2009).

A further heat exchange mechanism, in addition to convection or radiation at the surface, takes place on wet surfaces of fresh concrete exposed to evaporation, in particular horizontal concrete surfaces covered with bleeding water (which may accumulate on the top of fresh concrete) or covered with curing water (Hasanain et al. 1989). The phase change due to evaporation of water and the associated consumption of energy (heat of evaporation) together lead to evaporative cooling of concrete surfaces. By using a combination of experiments and simulations, Azenha

et al. (2007a, b) have demonstrated the importance of evaporative cooling in hot and dry environments, which enforced near-surface temperature drops of up to 7 °C when insulation was removed from previously sealed cement paste specimens (temperature of 36 °C and relative humidity of 30%). They have further shown that this effect is strongly diminished and becomes almost negligible when non-extreme environments are considered, e.g. temperature of 20 °C and relative humidity of 60%.

A rapid decrease of the surface temperature, as opposed to the self-heating bulk, may lead to the formation of high temperature gradient and cracking (Kovler 1995). To avoid this effect, limiting of early-age evaporation can be applied by means of covering the surface with, e.g., plastic sheets (McCarter and Ben-Saleh 2001). On the other hand, this effect was reported to be only very limited in time in the situations where bleeding water evaporates fast, especially with high ambient temperature and high wind speed (Hasanain et al. 1989).

To estimate the effect of heat exchange due to evaporative cooling, the mass exchange with the environment needs to be considered explicitly. In Azenha et al. (2007a), several numerical simulations with the DuCOM simulation framework were performed, and the near-surface temperature variations associated with evaporative cooling could be predicted by combining a hygrothermal analysis with a simple coupling term regarding the enthalpy of water evaporation.

3.2 Coefficient of Thermal Expansion (CTE)

In order to quantify the vulnerability of concrete to the restrained thermal deformations and therefore to the cracking risk, a coefficient expressing the tendency of concrete to deform due to temperature changes is used. Even though the term *coefficient of thermal expansion* (CTE) formally refers to the volume or length increase (expansion) upon heating only, it is often used in the literature to describe volume/length changes acting in both directions, due to both heating and cooling. The more general term *coefficient of thermal dilation* (CTD) is sometimes used and is formally more appropriate. Here, similarly as in most of the literature, the term CTE will be used to describe deformations in either direction and therefore will be considered as the equivalent of CTD. The CTE described thereafter, unless otherwise specified, refers to the linear coefficient expressing length change (contraction or expansion) at unit change of temperature (cooling or heating, respectively) (ARMY-COE 1981).

Different methods exist for the determination of the CTE based on the same principle: determining deformations and relating the deformation to the known temperature history, either applied as a part of a test, or self-induced by the hydrating material (Boulay 2003). The methods can be in general divided into linear and volumetric. It is normally assumed that the volumetric thermal expansion is isotropic; thus, the linear CTE can be approximated as one-third of the volumetric one. In the linear method, elongation and shortening of a sample exposed to

changing temperature are followed by either measurements of the sample length change with, e.g., LVDTs or optical systems or by strain measurements on the sample with, e.g., length comparators, strain gauges or vibrating wire extensometer, e.g. Kada et al. (2002); Buch and Jahangirnejad (2008); Maruyama and Teramoto (2011); ASTM (2012); AASHTO (2011); Azenha and Granja (2015). Linear techniques are often applied for in situ measurements of the CTE in the field, e.g. Yeon et al. (2013).

In the volumetric method, the sample is immersed in a bath containing a liquid of known density, see, e.g., Loser et al. (2010). By suspending the sample from a scale, the volume changes can be followed by measuring the apparent mass changes of the immersed sample. A systematic study of different factors influencing the volumetric method has been presented in Loser et al. (2010), where it was also shown that linear and volumetric methods give comparable results when all main artefacts are eliminated with care.

When thermal deformations are measured at early ages, they are often (especially for concretes with lower w/c) occurring simultaneously with autogenous shrinkage. Therefore, assuming the validity of the superposition principle, autogenous shrinkage needs to be subtracted from the total deformation to separate the thermal component (Bjøntegaard and Sellevold 2001; Loser et al. 2010; Wyrzykowski and Lura 2013a; Cusson and Hoogeveen 2007). Such assumption of superposition of thermal and autogenous components is valid when small temperature changes are considered (i.e. up to couple degrees) and the temperature steps are short (i.e. up to about 1–2 h) considering the ongoing hydration process. For larger temperature changes lasting longer, the dependence of the autogenous shrinkage upon temperature needs to be taken into account as well (Jensen and Hansen 1999; Bjøntegaard and Sellevold 2001; Maruyama and Teramoto 2011); in such case, the CTE is subject to possible bias due to an inaccurate estimation of autogenous shrinkage. General recommendations on testing procedures for CTE and autogenous shrinkage prepared based on the round robin test campaign of RILEM TC195-DTD are presented in Hammer and Bjøntegaard (2006).

It has long been observed that the CTE changes considerably during setting and hardening of concrete, e.g. Sellevold and Bjøntegaard (2006); Yeon et al. (2013). Similarly to other thermal properties (i.e. conductivity, heat capacity), since aggregates are inert, the evolution of the CTE is due to hardening and moisture state changes in the cement paste. Sellevold and Bjøntegaard (2006) have shown that hydration has only a negligible net effect on the evolution of the CTE, since concrete rewetted at the age of a couple of weeks had similar CTE as wet concrete shortly after setting time. Numerous studies have shown that the CTE of cement paste (and therefore also of concrete) changes considerably with the moisture state of the material (Kovler and Zhutovsky 2006; Sellevold and Bjøntegaard 2006;Grasley and Lange 2007; Maruyama and Teramoto 2012; Wyrzykowski and Lura 2013a, b). A general trend of the CTE evolution in cement paste is shown in Fig. 3.2.

It can be seen that the very high initial CTE is due to the contribution of water when concrete or cement paste is still in the plastic state. Shortly after setting time, a sudden decrease is observed. The value at this point corresponds to the CTE of the

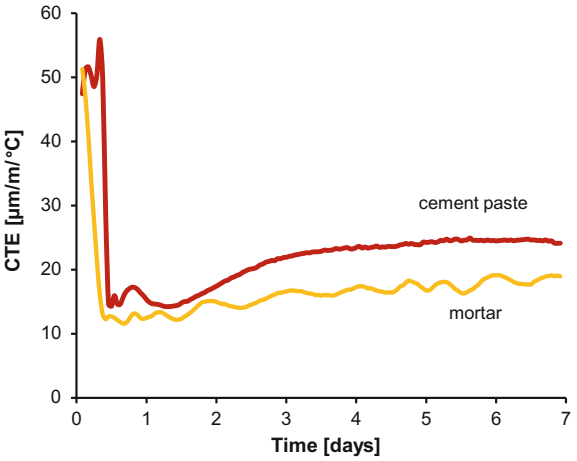

Fig. 3.2 Evolution of CTE of w/c 0.30 cement paste and mortar (with 40% vol. aggregates) during hardening in sealed conditions. For details, see Wyrzykowski and Lura (2013a)

solid skeleton, and, as already mentioned, should not change considerably due to hydration. An increase of the CTE is, however, further observed due to desaturation of the pores in the cement paste. In low *w/c* cement paste, an increase of more than 100% respect to the value at setting was observed in (Sellevold and Bjøntegaard 2006; Loser et al. 2010; Wyrzykowski and Lura 2013a, b). The moisture dependence of the CTE has been shown to be due to the temperature dependence of sorption. With increasing temperature, the RH in the pores increases, causing hygral swelling acting in addition to the thermal dilation of the solids. This effect becomes higher at RH decreasing from 100% to approximately 50%, see Sellevold and Bjøntegaard (2006); Radjy et al. (2003). The increase of the CTE is particularly important in low *w/c* pastes, in which the internal RH decreases considerably due to self-desiccation. Nevertheless, a considerable increase in CTE was observed in Wyrzykowski and Lura (2013b) for cement pastes with *w/c* as high as 0.45. In any case, desaturation of pores of concrete due to external drying will also result in a CTE increase (Sellevold and Bjøntegaard 2006).

Considering that the aggregates commonly used in concrete have lower CTE than the cement paste (see Table 3.3), due to the restraining effect of aggregates, the effect of the desaturation of the cement paste on the overall CTE of concrete is naturally lower than in cement paste or mortar (Sellevold and Bjøntegaard 2006; Wyrzykowski and Lura 2013b; Yeon et al. 2013). However, as reported by Sellevold and Bjøntegaard (2006), an increase from about 7 µm/m/°C at the time of setting to about 11 µm/m/°C after drying was observed in concrete with 72% vol. of aggregates. Furthermore, experimental results starting at the initial set are reported in Delsaute and Staquet (2017). It was found that the CTE increases from a minimum value varying between 7 and 9 µm/m/°C to a value varying between 10 and 12 µm/m/°C for concretes with w/c ranging from 0.4 to 0.6 during the hydration process, when the concrete is kept in sealed condition. Also, as shown by

Table 3.3 CTE of concrete and different types of aggregates as reported in the literature. Whenever the evolution of the CTE was followed, values after setting are reported here

Material/condition	CTE [μm/m/°C]	References
Concrete w/c 0.40, 72% vol. aggregates, 5% silica fume	7–11 (100–88% saturation degree)	Sellevold and Bjøntegaard (2006)
Concrete w/c 0.45, ~74% vol. aggregates, limestone coarse aggregate	5–7	Yeon et al. (2013)
Concrete w/c 0.45, ~71% vol. aggregates, river gravel coarse aggregate	8–9	Yeon et al. (2013)
Concretes w/c 0.30–0.45, ~66% vol. aggregates, metamorphic limestone-based coarse aggregate	6.5–7.6	Kada et al. (2002)
Concretes: normal (w/c 0.45) and high strength (w/c 0.25 and w/c 0.31), ~70% vol. aggregates (limestone)	10–11	Cook et al. (1993)
Concrete (recommendation)	11	ACI (2001)
Concrete, ~70% vol. aggregates, gravel coarse aggregate (6 different sources), w/b 0.40 (saturated, 28 d)	9.7–10.7	Naik et al. (2010)
Concrete, ~67% vol. aggregates, basalt coarse aggregate, w/b 0.40 (saturated, 28 d)	9.3	Naik et al. (2010)
Concrete (typical value)	10–12	Bentz (2008)
Aggregate: granite	7–9	Mindess et al. (2003)
Aggregate: basalt	6–8	Mindess et al. (2003)
Aggregate: limestone	6	Mindess et al. (2003)
Aggregate: dolomite	7–10	Mindess et al. (2003)
Aggregate: sandstone	11–12	Mindess et al. (2003)
Aggregate: quartzite	11–13	Mindess et al. (2003)

the numerical study by Yeon et al. (2013), the evolution of CTE due to desaturation in concrete can considerably affect the early-age thermal stresses.

As an efficient way for reducing the increase of CTE during hardening, internal curing has been proposed. It has been shown that the CTE can be reduced to values occurring shortly after setting, both using lightweight aggregates (Maruyama and Teramoto 2012) and superabsorbent polymers (Wyrzykowski and Lura 2013b).

It has been observed that, above the freezing point of water in the pores, the CTE increases slightly with temperature (Kodur 2014). However, for the temperature range normally encountered in massive structures, this effect is usually neglected (Briffaut et al. 2012; de Schutter 2002; Faria et al. 2006; Liu et al. 2014; Yuan and Wan 2002; Zreiki et al. 2010; ACI 2001).

The coefficient of thermal expansion of concrete varies strongly with concrete mix constituents (particularly aggregate type and amount) (CEB-FIP 2013;

Bangash 2001). A comprehensive study on the effect of different aggregates can be found in Buch and Jahangirnejad (2008). Some CTE values for concrete, either measured directly or assumed in calculations, are reported in Table 3.3.

As shown by Wyrzykowski and Lura (2013b), the dependence of the CTE upon the mix composition can be estimated with a good accuracy based on effective medium approaches, e.g. the Hobbs model (Hobbs 1971) or the Rosen–Hashin bounds (Rosen and Hashin 1970), when the CTE of the mix constituents is known, see Table 3.3. Zhutovsky and Kovler (2017) proposed a poromechanical model for the estimation of the CTE of concrete using the evolution of elastic properties obtained from ultrasonic measurements as input.

References

AASHTO. (2011). T 336 Standard method of test for coefficient of thermal expansion of hydraulic cement concrete. Washington, D.C.: American Association of State Highway and Transportation Officials.

Abdolhosseini Qomi, M. J., Ulm, F.-J., & Pellenq, R. J.-M. (2015). Physical origins of thermal properties of cement paste. *Physical Review Applied, 3,* 064010.

ACI. (2001). ACI 224.3R-95: Joints in concrete construction. Farmington Hills, MI.

ACI. (2005). ACI 207.1R-05: Guide to mass concrete. Farmington Hills, MI.

ARMY-COE CRD-C 39-81. (1981). *Handbook for Concrete and Cement Test Method for Coefficient of Linear Thermal Expansion of Concrete*.

ASTM C531-00. (2012). *Standard test method for linear shrinkage and coefficient of thermal expansion of chemical-resistant mortars, grouts, monolithic surfacings, and polymer concretes*. West Conshohocken, PA: ASTM International.

ASTM C1113/C1113M-09. (2013). *Standard test method for thermal conductivity of refractories by hot wire (Platinum resistance thermometer technique)*. West Conshohocken, PA: ASTM International.

Azenha, M., Maekawa, K., Ishida, T., & Faria, R. (2007a). Drying induced moisture losses from mortar to the environment. Part I: Experimental research. *Materials and Structures, 40,* 80–811.

Azenha, M., Maekawa, K., Ishida, T., & Faria, R. (2007b). Drying induced moisture losses from mortar to the environment. Part II: Numerical implementation. *Materials and Structures, 40,* 813–825.

Azenha, M. (2009). Numerical simulation of the structural behaviour of concrete since its early ages. Ph.D. thesis, Faculty of Engineering of the University of Porto, Portugal.

Azenha, M., Sousa, C., Faria, R., & Neves, A. (2011). Thermo–hygro–mechanical modelling of self-induced stresses during the service life of RC structures. *Engineering Structures, 33,* 3442–3453.

Azenha, M, & Granja, J. (2015). Characterization of concrete properties at early ages: Case studies of the University of Minho. *CMS Workshop "Cracking of Massive Concrete Structures", eBook of Presentations (RILEM)*, March 17, 2015. ENS-Cachan, Paris.

Bangash, M. Y. H. (2001). *Manual of numerical methods in concrete*. London, UK: Thomas Telford Ltd.

Baquerizo, L. G., Matschei, T., Scrivener, K. L., et al. (2015). Hydration states of AFm cement phases. *Cement and Concrete Research, 73,* 143–157.

Bentz, D. (2007). Transient plane source measurements of the thermal properties of hydrating cement pastes. *Materials and Structures, 40,* 1073–1080.

Bentz, D. (2008). A review of early-age properties of cement-based materials. *Cement and Concrete Research, 38*(2), 196–204.

Bentz, D., Peltz, M., Duran-Herrera, A., Valdez, P., & Juarez, C. (2011). Thermal properties of high-volume fly ash mortars and concretes. *Journal of Building Physics, 34*(3), 263–275.

Bentz, D. P., & Prasad, K. R. (2007). Thermal performance of fire resistive materials. I. Characterization with respect to thermal performance models. NISTIR 7401, National Institute of Standards and Technology, Gaithersburg, MD, USA.

Bjøntegaard, Ø., & Sellevold, E. J. (2001). Interaction between thermal dilation and autogenous deformation in high performance concrete. *Materials and Structures, 34,* 266–272.

Bohm, H. J., & Nogales, S. (2008). Mori-Tanaka models for the thermal conductivity of composites with interfacial resistance and particle size distributions. *Composites Science and Technology, 68*(5), 1181–1187.

de Borst, R., & van den Boogaard, A. H. (1994). Finite-element modeling of deformation and cracking in early-age concrete. *ASCE Journal of the Engineering Mechanics, 120*(12), 2519–2534.

Boulay, C. (2003). Determination of the coefficient of thermal expansion. Early age cracking in cementitious systems. Report of RILEM Technical Committee 181-EAS—Early age shrinkage induced stresses and cracking in cementitious systems (pp. 217–224). RILEM Publications SARL.

Branco, F. A., Mendes, P. A., & Mirambell, E. (1992). Heat of hydration effects in concrete structures. *ACI Materials Journal, 89*(2), 139–145.

van Breugel, K. (1980). *Artificial cooling of hardening concrete*. Delft University of Technology. Concrete Structures, Delft.

Briffaut, M., Benboudjema, F., Torrenti, J. M., & Nahas, G. (2012). Effects of the early age thermal behaviour on long term damage risk in massive concrete structures. *European Journal of Environmental and Civil Engineering, 16*(5), 598–605.

Buch, N. J., & Jahangirnejad, S. (2008). Quantifying coefficient of thermal expansion values of typical hydraulic cement concrete paving mixtures (No. RC-1503). Michigan Department of Transportation, Construction & Technology Division.

Campbell-Allen, D., & Thorne, C. P. (1963). The thermal conductivity of concrete. *Magazine of Concrete Research, 15*(43), 39–48.

CEB-FIP *fib*. (2013). Bulletin 70. State-of-the-art report: Code-type models for concrete behaviour. Background of MC2010.

Cerny, R., & Rovnanikova, P. (2002). *Transport processes in concrete*. CRC Press.

Choktaweekarn, P., & Tangtermsirikul, S. (2010). Effect of aggregate type, casting, thickness and curing condition on restrained strain of mass concrete. *Songklanakarin Journal of Science and Technology, 32,* 391–402.

Cook, W. D., Aitcin, P. C., & Mitchell, D. (1993). Thermal stresses in large high-strength concrete columns. *ACI Materials Journal, 89*(1), 61–68.

Côté, J., & Konrad, J.-M. (2005). A generalized thermal conductivity model for soils and construction materials. *Canadian Geotechnical Journal, 42,* 443–458.

Coussy, O. (2005). *Poromechanics*. Chichester: Wiley.

Craeye, B., de Schutter, G., Humbeeck, H. V., & Cotthem, A. V. (2009). Early age behaviour of concrete supercontainers for radioactive waste disposal. *Nuclear Engineering and Design, 239*, 23–35.

Cusson, D., & Hoogeveen, T. (2007). An experimental approach for the analysis of early-age behaviour of high-performance concrete structures under restrained shrinkage. *Cement and Concrete Research, 37,* 200–209.

Delsaute, B., & Staquet, S. (2017). Decoupling thermal and autogenous strain of concretes with different water/cement ratios during the hardening process. *Advances in Civil Engineering Materials, 6*(2), 1–22.

Faria, R., Azenha, M., & Figueiras, J. A. (2006). Modelling of concrete at early ages: Application to an externally restrained slab. *Cement and Concrete Research, 28,* 572–585.

Gawin, D., Majorana, C. E., & Schrefler, B. A. (1999). Numerical analysis of hygro-thermic behaviour and damage of concrete at high temperature. *Mechanics of Cohesive-Frictional Materials, 4,* 37–74.

Gawin, D., Pesavento, F., & Schrefler, B. A. (2006). Hygro-thermo-chemo-mechanical modelling of concrete at early ages and beyond. Part I: Hydration and hygro-thermal phenomena. *International Journal for Numerical Methods in Engineering, 67,* 299–331.

Gibbon, G. J., & Ballim, Y. (1998). Determination of the thermal conductivity of concrete during the early stages of hydration. *Magazine of Concrete Research, 50,* 229–235.

Guo, L., Guo, L., Zhong, L., & Zhu, Y. (2011). Thermal conductivity and heat transfer coefficient of concrete. *Journal of Wuhan University of Technology-Materials Science Edition, 26*(4), 791–796.

Grasley, Z., & Lange, D. (2007). Thermal dilation and internal relative humidity of hardened cement paste. *Materials and Structures, 40*(3), 311–317.

Hammer, T. A., & Bjøntegaard, Ø. (2006). Testing of autogenous deformation (AD) and thermal dilation (TD) of early age mortar and concrete—Recommended test procedure. In *International RILEM Conference on Volume Changes of Hardening Concrete: Testing and Mitigation* (pp. 341–346). RILEM Publications SARL.

Hammerschmidt, U. (2002). Guarded hot-plate (GHP) method: Uncertainty assessment. *International Journal of Thermophysics, 23*(6), 1551–1570.

Hamzah, M. O., Jamshidi, A., & Shahadan, Z. (2010). Evaluation of the potential of sasobit to reduce required heat energy and co2 emission in the asphalt industry. *Journal of Cleaner Production, 18*(18), 1859–1865.

Hasanain, G. S., Khallaf, T. A., & Mahmood, K. (1989). Water evaporation from freshly placed concrete surfaces in hot weather. *Cement and Concrete Research, 19*(3), 465–475.

Hobbs, D. (1971). The dependence of the bulk modulus, Young's modulus, creep, shrinkage and thermal expansion of concrete upon aggregate volume concentration. *Materials and Structures, 4*(2), 107–114.

Hollick, J. (2012). Nocturnal radiation cooling tests. *Energy Procedia, 30,* 930–936.

Holman, J. (2009). *Heat transfer* (10th ed.). Boston: McGraw-Hill Education.

Honorio, T. (2015). Modelling concrete behaviour at early-age: Multiscale analysis and simulation of a massive disposal structure. Ph.D. thesis, ENS Cachan, Univeristé Paris-Saclay.

Honorio, T., Bary, B., & Benboudjema, F. (2018). Thermal properties of cement-based materials: Multiscale estimations at early-age. *Cement and Concrete Composites, 87*, 205–219.

Jendele, L., Šmilauer, V., & Cervenka, J. (2014). Multiscale hydro–thermo–mechanical model for early-age and mature concrete structures. *Advances in Engineering Software, 72*, 134–146.

Jensen, O. M., & Hansen, P. F. (1999). Influence of temperature on autogenous deformation and relative humidity change in hardening cement paste. *Cement and Concrete Research, 29,* 567–575.

Jonasson, J.-E. (1994). Modelling of temperature, moisture and stress in young concrete. Ph.D. thesis, Luleå University of Technology, Luleå, Sweden.

Kada, H., Lachemi, M., Petrov, N., Bonneau, O., & Aitcin, P. C. (2002). Determination of the coefficient of thermal expansion of high performance concrete from initial setting. *Materials and Structures, 35,* 35–41.

Khan, M. I. (2002). Factors affecting the thermal properties of concrete and applicability of its prediction models. *Building and Environment, 37,* 607–614.

Kim, K. H., Jeon, S. E., Kim, J. K., & Yang, S. (2003). An experimental study on thermal conductivity of concrete. *Cement and Concrete Research, 33*(3), 363–371.

Klemczak, B. (2011). Prediction of coupled heat and moisture transfer in early-age massive concrete structures. *Numerical Heat Transfer, Part A: Applications, 60,* 212–233.

Kodur, V. (2014). Properties of Concrete at Elevated Temperatures. *ISRN Civil Engineering, 2014,* 468510.

Kovler, K. (1995). Shock of evaporative cooling of concrete in hot dry climate. *Concrete International, 17*(10), 65–69.

Kovler, K., & Zhutovsky, S. (2006). Overview and future trends of shrinkage research. *Materials and Structures, 39*(9), 827–847.

Kusuda, T. (1977). Fundamentals of building heat transfer. *Journal of Research of the National Bureau of Standards, 82*(2).

Kwak, H.-G., Ha, S.-J., & Kim, J.-K. (2006). Non-structural cracking in RC walls. Part I: Finite element formulation. *Cement and Concrete Research, 36*, 749–760.

Lee, Y., Choi, M. S., Yi, S. T., & Kim, J. K. (2009). Experimental study on the convective heat transfer coefficient of early-age concrete. *Cement and Concrete Composites, 31*(1), 60–71.

Litovsky, E. Y., & Shapiro, M. (1992). Gas pressure and temperature dependences of thermal conductivity of porous ceramic materials: Part 1, Refractories and ceramics with porosity below 30%. *Journal of American Ceramic Society, 75,* 3425–3439.

Liu, X., Jiang, W., de Schutter, G., Yuan, Y., & Su, Q. (2014). Early-age behaviour of precast concrete immersed tunnel based on degree of hydration concept. *Structural Concrete, 15*(1), 66–80.

Loser, R., Münch, B., & Lura, P. (2010). A volumetric technique for measuring the coefficient of thermal expansion of hardening cement paste and mortar. *Cement and Concrete Research, 40* (7), 1138–1147.

Lothenbach, B., Matschei, T., Möschner, G., & Glasser, F. P. (2008). Thermodynamic modelling of the effect of temperature on the hydration and porosity of Portland cement. *Cement and Concrete Research, 38,* 1–18.

Luca, J., & Mrawira, D. (2005). New measurement of thermal properties of superpave asphalt concrete. *Journal of Materials in Civil Engineering, 17*(1), 72–79.

Lura, P., & Van Breugel, K. (2001). Thermal properties of concrete: sensitivity studies. Report: Improved Production of Advanced Concrete (IPACS). Lulea University of Technology.

Marshall, A. L. (1972). The thermal properties of concrete. *Building Science, 7,* 167–174.

Maruyama, I., & Teramoto, A. (2011). Impact of time-dependant thermal expansion coefficient on the early-age volume changes in cement pastes. *Cement and Concrete Research, 41,* 380–391.

Maruyama, I., & Teramoto, A. (2012). Effect of water-retaining lightweight aggregate on the reduction of thermal expansion coefficient in mortar subject to temperature histories. *Cem Concr Compos, 34*(10), 1124–1129.

Matschei, T., Lothenbach, B., & Glasser, F. P. (2007). Thermodynamic properties of Portland cement hydrates in the system $CaO–Al_2O_3–SiO_2–CaSO_4–CaCO_3–H_2O$. *Cement and Concrete Research, 37,* 1379–1410.

McCarter, W. J., & Ben-Saleh, A. M. (2001). Influence of practical curing methods on evaporation of water from freshly placed concrete in hot climates. *Built Environment, 36*(8), 919–924.

Mehta P, Monteiro P (2005) Concrete: Microstructure, Properties, and Materials. McGraw-Hill.

Michell, D., & Biggs, K. L. (1979). Radiation cooling of buildings at night. *Applied Energy, 5*(4), 263–275.

Mindess, S., Young, J. F., & Darwin, D. (2003). *Concrete* (2nd ed.). Upper Saddle River: Prentice-Hall.

Modest, M. F. (2013). *Radiative heat transfer*. Academic press.

Morabito, P. (1989). Measurement of the thermal properties of different concretes. *High Temperatures High Pressures, 21*(1), 51–59.

Mounanga, P., Khelidj, A., & Bastian, G. (2004). Experimental study and modelling approaches for the thermal conductivity evolution of hydrating cement paste. *Advances in Cement Research, 16,* 95–103.

Naik, T. R., Kraus, R. N., & Kumar, R. (2010). Influence of types of coarse aggregates on the coefficient of thermal expansion of concrete. *Journal of Materials in Civil Engineering, 23*(4), 467–472.

Neville, A. M. (1997). *Properties of concrete* (4th ed.). London, UK: Wiley.

Pomianowski, M., Heiselberg, P., Jensen, R. L., Cheng, R., & Zhang, Y. (2014). A new experimental method to determine specific heat capacity of inhomogeneous concrete material with incorporated microencapsulated-PCM. *Cement and Concrete Research, 55,* 22–34.

Radjy, F., Sellevold, E. J., & Hansen, K. K. (2003). Isosteric vapor pressure—Temperature data for water sorption in hardened cement paste: Enthalpy, entropy and sorption isotherms at different temperatures. Report BYG-DTU R-057. Lyngby: Technical University of Denmark.

Reinhardt, H.-W., Blauwendraad, J., & Jongendijk, J. (1982). Temperature development in concrete structures taking account of state dependent properties. In *International Conference on Concrete at Early Ages*, RILEM, Paris (pp. 211–218).

Rosen, B. W., & Hashin, Z. (1970). Effective thermal expansion coefficients and specific heats of composite materials. *International Journal of Engineering Science, 8*(2), 157–173.

de Schutter, G. (2002). Finite element simulation of thermal cracking in massive hardening concrete elements using degree of hydration based material laws. *Computers & Structures, 80,* 2035–2042.

Ruiz, J., Schindler, A., Rasmussen, R., Kim, P., & Chang, G. (2001). Concrete temperature modeling and strength prediction using maturity concepts in the FHWA HIPERPAV software. In *7th International Conference on Concrete Pavements*, Orlando (FL), USA, 2001.

Sellevold, E. J., & Bjøntegaard, Ø. (2006). Coefficient of thermal expansion of cement paste and concrete: Mechanisms of moisture interaction. *Materials and Structures, 39,* 809–815.

Tatro, S. B. (2006). Thermal properties. In J. F. Lamond & J. H. Pielert (Eds.), *Significance of tests and properties of concrete and concrete-making materials, STP169D-EB* (p. 2006). West Conshohocken, PA: ASTM International.

Todd, S. (1951). Low-temperature heat capacities and entropies at 298.16 °K of crystalline calcium orthosilicate, zinc orthosilicate and tricalcium silicate. *Journal of the American Chemical Society, 73,* 3277–3278.

Ulm, F. J., & Coussy, O. (2001). What is a "massive" concrete structure at early ages? Some dimensional arguments. *Journal of Engineering Mechanics, 127,* 512–522.

Vargaftik, N. B. (1993) *Handbook of thermal conductivity of liquids and gases*. CRC Press.

Wojcik, G. S. (2001). The interaction between the atmosphere and curing concrete bridge decks. Ph.D. thesis, State University of New York at Albany, Dissertation Abstracts International (Vol. 63-01, Section: B).

Wojcik, G. S., Fitzjarrald, D. R., & Plawsky, J. L. (2003). Modelling the interaction between the atmosphere and curing concrete bridge decks with the SLABS model. *Meteorological Applications, 10*(2), 165–186.

Wyrzykowski, M., & Lura, P. (2013a). Moisture dependence of thermal expansion in cement-based materials at early ages. *Cement and Concrete Research, 53,* 25–35.

Wyrzykowski, M., & Lura, P. (2013b). Controlling the coefficient of thermal expansion of cementitious materials—A new application for superabsorbent polymers. *Cement and Concrete Composites, 35,* 49–58.

Xu, Y., & Chung, D. D. L. (2000). Effect of sand addition on the specific heat and thermal conductivity of cement. *Cement and Concrete Research, 30,* 59–61.

Yeon, J. H., Choi, S., & Won, M. C. (2013). In situ measurement of coefficient of thermal expansion in hardening concrete and its effect on thermal stress development. *Construction and Building Materials, 38,* 306–315.

Yuan, Y., & Wan, Z. L. (2002). Prediction of cracking within early-age concrete due to thermal, drying and creep behavior. *Cement and Concrete Research, 32,* 1053–1059.

Zreiki, J., Bouchelaghema, F., & Chaouchea, M. (2010). Early-age behaviour of concrete in massive structures—Experimentation and modelling. *Nuclear Engineering and Design, 240,* 2643–2654.

Zhutovsky, S., & Kovler, K. (2017). Application of ultrasonic pulse velocity for assessment of thermal expansion coefficient of concrete at early age. *Materials and Structures, 50*(5), 8.

Chapter 4
Mechanical Properties

Farid Benboudjema, Jérôme Carette, Brice Delsaute, Tulio Honorio de Faria, Agnieszka Knoppik, Laurie Lacarrière, Anne Neiry de Mendonça Lopes, Pierre Rossi and Stéphanie Staquet

Abstract Prediction of cracking by autogenous, drying shrinkage and thermal strain requires the knowledge of the development of mechanical properties. The main objective of this chapter is to describe the evolution of the mechanical properties, i.e., elastic properties, strengths, shrinkage, and creep, in cement-based materials. Mechanisms and experimental evidences are given thereafter. The influence of mix design, aging, stress level, cracking, etc., is reported. However, evolution of properties regarding interfaces in the case of prestress concrete, for instance, is not discussed (bond behavior). This chapter has strong interactions with the other chapters regarding the modeling (Chap. 2: hydration, Chap. 3: thermal strain, and Chap. 7: shrinkage, creep and cracking).

F. Benboudjema (✉)
LMT-Cachan/ENS-Cachan/CNRS/Université Paris Saclay, Paris, France
e-mail: farid.benboudjema@dgc.ens-cachan.fr

J. Carette · B. Delsaute · S. Staquet
Université Libre de Bruxelles (ULB), Service BATir, LGC, Brussels, Belgium

T. Honorio de Faria
CEA, DEN, DPC, SECR, Laboratoire d'Etude du Comportement des Bétons et des Argiles, 91191 Gif-sur-Yvette, France

A. Knoppik
Department of Structural Engineering, Silesian University of Technology, Gliwice, Poland

L. Lacarrière
UPS, INSA, LMDC (Laboratoire Matériaux et Durabilité des Constructions), Université de Toulouse, 135, avenue de Rangueil, 31 077 Toulouse Cedex 04 France

A. Neiry de Mendonça Lopes
Management of Research, Services and Technological Innovation, Furnas, Brazil

P. Rossi
IFSTTAR, Champs-sur-Marne, France

© RILEM 2019

E. M. R. Fairbairn and M. Azenha (eds.), *Thermal Cracking of Massive Concrete Structures*, RILEM State-of-the-Art Reports 27,
https://doi.org/10.1007/978-3-319-76617-1_4

4.1 Introduction

This chapter gives a description of the main mechanical properties that will govern cracking due to the restraint of strains (mainly shrinkages) in massive concrete structures. Delayed strains (free deformations and creeps) and quasi-static properties are summarized. Models are presented in Chap. 2 (hydration), Chap. 3 (thermal strain), and Chap. 7 (shrinkage, creep and cracking).

The total strain reads (see also Fig. 4.1):

$$\boldsymbol{\varepsilon} = \boldsymbol{\varepsilon}_e + \boldsymbol{\varepsilon}_{sh} + \boldsymbol{\varepsilon}_{th} + \boldsymbol{\varepsilon}_{cr} + \boldsymbol{\varepsilon}_{in} \tag{4.1}$$

where $\boldsymbol{\varepsilon}$, $\boldsymbol{\varepsilon}_e$, $\boldsymbol{\varepsilon}_{sh}$, $\boldsymbol{\varepsilon}_{th}$, $\boldsymbol{\varepsilon}_{cr}$, and $\boldsymbol{\varepsilon}_{in}$ are the total, elastic, shrinkages (autogenous and drying strains), thermal, creeps, and other inelastic (i.e., "cracking") strain tensors, respectively. Shrinkages and thermal strains are free strains. This strain model takes in account that the strain effects can be superimposed. In fact, these strains are linked: drying and hydration as well as cracking and (non linear) creep are coupled, for instance. Specific care should be taken in the case of complex analysis.

In order to predict the cracking risk if cracking is not taken into account, stresses (or elastic strains) have to be calculated and compared to the strength (or the strain) criteria. For unidimensional problem, stress reads (assuming that inelastic strains are equal to zero):

$$\dot{\sigma} = E_c(\dot{\varepsilon} - \dot{\varepsilon}_{sh} - \dot{\varepsilon}_{cr} - \dot{\varepsilon}_{th}) \tag{4.2}$$

where E_c is the Young modulus.

The shrinkage acts as the motor of cracking, but it is important to take into account the creep strains that may act positively here; i.e., they will lead to a global reduction of the amplitude of stresses during early age (Fig. 4.2 and Eq. 4.3). Note that creep strains have negative impacts; in general, they contribute to reduce the service life of the structures in cases like loss of prestress, generation of differential settlement in structures, excessive deflections.

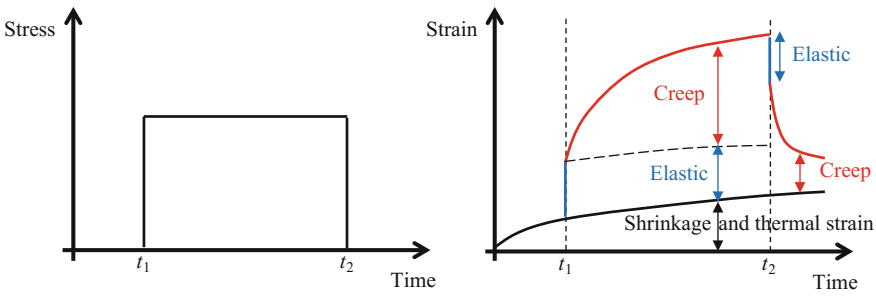

Fig. 4.1 Conventional decomposition of the strains: elastic, shrinkages, and creeps (without cracking)

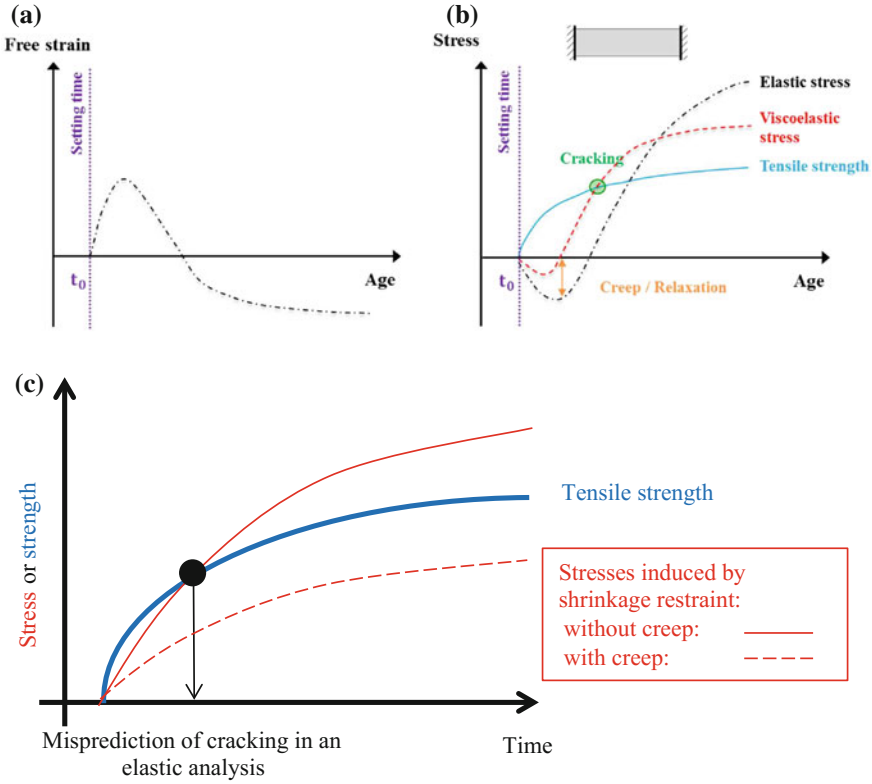

Fig. 4.2 Simplified evolutions in the case of an external restraint: free strain (**a**) and stresses (**b**) for a massive concrete structures (Delsaute et al. 2016a) with expansion (swelling, thermal strain) followed by contraction (autogenous shrinkage, thermal strain); stresses if only free contraction occurs (**c**)

Using the age-adjusted effective modulus method, without taking into account aging, a crack index, I_{cr}, can be roughly estimated (more details are given in Chap. 8):

$$I_{cr} = \frac{E_c R(\varepsilon_{sh} + \varepsilon_{th})}{f_{ct}(1 + \chi\varphi)} \tag{4.3}$$

where f_{ct} is the tensile strength, χ is an aging coefficient, φ is creep coefficient, and R is the restraint coefficient (see Chap. 8). Note that if R is equal to zero, there is no restraint (free shrinkage/thermal strain occur) and if R is equal to one the restraint is full (the total strain is equal to zero).

Note that the cracking index may have a different expression; in this case, more this coefficient is important more the cracking risk is high.

Then using numerical or code models, cracking opening and spacing can be estimated (see Chaps. 7 and 8).

4.2 Static Behavior of Concrete

Development of mechanical properties of concrete is related to the hydration process of cement. To express this dependency, development of mechanical properties can be defined as a function of maturity (with the effect of temperature expressed with the equivalent age) or degree of hydration (or degree of reaction, or degree of heat development). These two approaches are developed hereafter.

Time development of material properties is defined by the function β_c that expresses gain in time with respect to the reference value of a given property:

$$X(t) = [\beta_c(t)]^n \cdot X_{28} \tag{4.4}$$

where n is a material parameter (depending on the type of cement in particular), X is the material property at time t, and X_{28} is the material property at 28 days.

One of the formulations of the time-development functions is with the exponential function which was introduced by Reinhardt et al. (1982). The exponential time development is suggested by the European standards. Brazilian Standard NBR 6118, Model Code (1990, 2010), and Eurocode 2, for instance, propose the following function to describe the time development of mechanical properties:

$$\beta_c = \exp\left[s\left(1 - \sqrt{\frac{28}{t}}\right)\right] \tag{4.5}$$

where t is time (in days) and s is a coefficient dependent on the type of cement.

Alternatively, a hyperbolic function was introduced by Kee (1971). The ACI Report 209 and JSCE (2010) suggest the following function:

$$\beta_c = \frac{t}{a + bt} \tag{4.6}$$

where a and b are experimental coefficients dependent on the type of cement.

Recently, a new model has been proposed by Carette and Staquet (2016) for accurate evaluation of the very early-age development of the mechanical properties. The model uses an exponential function as it is expressed in the following equation:

$$\beta_c = \exp\left(-\left(\frac{p}{t}\right)^r\right) \tag{4.7}$$

where p and r are experimental coefficients dependent on the material and of the mechanical property. Parameter p (in days) is relative to the time at which the main increase of the property occurs, and is therefore affected by the type of cement. As shown in Fig. 4.3, the p parameter of a given cement is higher for compressive strength than for tensile strength and for the elastic modulus. On the other hand, the r parameter is equal to 1 for the compressive and tensile strength and must only be considered in the case of the elastic modulus, in which initial increase is fast in comparison with the strength development. For the elastic modulus, the value of r depends on the cement type and is generally in the range of 1 up to 1.5.

To account for the fact that concrete exhibits actual strength after it reaches a threshold age, t_s, corresponding to initiation of hardening (setting, see Chap. 2), the time component is replaced by the $t - t_s$ (for $t > t_s$) component (Rifai et al. 2016). The exponential formulation is used by numerous authors in Europe (Jonasson 1994; Larson 2003; Kanstad et al. 2003b; de Schutter and Vuylsteke 2004; Azenha et al. 2009; Craeye et al. 2009; Klemczak and Knoppik-Wróbel 2014). The hyperbolic formulation is popular among Far Eastern authors (Yuan and Wan 2002; Xiang et al. 2005). Nevertheless, both approaches prove to give results for development of strength and stiffness compliant with experimental data but material parameters which are dependent on the type of cement—especially the n exponent—should be adjusted based on the experimental data provided (*fib* Bulletin 70; Sofi et al. 2012; Klemczak and Knoppik-Wróbel 2014).

To account for the influence of temperature, the most popular approach is to apply the equivalent age t_e (related to maturity) instead of time t in definition of time dependence. This approach was applied in standards, e.g., Model Code (2010) or Eurocode 2, and is popular in the literature of the subject (Waller et al. 2004; de Schutter and Vuylsteke 2004; Craeye et al. 2009; Klemczak and Knoppik-Wróbel 2014):

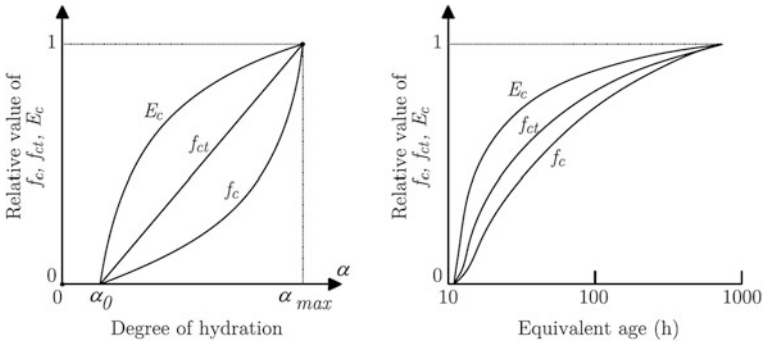

Fig. 4.3 Relative evolution of Young's modulus (E_c), tensile strength (f_{ct}), and compressive strength (fc) with respect to degree of hydration and equivalent age (Azenha 2009)

$$t_e(t) = \int_{\tau=0}^{\tau=t} e^{-\frac{E_a}{R}\left(\frac{1}{T}-\frac{1}{T_{ref}}\right)} d\tau \tag{4.8}$$

where E_a [J mol^{-1}] is the activation energy, R is the constant for perfect gas (8.314 J mol^{-1} K^{-1}), T is the temperature [K], and T_{ref} is a temperature reference [K]. In some standards, the activation energy is fixed at a constant value (e.g., E_a/R = 4000 K in Eurocode 2), whereas experimental results show that it depends significantly on the type of cement (Schindler 2004).

Some authors relate the change in mechanical properties of early-age concrete to the degree of hydration α, degree of reaction (which corresponds to β_c), or degree of heat development α_Q (de Schutter and Taerwe 1996; Gutsch and Rostásy 1994; Faria et al. 2006; Estrada et al. 2006; Benboudjema and Torrenti 2008; Briffaut et al. 2011; Buffo-Lacarriere et al. 2014, 2016). In that approach, development of material properties is related to the final value when the hydration process ends ($\alpha = \alpha_\infty$). The time development β_c is expressed with the function of hydration rate proposed by de Schutter and Taerwe (1996) after Carino (1982):

$$\beta_c(t) = \frac{\alpha(t) - \alpha_0}{\alpha_\infty - \alpha_0} \tag{4.9}$$

where α_0 is a threshold value (percolation threshold corresponding to the setting, see Chap. 2) of the degree of hydration below which no strength development occurs and α_∞ is the degree of hydration at infinite time (it can be replaced by the value at a reference time, 28 days for instance, especially in the case when dealing with the degree of heat development). This equation also can be expressed in terms of degree of reaction.

However, recent early-age measurements tend to show that the mechanical properties of concrete are affected by hydration even before the setting time. Carette and Staquet (2016) observed that after the dormant period, all newly formed reaction products induce an increase of mechanical property. For an accurate evaluation of the very early-age development of the mechanical properties, Carette and Staquet (2016) therefore highlight the relevance of Eq. (4.9). They propose to use this model since the very early age up to hardened concrete.

$$\beta_c(t) = \alpha(t) \tag{4.10}$$

As a matter of fact, this equation is equivalent to Eq. 4.9 in which α_0 is equal to 0 and where α_∞ is equal to 1.

Regardless of the approach used for estimating the relative evolution of mechanical properties (based on maturity/equivalent age or degree of hydration/reaction), it is generally admitted that the Young modulus E_c evolves faster than the

tensile strength f_{ct}, which in turn evolves faster than the compressive strength f_c, as it can be seen in Fig. 4.3.

4.2.1 Compressive Strength

Development of the compressive strength of concrete can be expressed with a time-development function with respect to its reference (usually 28 days) value (n = 1 in Eq. 4.4):

$$f_c(t) = \beta_c \cdot f_{c,28} \tag{4.11}$$

A comparison of different models was made by Klemczak and Batog (2014). Table 4.1 collectively presents the compared functions, and Tables 4.2 and 4.3 show the values of the parameters used. Figures 4.4 and 4.5 show the results of comparison of these models.

Table 4.1 Functions of time development of concrete strength

Code	Function of time and cement type	Function of strength development
CEB/FIP Model Code 1978	$\beta_c(t) = \left(\frac{t}{t+47}\right)^{1/2.45}$	$f_c(t) = \beta_c(t)\frac{f_{c28}}{0.669}$ $f_{ct}(t) = \beta_c(t)\frac{f_{ct28}}{0.669}$
CEB/FIP Model Code 1990/ 2010 Eurocode 2	$\beta_c(t) = \exp\left\{s\left[1 - \left(\frac{28}{t}\right)^{1/2}\right]\right\}$	$f_c(t) = \beta_c(t) f_{c28}$ $f_{ct}(t) = \beta_c(t) f_{ct28}$
ACI Committee 209	$\beta_c(t) = \frac{t}{a+b\cdot t}$	$f_c(t) = \beta_c(t) f_{c28}$ $f_{ct}(t) = 0.0069[w \cdot f_c(t)]^{0.5}$
JSCE	$\beta_c(t) = \frac{t}{a+b\cdot t}$	$f_c(t) = d\beta_c(t) f_{c28}$ $f_{ct}(t) = c\sqrt{10 f_c(t)}$

w is the unit weight of concrete, kg m^{-3}

Table 4.2 Functions of degree of hydration development of concrete strength

Model	Function of degree of hydration	Function of strength development	Coefficient
de Schutter, Taerwe Rostasy	$\beta_c = \left(\frac{\alpha-\alpha_0}{1-\alpha_0}\right)$	$f_c(\alpha) = [\beta_c]^a f_c(\alpha = 1)$ $f_{ct}(DoH) = [\beta_c]^b f_{ct}(\alpha = 1)$	$\alpha_0 = 0.17 \div 0.4$ $a = 1.4 \div 1.5$ $b = 0.88 \div 1.0$
Correction	$\beta_c = \left(\frac{\alpha-\alpha_0}{\alpha_{28}-\alpha_0}\right)$	$f_c(\alpha) = [\beta_c]^a f_{c28}$ $f_{ct}(\alpha) = [\beta_c]^b f_{ct28}$	As above

Table 4.3 Coefficients for function of concrete strength time development

Code	Coefficient	Strength class of cement[a]/Type of cement	Comment
CEB/FIP Model Code 1990/2010 Eurocode 2	$s = 0.20$	Class R (CEM 42.5R, CEM 52.5N, CEM 52.5R)	Class N may be assumed if ground granulated blast-furnace slag (GGBS) exceeds 35% of the cement combination of where fly ash (FA) exceeds 20%; Class S may be assumed if GGBS exceeds 65% or FA exceeds 35%
	$s = 0.25$	Class N (CEM 32.5R, CEM 42.5N)	
	$s = 0.38$	Class S (CEM 32.5N)	
ACI Committee 209	$a = 4.0$ $b = 0.85$ $a = 2.3$ $b = 0.92$	Cement Type I Cement Type III	Suggested coefficients range: $a = 0.05 \div 9.25$ $b = 0.67 \div 0.98$
JSCE	$a = 2.9$ $b = 0.97$ $c = 0.44$ $d = 1.07$	Class R	–
	$a = 4.5$ $b = 0.95$ $c = 0.44$ $d = 1.11$	Class N	–
	$a = 6.2$ $b = 0.93$ $c = 0.44$ $d = 1.15$	Class S	Class S can be assumed for ground granulated blast-furnace slag (GGBS)

[a]Class R = high early strength; Class N = normal early strength; Class S = slow early strength

Using Eq. 4.9, development of the compressive strength of concrete can be expressed as:

$$f_c(\alpha) = [\beta_c]^n \cdot f_{c\infty} \tag{4.12}$$

Depending on the concrete composition (especially the cement type), the value of n exponent ranges between 0.84 and 1.4 according to de Schutter and Taerwe (1996) and between 1.2 and 2.4 according to Carette and Staquet (2016).

4.2.2 Tensile Strength

Development of tensile strength can be also expressed with the same time-development function, β_c, adding a power term n:

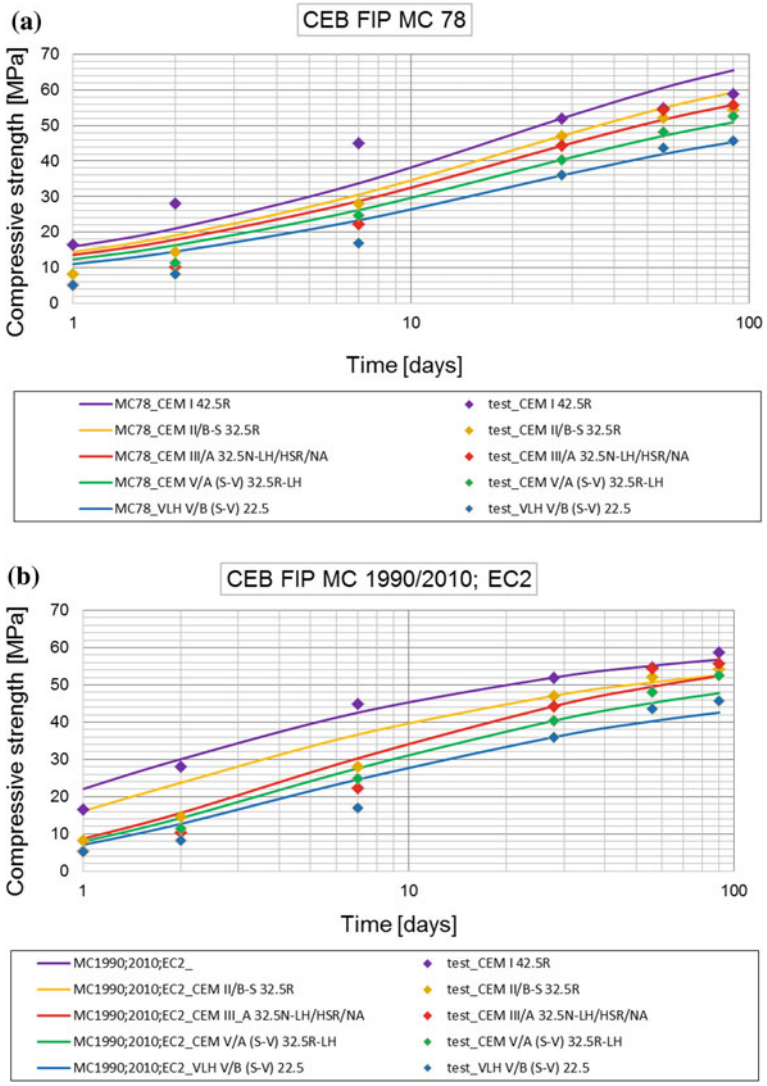

Fig. 4.4 Development of strength according to different time-based functions: comparison (Klemczak et al. 2016)

$$f_{ct}(t) = [\beta_c]^n \cdot f_{t,28} \tag{4.13}$$

For early-age concrete, Eurocode 2 suggests that the rate of tensile strength development is the same as the rate of compressive strength development ($n = 1$), although most of the authors suggest that tensile strength develops faster than compressive strength ($n < 1$). Depending on the concrete composition (especially

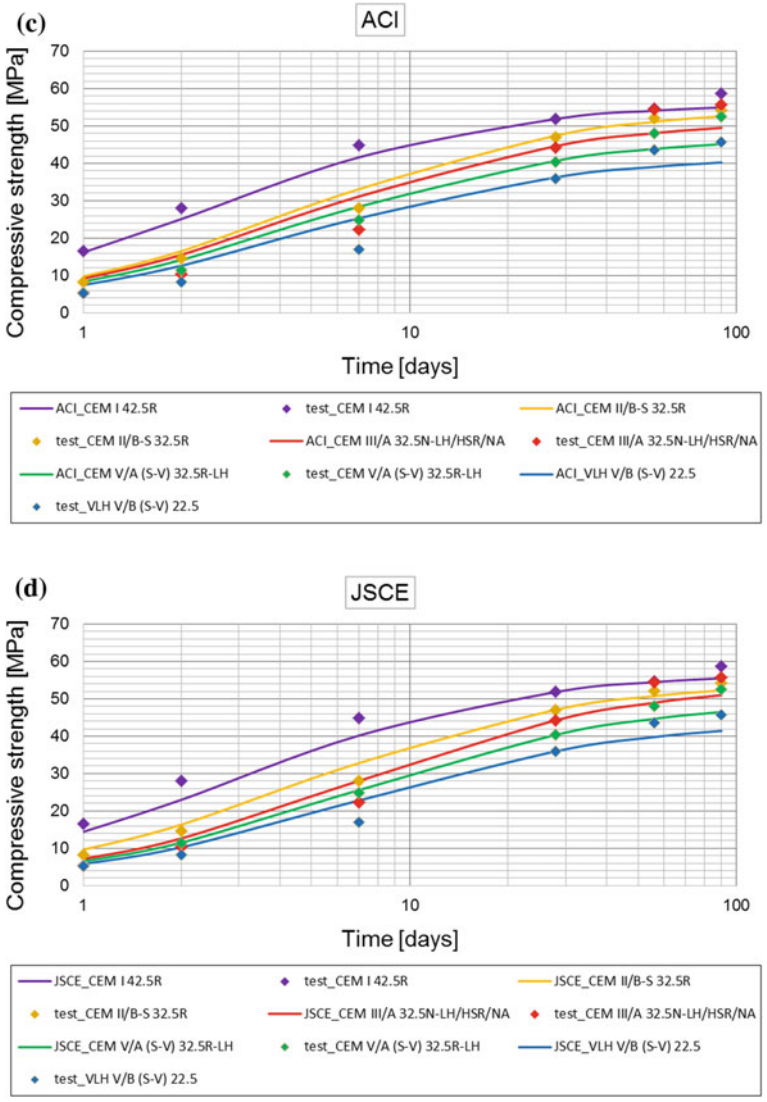

Fig. 4.4 (continued)

the cement type), the value of n exponent ranges between 0.50 and 0.67 according to Kanstad et al. (2003a, b).

Using Eq. 4.9, development of the tensile strength of concrete can be expressed as:

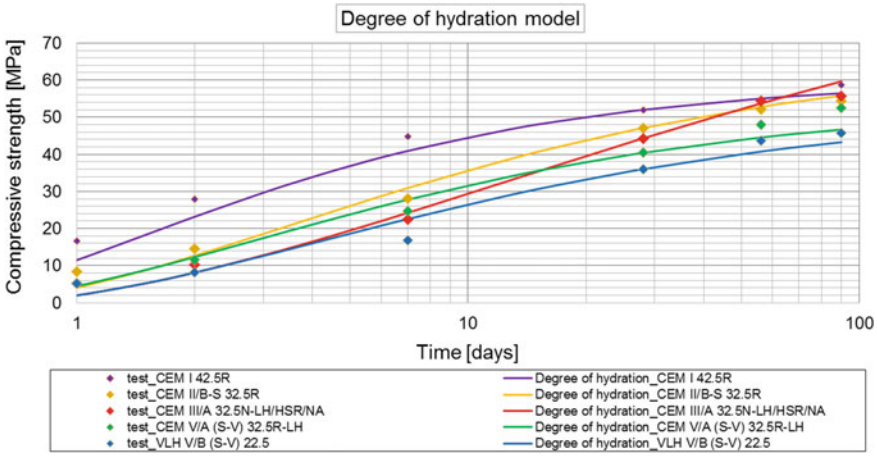

Fig. 4.5 Development of strength according to different degree of hydration-based functions: comparison (Klemczak et al. 2016)

$$f_{ct}(DoH) = [\beta_c]^n \cdot f_{t\infty} \tag{4.14}$$

Depending on the concrete composition (especially the cement type), the value of n exponent ranges between 0.46 and 0.88 according to De Schutter and Taerwe (1996) and between 1 and 2 according to Carette and Staquet (2016).

The tensile strength can be obtained from direct uniaxial test, splitting test, or bending test. The Eurocode 2 proposes that the uniaxial tensile strength is equal to 90% of the splitting test, whereas the Code Model 2010 assumes due to the variability of experimental results to take the same value. The bending strength is higher than the uniaxial tensile strength, which can be explained by the size effect (see thereafter). The tensile strength can be calculated in model code from the compressive strength, but the literature shows a significant scatter.

Several authors observe a significant size (scale) effect. According to Rossi et al. (1994), this effect on concrete in tension is a very important problem when the cracking process of a concrete structure is concerned. This scale effect results in the increasing concrete tensile strength with the decreasing volume of material stressed. This phenomenon is the consequence of the existence of two characteristics of the material: its strong heterogeneity and its important brittleness in tension (Weibull theory, based on the weakest link concept). Its heterogeneity is mainly due to the difference of Young's modulus between the cement paste and the largest aggregate of the concrete.

An experimental study, performed at Institut Français des Sciences et Technologies des Transports, de l'Aménagement et des Réseaux (IFSTTAR) twenty-five years ago (Rossi et al. 1994), concerned uniaxial tensile tests carried out on various concretes (different mix design and compressive strength) and on different specimens size. A strong scale effect was found. Similar results have been

obtained by van Vliet and van Mier (2000). In the framework of their study, Rossi et al. (1994) proposed relations to quantify this scale effect. These relations are the following:

$$m(f_{ct}) = a(\mathrm{V}_S/\mathrm{V}_A)^{-b} \tag{4.15}$$

$$\frac{\sigma(f_{ct})}{m(f_{ct})} = A(\mathrm{V}_S/\mathrm{V}_A)^{-B} \tag{4.16}$$

where $m(f_{ct})$ is the mean value of the uniaxial tensile strength, $\alpha(f_{ct})/\mathrm{m}(\mathrm{f_t})$ is the coefficient of variation related to the uniaxial tensile strength, V_S is the specimen volume, V_A is the largest aggregate volume, $a = 6.5$, $b = 0.25 - 3.6 \times 10^{-3} f_c + 1.3 \times 10^{-5} f_c^2$, $A = 0.35$, $B = 4.5 \times 10^{-2} + 4.5 \times 10^{-3} f_c - 1.8 \times 10^{-5} f_c^2$, f_c is the concrete compressive strength obtained from the French standardized specimen (cylinder with a height of 320 mm and a diameter of 160 mm).

These relations have been validated for 35 MPa $\leq \mathrm{f_c} \leq$ 130 MPa (they have not still been validated for early-age concretes).

In the framework of the same study, it was found that the mean value of the Young modulus of concrete in tension is independent of the volume of material stressed but its coefficient of variation increases with the decreasing volume stressed. This decreasing is quantified by the following relation:

$$\frac{\sigma(E_c)}{m(E_c)} = C(\mathrm{V}_S/\mathrm{V}_A)^{-D} \tag{4.17}$$

with $C = 0.15$ and $D = 0.16 + 2.7 \times 10^{-3} f_c - 3.4 \times 10^{-6} f_c^2$.

4.2.3 Young's Modulus

Time-development function can be also used for description of development of the Young modulus. Thus, this development is usually related to development of compressive strength of concrete (as in the case of tensile strength, the literature shows a significant scatter). Most often the square root function suggested, e.g., implicitly in Model Code (2010) as a square root of time-development function:

$$E_c(t) = [\beta_c]^{0.5} \cdot E_{c,28} \text{ and } E_{c,28} = E_{c,28}\left(f_{c,28}\right) \tag{4.18}$$

or explicitly in JSCE (2010) and ACI Report 209, respectively:

$$E_c(t) = 4.7 \cdot 10^3 \cdot \sqrt{f_c(t)} \tag{4.19}$$

$$E_c(t) = 0.043 \cdot \sqrt{\rho \cdot f_c(t)} \tag{4.20}$$

or explicitly in JSCE (2010) and ACI Report 209, respectively:

$$E_c(t) = [\beta_c]^{0.3} \cdot E_{c,28} \tag{4.21}$$

which complies with observations with other authors who show that the value of exponent of the time-development function, depending on the concrete mix composition, ranges between 0.30 and 0.43 (Kanstad et al. 2003a, b).

Some authors emphasize that the Young modulus differs in compression and tension. It is generally stated that the tensile Young's modulus is higher than the compressive Young's modulus (Brooks and Neville 1977; Atrushi 2003).

Using Eq. 4.9, development of the Young modulus of concrete can be expressed as:

$$E_c(\alpha) = [\beta_c]^n \cdot E_{c\infty} \tag{4.22}$$

Depending on the concrete composition (especially the cement type), the value of n exponent ranges between 0.26 and 0.62 according to de Schutter and Taerwe (1996). However, these values are determined considering a α_0 between 0.1 and 0.3. More recent measurements at very early ages of the elastic modulus indicate that E_c can reach significant values even for a degree of hydration lower than 0.05 (Krauss and Hariri 2006; Carette and Staquet 2016). Therefore, Carette and Staquet (2016) suggest lower values for α_0 (between 0.05 and 0.1) as well as higher values for the n exponent (between 0.4 and 0.8) (Carette and Staquet 2016).

Upscaling methods based on micromechanics have been used to estimate the Young modulus for different concrete compositions (Bernard et al. 2003; Constantinides and Ulm 2004; Sanahuja et al. 2007; Stefan et al. 2010). Such estimations are dependent on the precise knowledge of the cement composition and hydration kinetics as well as the elastic properties of the hydrates, cement, and aggregates.

4.2.4 Poisson's Ratio

Poisson's ratio is found to be very few dependent of the concrete mix and (Neville 2000) suggests using the value of 0.2 regardless the concrete mix (this value is also assumed in Eurocode 2). Regarding the elastic Poisson's ratio, according to Boumiz et al. (1996) and (Byfors 1980), the Poisson ratio decreases from 0.48 to about 0.15 with respect to the α. De Schutter and Taerwe (1996) report a sharp decrease from 0.5 (as in incompressible liquid) to 0.11 of the Poisson ratio, followed by an

increase up to 0.18. This sharp decrease has also been reported by Habib et al. (2002). According to Bernard et al. (2003), the decrease of Poisson's ratio occurs as long as the water phase is continuous and is due to the consumption of water during the hydration process. When the cement begins to set, the water phase becomes discontinuous and the evolution of Poisson's ratio is then governed by the solid stiffness evolution which will increase Poisson's ratio. It can be modeled using the degree of hydration (de Schutter and Taerwe 1996) or the equivalent time (Delsaute et al. 2016a):

$$v(\alpha) = 0.18 \sin \frac{\pi \alpha}{2} + 0.5 e^{-10\alpha} \tag{4.23}$$

$$v\left(t_{eq}\right) = 0.17 \cdot \exp\left(-\left(\frac{10.7h}{t_{eq}}\right)^{2.7}\right) + \left(\frac{1h}{t_{eq} - 13.8h}\right)^{2.6} \tag{4.24}$$

where t_{eq} is expressed in hour.

Similar to the Young modulus, homogenization methods have been applied to estimate the elastic Poisson's ratio (Bernard et al. 2003; Sanahuja et al. 2007; Stefan et al. 2010).

It should be emphasized that some numerical simulations (Azenha 2009; Briffaut et al. 2012) showed that the impact of the variation of Poisson's ratio is not significant and can be disregarded for the prediction of cracking at early age.

4.2.5 Strain Capacity

Strain capacity (named also the peak strain in tension) in tension defines the allowable magnitude of tensile strain of concrete before cracking. At any time t or degree of hydration $\alpha(t)$, it can be determined as a ratio between the tensile strength and the Young modulus of concrete (1D):

$$\varepsilon_{ctu}(t) = \frac{f_{ct}(t)}{E_c(t)} \tag{4.25}$$

where ε_{ctu} is the strain capacity. Note that, it can be extended to 3D and this approach is similar to the one used with a stress approach in the case of non-aging elasticity.

The strain capacity depends in a significant way on the aggregate's properties (see de Schutter and Taerwe (1996) and Roziere et al. (2015), for a review, for instance). Its evolution showed a minimum corresponding to the period that includes the setting time and early hardening, due to a very rapid increase of strength from the end of setting. Therefore, this is a critical stage for plastic shrinkage cracking (Roziere et al. 2015). However, Roziere et al. (2015) found that the strain capacity values are closely linked to the experimental procedure

(i.e., loading rate). From these results, they suggest that an approach based on strength and stresses would be more reliable if early-age cracking is concerned. Hammer et al. (2007) proposed the same conclusion.

4.2.6 *Fracture Energy*

Energy needed to create a localized macro-crack in concrete (fracture energy) is also modified by the hydration process at early ages. Very few results exist in the literature concerning the evolution of this property.

De Schutter and Taerwe (1996) presented some results on concrete with a degree of reaction quite high (0.8–1) and extrapolated a variation law similar to the one proposed for elastic and strength properties (see previously) to lower degree of reaction:

$$G_f(\alpha) = G_{fmax}\left[\frac{\alpha - \alpha}{\alpha_{max} - \alpha_0}\right]^n \tag{4.26}$$

where G_{fmax} is the maximal value of fracture energy that can be reached for the given formulation (in the same environmental conditions that the ones used for the test). This relationship is commonly used with cracking model (e.g., Benboudjema and Torrenti 2008; Buffo-Lacarriere et al. 2014, 2016). Some experimental results are given in Fig. 4.6.

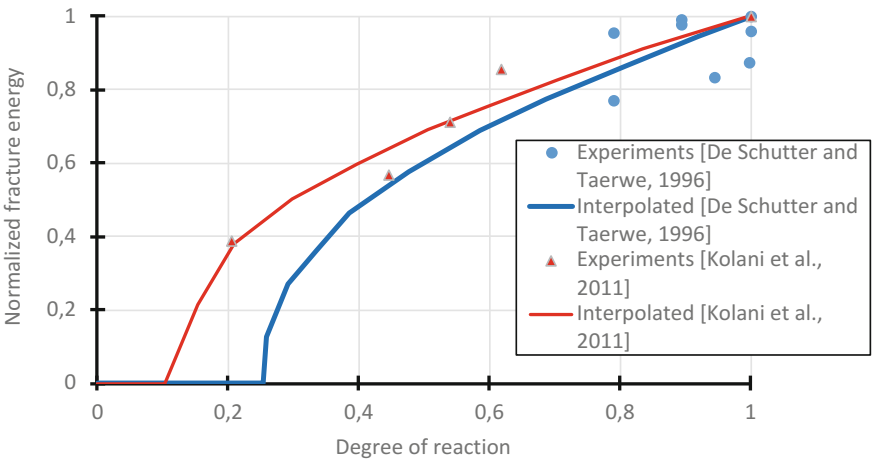

Fig. 4.6 Variation of fracture energy with degree of reaction for a CEM I 52.5 concrete (de Schutter and Taerwe 1996 and Kolani et al. 2011)

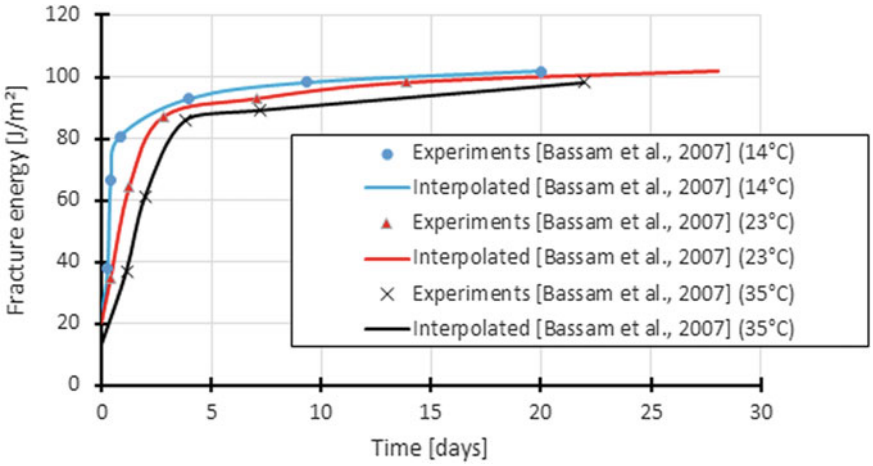

Fig. 4.7 Fracture energy according to time for different curing temperatures (Bassam et al. 2007)

Another approach based on the maturity concept was proposed by Bassam et al. (2007). The variation of fracture energy according to time is evaluated as follows using a thermal activation of mechanical development properties:

$$G_f = G_{fu} \frac{\beta e^{-\frac{E}{RT_k}}(t - t_s)}{1 + \beta e^{-\frac{E}{RT_k}}(t - t_s)} \tag{4.27}$$

where G_{fu} is the fracture energy reached at high ages for the given formulation of concrete and in environmental conditions similar to the test ones E/R is the relative activation energy, T_k is the temperature, and β is a fitting parameter.

This approach was validated on fracture energy measurements obtained at different curing temperatures (14, 23, and 35 °C) and at testing ages from 1 to 28 days (see Fig. 4.7).

The quick variation of fracture energy at very early age (in regard with the elastic properties or strength, for instance) that can be observed on Bassam's results is confirmed in Kim et al. (2004), especially for normal and high performance concrete (NS and HS, Fig. 4.8) and in Kolani et al. (2011), which compared for a same concrete, the development of fracture energy with the one of tensile strength (Fig. 4.9).

4.2.7 Multiaxial Stress State

Failure of concrete element should be analyzed in a complex, three-axial stress state allowing to determine the character of the occurring crack (*fib* Bulletin 70). The failure is referred to the failure surface, which is a spatial representation of possible

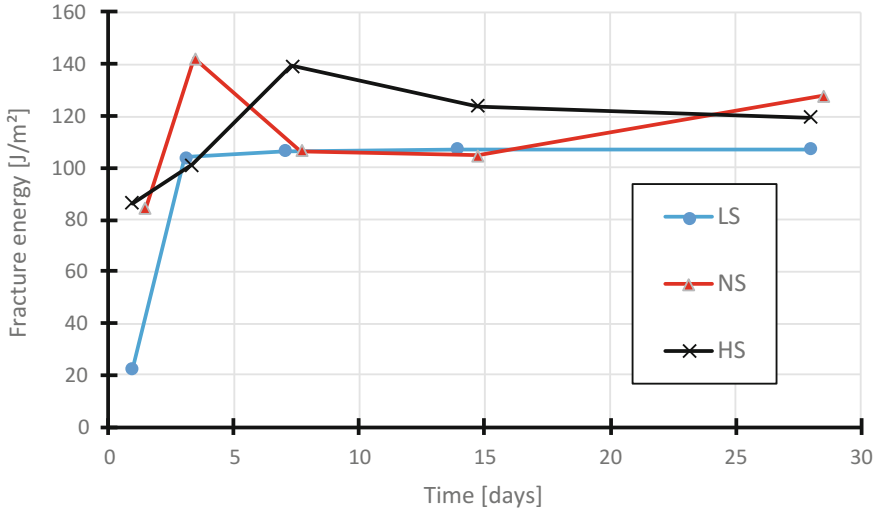

Fig. 4.8 Variation of fracture energy for low performance concrete (LS), normal concrete (NS), and high performance concrete (HS) (Kim et al. 2004)

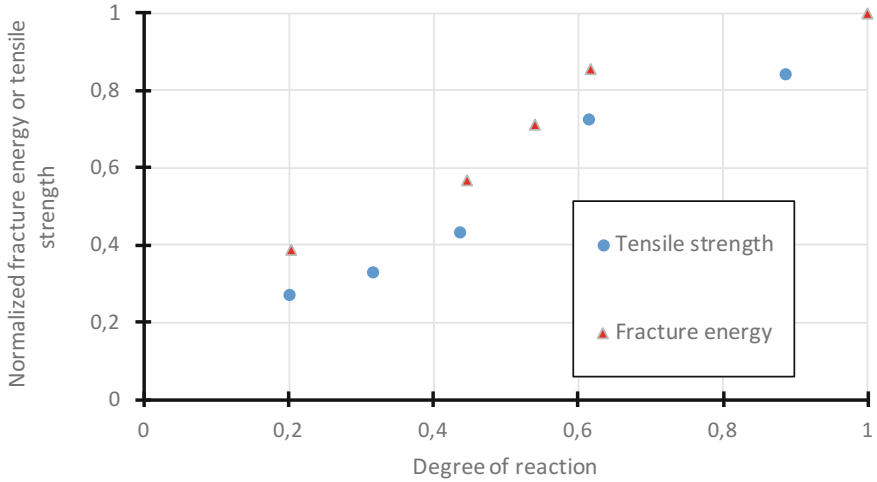

Fig. 4.9 Comparison of tensile strength and fracture energy development (Kolani et al. 2011)

states of stresses for a material. The strengths of the material in certain specific stress states, such as uniaxial compression or tension, or biaxial compression or tension, are the points on the surface.

The biaxial compressive strength can be calculated as follows (*fib* Bulletin 70):

$$f_{cc}(t) = \left[1.2 - \frac{f_c(t)}{1000}\right] f_c(t) \tag{4.28}$$

Regarding the biaxial tensile strength, it is similar to the one in uniaxial tension, suggesting that the orthogonal cracks do not interact significantly.

4.2.8 Experimental Test Methods

The test procedure to measure the Young modulus is not universal and differs according to the country. The different standards have in common to apply several consecutive loads on a sample. According to the European standard EN 12390-13, three preliminary loading cycles have to be applied in order to control the stability and the centering of the sample inside the press with a loading rate corresponding to (0.6 ± 0.2) MPa/s up to a load of 10–15% of the compressive strength. Then, three loading cycles are performed in order to define the secant Young's modulus. During these cycles, the stress varies between the maximal load applied during the preliminary loadings and the third of the compressive strength. For each loading, the load is kept constant during maximum 20 s. According to the ASTM Standard C469, at least two loading cycles have to be performed to define the chord Young's modulus. The load is applied at a constant loading rate within the range of (241 ± 34) kPa/s (hydraulically operated machine) or at constant displacement rate of about 1.25 mm/min (testing machines of the screw type). No preliminary loading is applied, and the load varies between 0 and 40% of the compressive strength. The longitudinal displacement is generally measured by means of strain gauges or an extensometer.

For the computation of Poisson's ratio, the transversal displacement is also necessary and is defined either by measuring the radial displacement (e.g., extensometer with elastic anchorage) or the circumferential displacement of the specimen (e.g., strain gauges and extensometer).

Currently, no recommendation or standard test method exists for the determination of the Young modulus for concrete at very early age. The experimental challenge lies in the fact that the monitoring must be fully automatic since the earliest age because the hardening process of the concrete takes place continuously over a period counted in hours and even in days after the casting time. Recently, new test procedures and devices were developed for the monitoring of the Young modulus since the casting or the final setting till several days by means of repeated loadings (Staquet et al. 2012; Boulay et al. 2012; Delsaute et al. 2016c; Boulay et al. 2014; Karte et al. 2015 and Irfan-ul-Hassan et al. 2016). Two different sorts of test protocol were developed. The first kind of protocol imposes a constant displacement (Boulay et al. 2014) or force (Karte et al. 2015) threshold for each loading during the whole test. The second protocol considers the evolution of the

compressive strength, and the load applied corresponds to 15 (Irfan-ul-Hassan et al. 2016) or 20% (Delsaute et al. 2016c) of the compressive strength.

To perform mechanical test since casting or setting, it is needed to test the sample directly in the mold. Such test was performed in Delsaute et al. (2016c) with a Temperature Stress Testing Machine (Staquet et al. 2012) for which the sample is loaded horizontally or with another vertical device BTJASPE (Boulay et al. 2012) for which the sample is loaded vertically. For each case, a thermal regulation surrounds the sample before and during the test in order to control the temperature inside the sample.

4.3 Shrinkage

Early-age cracking is generally due to volumetric changes, caused by autogenous and drying shrinkages, resulting from water movement and thermal gradients. If the cementitious material is free to move, concrete shrinkage and expansion produce few consequences. Nevertheless, deformation may occur if there are external or internal concrete restrictions. In these cases, the tensile stresses may induce the occurrence of micro-cracks, which can connect to each other to form cracking, seriously impairing the service life and aesthetics of the structure (Lopes et al. 2013). The origins of the deformation occurring in concrete are shown in Fig. 4.10. It should be noticed that the term "shrinkage" is generally used when referring to

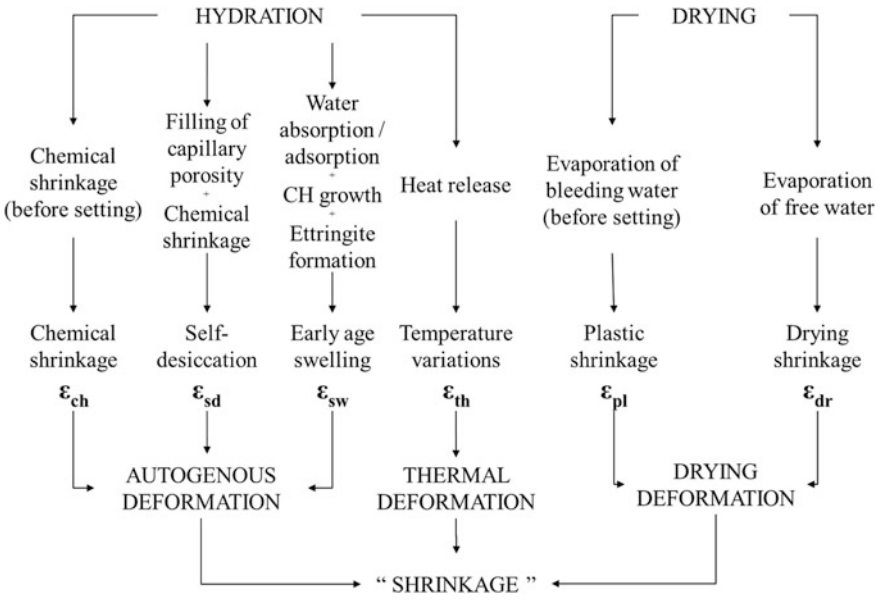

Fig. 4.10 Schematic view of the strain mechanisms contributing to the concrete shrinkages

the combination of the hydration- and drying-induced deformations due to the fact that they generally result in overall shrinkage. The terms "autogenous deformation" and "drying deformation" could be more appropriate.

The process of concrete hardening is accompanied with moisture migration which can lead to reduction of concrete volume and consequent shrinkage of a concrete element. The water is transported within and out of concrete element due to various phenomena. The loss of water through desiccation and evaporation at the surface of the element is called drying shrinkage. Desiccation of water is driven by concentration gradients within the elements caused by humidity difference between the element and the ambient surrounding with a RH lower than that found in the capillary pores. Water is transferred by vapor transfer and capillary transfer. On the other hand, in autogenous shrinkage, there is a decrease in internal RH by self-desiccation in the cement paste due to the consumption of evaporable water during hydration reactions. The autogenous deformation is governed by a combination of chemical shrinkage, self-desiccation, and swelling, with the influence of the former one more pronounced in the very early ages (before setting). Chemical shrinkage results from the reduction in material volume as water is consumed by hydration: When water and cement react, the volume of the products of this reaction is 7–10% less than that of cement (clinker) and water. After the setting time, this mechanism induces a decrease of the internal RH by self-desiccation. In parallel, some hydration products are known to generate expansion of the cement matrix at early age, thus resulting in overall swelling. The self-desiccation deformation is often considered proportional to the degree of hydration (Ulm and Coussy 1998; Mounanga et al. 2006; Benboudjema and Torrenti 2008; Briffaut et al. 2016; Honorio et al. 2016).

Thermal strains are analyzed in Chap. 3.

4.3.1 Autogenous Shrinkage

4.3.1.1 Mechanisms

Jensen and Hansen (2001) were among the first to propose a unified nomenclature regarding autogenous shrinkage and description of its mechanisms. A revision of the mechanisms supported with experimental and modeling studies was presented also by Lura et al. (2003).

During hydration of cement, reduction of volume of reaction products (hydrated cement) is observed with regard to the volume of the constituents (unhydrated cement and water). This phenomenon is referred to as chemical shrinkage and reaches approximately 6–7 ml per 100 g of cement (clinker) reacted ("le Châtelier" contraction, Taylor 1990). Before setting, when the material is still in plastic stage, chemical shrinkage manifests in overall volume reduction, and in this stage the cracking may be caused by the lack of deformability not by stress (phase 1 in Fig. 4.11).

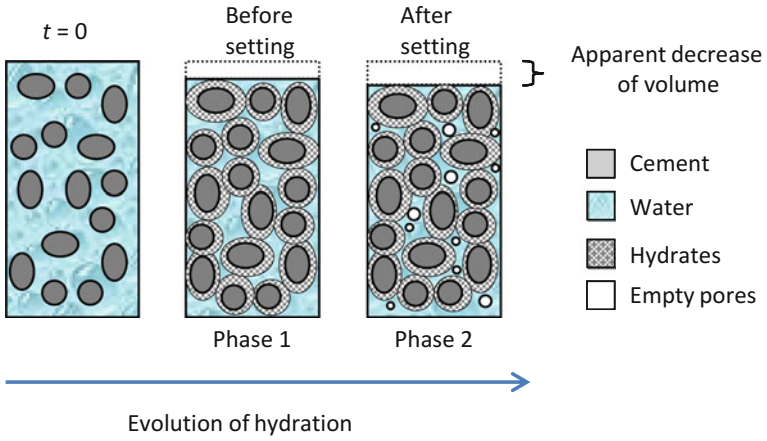

Fig. 4.11 Phases of autogenous shrinkage development

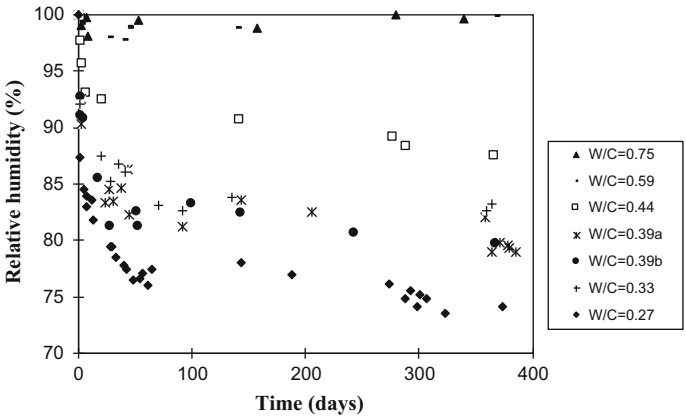

Fig. 4.12 Drop of relative humidity in autogenous conditions for different water-to-cement ratio (Yssorche-Cubaynes and Olivier 1999)

After setting takes place, the decrease in the absolute volume becomes incompatible with deformations mechanically permissible by the emerging mineral skeleton and thus chemical shrinkage manifests in creation of large empty pores (phase 2 in Fig. 4.11). A progressive desaturation of capillary pores due to hydration of the cement and a decrease in the internal relative humidity occur (called self-drying or self-desiccation; the Fig. 4.12 summarizes some experimental results of drop of relative humidity in autogenous conditions). This phenomenon stops usually at relative humidities below 75% (Hua et al. 1995). There are three physical mechanisms explaining this phenomenon (Hua et al. 1995):

1. With consumption of water from smaller and smaller pores in the course of hydration and formation of gas-filled pores, menisci form on the water–gas

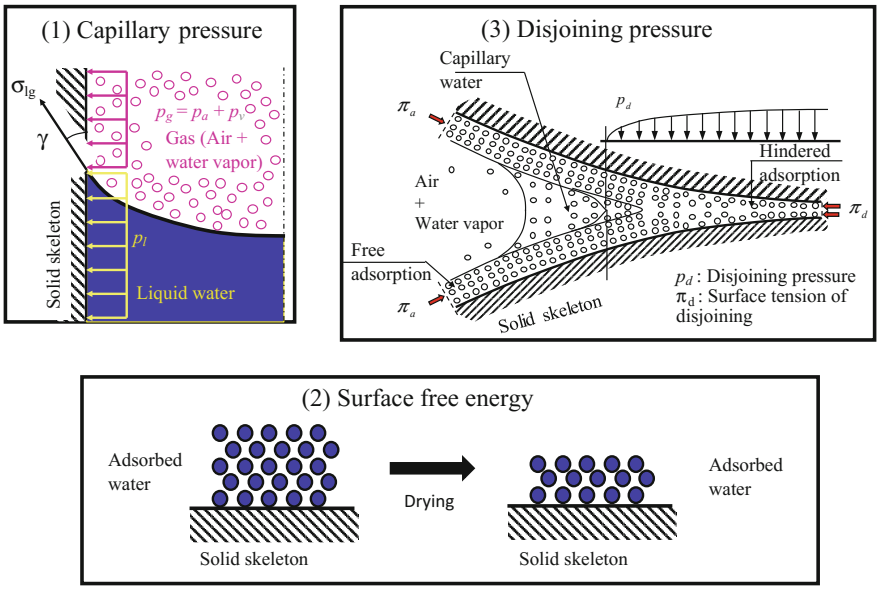

Fig. 4.13 Schematic representation of the capillary depression

interfaces due to the action of surface tension (Lura et al. 2003; Jensen and Hansen 2001). This leads to an increase of capillary tension in pore fluids in accordance with Young–Laplace law and corresponding decrease of RH in accordance with Kelvin law. Capillary tension in pore fluid is balanced by compressive stress in the solids ((1) in Fig. 4.13).

2. Reduction of thickness of water adsorbed on solid surfaces ((2) in Fig. 4.13), leading to increase of surface tension of the solids (mechanism leading to shrinkage) and
3. Decrease of the disjoining pressure ((3) in Fig. 4.13) in hindered adsorption areas (mechanism leading to shrinkage).

Although the mechanisms leading to autogenous shrinkage are still not fully understood, the three aforementioned mechanisms have been debated in an attempt to understand the driving forces behind autogenous shrinkage. However, there is agreement about relationship between autogenous shrinkage and changes in RH in the pores of hardened cement paste (Lopes et al. 2013). The dominating role of capillary tension has been shown in several studies (e.g., Lura et al. 2003; Hua et al. 1995; Gawin et al. 2008).

The thermodynamic approach to explain capillary pressure mechanism involves two aforementioned macroscopic laws: Kelvin law (Eq. 4.29) and Laplace law (Eq. 4.30). They describe directly the water liquid–vapor equilibrium and mechanical equilibrium of a meniscus set at both sides at different pressures, respectively. The Kelvin law reads:

$$P_c = P_l - P_g = \frac{\rho RT}{M} \ln RH \tag{4.29}$$

where P_c is the capillary pressure, P_l and P_g are pressures of liquid water and gas, respectively, R is a universal gas constant (8.314 J/(mol K)), M is the mass of a water molecule (18×10^{-3} kg/mol), T is the temperature (K), ρ is the specific volume of water (kg/m^{-3}), and RH is the relative humidity in the capillary pore. At a relative humidity of 90% and a temperature of 20 °C, the capillary pressure is equal to about −14 MPa.

The Laplace law reads:

$$P_l - P_g = \frac{2t \cos\theta}{r} \tag{4.30}$$

where t is superficial tension at the gas–liquid interface (N/m), θ is the contact angle (°), and r is the radius of the capillary pore (m). At a relative humidity of 90%, a temperature of 20 °C and a contact angle equal to zero, the radius of the pore is equal to about 12 nm (without taking into account the thickness of adsorbed water layer).

Based on these laws, it is possible to link the intensity of capillary pressure (P_c), the pore radius (r) in which the meniscus is located, and the internal relative humidity (RH). With simple calculations, it can be shown that the capillary depressions can reach high values for pore sizes commonly found in the cement matrix. Thus, it is possible to see the autogenous shrinkage as the mechanical deformation of the solid skeleton under the effect of capillary pressure. During the hydration, the intensity of the capillary depressions increases for two reasons (Boivin 1999):

1. Self-desiccation progresses throughout the material reaching narrower and narrower pores (decrease of the radius r of the capillary pores), causing a decrease in the internal relative humidity (RH) (Eq. 4.29).
2. The porosity of the cementitious matrix is refined (decrease of the radius r of the capillary pores) during the self-desiccation, leading to stronger capillary depressions during the self-drying process (Eq. 4.30).

Self-desiccation shrinkage and autogenous shrinkage were distinguished by Jensen and Hansen (2001), with the latter including also deformation due to initial swelling (that cannot be explained by the thermal deformations) of other mechanisms occurring in addition to self-desiccation. Swelling may be of utmost importance since the ability of a concrete to develop low shrinkage deformation can lead to significant durability improvement. Several mechanisms are proposed to explain this behavior (Carette 2015):

1. Water absorption by concrete leads to a swelling behavior due to the canceling of self-desiccation deformation (Bjøntegaard et al. 2004). In autogenous

conditions, this excess water can either come from bleeding or from the water contained in the aggregates.

2. In the presence of fine particles (fillers) in concrete, significant early-age swelling peaks can be observed. For instance, Esping (2008) observed swelling peaks up to 800 μm/m on self-compacting concrete. Similar observations were made with the incorporation of several filler fineness and nature (Craeye et al. 2010). According to Craeye et al. (2010), this swelling is due to the adsorption of water by the filler and the resulting disjointing pressure. He concluded that the swelling amplitude and kinetics were not only a function of the filler fineness but also to its nature.
3. It has been observed that slow early-age swellings can occur due to the formation and growth of large size portlandite crystals (Baroghel-Bouny et al. 2006). This observation is mostly related to the size of the crystals rather than to their amount, as observed on various water/cement mixtures. This swelling is mainly attributed to CH crystals.
4. The formation of ettringite is accompanied with an expansion. This property has led to the development of expansive concrete with the use of type K cements. Two mechanisms are proposed for this early-age expansion. First, it can be explained by the formation of ettringite around anhydrous or hydrated grains. Due to the porous aspect of ettringite (due to its needle-like structure), its volume occupies more space than its original constituents and therefore induces a matrix expansion as soon as it comes in contact with another ettringite layer (Bentur and Ish-Shalom 1974). In parallel, part of ettringite forms as colloidal particles in through-solution. These high specific surface particles result in water adsorption and therefore to an apparent cement expansion (Mehta 1973).

4.3.1.2 Main Influencing Parameters

The binder. Autogenous shrinkage depends strongly on the type of cement—its chemical composition and morphology (Baroghel-Bouny 1994). Increased amounts of C_3A and C_4AF visibly contribute to increased shrinkage at early age (Justnes et al. 1998, Parak et al. 1998) due to their high water consumption during hydration (Persson 2000; Beltzung and Wittman 2002).

The fineness of cement influences self-desiccation shrinkage due to its impact on the porosity of the material: For the same progress of hydration reactions, finer cement also leads to a finer porous network. The intensity of the capillary depressions caused by self-drying is therefore higher (van Breugel 1991). The reactivity of cement is also influenced by this parameter: Greater fineness of cement increases its reactivity, leading to accelerated development of autogenous deformation and an increase of its final value (Jensen 2000).

In addition to the chemical composition of cement, it is also necessary to consider the influence of mineral additions on autogenous deformation concerning their pozzolanic behavior and their role as filler. It should be noted, however, that in

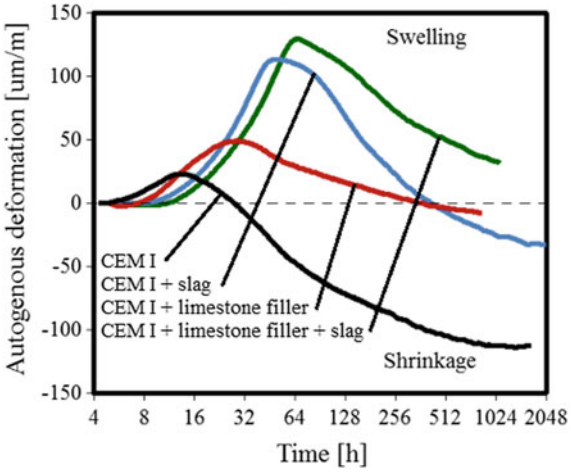

Fig. 4.14 Autogenous deformations including swelling and self-desiccation in presence of CEM I, limestone filler, and blast-furnace slag (Carette et al. 2017)

cementitious materials containing blast-furnace slag swelling of the cementitious matrix may appear at very early age (<24 h) (Darquennes et al. 2011; Aly and Sanjayan 2008; Carette et al. 2017) which may lead to a decrease in total autogenous shrinkage. As a matter of fact, such swelling can be observed even for usual concrete at very early age. Carette et al. (2017) observed this for various concrete compositions containing various amounts of blast-furnace slag and limestone filler. The high swelling deformations observed in Fig. 4.14 are attributed to the ettringite formation, which is highly increased in presence of blast-furnace slag. Limestone filler also contributes to the swelling by similar mechanisms (Carette et al. 2017).

W/C ratio. Autogenous shrinkage depends strongly on the water/cement ratio (*w/c*) due to its impact on reduction of the internal relative humidity. In concretes with low *w/c* ratio (less than 0.4), such as high performance concretes, autogenous shrinkage develops faster and reaches the final value at younger age than that of concretes with higher *w/c*. This behavior is caused by the decrease of the internal

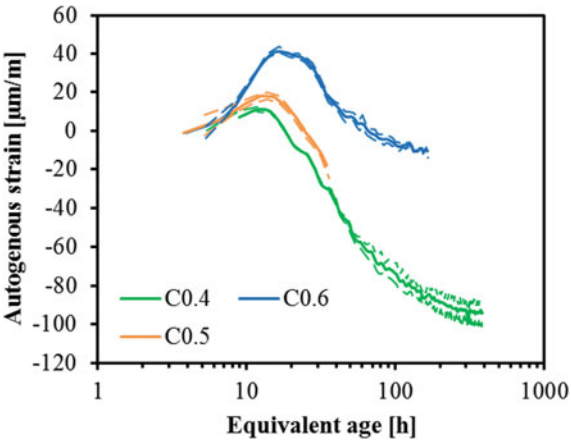

Fig. 4.15 Evolution of the autogenous strain for different water–cement ratios (0.4–0.5 and 0.6). Adapted from (Delsaute 2016b)

relative humidity which is more important for self-desiccation in a finer porous network (Boivin 1999; Holt 2005; Lopes et al. 2013). Generally, for concrete this type of deformation is significant only below a *w/c* ratio of 0.4 (Baroghel-Bouny and Kheirbek 2000).

For concretes with high w/c ratio (higher than 0.4), autogenous swelling develops just after the final setting. In Delsaute et al. (2016b), several tests on concrete with different w/c ratio were performed and are shown in Fig. 4.15. It is observed that the higher the w/c ratio, the greater the duration and the amplitude of swelling.

Aggregates. The porosity of aggregates and their humidity influence the value of shrinkage much more when the *w/c* ratio is low (Toma 1999). Dry aggregates will absorb water which remained available for the hydration, leading to a decrease in the *w/c* ratio producing a denser cement paste structure with finer pores. The capillary depressions will be higher, generating more significant shrinkage. The wet aggregates (porous) will play the role of reservoir and provide additional water when the water is partially consumed by the hydration of cement. This will result in an increase in the *w/c* ratio and reduced shrinkage.

4.3.1.3 Amplitude of Strains

Table 4.4 presents the magnitude of the autogenous shrinkage strain after 28 days for conventional concrete—based on the EC2 Part 1.1—and with additions. However, as observed previously, these values are the result of a combination of swelling and shrinkage. It is to be expected that specific concrete compositions might present overall swelling, especially in presence of high amount of blast-furnace slag and with high w/c ratio. For instance, Carette et al. (2017) observed amplitude of autogenous deformation of 100 μm/m for OC, of 50 for OC with slag, and a negative value of −50 for OC with slag and limestone filler.

4.3.1.4 Experimental Test Methods

Different methods exist for the determination of the autogenous deformations. The methods can be in general divided into linear and volumetric. It is normally assumed that the volumetric autogenous strain is isotropic; thus, the linear autogenous strain can be approximated as one-third of the volumetric one. In the linear method, elongation and shortening of a sample kept in isothermal condition are followed by either measurements of the sample length change with, e.g., LVDTs or

Table 4.4 Magnitude of the autogenous shrinkage strain

	OC	HPC	OC + slag	OC + silica fume
f_{ck} [MPa][a]	25	90	22	90
ε^{au} [μm/m]	24	131	150	289

[a]Characteristic compressive strength of concrete

optical systems or by strain measurements on the sample with, e.g., strain gauges or vibrating wire extensometer. In the volumetric method, the sample is immersed in the bath containing liquid of known density; see, e.g., (Loser et al. 2010). By suspending the sample from the balance, the volume changes can be followed by measuring apparent mass changes of the immersed sample.

Moreover, autogenous strain is very sensitive to the conditions of preservation of the specimen and to many factors related to the test rig. For that reason, several recommendations were developed in the past (Bjøntegaard et al. 2004; Hammer et al. 2007; ASTM Standard C1698; Jensen and Hensen 2001). The main common requirements for all the apparatus for free deformation test in sealed condition are their ability to:

- perfectly seal the specimen in order to avoid any external drying or water uptake;
- keep the temperature constant, which requires external control because the hydration of cement paste releases heat;
- limit the friction with the specimen.

It should be noted that only the ASTM C1698-09 standards exist for cement paste and mortar. No standard has been developed for concrete material.

4.3.2 Plastic and Drying Shrinkage

The concrete plastic and drying shrinkage is the deformation caused by drying (transport of liquid water/water vapor to the outside) due to the lack of equilibrium between the humidity of the material and the surrounding environment. The excess water that has not reacted with the cement is subjected to various phenomena: diffusion of water vapor, permeation of liquid water and moist air, etc.

Just after the casting of concrete, water at the surface of fresh concrete can be lost by evaporation. As soon as the content of evaporated water is larger than the one coming from bleeding, a plastic shrinkage occurs. By definition, it occurs before the end of setting, and drying shrinkage takes over. The risk of cracking is quite of importance for thin elements (rendering mortars, screeds, etc.) since evaporating surfaces are more larger than their volume.

Plastic and drying shrinkage can be a priori neglected in massive concrete structures (dams, liquefied natural gas (LNG) reservoirs, containments in nuclear power plants, etc.). On the one hand, water exchanges are 10^3–10^6 times slower than the thermal phenomena and have influence only in a thin layer of concrete located near the surface of a massive structure. The resulting cracking may be only superficial. This cracking is, however, more damaging for thin structures (repair layers, paving, facade mortar, etc.). The cracking risk can be largely reduced if efficient curing is undertaken.

This strain component is therefore not detailed in this STAR.

4.4 Creep

Creep is the time- and stress-dependent strain which occurs under prolonged application of load. Creep strains are generally split into three components: basic creep, drying creep, and thermal transient creep (called also load-induced thermal strain). Basic creep is defined as creep occurring under no moisture exchange between the concrete and the environment at constant temperature. When moisture is exchanged with the environment at constant temperature, there is an additional creep component referred to as drying creep or Pickett effect. When temperature variation occurs, there is an additional creep component referred to as thermal transient creep.

Note that these definitions are purely conventional and several couplings exist between these three components. Indeed, basic creep, for instance, depends upon internal relative humidity and temperature, which evolves because of hydration. The variation of temperature may lead to evaporation or condensation of water, inducing drying and wetting, and vice versa. The creep effect can also interfere significantly in structural analysis because it changes stress behavior inside of the structure and consequently can modify design projects. This effect is known as a viscoelastic behavior, and it is often considered in structural analysis by means of creep coefficients or functions that try to explain the phenomenon by simplified models.

4.4.1 Basic Creep

4.4.1.1 Mechanisms

The mechanisms at the origin of creep have been investigated for several decades, but they are still not fully understood. This may be due to the fact of the phenomena being associated with various internal and external intervenient factors of the concrete that correlate among themselves (coupled phenomena) as well as the fact that its origin is linked to behaviors at the nanoscale, in which observation, evaluation, and monitoring are very difficult. Nevertheless, there is a general agreement that creep of concrete has its source in hydrates (mainly C–S–H), involves water, and at especially high stress, interacts with micro-cracking and debonding of the cement paste–aggregate interface.

Several theories for (basic) creep mechanisms have been proposed over the years to explain the origin of creep in cement-based materials (see Neville et al. 1983 for a review), but it is generally agreed that none of the proposed theories is capable to account for all the observed phenomena. None of them can explain in a unified way the behavior of concrete under various environmental conditions and under various states of stress (compression, tension, and multiaxial). Several mechanisms may be involved to explain creep.

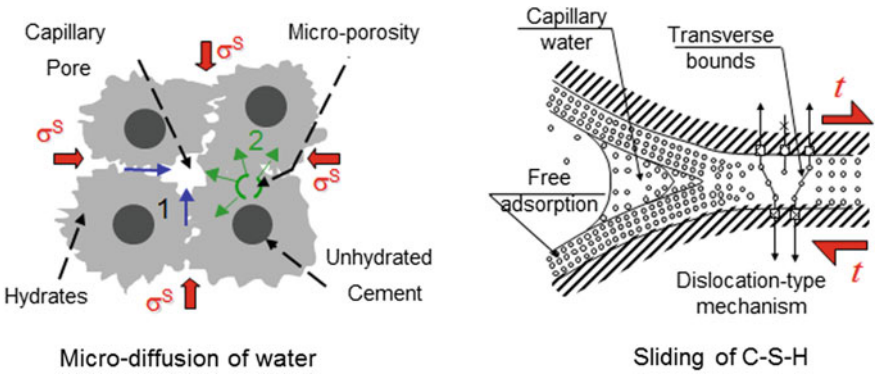

Fig. 4.16 An example of mechanisms for basic creep (Ruetz 1968; Lohtia 1970; Acker and Ulm 2001)

Recently, short- and long-term components of the viscoelastic behavior are generally separated (see Fig. 4.16). The short-term (characteristic time is about a few days) component is reported to occur due to a change of the hygral equilibrium in the gas-filled space which generates strains, stresses, and micro-cracking (Ruetz 1968; Lohtia 1970; Wittmann 1982). This internal state stress of the micropores, though evolutionary, due to the hydration process at early ages is even less significant due to the transient state of formation of the concrete stiffness matrix causing the creep to be more significant in this component. This component is generally associated with the reversible part of creep. The long-term component corresponds to an irreversible viscous behavior which may be related to slippage between layers of C–S–H, and which would increasingly fade in time (Ruetz 1968; Lohtia 1970), and is supposed to occur at constant volume according to Acker and Ulm (2001). The creep rate of this long-term phenomenon evolves as a power function t^n (Bažant 1984; Wittmann 1982) with an exponent n between −1 and −0.9 according to Bažant (1995), between −0.72 and −0.69 according to results of Wittmann (2015) on concrete, and an exponent n between −0.86 and −0.6 on cement paste according to results of Tamtsia et al. (2004). Nanoindentation tests were carried out on C–S–H by Vandamme and Ulm (2009). It was shown that C–S–H exhibits a logarithmic creep at short term which is in agreement with results obtained on concrete at long term. Vandamme (2015) compared also this logarithmic behavior with other heterogeneous and porous materials with porosity including several orders of magnitude (soils and wood). For these non-aging materials, a logarithmic long-term creep was also observed. It can then be assumed that this long-term creep is not linked to a hydration process or any chemical specificity of the C–S–H.

Other mechanisms have been proposed more recently to explain basic creep. Sellier et al. (2015) suggested that sliding of C–S–H induces reversible (due to reversible arrangement of inter-layer water molecules) and irreversible (break and restoration of inter-layer bonds as in plasticity theory) creep. During creep, some material rearrangement (interlocking phenomena) occurs leading to

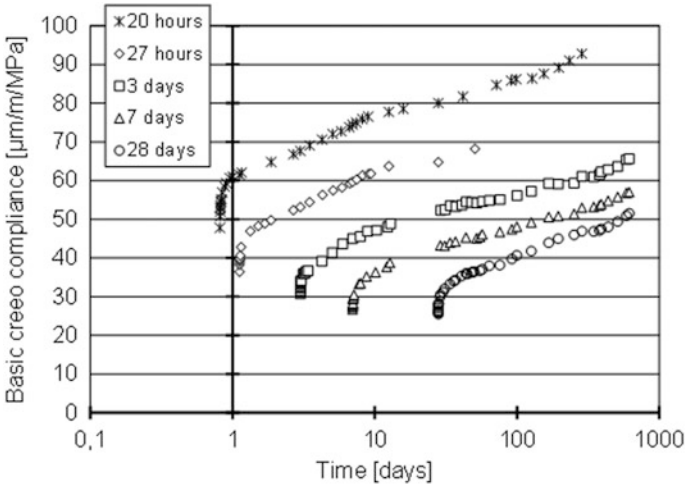

Fig. 4.17 Effects of loading age on basic creep in compression (Laplante 1993)

consolidation. Rossi et al. (2012) proposed an alternative mechanism related to flow of water in cracks generated during creep, since acoustic emission showed a relationship between the number of acoustic events and the amplitude of strains.

The creep behavior of cement-based materials is aging; i.e., it depends on the loading age (see Fig. 4.17). Prestress concrete structures are loaded at later age, and they will creep less as autogenous/thermal strain restraint leads to stresses just after setting. Different phenomena can lead to this aging character: solidification of hydration products due to hydration process (Bažant 1977; Carol and Bažant 1993) or consolidation and/or space-filling processes at the C–S–H scale (Masoero et al. 2012).

When shrinkage is restrained, tensile stresses occur. They can be preceded by compressive stresses if swelling or thermal expansion occurs. Therefore, it is important to assess if basic creep of concrete in tension and in compression occurs in the same manner. There is still no consensus in the literature on this topic as it is shown in Fig. 4.18. Due to the low tensile strength of concrete, micro-cracking may develop, propagate, and contribute more significantly to creep in tension: Effect of fiber content or cement paste content has inverse effects on total creep in tension and compression (Bissonnette et al. 2007).

4.4.1.2 Main Influencing Parameters

Temperature. Creep is affected by temperature in several ways:

- Creep for mature concrete is thermo-activated, and as the temperature increases, creep rate increases;

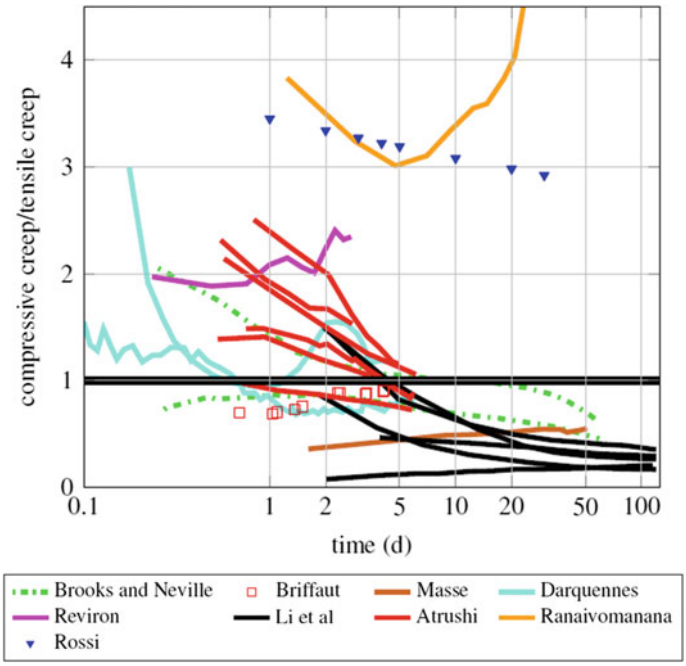

Fig. 4.18 Evolution of the ratio between specific compressive and tensile basic creep from different authors (Hilaire et al. 2014)

- At early age, since hydration is thermo-activated, mechanical properties are increasing faster, reducing the creep rate;
- If the temperature changes during the period of creep test, the creep rate may increase. This additional creep is named transient thermal creep or load-induced thermal strain.

Load-induced thermal strain has been extensively investigated for concrete at high temperature (in the context of concrete structures exposed to fire). However, results at early age are particularly scarce. The main mechanism may be related to the fact that temperature change leads to redistribution of inherent moisture in the cement paste as well as structural change—both of clear importance for creep. Illston and Sanders (1973) describe the rapid increase in creep, due to a positive change of temperature, as transitional thermal creep which is approximately independent of maturity, and is zero when the temperature decreases or when the temperature is raised to the given level for a second time. This means also that drop of temperature does not give any creep recovery. That a positive change in temperature of mature concrete increases creep is also confirmed by Arthanari and

Yu (1967). He also observed that increasing of the temperature by several steps gives a higher creep than a steady temperature after a certain period of loading

Cement and mineral additions. The type of cement and mineral additions influences the type of hydration products and the rate of hydration reaction. Thus, development of mechanical properties, shrinkage, and creep is also affected.

Creep tests performed by Botassi et al. (2012) showed different behavior for early age at loading. Concrete with mineral admixture at one-day loading showed creep of 58–316% greater than the reference for many types of admixtures, while loading ages at 3 and 7 days creep behavior is inversed. In those ages creep concrete is reduced with mineral additions of up to 77% for blast-furnace slag than reference.

Igarashi and Kawamura (2002) suggested that the lower potential of creep for concrete with silica fumes results from the higher strength and the dense microstructure for such concrete.

Aggregate. Since creep strains occur mainly in the cement paste, aggregates act as a restraint element and reduce the potential of basic creep. The Young modulus is thus an important factor. For lightweight aggregate for instance, since its Young modulus is lower than typical aggregate, this type of concrete exhibits larger creep.

On Very Young Concrete

By means of compressive creep tests on very early-age concrete, Delsaute et al. (2016b) have observed that short-term creep can be divided into two parts. The first part occurs during the first hours after loading with constant kinetic and variable amplitude which is inversely proportional to the age of the material at loading. The second part occurs on longer duration with amplitude increasing with the age at loading and a faster kinetic evolution for very early-age loading. The effect of the age at loading is significantly more marked for the first part of the short-term creep. By comparison with the evolution of the microstructure, it is observed that the first part of the short-term creep is associated with the state of the material (capillarity pores, C–S–H, etc.) when the load is applied and more specifically to the largest diameter pores. The second part of the short-term creep is associated with the solidification theory of Bažant and Prasannan (1989) which links the evolution of the C–S–H to the decrease of the creep for early-age loading.

Through these observations, a new advanced experimental methodology was developed on concrete (Delsaute et al. 2016b) to monitor the basic creep at very early age. The methodology is based on repeated minute-long loading which starts just after the final setting of the material. Every 30 min, a load corresponding to 20% of the compressive strength is applied and kept constant during 5 min and then finally removed. The amplitude of the aging creep for short duration of loading is defined with the value of the creep coefficient obtained after 5 min of loading.

Age at loading. Results of the compressive creep compliance for short duration loading of 5 min are presented in Fig. 4.19. The effect of the age at loading is significantly marked on the amplitude of the creep compliance, especially just after the setting time. Each compressive creep curves are normalized by their value reach at the end of the plateau of stress. All repeated minute-long loadings are

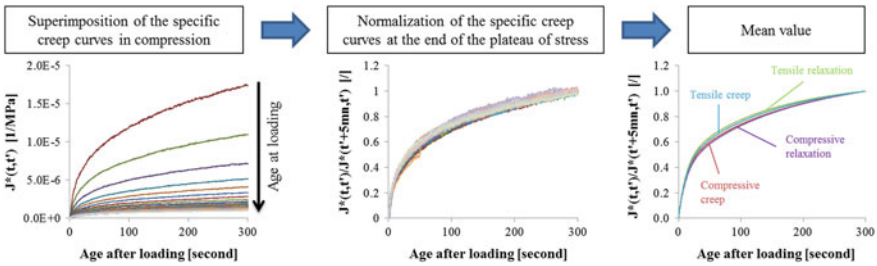

Fig. 4.19 Repeated minute-long loadings. Left to right: For each repeated minute-long loading, creep curves are superimposed and set to zero when the load is kept constant. For each repeated minute-scale loading, creep curves are normalized by the value obtained after 5 min of loading. Mean values of normalized curve for creep and relaxation repeated minute-scale loadings in tension and in compression (Delsaute et al. 2014)

quasi-superimposed which leads to the conclusion that the kinetic of the specific creep is independent of the age at loading during the early age for duration of loading limited to 5 min. The same data analysis has been made for compressive relaxation test, and no kinetic effect is detected for creep and relaxation test in compression. Tensile creep and relaxation were also carried out, and no difference was also observed in the kinetic for age at loading between the final setting time and 100 h.

For the analysis of the evolution of the creep or relaxation amplitude, the value of the creep coefficient or the relaxation coefficient after a plateau of 5 min with constant stress or mechanical strain was used. This value is called amplitude factor. Fig. 4.20 presents the evolution of the amplitude factor for several creep and relaxation tests in compression. A same evolution of the amplitude factor is observed for creep and relaxation. Just after setting, the value of the amplitude factor obtained a value of 0.3 which means that the creep strain or the relaxation stress represents after 5 min of loading 30% of the elastic strain/elastic stress.

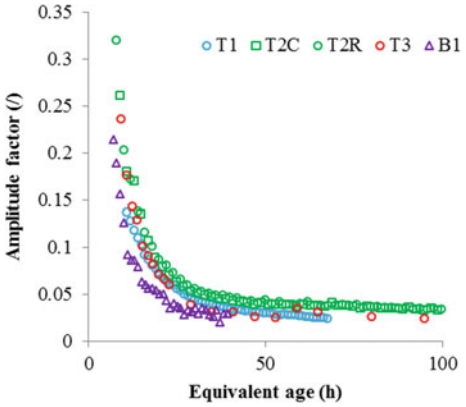

Fig. 4.20 Amplitude factor for creep and relaxation repeated minute-long loading tests in compression (Delsaute et al. 2016b)

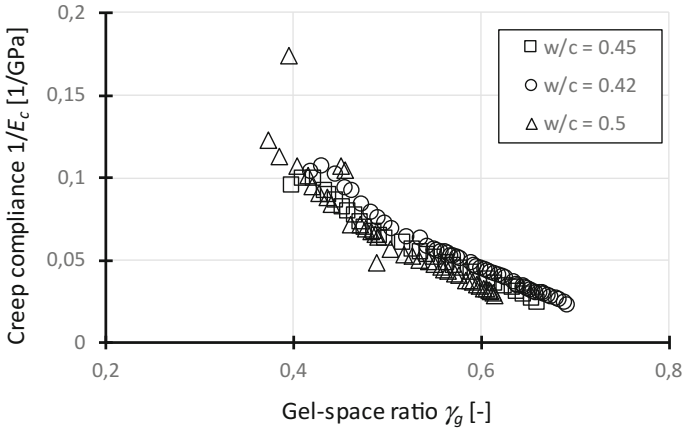

Fig. 4.21 Creep compliance in function of the gel–space ratio for three cement pastes with different w/c ratios (Irfan-ul-Hassan et al. 2016)

Water–cement ratio. A very similar methodology was also used by Irfan-ul-Hassan et al. (2016) in order to assess the aging of the viscoelastic behavior of cement pastes with three different water–cement ratios. The amplitude of the creep complaisance is influenced by the water–cement ratio. For high water–cement ratio, the creep complaisance obtained with short duration of loading (3 min) is higher for degree of hydration at loading between 0.3 and 0.65 (which corresponds to an age of the material varying between 24 and 168 h). However, when the

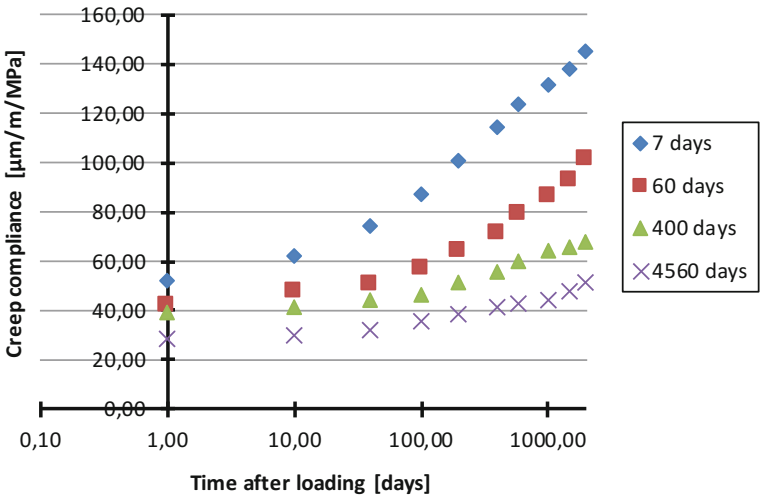

Fig. 4.22 Creep compliance for different age at loading (Browne and Blundell 1969)

evolution of the amplitude of the creep complaisance is compared to the gel–space ratio, a same general trend is observed as shown in Fig. 4.21.

On Hardened Concrete

Age of concrete. As shown in Fig. 4.22, concrete age at application of load is a very important factor: More the concrete is old, less the concrete will creep. This phenomenon is observed at early age and at long term. Therefore, this age effect is related to the degree of hydration, but also to another phenomenon (polymerization and micro-prestress relaxation theories have been proposed in the literature (Bažant et al. 1997)).

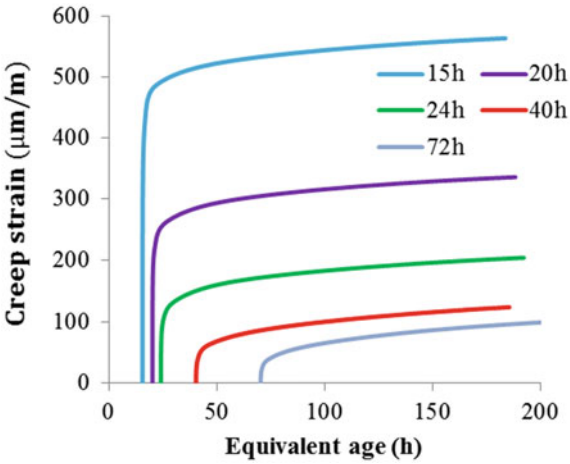

Fig. 4.23 Basic creep strain evolution for age at loading of 15–20–24–40 and 72 h for an ordinary concrete (Delsaute et al. 2016b)

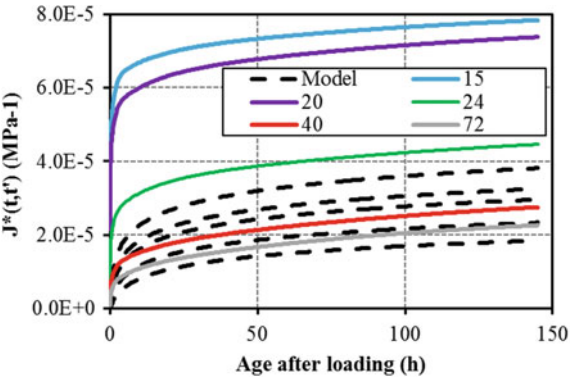

Fig. 4.24 Creep compliance evolution for age at loading of 15–20–24–40 and 72 h for an ordinary concrete (Delsaute et al. 2016a) and comparison with the Model Code 2010

4.4.1.3 Amplitude of Strains

Only few data are available in the literature for early-age concrete. Data obtained for very early age (<24 h) are nearly impossible to find. Recently, Delsaute et al. (2016b) have carried out several tests of long duration for age at loading of 15–20–24–40 and 72 h on an ordinary concrete with a CEM I 52.5 and a characteristic compressive strength of 40 MPa (Fig. 4.23).

Figure 4.24 presents the evolution of the creep compliance for several ages at loading of the same ordinary concrete. These results were compared to the value predicted by the Model Code 2010 (MC2010). For age at loading higher than 40 h, MC2010 is able to correctly predict the evolution of the basic compressive creep. However, for earlier ages, the amplitude of the creep can be underestimated by a factor 2.

4.4.1.4 Multiaxial Creep

Shrinkage strains are isotropic, and if they are restraint in 2 or 3 orthogonal directions, a biaxial or triaxial stress of state occurs. Even if there is no restriction in orthogonal directions, internal restrictions and the inherent internal balance of loads promoting tensions in all directions. It seems that there is no experimental data regarding the basic behavior of concrete in multiaxial tension. In most of the studies, multiaxial creep is dealt by using a creep or a relaxation Poisson's ratio (e.g., Granger 1996; Bažant et al. 1997) or by splitting the creep strain into a spherical and deviatoric component (e.g., Benboudjema et al. 2005; Sellier et al. 2015).

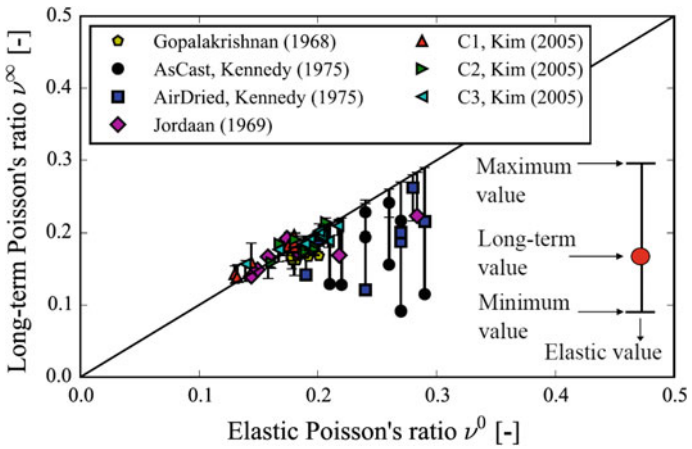

Fig. 4.25 Creep experiments on concrete: long-term asymptotic value of the viscoelastic Poisson's ratio versus elastic Poisson's ratio for each individual experiment; y-axis error bars indicate the maximum and minimum values of the viscoelastic Poisson's ratio during the experiment (Aili 2017)

Due to time-dependent effects, the Poisson ratio needs to be well defined in an aging viscoelastic framework (Hilton and Yi 1998). Aili (2017) showed that using available experimental data, the use of creep or relaxation Poisson's ratio leads to almost the same results. A literature review in compression shows some discrepancies (see Fig. 4.25).

4.4.1.5 Influence of the Stress Level and Interaction Between Creep and Cracking

As the concrete compressive and tensile strengths increase rapidly at early age as the applied stress remains constant, the stress/strength ratio decreases with time. Most of the experiments are performed in such case. However, the research by Botassi et al. (2012) concluded for concrete at early ages that more consistent tests results are obtained by maintaining the stress/strength constant over time, increasing the load test similar to the increased resistance. According to Botassi et al. (2012), this way of performing the assay evaluates the creep phenomenon, disregarding interference stiffness growth in the cement matrix, and allows the analysis to evaluate the behavior of creep from their main causes, (and not by stiffness increase of the concrete).

It is quite admitted in compression that creep is proportional linearly to the applied stress until a certain stress level. This threshold varies between 0.2 and 0.75 of the concrete compressive strength in compression (e.g., Hannant 1967; McDonald 1975; Smadi and Slate 1989; Ranaivomanana et al. 2013; Rossi et al. 2013). Above this threshold, micro-cracking develops in concrete, creep rates increase as the stress/stress ratio increases, and failure may occur.

There are less analyses in tension than in compression about the effect of stress level. Tensile creep strain remains proportional to the applied stress up to a stress

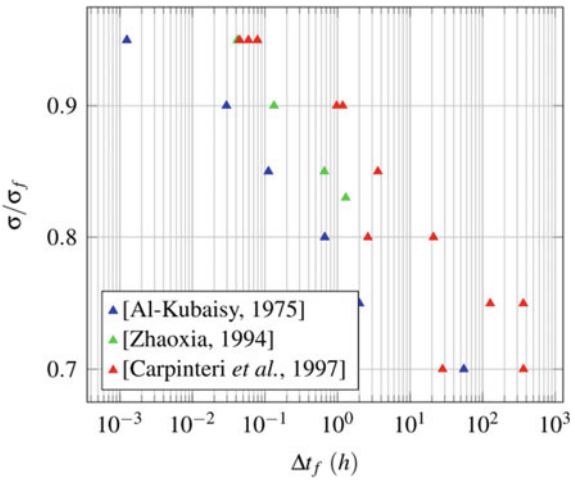

Fig. 4.26 Evolution of the applied stress σ/tensile or compressive strength σf ratio with respect to the time until failure Δtf in tension (Al-Kubaisy 1975; Carpinteri et al. 1997) or in compression (Zhaoxia 1994)

level between about 40 and 100% (Illston 1965; Domone 1974; Al-Kubaisy 1975; Neville et al. 1983; Bissonnette et al. 2007). As in compression, a sustained loading beyond this range of linearity may lead to failure. Note that some studies propose that creep induces micro-cracking (Rossi et al. 2012; Sellier et al. 2015) even for small level of stresses, leading eventually to internal drying shrinkage (Rossi et al. 2012). It is supported by acoustic emission (Rossi et al. 2012; Saliba et al. 2012; Al-Kubaisy 1975) and by observation in microscope (Shah and Chandra 1970).

Figure 4.26 displays the relationship between the applied stress (σ)/tensile or compressive strength (σf) ratio with respect to the time until failure Δtf for different authors in uniaxial tension or compression.

This result shows that the stress-to-strength ratio is proportional to the logarithm of time at failure. A similar result is observed also in bending (Carpinteri et al. 1997; Rossi et al. 2014). Micro-cracks during creep in tension may lead to their coalescence and result in a macro-crack and a corresponding failure. Note that the variability of properties is quite of great importance (coefficient of variation of 13% for 40 tested specimens coming from a construction site (Aït-Mokhtar et al. 2013)), since the tensile strength of the tested specimen is not known in advance: Reinhardt and Rinder (2006) observed in HPC for the same stress/strength ratio either a failure or not during tensile creep test at high stress level.

4.4.2 Drying Creep

Such as the drying shrinkage, this strain component is not detailed in this STAR.

4.4.3 Experimental Test Methods

The creep properties are very sensitive to the conditions of preservation of the specimen during the test and to many factors related to the test rig. For that reason, several recommendations were developed in the past (ASTM C512 2015; ISO 1920-9 2009; Subcommittee 4 1998) for hardened concrete. Currently, no recommendation or standard test method exists for the determination of the basic creep for concrete at very early age. The main common requirements for all the apparatus for testing basic creep in sealed condition are their ability to:

- ensure uniform stress distribution over the cross-section of the specimen;
- apply a load very quickly;
- operate in a room with controlled temperature and humidity;
- and maintain a constant known load during the whole testing period.

In addition, the measurement of the strain must be carried out in the central part of the specimen in order to eliminate the edge effects. As for the measurement of the

free deformations, the specimen must be perfectly sealed to avoid any external drying or water uptake. The instrumentation must be composed of material with very low coefficient of thermal expansion.

For the separation of the autogenous strain and the basic creep strain, a dummy specimen that is load free must be made for each creep test. A same instrumentation must be used for the loaded and the dummy specimen.

If sample is tested few hours after setting, special attention should be taken for the preparation of the sample (Delsaute et al. 2016b).

References

Acker, P., & Ulm, F.-J. (2001). Creep and Shrinkage of concrete: Physical origins and practical measurements. *Nuclear Engineering Design, 203,* 143–158.

ACI Report 209, ACI Committee 209. (1992). ACI 209R-92: Prediction of creep, shrinkage, and temperature effects in concrete structures (Reapproved 1997).

Aili, A. (2017). Shrinkage and creep of cement-based materials under multiaxial load: Poromechanical modeling for application in nuclear industry. Ph.D. thesis, University Paris Est (279 pp.).

Aït-Mokhtar, A., et al. (20 authors). (2013). Experimental investigation of concrete variability. *Cement and Concrete Research, 45*, 21–36.

Al-Kubaisy, M. A. (1975). Failure of concrete under sustained tension. *Magazine of Concrete Research, 27*(92), 171–178.

Aly, T., & Sanjayan, J. G. (2008). Shrinkage cracking properties of slag concretes with on-day curing. *Magazine of Concrete Research, 60,* 41–48.

Arthanari, S., & Yu, C. W. (1967). An analysis of the creep and shrinkage effects upon prestressed concrete members under temperature gradient and its application. *Magazine of Concrete Research, 19*(60), 157–164.

ASTM Standard C512, Standard Test Method for Creep of Concrete in Compression.

ASTM Standard C1698, Standard Test Method for Autogenous Strain of Cement Paste and Mortar.

ASTM Standard C469, Standard Test Method for Static Modulus of Elasticity and Poisson's Ratio of Concrete in Compression.

Atrushi, D. S. (2003). Tensile and compressive creep of early age concrete. Testing and modelling. Ph.D. thesis.

Azenha, M. (2009). Numerical simulation of the structural behavior of concrete since its early ages. Ph.D. thesis report, Faculty of Engineering of the University of Porto, 2009.

Azenha, M., Faria, R., & Ferreira, D. (2009). Identification of early-age concrete temperatures and strains: Monitoring and numerical simulation. *Cement & Concrete Composites, 31,* 369–378.

Baroghel-Bouny, V. (1994). Caractérisation des pâtes de ciment et des bétons, Méthodes, Analyse, Interprétation. Ph.D. thesis, Ecole Nationale des Ponts et Chaussées, France (467 pp.).

Baroghel-Bouny, V., & Kheirbek, A. (2000). Effect of mix-parameters on autogenous deformations of cement pastes—Microstructural interpretations. In V. Baroghel-Bouny & P. C. Aïtcin (Eds.), *Shrinkage Concrete-Shrinkage 2000, Proceedings of the International RILEM Workshop, PRO17*, October 16–17, Paris (pp. 115–141).

Baroghel-Bouny, V., Mounanga, P., Khelidj, A., Loukili, A., & Rafaï, N. (2006). Autogenous deformations of cement pastes: Part II. W/C effects, micro-macro correlations, and threshold values. *Cement and Concrete Research, 36*(1), 123–136.

Bassam, S. A., Yu, B-J., & Ansari, F. (2007). Fracture energy of concrete by maturity method. *American Concrete Institute Materials Journal*, Title no. 104-M10.

Bažant, Z. P. (1977). Viscoelasticity of solidifying porous material—concrete. *Journal of the Engineering Mechanics Division, ASCE*, *103*, 1049-10067; Disc., 1979, 725–728.

Bažant, Z. P. (1984). Double-power logarithmic law for concrete creep. *Cement and Concrete Research, 14,* 793–806.

Bažant, Z. P., & Prasannan, S. (1989). Solidification theory for aging creep. I: Formulation. *Journal of Engineering Mechanics, 115,* 1670–1691.

Bažant, Z. P. (1995). Creep and shrinkage prediction model for analysis and design of concrete structures—Model B-3. *Materials and Structures, 28,* 357–365.

Bažant, Z. P., Hauggaaed, A. B., Baweja, S., & Ulm, F. J. (1997). Microprestress-solidification theory for concrete creep. I: Aging and drying effects. *Journal of Engineering Mechanics, 123*(11), 1188–1194.

Beltzung, F., & Wittman, F. (2002). Influence of cement composition on endogenous shrinkage, Self-dessiccation and its importance in concrete technology. In *Proceedings of the Third International Research Seminar*, June 14–15, Lund, Sweden (pp. 113–125).

Benboudjema, F., Meftah, F., & Torrenti, J.-M. (2005). Interaction between drying, shrinkage, creep and cracking phenomena in concrete. *Engineering Structures, 27,* 239–250.

Benboudjema, F., & Torrenti, J.-M. (2008). Early-age behaviour of concrete nuclear containments. *Nuclear Engineering and Design, 238,* 2495–2506.

Bentur, A., & Ish-Shalom, M. (1974). Properties of type K expensive cement of pure components. II. Proposed mechanism of ettringite formation and expansion in unrestrained paste of pure expansive component. *Cement and Concrete Research, 4*(5), 709–721.

Bernard, O., Ulm, F.-J., & Lemarchand, E. (2003). A multiscale micromechanics-hydration model for the early-age elastic properties of cement-based materials. *Cement and Concrete Research, 33,* 1293–1309. https://doi.org/10.1016/S0008-8846(03)00039-5.

Bissonnette, B., Pigeon, M., & Vaysburd, A. M. (2007). Tensile creep of concrete: Study of its sensitivity to basic parameters. *Materials Journal, 104*(4), 360–368.

Bjøntegaard, Ø., Hammer, T., & Sellevold, E. J. (2004). On the measurement of free deformation of early age cement paste and concrete. *Cement & Concrete Composites, 26*(5), 427–435.

Boivin, S. (1999). Retrait au jeune âge du béton: Développement d'une méthode expérimentale et contribution à l'analyse physique du retrait endogène. Ph.D. thesis, Ecole Nationale des Ponts et Chaussées, France, (249 pp.).

Botassi, S. S., Silva Filho, L. C., & Calmon, J. L. (2012). Early-age creep of mass concrete: Effects of chemical and mineral admixtures. *ACI Materials Journal*, *V*(5), 109.

Boulay, C., Crespini, M., Delsaute, B., & Staquet, S. (2012). Monitoring of the creep and the relaxation behaviour of concrete since setting time. Part 1: Compression. In *SSCS 2012 Numerical Modelling Strategies for Sustainable Concrete Structures*, May 29–June 1, Aix-en-Provence, France.

Boulay, C., Staquet, S., Delsaute, B., Carette, J., Crespini, M., Yazoghli-Marzouk, O., et al. (2014). How to monitor the modulus of elasticity of concrete, automatically since the earliest age? *Materials and Structures, 47*(1), 141–155.

Boumiz, A., Vernet, C., & Cohen Tenoudji, F. (1996). Mechanical properties of cement pastes at early ages. *Advanced Cement Based Materials*, *3*.

Brazilian Standard NBR 6118, Projeto de estruturas de concreto - Procedimento. Rio de Janeiro (2014) (in Portuguese).

Briffaut, M., Benboudjema, F., Torrenti, J.-M., & Nahas, G. (2011). Numerical analysis of the thermal active restrained shrinkage ring test to study the early age behavior of massive concrete structures. *Engineering Structures, 33*(4), 1390–1401.

Briffaut, M., Benboudjema, F., Torrenti, J.-M., & Nahas, G. (2012). Concrete early age basic creep: Experiments and test of rheological modelling approaches. *Construction and Building Materials, 36,* 373–380.

Briffaut, M., Benboudjema, F., & D'Aloia, L. (2016). Effect of fibers on early age cracking of tunnel concrete lining. *Part II: Numerical simulations, Tunnelling and Underground Space Technology, 59,* 221–229.

Brooks, J. J., & Neville, A. M. A. (1977). comparison of creep, elasticity and strength of concrete in tension and in compression. *Magazine of Concrete Research, 29*(100), 131–141.

Browne, R., & Blundell, R. (1969). The influence of loading age and temperature on the long term creep behaviour of concrete in a sealed, moisture stable state. *Materials and Structures, 2,* 133–143.

Buffo-Lacarrière, L., Sellier, A., & Kolani, B. (2014). Application of thermo-hydro-chemo-mechanical model for early age behaviour of concrete to experimental massive reinforced structures with strain–restraining system. *European Journal of Environmental and Civil Engineering, 18*(7), 814–827.

Buffo-Lacarrière, L., El Bitouri, Y., & Sellier, A. (2016). Modelling of ageing behaviour of Supplementary Cementitious Materials. In *Materials, Systems and Structures in Civil Engineering. MSSCE2016 Proceedings*, August 2016, Lyngby, Denmark.

Byfors, J. (1980). *Plain concrete at early ages*. Stockholm: Swedish Cement and Concrete Research Institute.

Carette J. (2015) Towards early age characterisation of eco-concrete containing blast-furnact slag and limestone filler, PhD Thesis, Université Libre de Bruxelles, BATir department.

Carette, J., & Staquet, S. (2016). Monitoring and modelling the early age and hardening behaviour of eco-concrete through continuous non-destructive measurements: Part II. *Mechanical behaviour, Cement and Concrete Composites, 73,* 1–9.

Carette, J., Joseph, S., Cizer, Ö., & Staquet, S. (2017). Decoupling the autogenous swelling from the self-desiccation deformation in early age concrete with mineral additions: Micro-macro observations and unified modelling. *Cement & Concrete Composites, 85,* 122–132.

Carino, N. J. (1982). Maturity functions for concrete. In *Proceedings of the RILEM International Conference on Concrete at Early Ages*, Paris, France (pp. 111–115).

Carol, I., & Bažant, Z. P. (1993). Viscoelasticity with aging caused by solidification of nonaging constituent. *Journal of Engineering Mechanics, ASCE*, *119*(11), 2252–2269.

Carpinteri, A., Valente, S., Zhou, F. P., Ferrara, G., & Melchiorri, G. (1997). Tensile and flexural creep rupture tests on partially damaged concrete specimens. *Materials and Structures/ Matériaux et Constructions, 30,* 269–276.

Constantinides, G., & Ulm, F.-J. (2004). The effect of two types of C-S-H on the elasticity of cement based materials: Results from nanoindentation and micromechanical modeling. *Cement and Concrete Research, 34*.

Craeye, B., de Schutter, G., Humbeeck, H. V., & Cotthem, A. V. (2009). Early age behaviour of concrete supercontainers for radioactive waste disposal. *Nuclear Engineering and Design, 239,* 23–35.

Craeye, B., de Schutter, G., Desmet, B., Vantomme, J., Heirman, G., Vandewalle, L., et al. (2010). Effect of mineral filler type on autogenous shrinkage of self-compacting concrete. *Cement and Concrete Research, 40*(6), 908–913.

Darquennes, A. (2009). Comportement au jeune âge de bétons formulés à base de ciment au laitier de haut-fourneau en condition de déformations libre et restreinte. Thèse de doctorat, Université libre de Bruxelles.

Darquennes, A., Staquet, S., Delplancke-Ogletree, M.-P., & Espion, B. (2011). Effect of autogenous deformation on the cracking risk of slag cement concretes. *Cement & Concrete Composites, 33,* 368–379.

de Schutter, G., & Taerwe, L. (1996) Degree of hydration-based description of mechanical properties of early age concrete. *Materials and Structures, 29*.

de Schutter, G., & Vuylsteke, M. (2004). Minimisation of early age thermal cracking in a J-shaped non-reinforced massive concrete quay wall. *Engineering Structures, 26,* 801–808.

Delsaute, B., & Staquet, S. (2014). Early age creep and relaxation modelling of concrete under tension and compression. In L. Kefei, Y. Peiyu & Y. Rongwei (Eds.), *CONMOD 2014: Proceedings of the RILEM International Symposium on Concrete Modelling* (1 ed.) (Vol. 91, pp. 168–175). France: RILEM Publications S.A.R.L.

Delsaute, B., Torrenti, J.-M., & Staquet, S. (2016a). Monitoring and modeling of the early age properties of the vercors concrete. In *Technological Innovations in Nuclear Civil Engineering TINCE*, September 2016, Paris, France.

Delsaute, B., Boulay, C., & Staquet, S. (2016b). Creep testing of concrete since setting by means of permanent and cyclic loadings. *Cement and Concrete Research, 73,* 75–88.

Delsaute, B., Boulay, C., Granja, J., Carette, J., Azenha, M., Dumoulin, C., et al. (2016c). Testing concrete E-modulus at very early ages through several techniques: An inter-laboratory comparison. *Strain, 52*(2), 91–109.

Delsaute, B., Torrenti, J.-M., & Staquet, S. (2017). Modelling basic creep of concrete since setting time. *Cement & Concrete Composites, 83,* 239–250.

Delsaute, B., & Staquet, S. (2017). Decoupling thermal and autogenous strain of concretes with different water/cement ratios during the hardening process. *Advances in Civil Engineering Materials, ASTM Journal, 6*(2), 1–22.

Domone, P. L. (1974). Uniaxial tensile creep and failure of concrete. *Magazine of Concrete Research, 26*(88), 144–152.

EN 12390-13. Testing hardened concrete. Determination of secant modulus of elasticity in compression.

Esping, O. (2008). Effect of limestone filler BET(H_2O)-area on the fresh and hardened properties of self-compacting concrete. *Cement and Concrete Research, 38*(7), 938–944.

Estrada, C. F., Godoy, L. A., & Prato, T. (2006). Thermo–mechanical behaviour of a thin concrete shell during its early age. *Thin-Walled Structures, 44,* 483–495.

Eurocode 2—Design of Concrete Structures. Part 1-1: General Rules and Rules for Buildings, European Committee for Standardization. EN 1992-1-1—ENV 1992-1-1: 2004.

Faria, R., Azenha, M., & Figueiras, J. A. (2006). Modelling of concrete at early ages: Application to an externally restrained slab. *Cement & Concrete Composites, 28,* 572–585.

fib Bulletin 70, CEB-FIP. State-of-the-art report: Code-type models for concrete behaviour. Background of MC2010. 2013.

Gawin, D., Wyrzykowski, M., & Pesavento, F. (2008). Modeling hygro-thermal performance and strains of cementitious building materials maturing in variable conditions. *J. Build. Phys., 31,* 301–318.

Gopalakrishnan, K. S. (1968). Creep of concrete under multiaxial compressive stresses. Ph.D. thesis, Civil Engineering, University of Calgary.

Granger, L. (1996). Comportement différé du béton dans les enceintes de centrales nucléaires: analyse et modélisation. Ph.D. thesis, Ecole Nationale des Ponts et Chaussées.

Gutsch, A., & Rostásy, F. S. (1994). Young concrete under high tensile stresses—Creep, relaxation and cracking. In *Proceedings of the International RILEM Conference on Thermal Cracking in Concrete at Early Ages*, London, UK (pp. 111–118).

Habib, A., Lachemi, M., & Aitcin, P.-C. (2002). Determination of elastic properties of high-performance concrete at early ages. *ACI Materials Journal, 99*(1), 37–41.

Hammer, T. A., Fossa, K. T., & Bjøntegaard, Ø. (2007). Cracking tendency of HSC: Tensile strength and self generated stress in the period of setting and early hardening. *Materials and Structures, 40,* 319–324.

Hannant, D. (1967). *Strain behaviour of concrete up to 95 °C under compressive stresses* (pp. 57–71.

Hilaire, A., Benboudjema, F., Darquennes, A., Berthaud, Y., & Nahas, G. (2014). Modeling basic creep in concrete at early-age under compressive and tensile loading. *Nuclear Engineering Design, 269,* 222–230.

Hilton, H. H., & Yi, S. (1998). The significance of (an) isotropic viscoelastic Poisson ratio stress and time dependencies. *International Journal of Solids and Structures, 35,* 3081–3095.

Holt, E. (2005). Contribution of mixture design to chemical and autogenous shrinkage of concrete at early ages. *Cement and Concrete Research, 35,* 464–472.

Honorio, T., Bary, B., & Benboudjema, F. (2016). Factors affecting the thermo-chemo-mechanical behaviour of massive concrete structures at early-age. *Materials and Structures, 49*(8), 3055–3073.

Hua, C., Acker, P., & Ehrlacher, A. (1995). Analyses and models of the autogenous shrinkage of hardening cement paste: I. Modelling at macroscopic scale. *Cement and Concrete Research, 25,* 1457–1468.

Igarashi, S., & Kawamura, M. (2002). Effects of microstructure on restrained autogenous shrinkage behavior in high strength concretes at early ages. *Materials and Structures, 35*(2), 80–84.

Illston, J. (1965). The creep of concrete under uniaxial tension. *Magazine of Concrete Research, 17*(51), 77–84.

Illston, J. M., & Sanders, P. D. (1973). The effect of temperature change upon the creep of mortar under torsional loading. *Magazine of Concrete Research, 25*(84), 136–144.

Irfan-ul-Hassan, M., Pichler, B., Reihsner, R., & Hellmich, Ch. (2016). Elastic and creep properties of young cement paste, as determined from hourly repeated minute-long quasi-static tests. *Cement and Concrete Research, 82,* 36–49.

ISO 1920-9. Testing of concrete—Part 9: Determination of creep of concrete cylinders in compression.

Jensen, O. (2000). Influence of cement composition on autogenous deformation and change of relative humidity. In V. Baroghel-Bouny & P. C. Aïtcin (Eds.), *Shrinkage 2000, Proceedings of the International RILEM Workshop, PRO 17*, October 16–17, Paris, France (pp. 143–153).

Jensen, O. M., & Hansen, P. F. (2001). Autogenous deformation and RH-change in perspective. *Cement and Concrete Research, 31,* 1859–1865.

Jonasson, J.-E. (1994). Modelling of temperature, moisture and stress in young concrete. Ph.D. thesis, Luleå University of Technology, Luleå, Sweden.

Jordaan, I. J., & Illston, J. M. (1969). The creep of sealed concrete under multiaxial compressive stresses. *Magazine of Concrete Research, 21*(69), 195–204.

JSCE 2010, JSCE. Guidelines for Concrete. No. 15: Standard Specifications for Concrete Structures. Design (2011).

Justnes, H., Sellevold, E. J., Reyniers, B., Van Loo, D., Van Gemert, A., Verboven, F., et al. (1998). The influence of cement characteristics on chemical shrinkage, autogenous shrinkage of concrete. In *Proceedings of the International Workshop*, June 13–14, Hiroshima, Japan, Edité par Tazawa, E. (pp. 71–80).

Kanstad, T., Hammer, T. A., Bjøntegaard, Ø., & Sellevold, E. J. (2003a). Mechanical properties of young concrete. Part I: Experimental results related to test methods and temperature effects. *Materials and Structures, 36,* 218–225.

Kanstad, T., Hammer, T. A., Bjøntegaard, Ø., & Sellevold, E. J. (2003b). Mechanical properties of young concrete. Part II: Determination of model parameters and test program proposals. *Materials and Structures, 36,* 226–230.

Karte, P., Hlobil, M., Reihnsner, R., Dörner, W., Lahayne, O., Eberhardsteiner, J., et al. (2015). Unloading-based stiffness characterization of cement pastes during the second, third and fourth day after production. *Strain, 51*(2), 156–169.

Kee, C. F. (1971). Relation between strength and maturity of concrete. *ACI Journal Proceedings, 68*(3), 196–203.

Kennedy, T. W. (1975). *An evolution and summary of a study of the long-term multiaxial creep behavior of concrete*. Oak Ridge National Laboratory: Technical report.

Kim, J. K., Kwon, S. H., Kim, S. Y., & Kim, Y. Y. (2005). Experimental studies on creep of sealed concrete under multiaxial stresses. *Magazine of Concrete Research, 57*(10), 623–634.

Kim, J.-K., Lee, Y., & Yi, S.-T. (2004). Fracture characteristics of concrete at early ages. *Cement and Concrete Research, 34,* 507–519.

Klemczak, B., & Batog, M. (2014). Przewidywanie wczesnych wytrzymałości betonów na cementach wieloskładnikowych według Eurokodu 2. *Inżynieria i Budownictwo, 71*(3), 142–145.

Klemczak, B., & Knoppik-Wróbel, A. (2014). Analysis of early-age thermal and shrinkage stresses in reinforced concrete walls. *ACI Structural Journal, 111*(2), 313–322.

Klemczak, B., Batog, M., & Pilch, M. (2016). Assessment of concrete strength development models with regard to concretes with low clinker cements. *Archives of Civil and Mechanical Engineering, 16*(2), 235–247.

Kolani, B., Lacarrière, L., Sellier, A., Boutillon, L., & Linger, L. (2011). Crack initiation and propagation at early age. In *fib 2011 Symposium*, Prague (Czech Republic).

Krauss, M., & Hariri, K. (2006). Determination of initial degree of hydration for improvement of early-age properties of concrete using ultrasonic wave propagation. *Cement and Concrete Composites, 28,* 299–306.

Laplante, P. (1993). Propriétés mécaniques des bétons durcissants: analyse comparée des bétons classiques et à très hautes performances. Thèse de Doctorat de l'Ecole Nationale des Ponts et Chaussées, également en Etudes et Recherches des LPC, OA13.

Larson, M. (2003). Thermal crack estimation in early age concrete. Models and methods for practical application. Ph.D. thesis, Luleå University of Technology, Luleå, Sweden.

Li, H., Wee, T., & Wong, S. (2002). Early-age creep and shrinkage of blended cement concrete. *Materials Journal, 99*(1), 3–10.

Lohtia, R. P. (1970). Mechanism of creep in concrete. *Roorkee University Research Journal, 1–2* (12), 37–47.

Lopes, A. N. M., Fonseca Silva, E., Dal Molin, D. C. C., & Toledo Filho, R. D. (2013). Shrinkage-reducing-admixture: effect on durability of high-strength concrete. *ACI Materials Journal, 110*(4), 365–374.

Loser, R., Münch, B., & Lura, P. (2010). A volumetric technique for measuring the coefficient of thermal expansion of hardening cement paste and mortar. *Cement and Concrete Research, 40*(7), 1138–1147.

Lura, P., Jensen, O. M., & van Breugel, K. (2003). Autogenous shrinkage in high-performance cement paste: An evaluation of basic mechanisms. *Cement and Concrete Research, 33,* 223–232.

Masoero, E., Del Gado, E., Pellenq, R. J. M., Ulm, F. J., & Yip, S. (2012). Nanostructure and nanomechanics of cement: Polydisperse colloidal packing. *Physical Review Letters, 109*(15), 155503.

Masse, M. B. (2010). Étude du comportement déformationnel des bétons de réparation. Mémoire de D.E.A., École polytechnique de Montréal.

Mcdonald, J. (1975). Time-dependent deformation of concrete under multiaxial stress conditions. Final report. Technical report.

Mehta, P. (1973). Mechanism of expansion associated with ettringite formation. *Cement and Concrete Research, 3*(1), 1–6.

Model Code 1990, CEB-FIP *fib*. Model Code 1990, 1991.

Model Code 2010, CEB-FIP *fib*. Model Code 2010, 2013.

Mounanga, P., Baroghel-Bouny, V., Loukili, A., & Khelidj, A. (2006). Autogenous deformations of cement pastes: Part I. Temperature effects at early age and micro–macro correlations. *Cement and Concrete Research, 36,* 110–122.

Neville, A. M., Dilger, W. H., & Brooks, J. J. (1983). *Creep of plain and structural concrete*. Longman Group Ltd: Construction Press.

Neville, A. M. (2000). *Propriétés du béton*. Paris: Eyrolles.

Parak, K. B., Nogucht, T., & Tomosawa, F. (1998). A study on the hydration ration and autogenous shrinkage of cement paste, Autogenous shrinkage of concrete. In E. Tazawa (Ed.), *Proceedings of the International Workshop*, June 13–14, Hiroshima, Japan (pp. 281–290).

Persson, B. (2000). Consequence of cement constituents, mix composition and curing conditions for self-desiccation in concrete. *Materials and Structures, 33,* 352–362.

Ranaivomanana, N., Multon, S., & Turatsinze, A. (2013). Basic creep of concrete under compression, tension and bending. *Construction and Building Materials, 38,* 173–180.

Reinhardt, H., Blaauwendraad, J., & Jongedijk, J. (1982). Temperature development in concrete structures taking account of state dependent properties. In *Proceedings of RILEM International Conference on Concrete at Early Ages*, Paris, France (pp. 211–218).

Reinhardt, H.-W., & Rinder, T. (2006). Tensile creep of high-strength concrete. *Journal of Advanced Concrete Technology, 4*(2), 277–283.

Reviron, N. (2009). Etude du fluage des bétons en traction. Application aux enceintes de confinement des centrales nucléaires à eau sous pression. Ph.D. thesis, ENS de Cachan.

Rifai, F., Darquennes, A., Benboudjema, F., Muzeau, B., & Stefan, L. (2016). Study of shrinkage restraint effects at early-age in alkali activated slag mortars. In *FraMCoS-9*, Berkeley, USA, May 29–June 1, 2016.

Rossi, P., Wu, X., Le Maou, F., & Belloc, (1994). A. Scale effect on concrete in tension. *Materials and Structures, 27,* 437–444.

Rossi, J.-L., Tailhan, F. Le, Maou, L., & Gaillet, E. Martin. (2012). Basic creep behavior of concretes investigation of the physical mechanisms by using acoustic emission. *Cement and Concrete Research, 42*(1), 61–73.

Rossi, P., Tailhan, J., & Le Maou, F. (2013). Creep strain versus residual strain of a concrete loaded under various levels of compressive stress. *Cement and Concrete Research, 51,* 32–37.

Rossi, P., Charron, J., Bastien-Masse, M., Tailhan, J.-L., Le Maou, F., & Ramanich, S. (2014). Tensile basic creep versus compressive basic creep at early ages: comparison between normal strength concrete and a very high strength fibre reinforced concrete. *Materials and Structures, 47*(10), 1773–1785.

Roziere, E., Cortas, R., & Loukili, A. (2015). Tensile behaviour of early age concrete: New methods of investigation. *Cement & Concrete Composites, 55,* 153–161.

Ruetz, W. (1968). An hypothesis for the creep of the hardened cement paste and the influence of simultaneous shrinkage. In *Proceedings of the Structure of Concrete and its Behaviour Under Load*, Londres (pp. 365–387).

Saliba, J., Loukili, A., Grondin, F., & Regoin, J.-P. (2012). Experimental study of creep-damage coupling in concrete by acoustic emission technique. *Materials and Structures, 45*(9), 1389–1401.

Sanahuja, J., Dormieux, L., & Chanvillard, G. (2007). Modelling elasticity of a hydrating cement paste. *Cement and Concrete Research, 37*.

Schindler, A. K. (2004). Effect of temperature on hydration of cementitious materials. *ACI Materials Journal, 101*(1), 72–81.

Sellier, A., Multon, S., Buffo-Lacarrière, L., Vidal, T., Bourbon, X., & Camps, G. (2015). Concrete creep modelling for structural applications: Non-linearity, multi-axiality, hydration, temperature and drying effects. *Cement and Concrete Research*.

Shah, S. P., & Chandra, S. (1970). Fracture of concrete subjected to cyclic and sustained loading. *ACI Journal Proceedings, 67*.

Smadi, M., & Slate, F. O. (1989). Microcracking of high and normal strength concretes under short- and long-term loadings. *ACI Materials Journal, 86,* 117–127.

Sofi, M., Mendis, P. A., & Baweja, D. (2012). Estimation of early-age in situ strength development of concrete slabs. *Construction and Building Materials, 29,* 659–666.

Staquet, S., Delsaute, B., Darquennes, A., & Espion, B. (2012). Design of a revisited TSTM system for testing concrete since setting time under free and restrained conditions. In F. Toutlemonde & J.-M. Torrenti (Eds.), *Crack control of mass concrete and related issues concerning early-age of concrete structures (PRO, 85)*, March 15–16, 2012, Paris, France (pp. 99–110). Paris: RILEM Publications.

Stefan, L., Benboudjema, F., Torrenti, J. M., & Bissonnette, B. (2010). Prediction of elastic properties of cement pastes at early ages. *Computational Materials Science, 47*(3), 775–784.

Subcommittee 4: Standardized test methods for creep and shrinkage. *Materials and Structures, 31*, 507 (1998).

Tamtsia, B. T., Beaudoin, J. J., & Marchand, J. (2004). The early age short-term creep of hardening cement paste: Load-induced hydration effects. *Cement and Concrete Research, 26,* 481–489. https://doi.org/10.1016/S0958-9465(03)00079-9.

Taylor, H. F. W. (1990). *Cement chemistry*. London: Academic Press Limited.

Toma, G. (1999). Comportement des bétons au jeune âge. Ph.D. thesis, Université de Laval, Canada (264 pp.).

Ulm, F. J., & Coussy, O. (1998). Couplings in early-age concrete: From material modeling to structural design. *International Journal of Solids and Structures*, *35*(31–32), 4295–4311.

Van Breugel, K. (1991). Simulation of hydration and formation of structure in hardening cement-based materials, Ph.D. thesis, Delft Technical University, The Netherlands (305 pp.).

van Vliet, M. R., & van Mier, J. G. (2000). Experimental investigation of size effect in concrete and sandstone under uniaxial tension. *Engineering Fracture Mechanics, 65*(2), 165–188.

Vandamme, M., & Ulm, F.-J. (2009). Nanogranular origin of concrete creep. *Proceedings of the National Academy of Sciences of the United States of America, 106,* 10552–10557. https://doi.org/10.1073/pnas.0901033106.

Vandamme, M. (2004). A few analogies between the creep of cement and of other materials. *Concreep, 10*(2015), 78–83.

Waller, V., d'Aloïa, L., Cussigh, F., & Lecrux, S. (2004). Using the maturity method in concrete cracking control at early ages. *Cement & Concrete Composites, 26,* 589–599.

Wittmann, F. H. (1982). Creep and shrinkage mechanisms. In Z. P. Bažant & F. H. Wittmann (Eds.), *Creep and shrinkage in concrete structures* (pp. 129–161). Chichester: Wiley.

Wittmann, F. H. (2015). Useful fundamentals of shrinkage and creep of concrete. *Concreep, 10* (2015), 84–93.

Xiang, Y., Zhang, Z., He, S., & Dong, G. (2005). Thermal–mechanical analysis of a newly cast concrete wall of a subway structure. *Tunnelling and Underground Space Technology, 20,* 442–451.

Yssorche-Cubaynes, M.-P., & Olivier, J.-P. (1999). Self-desiccation microcracking and HPC and VHPC durability, *Materials and Structures/Matériaux et Constructions*, *32*, 14–21.

Yuan, Y., & Wan, Z. L. (2002). Prediction of cracking within early-age concrete due to thermal, drying and creep behavior. *Cement and Concrete Research, 32,* 1053–1059.

Zhaoxia, L. (1994). Effective creep Poisson's ratio for damaged concrete. *International Journal of Fracture, 66*(2), 189–196.

Chapter 5
Mixture Proportioning for Crack Avoidance

Stéphanie Staquet, Brice Delsaute, Eduardo M. R. Fairbairn, Roberto Torrent, Agnieszka Knoppik, Neven Ukrainczyk and Eduardus A. B. Koenders

Abstract In this chapter, the nature, the physical and chemical properties and the content of the concrete constituents will be discussed for the understanding of the way of making an optimized mixture proportioning of the concrete for massive applications where the temperature rise must be minimized.

5.1 Overview

Composition of concrete mix determines—to the great extent—physical and mechanical properties of the hardening and hardened concrete. Ones of particular importance are thermal properties of early-age concrete, such as the rate of heat development, q, and the total amount of heat, Q_{tot}, specific heat, C, thermal conductivity, λ, and coefficient of thermal expansion, CTE. It has also influence on other physical properties, such as autogenous shrinkage, ε_{ca}. Mechanical properties of concrete and the rate of their time development also depend strongly on the amount and properties of concrete components, especially the amount and type of cement. The following factors connected with the concrete mix design have an influence on the early-age concrete behaviour:

S. Staquet (✉) · B. Delsaute
BATir, LGC, Université Libre de Bruxelles, ULB, Brussels, Belgium
e-mail: sstaquet@ulb.ac.be

Eduardo M. R. Fairbairn
Federal University of Rio de Janeiro, Rio de Janeiro, Brazil

R. Torrent
Materials Advanced Services Ltd, Buenos Aires, Argentina

A. Knoppik
Silesian University of Technology, Gliwice, Poland

N. Ukrainczyk · E. A. B. Koenders
Institute of Construction and Building Materials, Technische Universität Darmstadt, Darmstadt, Germany

© RILEM 2019

E. M. R. Fairbairn and M. Azenha (eds.), *Thermal Cracking of Massive Concrete Structures*, RILEM State-of-the-Art Reports 27,
https://doi.org/10.1007/978-3-319-76617-1_5

- type, amount and fineness of cement, including type and amount of supplementary cementitious materials,
- water content and water-to-binder ratio,
- type and composition of aggregate,
- type, composition and amount of fibre reinforcement (discussed in detail in Chap. 10).

Design of the optimal concrete mix is considered as the easiest way to minimize negative effects in early-age concrete. The selection of adequate mixes to mitigate heat development is generally based on the control of one or several material variables mentioned just above. The optimal concrete mix design usually relates to application of low-heat cement, minimization of the total amount of cement per unit volume of concrete or partial replacement with SCMs and use of cement with low fineness (JCI Guideline 2008). The cement-to-binder ratio is also crucial—structures with denser cement paste matrix (lower *w/c*) are more prone to cracking (Bentz and Peltz 2008). Although the heat development and the subsequent temperature evolution and thermal gradient inside the structure are the most important factor for the design of mass concrete element, the consideration of other material properties is needed (e.g. strength, E-modulus, creep, autogenous strain) to prevent any early-age thermal cracking.

5.2 Aggregates

Early-age properties and behaviour of concrete elements are also governed by the characteristics of aggregate. The aggregates used for production of concrete vary in thermal properties and thus highly influence the magnitude of thermal strains in a concrete element (Riding et al. 2009; Klemczak and Knoppik-Wróbel 2012).

The thermal expansion coefficient (CTE) of concrete is directly linked to the thermal expansion coefficient of the aggregate used in the mix. The higher the CTE of the aggregate is, the higher the CTE of concrete is. Tables 5.1 and 5.2 illustrate the influence of aggregate CTE on hardened concrete CTE (Mehta and Monteiro 2006).

The development of tensile strength is an important property in the mitigation of early-age cracking in mass concrete. The tensile strength of concrete is strongly influenced by aggregate characteristics like texture. Concretes made of crushed or

Table 5.1 Influence of aggregate CTE on hardened concrete CTE (Mehta and Monteiro 2006)

CTE (μstrain/°C)	Limestone	Basalt gabbros	Granite	Air-cooled blast furnace slag
Aggregate	5	6	7	8
Concrete	6	7	8	9

Table 5.2 Influence of aggregate CTE on hardened concrete CTE (Mehta and Monteiro 2006)

CTE (μstrain/°C)	Dolerite	Sandstone gravels	Quartzite
Aggregate	9	10	11
Concrete	10	11	12

rough textured aggregates (basalt, granite) present higher strengths than those made of rounded or smoother aggregates.

The level of water saturation influences the magnitude of autogenous shrinkage of concrete: saturated aggregates are used to minimize autogenous shrinkage; however, there is no direct correlation between the degree of saturation of the aggregate and the magnitude of autogenous shrinkage (Cortas et al. 2014).

The porosity of the aggregate affects strongly the development and the magnitude of the properties of concrete. Lightweight aggregates are characterized by having a very high porosity in comparison with classical aggregate. When used instead of classical aggregate, the subsequent effects have been observed at concrete scale:

- large decrease of the self-weight of concrete which is very convenient for massive structure;
- decrease of the compressive strength;
- decrease of the thermal conductivity which depends mainly on the density and the water content of the concrete (Real 2016);
- decrease of the autogenous strain when the aggregate are saturated before mixing (Maruyama 2012; Liu 2016; Zhuang 2016). In such case, lightweight aggregate plays the role of water storage agent that refills capillarity pores during the hardening process and avoids or reduces the self-desiccation mechanism with the continuous release of water (Lura 2003; Bentur 2001). This phenomenon is all the more important when the water absorption rate of aggregate is important (Zhuang et al. 2016).

As for the autogenous strain, a reduction of the CTE is observed during the hardening phase when using saturated lightweight aggregate (Maruyama 2012).

Therefore, for mass concrete elements, lightweight aggregate must be used in saturated conditions in order to reduce the autogenous shrinkage and the increase in coefficient of thermal expansion due to the hydration process.

5.3 Water/Cement Ratio

It is well-known that the water-to-cementitious materials ratio affects strongly the development of concrete strength. Figure 5.1 illustrates the effect of this ratio on concrete compressive strength (Kosmatka et al. 2002). The higher the w/c is, the lower the compressive strength is.

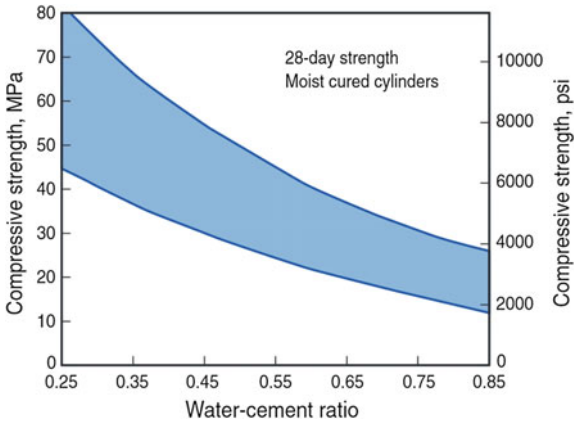

Fig. 5.1 Effect of water-to-cement ratio on compressive strength (Kosmatka et al. 2002)

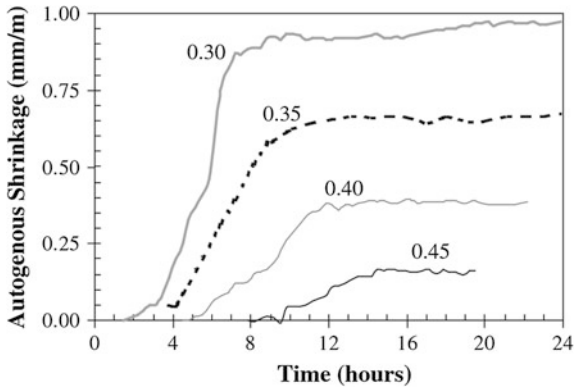

Fig. 5.2 Effect of water-to-cement ratio on autogenous shrinkage (Holt and Leivo 2004)

The water-to-cementitious materials ratio is also known to affect strongly the development of the autogenous shrinkage. Figure 5.2 shows that the higher the water-to-cementitious materials ratio is, the lower the magnitude of the autogenous shrinkage is (Holt and Leivo 2004).

For concretes with high w/c ratio (more than 0.4), autogenous swelling develops just after the final setting. In Delsaute (2017), several tests on concrete with different w/c ratio were performed and are shown in Fig. 5.3. It is observed that the higher the w/c ratio is, the greater the duration and the amplitude of swelling will be. The water-to-cement ratio has also an impact on the final setting of cement-based materials. For high water-to-cement ratio, setting occurs later (Saleh et al. 2017).

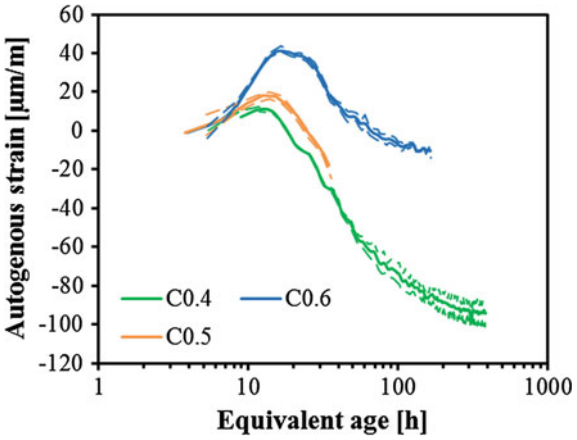

Fig. 5.3 Evolution of the autogenous strain for different water-to-cement ratios (0.4–0.5 and 0.6). Adapted from (Delsaute 2017)

5.4 Admixtures

During the whole hydration process, the water content is of major importance in the properties of cement-based materials such as the strength and the creep. During the hardening process or when concrete is exposed to the surrounding environment, volume contraction or expansion occurs with the change of relative humidity inside concrete. Such volume variation can be the cause of cracking in concrete structure. Moreover, damage caused by freeze/thaw cycle or alkali–silica reactions is strongly driven by the water content. Therefore, it is essential to well control the water content of cement-based materials since a fresh state till a hardened state.

Superabsorbent polymers (SAP) are polymeric materials which have the ability to control the water content by playing the role of curing agent serving as an internal reservoir of water. Standard SAP has a water absorption and/or water release capacity corresponding to 100–400 g of water for 1 g of dry SAP (Jensen 2013). When exposed to water, SAPs swell and inversely shrink when subjected to drying. SAPs were generally developed and used for high-performance concrete with low water-to-cement ratio (<0.45).

The introduction of SAP in cement-based materials changes the total porosity, the quantity of cement hydrated and the relative humidity. First, the SAP absorbs and is filled of water and acts as an aggregate. As a consequence, the introduction of SAP modifies the effective water-to-cement ratio in the early hydration stage. This changes the rheological aspect of the concrete at fresh state with the increase in both the yield stress and plastic viscosity (Jensen and Hansen 2002). Extra water can be added in order to compensate the loss of workability. During the hardening process, self-desiccation phenomenon occurs which causes a water release and shrinkage of the SAP. The water released from SAP promotes further hydration of cement particles which leads to an increase of the final hydration degree (Igarashi and Watanabe 2006). When water is released from SAP, additional voids are induced and a general increase of the porosity is observed (Mechterine et al. 2008). Finally,

even with high-performance concrete, the relative humidity stays high during the hardening phase with the presence of SAP.

Due to the change of effective water-to-cement ratio at very early age, the setting time is shifted. When extra water is added to keep a same effective water-to-cement ratio, the presence of SAP delayed the setting (Dudziak and Mechterine 2010a, b).

Several studies were performed on cement pastes (Jensen and Hansen 2002; Igarashi and Watanabe 2006; Lura et al. 2006a, b) and concrete (Igarashi and Watanabe 2006; Mechterine et al. 2008; Mechterine et al. 2009) to understand the effect of SAP on the autogenous deformation. Experimental results obtained in (Igarashi and Watanabe 2006) on cement pastes and concretes are shown in Figs. 5.4 and 5.5. Different water-to-cement ratios and percentage of SAP by mass

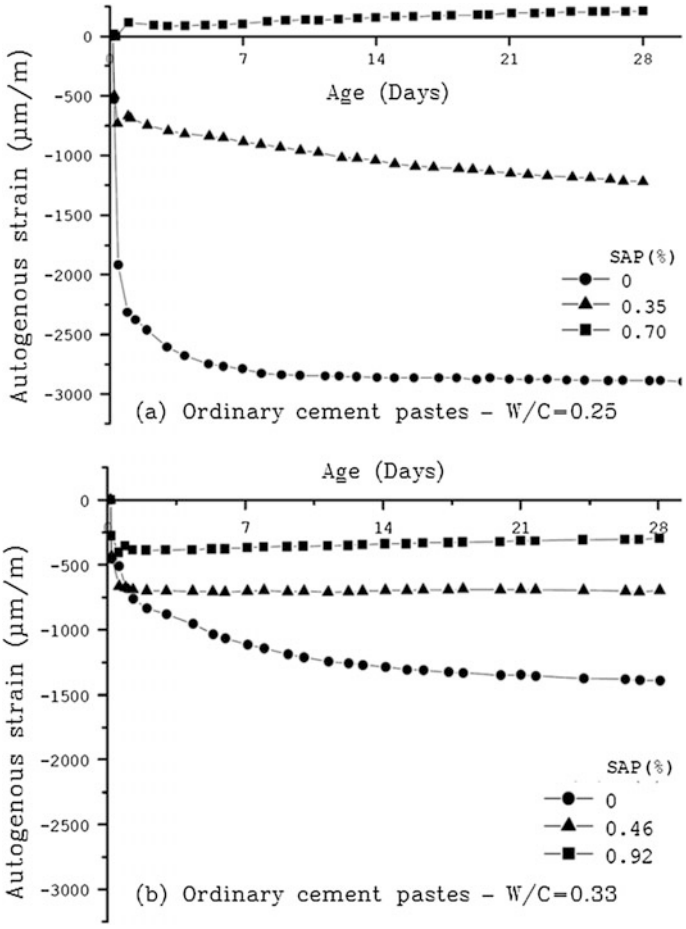

Fig. 5.4 Autogenous strain for cement pastes with and without SAP. **a** W/C = 0.25, **b** W/C = 0.33 (Igarashi and Watanabe 2006)

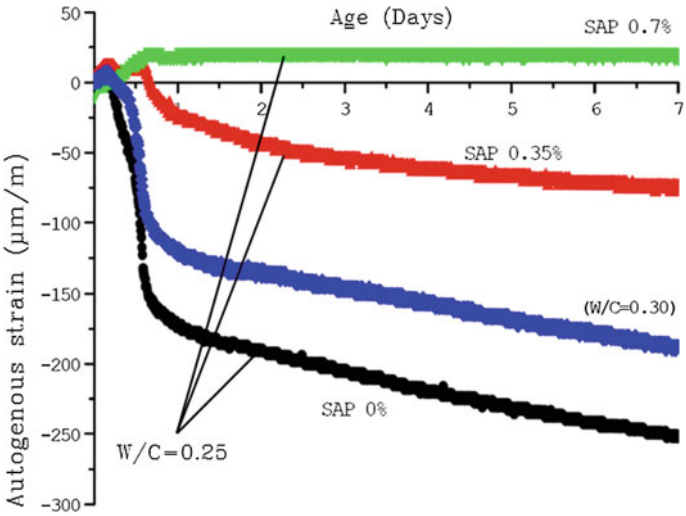

Fig. 5.5 Autogenous strains of concretes with different amounts of SAP (Igarashi and Watanabe 2006)

of cement were used. Extra water was added to keep a same effective water-to-cement ratio for composition with SAP.

It is generally observed for both scales that effect of SAPs is more pronounced on composition with very low water-to-cement ratio (composition for which the self-desiccation phenomenon is very consequent). A strong decrease of the autogenous shrinkage or even a swelling takes place at very early age for small (±0.3%) and high (±0.6%) addition of SAP, while for longer duration, a decrease of the autogenous shrinkage is only observed for composition with high addition of SAP. This is explained by the high part of the curing water of the SAP which is used during the first days after the final setting. For low addition of SAP, the whole curing water is consumed during the first days, while for high addition of SAP, the curing period is counted in weeks.

In Chap. 3, it has been shown that the CTE depends on the relative humidity. Wyrzykowski and Lura (2013) have pointed out that internal curing by means of SAP is an efficient method to avoid a significant increase of the CTE during the hardening process of high-performance concrete. Such application of the SAP allows decreasing the risk of cracking at early age caused by the restrained of thermal strain during the cooling of concrete structures.

The addition of SAP and extra water to keep a same effective water-to-cement ratio changes the mechanical properties of cement-based materials. At early age, the compressive strength is reduced with the higher porosity and moisture provided by the internal curing effect of SAP. For later ages, higher increase of the compressive strength was observed for composition with SAP by several authors (Mechterine et al. 2009; Lura et al. 2006b; Piérard et al. 2006; Igarashi and Watanabe 2006).

This can be explained by the general increase of cement hydrated, the hydration of cement particles in the void formed when SAP releases water (Reinhardt et al. 2008) or the reduction of the internal stresses resulting from the restrained of the autogenous strain of the cement paste by aggregates (Dudziak and Mechterine 2010b). Similar observations were achieved for the tensile strength (Lam and Hooton 2005). However, the order of magnitude of the increase provided by the SAP at later ages was found higher for the tensile strength in comparison with the compressive strength. On mortar and concrete scale, the elastic modulus seems to slightly decrease with the addition of SAP according to results of Dudziak and Mechtcherine (2010a, b). However, results of Wyrzykowski and Lura (2013) show significant decrease of the elastic modulus for cement pastes and mortars with the presence of SAP.

In Fig. 5.6, the global effect of SAP on main properties of concrete used for massive structures is presented. Even if the addition of SAP decreases the mechanical performance of cement-based materials at early age, a general positive effect is provided in terms of cracking risk by means of restrained shrinkage in concrete structures. Free deformations are reduced with the strong decrease of the autogenous strain and the CTE during the hardening phase. Such differences lead to a global reduction of the induced stresses in concrete. Ring tests performed by

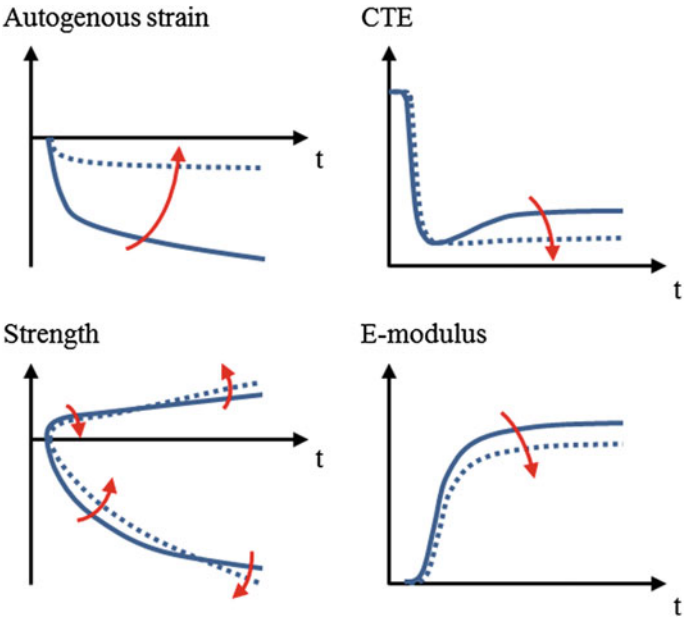

Fig. 5.6 Schematic representation of the effect of SAP on major parameters of mass concrete. Continuous lines correspond to the behaviour of a high-performance concrete, and dashed lines represent the corresponding high-performance concrete with the incorporation of SAP

Jensen and Hansen (2002) highlight this fact. For mortar compositions, a considerable decrease of the stresses induced by the restrained of the mortar free strain caused by the steel ring was observed for composition with SAP.

5.5 Cement

Cement composition is a major contributor to heat of hydration. Variables such as cement content and fineness of cement affect strongly the temperature rise in concrete because the chemical reaction between cement and water is highly exothermic. The adequate choice of these variables can be very efficient as means of temperature control techniques.

In Chap. 2, it has been shown that the relative proportions of the chemical compounds or Bogue compounds (such as C3S, C2S, C3A and C4AF) and their fineness determine the amount of heat they generate during hydration as well as the rate of heat generation. Additionally, the quantity of cement used directly affects the rate and magnitude of heat generation because that induces the quantity of reactive products available to hydrate and generate heat (ACI 207.2R 1997). The higher the cement content, the higher the temperature rise.

Cement fineness is a variable that affects more the rate of the temperature rise in concrete than the magnitude itself of the temperature rise (ACI 207.2R 1997). Indeed, higher fineness induces higher early strength and more rapid heat generation because the cement has more surface area to react with the water.

Concrete mixes made of coarser cements and with higher *w*/*c* ratio also exhibit slower development of mechanical parameters (tensile strength, modulus of elasticity) (Bentz 2008).

5.6 Supplementary Cementitious Materials

Above a threshold substitution (about 25% for the pozzolans), clinker replacement materials reduce hydration kinetics and exhibit lower early ages, but higher long-term mechanical properties, which is a desirable property for mass concretes. Slag and fly ash are the most abundant SCMs used today, but have limited resource, and the amounts produced are much less than the worldwide production of cement. Consequently, consideration should also be given to other replacement materials (Schneider et al. 2011), such as ground limestone (Lothenbach et al. 2008), and natural pozzolans (Ghrici et al. 2007), including calcined clays such as metakaolin (Paiva et al. 2012; Banfill et al. 2009; Antoni et al. 2012). Ground limestone additions of up to around 5% can react with cement and enhance most properties (Lothenbach et al. 2008).

At present, the production of low-clinker mass concrete based on ground limestone with 50% Portland cement substitution or more is beyond the limits of

contemporary concrete technology and can only be achieved by applying scientific methods and approaches to optimize binder and concrete composition and, finally, find the "bottom limit" on clinker content in concrete. There is an increased interest in developments on multi-component binders (Ghrici et al. 2007; de Weerdt et al. 2011; Bai et al. 2002; Menendez et al. 2003; Pipilikaki and Katsiot 2009; Mounanga et al. 2011; Damidot et al. 2011) with coupled clinker replacement, by f.e. ground limestone, fly ash and metakaolin. Literature (Paiva et al. 2012; Banfill et al. 2009; Antoni et al. 2012) demonstrates that metakaolin is not only environmental and economic cement replacement material but also an effective pozzolan which causes improvements in the microstructure and hence in the concrete durability. Metakaolin is normally produced by calcining pure clays at appropriate temperatures (around 750 °C). Highly reactive metakaolin can also be obtained by the calcination of waste sludge from the paper recycling industry as well as indigenous lateritic soils (Banfill et al. 2009; Antoni et al. 2012). Optimization of the novel quaternary binder composition together with their particle sizes will allow for higher levels of clinker substitution. Recent production of multi-composite binders has already produced a necessary shift in the manufacture process used in the cement industry.

As the high current market share of Portland limestone cement shows, **limestone** is a cheap convenient low-cost mineral substitute for Portland cement clinker which is available in almost unlimited quantities in the cement manufacturers' quarries. Moreover, a significantly lower energy input is required for grinding to the required fineness (Schneider et al. 2011) than for cement or other SCMs. Unfortunately, this material is much less reactive than slag making the production of good-quality concrete more difficult at high substitution levels (Table 5.3).

Table 5.3 Overview of some pozzolanic binders originating from primary waste streams

Type	Waste stream	Reactivity
Fly ash	Fine residues generated in coal (and biomass) (co-)combustion of electricity plants	Pozzolanic reactivity from silicate glass containing Al_2O_3, Fe_2O_3 and alkalies
Granulated blast-furnace slag	Obtained by quenching molten iron slag (a by-product of iron and steel-making) from a blast furnace in water or steam	Cementitious material from silicate glass containing mainly CaO, MgO, Al_2O_3 and SiO_2
Metakaolin	Calcination of kaolinite clay	Reactivity from Al2O3 and SiO2 dehydroxylated (amorphous 9 parts)
Silica fume	By-product of the induction arc furnaces in the silicon metal and ferrosilicon alloy industries	Pozzolanic reactivity from amorphous SiO_2

5.6.1 Slag/Fly Ash

Of many types of industrial **slags**, this report will focus only on the widely used ground-granulated blast-furnace slag (GGBFS), a by-product from iron production where iron ore, limestone and coke are heated up to 1500 °C. When slag is quenched (cooled down fast) during production, it forms amorphous (glassy) structure which exhibits good pozzolanic and hydration reactivity. On the other hand, when slag is cool down slowly it crystallizes essentially as melilite, a solid solution of akermanite (C_2S_2M) and gehlenite (C_2AS). Crystallized slag has poor reactivity and can only be used as an aggregate when making concrete, or as part of the raw meal in cement clinker production. Slag is further processed by drying and then ground to a very fine powder. Generally, grinding resistance of slag is higher than PC clinker or limestone and fly ash.

Fly ashes (FAs) are fine particles that are collected in power plants running on combustion of coal or lignite, as well as co-fired by biomass. The size of FA particles is largely dependent on the type of dust collection equipment and is usually equal or finer than PC cement. Fly ash generated in coal burning power plants is an inherently variable material because of the variability in type and mineralogical composition of the coal, degree of coal pulverization, type of furnace and oxidation conditions including air-to-fuel ratio, and the manner in which fly ash is collected, handled and stored before use. Some ash particles are fused and cooled quickly when they leave the flame to solidify in glassy spheres. Fly ashes that are clean (low carbon content), do not contain any non-reactive coarse crystalline particles and have low variability in quality are the ones suitable for cement and concrete industries. Fly ashes are classified as silico-aluminous rich fly ashes (Class F, generally produced from burning anthracite or bituminous coal) and silico-calcareous rich fly ashes (Class C, with more than 15% CaO, produced from lignite or sub-bituminous coal). Apart from high amorphous content in Cass F FA, main low reactive minerals are haematite, mullite, quartz, ferrite spinel. Class C FA comprises lower amount of amorphous phase (but more reactive) than class F, and following minerals: anhydrite, alkali sulphate, C2S, C3S, haematite, lime, periclase, mullite, merwinite, periclase, quartz, sodalite, ferrite spinel. Dead burnt MgO and CaO presented in fly ash affects the soundness of the resulting concrete through its expansive hydration to $Ca(OH)_2$ and $Mg(OH)_2$.

Above a threshold substitution of about 25% for the pozzolans, clinker replacement materials reduce hydration kinetics and exhibit lower early ages, but higher long-term mechanical properties, which is a desirable property for mass concretes. Slag and fly ash are the most abundant SCMs used today, but have limited resource, and the amounts produced are much less than the worldwide production of cement.

The use of low-heat cement, usually blended cement, is recommended mostly because the reduction of the total hydration heat results in smaller thermal strains. Supplementary cementitious materials (SCMs) such as fly ash and ground-granulated blast-furnace slag have been found to be effective in minimizing the

quantity of clinker and therefore reducing the hydration heat (ACI 207.2R 1997). Fly ash is used for mass concrete due to its effect on workability and its low heat generation (Sakai et al. 2005). In Schindler and Folliard (2005), many examples of reduction in heat release in case of cementitious systems containing fly ash and cement are provided. The use of ground-granulated blast-furnace slag has also been effective to mitigate the temperature rise in mass concrete (Schindler and Folliard 2005). The higher the slag content, the higher the reduction of heat release. The presence of slag also delays the occurrence of the peak of temperature due to the activation energy of the slag which increases the hydration rate in case of temperature higher than 20 °C and decreases the hydration rate in case of temperature lower than 20 °C.

The use of GGBFS as a substitute for cement clinker can improve technical properties, including strength, permeability and corrosion resistance (Shi and Qian 2000; Song and Saraswathy 2006). In a comprehensive German research into the slag/clinker ratio for a range of chemical composition of 72 different GGBFS and 16 PCs, the following facts were established: (1) CaO amount increases strength at all ages; (2) MgO has nearly the same effect but only below 10% of its total amount; (3) Al_2O_3 amount increases the early strength, but only below the 14% limit; (4) MnO amount decreases strength; (5) alkali amount increases strength.

Wainwright and Ait-Aider (1995) showed that addition of GGBFS in PC paste increases the setting times but reduces the paste consistency. Partial replacement of OPC with 40 and 70% of GGBFS led to increases in the bleeding of the concretes (Wainwright and Ait-Aider 1995, Olorunsogo and Wainwright 1998), more pronounced at the higher replacement levels. It was shown that addition of 55% slag in concrete mix (binder:sand:aggregate proportions 1:2.5:3.6, 300 kg/m3 cement, w/b = 0.56) increased the bleed capacity by 30% (compared to the plain PC mix) but had little effect on bleed rate. Moreover, increasing slag content 55–85% had no further significant effect on bleeding. They also reported that slag addition results in improved concrete workability. Wan et al. (2004) concluded that workability of mortar increased with the increase of the surface area of GGBFS, while the smoother the surface of particles, the better was the fluidity of mortar. Setting time increases with the increase in GGBFS content. In general, slag decreases the hydration rate of blended cement.

The improvement in strength of concrete containing 20–60% GGBFS occurs only after 28 days of curing, where similar or higher long-term strength was obtained as compared with that of normal PC concrete (Aldea et al. 2000; Miura and Iwaki 2000). Babu and Kumar (2000) reported that 28-day compressive strength of concretes containing GGBFS up to 30% replacement was all slightly above that of normal concretes, and at all other replacements (up to 80%) was below. Also, they observed that the variations due to the different percentages of slag replacement were smaller than the corresponding variations in the case of fly ash. The reduction of the volume porosity and the reconfiguration of the pore structure towards a more refined pore size results in a denser matrix (Manmohan 1981; Chen 2013). During the hydration process, internal pores dry with the self-desiccation phenomenon. With the use of GGBFS on concrete, self-desiccation

effect and a finer pore size are coupled and a net enhancement of the compressive stress occurs on the capillarity pores at microscale which leads to significant autogenous shrinkage at macro-scale (Tazawa 1993; Persson 1997). As a result, autogenous shrinkage increases with partial substitution of cement by slag in the long term (Tazawa 1995; Lim and Wee 2000; Lura et al. 2001; Lee et al. 2006; Hansen and Reinhardt 1991). Such increase can lead to a cracking in high-performance concrete (Pailere et al. 1989; Miyazawa et al. 1993; Jensen and Hansen 1996). Liu and Hansen (2016) have shown that the magnitude of autogenous shrinkage of concrete composition with GGBFS can be strongly reduced when used with lightweight aggregate. For mortar compositions with GGBFS and/or Portland cement and a water-to-binder ratio of 0.35, when 50% of the natural aggregate are replaced by lightweight aggregate, the autogenous shrinkage can be nullified.

Li and Zhao (2003) showed that concretes incorporating both GGBFS and FA can achieve adequate early strength, while maintaining a high long-term strength. Wan et al. (2004) indicated that strength of mortar incorporating GGBFS is not only related to the higher surface area, which of course increases strength, but also on particle size distribution (PSD) of GGBFS. For same slag surface area, the more fine particles (<3 μm) of slag, the higher its early strength was. Slag particles 3–20 μm improved the long-term strength. Compressive strength developments depend upon the GGBFS replacement percentage and the concrete age (Cheng et al. 2005). The amorphous part of slag reacts slowly, and it takes time to increase pH from the hydration of Portland cement to dissolve the glassy slag parcels at early age. Thus, incorporation of slag slows down the early strength development. However, GGBFS concrete had higher compressive strength than ordinary Portland cement concrete (OPC) after GGBFS hydration and pozzolanic reaction were almost accomplished. Higher GGBFS replacement percentage had higher ultimate strength. Cheng et al. (2005) also reported the beneficial influence of GGBFS on the rapid chloride permeability (RCPT) and water permeability of concrete. Khatib and Hibbert (2005) investigated the influence of incorporating GGBFS and metakaolin (MK) on the compressive strength of concrete. Khatib and Hibbert (2005) investigated the influence of incorporating GGBFS (0-80% partial replacement of PC) and metakaolin (MK, 0-20% replacement) on the compressive strength of concrete. There was a systematic decrease in compressive strength with the increase in GGBFS content during the early stages of hydration. Beyond 28 days and up to at least 90 days, the presence of GGBFS was highly beneficial at 40 and 60% replacement with a strength exceeding that of the control. A noticeable strength reduction at all ages is observed at 80% GGBFS. The decrease in compressive strength during the early ages of curing of GGBFS concrete was compensated by the inclusion of metakaolin (MK), without compromising the long-term strength. Although above 10% MK no further improvement in strength was observed, it was advantageous in increasing the flexural strength.

Coal fly ash lowers the rate of hydration reaction and thus also the rate of self-heating, but also the strength development (Flower and Sanjayan 2007). The lubricating effect of the glassy spherical fly ash particles, generally finer than

cement, and the increased ratio of solids to liquid make the concrete less prone to segregation (and bleeding) and increase concrete workability. The addition of low calcium Class F fly ashes generally show some degree of retarding effect on cement setting, but depends on the characteristics and amount of fly ash used. Increasing the replacement level of fly ash caused lower heat evolution effect in concrete (Atis 2002). The highly reactive fly ashes start their contribution to strength development almost from the onset of PC hydration. But usually the low calcium fly ashes do not exhibit significant pozzolanic activity and affect strength after about two weeks of hydration. For a typical low calcium fly ash, it was found that the pozzolanic reaction started at 11 days after hydration at 20 °C and the significant effect on compressive strength appeared to occur after 28 days of curing. However, some high calcium fly ashes, with calcium oxide content more than 15%, may start contributing to strength development as early as 3 days after mixing because of their self-hardening and pozzolanic properties. Fly ash in concrete may significantly improve the quality of the bulk paste microstructure and the transition zone between the paste and the aggregate. The favourable effects of fly ash in concrete cured at moderately elevated temperatures can be advantageously used in the construction of mass concrete. Poor curing conditions more adversely affect the strength of concrete made from pozzolanic cement than that of PC (Ozer and Ozkul 2004; Atis 2002).

Gajda, et al. (2014) developed and investigated a mass concrete without Portland cement. The binder is composed of fly ash (Class C) content of 658 kg/m^3 and a water-to-binder ratio of 0.29. Coarse limestone and natural sand were used as aggregates. Furthermore, a hydrocarboxylic acid salt (44.7 kg/m^3) was used in the mix. This composition was compared to a concrete for which 70% of the binder is replaced by Portland cement (Type I/II) and 30% by fly ash (Class F) in mass. The water-to-binder of the second mix 0.42. At early age, both compositions have obtained a compressive strength of around 18 MPa at an age of 1 day. Then, the composition with fly ash (class C) reaches a compressive strength of 50 MPa, while the second composition reaches a compressive strength of 35 MPa. Moreover, semi-adiabatic tests have been for both compositions. It results that the adiabatic temperature of the composition with Portland cement increases more strongly with a temperature of 83 °C at an equivalent age of 28 days instead of 58 °C for the composition with fly ash (class C).

Concrete strength where a fine aggregate (sand) was replaced by up to 50% with fly ash was higher than the plain concrete at all the ages up to 365 days (Siddique 2003), this difference becoming more distinct after 28 days. Maximal strength occured with 50% fly ash content at all ages and was 40.0 MPa at 28 days compared to the reference of 26.4 MPa. Saraswathy et al. (2003) improved the blended concrete strength by employing various FA activations: physical, thermal and chemical, although it was still lower than the reference one even after 90 days.

Moreover, higher rate of creep is observed in blended cement which reduces early-age stresses (Riding et al. 2008; Darquennes et al. 2011a, b, c, 2013; Carette 2015). In general, autogenous shrinkage is also decreased in blended cements (Pane and Hansen 2002; Nagy 2001) and it is lower when more than one SCM component

is used (Akkaya et al. 2007). However, it is reported that addition of some SCMs may increase the hydration rate and the total amount of hydration heat and consequently autogenous shrinkage and thermal strain (mainly silica fume is referred Pane and Hansen 2002; Kadri et al. 2009) and that drying shrinkage is higher in blended cements (Akkaya et al. 2007).

Furthermore, blended cements exhibit slower development of mechanical parameters (tensile strength, modulus of elasticity) (Nagy 2001; Knoppik-Wróbel 2012) with the rate of development decreasing with the increasing SCM content (Akkaya et al. 2007). Consequently, in elements made of these concrete mixes, despite smaller strains, cracking may occur almost as early and be as intense as in OPC concrete elements (Akkaya et al. 2007; Bentz and Peltz 2008; Knoppik-Wróbel 2012).

5.6.2 Silica Fume

Silica fume **SF** is often replaced only with 5% of clinker, due to its high pozzolanic activity, price and its small size inducing rheological constraints. It is used more to improve concrete properties in high-strength concrete rather than as a SCM used for clinker substitution. Moreover, SF availability is quite limited (global production of just 1 million tons (Kadri et al. 2009).

5.6.3 Multi-component Binder Blends

The simultaneous use of two or three mineral admixtures as a partial substituent of Portland cement in mortars and concretes has several advantages, in terms of mechanical performance and durability, compared with binary cements (Ghrici et al. 2007; de Weerdt et al. 2011a, b; Bai et al. 2002; Menendez et al. 2003; Pipilikaki and Katsiot 2009; Mounanga et al. 2011; Damidot et al. 2011). The synergic increase in solid volume and improvement in microstructural integrity in multiple limestone–pozzolan blends can be related to the reactive aluminous content of the pozzolan that increases the amount of reactive limestone (Antoni et al. 2012; Damidot et al. 2011). It was shown (Antoni et al. 2012) that 45% clinker replacement, of which 30% by metakaolin and 15% by limestone, gives better mechanical properties of standard mortars at 7 and 28 days than the pure reference cement. Even 60% substitution (40% metakaolin, 20% limestone) has 93% of the pure Portland reference strength at 28 days. Bai et al. (2002) demonstrated that judicious use of Portland cement–fly ash–metakaolin blends in concrete enables a much reduced clinker requirement while still maintaining or enhancing strength in the medium to long term. The metakaolin enhances early (28 days) strength, while fly ash retards early strength.

5.7 Mix Design Methods for Conventional Mass Concrete

5.7.1 General Principles of Mix Design

Concrete mix design can be defined as the appropriate selection and proportioning of constituents to produce a concrete with predefined characteristics in the fresh and hardened states. In general, concrete mixes are designed in order to achieve a defined workability, strength and durability.

The selection and proportioning of materials depend on:

- the structural requirements of the concrete,
- the environment to which the structure will be exposed,
- the job site conditions, especially the methods of concrete production, transport, placement, compaction and finishing,
- the characteristics of the available raw materials.

In mass concrete, an important element—usually disregarded for conventional structural concrete—is the need to keep volume changes low, in particular those arising from the thermal evolution of the concrete, so as to control the risk of cracking. For this, it is essential that the binder should generate a low heat of hydration and that its content in the mix is kept at a minimum.

Figure 5.7 shows the adiabatic temperature rise measured in several Brazilian dams (Tucurui and Itaipú among them) (Pacelli et al. 1982) and in an Argentine Dam (Piedra del Aguila) (Torrent 1985), as a function of the binder content of the mix. It is clear that keeping the binder content low is essential to achieve low thermal stresses in the structure.

After mixing, fresh concrete is a concentrated suspension of solids in water; the solids—typically denser than water—vary widely in dimensions (see Table 5.4). All these particles tend to settle in the water, but at different speeds (the larger ones tending to settle faster), with the smaller particles (fines and sand) "holding" the larger ones, thus providing cohesion to the conglomerate.

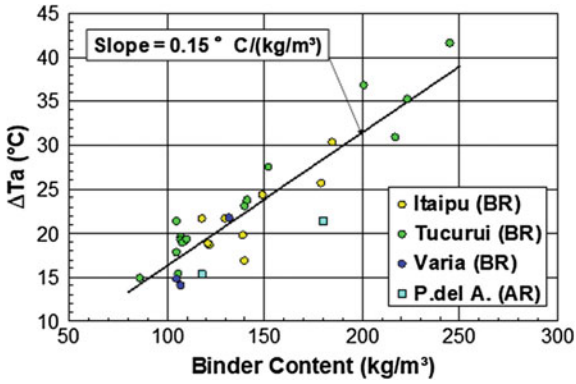

Fig. 5.7 Adiabatic temperature rise of different mass concretes as function of the binder content

Table 5.4 Range in size of solids in concrete

Size Range	Designation	Role in fresh concrete
1–100 μm	"Fines" (binders + dust in aggregates)	Surface → Cohesion
100 μm–5 mm	"Sand"	Surface → Cohesion + Filler
>5 mm (up to 150 mm)	"Gravel"	Filler

It is important to remark that, in conventional concrete, the aggregate particles are not in contact with each other, but covered by a thin layer of paste, the thickness and viscosity of which govern the mobility (slump) of the fresh concrete. The amount of paste required to achieve a certain mobility will depend on the compactness of the aggregate packing (minimizing interparticle voids) and on the specific surface (SS) of the combined particles. The lower the SS, the less paste is necessary to "coat" the particles with the lubricating layer of paste. However, as mentioned earlier, the stability of the fresh concrete requires a minimum SS, provided by the binders and sand in order to avoid segregation of the material. The aggregate design is, therefore, essential for the mix design.

5.7.2 *Specific Aspects of Mass Concrete Mix Design*

Different from structural concrete, mass concrete—especially for dams—is usually placed in vast areas, with ample space for the workers to place and vibrate the concrete (see Fig. 5.8).

This means that a concrete of very stiff consistency and large aggregate size can be used for dam construction, with several advantages.

First, a large maximum size (75 and 150 mm) means less cement paste, as the large aggregate particles occupy the volume otherwise occupied by smaller aggregates and paste (see Fig. 5.9), coupled to their low SS; this means less cement paste in the concrete and less heat generated.

Therefore, mass concrete for dams is characterized by large aggregate maximum size (up to 150 mm) and stiff mixes that can, nevertheless, be efficiently compacted by powerful, large diameter vibrators, in the ample space available (Fig. 5.10).

Now, designing or even testing a concrete containing aggregates of 75 or 150 mm poses some technical problems. The slump cone has a "mouth" diameter of 100 mm and is suitable for concretes with maximum size of aggregates up to 38 mm. Similarly, the conventional cylindrical or cubic moulds used for testing strength cannot accommodate concretes with aggregate particles larger than 30–40 mm. In the case of strength, the mass concrete has to be tested in very large specimens, typically cylinders Ø450 × 900 mm, suitable for aggregates up to 150 mm maximum size.

Fig. 5.8 Preparation for concrete placement in Xiluodu Dam, China

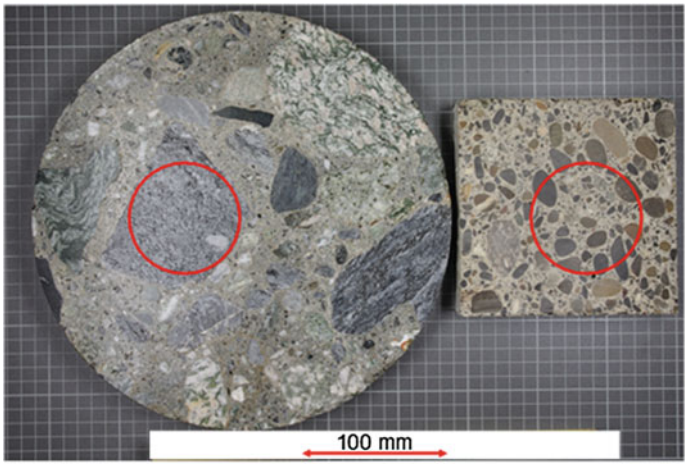

Fig. 5.9 Substitution of small aggregates and paste by large aggregate particles

For routine mix design and quality control, both the slump and the strength are not measured on the integral concrete, but on a sample fresh-sieved through a 38 mm sieve. Regarding strength, a relation is established experimentally between the strength of the integral concrete (f'_{ci}) and that of the sieved concrete (f'_{cs}) under the form $f'_{ci} = k.\ f'_{cs}$, with k typically around 0.85 (k is less than 1 due to

Fig. 5.10 Placing stiff consistency concrete in Yacyretá Dam (Argentina—Paraguay)

the larger aggregates and the size effect of the big specimen for the integral concrete, as shown in Fig. 5.11).

Based on the structural requirements of the dam, a value of f'_{ci} is established, which is converted into a corresponding value of $f'_{cs} = f'_{ci}/k$. A slump value is also specified for the sieved concrete, which is often relatively low, typically 50 mm.

The large maximum size of the aggregate and rather stiff consistency of the mix allow to keep the water content low (helped by the use of suitable water reducer and air entrainer) and, consequently, the cement content too. Cement contents of 100 kg/m^3 or even less (see Fig. 5.13) can be achieved by a proper mix design.

5.7.3 Approaches for Mass Concrete Mix Design

At this point, it must be stated that designing a concrete mix is not a scientific endeavour, but rather the application of a combination of technical concepts coupled to subjective expert judgement (technique and art) (Neville 1995), as sketched in Fig. 5.12. This applies also to very sophisticated mix design tools, such as the ones developed by (de Larrard 1999; Day 1999; Torrent 2010); in the end, trial mixes are required to assess sensorially (looking, touching) the aspect of the fresh concrete, combined with proper testing.

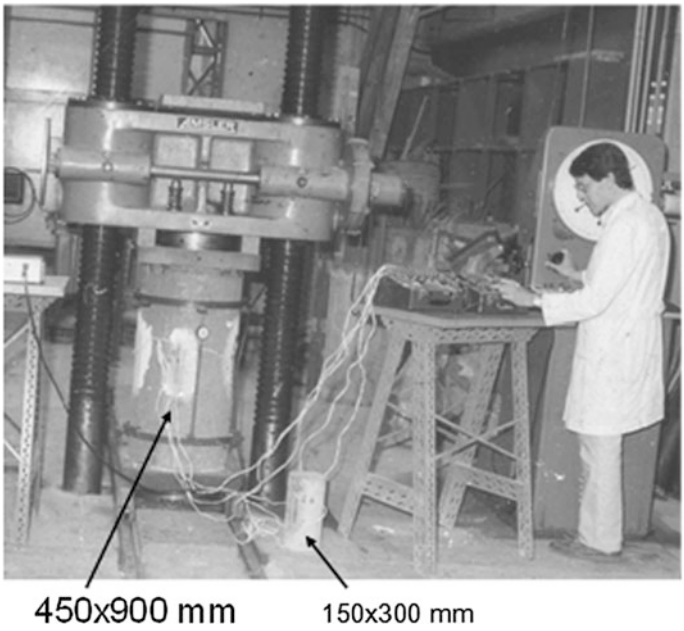

Fig. 5.11 Compression test of integral concrete, comparing the specimens' sizes

Fig. 5.12 Mix design requires a mixture of technical and subjective judgement

The method described below is based on that developed at the National Institute of Industrial Technology, Buenos Aires, Argentina, and implemented in a computer routine. It was used to successfully design mass concrete mixes for several dams: Salto Grande (Argentina–Uruguay), Yacyretá (Argentina–Paraguay) and Piedra del Águila (Argentina). It was presented in Alvaredo et al. (1984, 1987).

Mix requirements are:

- Maximum size of the aggregate,
- Slump of the fresh-sieved concrete,
- Strength of the fresh-sieved concrete (f'cs),
- Optionally, air content of the fresh-sieved concrete.

The first important step is to design the integral aggregate. Several methods can be employed, such as trying to maximize the packing of the aggregate (although this tends to lead to unworkable concretes) because the separation between the aggregate particles in the fresh concrete is often not taken into account.

A safe approach is to proportion the aggregate fractions to fit as closely as possible the Fuller grading, expressed as:

$$p = 100 \cdot \left(\frac{d}{D}\right)^n \tag{T1}$$

p = proportion (%) of material passing sieve with opening d (mm)
D = maximum size of the aggregate (mm)
n = exponent, typically n = 0.5 for rounded particles and n = 0.4 for crushed particles

This can be done manually or, given that sometimes the amount of fractions to be combined may be high, by applying some mathematical tool (Torrent et al. 1984). The mass concrete mix design procedure will be illustrated by an example.

Figure 5.13 shows the grading curves (black lines labelled I to VI) of 6 aggregate fractions (4 gravels and 2 sands), as well as the resulting combined grading (red lined labelled C) of proportioning them as shown in Fig. 5.14 (it comes close to Fuller curve for exponent n = 0.4, not shown in the chart). Figure 5.13 shows also (dotted lines) the grading curves resulting of sieving the combined aggregate through a 38 mm sieve, one passing (green labelled <38) and one retained (blue labelled >38). Fractions I to V are crushed, and fraction VI is rounded.

A mass concrete mix has to be designed with the combined grading indicated in red in Fig. 5.13, so that its properties in the fresh-sieved concrete are:

- Compressive strength at 90 days: 15 MPa,
- Slump: 50 mm,
- Air content: 5% (air is usually entrained to reduce water content and improve workability of the mass concrete lean mixes).

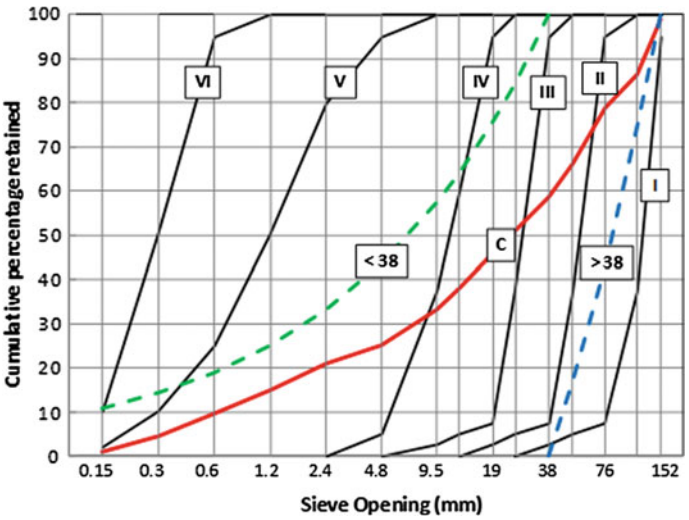

Fig. 5.13 Grading curves of individual (black), combined (red C) and sieved (dotted lines) fractions (Color figure online)

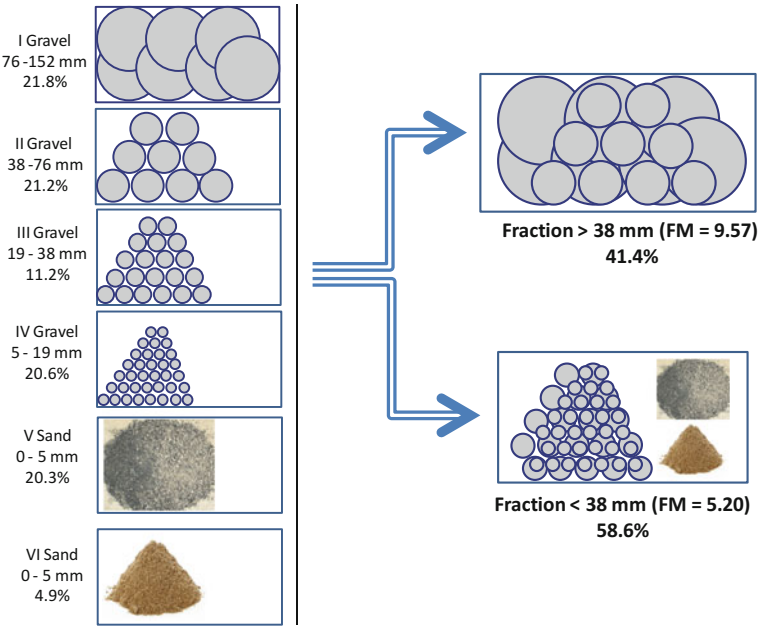

Fig. 5.14 Original aggregate fractions and proportions (l.) and split after fresh-sieving through 38 mm (r.)

Table 5.5 From fresh-sieved mix to integral concrete mix

Row	Column	A	B	C	D	E	F
	Component	Fresh-Sieved mix		Added for integral mix	Integral mix		
		(kg/m^3)	(dm^3/m^3)	(kg)	(kg)	(dm^3)	(kg/m^3)
1	Water	153	153	10	163	163	**107**
2	Cement	216	72	14	230	77	**151**
3	Fraction <38	1885	725	0	1885	725	1234
4	Air Content		50		0	50	–
5	Fraction >38			1332	1332	512	872
6	Fraction I		0		0		**459**
7	Fraction II		0		0		**447**
8	Fraction III		0		0		**236**
9	Fraction IV		0		0		**434**
10	Fraction V		0		0		**428**
11	Fraction VI		0		0		**103**
	TOTAL	2254	**1000**			1527	2364

Any conventional mix design method can be used to design such mix for an aggregate having the grading shown in Fig. 5.13 as "<38". One such mix design is shown in Table 5.5, columns A and B (in mass and volume, respectively). Densities are assumed = 3.00 for cement and 2.60 for all aggregate fractions.

Now, to compose the integral concrete, we have to add not just the aggregate (>38) removed by the sieving, but also the cement paste that coats each of its particles.

Experimental investigations carried out at the National University of Rosario (Argentina) (Sabesinsky 1969) yielded equations relating the water retained at the surface of different aggregates as function of their fineness modulus, of the form:

$$WR = \frac{1}{1000} \cdot 10^{(a-b.FM)} \qquad \text{(T2)}$$

WR water retained on the surface of the aggregates (dm^3 water/kg of aggregate)
FM fineness modulus of the aggregate
a parameter (2.6 for rounded and 2.8 for crushed particles)
b parameter (0.21 for rounded and 0.20 for crushed particles)

In our case, the fineness modulus of the fraction retained on 38 mm sieve is FM = 9.57 and, for crushed aggregate, the water retained on the surface is, from Eq. T2, WR = 0.0077 dm^3/kg.

To compose the integral concrete, we have to add the following to the fresh-sieved concrete:

- The aggregate >38 mm, respecting the proportions of the combined grading, i.e. 1885 kg/0.586 * 0.414 = 1332 kg, see Fig. 5.14
- The water retained on the surface of the aggregate >38 mm, i.e. 1332 * 0.0077 = 10 dm^3
- The cement included in the paste coating the particles, respecting the same w/c of the concrete, i.e. 216/153 * 10 = 14 kg.

This has been done in Column C of Table 5.5. Column D and C provides now the composition of the integral concrete in mass and volume, respectively; obviously, now the volume exceeds 1 m^3. Column E gives the final composition of the integral mass concrete in kg/m^3, including the quantity of each of the 6 aggregate fractions, using the proportions established earlier for the combined grading, see Fig. 5.14 (l.).

In this manner, it is possible to compose the proportions of a mass concrete that has to comply with certain properties in the fresh-sieved portion. Summarizing:

1. Compose the aggregate fractions to fit a desired combined grading (e.g. Fuller curve),
2. Separate the combined aggregate in one retained (>38) and another passing (<38) the 38 mm sieve,
3. Design, with any method the user likes, the conventional concrete with the <38 mm aggregate fraction, to achieve the slump and strength (eventually air content) specified,
4. Recompose the integral concrete by adding the >38 mm aggregate fraction and the water and cement making the paste that coat this fraction's particles,
5. Resize the volume of the mix to 1 m^3 and allocate the proportions of the different aggregate fractions according to step 1.

The design of a suitable binder composition for low-clinker concrete requires in-depth knowledge of (a) the physical packing of the binder particles together with (b) the development of the crystalline and amorphous phases formed during hydration. The latter also depends on particle fineness due to, for example, heterogeneous nucleation of hydration products and coupling of reaction kinetics to microstructure development. These chemical and physical processes not only affect the hydration kinetics, development of porosity, strength and thus the durability of hardened concrete in service, but also fresh concrete workability, i.e. rheology. Thus, complementary studies are required to determine the optimum cementitious binder and concrete composition leading to the best synergy between the various components.

Generally, a mass concrete mix design considers a big maximum aggregate size (above 32 mm), even above 60 mm, but limited by an employed mixing or pumping technology. The main reason for such big aggregates is the lowering of the

aggregate surface area, thus allowing for a reduction in cement paste content needed to surround (wrap around) the aggregates.

The addition of fine mineral admixtures to clinker can complete the fine fraction in the granulometric curve of cement improving the particle packing that can decrease water demand for a targeted workability (indicating that water demand is not just solid surface area related) (Fennis 2011; de Larrard 1999). Partial replacement by ultra-fine inert particles results in a reduction in the strength of pastes due to the dilution effect but an increase in the strength of concrete due to an improved transition zone. If the fine mineral admixtures are slow reactive pozzolans, then they further improve microstructural integrity without increasing the overall hydration reaction rate.

Methods for optimizing the granular mixtures can be divided into three groups: (1) optimization curves ('ideal' grading curves worked out on the basis of practical experiments and theoretical calculations); (2) particle packing models (analytical models to calculate the overall packing density of a mixture based on the geometry of the combined particle groups); and (3) 3D computer simulations (numerical models, e.g. discrete element models, that generate a "virtual" particle structure from a given particle size distribution—a fundamental approach, but large computational cost limits the particle size range).

Among these models, the model developed by de Larrard (2nd group), called the Compressible Packing Model (CPM), is the most promising model as it considers the mutual influence of compaction and interactions in the particle structure as well as particle shape. These interactions are ascribed by the wall effect (when the fine particles are butting into the surfaces of very large size particles) and the loosening effect (when the fine particles cannot fit themselves perfectly into the gaps of the larger size particles). This model has been found useful to optimize the packing density of granular mixtures of ecological concrete. The model requires the particle size distribution (PSD) to be measured for all constituent materials and a calibration of the eigenpacking density of each constituent material using its PSD and its (measured) packing density. For small particles, surface forces become increasingly important compared to gravitation and shear forces. These interparticle forces can cause agglomeration of particles, thus lowering the packing density. Recently, Fennis (2011) modified the Compressible Packing Model to include these additional (electrostatic) interactions. A discrete element modelling was employed to investigate the influence of interparticle forces on the particle packing density, wall effect and loosening effect.

The rate and total amount of evolved heat in concrete generally decreases with decreasing C3S and C3A contents of cement. On the other hand, the pozzolanic reaction is slower than C3S hydration and it produces less total potential heat than does cement hydration (Nili and Salehi 2010). Concrete containing SCMs generally exhibits low rate of hydration heat development and thus a small increase in material temperature due to self-heating. Schindler and Folliard (2005) showed that the use of FA and GGBFS retards the hydration process and reduces the amount of heat generated during the acceleration stage. Wang and Lee (2010) demonstrated

that FA is more effective in reducing the heat of hydration in concrete than GGBFS. Atis (2002) showed that 50% FA reduces the peak temperature of concrete by 23% as compared with OPC, indicating that the moderate levels (10–30%) of FA currently used in cement production may not provide sufficient reduction in the heat evolution of concrete. The use of large amounts of SCMs also significantly contributes to the sustainability of mass concrete (Yang et al. 2016) in terms of low CO2 emissions, recycling of by-products, and conservation of natural resources as well as the enhancement of workability and durability of concrete (Zhao et al. 2015).

The design of mass concrete structural elements requires the good prediction of the temperature within the mass concrete in order to avoid early-age thermal cracking and delayed ettringite formation. Thermal analysis of mass concrete is often performed by using finite element method (FEM) models in combination with cement hydration models (more information about such approach is given in Chap. 7). However, for the preliminary mixture design, such method is not practical because of time constraints. For that reason, simplified models were developed in order to rapidly estimate the evolution of the temperature or the maximal temperature of a concrete structure during the hydration process. Three methods are generally used: the Portland Cement Association's temperature estimation method (PCA method), the ACI graphical method and the Schmidt method. The PCA method estimates fast the value of the maximum temperature but not when this temperature is reached in a concrete without considering the type of cement. By means of several equations and charts, the ACI graphical method (207.2R-07 2007) predicts temperature rise for a variety of conditions with constraints on the empirical equations. The Schmidt method (ACI 207.2R-07 2007) computes the temperature evolution for discrete nodes at discrete time steps and is based on a numerical solution for the heat transfer equation. According to Riding et al. (2006), these three methods underestimate the maximum temperature of concrete structure. Based on this observation, Bobko et al. (2015) implemented a new version of the Schmidt method in which the effect of the temperature on heat of hydration is considered and some empirical equations that predict heat of hydration has been adjusted.

Leal da Silva and Šmilauer (2015) elaborated a nomogram in Fig. 5.15 which provides a quick preliminary maximum temperature inside a mass concrete structure for different types and amounts of cementitious material. The nomogram is based on a 1D numerical analysis with FEM and the affinity hydration model considering six factors (cement type, unit mass of total binder content, effective percentage and type of supplementary cementitious material, element thickness, initial concrete temperature and average ambient temperature). However, these tools have some limitations such as the consideration of cooling system (see Chap. 6) on the evolution of the temperature. For an accurate determination of the thermal gradient inside the concrete structure, FEM simulation must be performed.

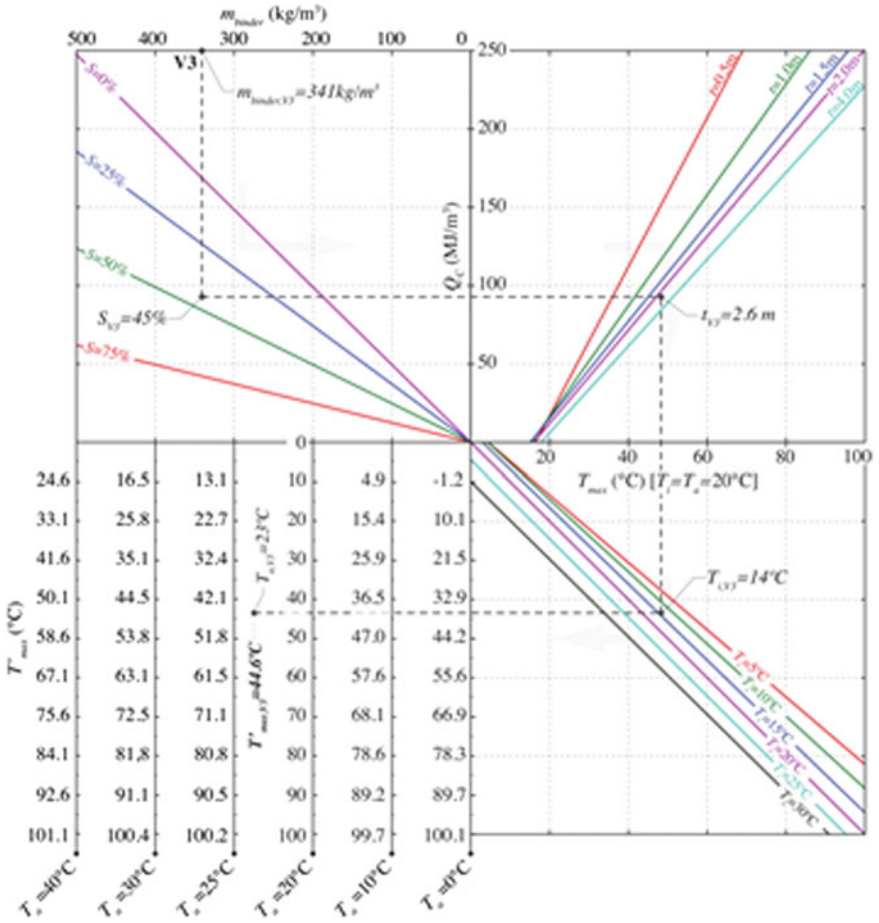

Fig. 5.15 Nomogram for predicting maximum temperature of mass concrete structures taking into account six influencing factors

5.8 Mix Design Methods for Roller Compacted Mass Concrete

Rolled compacted concrete (RCC) mix design seeks to obtain a maximum aggregate content and a minimum amount of cementitious material, in a suitable condition to obtain the required properties for the fresh and hardened concrete. As stated by ACI 207.5R-11 (2011), the following characteristic should be addressed: workability, strength, segregation, permeability, heat generation, construction conditions.

Two main mix design philosophies can be identified for CCR mix design: the one known as concrete approach and the soil mechanics or geotechnical approach (US Department of the Interior Bureau of Reclamation 2005). The first design philosophy leads to more fluid and workable mixtures, although both mix design approaches produce concrete with zero slump. The concrete approach, as the name implies, regards RCC as a true concrete, following, essentially, the same mix design procedures. However, the mix design methods based on the geotechnical philosophy uses compaction concepts similar to those used in soil mechanics. Thus, among the laboratory tests used to evaluate the concrete in its fresh state are the modified Vebe, modified Proctor and permeability of the wet granular mixture (Farias 2006).

According to Hansen and Reinhardt (1991), in the 1970s, three different directions for the design of a RCC dam were introduced: in the USA, the procedure for a dry concrete based on soil technology was developed by the US Army Corps of Engineers (USACE method); English engineers, on the other hand, evaluated the high paste alternative, which would be a mixture of conventional concrete mix design and constructive methods of land and rock fill dams, named the US Bureau of Reclamation high paste method; Japanese researchers studied the rationalization of concrete dam construction methods, creating the roller compacted dam (RCD) method. Since then, other methods have been applied to RCC mix proportioning (ACI 207.5R-11 2011; US Department of the Interior Bureau of Reclamation 2005), such that the Maximum Density Method and the Brazilian High Content of Fines method (Andriolo 2015).

Besides the traditional methods of mixture proportioning for Roller Compacted Concrete (RCC), one can refer to the Compressive Packing Model (CPM) developed by de Larrard and co-authors (de Larrard 1999). As already mentioned above in this chapter, CPM allows the simulation of concrete mix proportioning by means of a computer code. Besides the applications to conventional concrete, this method has been used to RCC mix design since the early 2000s when applications to road building materials have been reported (Pouliot et al. 2001). This type of application would require a much larger quantity of cementious material and a lower w/c ratio than for a dam, since the characteristics of the loads (mechanical and thermal) as well as the needs of surface finishing are more demanding for the road building materials.

An application of the CPM for the mix design of RCC used to dams can be seen in Farias (2006). This research was developed at the laboratories of FURNAS, the company responsible for the generation and distribution of electrical energy in the Brazilian south-eastern region. Concretes with contents ranging from 70 to 120 kg/m^3 have its raw materials characterized in such a way that the parameters required by the CPM (virtual packing density, loosening effect and wall effect) have been determined allowing the optimization of maximum compactness. In this way, several lithological types of aggregates were used, including biotite-gneiss, granite, limestone and basalt

Fig. 5.16 Aggregates of several lithological types with 12.5 mm of maximum diameter

with diameters ranging from 1.18 mm to 31.5 mm. These types of aggregates displayed different heuristics for its particular shapes (see Fig. 5.16) and consequently its packing characteristics.

A software specially developed for this purpose (CCR_FURNAS) was used to obtain the maximum packing density of the mixes (Fig. 5.17).

Having all the parameters necessary to model the mixtures using CPM, the several RCC mixes were designed and submitted to a battery of laboratory tests that characterized them in the fresh and hardened states, such that Cannon time, Vebe, nuclear densometer, strength, permeability. The compressive strengths obtained for the several cement contents are shown in Fig. 5.18.

This study indicated that the Compressive Packing Model is a valuable tool to design mixtures of RCC aiming its application to dams. The mixtures designed with CPM presented good properties in the fresh state and also mechanical properties compatible with applications to hydropower plants.

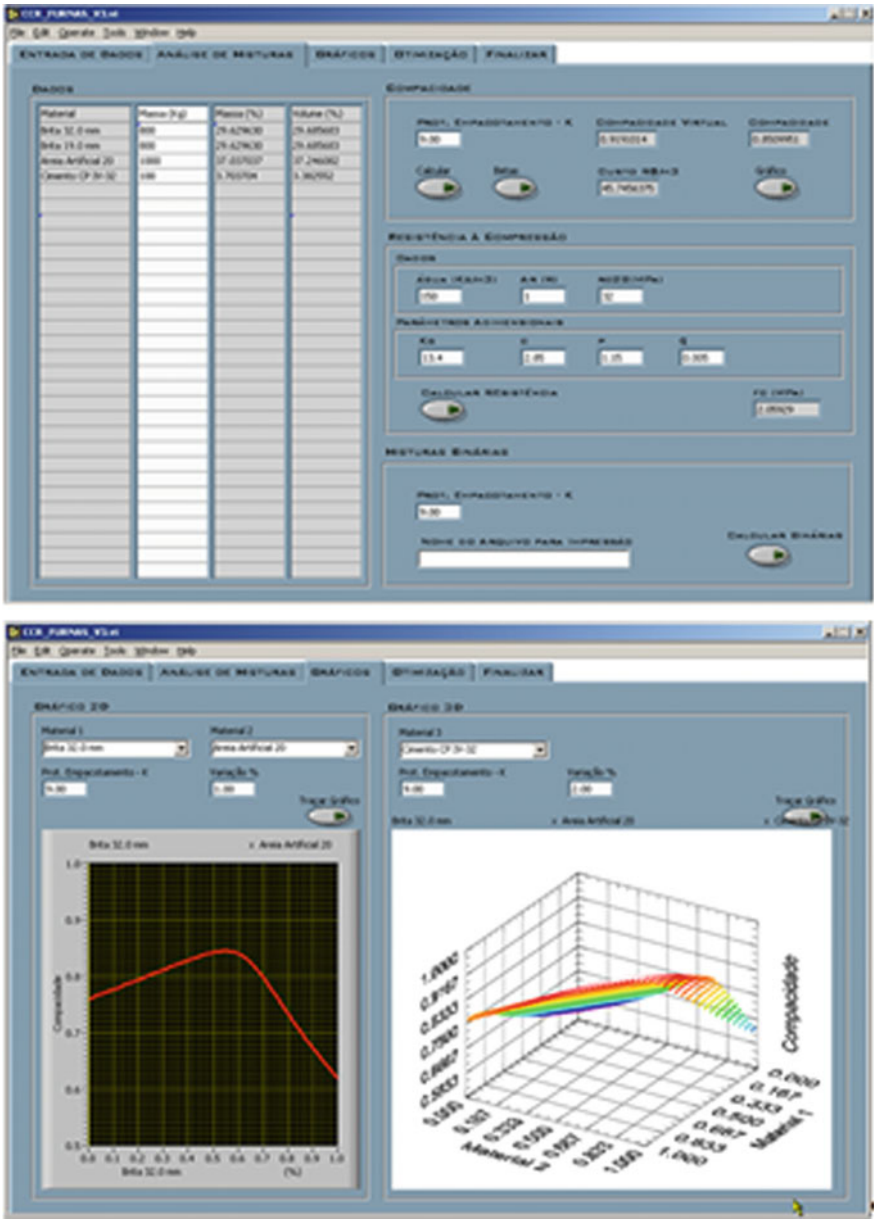

Fig. 5.17 Optimization of RCC mixes using the compressive packing model

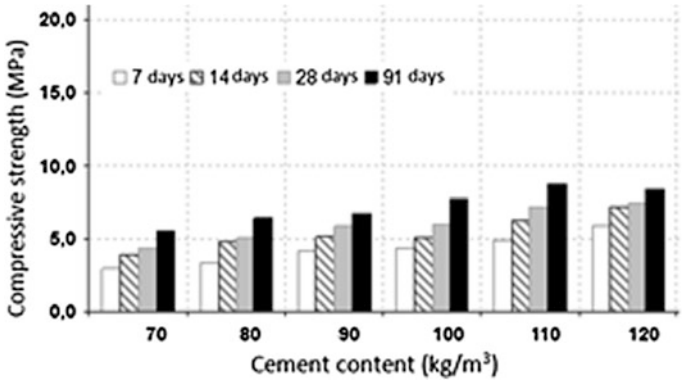

Fig. 5.18 Compressive strains obtained with CPM

5.9 Conclusions

The design of mass concrete structural elements requires the good prediction of the temperature within the mass concrete in order to avoid early-age thermal cracking and delayed ettringite formation.

The use of GGBFS and coal FA as a substitute for cement clinker can improve technical properties, including workability, strength and durability. Special care should be taken for use of SCMs in mass concrete, as poor curing conditions more adversely affect the properties of mass concrete made from pozzolanic blended cement than that of ordinary Portland cement.

Conventional SCMs like coal fly ashes and GGBFS have a market value, and consequently, a percentage of the power plant's flows should be allocated to their productions. On the other hand, for waste utilization in mass concrete there are no flows from their producers allocated to its production.

Thus, complementary studies are required to determine the optimum cementitious binder and concrete composition leading to the best synergy between the various components.

Generally, a mass concrete mix design considers a big maximum aggregate size (above 32 mm), even above 60 mm, but limited by an employed mixing or pumping technology.

References

ACI Committee 207.2R. (1997). *Effect of restraint, volume change, and reinforcement on cracking of mass concrete*. Farmington Hills, MI: American Concrete Institute.

ACI Committee 207.2R-07. (2007). *Report on thermal and volume change effects on cracking of mass concrete*. Farmington Hills, MI: American Concrete Institute.

ACI Committee 207.5R-11. (2011). *report on roller-compacted mass concrete*. Farmington Hills, MI: American Concrete Institute.

Akkaya, Y., Ouyang, C., & Shah, S. P. (2007). Effect of supplementary cementitious materials on shrinkage and crack development in concrete. *Cement & Concrete Composites Journal, 29,* 117–123.

Aldea, C., Young, F., Wang, K., & Shah, S. P. (2000). Effect of curing conditions on properties of concrete using slag replacement. *Cement Concrete Research, 30,* 465–472. https://doi.org/10.1016/S0008-8846(00)00200-3.

Alvaredo, A., Di Pace, G., & Torrent, R (1984). *Método de dosificación por computadora para hormigones masivos y convencionales, 6a*. Bahía Blanca, Argentina: Reunión Técnica de la AATH.

Alvaredo A., Di Pace, G., & Torrent, R. (1987) Mix design computer method for mass and conventional concrete, Rilem TC 70-OMD 'Optimized Mix Design'. *Materials and Structures*, *20*(115), 51–53.

Andriolo, F. R. (2015). Aspects of the use of RCC in Brazilian dams. In *7th International Symposium on Roller Compacted Concrete (RCC) Dams, Chengdu, China*, (in Portuguese).

Antoni, M., Rossen, J., Martirena, F., & Scrivener, K. (2012). Cement substitution by a combination of metakaolin and limestone. *Cement and Concrete Research, 42,* 1579–1589. https://doi.org/10.1016/j.cemconres.2012.09.006.

Atis, C. D. (2002). Heat evolution of high-volume fly ash concrete. *Cement and Concrete Research, 32*(5), 751–756. https://doi.org/10.1016/S0008-8846(01)00755-4.

Babu, K. G., & Kumar, V. S. R. (2000). Efficiency of GGBS in concrete. *Cement and Concrete Research, 30,* 1031–1036. https://doi.org/10.1016/S0008-8846(00)00271-4.

Bai, J., Wild, S., & Sabir, B. B. (2002). Sorptivity and strength of air-cured and water-cured PC–PFA–MK concrete and the influence of binder composition on carbonation depth. *Cement and Concrete Research, 32,* 1813–1821. https://doi.org/10.1016/S0008-8846(02)00872-4.

Banfill, P. F. G., Rodríguez, O., Sánchez de Rojas, M. I., & Frías, M. (2009). Effect of activation conditions of a kaolinite based waste on rheology of blended cement pastes. *Cement and Concrete Research, 39,* 843–848. https://doi.org/10.1016/j.cemconres.2009.06.010.

Bentur, A., Igarashi, S. I., & Kovler, K. (2001). Prevention of autogenous shrinkage in high strength concrete by internal curing using wet lightweight aggregates. *Cement and Concrete Research, 31*(11), 1587–1591.

Bentz, D. P., & Peltz, M. A. (2008). Reducing thermal and autogenous shrinkage contributions to early-age cracking. *ACI Materials Journal, 105*(4), 414–420.

Bobko, C. P., Zanjani, Zadeh V., & Seracino, R. (2015). Improved Schmidt method for predicting temperature development in mass concrete. *ACI Materials Journal, 112*(4), 579–586.

Carette, J. (2015). Towards Early Age Characterization of Eco-Concrete containing blast-furnace slag and limestone filler. Ph.D. Thesis, ULB, BATir, Brussels, Belgium, 187 pp.

Chen, X. D., & Wu, S. X. (2013). Influence of water-to-cement ratio and curing period on pore structure of cement mortar. *Construction and Building Materials, 38,* 804–812.

Cheng, A., Huang, R., Wu, J. K., & Chen, C. H. (2005). Influence of GGBS on durability and corrosion behavior of reinforced concrete. *Materials Chemistry and Physics, 93,* 404–411. https://doi.org/10.1016/j.matchemphys.2005.03.043.

Cortas, R., Rozière, E., Staquet, S., Hamami, A., Loukili, A., & Delplancke-Ogletree M.-P. (2014). Effect of the water saturation of aggregates on the shrinkage induced cracking risk of concrete at early age. *Cement & Concrete Composites Journal*, *50*, 1–9.

Damidot, D., Lothenbach, B., Herfort, D., & Glasser, F. P. (2011). Thermodynamics and cement science. *Cement and Concrete Research, 41,* 679–695. https://doi.org/10.1016/j.cemconres.2011.03.018.

Darquennes, A., Staquet, S., Delplancke-Ogletree, M.-P., & Espion, B. (2011). Effect of autogenous deformation on the cracking risk of slag cement concretes. *Cement & Concrete Composites Journal*, *33*, 368–379.

Darquennes, A., Staquet, S., & Espion, B. (2011). Determination of time-zero and its effect on autogenous deformation evolution. *EJECE Journal*, *15*, 787–798.

Darquennes, A., Staquet, S., & Espion, B. (2011). Behaviour of slag cement concrete under restraint conditions. *EJECE Journal*, *15*, 1017–1029.

Darquennes, A., & Benboudjema, F. (2013). Cracking sensibility of slag cement concrete at early age. In *Third International Conference on Sustainable Construction Materials and Technologies (SCMT3)*, Kyoto, Japon, August 2013.

Day, K. W. (1999). *Concrete mix design, quality control and specification* (p. 391). London: E&FN Spon.

de Larrard. (1999). *Concrete mixture proportioning: a scientific approach* (448 p). London: E&FN SPON.

Delsaute, B., & Staquet, S. (2017). Decoupling thermal and autogenous strain of concretes with different water/cement ratios during the hardening process. *Advances in Civil Engineering Materials*. https://doi.org/10.1520/ACEM20160063, ISSN 2379-1357.

De Weerdt, K. (2011). *Blended cement with reduced CO_2 emission—Utilizing the fly ash-limestone synergy* (171 pp). Ph.D. thesis, NTNU, Trondheim, Norway.

De Weerdt, K., Ben Haha, M., Le Saout, G., Kjellsen, K. O., Justnes, H., & Lothenbach, B. (2011a). Hydration mechanisms of ternary Portland cements containing limestone powder and fly ash. *Cement and Concrete Research, 41,* 279–291.

De Weerdt, K., Kjellsen, K. O., Sellevold, E., & Justnes, H. (2011b). Synergy between fly ash and limestone powder in ternary cements. *Cement & Concrete Composites, 33,* 30–38. https://doi.org/10.1016/j.cemconcomp.2010.09.006.

Dudziak, L., & Mechtcherine, V. (2010). Deliberations on kinetics of internal curing water migration and consumption based on experimental studies on SAP-enriched UHPC. In *International RILEM Conference on Use of Superabsorbent Polymers and Other New Additives in Concrete*. August 15–18, 2010, Lyngby, Denmark (pp. 3343).

Dudziak, L., & Mechtcherine, V. (2010b). Reducing the cracking potential of ultra-high performance concrete by using super absorbent polymers (SAP). In G. P. A. G. van Zijl, & W. P. Boshoff, (Eds.), *Advances in Cement-Based Materials* (pp. 11–19). London, UK: Taylor and Francis Group.

Farias, L. A. (2006). Implementation of scientific concrete mix design for roller compacted concrete applied to dams. M.Sc. thesis, Federal University of Goiás (UFG), Brazil. http://www.dominiopublico.gov.br/.

Fennis-Huijben, S. (2011). Design of ecological concrete by particle packing optimization (255 pp). Ph.D. thesis, TU Delft, The Netherlands.

Flower, D. J. M., & Sanjayan, J. G. (2007). Green house gas emissions due to concrete manufacture. *International Journal Life Cycle Assesment, 12*(5), 282–288. https://doi.org/10.1065/lca2007.05.327.

Gajda, J., Weber, M., & Diaz-Loya, I. (2014). A low temperature rise mixture for mass concrete, fly ash-based hydraulic cement generates significantly less heat than Portland cement. *Concrete International Journal, 36*(8), 48–53.

Ghrici, M., Kenai, S., & Said-Mansour, M. (2007). Mechanical properties and durability of mortar and concrete containing natural pozzolana and limestone blended cements. *Cement & Concrete Composites, 29,* 542–549. https://doi.org/10.1016/j.cemconcomp.2007.04.009.

Hansen, D. K., & Reinhardt, W.G. (1991). *Roller compacted concrete* (1st ed.). McGraw-Hill.

Holt, E., & Leivo, M. (2004). Cracking risks associated with early age shrinkage. *Cement & Concrete Composites Journal*, *26*(5), 521–530.

Igarashi, S., & Watanabe, A. (2006). Experimental study on prevention of autogenous deformation by internal curing using super-absorbent polymer particles. In O. M. Jensen, P. Lura, K. Kovler (Eds.), *Proceedings of International RILEM Conference on Volume Changes of Hardening Concrete: Testing and Mitigation*, August 20–23, 2006, Lyngby, Denmark, (pp. 77–86).

Japanese Concrete Institute. (2008). *Guidelines for control of cracking of mass concrete*.

Jensen, O. M., & Hansen, P. F. (1996). Autogenous deformation and change of the relative humidity in silica fume-modified cement paste. *ACI Materials Journal, 93*(6), 1238–1249.

Jensen, O. M., & Hansen, P. F. (2002). water-entrained cement-based materials: II. experimental observations. *Cement and Concrete Research, 32*(6), 973–978.

Jensen, O. M. (2013). Use of superabsorbent polymers in concrete. *Concrete International, 15*(1), 48–52.

Kadri, E.-H., Duval, R., Aggoun, S., & Kenai, S. (2009). Silica fume effect on hydration heat and compressive strength of high-performance concrete. *ACI Materials Journal, 106*(2), 107–113.

Khatib, J. M., & Hibbert, J. J. (2005). Selected engineering properties of concrete incorporating slag and metakaolin. *Construction and Building Materials, 19,* 460–472. https://doi.org/10.1016/j.conbuildmat.2004.07.017.

Klemczak, B., & Knoppik-Wróbel, A. (2012). Wpływ wybranych czynników materiałowo–technologicznych na temperatury twardnienia betonu w masywnej płycie fundamentowej (Influence of chosen material–technological factors on hardening temperatures in massive foundation slab). In *Proceedings of "Dni Betonu"*,Wisła, Poland (pp. 291–301) (in Polish).

Knoppik-Wróbel, A. (2012). Cracking risk in early-age RC walls. In: *Proceedings of the 9th fib International PhD Symposium in Civil Engineering*, Karlsruhe, Germany (pp. 129–135).

Kosmatka, S. H., Kerkhoff, B & Panarese, W. C. (2002). *Design and control of concrete mixtures* (14th ed.). PCA.

Lam, H., & Hooton, R.D. (2005). Effects of internal curing methods on restrained shrinkage and permeability. In B. Persson, D. Bentz, & L. O. Nilsson (Eds.), *Proceedings of the 4th I*nternational *Research Seminar on Self-desiccation and Its Importance in Concrete Technology* (pp. 210–228). Lund, Sweden: Lund University.

Leal da Silva, W. R., & Šmilauer, V. (2015). Nomogram for maximum temperature of mass concrete. *Concrete International, 37*(5), 30–36.

Lee, K. M., Lee, H. K., Lee, S. H., & Kim, G. Y. (2006). Autogenous shrinkage of concrete containing granulated blast-furnace slag. *Cement and Concrete Research, 36,* 1279–1285.

Li, G., & Zhao, X. (2003). Properties of concrete incorporating fly ash and ground granulated blastfurnace slag. *Cement & Concrete Composites, 25,* 293–299. https://doi.org/10.1016/S0958-9465(02)00058-6.

Lim, S. N., & Wee, T. H. (2000). Autogenous shrinkage of ground-granulated blast-furnace slag concrete. *ACI Materials Journal, 97,* 587–593.

Liu, Z., & Hansen, W. (2016). Aggregate and slag cement effects on autogenous shrinkage in cementitious materials. *Construction and Building Materials Journal, 121*(15), 429–436.

Lothenbach, B., Le Saout, G., Gallucci, E., & Scrivener, K. (2008). Influence of limestone on the hydration of Portland cements. *Cement and Concrete Research, 38,* 848–860. https://doi.org/10.1016/j.cemconres.2008.01.002.

Lura, P., Van Breugel, K., & Maruyama, I. (2001). Effect of curing temperature and type of cement on early-age shrinkage of high-performance concrete. *Cement and Concrete Research, 31,* 1867–1872.

Lura, P., Durand, F., & Jensen O. M. (2006a). Autogenous strain of cement pastes with superabsorbent polymers. In: O.M. Jensen, P. Lura & K. Kovler (Eds.), *Proceedings of International RILEM Conference on Volume Changes of Hardening Concrete: Testing and Mitigation*, August 20–23, 2006, Lyngby, Denmark (pp. 57–66).

Lura, P., Durand, F., Loukili, A., & Jensen, O.M. (2006b). Compressive strength of cement pastes and mortars with superabsorbent polymers. In O. M. Jensen, P. Lura & K. Kovler (Eds.), *RILEM Proceedings of PRO 52 Volume Changes oh Hardening Concrete: Testing and Mitigation* (pp. 117–126). Bagneux, France: RILEM Publications S.A.R.L.

Lura, P. (2003). Autogenous deformation and internal curing of concrete (Ph.D thesis), Delft University of Technology, Delft, the Netherlands.

Manmohan, M., & Mehta, P. K. (1981). Influence of pozzolanic, slag, and chemical admixtures on pore size distribution and permeability of hardened cement pastes. *Cement, Concrete and Aggregates, 3*(1), 63–67.

Maruyama, I., & Teramoto, A. (2012). Effect of water-retaining lightweight aggregate on the reduction of thermal expansion coefficient in mortar subject to temperature histories. *Cement and Concrete Composites*, *34*, 1124–1129.

Mechterine, V., Dudziak, L., & Hempel, S. (2008). Mitigating early age shrinkage of concrete by using super Absorbent Polymers (SAP). In: T. Tanabe et al. (Ed.), *Proceedings of the 8th*

International conference on Creep, Shrinkage and Durability Mechanics of Concrete and Concrete Structures—CONCREEP-8, 30 September 30 –October2, 2008 (Ise-Shima, Japan) pp. 847–853.

Mechterine, V., Dudziak, L., & Hempel, S. (2009). Reducing cracking potential of ultra high performance concrete (UHPC) by using Super absorbent Polymers. In K. Kovler et al (ed.), *Proceedings of the 2nd International RILEM workshop on Concrete Durability and Service Life Planning. ConLife'09*, September 7–9, 2009 (Haifa, Israel) (pp. 31–38).

Mehta and Monteiro. (2006). *Concrete: Microstructure, properties, and materials* (3rd ed.). New York, NY: McGraw-Hill, Inc.

Menendez, G., Bonavetti, V., & Irassar, E. F. (2003). Strength development of ternary blended cement with limestone filler and blast-furnace slag. *Cement & Concrete Composites, 25,* 61–67. https://doi.org/10.1016/S0958-9465(01)00056-7.

Miura, T., & Iwaki, I. (2000). Strength development of concrete incorporating high levels of ground granulated blast-furnace slag at low temperatures. *ACI Materials Journal, 97*(1), 66–70.

Miyazawa, S., Tazawa, E., Sato, T., & Sato, K. (1993). Autogenous shrinkage of ultra high strength concrete caused by restraint of reinforcement. *Transactions of the Japan Concrete Institute, 15,* 115–122.

Mounanga, P., Irfan, M., Khokhar, A., El Hachem, R., & Loukili, A. (2011). Improvement of the early-age reactivity of fly ash and blast furnace slag cementitious systems using limestone filler. *Materials and Structures, 44,* 437–453. https://doi.org/10.1617/s11527-010-9637-1.

Nagy, A. (2001). *Parameter study of thermal cracking in HPC and NPC structures* (Vol. 26, pp. 1–13). Nordic Concrete Research.

Neville, A. M. (1995). *Properties of concrete* (4th ed., p. 844). Essex: Longman Group Ltd.

Nili, M., & Salehi, A. M. (2010). Assessing the effectiveness of pozzolans in massive high strength concrete. *Construction and Building Materials, 24*(11), 2108–2116. https://doi.org/10.1016/j.conbuildmat.2010.04.049.

Olorunsogo, F. T., & Wainwright, P. J. (1998). Effect of GGBFS particle-size distribution on mortar compressive strength. *Journal of Materials in Civil Engineering*, *10*. https://doi.org/10.1061/(asce)0899-1561(1998)10:3(180).

Ozer, B., & Ozkul, M. H. (2004). The influence of initial water curing on the strength development of ordinary Portland and pozzolanic cement concretes. *Cement and Concrete Research, 34,* 13–18. https://doi.org/10.1016/S0008-8846(03)00185-6.

Pacelli de Andrade, W., Tomaz França Fontoura, J., Machado Bittencourt, R., & Antonio Guerra, E. (1982). Thermal properties of concrete for some Brazilian dams. In *14th congress of large Dams*, Rio de Janeiro, Brazil, 1982, C3 (pp. 1111–1138).

Pailere, A. M., Buil, M., & Serrano, J. J. (1989). Effect of fiber addition on the autogenous shrinkage of silica fume concrete. *ACI Materials Journal, 86*(2), 139–144.

Paiva, H., Velosa, A., Cachim, P., & Ferreira, V. M. (2012). Effect of metakaolin dispersion on the fresh and hardened state properties of concrete. *Cement and Concrete Research, 42,* 607–612. https://doi.org/10.1016/j.cemconres.2012.01.005.

Pane, I., & Hansen, W. (2002). Early age creep and stress relaxation of concrete containing blended cements. *Materials and Structures Journal*, *35*, 92–96.

Persson, B. (1997). Self-desiccation and its importance in concrete technology. *Materials and Structures, 30,* 293–305.

Piérard, J., Pollet, V., & Cauberg, N. (2006). Mitigating autogenous shrinkage in HPC by internal curing using superabsorbent polymers. In O. M. Jensen, P. Lura, K. Kovler, (Eds.), *RILEM Proceedings of the PRO 52 Volume Changes oh Hardening Concrete: Testing and Mitigation* (pp. 97–106). Bagneux, France: RILEM Publications S.A.R.L.

Pipilikaki, P., & Katsiot, M. (2009). Study of the hydration process of quaternary blended cements and durability of the produced mortars and concretes. *Construction and Building Materials, 23,* 2246–2250. https://doi.org/10.1016/j.conbuildmat.2008.11.015.

Pouliot, N., de Larrard, F., Sedran, T., & Marchand, J. (2001). *Prediction of the compactness of roller-compacted concrete using a granular packing model* (Vol. 233, Réf. 4370, pp. 23–36). Bulletin des Laboratoires des Ponts et Chaussées.

Real, S., Glória Gomes, M., Moret Rodrigues, A., & Alexandre Bogas, J. (2016). Contribution of structural lightweight aggregate concrete to the reduction of thermal bridging effect in buildings. *Construction and Building Materials*, *121*, 460–470. ISSN 0950-0618, http://dx.doi.org/10.1016/j.conbuildmat.2016.06.018.

Reinhardt, H. W., Assman, A., & Mönnig, S. (2008). Superabsorbent polymers (SAPS)—An admixture to increase the durability of concrete. In *Proceedings of the 1st International Conference*.

Riding, K. A., Poole, J. L., Schindler, A. K., Juenger, M. C. G., & Folliard, K. J. (2008). Quantification of effects of fly ash type on concrete early-age cracking. *ACI Materials Journal, 105*(2), 149–1550.

Riding, K. A., Poole, J. L., Schindler, A. K., Juenger, M. C. G., & Folliard, K. J. (2009). Effects of construction time and coarse aggregate on bridge deck cracking. *ACI Materials Journal, 106*(5), 448–454.

Sabesinsky Felperín, M. (1969). *Composición de agregados compactos y compuestos para proyecto de hormigones normales de distintas consistencias y relaciones agua/cement0, Publicación N° 33, IMAE* (p. 22). Argentina: National University of Rosario.

Sakai, E., Miyahara, S., Lee, S., & Daimon, M. (2005). Hydration of fly ash cement. *Cement & Concrete Research Journal, 35*(6), 1135–1140.

Saleh, M., Carette, J., Delsaute, B., & Staquet, S. (2017). Applicability of ultrasonic measurement on the monitoring of the setting of cement pastes: Effect of water content and mineral additions. *Advances in Civil Engineering Materials*. ISSN 2379-1357, https://doi.org/10.1520/ACEM20160062.

Saraswathy, V., Muralidharan, S., Thangavel, K., & Srinivasan, S. (2003). Influence of activated fly ash on corrosion-resistance and strength of concrete. *Cement & Concrete Composites, 25,* 673–680. https://doi.org/10.1016/S0958-9465(02)00068-9.

Schindler, A., & Folliard, K. (2005). Heat of Hydration models for cementitious materials. *Journal of American Concrete Institute, 102*(1), 24–33.

Schneider, M., Romer, M., Tschudin, M., & Bolio, H. (2011). Sustainable cement production—Present and future. *Cement and Concrete Research, 41,* 642–650. https://doi.org/10.1016/j.cemconres.2011.03.019.

Shi, C., & Qian, J. (2000). High performance cementing materials from industrial slags a review. *Resources, Conservation and Recycling, 29,* 195–207. https://doi.org/10.1016/S0921-3449(99)00060-9.

Siddique, R. (2003). Effect of fine aggregate replacement with class F fly ash on mechanical properties of concrete. *Cement and Concrete Research, 33,* 539–547. https://doi.org/10.1016/S0008-8846(02)01000-1.

Song, H.-W., & Saraswathy, V. (2006). Studies on the corrosion resistance of reinforced steel in concrete with ground granulated blast-furnace slagdan overview. *Journal of Hazardous Materials, 138,* 226–233. https://doi.org/10.1016/j.jhazmat.2006.07.022.

Tazawa, E., & Miyazawa, S. (1993). Autogenous shrinkage of concrete and its importance in concrete technology. In *Proceedings of the Fifth International RILEM Symposium on Creep and Shrinkage of Concrete, Barcelona, Spain* (pp. 159–168).

Tazawa, E., & Miyazawa, S. (1995). Influence of cement and admixture on autogenous shrinkage of cement paste. *Cement and Concrete Research, 25,* 281–287.

Torrent, R. (1985). *Estudio de alternativas para la altura máxima de tongada*. Buenos Aires, Argentina: Informe Técnico, INTI.

Torrent, R. J., Alvaredo, A., & Poyard, E. (1984). Combined aggregates: A computer-based method to fit a desired grading. *Materials and Structures, 17*(98), 139–144.

Torrent, R., & Griesser, A. (2010). Introduction into MixMaster 2.0 Software, Holcim Group Support, 2010, 12 slides.

U.S. Department of the Interior Bureau of Reclamation. (2005). Roller-Compacted concrete design and construction *Considerations for Hydraulic Structures*.

Wainwright, P. J., & Ait-Aider, H. (1995). The influence of cement source and slag additions on the bleeding of concrete. *Cement and Concrete Research*, *25*(7), 1445–1456. ISSN 0008-8846, https://doi.org/10.1016/0008-8846(95)00139-4.

Wan, H., Shui, Z., & Lin, Z. (2004). Analysis of geometric characteristics of GGBS particles and their influences on cement properties. *Cement and Concrete Research, 34,* 133–137. https://doi.org/10.1016/S0008-8846(03)00252-7.

Wang, X. Y., & Lee, H. S. (2010). Modeling the hydration of concrete incorporating fly ash or slag. *Cement and Concrete Research, 40*(7), 984–996. https://doi.org/10.1016/j.cemconres.2010.03.001.

Wyrzykowski, M., & Lura, P. (2013). Controlling the coefficient of thermal expansion of cementitious materials—A new application for superabsorbent polymers. *Cement and Concrete Composites*, *35*(1), 49–58. ISSN 0958-9465, http://dx.doi.org/10.1016/j.cemconcomp.2012.08.010.

Yang, K. H., Moon, G. D., & Jeon, Y. S. (2016). Implementing ternary supplementary cementing binder for reduction of the heat of hydration of concrete. *Journal of Cleaner Production, 112,* 845–852. https://doi.org/10.1016/j.jclepro.2015.06.022.

Zhao, H., Sun, W., Wu, X., & Gao, B. (2015). The properties of the self-compacting concrete with fly ash and ground granulated blast furnace slag mineral admixtures. *Journal of Cleaner Production, 95,* 66–74. https://doi.org/10.1016/j.jclepro.2015.02.050.

Zhuang, Y.-z., Zheng, D.-d., Zhen, N. g, Tao, J. i., & Chen, X.-f. (2016). Effect of lightweight aggregate type on early-age autogenous shrinkage of concrete. *Construction and Building Materials*, *120*, 373–381, ISSN 0950-0618, http://dx.doi.org/10.1016/j.conbuildmat.2016.05.105.

Chapter 6
Temperature Control

Miguel Azenha, Ioannis P. Sfikas, Mateusz Wyrzykowski, Selmo Kuperman and Agnieszka Knoppik

Abstract Temperature rises are definitely one of the most important driving forces for thermal cracking in mass concrete, together with the restraint to deformation. Therefore, amongst the most widespread measures that can be taken to minimize the risks of thermal cracking, the temperature control of concrete since its production and throughout construction is of utmost significance. Following Chap. 5 where temperature control of concrete by limiting the heat generation potential of the binder in the mixture was already addressed, this chapter is dedicated to a review on measures that can be taken to control concrete temperature at several levels, mainly focused in limiting temperature rises due to cement hydration heat: (i) pre-cooling of mix constituents; (ii) cooling concrete during the mixing procedures; (iii) controlling temperature during transport and placement; (iv) selecting and designing suitable surface measures for temperature control; (v) post-cooling with water or air; (vi) scheduling of construction stages.

M. Azenha (✉)
ISISE, University of Minho, Guimarães, Portugal
e-mail: miguel.azenha@civil.uminho.pt

I. P. Sfikas
Mott MacDonald Ltd., Croydon, UK

M. Wyrzykowski
Empa, Swiss Federal Laboratories for Materials Science and Technology, Dübendorf, Switzerland

S. Kuperman
Desek Ltda, São Paulo, Brazil

A. Knoppik
Silesian University of Technology, Gliwice, Poland

© RILEM 2019

E. M. R. Fairbairn and M. Azenha (eds.), *Thermal Cracking of Massive Concrete Structures*, RILEM State-of-the-Art Reports 27,
https://doi.org/10.1007/978-3-319-76617-1_6

6.1 Introduction

6.1.1 General Considerations

Curing in mass concrete is mostly related to three issues:

i. ensuring adequate moisture conditions for concrete hydration, through formwork selection for formed surfaces or proper evaporation hindering (or even watering) of freely exposed (unformed) surfaces. Wet/moisture curing, in addition to promoting hydration and reducing early shrinkage cracking, also reduces the coefficient of thermal expansion considerably, therefore reducing the risk of thermal cracking;
ii. controlling temperature differentials below a maximum level as to avoid excessive temperature gradients, either cross sectional or along time, which can potentially result in thermal cracking (Bamforth 2007);
iii. limiting maximum temperature in concrete, which is also critical in order to mitigate long-term cracking due to the delayed ettringite formation (DEF) and avoid hydration at higher temperatures that leads to the production of a poorer quality of hydrate that can compromise long-term strength capacity.

While issue (i) can normally be handled by good practices of application/workmanship and quality control, including direct application of suitable formwork materials (ACI 2014), such as controlled permeability formwork (CPF), physical curing membranes or even anti-evaporating agents/curing compounds or liquid membranes (ACI 2011; Buenfeld and Yang 2001; Concrete Society 2014; Vicroads 2000), issues (ii) and (iii) are more complex to tackle. In fact, maintaining maximum levels of temperature and temperature differentials within concrete are considered to be challenging to control, in view of the multiplicity of climatological factors that contribute to the temperature development (e.g. cold or hot weather concreting, relative humidity, wind velocity, solar radiation), as well as the influence of the initial temperature of concrete (fresh concrete temperature), the heat generation potential of the hydrating binder in the concrete mix, the effectiveness of curing and post-cooling measures and also the size of the structural element itself (often dictated by the adopted construction phasing strategy), as well as the anticipated construction stages (new concrete on previously constructed elements).

The present chapter is targeted to issues related to approaches that may be adopted during the construction phase of a concrete project in order to control temperature, comprising the set of influencing factors mentioned above. As mass concrete temperature issues are normally related to cooling necessities or minimization of peak temperature and associated temperature gradients, the present chapter is mainly focused on such aspects.

6.1.2 Outline of Strategies for Temperature Control

The selection of appropriate constituent materials for the concrete mix production targeting the reduction of heat generation potential has been discussed in detail in Chapter 5 and will not be further discussed. Apart from this method, different strategies or combination of strategies for temperature control can be followed and they are summarized in the list below, linking to sections where they are discussed:

1. Pre-cooling methods, including cooling of ingredients and cooling during the mixing procedures, to reduce the concrete temperature at the time of delivery (Sects. 6.2 and 6.3);
2. Post-casting measures to control heat fluxes from concrete and thus limit the temperature rise and associated differentials (Sects. 6.4 and 6.5);
3. Construction management, including scheduling of construction stages and procedures to achieve lower temperatures and associated differentials (Sect. 6.6).

6.1.3 Regulatory and Non-regulatory Frameworks of Temperature Control

In Europe, the general purpose specification for normal concrete, EN 206:2013 (CEN 2013), solely establishes a minimum temperature of 5°C for concrete upon delivery. According to EN 206:2013, if a different minimum temperature is necessary or a maximum temperature needs to be established, such limits should be specified (together with permitted tolerances), and any requisites for the artificial heating or cooling of concrete constituents and/or concrete mix should be agreed amongst the producer and the user.

The ACI 301-16 specification (ACI 2016) for structural concrete sets minimum temperature immediately after placement that varies between 4.4 °C (40 °F) and 12.8 °C (55 °F), depending on ambient conditions to be encountered on site and size of structural element (least dimension), along with a permitted tolerance. A maximum temperature of the delivered concrete is also specified, as 35 °C (95 °F).

The recommendations of the Japanese Society for Civil Engineers for concrete (JSCE 2010a, b) point to a minimum placement temperature of 10 °C (that may be further reduced to 5 °C in mass concrete) and a maximum casting temperature of 35 °C.

In the scope of recommendations for concrete temperature upon placement in mass concrete, the following documents and guidelines can be highlighted as examples, which though cover a great range of areas on a worldwide scale:

- ACI 207.2R-07 (ACI 2007) provides recommendations for maximum temperature limits according to several factors, such as the properties of concrete and the type of restraint to deformation.
- ACI 301-16 (ACI 2016) sets maximum limits both for concrete temperature after placement and for temperature differentials between the centre and surface

of placement. Specifically, the maximum temperature should not exceed 158 °F (57 °C) and the temperature differential should not exceed 35 °F (19 °C).

- The Florida Department of Transportation Specifications (FDOT 2010) establish a maximum allowable temperature for concrete of 82 °C, while ensuring that the temperature differential between the concrete core and the exterior surface does not exceed 20 °C.
- The JSCE guidelines for Dam Concrete (JSCE 2010a) recommend minimum and maximum placing temperatures of 5 °C and 25 °C, respectively.
- The Japanese Concrete Institute Guidelines (JCI 2012) are based on stress computations to evaluate the risk of cracking, rather than providing specific recommendations on temperature placement/variation limits. It is nonetheless quite relevant to address the temperature-based criterion for formwork removal. In fact, it is recommended that formwork can only be removed when the temperature difference between the inside of concrete and the ambient air is less than approximately 15–20 °C.
- CIRIA C660 (Bamforth 2007) acknowledges the 'rule of thumb' of limiting temperature rises in concrete to 20 °C and explains the limitations of such approach. It provides an integrated methodology for cracking calculation based mainly on mix parameters, heat of hydration and exposure and restraint conditions.
- The Qatar Construction Specifications (QCS 2014) limit fresh concrete temperature at placing to a maximum of 21 °C to minimize thermal cracking, but allowing for a temperature up to 27 °C, subject to demonstrating a satisfactory performance of concrete, including mock-up and thermal calculations. Furthermore, a maximum differential temperature between the interior and the exterior of the mass concrete element is specified as 20 °C. Finally, the drop in concrete surface temperature during, and at the conclusion of the specified curing period, is not allowed to exceed 11 °C in any 24 h period.

As stated in the beginning of the current subsection, the decisions about requisites should be agreed amongst the contractor and the owner. It is indeed frequent to observe the existence of specific demands on behalf of owners of mass concrete structures (such as electricity companies that own massive structures such as dams or nuclear containments). These demands tend to vary in value and type of restriction amongst different countries and companies.

6.2 Pre-cooling of Mix Constituents and Cooling During Mixing

6.2.1 General Considerations

An important factor in temperature control of mass concrete is the initial temperature of the concrete mix. Due to the temperature increase during hydration, the difference between the temperature of the concrete element and the ambient temperature

increases. That is why it is advised to cool the concrete mix before placement in order to reduce both the maximum temperature in the core and the thermal gradients (along space and time), and thus mitigate the risk of thermal cracking.

Pre-cooling can be achieved by one of two methods (or, as a combination of the two): pre-cooling the components of concrete before the actual mixing, or by cooling the freshly mixed concrete before placing. The choice of the method for pre-cooling depends on the local conditions, on the capacity, competence and experience of the concrete supplier and contractor, but also on other project-related parameters, such as acceptable levels for cracking, extent of repairs.

Even though the effectiveness of pre-cooling of concrete depends on the mix design (e.g. cement quantity, binder type and content, total aggregate volume, etc.) and on several other parameters that are related to further heat exchange with the environment, such as the thickness of the concrete element, the climatological conditions and the activation energy, some rules of thumb of expectable benefits of reducing the initial temperature can be established. It is normally considered that a reduction of 1 °C in the placing temperature decreases the peak concrete temperature by approximately 1 °C (Gajda and Vangeem 2002).

6.2.2 *Prediction of Mix Temperature*

In order to make decisions in regard to the most desirable measures to take for pre-cooling (or preheating) concrete before/while mixing, it is desirable to have a predictive tool that assists on the evaluation of the expectable temperature of the mix based on the temperatures of the constituents. Based on such predictive tools, contractors can take sustained decisions on the constituent that should be cooled/heated and the best method to apply for such purpose, always taking into account both technical and economic feasibilities.

Several predictive models exist to allow the estimation of the temperature of the concrete mix and they are mostly based on weighted averages of the temperature of the individual constituents, with the critical factor being the specific heat of each constituent (ACI 2010; JCI 2012; Bofang 2013).

By using the model suggested by ACI 305R-10 (ACI 2010), the initial temperature of the concrete mix can be then estimated as follows:

$$T = \frac{0.22 \cdot (T_a W_a + T_c W_c) + T_w W_w + T_a W_{wa}}{0.22 \cdot (W_a + W_c) + W_w + W_{wa}} \tag{6.1}$$

where W is mass (kg/m^3) and T is temperature (°C) of the mix components, denoting by subscripts a—aggregate, c—cement, w—water added to the mixture (excluding ice and absorbed water in aggregates) and wa—free and absorbed water by the aggregates. This expression underlies that the relation between the specific heat of cement and aggregate with respect to water can be assumed as 0.22. If the actual situation deviates from such a typical relationship, the equation needs to be

revised. It is additionally remarked that, in the absence of solar shielding or cooling measures, the temperature of aggregates to be considered in the equation is normally higher than the average daily temperature. For example, Bofang (2013) recommends adding 5 °C to the temperature of the aggregates used in middle China over the summer period.

The above-described method for predicting the temperature of the mix does not take into account that, typically, the initial temperature of a concrete mix is slightly higher than the ambient temperature (1–2 °C in accordance with JCI 2012) because of the mechanical work made during the process of the concrete mix preparation. It is therefore advised that such a correction is made at the end of the calculation process. It should also be noted that Bofang (2013) recommends an additional term to the predictive equation that takes into account the power of the motor of the concrete mixer, the time of mixing and the effective volume of concrete in the mixer.

Based on the predictive equation, and the usual proportion of the components of concrete mixes, it is possible to infer that the most influential factors in the final temperature of the mix are:

- the aggregates, because of their large mass contribution within the mix;
- the liquid components of the mix (i.e. mixing water and other liquid additions, such as superplasticizers) because of the fact that their heat capacity is practically five times higher than that of solid components.

When the cooling of the concrete mix is performed by addition of chipped ice, the prediction of temperature of the mix needs to take into account the energy absorbed during the process of phase change that further enhances the capacity of ice to decrease concrete temperature (ACI 2010) and Eq. (6.1) is amended as follows:

$$T = \frac{0.22 \cdot (T_a W_a + T_c W_c) + T_w W_w + T_a W_{wa} - 79.6 \cdot W_i}{0.22 \cdot (W_a + W_c) + W_w + W_i + W_{wa}} \tag{6.2}$$

where W_i corresponds to the mass of added ice (kg/m^3). The above expression makes the simplifying assumption that ice is at its melting temperature. If more accurate predictions are desirable, ACI 305R-10 (ACI 2010) provides alternative predictive equations. In concern to alternative ways of estimating concrete mix temperatures, it is also worth mentioning the nomogram suggested by CIRIA Report 135 (Bamforth and Price 1995).

The introduction of liquid nitrogen for cooling concrete mixtures, which is further discussed in Sect. 6.2.7, is usually done after the mixing process, when concrete is already in a truck. The quantity of liquid nitrogen varies according to the proportion and the extent of concrete temperature reduction that is intended. Normally, the use of 10 kg of liquid per m^3 of concrete allows reducing its temperature by approximately 1 °C.

If phase-change materials (Bentz and Turpin 2007; Choi et al. 2014) are being added to the mix, their melting temperature is usually higher than mixing temperatures, so their latent heat does not need to be taken into account in computations

of Eqs. (6.1) or (6.2). However, due account should be taken in regard to the mass of phase-change materials added, as well as their initial temperature and specific heat (outside the range of phase change).

6.2.3 Cooling Mixing Water

Most of the times, water is the easiest constituent of concrete to cool (Juenger et al. 2010; ACI 2005a, b). Moreover, its impact on the final temperature of the mix is quite efficient in view of the high heat capacity of water. Lowering water temperature by 2 ~ 2.2 °C usually allows reducing the mix temperature by approximately 0.5 °C. Nonetheless, as water usually represents a relatively small mass fraction in concrete, it is hard to lower the overall concrete temperature by more than 4.5 °C through the use of water cooling alone. The technology behind the industrial water coolers falls beyond the scope of this chapter. However, it can be mentioned that this technology is mostly based on combination of several other technologies (depending on the manufacturer), such as heat exchangers, compressors and evaporators. It is nonetheless relevant to remark that nowadays commercial products can assist the production of a few tens of cubic metres of concrete per day up to more than 3000 m^3 of concrete with one single piece of equipment. The cooling capacity of these systems allows them to cool water from the environmental temperature to values as low as 4 °C or even 1 °C. It is nonetheless remarked that, even when the refrigerating unit is installed within the concrete plant, thermal gains occurring between the outlet of the cooling system and the entrance of the concrete mixer are normally responsible for an increase of approximately 1 °C in water temperature.

6.2.4 Introduction of Ice in the Mix

As an alternative to the use of liquid water alone, it is possible to partially replace it by ice in the form of shaved, chipped or flaked ice. These forms of ice are more attractive than crushed ice because of their high slenderness and specific surface that facilitate the melting process within the concrete mixer. The partial substitution of liquid water with the recommended forms of ice offers additional cooling capacity, not only due to its lower temperature as compared to liquid water, but mainly because of the energy (enthalpy ~333 J/g) involved in the phase-change process from the solid state to the liquid state (endothermic). In effect, ice can substitute up to about 75% of the mix water to reduce the concrete temperature by up to 20 °C (Neville 2011; ACI 2005a, b). For reference, it is usually considered that each 7.5 kg of added ice (per m^3) allows reducing the temperature of fresh concrete by 1 °C. Taking into account that the normal range of ice added to concrete for cooling is within 35–100 kg/m^3, temperature reductions from ~5

to ~14 °C may be expected (ICOLD 1990; Vallarino 1998). It should, however, be taken into account that the times for mixing can increase due to the necessity of liquefying the ice. From a practical point of view, this can represent losses in the efficiency of the concrete plant by up to approximately 20%. Care should, however, be taken in ensuring that the mixing process effectively melts all the ice, which would otherwise cause problems in casting or even generate voids if large pieces of ice remain intact until setting. That is why the ice to be introduced in the mix should always have a high surface area (such as thin chips, flakes) to allow its quick melting upon contact with other concrete constituents within the mixer.

The manufacturers of cooling systems for water are normally also suppliers of systems to produce ice in several forms suitable for adding in concrete mixers. Currently existing ice plants vary in size and capacity, but they are able to produce daily outputs of as much as 150 tons of ice per unit. Specific information about ice replacement in the mixture, with particular focus on construction site requirements (e.g. machinery, energy) can be found in Oliveira (2015). It is further remarked that be aforementioned reference also provides practical information for other pre- and post-cooling techniques relevant to the present chapter.

6.2.5 *Cooling Aggregates*

Aggregates have a pronounced effect on the final temperature of the concrete mix because of the fact that they usually represent a large proportion (up to 70–85%) of the overall concrete mass. As a rule of thumb, in order to lower the temperature of the mix by ~0.5 °C, it is usually necessary to cool the aggregates by between 0.8 and 1.1 °C. Aggregates can be cooled using different methods, such as processing and stockpiling of aggregates during colder seasons (when applicable), shading aggregate stockpiles from the direct solar radiation, processing in chilled water during final classification, controlled misting or water sprinkling of coarse aggregate stockpiles, immersion cooling of coarser aggregates, chilled water spraying when on the belt conveyor, vacuum cooling/cold air circulation or use of liquid nitrogen (Bamforth 2007; ACI 2005a, b, 2010).

Some of the aforementioned methods, such as retaining aggregates in shadowed zones, and regularly sprinkling them with water to promote evaporative cooling, are fairly simple and cost efficient. The evaporation of water from the aggregates removes heat from them because of the enthalpy of the phase-change process. This process is especially effective when the environmental relative humidity is low.

The use of air circulation cooling systems is another alternative. However, it requires dedicated equipment. Even though this is a relatively economic system, and it does not require the consumption of resources such as water, it has a limited cooling capacity associated to the low heat capacity of air (Andriolo and Skwarczynski 1988).

It is also possible to submerge aggregates in silos, in which cool water is circulated. This technique allows very fast cooling of the aggregates due to the high

heat capacity of water. However, the cost is relatively high, it involves significant water consumption and is, therefore, a less sustainable solution. Furthermore, after the cooling process, some drying is usually necessary to reduce the humidity of aggregates. This drying process can reduce the effectiveness of cooling due to exposure to the environmental temperature, particularly in fine aggregates. The design of silo-based cooling systems can be performed with the method proposed by ACI 207.2R-07 (ACI 2007). Significant applied information, based on extensive application of aggregate cooling methodologies of several types, can be found in the report of Andriolo and Skwarczynski (1988).

6.2.6 Cooling Other Constituents

The volumetric content of cement in concrete is relatively low, and the heat capacity of cement is also low when compared with that of water. Therefore, cooling cement has a low impact on the overall temperature of the mix. In fact, a reduction of 5 °C in the temperature of cement usually only allows a reduction of approximately 0.5 °C in the mix. For similar reasons, there is usually no use in cooling other binders (e.g. fly ash, slag), or minor constituents such as admixtures.

6.2.7 Cooling by Injection of Liquid Nitrogen

One of the methods of pre-cooling concrete before placement consists of cooling either the fresh concrete or its constituents with liquid nitrogen (LN), also referred to as cryogenic cooling of concrete (Beaver 2004; Gajda and Vangeem 2002). Liquid nitrogen is a cryogenic fluid with boiling temperature of −196 °C obtained industrially from cryogenic fractional distillation of liquefied air or by liquefying the nitrogen obtained from separation of gaseous air. The low boiling temperature together with its non-reactivity makes LN a commonly used refrigerating agent in industrial and laboratory applications. Using LN for cooling concrete has been proposed as early as in the 1970s (Koudelka and Kelly 1971). Nevertheless, the widespread application of the method has been initially limited, mainly due to safety concerns regarding operating the cryogenic gas at the construction sites and the high costs. Since recently, specialized companies offer LN cooling technologies aimed at pre-cooling concrete directly at the construction site, allowing for reduction of costs and relieving safety-related issues, thus increasing the disseminated use of LN (Beaver 2004). A typical example of application of LN cooling in site can be seen in Fig. 6.1.

In fact, LN cooling may be in some regions cheaper than chilled water or ice cooling (Beaver 2004; Luff and Bhasin 1983). Cooling by LN is also recognized by ACI 305R-10 (ACI 2010). In practice, cooling by means of LN may be realized in one of the following ways (or as combination of them): cooling of mixing water

Fig. 6.1 Photograph of typical in-site application of LN cooling in concrete truck (courtesy of O. Kunc, TBG Metrostav)

before mixing, cooling of dry cement in a truck or a silo (Luff and Bhasin 1983), cooling aggregates (Kurita et al. 1990) or cooling the mixed concrete in a central mixer or in a truck drum (Beaver 2004). The latter method seems practically most feasible for adjusting appropriate placing temperature and is obtained by placing a lance into the mixer/drum and spraying the LN directly on concrete surface for a required time while mixing. Relatively short cooling times are required, e.g. as reported by Beaver (2004): 8 min LN spraying was needed to cool down 6 m^3 of concrete from initial 35 °C–24 °C and reach the placing temperature after transportation equal to 26 °C (15 min from batching). The quantity of LN varies according to the mixture proportions and the targeted temperature reduction. Normally, 10–12 kg of LN per m^3 of concrete allows reducing its temperature by 1 °C (Bamforth and Price 1995). Regarding the injection of LN into mixing water, it has been suggested (ACI 2005b) that, in most cases, a placing temperature of less than 18 °C can be normally achieved.

It has been reported by Juenger et al. (2010) that cooling can take place even up to 1 h from the end of mixing which allows applying it directly before placement (e.g. in the mixing drum of a concrete truck) and compensate for the prolonged transportation time.

It is important that the LN is not sprayed on the equipment (mixer walls) since thermal shock can cause cracks as cooled metal loses its ductility (Juenger et al. 2010).

Even though LN is an inert gas, and therefore its influence per se on concrete properties should not be an issue, the influence of cryogenic cooling should be considered. This may in particular regard performance of admixtures if local temperature of concrete during cooling is lower than specified by the manufacturer. Further, too intense cooling may lead to partial freezing of the mixture and cause its inhomogeneity or problems with pumping, compaction, etc. A comprehensive study on the effects of LN cooling in laboratory conditions and at the site on the properties of concrete, both at early age and hardened, can be found in Juenger et al. (2010). In the study, it has been shown that LN cooling shows no significant negative influence on the properties and performance of concrete. In particular, no negative influence on hydration and microstructure evolution, workability, setting time, yield (volume loss due to cooling), strength, chloride penetration. Some reduction of air content for LN-cooled concretes was, however, a case.

6.3 Transport and Placement

6.3.1 Temperature Issues During Transport

The transport of concrete from the mixer to the placement point can sometimes be a relatively lengthy process in terms of duration. This is particularly the case when the concrete plant is not directly located in the same place as the construction site itself. In such cases, the transport is usually made by trucks. In cases where the ambient temperatures are high, and particularly during the day in sunny conditions, concrete temperatures are bound to rise. Under such conditions, it is then recommended to minimize transport distances and to use light-coloured vehicles, or place reflective aluminium insulation in the concrete drums (low absorptivity that reduces the effects of solar radiation), or favour night time for transport and casting (when feasible). To avoid rejection of batches, suitable on-site measures may be taken, such as the provision for a liquid nitrogen injection system, as mentioned in Sect. 6.2.7.

According to ICOLD (1990), it is possible to obtain an estimate of the temperature increase per hour (ΔT), based on a formula that depends on the ambient (T_a), the initial temperature of concrete (T) and a coefficient K that varies between 0.1 and 0.2 (empirical nature):

$$\Delta T = K \cdot (T - T_a) \tag{6.3}$$

An alternative more complex prediction model for concrete temperature has been proposed by Bofang (2013), which specifically takes into account the solar radiation, the conductance of the transporting vessel, and a variable number of empiric coefficients related to episodes of loading/unloading and change of transporter and duration of the transport process.

6.3.2 Temperature Issues During Placement

There are two fundamental temperature issues that can be brought about when concrete placement is under discussion: (i) the thermal exchanges that occur when concrete is moved from the transporting container (e.g. truck drum, blondin bucket) or the concrete plant itself to the placement spot; (ii) the thermal exchanges that occur during the placement itself, which tends to span through several hours in mass concrete castings.

Regarding issue (i), one has to take into account the possible means of moving concrete from the transporting container or the concrete plant itself to the placement spot. Indeed, several techniques exist, such as pumped concrete, transfer belts/conveyors, buckets and hoppers, buggies, (drop) chutes (ACI 2000). Regardless of the adopted moving technique, the basic intent is normally to keep concrete within the same temperature as it was inside the transporting container. Therefore, it is advisable to minimize distances, speed up the process (e.g. by preferring bucket transport to belt transport) and ensure thermal insulation and solar shielding throughout the process (e.g. insulation material around the transportation belt, which could also include active cooling measures ACI 2005a, b). In some cases, the pipes through which concrete is pumped may be surrounded by ice, as to minimize heating effects, or even ensure some degree of cooling during transport. Transport of concrete in refrigerated boxes has also been reported (Schrader and Swiger 1988; Schleiss 2011).

Of course, when concrete heating is to be avoided, it is advised to commence concreting at night, especially in summer, both due to the lowest diurnal temperature and solar action (Riding et al. 2009; Klemczak and Knoppik-Wróbel 2012; Witakowski 2001; JCI 2012).

Another important issue raised above (ii) pertains to the fact that casting mass concrete is usually a relatively lengthy process, mostly due to the relevant thickness of the concrete layers that may easily span from 1 to 3 m. Therefore, the casting of a given layer is normally done in sequential sub-layers of approximately 15–30 cm height that are cumulatively placed and vibrated. During this process, the top surface of each sub-layer is normally relatively large and subject to thermal exchanges with the surrounding environment before the placement of the subsequent layer commences. These heat exchanges can be minimized by: (a) prioritizing night castings, thus avoiding solar energy intakes and the higher temperatures during daytime; (b) using solar shielding panels when diurnal times of casting are involved; (c) accelerating construction by increasing casting rates and multiple casting points (by deploying additional workforce and equipment). In regard to the potential prediction of temperature rises of concrete during this placement process, Bofang (2013) proposes a predictive equation, with a set of empirical coefficients, that depend on the air temperature, the solar radiation, as well as the time to spread the layer.

6.4 Surface Measures for Temperature Control

After placement, the boundaries between concrete surfaces and the surrounding environment tend to be regularly cooler than the interior regions of mass concrete elements, in which near-adiabatic conditions are normally endured in mass concrete. Therefore, when the temperature of near-surface regions is significantly lower than that of the inner core, the thermal gradients induce differential volumetric changes between surface and core that can generate thermal stresses. These surface-induced thermal stresses are naturally more significant in cold weather conditions that maximize the thermal gradients. The typical approach to this problem is to provide surface insulation to concrete, which limits thermal exchanges and thus keeps the surface temperatures higher (Bofang 2013; ACI 2005a, b; ICOLD 1990). As a consequence of the insulation, the peak temperature of concrete in its inner core is retained for a longer period, and the duration of the hydration heat dissipation is prolonged. As the insulation measures are preferably taken in cold weather conditions, the increase in peak temperature and the extended cooling period are not usually considered problematic.

The insulation issue is also relevant in formed surfaces, which need to ensure adequate thermal resistance as to hinder excessive thermal fluxes. Furthermore, surface concrete may be susceptible to thermal shocks upon formwork removal (e.g. at ordinary stripping ages, that often vary between 1 and 3 days of age). Such thermal shocks may also be responsible for potential cracking and thus the application of surface insulation immediately after formwork removal, or, alternatively, a delay in formwork removal is advisable (Huo and Wong 2006; Lawrence et al. 2014; Klemczak and Knoppik-Wróbel 2011). The formwork removal issue can also bring about added thermal shock hazard associated to the intense evaporation that occurs from the wet concrete surface to the surrounding environment. In hot and dry climates, this evaporation induces significant rapid cooling of concrete (several °C) and may provoke relevant stresses, thus contributing to cracking. This phenomenon has been documented as the shock of evaporative cooling (Kovler 1995) and should be carefully taken into account in hot and dry climates through adequate curing measures immediately after formwork removal.

For insulation, in most cases concrete insulating blankets are used; however, any insulating material is usually acceptable; cracking risk decreases with lowering the value of thermal conductivity of the covering material (Liu et al. 2014a, b). The important issue is that insulation should be kept in place until the hottest portion of concrete cools to the ambient temperature (Klemczak and Knoppik-Wróbel 2011). The effectiveness of the insulation on the reduction of the temperature difference and thermal stresses depends on the thickness of the insulation layer but also on the size of the insulated element: it was observed that the effectiveness of the increase of the insulation thickness is greater in thicker elements (Lawrence et al. 2014). The same research team (Tu et al. 2014) has further performed a numerical sensitivity analysis that led them to the proposal of recommendable insulation thicknesses

(using expanded polysterene products) for temperature control in concrete footings, based on the ratio between volume and surface area of the concrete element.

An important point to take into account when selecting the system (material, thickness, etc.) for providing adequate thermal protection is its thermal resistance, R. The R-value is normally addressed in building physics to express the thermal resistance of a given element to heat fluxes. It is calculated by dividing the thickness of the material (measured perpendicularly to the heat flux) [m] by the thermal conductivity [W/(mK)]. According to (ACI 2005a, b), a minimum R-value of 0.70 m^2 K/W has been found to be adequate for surface thermal insulation in the context of mass concrete in moderate climate countries, whereas in severe climates, a minimum R-value of 1.76 m^2 K/W is recommended. These values are clearly not achievable by typical plywood formwork solutions: for example, a 21 mm thick plywood board (with thermal conductivity 0.15 W/mK) has a R-value of only 0.14 m^2 K/W. Therefore, even formed surfaces usually need to deploy specialized insulation materials such as (Bofang 2013): foamed polystyrene boards, namely expanded polystyrene (EPS) and extruded polystyrene (XPS) with typical conductivity ranging 0.03–0.04 W/mK; foamed polythene wadded quilt; polyurethane foamed coating ($k \sim 0.02$ W/mK). Formwork removal should be done carefully, preferably during the hottest time of the day to reduce the thermal shock. If inner temperatures of concrete are still elevated, the formerly formed surface should be immediately insulated with an adequate system (usually boards or blankets) (ACI 2005a, b).

Additional challenges are placed in the case of horizontal surfaces of fresh concrete that are not formed, and that are supposed to support the upcoming stages of construction. In these cases, applying insulation is more challenging and typical approaches involve the use of straw bags or blankets (mineral/glass wool blankets or batting in thicknesses up to 50 ~ 100 mm, or roll-on rubber-type materials) (ACI 2005a, b; Bofang 2013). These alternatives demand more than one layer of bags/blankets to be applied in order to achieve the desirable insulation. This multiple layer approach is considered by ACI (2005a, b) as an interesting feature in the sense that it allows mismatching the joints between adjacent bags/blankets in consecutive layers and also allows a progressive removal of the bags/blankets, thus minimizing the thermal shock of a sudden/instant removal. The application of these insulations should be made immediately after walking over the fresh concrete is possible and should allow easy removal/re-collocation for the preparative works of the next lift. The lightweight character of typical insulation materials can often induce the necessity of measures to avoid uplift by wind, such as anchors (ICOLD 1990). As an alternative to bags/blankets, sand can be used for thermal insulation. However, this method demands more workmanship for removal, even if a geotextile membrane is used below the soil. It is therefore usually only recommended when a relatively long pause in the construction is foreseen (ACI 2005a, b). Other less conventional techniques of ensuring adequate temperature at the surface of mass concrete can involve hot fog spraying or even actively heated insulation materials (ICOLD 1990; Bofang 2013).

The protection of the insulation system from solar radiation can be a relevant issue. In fact, the point of the insulation is avoiding strong heat dissipation, and not

necessarily feeding concrete with additional heat. Therefore, solar shielding through reflective or light-coloured materials might be desirable in critical cases (ACI 2005a, b).

6.5 Post-cooling of Mass Concrete

6.5.1 Strategic Background of Post-cooling

Post-cooling of concrete with embedded pipes has been applied since the 1930s (ACI 2005a, b). The point is to control the internal temperature of concrete within specified limits by actively circulating water (or another cooling fluid) through the embedded pipes, as to mitigate the risk of thermal cracking. It is usually oriented towards the reduction of the peak temperatures of concrete during the hydration period, thus minimizing the volumetric variations associated to the corresponding temperature variations. The design of post-cooling systems comprises the optimization of pipework properties (geometrical layout, heat transfer, fluid flow rate, inflow/outflow temperatures) to achieve the desired peak temperature reduction with the minimum possible energy consumption. Examples of structures and their corresponding typical piping layouts can be seen in Fig. 6.2. The output of this design can then be directly provided to suppliers for sizing of cooling pipe systems and procurement of suitable generators (Sfikas et al. 2016).

The technique is quite effective, but it has relevant costs of effective design, material procurement, installation and operation. For that reason, its area of application is generally limited to bigger structures, such as arch dams that require internal cooling before joint filling/sealing (ICOLD 1990); the cooling system can be activated during the early days/weeks after casting, thus allowing thermal control of concrete. Other applications of post-cooling include, but are not limited to, production of concrete segments for immersed tunnels, retaining walls and slabs (Baber et al. 1998; Kim et al. 2001; Lunniss and Baber 2013), which are nowadays commonly analysed and designed using dedicated finite-element analysis (FEA) software. An extended review of the current state-of-the-art for the use of

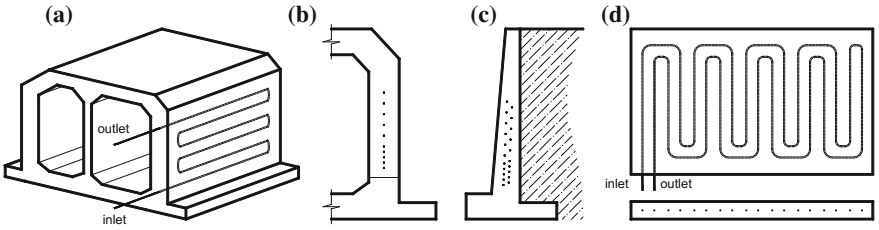

Fig. 6.2 Examples of embedded concrete pipe systems layouts for **a** tunnel segment, **b** gallery wall (linear set-up), **c** retaining wall (staggered set-up) and **d** slab. (Sfikas et al. 2016)

FEA for thermal dynamics and a briefing paper have been recently published by Sfikas et al. (2016, 2017).

6.5.2 Post-cooling with Water Circulation

The control capacity that the embedded pipes permit can provide interesting alternative insights into construction phasing that would be unthinkable with pre-cooling techniques alone. A good example of such situation is the application of embedded pipes in the walls of a reservoir in Germany, with 1.2 m thick walls and 12 m tall (Bamforth 2007). Through judicious placement and activation of the embedded pipes, it was possible to cast the entire wall simultaneously with its foundation slab (2 m × 27.4 m × 28.2 m), in a total of 1100 m^3 of concrete applied within 32 h.

Most applications reported in the literature for post-cooling with water use 1″ (2.54 cm) diameter steel pipes with wall thickness of 1.5 mm. According to ACI 207.4R-05 (ACI 2005a, b), the alternative of using aluminium pipes is only recommendable for cooling applications with durations of less than 3 months, as these may tend to degrade due to reaction with the alkalis from cement. It is further possible to apply PVC, polyethylene or other plastic-based pipes (Zhu 1999), but it is recommended to take special care in respect to the mechanical strength of the piping system to apply, in order to avoid unwanted damages. Apart from being cheaper than steel pipes, the plastic pipes have lower thermal conductivity, thus minimizing the heat absorption of the flowing fluid along the embedded path of the pipe. This advantage allows to apply longer piping systems (i.e. less inlets/outlets), but it also carries the drawback of limiting the cooling capacity in comparative terms to that of steel pipes. The plastic-based pipes usually have the advantage of being flexible thus allowing a much easier and fast placement than that of steel pipes (that require 'knees', 'turns', etc.) but may be more vulnerable to unintended movements during casting.

In mass concrete structures, where layered casting is made, cooling pipes are usually placed on the top level of each casting phase, corresponding to the bottom plane of the subsequent casting phase. This option is mostly related to the ease of application of the pipes, and the potential added difficulties that would be faced in holding the pipes at an intermediate level, as mass concrete structures do not usually have enough inner reinforcement for such kind of support (thus demanding for dedicated supports). Typical layouts of pipes can be seen in Fig. 6.3. The efficiency is related to the layout of the pipes and number of individual pipe networks. In effect, several independent piping systems, both in terms of their layout in plan and their distribution over the depth of the element, can be used within the body of mass concrete.

The horizontal spacing between adjacent pipes varies according to the thermal design. However, according to CIRIA C660 (Bamforth 2007), spacings of 1.0 m are usual in large castings of low-heat cement, as opposed to smaller spacings of

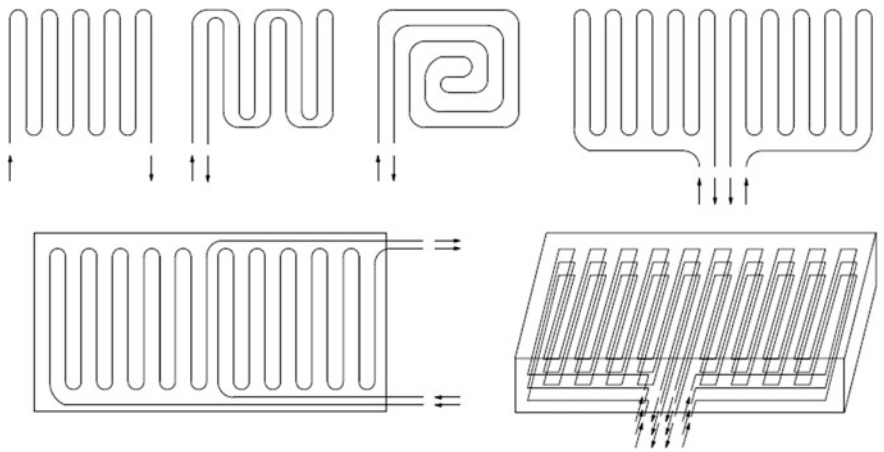

Fig. 6.3 Examples of cooling pipe layout

approximately 0.5 m when concrete with high quantities of rich cement is used. The reason for these relatively small spacings is related to the low thermal diffusivity of concrete, which makes the influence zone of each pipe to be small in the context of the early ages of concrete. In fact, if the placement of pipes were solely related to the cooling of a dam for joint sealing purposes, the spacing could easily be enlarged to 2–3 m as the cooling can be much slower in such cases (there is no competition with the pace of hydration heat development).

Under optimum conditions, the horizontal and vertical spacing of pipes should be identical, with quincunx arrangement as shown in Fig. 6.4. This is however not always possible due to restraints to the height of lifts.

The total embedded length of a water cooling pipe should avoid significant heating of the circulating water. In spite of that, pipes as long as 180–350 m can be applied without relevant heating problems (ACI 2005a, b). The flow rate of water is usually fixed amongst 15–17 L/min. The water that circulates in the pipes is normally originated in a natural source such as a river (quite easy in the particular case of dam construction), with adequate filtering measures as to avoid clogging of the pumping/piping system. When river water is used, the natural water temperature is normally adequate for the purposes of concrete cooling (Bamforth 2007). If water

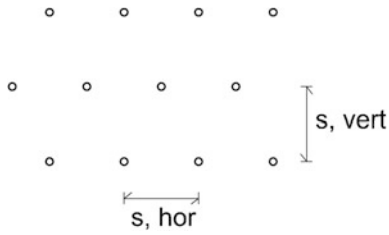

Fig. 6.4 Quincunx arrangement of adjacent cooling pipes for optimized performance

cooling is necessary, it is required to ensure a water chilling system with enough capacity for the flow rates of the several pipes that might need to be active simultaneously. Even though it is known that the capacity of cooling may be increased by increasing pipe diameter, using higher water velocity and diminishing the temperature of water, it is necessary to take into account that excessive coolness can induce thermal shock to the concrete surrounding the cooling pipes and induce thermal cracking around the pipes. The recommendations of JCI (2012) point to a maximum admissible difference of 20 °C between the temperature of the circulating water and its surrounding concrete.

The operation of cooling pipe systems demands for a watertightness test to be made before casting, with the corresponding repairs being made before pouring operations. The pressure inside the pipes should be monitored as to ensure that the intended flow rates are met during operation. The measurement of water temperature at the inlets and outlets, as well as several points of the cooled concrete is desirable for assessment of the operational conformity. Particularly for the cases in which the cooling water suffers relevant heating along its embedded path, it is recommendable to invert the direction of the circulation flow according to intervals around 12–24 h, as to avoid inducing significant thermal imbalances in concrete (JCI 2012).

The activation of water circulation can be made simultaneously with the casting operations (Korol 1968). The adequate fixation of the pipes together with the relatively small internal flow rate can ensure that no damaging vibrations are transmitted to the fresh concrete. However, as the heat generation of concrete is quite low before the setting point, it is possible to await for such threshold in order to activate the circulation of water. The water circulation should be kept at least until the peak temperature of concrete is reached. After the core concrete reaches thermal equilibrium with either the outer environment or the water in the pipes (similar temperature), there is no point in continuing the water circulation. However, care should be taken of avoiding that the internal cooling causes excessive rates of temperature drop in concrete, which could be potential causes for thermal cracking. According to recommendations of ICOLD (1990), during the first 3–4 weeks after placement, the cooling rate of concrete should not exceed 0.5 °C/day as to prevent thermal cracking. In case the water circulation is stopped when the peak temperature is reached in concrete, it may be re-activated if the peak temperature is reached again (ACI 2005a, b; Korol 1968).

Even though there are simplified design methods for water pipe cooling systems, they are mostly targeted to the cooling period that precedes the sealing of joints in dams. The simplified solutions that have been proposed for the context of concrete at early ages (Yang et al. 2012) still have very limited applicability due to their subjacent simplifications. The most precise way to design and optimize post-cooling systems is definitely the explicit spatial simulation of temperature development, which is most frequently achieved through the finite-element method. The numerical simulation tools that are nowadays available to the practising community allow for the explicit simulation of thermal fluxes occurring between concrete and the embedded pipes, which inclusively allow to calculate the increases in water temperature along the cooling pipe.

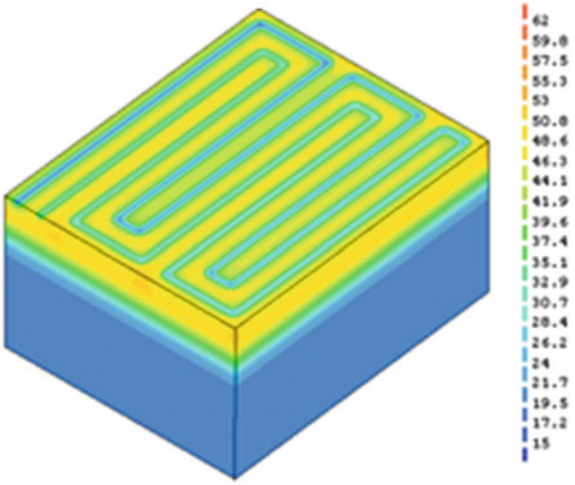

Fig. 6.5 Temperature map of a mass concrete element at the age of 30 h after casting: cutaway view through the place of the cooling pipes [Units: °C]—study made at the University of Minho (unpublished)

An example of such computation capacity is shown in Fig. 6.5, where a cutaway view of the temperature map of a mass concrete element through the plane of the cooling pipes is shown. The effect of the cooling pipes on concrete temperature is easily identifiable in the figure, as well as the inlet and the outlet of the cooling pipes through observation of the increasing temperature along the pipe.

A typical design for an immersed tunnel gallery wall design is shown in Fig. 6.6. It is evident that the incorporation of a cooling pipe system in the wall, with carefully designed geometrical and operation parameters using dedicated FEA software, can mitigate the risk of cracking by reducing the developed out-of-plane stresses over the curing period below the design tensile strength (ultimate tensile strength, usually factored by 50–70%). Another recent application of cooling pipes was reported by Du (2016).

The use of cooling pipes is frequently adopted as to allow thicker casting lifts and therefore accelerate construction cycles. An example of the advantages that can be obtained can be supported in a recent study conducted for a contractor on behalf of the University of Minho in Portugal. The study evaluated the possibility of increasing the thickness of casting lifts of a massive concrete element (spillway wall) from the originally planned value of 1.5 m, to a larger value of 2.4 m without increasing the associated cracking risk. The study allowed concluding that it was possible to increase the thickness of the lift by applying a single layer of high-density polyethylene (HDPE) pipes located at mid-height of the lift (1″ diameter and flow rate of 0.5 m/s), fed directly with river water and horizontally spaced by approximately 0.8 m. The computed temperature maps for the instant of peak temperature are shown in Fig. 6.7 for both the reference case (1.5 m thick lift without cooling measures) and the alternative scenario of 2.4 m lift thickness with active cooling. It can be confirmed that both the peak temperatures and the spatial thermal gradients in concrete are quite similar, thus confirming feasibility of the proposed alternative with cooling.

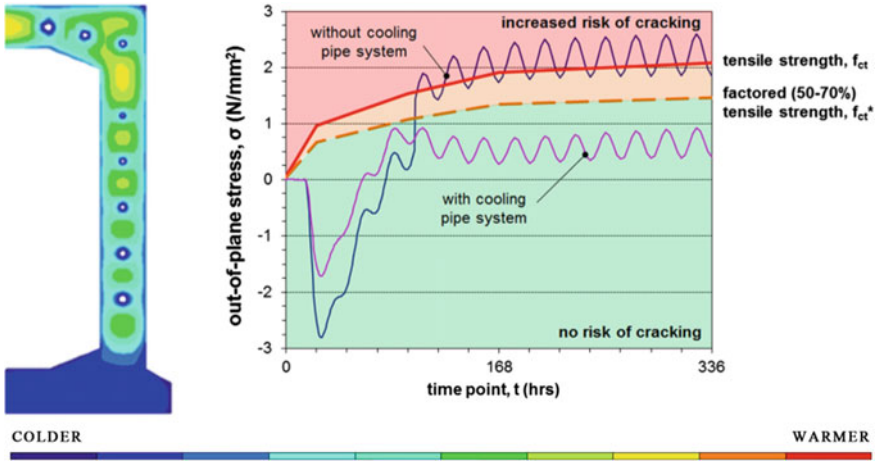

Fig. 6.6 Typical linear arrangement of cooling pipes in immersed tunnel gallery wall and assessment of the risk of cracking due to developed out-of-plane stresses (Sfikas et al. 2016)

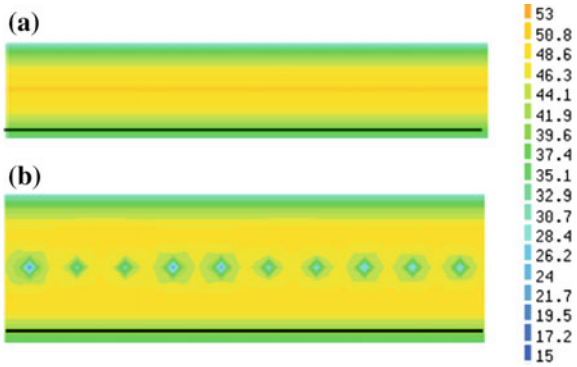

Fig. 6.7 Calculated temperatures for the instant of peak temperature (t = 24 h): **a** 1.5 m lift thickness without cooling pipes; 2.4 m lift thickness with cooling pipes [Units: °C]—study made at the University of Minho (unpublished)

Amongst water circulation techniques, it is relevant to pinpoint the possibility of increasing the cooling effectiveness by using a water suspension of 'phase-change materials' (PCM) circulating in the cooling pipes. The principle is relatively simple, as the PCMs absorb and release heat upon passing through their phase-change temperature, which is selected to be somewhat above the casting/environmental temperature. If cooled PCMs (solid) are circulated within cooling pipes, the heat of the surrounding concrete tends to melt them and induces a significant heat absorption by the PCM because of the phase change, thus enhancing the heat exchange. The PCM should then be cooled down outside concrete and the cycle can be repeated. Such technique has been applied by Qian et al. (2015), who used a PCM with phase-change range 16–24 °C, and compared the performance of this method with the classic water circulation technique in two prototypes. The cooling with PCMs has shown a slightly better capacity of reducing the peak temperature in

concrete. Even though the benefits were not outstandingly good, the technique has a good potential because the PCMs can be re-used in several cycles of circulation.

Qian et al. (2015) have also attempted the use of closed cylindrical cavities within concrete (without any kind of circulation), containing the PCM for temperature control in mass concrete. However, this approach has two major downsides: (i) the PCM only operates a single time upon its phase change; (ii) the quantity of PCM necessary to induce relevant effects on temperature ended up being very large and this impracticable.

6.5.3 *Post-cooling with Air Circulation*

The use of air as cooling fluid for hardening concrete has been initially proposed by Hedlund and Groth (1998). In such initial proposal, the authors proved the viability of the system with both laboratory and in situ applications. The use of air instead of water can be quite interesting in several applications because of the ease of application and lower cost. The piping itself can be quite cheap due to the possibility of using prestressing ducts, which have the interesting characteristic of having a well-proven long-term behaviour when embedded into concrete (both in terms of mechanical strength and tightness, as well as in terms of compatibility and durability). However, as air is a fluid with a much lower specific heat capacity as compared to water, it is necessary to use much higher circulation speeds (around 8 m/s for example) and larger diameter piping (8 cm diameter or more) to ensure similar cooling capacity. Based on the mentioned limitations, this type of cooling fluid becomes quite attractive for extremely massive constructions, such as dams. However, in the particular case of thick laminar concrete elements such as foundation slabs, tunnel or spillway walls, this type of cooling fluid can reveal an interesting attractiveness. An example of a successful application in a foundation slab in Qatar was reported by Ishikawa et al. (2007).

More recently, a more comprehensive application has been applied in Portugal, in the scope of the dam spillway (Azenha et al. 2014). The central wall of the spillway had a maximum thickness of approximately 2.7 m and longitudinal length of $\sim$27.5 m. One of the lifts of this wall required internal heating to ensure the safety to thermal cracking of its 2.5 m height. The option for a air-based post-cooling system was based on the low cost of the system and the easy availability of the necessary material: (i) prestressing ducts used as cooling pipes; (ii) industrial fans that had been used in the construction of a nearby tunnel. The cooling system consisted of six ducts with 90 mm diameter spaced by 80 cm from each other (at the thickest section of the wall)—see layout in Fig. 6.8.

The air intake was made through the downstream extremity of the wall, and the air outlet was placed in the upper surface of concrete, in the vicinity of the upstream extremity. The industrial fan had a diameter of 60 cm, and a ventilation capacity of 1200 m^3/h. In order to avoid unwanted vibrations in the fresh concrete, the ventilation system was only activated 14 h after the beginning of casting operations.

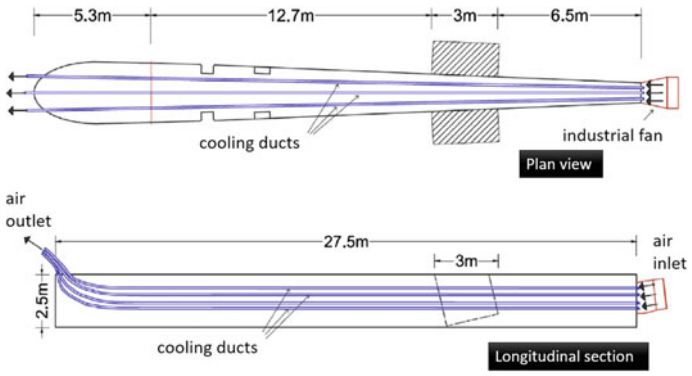

Fig. 6.8 Layout of the cooling ducts in the spillway wall. Adapted from Azenha et al. (2014)

The ventilation was turned off at the age of 8.6 days, in correspondence to the thermal equilibrium between core concrete and the surrounding environment. Before the placement of concrete in the subsequent casting phase, the prestressing ducts were filled with mortar with the same type of procedures that are normally applied to post-tensioning cables.

Through numerical simulation based on the finite-element method (duly validated by comparison with in situ temperature measurements), it was possible to confirm that the peak temperature of concrete at its hottest point was roughly 5 °C lower than that which would have occurred if pipe cooling had not been applied. Such difference can be appreciated along time in the comparison of both scenarios shown in Fig. 6.9. Additionally, Fig. 6.10 shows the same comparison in the shape of a temperature map plotted for the instant of peak temperature for both studied scenarios.

The field application that has just been reported allowed to confirm the viability of the air cooling technique, but it also allowed identifying another drawback in addition to the ones presented before: there is a significant heat gain in air along the cooling duct. Therefore, for optimized cooling efficiency, it is recommendable that the embedded path of each independent pipe should not be larger than approximately 10 m. In spite of the reported limitations, the low cost and ease of

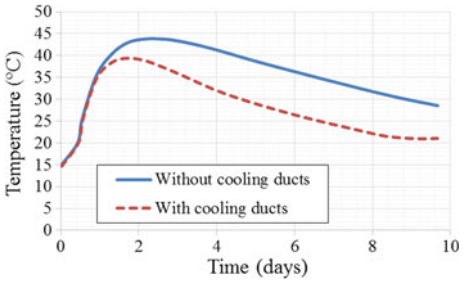

Fig. 6.9 Temperature evolution in the hottest point of the wall for the case in which the cooling pipes were used, and for the hypothetical case of absence of such pipes (simulation) Adapted from Azenha et al. (2014)

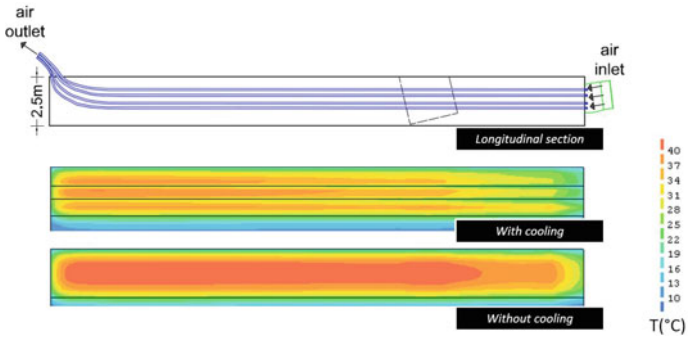

Fig. 6.10 Temperature maps for the longitudinal symmetry plane of the 2.5 tall casting phase for the two scenarios under study: with cooling pipes; without cooling pipes. [Units: °C]

application inherent to this cooling technique based on ventilated prestressing ducts make this an attractive solution in several situations for which the costs associated to water-based systems are not bearable.

6.6 Construction Phasing

Regardless of the temperature control measures taken in the production, transport, and placement, or even through the use of post-cooling, the thermal cracking risk is broadly affected by the strategies adopted for construction, especially in regard to the height of lifts and the waiting interval (dormant period) between consecutive/adjacent casting blocks. Indeed, these two factors have a major impact on temperature development of mass concrete structures. However, unlike previous factors that have been analysed in an almost-individual manner throughout the document, in the sense that their impact could be assessed in a relatively easy manner, the only way of truly understanding the consequences of construction phasing on cracking risk (lift height and casting frequency) before the actual construction itself, is to conduct numerical simulations of temperature and stress fields. These simulation should aim at evaluating the merits and comparing the risks of each possible alternative scenario. In the end, it is always a matter of establishing a trade-off between the desirable tall lift heights combined with small waiting periods for casting, and the undesirable elevated cracking risk, when such bold construction measures are taken. Naturally, the simulation of construction scenarios demands that all variables are taken into account, including the relevant effects of initial concrete temperature, and the potential use of post-cooling measures. The number of potentially involved variables in a process of optimization of mass concrete construction could prove to be next-to-infinite, and therefore practitioners normally tend to rely on their intuition to set up a small group of potential scenarios of construction (as small as 2, 3 or 4). The subject of optimization of construction

phasing in mass concrete has been tackled very few times in the literature. The most extensive work done on the subject was made by Fairbairn et al. (2004) through the application of genetic algorithms for the optimization of mass concrete construction. They have set up a group of variables for optimization aiming of minimization of costs, while keeping adequate cracking risk for construction: cost of the raw material and the construction costs associated to placing, cooling, formwork, lift height and time intervals between consecutive lifts. They have used a genetic algorithm to optimize global costs and applied their proposed framework to the 2D simulation of the cross-sectional thermo-mechanical behaviour of a small concrete gravity dam, reaching a set of recommended construction parameters, including the lift height and waiting periods. The example cannot be directly extrapolated for other situations worldwide because of its inherent specificities (e.g. types of concrete, climatic conditions). In spite of the encouraging results, this practice was not found in any work of the literature (practical or research) meanwhile.

In spite of the absence of works specifically targeted to the optimization of construction phasing of mass concrete structures, it is relevant to highlight the recent works of Klemczak and Knoppik-Wróbel (2015), Knoppik-Wróbel (2015) and Hónorio et al. (2016), who present insights into the relative relevance of construction parameters in the scope of mass concrete analyses through sensitivity analyses through numerical simulations.

Acknowledgements The kind contribution of the construction company SOMAGUE in sharing their experience in concert with temperature control in concrete is gratefully acknowledged. The sharing of information on behalf of the colleagues José Conceição and Shingo Asamoto is also acknowledged. This work was partially supported by: project POCI-01-0145-FEDER-007633 (ISISE), funded by FEDER funds through COMPETE2020—Programa Operacional Competitividade e Internacionalização (POCI), and by Portuguese funds through FCT—Fundação para a Ciência e a Tecnologia. FCT and FEDER (COMPETE2020) are also acknowledged for the funding of the research project IntegraCrete PTDC/ECM-EST/1056/2014 (POCI-01-0145-FEDER-016841).

References

American Concrete Institute ACI. (2005a). 207.4R-05 Cooling and insulating systems for mass concrete. ACI Committee 207. ISBN: 9780870311918.

American Concrete Institute ACI. (2005b). 207.1R-05 Guide to mass concrete. ACI Committee 207. ISBN: 9780870312014.

American Concrete Institute ACI. (2007). 207.2R-07 Report on thermal and volume change effects on cracking of mass concrete. ACI Committee 207. ISBN: 9780870312588.

American Concrete Institute ACI. (2000). 304R-00: Guide for Measuring, Mixing, Transporting, and Placing Concrete (Reapproved 2009), ACI Committee 304. ISBN: 9780870313080.

American Concrete Institute ACI. (2016). 301–16 Specifications for Structural Concrete. ACI Committee 301. ISBN: 9781942727866.

American Concrete Institute ACI. (2010). 305R-10 Guide to hot weather concreting. ACI Committee 305. ISBN: 9780870313967.

American Concrete Institute ACI. (2011). 308.1–11 Specification for Curing Concrete. ACI Committee 308. ISBN: 9780870314391.

American Concrete Institute ACI. (2014). 347R-14 Guide to Formwork for Concrete. ACI Committee 347. ISBN: 9780870319105.

Andriolo, F. M., & Skwarczynski, T. M. (1988). *Concreto pré-refrigerado no Brasil: Uma evolução com mais de 20 anos. (Pre-cooled concrete in Brazil: An evolution of more than 20 years) Grapho*, São Paulo, Brazil.

Azenha, M., Lameiras, R. M., Sousa, C., & Barros, J. (2014). Application of air cooled pipes for reduction of early age cracking risk in a massive RC wall. *Engineering Structures*, *62–63*, 148–163.

Baber, J., Salet, T. A. M., & Lundberg, J. K. (1998). Øresund tunnel control of early age cracking. In *Proceedings of the IABSE Stockholm Colloquium: Tunnel Structures*, Stockholm, Sweden (IABSE Report 78) (pp. 175–180). Zürich, Switzerland: IABSE.

Bamforth, P., & Price, W. (1995). *Report 135. Concreting deep lifts and large volume pours*. London: CIRIA (Construction Industry Research and Information Association). ISBN-13: 978-0727720252.

Bamforth, P. (2007). CIRIA *C660: Early-age thermal crack control in concrete*. London: CIRIA (Construction Industry Research and Information Association). ISBN: 978-0-86017-660-2.

Beaver, W. (2004). Liquid nitrogen for concrete cooling. *Concrete International, 26,* 93–95.

Bentz, D. P., & Turpin, R. (2007). Potential applications of phase change materials in concrete technology. *Cement & Concrete Composites, 29*(7), 527–532.

Bofang, Z. (2013). *Thermal stresses and temperature control in mass concrete*. Tsinghua University Press, published by Butterworth-Heinemann. ISBN-13: 978-0124077232.

Buenfeld, N. R., & Yang, R. (2001). *C530 On-site curing of concrete—microstructure and durability*. London: CIRIA (Construction Industry Research and Information Association). ISBN: 9780870314391.

CEN. (2013). EN 206: Concrete: Specification, performance, production and conformity.

Choi, W., Khil, B., Chae, Y., Liang, Q., & Yun, H. (2014). Feasibility of using phase change materials to control the heat of hydration in massive concrete structures. *The Scientific World Journal*, *2014*, Article ID 781393, 6 p. http://dx.doi.org/10.1155/2014/781393.

Concrete Society. (2014). CAS20 Curing concrete. Concrete advice n.20. Concrete Society.

Du, C. (2016). Temperature control for the Gomal Zam RCC Arch-Gravity Dam. *Concrete International, 38*(11), 31–36.

Fairbairn, E., Silvoso, M., Toledo Filho, R., Alves, J. L. D., & Ebecken, N. F. F. (2004). Optimization of mass concrete construction using genetic algorithms. *Computers & Structures, 82,* 281–289.

FDOT. (2010). *Standard specifications for road and bridge construction*. Tallahssee, FL: Florida Department of Transportation.

Gajda, J., & Vangeem, M. (2002). Controlling temperatures in mass concrete. *Concrete International, 24*(2002), 58–62.

Hedlund, H., & Groth, P. (1998). Air cooling of concrete by means of embedded cooling pipes-Part I: Laboratory tests of heat transfer coefficients. *Materials and Structures*, *31*, 329–334.

Honório, T., Bary, B., & Benboudjema, F. (2016). Factors affecting the thermo-chemo-mechanical behaviour of massive concrete structures at early-age. *Materials and Structures, 49,* 3055–3073.

Huo, X. S., & Wong, L. U. (2006). Experimental study of early-age behavior of high performance concrete deck slabs under different curing methods. *Construction and Building Materials*, *20*, 1049–1056.

ICOLD. (1990). *Bulletin n°76, conventional methods in dam construction*. International Commission on Large Dams.

Ishikawa, S., Matsukawa, K., Nakanishi, S., & Kawai, H. (2007). Air pipe cooling system. *Concrete International, 29*(12), 46–49.

Japanese Concrete Institute JCI. (2012). Guidelines for control of cracking of mass concrete, 2012 (English version translated from the Japanese Version of 2008).

JSCE. (2010a). Guidelines for concrete N. 16. *Standard specifications for concrete structures 2007—Materials and construction*. Tokyo: Japan Society of Civil Engineers.

JSCE. (2010b). Guidelines for concrete No. 18. *Standard specifications for concrete structures-2007, Dam Concrete*. Tokyo: Japan Society of Civil Engineers: Tokyo.

Juenger, M., Solt, S., & Hema, J. (2010). Effects of liquid nitrogen cooling on fresh concrete properties. *ACI Materials Journal*, *107*.

Kim, J. K., Kim, K. H., & Yang, J. K. (2001). Thermal analysis of hydration heat in concrete structures with pipe cooling system. *Computers and Structures*, *79*(2), 163–171. http://dx.doi.org/10.1016/S00457949(00)00128-0.

Klemczak, B., & Knoppik-Wróbel, A. (2011). Early-age thermal and shrinkage cracks in concrete structures—influence of curing conditions. *Architecture–Civil Engineering–Environment*, *4*(4), 47–58.

Klemczak, B., & Knoppik-Wróbel, A. (2012). Wpływ wybranych czynników materiałowo–technologicznych na temperatury twardnienia betonu w masywnej płycie fundamentowej. In *Proceedings of "Dni Betonu" Wisła, Poland*, (pp. 291–301).

Klemczak, B., & Knoppik-Wróbel, A. (2015). Reinforced concrete tank walls and bridge abutments: Early-age behaviour, analytic approaches and numerical models. *Engineering Structures, 84,* 233–251.

Knoppik-Wróbel, A. (2015). Analysis of early-age thermal–shrinkage stresses in reinforced concrete walls. Ph.D. thesis, Silesian University of Technology, Gliwice, Poland.

Korol, S. I. (1968). Technology of pipe refrigeration for the Krasnoyarsk hydroelectric station dam. *Hydrotechnical Construction*, *2*, 961–966.

Koudelka, R. E., & Kelly, L. L. (1971). *Cryogenic cooling of concrete*, US Patent 3,583,172.

Kurita, M., Goto, S., Minegishi, K., Negami, Y., & Kuwahara, T. (1990). In *Precooling concrete using frozen sand, concrete international*, (Vol. 12).

Kovler, K. (1995). Shock of evaporative cooling of concrete in hot dry climates. *Concrete International, 17*(10), 65–69.

Lawrence, A. M., Tia, M., & Bergin, M. (2014). Considerations for handling of mass concrete: control of internal restraint. *ACI Materials Journal*, *111*(1), 3–12.

Liu, X., Jiang, W., de Schutter, G., Yuan, Y., & Su, Q. (2014a). Early-age behaviour of precast concrete immersed tunnel based on degree of hydration concept. *Structural Concrete*, *15*(1), 66–80.

Liu, X., Yuan, Y., & Su, Q. (2014b). Sensitivity analysis of the early-age cracking risk in an immersed tunnel. *Structural Concrete*, *15*(2), 179–190.

Luff, B. A., & Bhasin, D. P. (1983). Cooling concrete with liquid nitrogen. *Concrete Construction*, *28*, 391.

Lunniss, R., & Baber, J. (2013). *Immersed tunnels*. London, UK: CRC Press, Taylor & Francis Group.

Neville, A. (2011). *Properties of concrete*. Pearson Education Limited. ISBN: 978-0-273-75580-7.

Oliveira, J. P. (2015). Betão em massa. Pré-refrigeração e pós refrigeração. Master Thesis in Civil Engineering. Universidade Nova de Lisboa. 104 pp. http://hdl.handle.net/10362/15558.

QCS. (2014). *Qatar construction specifications*. Qatar: Ministry of Environment.

Qian, C., Gao, G., He, Z., & Li, R. (2015). Feasibility research of using phase change materials to reduce the inner temperature rise of mass concrete. *Journal of Wuhan University of Technology-Materials Science Edition*, *30*(5), 989–994.

Riding, K. A., Poole, J. L., Schindler, A. K., Juenger, M. C. G., & Folliard, K. J. (2009). Effects of construction time and coarse aggregate on bridge deck cracking. *ACI Materials Journal*, *106* (5), 448–454.

Schrader, E., & Swiger, W. (1988). Concrete dam construction and foundation treatment. In R. Jansen (Ed.), *Advanced dam engineering for design, construction, and rehabilitation* (pp. 540–577). New York: Van Nostrand Reinhold.

Schleiss, A. (2011). *Les barrages: du projet à la mise en service*. Lausanne: Presses Polytechniques et Universitaires Romandes.

Sfikas, I. P., Ingham, J., & Baber, J. (2016). Simulating thermal behaviour of concrete by FEA: state-of-the-art review. In *Proceedings of the ICE: Construction Materials*. http://dx.doi.org/10.1680/jcoma.15.00052.

Sfikas, I., Ingham, J., & Baber, J. (2017). Using finite-element analysis to assess the thermal behaviour of concrete structures. *The Concrete Society: Concrete Magazine, February,* 50–52.

Tu, D., Lawrence, A., Tia, M., & Bergin, M. (2014). Determination of required insulation for preventing early-age cracking in mass concrete footings. *Transportation Research Record: Journal of the Transportation Research Board*, (2441), 91–97.

Vallarino, E. (1998). Tratado básico de presas, tomo II., Madrid: Colegio de Ingenie-ros de Caminos, Canales y Puertos.

Vicroads. (2000). Technical Bulletin TB 42. Curing of Concrete. State Government of Victoria. ISBN: 0731129253.

Witakowski, P. (2001). Technologia budowy konstrukcji masywnych z betonu. In *Proceedings of the 13th Scientific Conference on Computer Methods in Design and Analysis of Hydrotechnic Structures*, Korbielów, Poland.

Yang, J., Hu, Y., Zuo, Z., Jin, F., & Li, Q. (2012). Thermal analysis of mass concrete embedded with double-layer staggered heterogeneous cooling water pipes. *Applied Thermal Engineering*, *35*, 145–156, 3.

Zhu, B. (1999). Effect of cooling by water flowing in nonmetal pipes embedded in mass concrete. *Journal of Construction Engineering and Management*, *125*, 61–68.

Chapter 7
Numerical Modelling

Francesco Pesavento, Agnieszka Knoppik, Vít Šmilauer, Matthieu Briffaut and Pierre Rossi

Abstract This chapter deals with the problem of modelling the behaviour of massive concrete structures. In the last decades, the developments in the field of computational mechanics were significant, so nowadays several numerical techniques are available to this goal, depending on the scale level considered but also on which phenomena/processes are taken into account. In this chapter, we limit the description to approaches/models that can be implemented using the Finite Element Method, which is still the worldwide most used numerical technique. This chapter presents two distinct groups of models. The first group covers deterministic models starting from the simplest ones, which consider simply the thermo-chemo-mechanical behaviour of the material, to more sophisticated approaches which consider also the fluid phases; i.e., they consider concrete as a multiphase porous material. In this first part, a specific section is dedicated to mechanical behaviour modelling considering damage of the material, plasticity, etc. The second group of the models takes into consideration stochastic nature of cracking. These models are formulated specifically for giving a detailed information about cracks spacing and opening in concrete structures in service life conditions.

F. Pesavento (✉)
University of Padova, Padova, Italy
e-mail: francesco.pesavento@dicea.unipd.it

A. Knoppik
Silesian University of Technology, Gliwice, Poland

V. Šmilauer
Czech Technical University in Prague, Prague, Czech Republic

M. Briffaut
CNRS, University Grenoble Alpes, Grenoble, France

P. Rossi
IFSTTAR, University Paris-Est, Champs-sur-Marne, France

© RILEM 2019

E. M. R. Fairbairn and M. Azenha (eds.), *Thermal Cracking of Massive Concrete Structures*, RILEM State-of-the-Art Reports 27,
https://doi.org/10.1007/978-3-319-76617-1_7

7.1 Introduction

Computational analysis has become crucial in almost all disciplines, together with theory and experimental analysis. Every model is a simplification of reality intended to promote its understanding. A model uses a simplified physical formulation, mathematical framework and numerical tools in order to find the solution. Successful models pass the validation stage where modelling results correspond sufficiently well to reality.

Computational approaches are also playing an increasing role in industry. In fact, validated models can save significant amount of experiments, time, and resources, can mitigate potential problems and even find optimal solution. For instance, in the case of massive concrete structures, numerical modelling often follows objectives such as determination of temperature field during hardening, effect of concrete composition, estimation of cracking potential with consequences to durability, economical benefits.

In civil and environmental engineering, most of the processes/phenomena are mathematically described by a set of partial differential equations (PDEs), usually nonlinear in material laws. For example, a set of PDEs describes heat and mass transfer, mechanical effects, hydrodynamic effects, electric and magnetic fields, and all their interactions (multiphysics problems). There exists a significant amount of numerical techniques for solving such a kind of complex mathematical systems, some of them limited to the research world. In the context of this state-of-the-art report, we consider the most commonly used numerical method—the Finite Element Method. Often, obtaining a prediction from a theory requires massive computing, so it is necessary to develop and implement special algorithms for parallel computation to be able to exploit the full potential of the technology and maintain scientific and productive competitiveness. Virtually, all manufacturers of high-end chips in the last few years have adopted a multiprocessor organisation, typically with 4–8 processors per chip (but solutions with up to 18 cores are available). This number is expected to grow to 100–1000 in the next decade. Hence, high-parallelism and low-communication algorithms are no longer the prerogative of supercomputing and are instead becoming pervasive, but a description of such kind of solvers and tools is beyond the scope of this chapter.

Hardening concrete is undoubtedly one of the most difficult structural materials for modelling. The difficulties arise from a complex concrete microstructure, which is additionally subjected to transformations as a result of cement hydration. Initially, it is a mixture of liquids and solids of varying diameters and shapes. Such a multiphase medium is characterised by strong viscous and plastic properties. With progressing cement, hydration concrete becomes a solid, with elastic, viscous and plastic characteristics, where the mutual proportions of these features depend on the progress of the concrete hardening process. Moreover, in addition to the chemical reactions resulting in the hydration of the material, several physical phenomena take place (e.g. phase changes) and numerous fields are interacting with each other

(thermal, hygral, mechanical, etc.) making the problem a typical multifield–multiphysics problem (Gawin et al. 2006a).

Concrete represents a multiscale material which spans characteristic lengths from about 10^{-10} to 10^{-2} m. The finest atomistic scale of C-S-H determines several macroscopic properties such as elasticity, strength, creep, shrinkage, which manifest on higher scales (Bernard et al. 2003; Pichler et al. 2011). Hydration takes place up to micrometre scale of cement paste, and large aggregates have impact on fracture properties.

Recent advances in multiscale models demonstrated models' capabilities to capture those effects and to set up microstructure-property link. Indeed, nowadays several multiscale technics, of mathematical or numerical nature, are available for considering the material behaviour at different scales: the formulation of constitutive relationships starting from the microcomponents of the material up to the macroscale is an example of the application of multiscale strategy (see Chap. 3 for thermal properties).

Taking into account only concrete scale and its changes during hardening, two possibilities appear to model its early-age behaviour:

- to use pure thermo-chemical, and possibly mechanical, models, or
- to formulate a multifield model.

In the first class of models, concrete is treated as a continuum at macroscopic level and only the solid phase of the material is considered, taking into account the thermal field and the chemical reactions (e.g. the hydration process), which affect the mechanical performance of the material for a large extent.

The second group of models is based on the multifield concept; i.e., they consider one or more phases: not only the solid phase, which is typically the concrete skeleton, but also the liquid and gaseous components filling the pores of the material. Depending on the number of the phases considered and on the scale level chosen for the initial formulation of the mathematical model, the multifield models can be subdivided into two main groups corresponding to two different approaches.

The first approach is related to phenomenological models, where concrete is treated as a continuous medium. A detailed analysis of physical processes related to phase transitions and chemical processes occurring in hardening concrete is neglected in these models, and a macroscopic description of the thermal–moisture–mechanical phenomena is used as a multiphysical description.

The second approach is related to multiphase models based on Multiphase Porous Media Mechanics (MPMM), in which a precise analysis of the physical phenomena and the influence of the material's internal structure on these phenomena are made. Starting from the microscopic level, appropriate constitutive equations are defined for the solid, liquid and gaseous phases of the medium and then averaged at macroscopic scale for a multiphase medium.

This state-of-the-art report gives a basic overview of the main approaches available in the literature for modelling the behaviour of concrete at early ages and beyond, starting from the simplest ones and then increasing the level of complexity.

First, the pure thermo-chemo-mechanical models are introduced in Sect. 7.2. Then, multifield single-fluid phase thermo-chemo-mechanical models and their extension with a moisture transport are presented and described in Sect. 7.3. Both these groups of models can be considered based on a typical phenomenological approach (i.e. concrete is treated as a homogeneous medium directly at macroscopic level). The last class of deterministic models taken into consideration is the one of multifield multiphase models described in Sect. 7.4 based on porous media mechanics. Each model group contains validation examples showing its effectiveness in the numerical simulation of the main phenomena/processes taking place in massive concrete structures.

Whatever is the model adopted for the description of the general behaviour of the material, it is needed to consider the effects of thermal field, chemical reactions and solid skeleton-fluid phase interactions on its mechanical performance. This means the necessity to choose an appropriate constitutive relationship, describing specifically its mechanical behaviour. Thus, damage and plasticity material models are briefly discussed in Sect. 7.5 in connection with Chap. 4. Section 7.6 focuses on models with stochastic nature. These models are formulated specifically for giving a detailed information about cracks' spacing and opening in concrete structures in service life conditions.

7.2 Thermo-Chemo-Mechanical Models

Thermo-chemo-mechanical models consider coupling among heat transport, evolution of underlying microstructure via chemical reactions and solid mechanics. Moisture (humidity, water) transport is neglected, leading to zero drying shrinkage. Such simplification is feasible for massive structures in their early age (except for element surface), while for long-term calculation a chemo-hydro-thermo-mechanical model should be preferred (see Sects. 7.3 and 7.4).

During early age, several phenomena occur simultaneously. In thermal-chemo-mechanical models, the following ones are generally taken into account: hydration linked to the temperature evolution due to exothermic cement reaction, thermal conduction and dilatation, autogenous shrinkage, mechanical properties evolution and mechanical degradation due to cracks and/or damage (which could be visco-elastic damage models or plastic models).

7.2.1 Thermal Conduction Through the Concrete

The prediction of temperature evolution in a massive concrete structure is based on the heat equation with a source term:

$$c\dot{T} = \nabla(k\nabla T) + Q_{\xi}\dot{\alpha} \tag{7.1}$$

in which Q_{ξ} is the latent heat of hydration [Jm^{-3}], T [K] is the temperature, α is the hydration degree, k is the thermal conductivity [$Wm^{-1}K^{-1}$], and c is the volumetric heat capacity [$Jm^{-3}K^{-1}$]. The latent heat of hydration, the thermal conductivity and the volumetric heat capacity could be kept constant (see Waller 2000; Mounanga 2004; Mounanga et al. 2006) or evolve slightly with the temperature (Morabito 2001) and the hydration (see Faria et al. 2006; Ruiz et al. 2001; Lura and Van Breugel 2001).

7.2.2 Constitutive Relationships/Couplings

One can distinguish between two types of couplings: thermo-chemical and chemo-mechanical couplings with the corresponding constitutive relationships, which are analysed and discussed in the following sections.

Thermo-chemical Coupling

The thermal properties, namely thermal conductivity, heat capacity and coefficient of thermal expansion, are generally functions of the temperature and also evolve at early age with the changes in the microstructure of the cement-based materials. For instance, Hansen et al. (1982) reported a decrease of thermal conductivity from 0.88 to 0.78 W/(mK) during hydration of rapid hardening Portland cement, $w/c = 0.5$ at $T = 30$ °C, while Mounanga (2004) obtained an increase. Generally, this aspect is not explicitly taken into account in simulations or even experimentally, but different authors report an impact of the variation of these properties on the structural response. For instance, Briffaut et al. (2012) performed simulations, at the structure level, in which the heat capacity and the thermal conductivity evolved with respect to the degree of hydration. In their simulation, the evolution of the heat capacity impacted the stress response more strongly than the evolution of the thermal conductivity. Lura and van Breugel (2001) reported that a given variation of the heat capacity may lead to a variation of the same order of magnitude in the computed temperatures and stresses. The same authors also found that up to 5% of variation in the thermal conductivity, an almost negligible effect is observed on the temperature and stress responses and that the CTE affects actively the thermo-chemo-mechanical response (a variation of 16% in the CTE is reported to increase the cracking risk by about 15%) (see Lura and Van Breugel 2001). On the other hand, Hilaire (2014) reported a not very pronounced impact of the CTE evolution on the mechanical response at early age.

The thermal source of the heat equation depends on the evolution of hydration which is achieved using chemical affinity (see Ulm and Coussy 1998, 2001; Lackner and Mang 2004; Regourd and Gauthier 1980):

$$\dot{\alpha} = \tilde{A}(\alpha) \exp\left(-\frac{E_a}{RT}\right) \tag{7.2}$$

where E_a is the activation energy [Jmol^{-1}], R is the ideal gas constant 8.3145 [JK^{-1}mol^{-1}], T is the temperature [K], α is the hydration degree, and $\tilde{A}(\alpha)$ is the chemical affinity [s^{-1}].

Many kinds of expression describing the evolution of the chemical affinity have been used (see among others Lackner and Mang 2004; Cervera et al. 1999a; Benboudjema and Torrenti 2008; Briffaut et al. 2012; Sciumè et al. 2013), but there remains experimental fitting. Buffo-Laccarière et al. (2007) proposed an expression for multiphasic hydration degree evolution linked to chemical activation and physical water accessibility to anhydrous cement product which allows for composed cement.

The energy of activation is also a function of the temperature and may vary as a function of the mechanisms deemed to drive hydration (Lothenbach et al. 2008). Again, the variation of the energy of activation with respect to age and temperature is often neglected in TC analyses.

Chemo-mechanical Coupling/Evolution of Mechanical Properties (Elastic, Plastic or Damage)

This kind of model is generally based on uncoupled strains decomposition:

$$\boldsymbol{\varepsilon} = \boldsymbol{\varepsilon}_M + \boldsymbol{\varepsilon}_{bc} + \boldsymbol{\varepsilon}_{au} + \boldsymbol{\varepsilon}_T \tag{7.3}$$

where $\boldsymbol{\varepsilon}_M$ is the mechanical strain tensor, $\boldsymbol{\varepsilon}_{bc}$ is the basic creep strain tensor, $\boldsymbol{\varepsilon}_{au}$ is the autogenous strain tensor, $\boldsymbol{\varepsilon}_T$ is the thermal strain tensor, and finally, $\boldsymbol{\varepsilon}$ is the total strain tensor. Nevertheless, some authors used coupling between creep and damage (see Chap. 4) and between creep and hydration (chemo-visco-elastic coupling see Chap. 4).

Autogenous shrinkage is directly related to the evolution of hydration in the material. Experimental results show that autogenous shrinkage evolution is almost linear with respect to the hydration degree as soon as the percolation threshold has been overcame (see Laplante 1993; Mounanga 2004; Mounanga et al. 2006). Therefore, autogenous shrinkage can be modelled by the following equation (Ulm and Coussy 1998):

$$\varepsilon_{ij}^{au} = -\kappa \bar{\alpha} \delta_{ij} \quad \text{with} \quad \bar{\alpha} = \left\langle \frac{\alpha - \alpha_0}{\alpha_\infty - \alpha_0} \right\rangle_+ \tag{7.4}$$

where κ is a constant material parameter [-], α_0 is the mechanical percolation threshold [-] (Torrenti and Benboudjema 2005), α_∞ is the final hydration degree (which depends on the concrete mix Waller 2000), and $\langle \cdot \rangle_+$ is the positive part operator. A small expansion (so-called swelling) can also be measured at the beginning of hydration, depending on the *w/c* ratio and the type of cement.

The mechanical strains could be elastic ones (Faria et al. 2006) but could also consider plasticity (Ulm and Coussy 1998, 2001; Lackner and Mang 2004) or damage (Benboudjema and Torrenti 2008; Briffaut et al. 2011; Cervera et al. 1999b). In this last case, the relationship between apparent stress $\boldsymbol{\sigma}$, effective stress $\tilde{\boldsymbol{\sigma}}$, damage D, elastic stiffness tensor $\mathbf{E}$, elastic strain and previously defined strain reads:

$$\boldsymbol{\sigma} = (1 - D)\tilde{\boldsymbol{\sigma}} \tag{7.5}$$

$$\dot{\tilde{\boldsymbol{\sigma}}} = \mathbf{E}(\alpha)\dot{\boldsymbol{\varepsilon}}_{el} = \mathbf{E}(\alpha)(\dot{\boldsymbol{\varepsilon}} - \dot{\boldsymbol{\varepsilon}}_{bc} - \dot{\boldsymbol{\varepsilon}}_{ttc} - \dot{\boldsymbol{\varepsilon}}_{au} - \dot{\boldsymbol{\varepsilon}}_{T}) \tag{7.6}$$

where $\boldsymbol{\varepsilon}_{ttc}$ is the transient thermal creep strain.

The Young's modulus E and the tensile strength f_t increase due to hydration as follows (De Schutter 1999; Stefan et al. 2010, see also Chap. 4):

$$E(\alpha) = E_{\infty}\bar{\alpha}^{a_E} \tag{7.7}$$

$$f_t(\alpha) = f_{t\infty}\bar{\alpha}^{a_{ft}} \tag{7.8}$$

where $f_{t\infty}$ is the final tensile strength (i.e. when $\alpha = \alpha_{\infty}$) [Pa], E_{∞} is the final Young's modulus [GPa], $\bar{\alpha}^{a_E}$, and $\bar{\alpha}^{a_{ft}}$ are constant material parameters.

The Poisson's ratio is relatively stable for mature concrete. Neville et al. (1983) recommend a value equal to 0.2 for most of concrete mixes. However, De Schutter and Taerwe (1996) suggests an evolution depending on the hydration degree:

$$v(\alpha) = 0.18\sin\frac{\pi\alpha}{2} + 0.5\exp(-10\alpha) \tag{7.9}$$

where v is the Poisson's ratio and α is the hydration degree. Note that for a hydration degree equal to 0, the Poisson's ratio is equal to 0.5 which is the common value for an incompressible fluid.

The evolution of the damage is linked to the elastic equivalent tensile strain and could use strain from Rankine criterion (Cervera et al. 1999b) or Mazars approach (Benboudjema and Torrenti 2008; Briffaut et al. 2011).

Strain softening induces inherent mesh dependency and produces failure without energy dissipation (see Pijaudier-Cabot and Bažant 1987). In order to dissipate the same amount of energy after mesh refinement, when strains localise in one row of finite elements, a characteristic length l_c is introduced as a localisation limiter (Rots 1988; Cervera and Chiumenti 2006). Fracture energy of an element g_f is related to the material fracture energy G_f and the characteristic length l_c:

$$g_f(\alpha) = \frac{G_f(\alpha)}{l_c} \tag{7.10}$$

$$l_c = \sqrt[3]{V_{ef}} \tag{7.11}$$

where V_{ef} is the volume of the finite element.

The fracture energy also depends on the hydration degree (De Schutter and Taerwe 1997):

$$G_f(\alpha) = G_{f\infty}\bar{\alpha}^{\delta} \tag{7.12}$$

where δ is a material property that must be fitted from experimental data and $G_{f\infty}$ is the material fracture energy at the end of hydration process.

Ulm and Coussy (1998) propose a chemo-mechanical cross-effect in a context where plasticity is considered. These authors link the chemo-plastic cross-effects to the strength growth and plastic hardening/softening properties of the material when irreversible skeleton evolutions occur.

Thermo-mechanical Coupling

The thermal strain $\boldsymbol{\varepsilon}_{th}$ is linked to the temperature variation and to the coefficient of thermal expansion *CTE* which is a function of the hydration degree and of the temperature. Nevertheless, constant value allows to obtain sufficiently accurate prediction (Loukili et al. 2000):

$$\varepsilon_{ij}^{T} = CTE(\alpha) \cdot (T - T_0)\delta_{ij} \tag{7.13}$$

where T_0 is the reference temperature [K].

Thermo-chemo-mechanical Coupling

In thermo-chemo-mechanical model, when creep is taken into account, viscous parameter could also be affected by the hydration degree and the temperature. For instance, when rheological modelling is used, the viscosity and the stiffness of the component should be affected (Benboudjema and Torrenti 2008; Briffaut et al. 2012).

It is noteworthy that the properties such as heat capacity and CTE are, for thermo-elastic composites, linked according to some cross-relationships (Chen et al. 2012).

An additional thermo-chemo-mechanical coupling arises on the light of Bažant and collaborators micro-prestress solidification theory (Bažant et al. 1997, 2004). According to these authors, a micro-prestress relaxation within the concrete matrix appears at the microlevel and is related to the hydration reaction. This effect is thermo-activated per se (Bažant et al. 2004).

7.2.3 *Validation of the Thermo-Chemo-Mechanical Models on Massive Structures at Early Age*

The chemo-thermal problem is often decoupled from the mechanical problem. Several comparisons of model estimations and experimental measurements can be

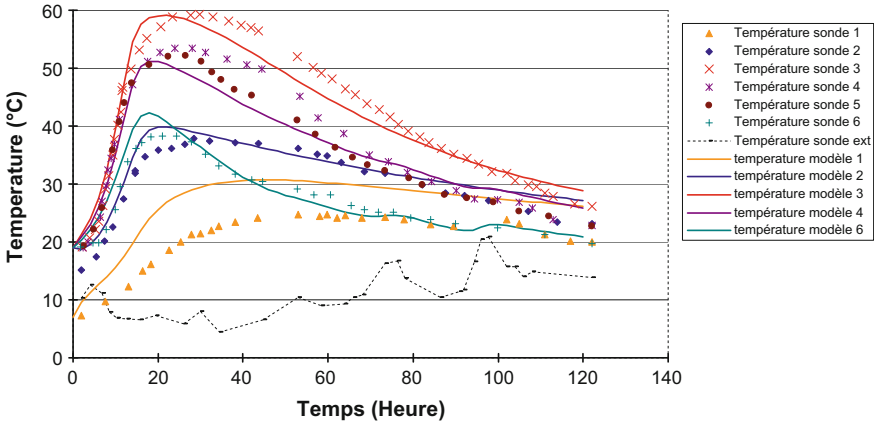

Fig. 7.1 Temperature prediction on Civaux Wall (thickness 1.2 m; height 2.4 m) during hydration (Briffaut 2010)

found in the literature (e.g. Craeye et al. 2009; Fairbairn et al. 2004; Faria et al. 2006; Honorio et al. 2014; Ulm and Coussy 1998, 2001). An example of thermal prediction on a massive concrete structure (wall thickness 1.2 m; height 2.4 m) is given in Fig. 7.1.

7.3 Multifield Models: Single-Fluid Models

This group of multifield models deals with the heat and moisture transport in a porous material accompanied with mechanical response. The material can represent cement paste, mortar, or concrete as a continuum directly defined at macroscale. Even if the model is a multifield model, it is still based on a phenomenological approach. In the view of the model description, thermo refers to heat transport, chemo stands for chemical reactions occurring due to cement hydration, and hygro describes moisture or water vapour transport as a single transported fluid phase, followed with solid mechanical analysis.

In the simplest approach, thermo-(chemo)-hygro models proceed using a staggered approach where temperature and relative humidity fields are computed first. Both fields are then passed to mechanical model which accounts for strain-related quantities, such as thermal strain caused by temperature, drying strain originating from relative humidity, autogenous shrinkage strain due to drop in relative humidity. Several mechanical parameters may depend on the microstructure evolution, such as increasing Young's modulus or increasing tensile strength (de Shutter 2002). This section shows several examples of material sub-models, their coupling and validations on real structures.

7.3.1 Phenomena Taken into Consideration

Heat transport (*thermo*-) takes into account heat conduction (diffusion), heat convection and radiation. The transport is often enhanced with heat generated due to mostly exothermic cement hydration, or extended for enthalpy of water evaporation from concrete surface (Černý and Rovnaníková 2002). Modelling heat transport solely in hydrating concrete is used rarely; it finds its place especially in massive concrete structures where moisture gradient could be neglected and thermal gradients present substantial strains (Park et al. 2008).

Chemical phenomena deal mainly with the evolution of hydrating microstructure; i.e., it describes kinetics of hydrating clinker minerals, their hydration, evolution of volume fractions or generated heat. The most elaborated hydration models take into account cement chemistry, cement fineness, temperature, supplementary cementitious materials, and water availability (Thomas et al. 2011). Temperature acceleration often requires coupling with a heat transport model since reaction speed approximately doubles with a 10 °C increase (Černý and Rovnaníková 2002).

Moisture transport describes gas diffusion, effusion and solution diffusion, being driven by a gradient of water vapour pressure (Künzel 1995). The moisture in a porous material can be present in the form of solid, liquid or vaporous form, and it becomes convenient to quantify moisture as a total water content in this single-fluid model. Most hygral models express total water content as a relative humidity, using water vapour sorption isotherm for recalculation (Künzel 1995).

Mechanical part describes the effect of strains on structural behaviour in hydrating concrete. Under standard circumstances, strains contain autogenous shrinkage, temperature expansion/contraction or drying shrinkage. Mechanical models used in the analysis compute time-dependent material behaviour (creep, shrinkage) and time-independent load response (plasticity, damage).

Each part is represented with more or less sophisticated sub-model, which could operate on different scales using a multiscale formulation. For example, concrete can be treated as a heterogeneous material for prediction of hydration heat (Park et al. 2008), and elasticity and strength can be linked to cement hydration (Shutter 2002).

7.3.2 Coupled Formulation and Data Flow

The multiphysical thermo-(chemo)-hygro-mechanical formulation leads at least to three governing equations. Each sub-model contains a state variable to be solved and may depend on other state variable, leading to mutual coupling:

- *Thermo*: enthalpy balance equation with unknown temperature field T [K], see Eq. 7.1.

- *Chemo*: hydration kinetic equation could be added, with, e.g., unknown degree of hydration α [-], see Eq. 7.2.
- *Hygro*: mass balance equation for moisture transport with unknown relative humidity h [-]. Some models use moisture content by mass w $[\mathrm{kg}_{H_2O}/m^3_{concrete}]$ instead, being a thermodynamically equivalent quantity related to h by sorption/desorption isotherm.
- Linear momentum conservation equation (static equilibrium) with unknown displacement field $\boldsymbol{u}$[m]. Various material constitutive laws (viscoelastic, plastic, damage) define stress/strain relationship between displacement field $\boldsymbol{u}$ and stress $\boldsymbol{\sigma}$, see Sect. 7.5.

A monolithic formulation of thermo-(chemo)-hygro-mechanical problem requires that all unknowns are solved in one system of equations, leading generally to large systems. A simpler strategy for approximate solution is often employed, using one-way coupling when outputs from one sub-model are passed to another one, solving sub-models' set of equations separately. Such staggered solution strategy is the most popular method of decoupling (Baggio et al. 1995; Červenka et al. 2014; Wu et al. 2014).

A characteristic thermo-hygro-mechanical model using a staggered approach is shown in Fig. 7.2. First, heat transport sub-model with a possible hydration sub-model computes temperature field T. Second, moisture transport sub-model evaluates field of relative humidity h which also depends on temperature. Alternatively, if hydration is formulated such as humidity-dependent, the corrector phase may be added to find equilibrium in both sub-models with compatible humidity field. Temperature and relative humidity fields are passed further to time-dependent mechanical sub-model.

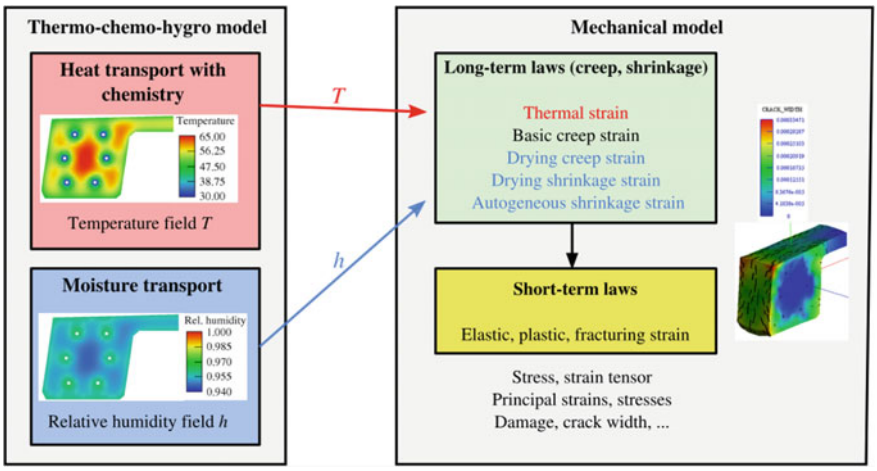

Fig. 7.2 A classical setup of thermo-chemo-hygro-mechanical model implementing a staggered solution strategy

Strain decomposition belongs to the key assumptions of the mechanical model. Under small deformations, total strain tensor could be decomposed to (Thelandersson 1987)

$$\boldsymbol{\varepsilon} = \boldsymbol{\varepsilon}_e(T) + \boldsymbol{\varepsilon}_f + \boldsymbol{\varepsilon}_p + \boldsymbol{\varepsilon}_{cr}(T,h) + \boldsymbol{\varepsilon}_T(T) + \boldsymbol{\varepsilon}_{au}(T) + \boldsymbol{\varepsilon}_{d,sh}(T,h) \tag{7.14}$$

where the indices denote elastic, fracture, plastic, creep, thermal, autogenous, and drying shrinkage strain components, respectively. Several strain components may depend on temperature, such as creep, and on humidity, such as drying shrinkage strain (Bažant et al. 2015). T and h are known from the underlying sub-models.

Analysis of Eq. 7.14 shows that strain components could be separated into long-term and short-term contributions. Long-term (time-dependent) mechanical laws define strain evolution in time such as strains $\boldsymbol{\varepsilon}_{cr}$, $\boldsymbol{\varepsilon}_T$, $\boldsymbol{\varepsilon}_{au}$, $\boldsymbol{\varepsilon}_{d,sh}$. On the other hand, short-term (time-independent, frozen time) mechanical laws have no notion of time and evaluate $\boldsymbol{\varepsilon}_e$, $\boldsymbol{\varepsilon}_f$, $\boldsymbol{\varepsilon}_p$ strains. These strains are related to concrete elasticity, concrete cracking and concrete crushing, where time-dependent evolution of concrete properties is often accounted for inside the constitutive laws (Červenka et al. 2014). Most of short-term constitutive laws are based on stress criteria, such as principal stress/tensile strength or plasticity surface.

7.3.3 *Mathematical Formulation and Constitutive Relationships*

7.3.3.1 Stand-Alone Heat Transport

Chapter 3 describes in detail the heat balance equation, heat source, boundary conditions with thermal properties of concrete and its components.

7.3.3.2 Stand-Alone Moisture Transport

Moisture transport in concrete has been modelled since the 1930s, and since that time, it has been recognised that concrete moisture diffusivity strongly depends on moisture content (Pickett 1942). Moisture transport model has been formulated by Bažant and Najjar (1972) who quantified nonlinear concrete diffusivity and showed it decreases an order of magnitude when passing from saturated to dry concrete state. The mass balance equation for water vapour transport reads:

$$\frac{\partial w}{\partial t} = -\nabla \cdot J_w + \frac{\partial w_s}{\partial t} \tag{7.15}$$

where w [kg/m^3] is moisture (evaporable water) content, t [s] is time, J_w [kg/(m^{2}s)] is moisture flux, and w_s [kg/m^3] is water source, e.g. water consumption during

hydration. Defining concrete moisture capacity C_h [kg/m^3], one can relate moisture content w with relative humidity h [-] as

$$\frac{\partial w}{\partial t} = C_h \frac{\partial h}{\partial t} \tag{7.16}$$

Bažant and Najjar (1972) assumed C_h being a constant over the whole desorption range, see Fig. 7.3 for three w/cs.

They arrived to the mass balance equation for moisture transport with h as the unknown:

$$\frac{\partial h}{\partial t} = -\nabla \cdot J + \frac{\partial h_s}{\partial t} + K \frac{\partial T}{\partial t} \tag{7.17}$$

$$J = -C(h)\nabla h \tag{7.18}$$

where J [m/s] is the liquid and vapour diffusion flux density, C [m^2/s] is diffusivity depending on h, h_s captures humidity decrease due to self-desiccation during hydration, and K is a hygrothermic coefficient [K^{-1}]. Bažant and Najjar proposed S-shape function for diffusivity as:

$$C(h) = C_1 \left(\alpha_0 + \frac{1 - \alpha_0}{1 + \left(\frac{1-h}{1-h_c} \right)^N} \right) \tag{7.19}$$

with characteristic values for mature concrete $C_1 = 150 \times 10^{-12} - 2200 \times 10^{-12}$ m^2/s, $\alpha_0 = 0.05 - 0.10$ (it is the initial hydration degree), $h_c = 0.75 - 0.90$, $N = 6 - 16$ (Bažant and Najjar 1972). Figure 7.4 shows such an example for structural concrete. More refined values for structural concrete were proposed (Fib 2010; Abbasnia et al. 2013) as well as simpler approximations (Ayano and

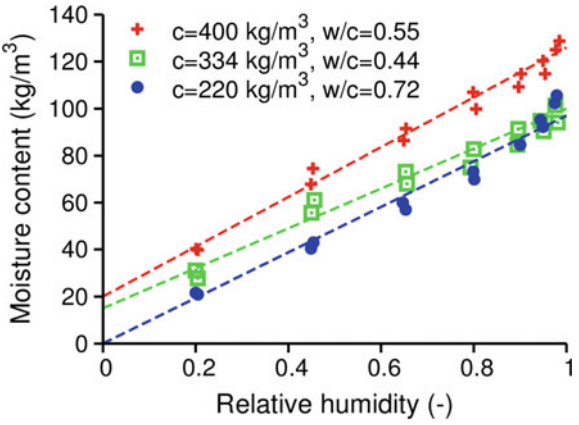

Fig. 7.3 Example of desorption isotherms for structural concrete (Hansen 1986) and linearisation

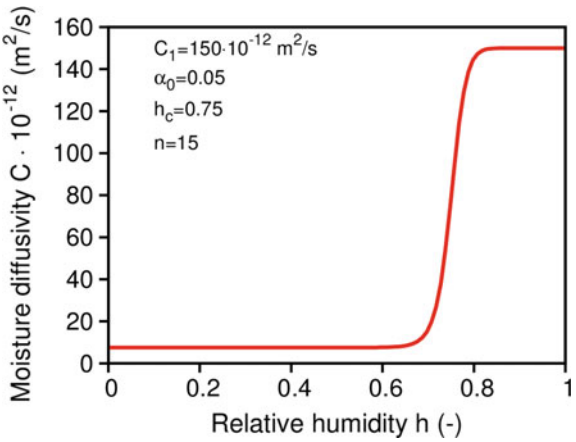

Fig. 7.4 Example of concrete moisture diffusivity (Bažant and Najjar 1972)

Wittman 2002; Xi et al. 1994). Note that the *S*-shape function gives a nonlinear stationary profile of relative humidity across a concrete member, favouring higher relative humidity.

Dirichlet boundary condition for (7.17) prescribes a fixed value of h, while humidity convection on a surface can be conveniently approximated with a humidity transfer coefficient as:

$$J = \beta_p(h - h_\infty) \tag{7.20}$$

where h_∞ is relative humidity far away from a surface. β_p can be approximated for concrete (Kwak et al. 2006):

$$\beta_p = 6.028 \times 10^{-7} w/c - 2.378 \times 10^{-7} \text{ [m/s]} \tag{7.21}$$

which gives a value $\beta_p = 2.74 \times 10^{-8}$ m/s for $w/c = 0.44$, advised also by other authors (Andreasik 1982; Aurich et al. 2009).

7.3.3.3 Heat and Moisture Coupled Transport

Coupling of heat and moisture transport leads generally to a system of two differential balance equations for heat and moisture transport

$$\frac{\partial H}{\partial t} = -\nabla \cdot q + Q_H \tag{7.22}$$

$$\frac{\partial w}{\partial t} = -\nabla \cdot J + Q_w \tag{7.23}$$

where H is the total enthalpy [J/m^3], q is the heat flux density [W/m^2], Q_H is the heat source [W/m^3], J is the liquid and vapour diffusion flux density [kg/(m^{2}s)], and Q_w is the moisture source [kg/(m^{3}s)]. Constitutive equations defining flux densities q and J have been used by several authors (Andreasik 1982; Klemczak 2011), and their general forms yield:

$$q = -d_{TT}\nabla T - d_{Tw}\nabla w \tag{7.24}$$

$$J = -d_{wT}\nabla T - d_{ww}\nabla w \tag{7.25}$$

where d_{ij} are diffusion coefficients for heat or moisture transport.

Further, attention is focused to quite popular coupled model for building materials which was pioneered by Künzel (1995). He defined constitutive equations by taking into account separate liquid and moisture transport in a porous material, quantifying dependence of thermal conductivity on moisture content and dependence of water vapour permeability on temperature. Elaboration of Eqs. 7.22–7.25 leads to the final form:

$$\frac{\partial H}{\partial T}\frac{\partial T}{\partial t} = \nabla\cdot(\lambda\nabla T) + \frac{\partial Q_s}{\partial t} + h_v\nabla\cdot\left(\delta_p\nabla(h\cdot p_{sat})\right) \tag{7.26}$$

$$\frac{\partial w}{\partial h}\frac{\partial h}{\partial t} = \nabla\cdot\left(D_\varphi\nabla h + \delta_p\nabla(h\cdot p_{sat})\right) - w_n \tag{7.27}$$

where dH/dT [J/(m^{3}K)] is a heat capacity, λ [W/(mK)] is a thermal conductivity, dQ_s/dt [W/m^3] is an outflow of heat per unit volume, e.g. hydration heat source, h_v [J/kg] is evaporation enthalpy of water, δ_p [kg/(msPa)] is water vapour permeability, p_{sat} [Pa] is water vapour saturation pressure depending on temperature, dw/dh [kg/m^3] is moisture storage capacity, D_φ [kg/(ms)] is liquid conduction coefficient, and w_n [kg/m^3/s] is non-evaporable (chemically bound) water flux density, i.e. consumed water due to hydration. The moisture diffusivity depends again on relative humidity, in a similar fashion as in Fig. 7.4.

7.3.4 Validations of Single-Fluid Models

7.3.4.1 Validation of a Stand-Alone Moisture Transport Model

A short example of drying concrete cylinder illustrates the Bažant-Najjar's model for moisture transport (Bažant and Najjar 1972). A concrete cylinder with 6 inches in diameter was exposed at 7 days to environmental humidity with 0.5 (Hanson 1968). The best fit over all datapoints gave parameters from Eq. 7.19 as $C_1 = 579 \times 10^{-12}$ m^2/s, $\alpha_0 = 0.002, h_c = 0.85, N = 3$, better than in the original article (Bažant and Najjar 1972) (Fig. 7.5).

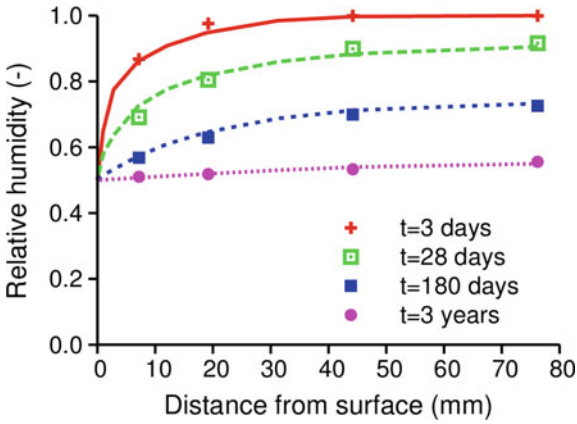

Fig. 7.5 Validation of cylinder drying (Hanson 1968)

7.3.4.2 Validation of Oparno Bridge's Arch

A reinforced concrete arch bridge, completed in 2010, was erected in the Czech Republic, on a highway between Prague and Dresden. Two arches with a span of 135 m support prestressed bridge decks, as shown in Fig. 7.6.

Emphasis on durability with reduced cracking and application of concrete with OPC 431 kg/m^3 led to the need for internal cooling during concrete hardening. The analysed cross section is located above the scaffolding as shown in Fig. 7.6. The left symmetric part has outer dimensions of 3.5 × 2.17 m, the analysis considered first a 2D cross-sectional model (Červenka et al. 2014). The most critical time for the temperature evolution occurred during summer casting with the peak ambient air temperature over 30 °C. CEM I 42.5R was used for concrete C45/55, and its reaction kinetics was well known.

Figure 7.7 shows the temperature T and the moisture fields at 0, 32, 42, 60 h of hydration. It was exercised that water cooling efficiently mitigated hydration heat and maintained the core temperature under 65 °C. Without water cooling, the

Fig. 7.6 Two arches of Oparno Bridge during construction (Photograph by Jan L. Vítek)

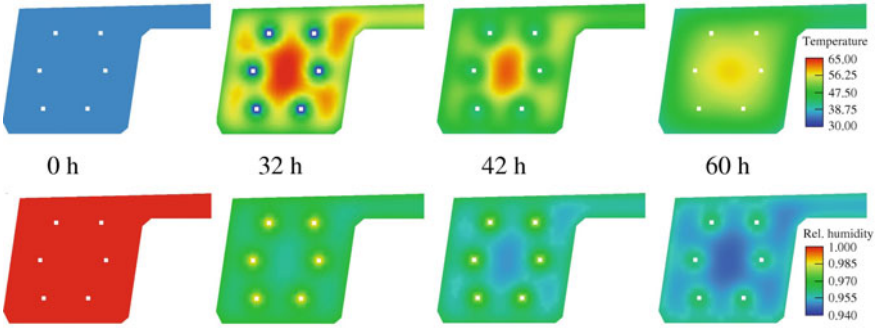

Fig. 7.7 Temperature (top) and relative humidity (bottom) fields in the left symmetric part of the arch cross section. The outer dimensions of the displayed cross section are 3.5 × 2.17 m. Six cooling pipes are embedded, and the cooling water was turned off at 40 h

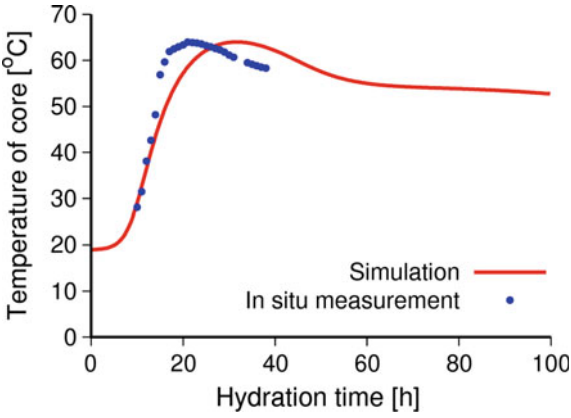

Fig. 7.8 Temperature validation in the core of the bridge arch

maximum temperature would exceed 85 °C, which was unacceptable. Figure 7.8 validates temperatures from the thermo-hygral model.

The results of the transport analysis entered mechanical analysis which computed cracks (see Fig. 7.8 for the evolution of temperature). The cracks' pattern originates from heat dissipation through the surface (Fig. 7.9).

7.3.4.3 Validation of ConCrack's Restrained Beam

The validation of the coupled hydro-thermo-hydro-mechanical analysis originates from the well-documented RG8 ConCrack experiment (Mazars 2014). Figure 7.10 shows the overall geometry of the RG8 beam with two massive heads on both sides and two restraining steel struts. The central beam part was made of reinforced concrete C50/60, $w/c = 0.46$, with dimensions of $0.5 \times 0.8 \times 5.1$ m. The

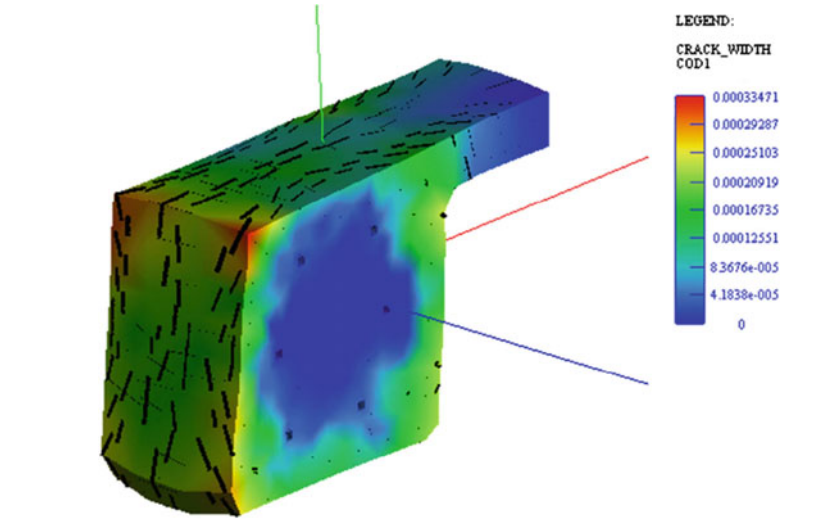

Fig. 7.9 Crack pattern in a 1-m long segment in the Oparno Bridge

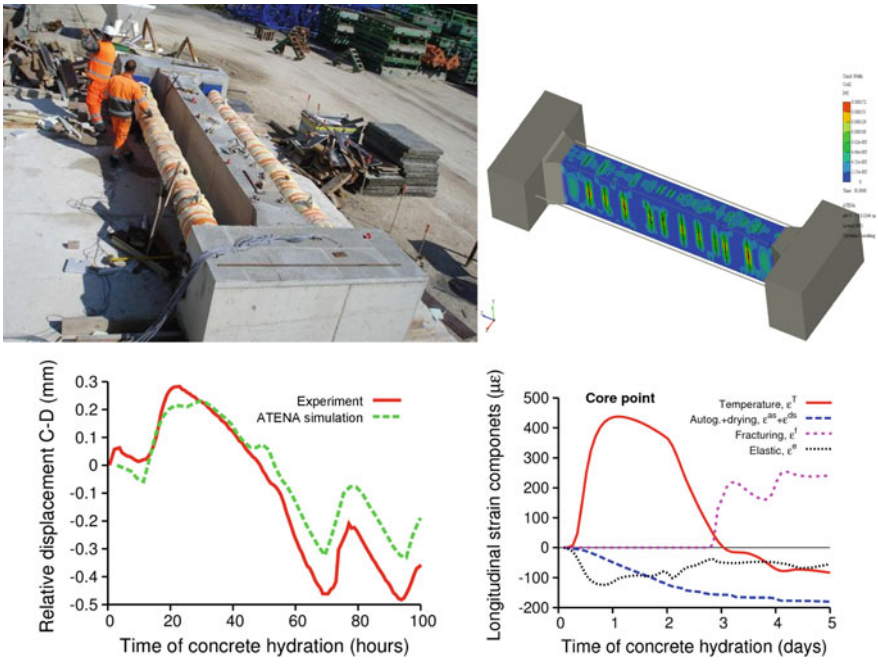

Fig. 7.10 Validation of RG8 ConCrack experiment—experiment overview (by CEOS.fr), cracks at 30 days, displacement of points C-D and strain decomposition at the core point

benchmark experiment provided material and structural data, internal temperature in three points, and displacements of two points C, D located on the beam axis 2.5 m apart. Maximum temperature in the core attained 53.7 °C at 30 h.

Thermo-hygro-mechanical simulation used Künzel's heat-moisture model, B3 creep model and fracture-plastic material model in ATENA software (Červenka et al. 2014). Figure 7.10 validates further C-D displacement and displays strain decomposition in the core point. Note that thermal strain with subsequent cooling contributes the most to cracking at early ages.

7.3.4.4 Validation of a Restrained Wall in Oslo

A restrained wall served as a forerunner experiment for Bjørvika submerged tunnel project, built in Oslo between 2005 and 2012. The wall utilised low-heat concrete with a minimal risk of early-age cracking and high watertightness. Figure 7.11 shows two walls built on a raft concrete slab (Ji 2008). The left wall is made from SV-40 concrete containing low-heat OPC I with silica fume at the amount of 424 kg/m^3. This left wall is validated using a thermo-chemo-mechanical model

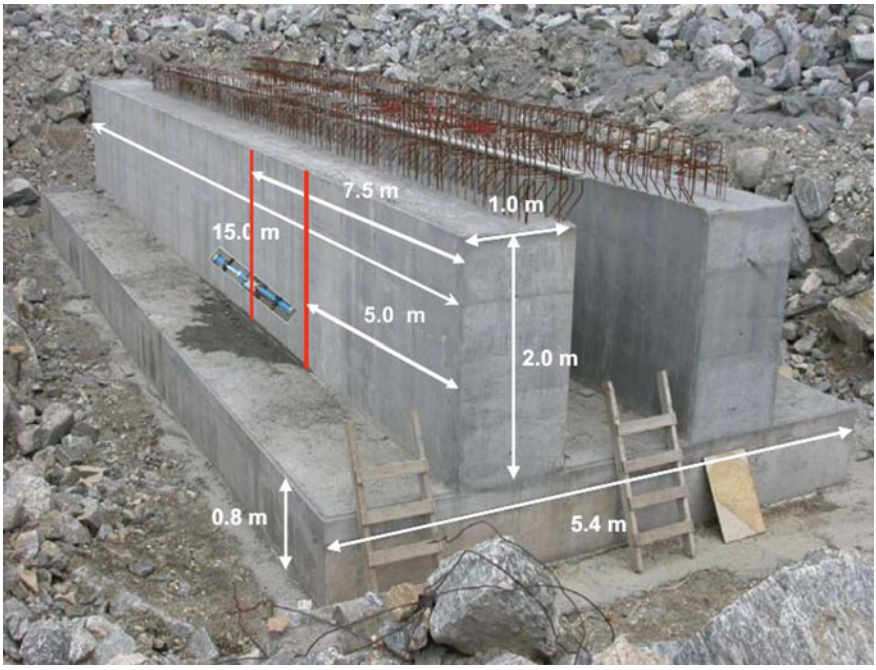

Fig. 7.11 Field test of a restrained wall in Oslo (Ji 2008)

implemented in OOFEM (Patzák and Rypl 2012), neglecting moisture transport (Šmilauer et al. 2016).

A semi-adiabatic calorimeter gave temperature evolution on a concrete cube with 247-mm edge. This small-scale test served for calibration of affinity hydration model with perfect result (Leal da Silva et al. 2015).

The restrained concrete wall was cast on older concrete raft slab according to Fig. 7.11. The quarter-simulated wall had reduced dimensions of 0.5 × 2 × 7.5 m due to symmetry conditions. A fixed temperature 20 °C served at the bottom, fluctuating temperature between 8 and 21 °C provided ambient temperature-exposed surfaces. Heat transfer coefficients of 3.75 W/(m^{2}K) acted on vertical surfaces covered with a formwork, the top had 5.75 W/(m^{2}K) with a foil cover, and the bottom had 10 W/(m^{2}K). The formwork removal at 216 h increased the coefficients to 19 W/(m^{2}K). Figure 7.12 shows temperature field with the maximum temperature at 30 h and temperature validation in gage 15 which is located in the middle of the wall, 1.2 m above the bottom.

The mechanical part used B3 creep model for concrete with corresponding parameters, coefficient of thermal expansion of 10^{-5} K^{-1}. The evolution of autogenous shrinkage, tensile strength and fracture energy was defined accordingly (Fib 2010). The wall's bottom was supported with horizontal stiffness of 1000 MN/m^3 to mimic high stiffness of the underlying old concrete. The first cracks on the surface appeared already in 12 h, but they closed by 60 h due to cooling. Minor cracks formed after 70 h close to the interface with the old concrete, where high shear stress led to tension on inclined planes. At time 260 h, vertical cracks formed through the whole beam section close to gage 15, leading to a drop of principal stress (Fig. 7.13). The widest cracks attained the width of 0.42 mm, and the maximum tensile stress in reinforcement reached 25 MPa (Fig. 7.14). The localisation into crack bands was not indicated in the experiment signalising better tensile strength of concrete than that adopted from Model Code (Fib 2010).

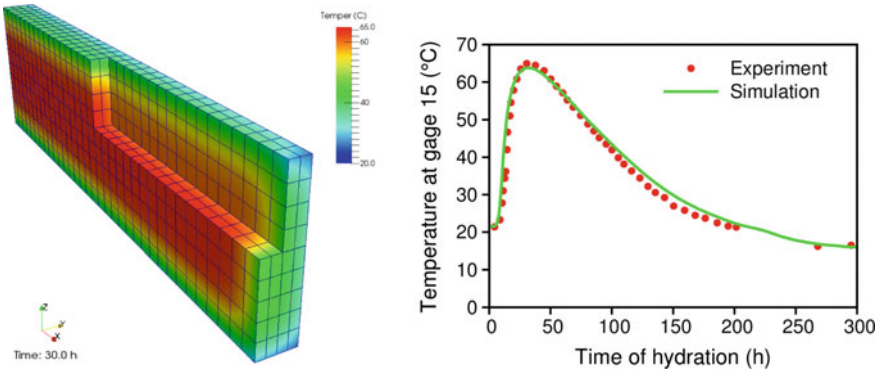

Fig. 7.12 Temperature field at 30 h and the validation

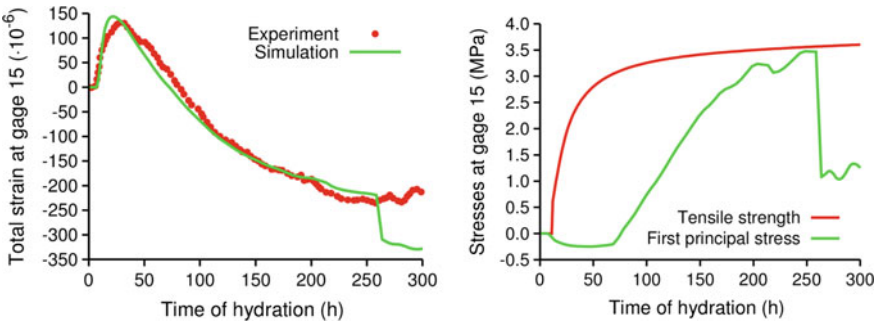

Fig. 7.13 Validation of horizontal strain, principal stress and tensile strength at gage 15

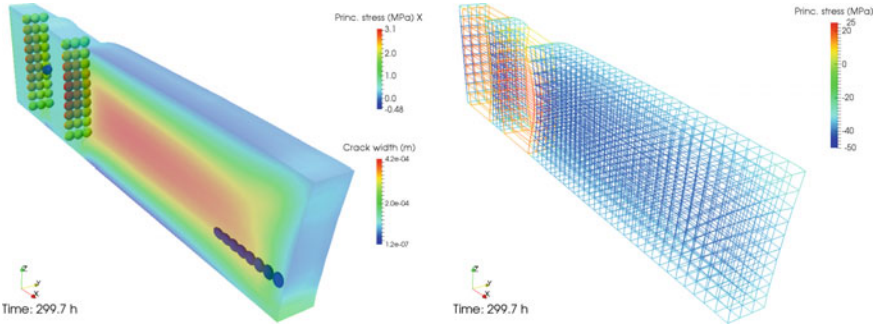

Fig. 7.14 First principal stress, cracks and stress in reinforcement at 300 h

7.4 Multifield Models: Advanced Multiphase Modelling

In this part, the models will be discussed considering more than one fluid inside the pore network of concrete. This class of models regards concrete as a porous material and is based essentially on the mechanics of porous media.

This group of models aims at the simulation of the overall thermo-hygral and mechanical behaviour of the material, considering sometimes also some chemical aspects (e.g. the reactions of hydration and dehydration). To analyse hygro-thermal phenomena in porous media, two different approaches are currently used: phenomenological and mechanistic ones. In phenomenological approaches (e.g. Bažant and Thonguthai 1978, 1979; Bažant and Kaplan 1996), moisture and heat transport are described by diffusive-type differential equations with temperature- and moisture content-dependent coefficients. The model coefficients are usually determined by inverse problem solution, starting from experimental tests results, to obtain the best agreement between theoretical prediction and experimental evidence. An advantage of such a kind of models is that they are very accurate for interpolation but rather poor for extrapolation of the known experimental results. Moreover,

various physical phenomena are lumped together and important processes, such as phase changes, are neglected. An example of such a class of models is described in Sect. 7.3.

Mechanistic models (Gawin et al. 2002, 2003, 2006a, b, c, 2008, 2009) are more complicated from the mathematical point of view, and contrary to phenomenological ones, their coefficients have a clear physical meaning. This kind of models is often obtained from microscopic balance equations written for each constituent of the medium, which are then averaged in space by applying special averaging operators.

Several mathematical and numerical models, usually based on extensive laboratory tests, have been developed for the analysis of heat and mass transfer in concrete at early ages and beyond, e.g. Benboudjema and Torrenti (2008), Cervera et al. (1999a, b), Gawin et al. (2006a, b). However, one should remember that every interpretation possesses all limitations and simplifications that are assumed in the mathematical model which the simulation is based on. Thus, for this purpose one should use models considering possibly the whole complexity and mutual interactions of the analysed physical processes. Hence, a proper choice may be models based on mechanics of multiphase porous media, taking into account chemical reactions (e.g. reactions related to hydration, silica-alkali reactions and other reactions due to chemically aggressive environments), phase changes, cracking and thermo-chemical material degradation, as well as their mutual couplings and influence on the hygral, thermal, chemical and mechanical properties of concrete. These physical aspects of the behaviour of concrete treated as a multiphase porous material are described in the following sections.

7.4.1 Concrete as Multiphase Porous Material

Concrete is essentially a mixture of two components: aggregates and paste. The aggregate component is usually sand, gravel or crushed stone. It is mainly responsible for the unit weight, the elastic modulus and the dimensional stability of concrete. The paste component is typically used to bind aggregates in concrete and mortar. It is a porous medium, which is composed of a solid skeleton, produced from the hydration of Portland cement, and pores, which are filled by different fluid phases. The principal solid phases generally present in the hydrated cement paste (*hcp*) that can be resolved by an electron microscope are the calcium silicate hydrates C-S-H which are very important in determining the properties of the paste such as strength and permeability, and the calcium hydroxide $Ca(OH)_2$ (also called portlandite). The pore structure is relevant for concrete. It contributes to the mechanical strength of concrete, but it also allows the interaction with the external environment which takes place through the connected pores. Besides, it is the container of the liquid water and gas phases (vapour and dry air). Figure 7.15 gives a schematic representation of cement paste seen as a partially saturated medium.

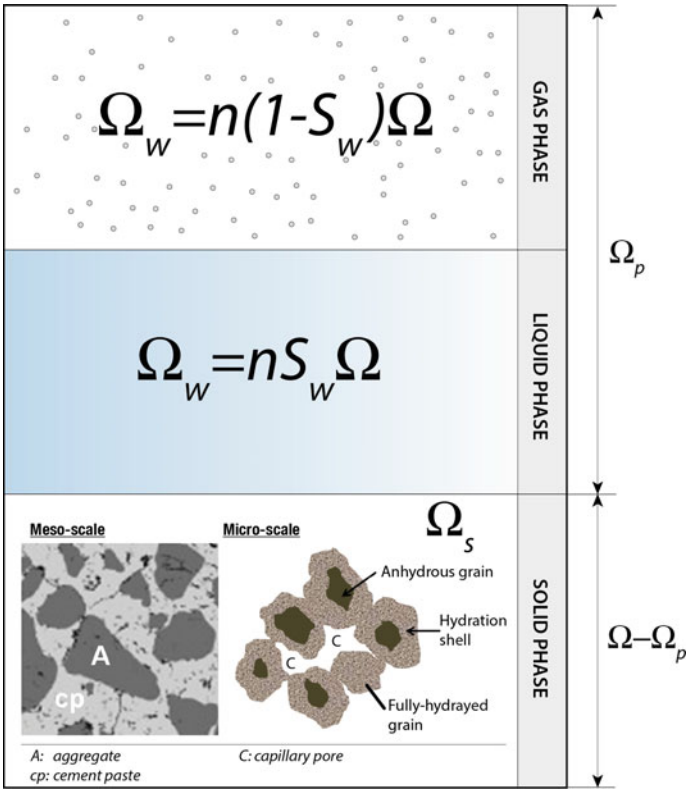

Fig. 7.15 Schematic representation of a non-saturated porous material

For a given representative elementary volume (REV)Ω, the volume of pores Ω_p allows to define the porosity $n = \Omega_p/\Omega$. Furthermore, the degree of saturation of pores with liquid water is introduced as $S_w = \Omega_w/\Omega_p$. It is an experimentally determined function of the relative humidity RH (obtained through the sorption isotherms). The remaining volume of pores is filled with a gaseous mixture with a gas saturation: $S_g = (1 - S_w) = \Omega_g/\Omega_p$ (Ω_w and Ω_g are the volumes of the liquid and gas phases, respectively).

The interfacial surface tension of water in a capillary pore leads to a concave meniscus between liquid water and gas phase, as shown in Fig. 7.16. This may give rise to a discontinuity in fluid pressure. The difference between the liquid water pressure p_w and the gas pressure (dry air p_a + vapour p_v) is called the capillary pressure p_c and is a function of the liquid water saturation S_w:

$$p_c(S_w) = p_v + p_a - p_w \tag{7.28}$$

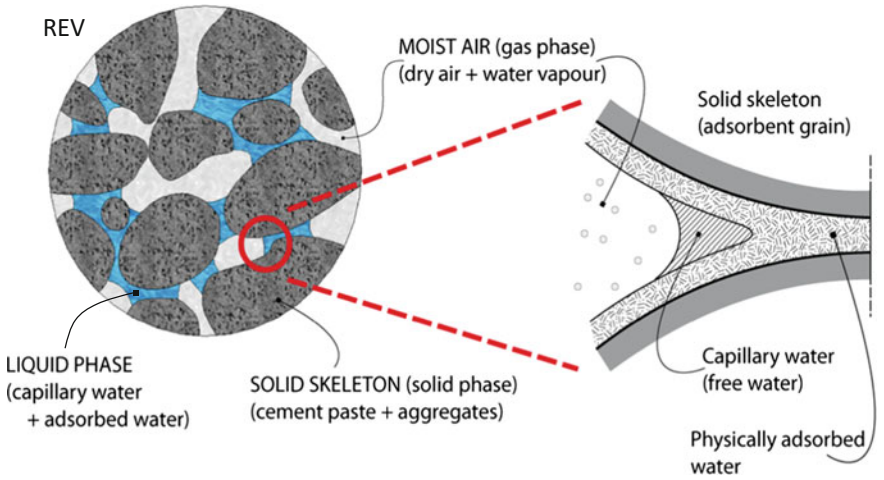

Fig. 7.16 Schematic representation of the representative elementary volume (REV)

Assuming the contact angle γ between liquid phase and solid matrix to be zero, the capillary pressure of water p_c can be related to the pore radius r with the Laplace equation:

$$p_c = \frac{2\sigma(T)}{r}\cos\gamma = 2\sigma(T)\cos\gamma\,\chi \tag{7.29}$$

where $\sigma(T)$ is the surface tension of water which depends upon temperature and χ is the curvature of the meniscus. Any change in the curvature of meniscus will change the equilibrium between liquid and vapour phases. A relation between the liquid water and the vapour can be obtained by means of Kelvin's equation considering that liquid is incompressible and the vapour is a perfect gas.

Water can exist in the hydrated cement paste in many forms:

- capillary and physically adsorbed water; their loss is mainly responsible for the shrinkage of the material while drying;
- interlayer water; it can be lost only during strong drying, which leads to considerably shrinkage of the C-S-H structure.

All these types of water can evaporate up to 105 °C (at atmospheric pressure and slow rate of heating). Another type of water, which is non-evaporable water, is chemically bound water. It is considered to be an integral part of the structure of various cement hydration products, and it is released when the hydrates decompose on heating. Based on the Feldman–Sereda model (Feldman and Sereda 1968), the different types of water associated with the C-S-H are illustrated in Fig. 7.17.

In fact, there is a third phase in the concrete microstructure, known as transition zone, which represents the interfacial region between the particles of coarse aggregates and the *hcp*. Concrete has microcracks in the transition zone even before

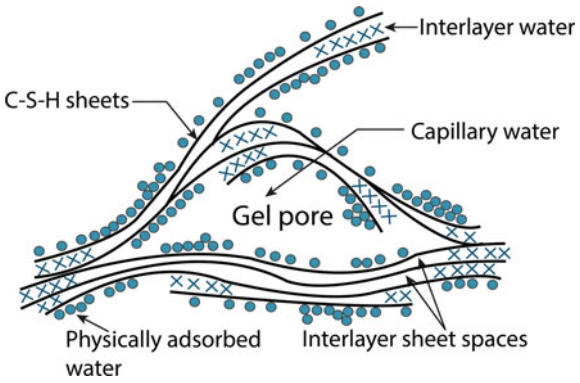

Fig. 7.17 Probable structure of hydrated silicates (based on Feldman and Sereda 1968)

a structure is loaded. This has a great influence on the stiffness of concrete. In the composite material, the transition zone serves as a bridge between the two components: the mortar matrix and the coarse aggregate particles. Therefore, the broken bridges (i.e. voids and microcracks in this zone) would not permit stresses transfer.

For what has been described above, concrete can be treated as a multiphase/multicomponent porous material. Because of this, in the last fifteen years, mechanics of multiphase porous media proved to be a theory enabling an efficient modelling of cement-based materials (Gawin et al. 2003, 2006a, b, 2008, 2009; Pesavento et al. 2008, 2012). It allows for considering the porous and multiphase nature of the materials, their chemical transformations, water phase changes and different behaviour of moisture below and above the critical temperature of water, mutual interactions between the thermal, hygric and degradation processes, as well as several material nonlinearities, especially those due to temperature changes, material cracking and thermo-chemical degradation.

In modelling, it is usually assumed that the material phases are in thermodynamic equilibrium state locally. In this way, their thermodynamic state is described by one common set of state variables and not by separate sets for every component of the material, which allows reducing the number of unknowns in a mathematical model. Thus, there is, for example, one common temperature for the multiphase material and not different temperature values for the skeleton, liquid water, vapour and dry air, etc. When fast hygro-thermal phenomena in a material are analysed (e.g. during a rapid heating and/or drying), the assumption is debatable, but it is almost always used in modelling, giving reasonable results from a physical point of view and in part confirmed by the available experimental results.

Concrete is here considered to be a multiphase medium where the voids of the solid skeleton could be filled with various combinations of liquid and gas phases as in Fig. 7.16. In the specific case, the fluids filling pore space are the moist air (mixture of dry air and vapour), capillary water and physically adsorbed water. The chemically bound water is considered to be part of the solid skeleton until it is released on heating.

Below the critical temperature of water T_{cr}, the liquid phase consists of physically adsorbed water, which is present in the whole range of moisture content, and

capillary water, which appears when degree of water saturation S_w exceeds the upper limit of the hygroscopic region, S_{ssp} (i.e. below S_{ssp} there is only physically adsorbed water). Above the temperature T_{cr}, the liquid phase consists of the adsorbed water only. In the whole temperature range, the gas phase is a mixture of dry air and water vapour.

Thanks to the mechanics of porous media and the schematisation of the material described above, it is possible to analyse three different classes of phenomena which characterises the behaviour of concrete at early ages and beyond:

- hygral phenomena,
- thermal phenomena,
- mechanical phenomena,
- chemical processes.

7.4.1.1 Hygral Phenomena

In order to analyse the physical processes taking place in the material under variable conditions in terms of temperature and pressure, we can consider a concrete element heated from the environment.

When temperature increases in a concrete structure (e.g. in a wall), water vapour pressure is continuously increasing in a zone close to the heated surface. This derives principally from the evaporation of water inside the wall, when the temperature reaches and passes the boiling point of water. Vapour pressure is also due to the water that is liberated during the dehydration of cement paste. This increase in the water vapour pressure in the hot region will create a thermodynamic imbalance between the hot and the cold regions. This will entail a diffusion process of the water vapour and of the dry air through the wall and towards the external atmosphere to maintain the equilibrium between liquid and vapour (see Fig. 7.18).

For appropriate prediction of the moisture distribution in a concrete structure, one needs to know the material properties that control the movement of the fluids inside a porous medium. Permeability and diffusivity are the most important properties of the cementitious materials, from this point of view. These are very sensitive to porosity changes or microcracking phenomena. In fact, the increases in permeability and porosity of such materials are currently accepted as providing a reliable indication of their degradation whether it has thermal, mechanical or physicochemical origins. Therefore, in this document these properties and their evolutions will be analysed also in the view of what is described in Chaps. 3 and 4.

7.4.1.2 Thermal Phenomena

Concerning thermal phenomena, it can be stated that in most cases the main mechanism for heat transport is heat conduction. Heat conduction responds to

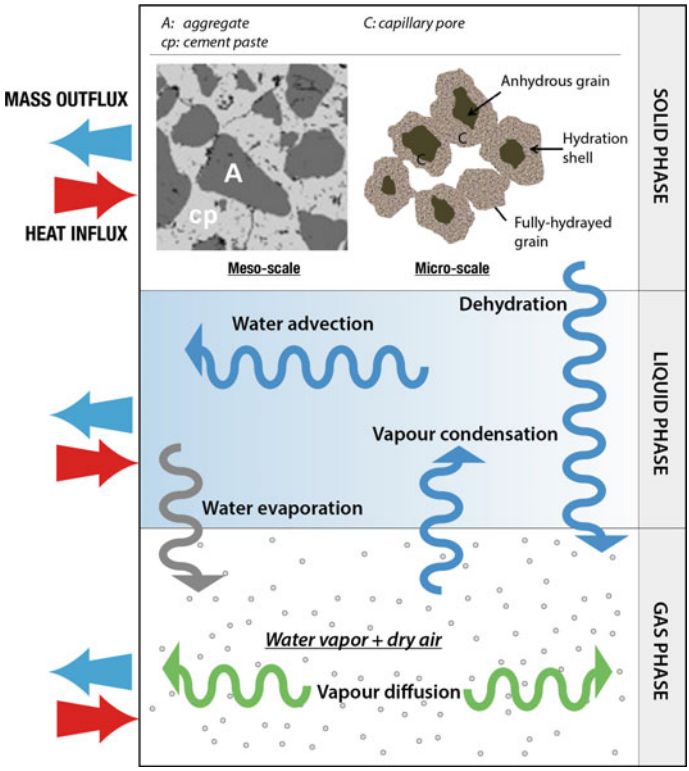

Fig. 7.18 Mass sources/sinks and mass transport mechanisms in a non-saturated porous medium subjected to heating

gradients of temperature T. However, additional heat transfer will also be accomplished by advection due to the movement of the three phases: solid, liquid and gas. The latent heat inherent to phase changes may also have significant thermal effects (Gawin et al. 2003), see also Fig. 7.19.

The evolution of the temperature distribution in any structure is governed by the thermal properties of the material, particularly heat capacity and thermal conductivity. In case of concrete, it is difficult to determine these properties because of the numerous phenomena that occur simultaneously within the microstructure of concrete and cannot be separated easily. These phenomena are affected in particular by the evolution of the porosity, by the moisture content, by the type and amount of aggregate, by changes in the chemical composition and by the latent heat consumption generated by certain chemical phenomena. Because of these effects, a unique relation cannot rigorously describe the dependence of concrete properties on temperature.

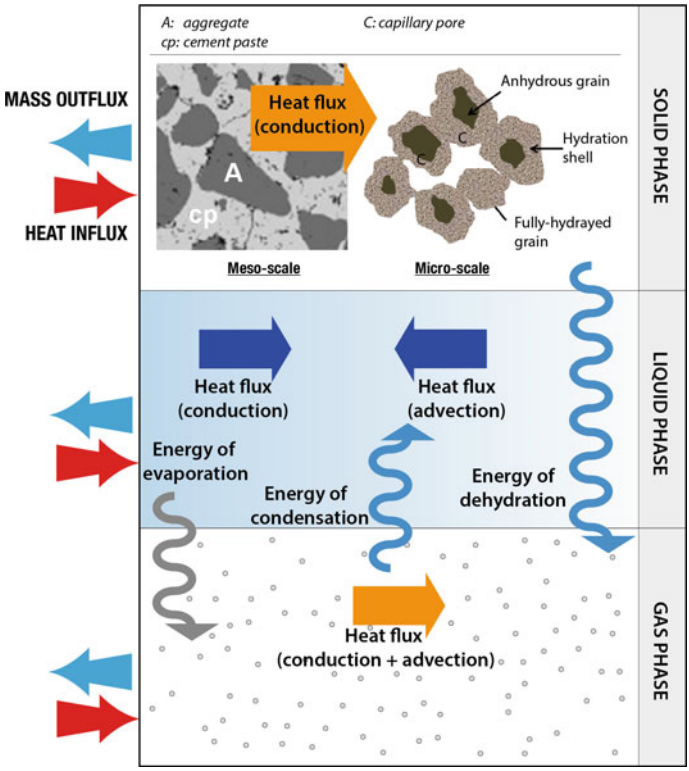

Fig. 7.19 Heat sources/sinks and heat transport mechanisms in a porous medium

7.4.1.3 Mechanical Phenomena

When mechanically loaded and simultaneously heated, the overall measured strain of concrete is assumed as an additive combination of different components. These components can be conventionally classified into three families according to the origin of driving mechanisms:

- Mechanical strains that occur due to an applied mechanical load only. Elastic strain, cracking strain and basic creep strain are main mechanical components.
- Thermo-hygral strains related to the occurrence of physicochemical processes within the material such as drying, temperature raising, hydration and other chemical reactions. Thermal expansion and shrinkage (both capillary and chemical shrinkage) are the most important components. They are carried out in (mechanically) load-free configurations.
- Interaction strains are additional components generated when the above-mentioned physicochemical processes occur during a concomitant applied load. In this case, indeed, the overall measured strain differs from the

sum of all strains induced by each single mechanism. For instance, additional elastic strain, due to the evolution of Young's modulus with temperature, is an illustration of interaction strains. Also, drying and creep strains belong to this category. For example, drying creep is shown when the structural element can exchange water with the environment (i.e. shrinkage is taking place) and is loaded at the same time.

7.4.1.4 Chemical Processes

Description of chemical reactions taking place in concrete at early ages (and beyond) and their couplings with the thermo-hygral state of the material (e.g. self-drying) can be found in Chap. 3. Here, one underlines that in the numerical modelling the hydration is often considered as a single chemical reaction; i.e., only the overall process is described through the formulation of a proper evolution equation.

7.4.2 Heat and Mass Transfer

The general approach to heat and mass transfer processes in a partially saturated open porous medium is to start from a set of balance equations governing the time evolution of mass and heat of solid matrix and fluids filling the porous network, taking into account the exchange between the phases and with the surrounding medium. These balance equations are supplemented with an appropriate set of constitutive relationships, which permit to reduce the number of independent state variables that control the physical process under investigation.

The formulation of the mathematical model is based usually on here main approaches:

(1) Mixture theories (Bear 1988);
(2) Volume averaging theories (Whitaker 1980);
(3) Hybrid mixture theories (Hassanizadeh and Gray 1979a, b, 1980).

In the first approach, the governing equations of the model and its constitutive equations are both formulated directly at macroscale. In the second and in the third approach, the governing equations are defined at microscopic level and then upscaled at macrolevel by applying some averaging operators (mass, volume, area operators, mainly). In the case of volume averaging approach also the constitutive relationships are formulated at microscale.

The Hybrid Mixture Theory and the Volume Averaging Theory allow for taking into account both bulk phases and interfaces of the multiphase system, assure that the Second Law of Thermodynamics is satisfied at macrolevel, that no un-wanted dissipations are generated and that the definition of the relevant quantities involved is thermodynamically correct.

Recently, it has been shown that with the combination of Hybrid Mixture Theory and the Thermodynamically Constrained Averaging Theory (TCAT, Gray and Miller 2005), also the satisfaction of the second law of thermodynamics for all constituents at microlevel is guaranteed (Gray et al. 2009).

Starting from this latter approach, in the following section a full set of balance equations is presented. They can be obtained by using the procedure of space averaging of the microscopic balance equations, written for the individual constituents of the medium (i.e. the governing equations at local level). The theoretical framework is based on the works of Lewis and Schrefler (1998), Gray and Schrefler (2007). A detailed description of the procedure can be found in (Pesavento 2000; Gawin et al. 2003, 2006a, b, c, 2008, 2009; Pesavento et al. 2008, 2012).

7.4.2.1 Final Form of the Governing Equations

The hygro-chemo-thermal state of cement-based materials considered as multiphase porous media is described by three primary state variables: the capillary pressure p_c, the gas pressure p_g and the temperature T, as well as one internal variable describing advancement of the hydration processes, i.e. degree of hydration, α. This choice is of particular importance: the chosen quantities must describe a well-posed initial-boundary value problem, should guarantee a good numerical performance of the solution algorithm and should make their experimental identification simple. A detailed discussion about the choice of state (i.e. primary) variables can be found in Sect. 7.4.3.

The mathematical model describing the material performance consists of three equations: two mass balances (continuity equations of water and dry air), enthalpy (energy) balance and one evolution equation (degree of dehydration). For convenience of the reader, the final form of the model equations, expressed in terms of the primary state variables, is listed below. The full development of the equations is presented in (Gawin et al. 2006a, b).

Mass balance equation of dry air takes into account both the diffusive (described by the term L.30.7) and advective air flow (L.30.8), the variations of the saturation degree of water (L.30.1) and air density (L.30.4), as well as the variations of porosity caused by: hydration process (L.30.5), temperature variation (L.30.2), skeleton density changes due to dehydration (L.30.6) and by skeleton deformations (L.30.3). The mass balance equation has the following form:

$$\begin{aligned} &\underbrace{-n\frac{\partial S_w}{\partial t}}_{\text{L.30.1}} \underbrace{-\beta_s(1-n)S_g\frac{\partial T}{\partial t}}_{\text{L.30.2}} + \underbrace{S_g\nabla\cdot\mathbf{v}^s}_{\text{L.30.3}} + \underbrace{\frac{S_g n}{\rho_a}\frac{\partial \rho_a}{\partial t}}_{\text{L.30.4}} \underbrace{-\frac{\dot{m}_{hydr}}{\rho_s}S_g}_{\text{L.30.5}} \\ &\underbrace{-\frac{(1-n)S_g}{\rho_s}\frac{\partial \rho_s}{\partial \alpha}\frac{\partial \alpha}{\partial t}}_{\text{L.30.6}} + \underbrace{\frac{1}{\rho_a}\nabla\cdot\mathbf{J}_g^a}_{\text{L.30.7}} + \underbrace{\frac{1}{\rho_a}\nabla\cdot\left(n\,S_g\rho_a\mathbf{v}^{gs}\right)}_{\text{L.30.8}} = 0 \end{aligned} \tag{7.30}$$

in which ρ_π is the density of the π-phase ($\pi = s,\ w,\ g$) and β_s is the thermal expansion coefficient of the solid phase, ρ_a is the dry air density, α the hydration degree, and $\mathbf{J}_g^a$ the dry air diffusive flux. In the previous equation and in the following ones, $\mathbf{v}^s$ is the velocity of the solid phase, while $\mathbf{v}^{\pi s}$ is the relative velocity of the π-fluid phase ($\pi = w,\ g$) with respect to the solid skeleton.

Mass balance equation of water species (vapour + liquid water) considers the diffusive (L.31.6) and advective flows of water vapour (L.31.7) and water (L.31.8), the mass sources related to phase changes of vapour (evaporation–condensation, physical adsorption–desorption) (the sum of those mass sources equals to zero) and hydration (R.31.1), and the changes of porosity caused by variation of: temperature (L.31.3), hydration process (L.31.10), variation of skeleton density due to hydration (L.31.9) and deformations of the skeleton (L.31.2), as well as the variations of: water saturation degree (L.31.1) and the densities of vapour (L.31.4) and liquid water (L.31.5). This gives the following equation (Gawin et al. 2006a, b):

$$\begin{aligned}
&\underbrace{n(\rho_w - \rho_v)\frac{\partial S_w}{\partial t}}_{\text{L.31.1}} + \underbrace{\left(\rho_w S_w + \rho_v S_g\right)\nabla\cdot\mathbf{v}^s}_{\text{L.31.2}} - \underbrace{\beta_{swg}\frac{\partial T}{\partial t}}_{\text{L.31.3}} + \underbrace{S_g n\frac{\partial \rho_v}{\partial t}}_{\text{L.31.4}} \\
&+ \underbrace{S_w n\frac{\partial \rho_w}{\partial t}}_{\text{L.31.5}} + \underbrace{\nabla\cdot\mathbf{J}_g^v}_{\text{L.31.6}} + \underbrace{\nabla\cdot\left(n\,S_g\rho_v\mathbf{v}^{gs}\right)}_{\text{L.31.7}} + \underbrace{\nabla\cdot\left(n\,S_w\rho_w\mathbf{v}^{ws}\right)}_{\text{L.31.8}} \\
&- \underbrace{\left(\rho_w S_w + \rho_v S_g\right)\frac{(1-n)}{\rho_s}\frac{\partial \rho_s}{\partial \alpha}\frac{\partial \alpha}{\partial t}}_{\text{L.31.9}} - \underbrace{\frac{\dot{m}_{hydr}}{\rho_s}\left(\rho_w S_w + \rho_v S_g\right)}_{\text{L.31.10}} = -\underbrace{\dot{m}_{hydr}}_{\text{R.31.1}}
\end{aligned} \tag{7.31}$$

where ρ_v is the water vapour density, $\mathbf{J}_g^v$ is the water vapour diffusive flux, and $\dot{m}_{hydr}$ is the water mass source/sink due to hydration process.

In Eq. 7.31, β_{swg} is the thermal expansion coefficient of the multiphase porous medium, defined by:

$$\beta_{swg} = \beta_s(1-n)\left(S_g\rho_v + S_w\rho_w\right) + n\,\beta_w S_w \rho_w \tag{7.32}$$

in which β_π is the thermal expansion coefficient of each phase ($\pi = s,\ w,\ g$).

Enthalpy balance equation of the multiphase medium, accounting for the conductive (L.33.3) and convective (L.33.2) heat flows, the heat effects of phase changes (R.33.1) and dehydration process (R.33.2), and the heat accumulated by the system (L.33.1), can be written as follows:

$$\begin{aligned}
&\underbrace{\left(\rho C_p\right)_{eff}\frac{\partial T}{\partial t}}_{\text{L.33.1}} + \underbrace{\left(\rho_w C_p^w \mathbf{v}^w + \rho_g C_p^g \mathbf{v}^g\right)\cdot\nabla T}_{\text{L.33.2}} - \underbrace{\nabla\cdot(\widetilde{\mathbf{q}})}_{\text{L.33.3}} \\
&= -\underbrace{\dot{m}_{vap}\Delta H_{vap}}_{\text{R.33.1}} + \underbrace{\dot{m}_{hydr}\Delta H_{hydr}}_{\text{R.33.2}}
\end{aligned} \tag{7.33}$$

where $\widetilde{\mathbf{q}}$ is the conductive thermal flux, $\mathbf{v}^w$ and $\mathbf{v}^g$ are the velocities of the liquid and gas phase, respectively, and the thermal capacity of the multiphase porous medium $(\rho C_p)_{eff}$ and the enthalpies of vaporisation ΔH_{vap} and hydration ΔH_{hydr} are:

$$\begin{aligned} \left(\rho C_p\right)_{eff} &= \rho_s C_p^s + \rho_w C_p^w + \rho_g C_p^g, \\ \Delta H_{vap} &= H^{gw} - H^w, \\ \Delta H_{hydr} &= H^w - H^{ws} \end{aligned} \tag{7.34}$$

in which C_p^π is the specific heat of the π-phase (π = *s, w, g*).

In Eq. 7.33, the vapour mass source is given by (Gawin et al. 2006a, b):

$$\begin{aligned} \underbrace{\dot{m}_{vap}}_{\text{L.35.1}} = &- \underbrace{\rho_w n \frac{\partial S_w}{\partial t}}_{\text{R.35.1}} - \underbrace{\rho_w S_w\, b\, \nabla \cdot \mathbf{v}^s}_{\text{R.35.2}} + \underbrace{\beta_{sw} \frac{\partial T}{\partial t}}_{\text{R.35.3}} - \underbrace{\nabla \cdot \left(n\, S_w \rho_w \mathbf{v}^{ws}\right)}_{\text{R.35.4}} \\ &\underbrace{- (1-n) \frac{\rho_w S_w}{\rho_s} \frac{\partial \rho_s}{\partial \alpha} \frac{\partial \alpha}{\partial t}}_{\text{R.35.5}} - \underbrace{\dot{m}_{hydr} \frac{\rho_w S_w}{\rho_s}}_{\text{R.35.6}} + \underbrace{\dot{m}_{hydr}}_{\text{R.35.7}} \end{aligned} \tag{7.35}$$

with:

$$\beta_{sw} = \rho^w S_w [(1-n)\beta_s + n\beta_w] \tag{7.36}$$

Equation 7.35 considers the advective flow of water (R.35.4), the mass sources related to dehydration (R.35.7) and the changes of porosity caused by: variation of temperature (R.35.3), dehydration process (R.35.6), variation of skeleton density due to dehydration (R.35.5) and deformations of the skeleton (R.35.2), as well as the variations of water saturation degree (R.35.1).

The governing equations in the form described above are now complemented by the constitutive equations.

7.4.2.2 Constitutive Equations

Fluid state equations

The liquid water is considered to be incompressible such that its density depends on the temperature only. The vapour, dry air and the gas mixture are considered to behave as ideal gases, which gives (π = *v, a, g*):

$$p_\pi = \rho_\pi T R / M_\pi \tag{7.37}$$

where p_π is the pressure, M_π is the molar mass, and R is the universal gas constant. Furthermore, the pressure and density of the gas mixture can be related to the partial pressures and densities of the constituents through the Dalton's law:

$$p_g = p_a + p_v \quad \rho_g = \rho_a + \rho_v \tag{7.38}$$

which gives:

$$M_g = M_a + (M_v - M_a)\frac{p_v}{p_g} \tag{7.39}$$

Liquid–Vapour Equilibrium

By assuming that the evaporation process occurs without energy dissipation, that is, liquid and vapour water have equal free enthalpies, one can derive the generalised Clausius–Clapeyron equation, which is a relationship between liquid and vapour pressure:

$$p_v = p_{vs} exp\left(\frac{M_v}{\rho_w RT}\left(p_g - p_c - p_{vs}\right)\right) \tag{7.40}$$

where the capillary pressure at equilibrium

$$p_c = p_g - p_w \tag{7.41}$$

has been introduced for the porous medium and p_{vs} is the saturation vapour pressure, which only depends on temperature.

Mass fluxes

According to the definition of the velocities in the governing equations (7.30) (Gawin et al. 2006a), the mass fluxes can be as follows:

$$\mathbf{J}^{\pi s} = nS_\pi \rho_\pi \mathbf{v}^{\pi s} = \rho_\pi \frac{k_{r\pi}\mathbf{k}}{\mu_\pi}\left(-\nabla p_\pi + \rho_\pi \mathbf{g}\right) \tag{7.42}$$

which represents the Darcy's law for the liquid ($\pi = w$) and gaseous ($\pi = g$) phases, respectively, and where $\mathbf{k}$ is the intrinsic permeability, $k_{r\pi}$ is the relative permeability, μ_π is the dynamic viscosity, and $\mathbf{g}$ is the gravity acceleration.

The mass fluxes related to the diffusion are defined as:

$$\mathbf{J}_g^a = -\rho_g \frac{\mathrm{M_a M_w}}{\mathrm{M_g^2}} \mathbf{D}_g^a \nabla\left(\frac{p_a}{p_g}\right) = -\mathbf{J}_g^v \tag{7.43}$$

where $\mathbf{J}_g^a$ and $\mathbf{J}_g^v$ are the fluxes of the dry air and water vapour in the gas phases (i.e. the humid air), respectively, and $\mathbf{D}_g^a$ is the diffusion tensor of the dry air.

Conductive Heat Flux

In the energy balance Eq. 7.33, the heat conduction process in the porous medium can be described by Fourier's law which relates the temperature to the heat flux as follows:

$$\widetilde{\boldsymbol{q}} = -\lambda(S_w, T)\nabla T \tag{7.44}$$

where $\lambda(S_w,T)$ is the effective thermal conductivity which in general is a function of the temperature and of the degree of saturation with liquid water of the pores.

Sorption–desorption isotherm

Solving the presented equations aims at determining the spatial and temporal distribution of temperature, masses of constituents and corresponding pressures within the porous medium. By introducing the previous constitutive equations, the problem involves, at this stage, as main unknowns (S_w, p_c, p_g, T, m_{vap}) or alternatively (S_w, p_v, p_a, T, m_{vap}). This set is reduced by introducing an additional explicit relationship (van Genuchten 1980; Baroghel-Bouny et al. 1999; Pesavento 2000; Gawin et al. 2003):

$$S_w = S_w(p_c, T) \tag{7.45}$$

which is the sorption–desorption isotherm, characterising phenomenologically the microstructure of the porous medium (pore size distribution).

Moreover, it is needed to consider that the microstructure of the cement paste shows important changes during hydration (refinement of the porous network), so it is important to take into account this aspect in the mathematical formulation of the isotherms.

To do this, the classical analytical expression proposed by Van Genuchten (1980) can be slightly modified to take into account the hydration degree (see Fig. 7.20), which is a measure of the hydration extent (see the next subsections for its definition):

$$S_w = \left\{1 + \left[\frac{p_c}{a}\left(\frac{\Gamma + \Gamma_i}{1 + \Gamma_i}\right)^{-c}\right]^{\frac{b}{b-1}}\right\}^{-\frac{1}{b}} \tag{7.46}$$

where a and b are the classical parameters of the Van Genuchten's law, and c and Γ_i are the newly introduced parameters (Sciumè et al. 2013).

Using this additional relationship, the reduced set of unknowns is then (p_c, p_g, T, m_{vap}) where a choice is made here to retain the state variables (p_c, p_g) instead of (p_v, p_a) or (p_w, p_a). Moreover, the set of unknowns can be further reduced. Because of this, mass conservation equations of liquid and vapour defined as in (Schrefler 2002; Gawin et al. 2003) have been summed to eliminate the evaporation source

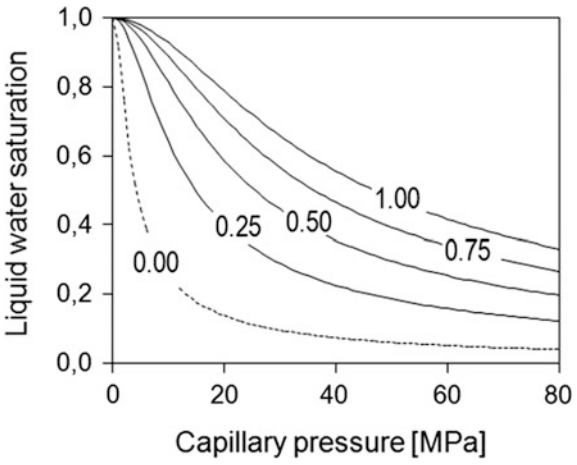

Fig. 7.20 Desorption isotherms: the numbers in the diagram indicate the hydration degree. (Adapted from Sciumé et al. 2013)

term m_{vap} and thus obtain the mass balance equation for the water species (that means liquid water plus water vapour), Eq. 7.31.

7.4.3 Key Points for Modelling Cement-Based Materials as Multiphase Porous Media

Dealing with cement-based materials as multiphase porous media introduces some physical and theoretical difficulties, which should be overcome to be able to formulate a mathematical model giving reliable results for the material. These key points are discussed in the following subsections.

Choice of state variables

A proper choice of state variables for description of the multiphase porous materials is of particular importance. From a practical point of view, the physical quantities used should be possibly easy to measure during experiments, and from a theoretical point of view, they should uniquely describe the thermodynamic state of the medium. They should also assure a good numerical performance of the computer code based on the resulting mathematical model. As already mentioned previously, the necessary number of state variables may be significantly reduced if the existence of local thermodynamic equilibrium at each point of the medium is assumed (Schrefler 2002). In such a case, the physical state of different phases of water can be described by the same variable.

Having in mind all the aforementioned remarks, the state variables chosen for the presented model will be now briefly discussed. Use of temperature, which is the same for all constituents of the medium because of the assumption about the local thermodynamic equilibrium state, and use of solid skeleton displacement vector are rather obvious; thus, it needs no further explanation. As a hygrometric state variable,

various physical quantities which are thermodynamically equivalent may be used, e.g. moisture content by volume or by mass, liquid water saturation degree, vapour pressure, relative humidity or capillary pressure. Analysing materials in the whole range of temperatures, one must remember that at temperatures higher than the critical point of water (i.e. 374.15 °C or 647.3 K) there is no capillary (or free) water present in the material pores, and there exists only the gas phase of water, i.e. vapour. Then, very different moisture contents may be encountered at the same moment in a cement-based material, ranging from full saturation with liquid water (e.g. in some nuclear vessels or in so-called moisture clog zone in a heated concrete, see England and Khoylou 1995, or in concrete at early ages), up to almost completely dry material. Moreover, some quantities (e.g. saturation or moisture content) which can be chosen as primary variables are not continuous at interfaces between different materials.

For these reasons, apparently it is not possible to use, in a direct way, one single variable for the whole range of moisture contents. However, it is possible to use a single variable that has a different meaning depending on the state. The moisture state variable selected in the model is capillary pressure (Gawin et al. 2002, 2003, 2006a) that was shown to be a thermodynamic potential of the physically adsorbed water and, with an appropriate interpretation, can be also used for description of water at pressures higher than the atmospheric one. The capillary pressure has been shown to assure good numerical performance of the computer code (Gawin et al. 2002, 2003, 2006a, b, c) and is very convenient for analysis of stress state in concrete, because there is a clear relation between pressures and stresses (Gray et al. 2009).

Therefore, as already shown, the chosen primary state variables of the presented model are the volume averaged values of: gas pressure, p_g, capillary pressure, p_c, temperature, T, and displacement vector of the solid matrix, $\mathbf{u}$.

For temperatures lower than the critical point of water, $T < T_{cr}$, and for capillary saturation range, $S_w > S_{ssp}(T)$ (S_{ssp} is not only the upper limit of the hygroscopic moisture range as mentioned earlier, but also the lower limit of the capillary one), the capillary pressure is defined according to Eq. 7.41.

For all other situations, and in particular for $T \geq T_{cr}$ or where condition $S_w < S_{ssp}$ is fulfilled (there is no capillary water in the pores), the capillary pressure substitutes—only formally—the water potential Ψ_c, defined as:

$$\Psi_c = \frac{RT}{M_w} ln\left(\frac{p_v}{f^{vs}}\right) \tag{7.47}$$

where M_w is the molar mass of water, R is the universal gas constant, and f^{vs} is the fugacity of water vapour in thermodynamic equilibrium with a saturated film of physically adsorbed water (Gawin et al. 2002). For physically adsorbed water at lower temperatures ($S_w < S_{ssp}$ and $T < T_{cr}$), the fugacity f^{vs} should be substituted in the definition of the potential Ψ_c, by the saturated vapour pressure p_{vs}. Having in mind Kelvin's equation, valid for the equilibrium state of capillary water with water vapour above the curved interface (meniscus) we can notice that in the situations where Eq. 7.47 is valid, the capillary pressure may be treated formally as the water potential multiplied by the density of the liquid water, according to the relation:

$$ln\left(\frac{p_v}{p_{vs}}\right) = -\frac{p_c}{\rho_w}\frac{M_w}{RT} \tag{7.48}$$

$$p_c = -\Psi_c \rho_w \tag{7.49}$$

Thanks to this similarity, it is possible to "formally" use the capillary pressure during computations even in the low moisture content range, where the capillary water is not present in the pores and capillary pressure has no physical meaning.

7.4.4 Constitutive Laws for Crack Evolution

In the following, some peculiar aspects of the mechanical behaviour of the material strictly related to its porous nature are illustrated, taking into account that most of the phenomena/processes involved are described in Chap. 4, e.g. creep and microfracturing.

Furthermore, a more detailed discussion about the formulation of proper constitutive relationships for describing damage mechanics and visco-plasticity can be found in Sect. 7.5.

7.4.4.1 Momentum Balance

For completeness, the momentum balance equation is recalled here. Introducing the Cauchy stress second-order tensor $\boldsymbol{\sigma}^{total}$ ($\mathbf{x}$, t) at any point $\mathbf{x}$ in the studied domain Ω, and at time t, and the applied forces per unit volume vector $\mathbf{f}$ ($\mathbf{x}$, t), the momentum balance equations can be written, in a quasi-static case, i.e. neglecting the inertia effects, as:

$$\nabla \cdot \boldsymbol{\sigma}^{total} + \mathbf{f} = \mathbf{0} \tag{7.50}$$

These equations are complemented by the boundary conditions, which are either the prescription of displacements on some part of the boundary of the studied domain $\Gamma_u = \partial\Omega_u$:

$$u_i = \bar{u}_i \quad \forall \boldsymbol{x} \in \Gamma_u = \partial\Omega_u \tag{7.51}$$

or the prescription of surface forces on the complementary part $\Gamma_u^q = \partial\Omega_u^q$ the boundary:

$$\sigma_{ij}^{total} n_j = \bar{\sigma}_i \quad \forall \boldsymbol{x} \in \Gamma_u^q = \partial\Omega_u^q \tag{7.52}$$

where $\boldsymbol{n}$ denotes the outward normal vector.

7.4.4.2 Effective Stress Principle

Here, cement-based materials are treated as multiphase porous media; hence, for analysing the stress state and the deformation of the material, it is necessary to consider not only the action of an external load, but also the pressure exerted on the skeleton by fluids present in its voids. Hence, the total stress tensor $\boldsymbol{\sigma}^{total}$ acting in a point of the porous medium may be split into the effective stress $\varepsilon_s \boldsymbol{\tau}_s$, which accounts for stress effects due to changes in porosity, spatial variation of porosity and the deformations of the solid matrix, and a part accounting for the solid phase pressure exerted by the pore fluids (Pesavento et al. 2008; Gray et al. 2009)

$$\boldsymbol{\sigma}^{total} = \varepsilon_s \boldsymbol{\tau}_s - b_H p_s \mathbf{I}, \tag{7.53}$$

where $\mathbf{I}$ is the second-order unit tensor, b_H is the Biot coefficient, and p_s is some measure of solid pressure acting in the system, i.e. the normal force exerted on the solid surface of the pores by the surrounding fluids.

Taking into account several simplifications (Pesavento et al. 2008; Gray et al. 2009), the relationship describing the effective stress principle can be written in the following manner:

$$\varepsilon_s \boldsymbol{\tau}_s = \boldsymbol{\sigma}^{total} + P_s \mathbf{I} = \boldsymbol{\sigma}^{total} + \left(p_g - x_s^{ws} p_c\right)\mathbf{I} \tag{7.54}$$

where x_s^{ws} is the fraction of skeleton area in contact with the water and P_s is an alternative measure of the "solid pressure". The effective stress principle in the form of Eq. 7.54 allows to consider not only the capillary effects but also the disjoining pressure (Gawin et al. 2004; Pesavento et al. 2008; Gray et al. 2009).

7.4.4.3 Strain Decomposition

As already mentioned in Sect. 7.4.1.3, different strain components can be identified in a maturing element of concrete, both at early ages or at long term. Accordingly, the overall measured strain tensor $\boldsymbol{\varepsilon}$ may conventionally be split as following (Gawin et al 2004):

$$\boldsymbol{\varepsilon} = \boldsymbol{\varepsilon}_{el} + \boldsymbol{\varepsilon}_f + \boldsymbol{\varepsilon}_T + \boldsymbol{\varepsilon}_{chem} + \boldsymbol{\varepsilon}_{sh} + \boldsymbol{\varepsilon}_{cr} + \cdots \tag{7.55}$$

where $\boldsymbol{\varepsilon}_{el}$ is the elastic strain, $\boldsymbol{\varepsilon}_f$ is the cracking induced strain, $\boldsymbol{\varepsilon}_T$ is the thermal strain, $\boldsymbol{\varepsilon}_{chem}$ is the chemical strain (i.e. due to the hydration), $\boldsymbol{\varepsilon}_{cr}$ is the creep strain which can be split into two parts: basic creep and drying creep.

In the following, some of these strain components will be analysed and discussed in view of a specific formulation of a mechanical constitutive model, also taking into account what has been presented in Chaps. 3 and 4.

7.4.4.4 An Example of a Mechanical Constitutive Model for Concrete

Concrete is modelled as a visco-elastic damageable material, whose mechanical properties depend on the hydration degree (De Schutter and Taerwe 1996). The relationship between apparent stresses $\boldsymbol{\sigma}^{total}$, effective stresses $\tilde{\boldsymbol{\sigma}}$ (in the sense of damage mechanics), damage D, elastic stiffness matrix $\mathbf{E}$, elastic strains $\boldsymbol{\varepsilon}_{el}$, creep strains $\boldsymbol{\varepsilon}_{cr}$, shrinkage strains $\boldsymbol{\varepsilon}_{sh}$ (caused by the fluid pressures as shortly described in Sect. 7.4.4.2), thermal strains- $\boldsymbol{\varepsilon}_T$ and total strains $\boldsymbol{\varepsilon}$ reads:

$$\boldsymbol{\sigma}^{total} = (1 - D)\tilde{\boldsymbol{\sigma}} \tag{7.56}$$

$$\dot{\tilde{\boldsymbol{\sigma}}} = \mathbf{E}_{(\alpha)}\dot{\boldsymbol{\varepsilon}}_{el} = \mathbf{E}_{(\alpha)}(\dot{\boldsymbol{\varepsilon}} - \dot{\boldsymbol{\varepsilon}}_{cr} - \dot{\boldsymbol{\varepsilon}}_T - \dot{\boldsymbol{\varepsilon}}_{sh}) \tag{7.57}$$

Young's modulus E, the tensile strength f_t and the Poisson's ratio v vary due to hydration according to the equations proposed by De Schutter and Taerwe (1996) and De Schutter (2002).

Creep strain is computed using a rheological model made of a Kelvin-Voigt chain and two dashpots combined in serial way (see Fig. 7.21). The first two cells (aging Kelvin-Voigt chain and one single dashpot) are used to compute the basic creep, and the last cell (single dashpot) is dedicated to the drying creep strain. The scalar model in Fig. 7.21 is extended in 3D through the definition of a creep Poisson's ratio (Sciumè et al. 2013).

The thermal strain $\boldsymbol{\varepsilon}_{th}$ is related to the temperature variation:

$$\dot{\boldsymbol{\varepsilon}}_T = \beta_s \dot{T}\mathbf{1} \tag{7.58}$$

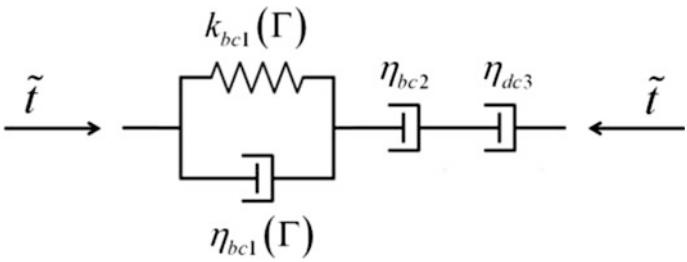

Fig. 7.21 Creep rheological model

in which β_s is the thermal dilatation coefficient (kept constant) and $\mathbf{1}$ is the unit tensor.

To compute shrinkage, the elastic and the viscous parts have to be considered:

$$\boldsymbol{\varepsilon}_{sh} = \boldsymbol{\varepsilon}_{sh}^{inst} + \boldsymbol{\varepsilon}_{sh}^{visc} \tag{7.59}$$

taking into account the solid pressure (see Eqs. 7.53–7.54), the constitutive model to compute the elastic shrinkage reads

$$\dot{\boldsymbol{\varepsilon}}_{sh}^{inst} = -\frac{\mathbf{1}}{3K_T}\frac{\partial(b_H p^s)}{\partial t} \tag{7.60}$$

where K_T is the bulk modulus of the solid skeleton and b_H is the Biot modulus. The viscous part of shrinkage strain, $\dot{\boldsymbol{\varepsilon}}_{sh}^{visc}$, is computed using the creep rheological model (represented in Fig. 7.21) in which the stress is now $\dot{\boldsymbol{\varepsilon}}_{sh}^{visc}$.

Damage D is linked to the elastic equivalent tensile strain, $\hat{\varepsilon}$. To take into account the coupling between creep and cracking, the expression of $\hat{\varepsilon}$ proposed by Mazars (1986) is modified by Mazzotti and Savoia (2003) and reads:

$$\hat{e} = \sqrt{\langle \boldsymbol{\varepsilon}_{el} \rangle_+ : \langle \boldsymbol{\varepsilon}_{el} \rangle_+ + \beta \langle \boldsymbol{\varepsilon}_{cr} \rangle_+ : \langle \boldsymbol{\varepsilon}_{cr} \rangle_+} \tag{7.61}$$

where β is a coefficient calibrated experimentally, which allows for considering that often cracking may occur even at lower tensile stress than the expected tensile strength. The damage criterion is given by:

$$f = \hat{e} - \kappa_0(\alpha) \tag{7.62}$$

where $\kappa_0(\alpha)$ is the tensile strain threshold, which is computed from the evolution of tensile strength, and the Young's modulus (De Schutter and Taerwe 1996). Considering the equivalent tensile strain, $\hat{\varepsilon}$, and with respect to criterion Eq. 7.62 D is given by the equations proposed by Benboudjema and Torrenti (2008); the adopted damage model allows taking into account also evolution of fracture energy during hydration (De Schutter and Taerwe 1997).

To overcome the mesh dependency related to the local damage formulation, the model is regularised in tension with the introduction of a characteristic length related to the size of each finite element (Rots 1988; Cervera and Chiumenti 2006).

7.4.5 Boundary Conditions

With the momentum balance equation, the set of governing equations is complete, Eqs. 7.30, 7.31, 7.33 and 7.50. For the model closure, we need the initial and boundary conditions. The initial conditions (ICs) specify the values of primary state

variables at time instant $t = 0$ in the whole analysed domain Ω and on its boundary Γ, ($\Gamma = \Gamma_\pi\ \Gamma_\pi \cup \Gamma_\pi^q$; π = g, c, t, u):

$$p_g = p_{go},\ p_c = p_{co},\ T = T_o,\ \mathbf{u} = \mathbf{u}_o, \quad \text{on } (\Omega \cup \Gamma), \tag{7.63}$$

The boundary conditions (BCs) describe the values of the primary state variables at time instants $t > 0$ (Dirichlet's BCs) on the boundary Γ_π:

$$\begin{aligned} p_g(t) &= \bar{p}_g(t) \text{ on } \Gamma_g, \\ p_c(t) &= \bar{p}_c(t) \text{ on } \Gamma_c, \\ T(t) &= \bar{T}(t) \text{ on } \Gamma_t, \\ \mathbf{u}(t) &= \bar{\mathbf{u}}(t) \text{ on } \Gamma_u, \end{aligned} \tag{7.64}$$

or heat and mass exchange, and mechanical equilibrium condition on the boundary Γ_π^q (the BCs of Cauchy's type or the mixed BCs):

$$\begin{array}{ll} \left(n S_g \rho_a \mathbf{v}^{gs} + \mathbf{J}_d^a\right) \cdot \mathbf{n} = q^a, & \text{on } \Gamma_g^q \\ \left(n S_w \rho_w \mathbf{v}^{ws} + n S_g \rho_v \mathbf{v}^{gs} + \mathbf{J}_d^v\right) \cdot \mathbf{n} = q^v + q^w + \beta_c\left(\rho_v - \rho_{v\infty}\right), & \text{on } \Gamma_c^q \\ \left(n S_w \rho_w \mathbf{v}^{ws} \Delta H_{vap} + \tilde{\mathbf{q}}\right) \cdot \mathbf{n} = q^T + \alpha_c (T - T_\infty) + e\,\sigma_o\left(T^4 - T_\infty^4\right), & \text{on } \Gamma_T^q \\ \left[\varepsilon_s \boldsymbol{\tau}_s - \left(p_g - x_s^{ws} p_c\right)\mathbf{I}\right] \cdot \mathbf{n} = \bar{\boldsymbol{\sigma}}, & \text{on } \Gamma_u^q \end{array} \tag{7.65}$$

where $\mathbf{n}$ is the unit normal vector, pointing towards the surrounding gas, q^a, q^v, q^w and q^T are respectively the imposed fluxes of dry air, vapour, liquid water and the imposed heat flux, and $\bar{\boldsymbol{\sigma}}$ is the imposed traction, $\rho_{v\infty}$ and T_∞ are the mass concentration of water vapour and the temperature in the far field of undisturbed gas phase, e is emissivity of the interface, and σ_o the Stefan–Boltzmann constant, while α_c and β_c are convective heat and mass exchange coefficients.

The boundary conditions, with only imposed fluxes given, are called Neumann's BCs. The purely convective boundary conditions for heat and moisture exchange are also called Robin's BCs.

7.4.6 Numerical Formulation

The set of nonlinear partial differential equations that controls the processes of mass and heat transport (Eqs. 7.30 and 7.31) plus the one Eq. 7.33 is usually discretised in the space domain by means of Finite Element Method. Also Equation 7.50 is usually discretised in the space domain by means of Finite Element Method.

According to the FEM procedure, the governing equations are written by using the weighted residual method, and the standard Galerkin procedure is usually adopted. Time discretisation is achieved by means of the standard Finite Difference Method. A non-symmetric, nonlinear system is finally obtained, and linearisation,

usually by means of the Newton–Raphson method, is required (Zienkiewicz and Taylor 2000).

The final set of discretised, linearised governing equations is solved as a monolithic system or, alternatively, by means of a staggered coupled procedure (see Gawin et al. 2003, 2006a, b, 2008; Sciumè et al. 2013).

Starting from the previous initial-boundary value problem, the variational formulation can be obtained. Then, the standard Galerkin discretisation, replacing the weighting functions with the shape functions, is adopted. For the state variables, we can write:

$$\begin{aligned} p_g(t) &\cong \mathbf{N}_p\,\overline{\mathbf{p}}_g(t), \qquad & p_c(t) &\cong \mathbf{N}_p\,\overline{\mathbf{p}}_c(t), \\ T(t) &\cong \mathbf{N}_t\,\overline{\mathbf{T}}(t), \qquad & \mathbf{u}(t) &\cong \mathbf{N}_u\,\overline{\mathbf{u}}(t). \end{aligned} \tag{7.66}$$

The resulting system of equations can be written in the following concise discretised matrix form:

$$\mathbf{C}_{ij}(\mathbf{x}_j)\frac{\partial \overline{\mathbf{x}}_j}{\partial t} + \mathbf{K}_{ij}(\mathbf{x}_j)\overline{\mathbf{x}}_j = \mathbf{f}_i(\mathbf{x}_j), \tag{7.67}$$

with

$$\begin{aligned} \mathbf{C}_{ij} &= \begin{bmatrix} \mathbf{C}_{gg} & \mathbf{C}_{gc} & \mathbf{C}_{gt} & \mathbf{C}_{gu} \\ \mathbf{0} & \mathbf{C}_{cc} & \mathbf{C}_{ct} & \mathbf{C}_{cu} \\ \mathbf{0} & \mathbf{C}_{tc} & \mathbf{C}_{tt} & \mathbf{C}_{tu} \\ \mathbf{0} & \mathbf{0} & \mathbf{0} & \mathbf{0} \end{bmatrix}, \quad \overline{\mathbf{x}}_j = \begin{Bmatrix} \overline{\mathbf{p}}^g \\ \overline{\mathbf{p}}^c \\ \overline{\mathbf{T}} \\ \overline{\mathbf{u}} \end{Bmatrix}, \\ \mathbf{K}_{ij} &= \begin{bmatrix} \mathbf{K}_{gg} & \mathbf{K}_{gc} & \mathbf{K}_{gt} & \mathbf{0} \\ \mathbf{K}_{cg} & \mathbf{K}_{cc} & \mathbf{K}_{ct} & \mathbf{0} \\ \mathbf{K}_{tg} & \mathbf{K}_{tc} & \mathbf{K}_{tt} & \mathbf{0} \\ \mathbf{K}_{ug} & \mathbf{K}_{uc} & \mathbf{K}_{ut} & \mathbf{K}_{uu} \end{bmatrix}, \quad \mathbf{f}_i = \begin{Bmatrix} \mathbf{f}_g \\ \mathbf{f}_c \\ \mathbf{f}_t \\ \mathbf{f}_u \end{Bmatrix}, \end{aligned} \tag{7.68}$$

where the nonlinear matrix coefficients $\mathbf{C}_{ij}(\mathbf{x}_j)$, $\mathbf{K}_{ij}(\mathbf{x}_j)$ and $(\mathbf{x}_j)$ are defined in detail in Pesavento (2000), Gawin et al. (2003, 2006a, b).

The time discretisation is accomplished through a fully implicit finite difference scheme (backward difference):

$$\boldsymbol{\Psi}_i\left(\overline{\mathbf{x}}_{n+1}\right) = \mathbf{C}_{ij}\left(\mathbf{x}_{n+1}\right)\frac{\overline{\mathbf{x}}_{n+1} - \overline{\mathbf{x}}_n}{\Delta t} + \mathbf{K}_{ij}\left(\mathbf{x}_{n+1}\right)\overline{\mathbf{x}}_{n+1} - \mathbf{f}_i\left(\mathbf{x}_{n+1}\right) = \mathbf{0}, \tag{7.69}$$

where superscript i ($i = g, c, t, u$) denotes the state variable, n is the time step number, and Δt is the time step length.

The equation set (7.69) can be linearised according to the following scheme:

$$\boldsymbol{\Psi}_i\left(\overline{\mathbf{x}}_{n+1}^{k}\right) = -\left.\frac{\partial \boldsymbol{\Psi}_i}{\partial \mathbf{x}}\right|_{\overline{\mathbf{x}}_{n+1}^{k}} \Delta\overline{\mathbf{x}}_{n+1}^{k}, \quad \overline{\mathbf{x}}_{n+1}^{k+1} = \overline{\mathbf{x}}_{n+1}^{k} + \Delta\overline{\mathbf{x}}_{n+1}^{k}, \tag{7.70}$$

where k is the iteration index and $\frac{\partial \boldsymbol{\Psi}_i}{\partial \mathbf{x}}$ is Jacobian matrix.

More details concerning numerical techniques used for solution of the model equations can be found in Pesavento (2000) Gawin et al. (2003, 2006a, b, 2008, 2009).

7.4.6.1 Solution Strategy

A monolithic approach is often adopted for solution of the linearised system. In this approach, all the equations are solved at the same time and all the state variables are updated simultaneously during the iterative procedure. This approach guarantees the optimal convergence of the system especially when dealing with strong non-linearities (Pesavento 2000; Gawin et al. 2003; Bianco et al. 2003).

Alternatively, the system can be solved using a staggered procedure that permits to solve the equations sequentially (Sciumè et al. 2013). A specific iterative algorithm to account for the interaction between all the transfer processes to conserve their full coupling is required. Staggered procedures show a superior flexibility compared to monolithic ones if successive fields have to be introduced in the problem. Moreover, an appropriate partitioning reduces the size of the discretised problem to be solved at each time step. For further details, see Sciumè et al. (2013).

7.4.7 Application of the Proposed Approach

In this section, two application cases are presented. The mechanical constitutive law used for this purpose is the one described in Sects. 7.4.2 and 7.4.4. For sake of brevity tables with the assumed parameters that are not reported here, can be found in the referred papers.

7.4.7.1 Cracking of a Reinforced Concrete Beam Under Variable Environmental Condition

As typical application of the approach based on TCAT and validation of the resulting model, the results of the numerical simulation of cracking of a massive concrete beam are shown. The analysed test is a large beam specimen built for ConCrack (2011): the international Benchmark for Control of Cracking in Reinforced Concrete Structures (Fig. 7.22). This benchmark has been organised within the French national project CEOS (*Comportement et Evaluation des*

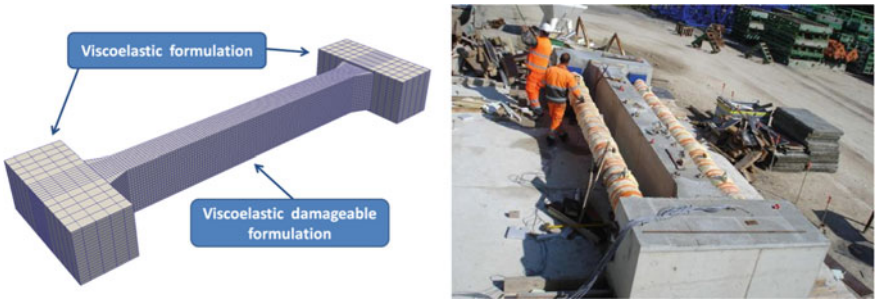

Fig. 7.22 Experimental specimen (right) and finite elements mesh (left)

Ouvrages Speciaux vis-à-vis de la fissuration et du retrait) dedicated to the analysis of the behaviour of special large specimens concerning cracking and shrinkage.

Here, one of the experiments of the benchmark programme and its numerical simulation are presented. The test is divided in two phases. During the first 48 h after casting, the structure is thermally isolated and protected from drying. Then, after two days the isolation and the formwork are removed and the structure is conserved during two months in the open environment. During the two phases of the test, the longitudinal strains of the structure are globally restrained by two metallic struts. After two months, the structure is loaded by a static bending test. For more details on the analysed test, see the reference Web page of the benchmark (https://www.concrack.org). The mesh of concrete is made of 3D elements (Fig. 7.22, left). Truss elements rigidly linked with the concrete 3D mesh are used to model the struts. The local damage model of Mazars (1986) has been used. This approach allows predicting cracking in mode I (De Sa et al. 2008; De Sa and Benboudjema 2012) which is the case here, since cracking is induced by shrinkage restraint. The model is regularised in tension with the introduction of a characteristic length, l_c, related to the size of each finite element (Rots 1988; Cervera and Chiumenti 2006) to overcome the possible mesh dependency. The model for concrete at early age is that of Sciumè et al. (2013).

The boundary conditions are assumed to be of convective type for both heat and mass exchange, see Simoni and Schrefler (2014) for details. For the material parameters, see Sciumè et al. (2012).

During the first and second phases, the longitudinal displacements of the specimen have been globally restrained by the two metallic struts. Therefore, during hydration the thermal extension of the concrete has been restrained and so in this phase the concrete cross section was compressed. After the hydration, it is the shrinkage of the beam that has been contrasted. The position of the displacement measurement points are depicted in Fig. 7.23 and the deformed configuration and the damage at day 60 in Fig. 7.24. The solution is not symmetric due to the non-symmetric solar irradiation: this has been experimentally measured by the benchmark organizers and taken into account in the modelling process.

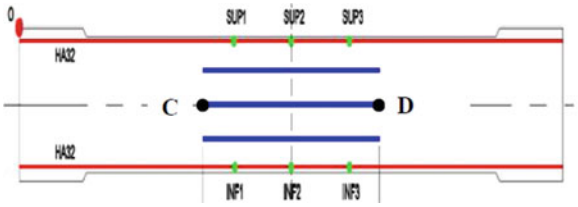

	x (m)	y (m)	z (m)
C	1.26	2.6	0.49
D	1.26	5.1	0.49

Fig. 7.23 Position of the displacement measurement points (and coordinates)

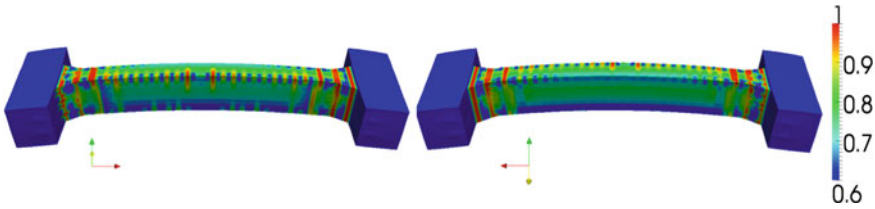

Fig. 7.24 Deformed configuration (× 500) and damage after 60 days. Face exposed to the sun (left) and face not exposed to the sun (right)

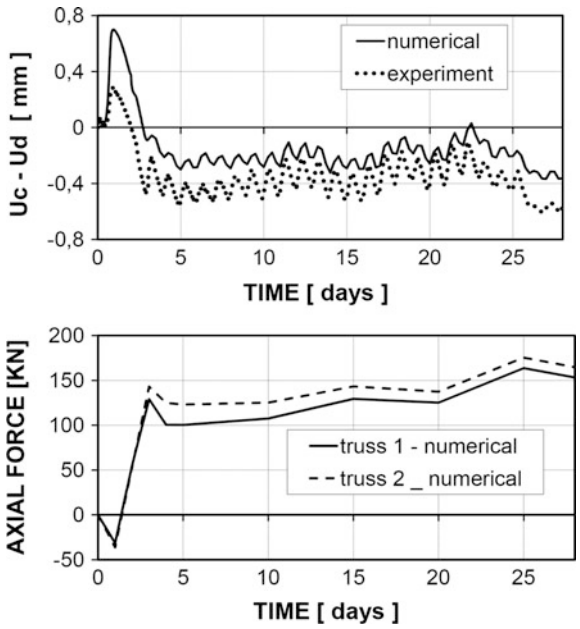

Fig. 7.25 Relative displacement between the point C and D (left). Axial force in the two metallic struts that restrain shrinkage (right)

The comparison between the experimentally and numerically obtained relative displacements and axial force is shown in Fig. 7.25. Note the complex displacement evolution.

After two months, a static four-point bending test has been carried out until rupture. Compression has been applied by eight jacks and live controlled by a pressure sensor with an independent data registration system. The load was applied with increments of 50 kN, and each loading step is kept during 20 min. The comparison between the experimental and numerical crack pattern and the force versus displacement diagram is shown in Fig. 7.26. The comparison in Figs. 7.25 and 7.26 with experimental results shows that the adopted approach is able to simulate such complicated multifield fracture phenomena in realistic engineering structures. For more results concerning hydration and thermal field, the reader is referred to the Website of ConCrack (2011) and the final report.

7.4.7.2 Modelling of Repaired Beam

The numerical simulation of the thermo-hygro-mechanical behaviour of two repaired beams is presented in this subsection (see Sciumè et al. 2013). Numerical results are compared with the experimental ones of the reference experiment performed by Bastien Masse (2010).

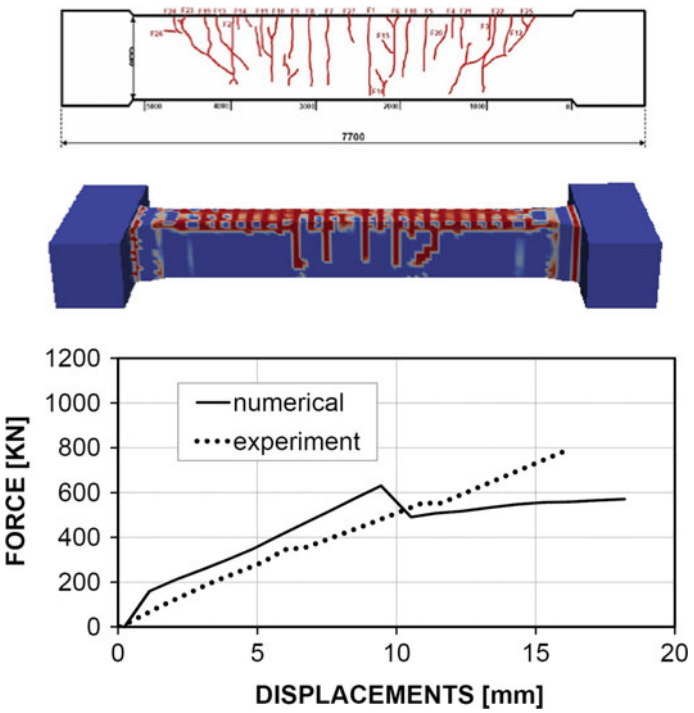

Fig. 7.26 Comparison between the numerical and experimental crack pattern (left). Force versus displacements during the bending test (right)

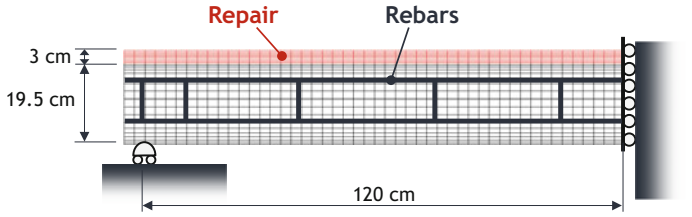

Fig. 7.27 Geometry and FE mesh of the repaired beam

The geometry of the reinforced beams is represented in Fig. 7.27. Three identical reinforced beams were cast for the experiment. At thirty days after the casting, two of these beams, after the hydrodemolition of 30 mm of the upper part, had been repaired: one using the ordinary concrete (OC) (very similar to that using to cast the three beams) and the other using the ultra-high-performance fibre-reinforced concrete (UHPC). The third beam is the reference specimen. Two fibre-optic sensors (FO-h and FO-b) were placed inside the beams. More details on the experimental procedure (laboratory conditions, specimen equipment, etc.) can be found in Bastien Masse (2010).

The beams have been modelled in 2D plane stress; for more information about the assumed boundary conditions and the FE discretization, refer to Sciumè et al. (2013).

Is important to highlight that the THCM history of the two beams before the repair and the wetting procedure for the preparation of the substrate have been also taken into account within the modelling process (the numerical simulations start from the casting of the beams), and this has been critical to succeed in predictive numerical results.

Before performing the simulation of the beams, the input parameters for the two considered concretes have been identified. This has been done exploiting experiments performed by Bastien Masse (2010) for the characterisation of the two repair materials. Comparison between experimental results and numerical ones for adiabatic calorimetry, creep properties, Young's modulus and Poisson's ration evolution, autogenous and drying shrinkage is shown in Fig. 7.28.

In Fig. 7.29, for the two repair cases, relative humidity at 1 h, 1 week and 1 month after repair is depicted. In the UHPC, self-desiccation has also a relevant impact on the decrease of relative humidity.

Figure 7.30 shows the numerical and the experimental results for the vertical displacement of the three beams measured using the linear potentiometer placed in the lower middle point of the beams. A good agreement between the experimental results and the numerical ones can be observed. The deflection of the reference beam is mainly due to its weight and also to the not symmetric position of the steel reinforcements: in other words the shrinkage of the upper and lower part of the beam generates an eccentric force which increases the deflection of the beam. In the repaired beams, the deflections are accentuated by the autogenous and drying shrinkage of the fresh restoration materials.

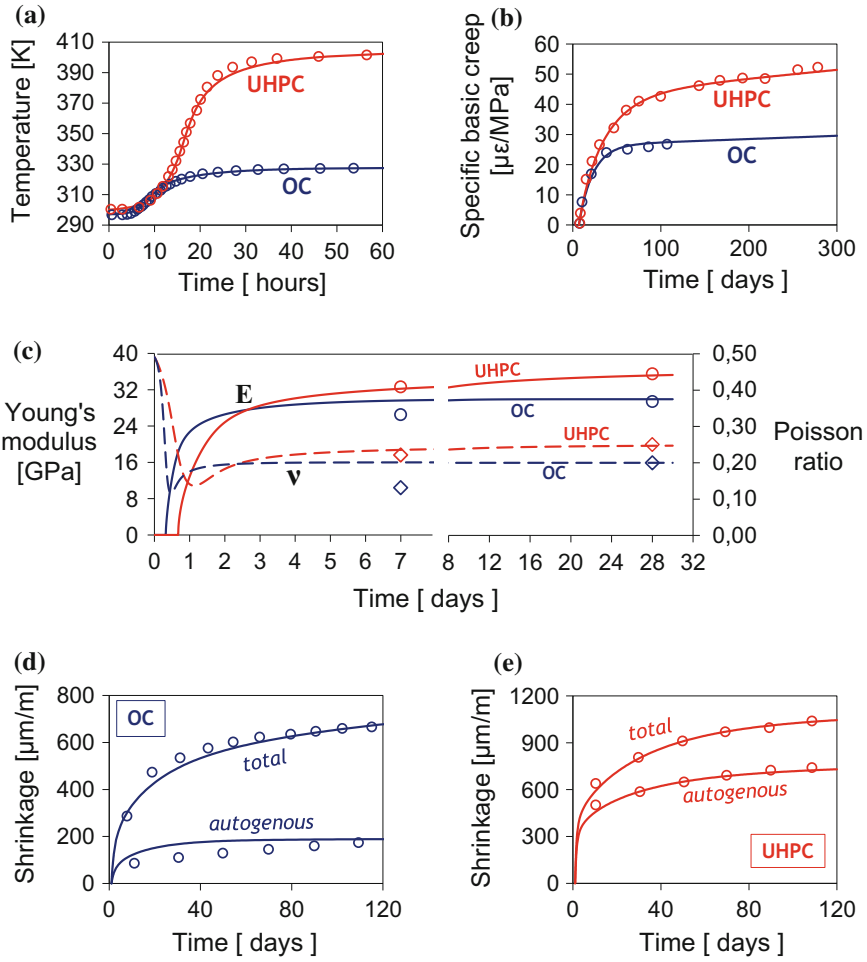

Fig. 7.28 Experimental tests exploited to identify the model parameters: **a** adiabatic calorimetry, **b** creep test, **c** Young's modulus and Poisson's ration evolution, **d** autogenous and drying shrinkage for OC, **e** autogenous and drying shrinkage for UHPC. Symbols are experimental data, while solid and dashed lines are numerical results. (Adapted from Sciumé et al. 2013)

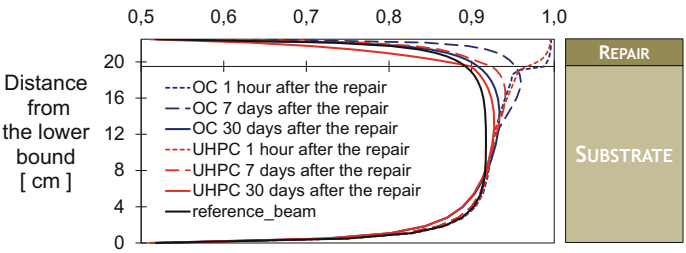

Fig. 7.29 Relative humidity at 1 h, 1 week and 1 month after repair for the two simulated cases. (Adapted from Sciumé et al. 2013)

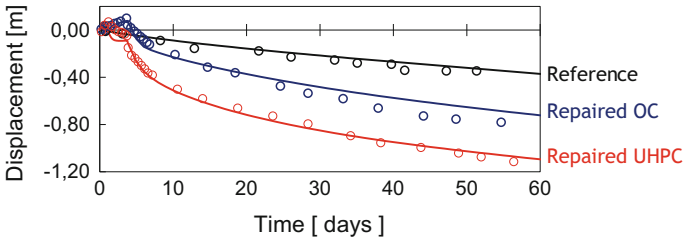

Fig. 7.30 Experimental (open symbols) and numerical results (solid lines) for the vertical displacement of the middle points of the three beams. The time "zero" corresponds to the application of the repairs. (Adapted from Sciumé et al. 2013)

After 2 months, the two repaired beams have been submitted to a three-point bending test, and also in this case, the presented model has shown good accuracy in predicting experimental results (Sciumè et al. 2013).

7.5 Constitutive Laws for Crack Evolution

Damage of concrete is connected with formation of discrete cracks. The study of damage in which damage is modelled in a discrete manner is the interest of fracture mechanics. Discrete crack models perform well in representation of structural behaviour governed by a few dominant cracks with large crack widths and which location and direction of propagation can be known a priori, and as such are suitable for modelling of laboratory tests. More often damage of concrete due to crack formation is represented with smeared models of cracking. Smeared crack models are good for representation of typical, properly designed reinforced concrete structures characterised by many cracks of small widths. The cracked material is treated as continuum, and its cracked parts are assigned with modified properties. Usually, it is assumed that the cracked element can no longer transfer the load in the direction perpendicular to the crack plane (tensile stresses) but can still transfer the parallel (shear) stresses (Hofstetter and Mang 1995).

7.5.1 Damage Models

The failure of concrete is connected with formation of a crack under certain level of stress. Formation of the crack is a local phenomenon; however, homogenisation techniques can be used to transform a cracked element into a continuum medium and apply non-local damage models. Continuous damage models are based on phenomenological approach to description of an elastic material containing cracks, in which the effect of microcracking on the elastic stiffness of concrete

(a quasi-brittle material) is introduced with internal state variables which act on the elastic stiffness of the material (Pijaudier-Cabot 1995). In the simplest damage model, the effect of damage is represented as degradation of the modulus of elasticity of concrete:

$$\sigma_{ij} = E_{ijkl}^{damaged} \varepsilon_{kl} \tag{7.71}$$

where σ_{ij} is the stress component, ε_{kl} is the strain component, and $E_{ijkl}^{damaged}$ is the stiffness coefficient of the damaged material. Ladevèze (1983) has introduced a model which contains two damage variables d and δ, which are equal to 0 in undamaged material and reach 1 at complete failure. By assuming $d = \delta$, Mazars (1984) has proposed a simplified formulation of this model which reads:

$$\varepsilon_{ij} = \frac{1 + \nu_0}{E_0(1-d)} \sigma_{ij} - \frac{\nu_0}{E_0(1-d)} \left[\sigma_{kk} \delta_{ij}\right] \tag{7.72}$$

where E_0 and ν_0 are elastic modulus and Poisson's ratio of undamaged isotropic material and δ_{ij} is a Kronecker delta.

Most commonly used non-local damage models are scalar isotropic models, which introduce a scalar variable to represent damage. Nevertheless, there are formulations based on plasticity models (see, e.g. Leblond et al. 1992) or anisotropic damage models (see, e.g. Pijaudier-Cabot et al. 1994; Valanis 1991).

Damage can be controlled by either energy release rate or by tensile strain. In the first approach, there is no distinction between the effect of damage in compression and tension, while the other model does not have such limitations; thus, it is more suitable for modelling of concrete. However, since the level of the compressive stresses induced by the early-age effects is relatively small in the discussed massive concrete structures, many authors apply damage criteria which account for material degradation only in tension. For that purpose, stress–strain relationship with strain softening in tension is used (such relationships were proposed, e.g., by Bažant and Oh (1983) or Gutsch and Rostásy (1994)). These models involve tensile strength of concrete, f_t, and fracture energy, G_f.

The most popular strain-based damage model was introduced by Mazars (1984) and developed by Mazars and Bournazel (1996) for the purpose of modelling early-age concrete, modified and presented in its latest form by Benboudjema and Torrenti (2008). The damage criterion which determines the formation of cracking is defined as:

$$f = \underline{\varepsilon} - \varepsilon_{ctu}(\alpha) \tag{7.73}$$

where $\underline{\varepsilon}$ is the equivalent tensile strain and $\varepsilon_{ctu}(\alpha)$ is the tensile strain capacity defined as a ratio between the tensile strength, $f_t(\alpha)$, and the modulus of elasticity, $E(\alpha)$, at the time of analysis, t, expressed as a function of degree of hydration, $\alpha(t)$:

$$\varepsilon_{ctu}(\alpha) = \frac{f_t(\alpha)}{E(\alpha)} \tag{7.74}$$

After the threshold strain is exceeded $\underline{\varepsilon} > \varepsilon_{ctu}(\alpha)$, cracking appears. It is assumed that part of the element is sound and part of the element is cracked; only the sound part of the element can transfer the stress, which is the effective stress, $\underline{\sigma}$:

$$\underline{\sigma} = E\underline{\varepsilon} \tag{7.75}$$

The influence of progressing cracking on stress, σ, is expressed with the damage, D, and effective stress $\underline{\sigma}$:

$$\sigma = (1 - D)\underline{\sigma} \tag{7.76}$$

The damage, D, describing the softening behaviour of concrete in tension is given by the formula:

$$D = 1 - \frac{\varepsilon_{ctu}}{\underline{\varepsilon}}[(1 + A_t)exp(-B_t t) - A_t exp(-2B_t t)] \tag{7.77}$$

where A_t and B_t are material parameters defining softening branch of $\sigma - \varepsilon$ diagram.

When modelling softening of concrete as damage progresses, it must be remembered that the results of numerical analysis are strongly mesh-dependent (Azenha et al. 2009, 2011; Benboudjema and Torrenti 2008; Jendele et al. 2014). It is advised to discretise the analysed structure based on the density of the fracture energy, G_f, and internal length, l_c (Hillerborg et al. 1976). The internal length bridges the gap between damage and fracture mechanics as the fracture energy is a function of this length (Pijaudier-Cabot 1995).

In order to apply damage models, two characteristics of the material need to be defined (Pijaudier-Cabot 1995): softening stress–strain curve and internal length of the non-local continuum. These characteristics can be obtained either experimentally or with the inverse analysis (FEM calculations on simple structural elements).

7.5.2 Plasticity Models

Other approach to modelling early-age concrete is based on plasticity models, defined for three-dimensional complex stress states in which damage of the element —its occurrence and character—is defined by a failure criterion. Failure criterion can be graphically represented by a spatial surface, called failure surface. Behaviour of concrete element after reaching failure surface is defined by the appropriate material model, as is its behaviour before damage.

In modelling early-age concrete, the simplest material model is viscoelastic model, which extensions led to definition of other models based on plasticity,

i.e. viscoelastic–plastic, elasto-viscoplastic and viscoelasto-viscoplastic models. A concise presentation and comparison of these models were presented by Klemczak (2007). In the viscoelastic model, the stress–strain relationship has a form:

$$\Delta\boldsymbol{\sigma}(t_{i+1}) = \mathbf{D}^{\mathrm{ve}}(t_{i+1})[\Delta\boldsymbol{\varepsilon}(t_{i+1}) - \Delta\boldsymbol{\varepsilon}_{\mathrm{n}}(t_{i+1}) - \Delta\boldsymbol{\varepsilon}_{\mathrm{cr}}(t_{i+1})] \tag{7.78}$$

where notation $\Delta\varepsilon_{\mathrm{cr}}$ $(t_{\mathrm{i+1}})$ is given by the formula:

$$\begin{aligned}\Delta\boldsymbol{\varepsilon}_{\mathrm{cr}}(t_{i+1}) = \mathbf{D}^{-1}\Bigg[&\int_0^{t_i} \frac{-\partial C(t_{i+1},\tau)}{\partial\tau}\boldsymbol{\sigma}(\tau)d\tau + \boldsymbol{\sigma}(t_i)\int_0^{t_{i+1}} \frac{-\partial C(t_{i+1},\tau)}{\partial\tau}d\tau \\ &- \int_0^{t_i} \frac{-\partial C(t_i,\tau)}{\partial\tau}\boldsymbol{\sigma}(\tau)d\tau\Bigg]\end{aligned} \tag{7.79}$$

$\mathbf{D}^{\mathrm{ve}}$ is a viscoelasticity matrix:

$$\mathbf{D}^{\mathrm{ve}}(t_{i+1}) = \frac{\mathbf{D}^{\mathrm{e}}(t_{i+1})}{1 + 0.5E(t_{i+1})[(1/E(t_i)) - (1/E(t_{i+1})) + H(t_{i+1},t_i)]} \tag{7.80}$$

where

$$H(t_{i+1},t_i) = \int_{t_i}^{t_{i+1}} \frac{-\partial C(t_{i+1},\tau)}{\partial\tau}d\tau \tag{7.81}$$

in which $C(t,\ \tau)$ is a creep function.

In viscoelastic–plastic model, the strain tensor consists additionally of a plastic strain component:

$$d\boldsymbol{\varepsilon} = d\boldsymbol{\varepsilon}_{\mathrm{e}} + d\boldsymbol{\varepsilon}_{\mathrm{ve}} + d\boldsymbol{\varepsilon}_{\mathrm{p}} + d\boldsymbol{\varepsilon}_{\mathrm{n}} \tag{7.82}$$

The magnitude of plastic strain is determined by the law of plastic flow:

$$d\boldsymbol{\varepsilon}_{\mathrm{p}} = d\lambda\frac{\partial g}{\partial\boldsymbol{\sigma}} \tag{7.83}$$

where $d\lambda$ is a scalar proportionality coefficient and g is the surface of plastic potential, defined in the stress space as:

$$g = g(\boldsymbol{\sigma},\kappa,t) \tag{7.84}$$

The yield surface evolution, which characterises plastic behaviour of concrete, for maturing concrete depends on the plastic parameter $\kappa = \kappa(\varepsilon^p)$ and the age of concrete t:

$$f(\boldsymbol{\sigma}, \kappa, t) = 0 \tag{7.85}$$

The yield surface f represents real physical states; thus, the point representing the current state of stress in the stress space must always remain on the yield surface. This means that each load must correspond to such a change of hardening parameter that the point representing the state of stress is located on the yield surface. This consistency condition may be written as:

$$df(\boldsymbol{\sigma}, \kappa, t) = 0 \tag{7.86}$$

The stress–strain relationship for the viscoelasto-plastic model can be defined as:

$$d\boldsymbol{\sigma} = \mathbf{D}^{\mathrm{ve}}\left[d\boldsymbol{\varepsilon} - d\boldsymbol{\varepsilon}_{\mathrm{n}} - d\boldsymbol{\varepsilon}_{\mathrm{cr}} - d\boldsymbol{\varepsilon}_{\mathrm{p}}\right] \tag{7.87}$$

or in the following form:

$$d\boldsymbol{\sigma} = \mathbf{D}^{\mathrm{vep}}(d\boldsymbol{\varepsilon} - d\boldsymbol{\varepsilon}_{\mathrm{n}}) - \mathbf{A}_1 - \mathbf{A}_2 \tag{7.88}$$

with:

$$\mathbf{D}^{\mathrm{vep}} = \left(\mathbf{D}^{\mathrm{ve}} - \frac{\mathbf{D}^{\mathrm{ve}}\mathbf{m}\mathbf{n}^{\mathrm{T}}\mathbf{D}^{\mathrm{ve}}}{h + \mathbf{n}^{\mathrm{T}}\mathbf{D}^{\mathrm{ve}}\mathbf{m}}\right) \tag{7.89}$$

$$\mathbf{A}_1 = \left(\mathbf{D}^{\mathrm{ve}} - \frac{\mathbf{D}^{\mathrm{ve}}\mathbf{m}\mathbf{n}^{\mathrm{T}}\mathbf{D}^{\mathrm{ve}}}{h + \mathbf{n}^{\mathrm{T}}\mathbf{D}^{\mathrm{ve}}\mathbf{m}}\right) d\boldsymbol{\varepsilon}_{\mathrm{cr}} \tag{7.90}$$

$$\mathbf{A}_2 = \frac{\mathbf{D}^{\mathrm{ve}}\mathbf{m}(\partial f/\partial t)dt}{h + \mathbf{n}^{\mathrm{T}}\mathbf{D}^{\mathrm{ve}}\mathbf{m}} \tag{7.91}$$

where $\mathbf{n}$ is a vector normal to the yield surface, $\mathbf{m}$ is a vector normal to the plastic potential surface, and h is the hardening modulus given as:

$$h = -\frac{\partial f}{\partial \kappa}\frac{d\kappa}{d\lambda} \tag{7.92}$$

The failure criterion for a viscoelasto-plastic model is defined as follows:

$$F(\sigma, t) = 0 \tag{7.93}$$

$$dF(\sigma, t) = 0 \tag{7.94}$$

Finally, viscous behaviour of concrete can be considered in the plastic phase, which led to formulation of viscoplastic models. One approach to determination of viscoplastic strains is based on the overstress concept, which states that viscoelastic strain develops only when a stress path goes outside the yield surface. The viscoelastic strain rate is proportional to the excess stress. There are two main proposal of models based on this concept: Perzyna model (Perzyna 1966) and Duvant-Lions model (De Borst et al. 2001). The first model is more general by assuming a function of the excess stress, while in the other one the viscoelastic strain rate is directly proportional to the vector of stress increase above plastic state. It must be, however, emphasised that in both proposals it is possible that stress path goes outside the yield surface; thus, the consistency condition $df = 0$ is not satisfied.

The consistency condition is satisfied in a consistency concept of the viscoplastic model in which the viscoplastic strain is defined as:

$$\dot{\boldsymbol{\varepsilon}}_{\mathrm{vp}} = \dot{\lambda}\frac{\partial f}{\partial \boldsymbol{\sigma}} \tag{7.95}$$

where $\dot{\lambda}$ is a positive scalar called a consistent parameter (De Borst et al. 2001; Winnicki 2001).

Stress–strain relationship can be expressed in the following rate form:

$$\dot{\boldsymbol{\sigma}} = \mathbf{D}^{\mathrm{ve}}\left(\dot{\boldsymbol{\varepsilon}} - \dot{\boldsymbol{\varepsilon}}_{\mathrm{n}} - \dot{\boldsymbol{\varepsilon}}_{\mathrm{cr}} - \dot{\lambda}\mathbf{n}\right)$$

The yield surface and failure surface are expressed as functions of hardening parameter and its rate:

$$f(\boldsymbol{\sigma}, \kappa, \dot{\kappa}) = 0$$

$$F(\boldsymbol{\sigma}, \kappa, \dot{\kappa}) = 0$$

Such formulation satisfies the consistency condition. The age of concrete is implicitly considered in the adopted hardening law $\kappa = \kappa(\varepsilon^{vp}, t)$.

Damage of the element is defined by failure criterion. When defining the failure surface for concrete, it was observed in the experimental tests (Chen 1982; Majewski 2003) that the shape of deviatoric section is close to triangular in the zone of tensile and low-compressive stresses and similar to circular in the zone of high-compressive stresses. The deviatoric section is smooth and convex, but it is not a circle and the surface is not a solid of revolution. The meridians are smooth, convex and curvilinear but for practical ranges can be approximated with straight lines.

There have been multiple proposals for the failure surface to represent the behaviour of concrete under the complex stress state. The single- and double-parameter failure criteria used for description of the failure surface for concrete, such as the Rankine, Mohr–Coulomb and Drucker–Prager failure criteria, are commonly applied for description of the failure surface of concrete (Jendele et al. 2014; Lackner and Mang 2004); however, each of them fails to represent some major

characteristic of the concrete behaviour. Thus, more advanced approaches are used, e.g. three- or five-parameter Willam–Warnke criterion or four-parameter Ottosen criterion. The criteria are expressed either with stress invariants (I_1, J_2 and θ) or by means of the mean and octahedral stress (σ_m, τ_{oct} and θ).

The three-parameter Willam–Warnke criterion provides good representation of concrete behaviour within the range of mean stresses from $4/3f_c$ to $1/3f_t$. However, because of the assumption of linearity of meridians, the strength within bi- and three-axial tensile stresses and three-axial compression is overestimated (Majewski 2003). This shortcoming is removed in Ottosen failure criterion and five-parameter Willam–Warnke criterion where curvilinear meridians are defined. According to the five-parameter Willam–Warnke criterion, deviatoric section is still defined with a triple elliptical shape, but the ratio of the meridians radii is not constant but depends on the level of mean stresses. Meridians are defined with curved lines (second-order

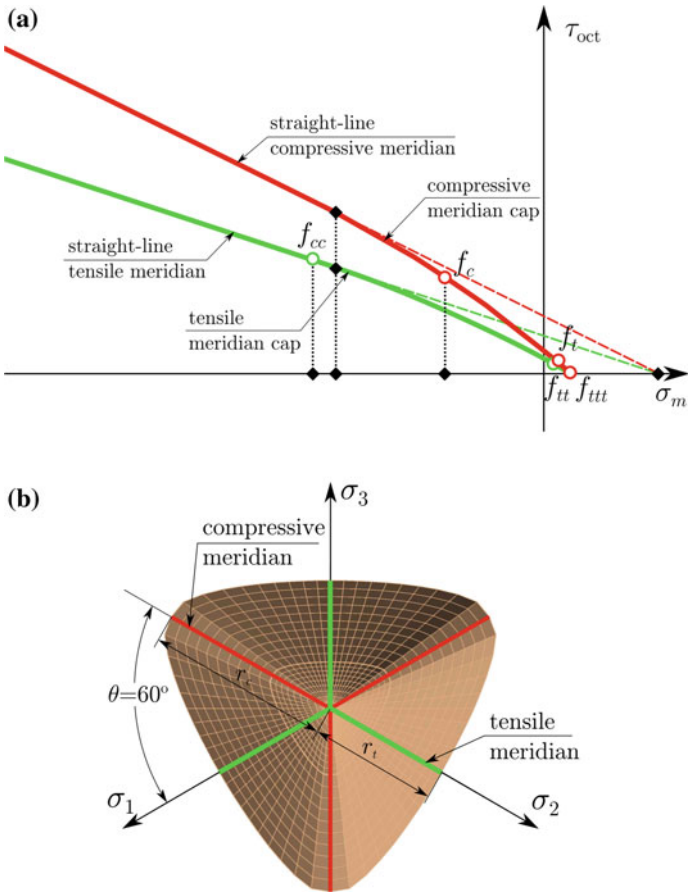

Fig. 7.31 Deviatoric and axiatoric sections of failure surface with the modified three-parameter Willam–Warnke criterion (MWW3, adopted after Majewski 2003)

parabolas) which requires introduction of two additional parameters. Both failure surfaces are "open" in the direction of compressive stresses on the mean stresses axis.

To remove the shortcomings of these criteria and limit the complexity of the model, Majewski proposed a modified three-parameter Willam–Warnke failure criterion (Majewski 2003, 2004). In his approach, meridians are straight lines, but instead of defining meridians in such a way that meridian crosses the points representing the values of appropriate strengths of concrete, the best straight-line approximation was derived. Moreover, to limit the stresses in high-compressive stresses range, a closing cap was defined (tension cutoff) (see Fig. 7.31).

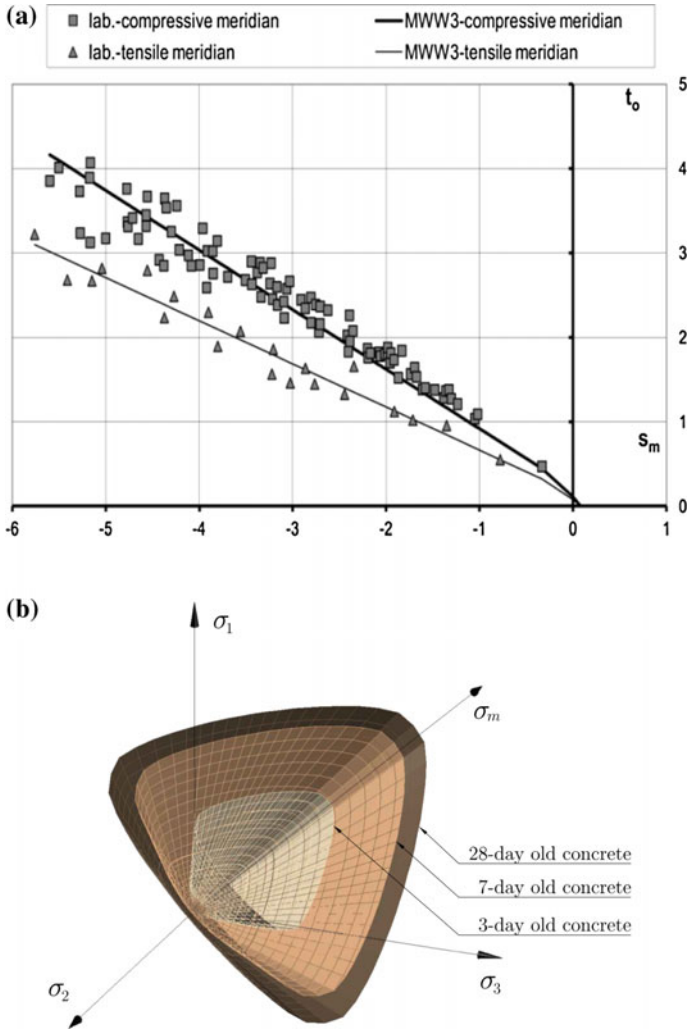

Fig. 7.32 MWW3 failure surface for hardening concrete: **a**. calibration based on experimental results, **b**. development during hardening process. (Adopted after Klemczak 2007)

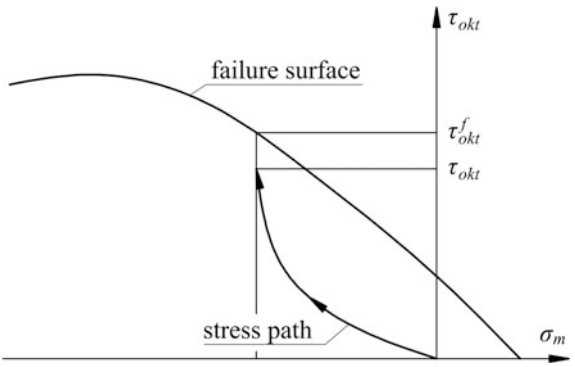

Fig. 7.33 Graphical interpretation of damage intensity factor. (Adopted after Majewski 2003)

Under the same assumptions, the modified Willam–Warnke criterion was adopted by Klemczak (2007) for early-age concrete. MWW3 was calibrated based on the laboratory tests (see Fig. 7.32a). Development of the failure surface was considered as mechanical properties defining the shape of the surface (compressive and tensile strengths) change in time (see Fig. 7.32b).

Damage intensity factor was proposed by Majewski (2003) to determine the level of damage of the element. DIF relates the actual stress level τ_{oct} with respect to the stress at failure surface τ^f_{okt} (Fig. 7.33):

$$DIF = \frac{\tau_{okt}}{\tau^f_{okt}} \tag{7.96}$$

The value of the damage intensity factor equal to unity signifies reaching of failure surface and damage, which character depends on the location where the failure surface was reached. In case of massive concrete structures under early-age effects, failure surface is predominantly reached within hydrostatic tensile stresses, which is equivalent with formation of a splitting crack in the direction perpendicular to the principal tensile stress.

Behaviour of concrete after damage (i.e. reaching failure surface) is governed by the applied softening law. If the stress path reaches the failure surface in the area of mean tensile stress, where failure manifests as a splitting crack, a substantial anisotropy of the concrete appears. Then, when describing material after failure the law of softening and material anisotropy is considered.

7.6 Probabilistic Modelling of Mechanical Behaviour

This section presents some alternative methods to modelling the mechanical behaviour of concrete structures in service life conditions. On the contrary of what was described in Sect. 7.5, in which all the models and constitutive laws have a

deterministic nature, this new class of models is based on a probabilistic approach. They are capable to give a detailed information about cracks spacing and opening.

7.6.1 Probabilistic Explicit and Semi-Explicit Cracking Model for Concrete

7.6.1.1 Probabilistic Explicit Cracking Model

The presented model was first developed at IFSTTAR by Rossi and Richer (1987) and Rossi and Wu (1992) and recently improved by Tailhan et al. (2010). It describes the behaviour of concrete via its two major characteristics: heterogeneity and sensitivity to scale effects (see Rossi et al. 1994). The physical basis of the model (presented in detail in Rossi and Richer 1987; Rossi and Wu 1992) can be summarised as follows:

- The heterogeneity of concrete is due to its composition. The local mechanical characteristics (Young's modulus E_b, tensile strength f_t, shear strength τ_c) are randomly distributed.
- The scale effects are a consequence of the heterogeneity of the material. The mechanical response directly depends on the volume of material that is stressed.
- The cracking process is controlled by defects in the cement paste, by the heterogeneity of the material, and by the development of tensile stress gradients.

The following points specify how the numerical model accounts for these physical evidences:

- The model is developed in the framework of the finite element method, each element representing a given volume of (heterogeneous) material.
- The tensile strength is distributed randomly on all elements of the mesh using a probability distribution function whose characteristics depend on the ratio: volume of the finite element/volume of the largest aggregate and the compressive strength (as a depends on the mesh, while the volume of the largest aggregate is a property of the concrete, see Rossi and Richer 1987; Rossi and Wu 1992; Tailhan et al. 2010).
- The shear strength is also distributed randomly on all elements using a distribution function: (1) its mean value is independent of the mesh size and is assumed equal to the half of the average compressive strength of the concrete, and (2) its deviation depends on the element's size and is the same (for elements of same size) as that of the tensile strength.
- In the explicit cracking model, developed, in priority, to perform 2D simulations, the cracks are explicitly represented by interface elements of zero thickness. These elements connect volume elements representing uncracked plain concrete. Failure criteria of Rankine in tension and Tresca in shear are used. As far as tensile or shear stresses remain lower than their critical values, the

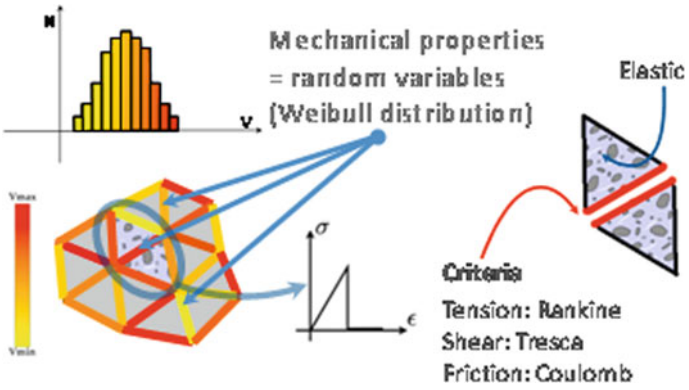

Fig. 7.34 Probabilistic concrete cracking model

interface element ensures the continuity of displacements between the nodes of the two neighbouring volume elements. The material cell gathering these two volume elements and the interface element remains therefore elastic. Once one of the preceding failure criteria is reached, the interface element opens and an elementary crack is created. Its tensile and shear strengths as well as its normal and tangential stiffness values become equal to zero (Rossi and Richer 1987; Rossi and Wu 1992; Tailhan et al. 2010). In case of crack reclosure, the interface element recovers its normal stiffness and follows a classical Coulomb's law (Rossi et al 1996).

Note that in this model, the creation and the propagation of a crack is the result of the creation of elementary failure planes that randomly appear and can coalesce to form the macroscopic cracks (see Fig. 7.34). Note also that, in fact, the finite element volume considered to determinate the tensile strength distribution function is, in the explicit cracking model, the total volume of two volume elements interfaced by one interface element (see Fig. 7.34).

To conclude, it can be said that this probabilistic model is in fact a deterministic one with probabilised parameters. Hence, it is necessary to perform a large number of computations to statistically validate the results following a Monte Carlo method, because only one simulation is not relevant when a probabilistic model is used. The number of numerical simulations needed is related to the structural problem concerned and the scattering of the structural response. In this way, it is easy to perform a safety analysis of the loaded structure.

7.6.1.2 Probabilistic Semi-Explicit Cracking Model

The semi-explicit cracking model is based on the same physical assumptions than the explicit one. The main difference between the two approaches is related to the way of modelling the cracks. As a matter of fact, in the semi-explicit cracking

model, cracks are not modelled by using interface elements but by using volume elements (linear triangles in 2D or linear tetrahedron in 3D).

The failure criteria of Rankine in tension and Tresca in shear are thus applied at the gravity centre of the elements. When one of these criteria is reached in one element, all the components of the matrix of rigidity of the volume element become equal to zero. It is a "kill element" approach. By this way, a crack is modelled by a hole.

Note that, in the frame of this semi-explicit cracking model, the finite element volume considered to determinate the tensile strength distribution function is the volume of the volume element itself.

7.6.2 Concrete-Rebar Bond Model

A simple and robust model has been developed and validated at IFSTTAR (see Phan et al. 2013a, b, 2015). It takes into account the nonlinear behaviour of the concrete-rebar bond in the frame of damage mechanics. It can represent physical phenomena such as interface sliding, cracks appearance and degradation process. The concrete-rebar bond is modelled as interface elements. Their role is to:

- Ensure the displacement continuity between the concrete and the steel before the slip of the interface and before the cracking of the concrete, thus ensuring the transfer of stresses between steel and concrete.
- Represent the macroscopic mechanical effect of the rebar at the ribs—which is not explicitly represented in the mesh.
- Simulate a local failure between steel and concrete along the rebar resulting from a loss of the local adhesion due to shear cracking.
- Simulate the local friction between the concrete and the steel after the interface failure.

The model is implemented in 2D and 3D. It models the concrete-rebar bond as a material zone that progressively degrades in shear (the tensile failure is neglected). Prior to total failure, stresses are continuously transmitted through the interface.

The interface model is based on a damage model that maintains a constant level of stress when the critical shear has been reached (see Fig. 7.35). When the relative tangential displacement between the concrete and the rebar exceeds a critical value, the interface element is declared broken (Rossi 1993). After failure, a Mohr–Coulomb type of friction behaviour is maintained (see Fig. 7.36).

The interface model is deterministic. This is a valid approximation because the cracking process around the rebar is governed by the presence of the ribs (rather than the heterogeneity of concrete) (Rossi 1993).

Only the values of the maximum shear stress, C, and of the tangential critical relative displacement, δ_t^{cri}, have to be determined. This is done by numerical inverse analysis of tie-beam tests.

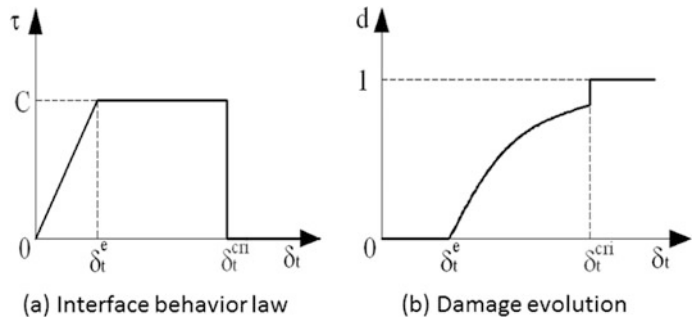

Fig. 7.35 **a** Steel–concrete interface behaviour law and **b** damage evolution

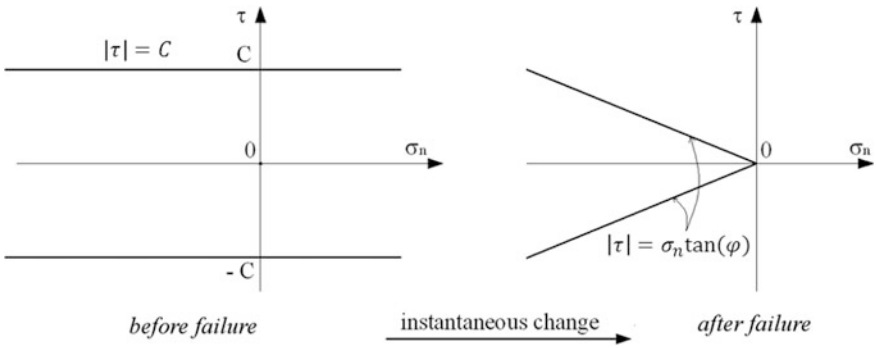

Fig. 7.36 Mohr–Coulomb friction after failure of the steel–concrete interface

7.6.3 Probabilistic Explicit Cracking Model for FRC

The extension of the probabilistic explicit model to analyse the cracking process of FRC structures is very simple.

The first step is to create cracks in the matrix, that means, in the concrete. It is realised by opening the interface elements as described in Sect. 7.6.1.

Thus, after cracking, the interface element rigidity is considered different for normal and tangential displacements. In 2D, normal and tangential rigidities of the interface element are $K_n^{'}$ and $K_t^{'}$, respectively. This post-cracking elastic behaviour exists until it reaches a limit, δ_0, related to the normal displacement. Once this limit value is reached, the mechanical behaviour of the interface element changes. As a matter of fact, the normal stress is considered as linearly decreasing with the normal displacement in order to take into account the damage of the bond between the concrete and the fibre and the pull-out of the fibre. The decreasing evolution is obtained with a damage model.

Finally, the interface element is considered definitely broken, and its normal and tangential rigidities are equal to zero, when the normal displacement occurring during the damage step reaches a critical value δ_c. This value corresponds to the state where the effect of fibres is considered negligible.

The post-cracking total energy dissipated during the linear increase and followed by the linear decrease of the normal stress is considered randomly distributed on the mesh elements as for the material tensile strength. However, the random distribution results from a log-normal distribution function with a mean value independent of the mesh elements size and a standard deviation increasing with the decrease in the mesh elements size, which is physically logical (see Rossi 2012). In practice, to model a given structure, the distribution function is determined in the following manner:

- The mean value is directly obtained by performing a certain number of uniaxial tensile tests on notched specimens (the post-cracking energy is classically determined from the load-crack opening curve) or indirectly by performing an inverse approach based on numerical simulations of bending test.
- The standard deviation, which depends on the mesh elements size, is determined by an inverse analysis approach that consists of simulating uniaxial tests (on notched specimens) or bending tests with different element mesh sizes. As a matter of fact, knowing from the mean value of the post-cracking energy, several numerical simulations are realised for each mesh size and the standard deviation related to each mesh size is obtained by fitting the experimental results (in terms of mean and standard deviation of the numerical responses compared to their corresponding experimental values). By this way, it is possible to find a relation between the standard deviation and the finite element mesh size.

The numerical mechanical behaviour adopted for the post-cracking step is illustrated in Fig. 7.37. Only the normal stress–normal displacement curve is considered in this figure.

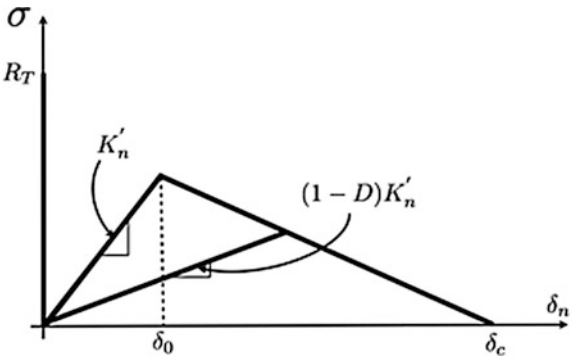

Fig. 7.37 Modelling of the post-cracking behaviour of FRC

7.6.4 Example of Application of the Numerical Model Related to RC Structures

This example of validation of the numerical model was published in Phan et al. (2013b).

The structure concerned is a reinforced slab–beam submitted to three-point bending, 3.30 m long (3.00 m between supports), 0.80 m wide, and 0.15 m thick (an element must have a thickness $\leq$ 1/5 of its width to be considered a slab). All details (geometry, reinforcement, loading conditions, etc.) concerning this RC structure are given in Fig. 7.38.

The mean compressive strength of the concrete studied was 55 MPa.

The mechanical properties of the steel rebars were:

- Young's modulus: 200000 MPa,
- Linear hardening modulus 1120 MPa,
- Elastic limit strength: 640 MPa,
- Ultimate limit strength: 720 MPa,
- Ultimate strain: 12%.

Tie-beam tests were performed in parallel of this structural test to get (by inverse approach, see Sect. 7.6.3) the values of the parameters of the concrete-rebars bond model.

These values were the following: C = 16 MPa and δ_t^{cri} = 23 µm.

3D simulation of the beam–slab was performed. The finite element mesh used is shown in Fig. 7.39.

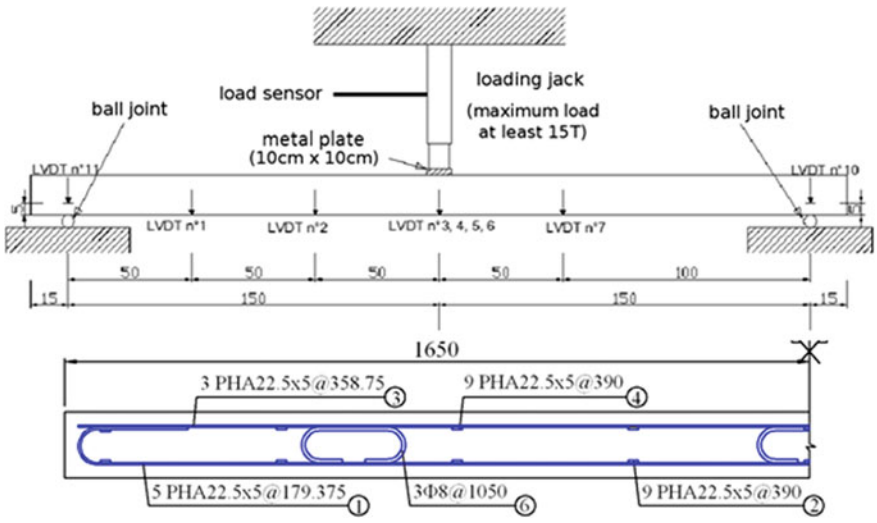

Fig. 7.38 Slab–beam dimensions, type of reinforcement and loading conditions

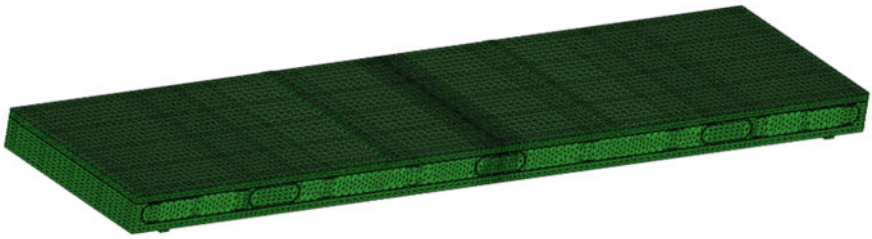

Fig. 7.39 3D finite elements mesh of the beam–slab

The finite elements used were:

- hexahedral linear elements for the steel bar,
- 3D linear interface elements for the concrete/steel bond,
- tetrahedral linear elements for the concrete.

Figure 7.40 shows a comparison between experience and numerical simulation concerning the global behaviour of the structure represented by the load–deflection curve.

Figure 7.41 shows an example of cracking profile obtained with the numerical simulations.

Figures 7.42 and 7.43 summarise comparison between numerical simulations and experimental tests in terms of mean, min and max curves related, respectively, to the number of cracks versus load and to the cracks opening versus load.

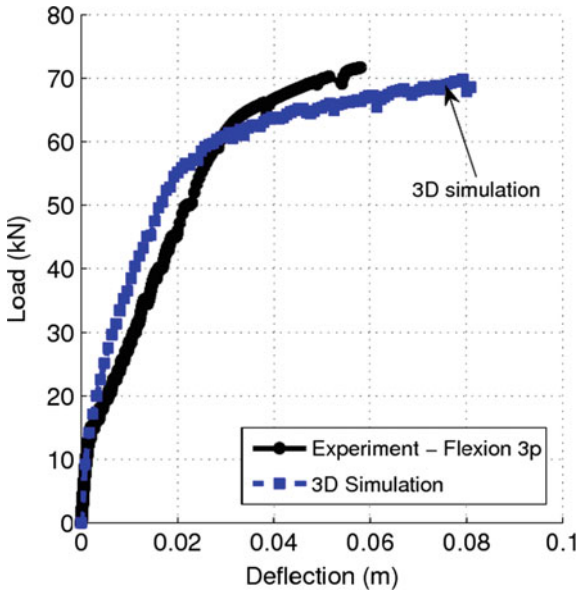

Fig. 7.40 Load–deflection curves—comparison between experience and numerical simulation

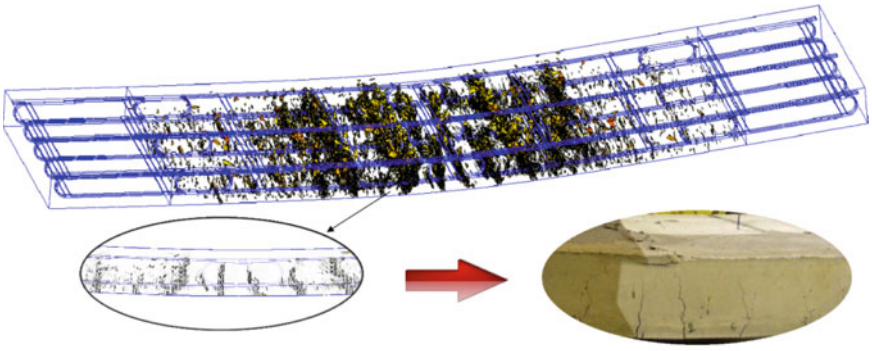

(a) Side view

(b) Underside view

Fig. 7.41 Slab–beam test—example of cracking profile obtained with the 3D simulations

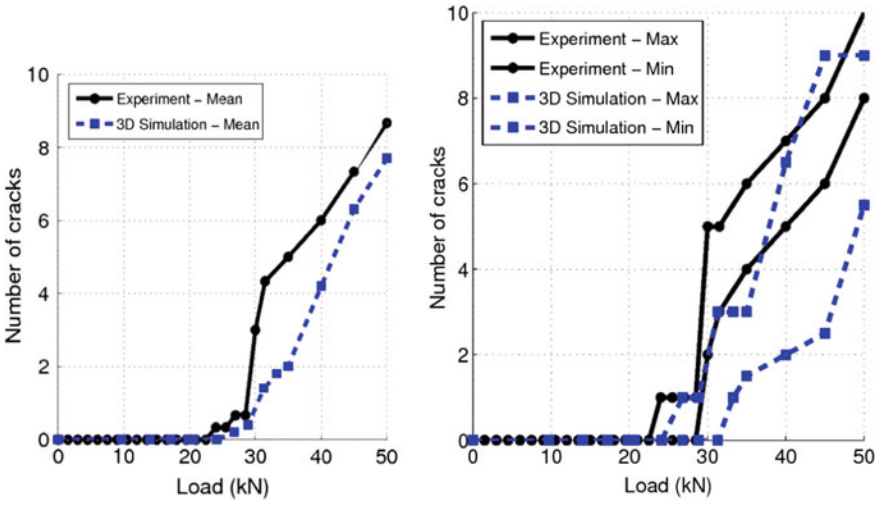

Fig. 7.42 Slab–beam test—number of cracks versus load—mean, min, max curves—comparison between experience and numerical simulations

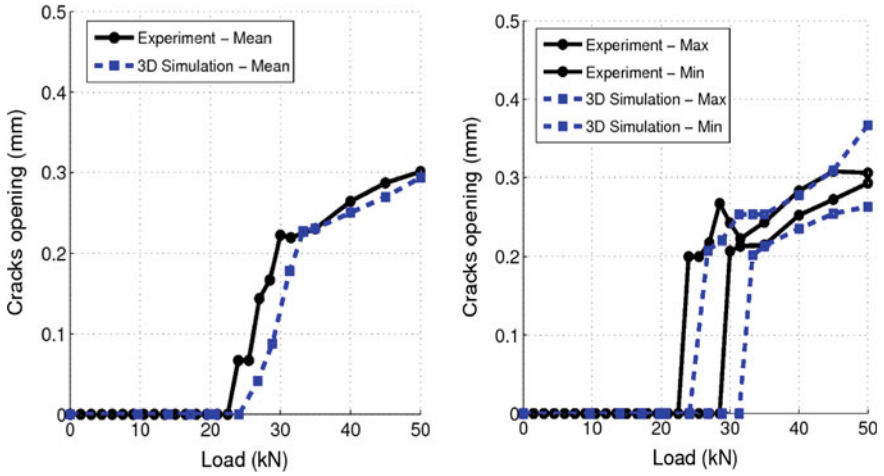

Fig. 7.43 Slab–beam test—cracks opening versus load—mean, min, max curves—Comparison between experience and numerical simulations

7.6.5 *Example of Application of the Numerical Model Related to FRC Structures*

This example of validation of the numerical model has been published in (Rossi et al. 2015). The FRC structure concerned was a steel fibre-reinforced concrete (SFRC) beam submitted to four-point bending. The experimental campaign that allows the comparison of experimental and numerical results was conducted at Ecole Polytechnique de Montréal, Canada (de Montaignac de Chauvance 2011). The dimensions (length, width, height) of the beam were the following: 2600 × 400 × 300 mm. The testing apparatus used for this experimental campaign is shown in Fig. 7.44.

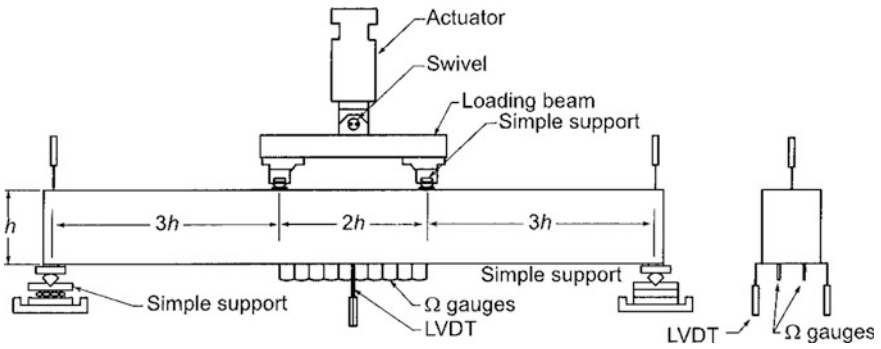

Fig. 7.44 Beams' dimensions, testing apparatus and instrumentation related to the experimental tests

The SFRC used was a self-compacting one containing 78 kg/m^3 of hooked-end steel fibres. These fibres were 35 mm long and had a diameter of 0.55 mm. This SFRC achieved an average compressive strength of approximately 60 MPa at 28 days.

In order to characterise the tensile behaviour, uniaxial tension tests were performed on this SFRC. The RILEM uniaxial tension test was conducted on notched core cylinders (h = 100 mm and Ø = 85 mm). Six specimens for each mix were cored horizontally from a 500 × 600 × 400 mm block casted in addition to the beams.

These tensile tests were performed to determinate, by inverse approach, the parameters of tensile behaviour model of the SFRC (Sect. 7.6.4).

The parameters of the tensile behaviour model related to the studied SFRC were the following:

- Average tensile strength: 2.46 MPa,
- Tensile strength standard deviation: 0.34 MPa,
- Average post-cracking energy: 4.26 MPa.mm,
- Post-cracking energy standard deviation: 0.88 MPa.mm,

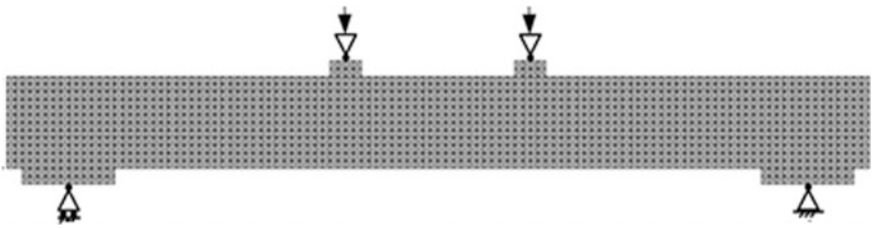

Fig. 7.45 Finite elements mesh of the SFRC beam

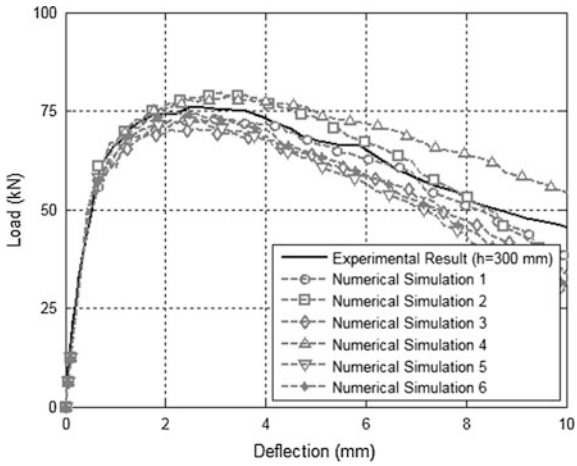

Fig. 7.46 Load–deflection curve—comparison between experience and numerical simulation

- δ_0: 0.05 mm,
- δ_C: 4 mm.

The finite element mesh used to simulate the beam behaviour is shown in Fig. 7.45.

Figure 7.46 shows a comparison between the global behaviour of the SFRC beam obtained with the experience and with the numerical simulation. This global behaviour is considered in the frame of the load–deflection curve of the beam.

Figure 7.47 shows an example of cracking pattern obtained with the numerical simulation.

Figure 7.48 proposes a comparison between the evolution (with the loading moment) of the maximum crack opening displacement obtained experimentally with the one obtained numerically.

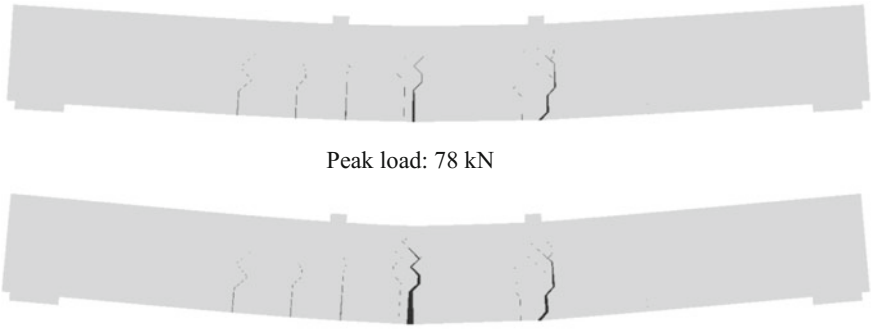

Fig. 7.47 Example of cracking pattern obtained with the numerical simulation

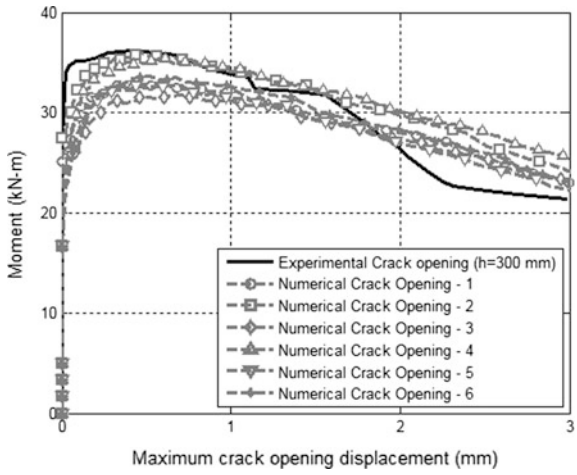

Fig. 7.48 Maximum crack opening displacement versus loading moment—comparison between experience and numerical simulation

References

Abbasnia, R., Shekarchi, M., & Ahmadi, J. (2013). Evaluation of concrete drying shrinkage related to moisture loss. *ACI Materials Journal, 110,* 269–277.

Andreasik, M. (1982). Naprężenia termiczno–skurczowe w masywach betonowych. Ph.D. thesis. Cracow University of Technology, Cracow, Poland.

Aurich, M., Filho, A. C., Bittencourt, T. N., & Shah, S. P. (2009). Finite element modeling of concrete behaviour at early age. *Revista IBRACON de Estruturas e Materiais, 2,* 37–58.

Ayano, T., & Wittmann, F. H. (2002). Drying, moisture distribution, and shrinkage of cement-based materials. *Materials and Structures, 35,* 134–140.

Azenha, M., Faria, R., & Ferreira, D. (2009). Identification of early-age concrete temperatures and strains: Monitoring and numerical simulation. *Cement & Concrete Composites, 31,* 369–378.

Azenha, M., Sousa, C., Faria, R., & Neves, A. (2011). Thermo–hygro–mechanical modelling of self-induced stresses during the service life of RC structures. *Engineering Structures, 33,* 3442–3453.

Baggio, P., Majorana, C. E., & Schrefler, B. A. (1995). Thermo-hygro-mechanical analysis of concrete. *International Journal for Numerical Methods in Fluids, 20,* 573–595.

Baroghel-Bouny, V., et al. (1999). Characterization and identification of equilibrium and transfer moisture properties for ordinary and high-performance cementitious materials. *Cement and Concrete Research, 29,* 1225–1238.

Bastien Masse, M. (2010). Étude du comportement déformationnel des bétons de réparation. Master Thesis. Université de Montréal.

Bažant, Z. P., Cusatis, G., & Cedolin, L. (2004). Temperature effect on concrete creep modeled by microprestress-solidification theory. *Journal of Engineering Mechanics, 130,* 691–699.

Bažant, Z. P., Hauggaard, A. B., Baweja, S., & Ulm, F.-J. (1997). Microprestress-solidification theory for concrete creep. I: Aging and drying effects. *Journal of Engineering Mechanics 123,* 1188–1194.

Bažant, Z. P., Jirásek, M., et al. (2015). RILEM draft recommendation: TC-242-MDC multi-decade creep and shrinkage of concrete: material model and structural analysis. *Materials and Structures, 48,* 753–770.

Bažant, Z. P., & Najjar, L. J. (1972). Nonlinear water diffusion in nonsaturated concrete. *Materials and Structures, 5,* 3–20.

Bažant, Z. P., & Oh, B. H. (1983). Crack band theory for fracture of concrete. *Materials and Structures, 16,* 155–177.

Bažant, Z. P., & Thonguthai, W. (1978). Pore pressure and drying of concrete at high temperature. *Journal of the Engineering Mechanics Division ASCE, 104,* 1059–1079.

Bažant, Z. P., & Thonguthai, W. (1979). Pore pressure in heated concrete walls: theoretical prediction. *Magazine of Concrete Research, 31*(107), 67–76.

Bažant, Z. P., & Kaplan, M. F. (1996). *Concrete at high temperatures: material properties and mathematical models*. Harlow: Longman.

Bear, J. (1988). *Dynamics of fluids in porous media*. New York: Dover.

Benboudjema, F., & Torrenti, J. M. (2008). Early-age behaviour of concrete nuclear containments. *Nuclear Engineering and Design, 238*(10), 2495–2506.

Bernard, O., Ulm, F.-J., & Lemarchand, E. (2003). A multiscale micromechanics-hydration model for the early-age elastic properties of cement-based materials. *Cement and Concrete Research, 33,* 1293–1309.

Bianco, M., Bilardi, G., Pesavento, F., Pucci, G., & Schrefler, B. A. (2003). A frontal solver tuned for fully-coupled non-linear hygro-thermo-mechanical problems. *International Journal of Numerical Methods in Engineering, 57*(13), 1801–1818.

Briffaut, M. (2010). Etude de la fissuration au jeune âge des structures massives: influence de la vitesse de refroidissement, des reprises de bétonnage et des armatures. Dissertation (in French), ENS Cachan.

Briffaut, M., Benboudjema, F., Torrenti, J.-M., & Nahas, G. (2011). Numerical analysis of the thermal active restrained shrinkage ring test to study the early age behavior of massive concrete structures. *Engineering Structures, 33*(4), 1390–1401.

Briffaut, M., Benboudjema, F., Torrenti, J.-M., & Nahas, G. (2012). Effects of early-age thermal behaviour on damage risks in massive concrete structures. *European Journal of Environmental and Civil Engineering, 16,* 589–605. https://doi.org/10.1080/19648189.2012.668016.

Buffo-Lacarrière, L., Sellier, A., Escadeillas, G., & Turatsinze, A. (2007). Multiphasic finite element modeling of concrete hydration. *Cement and Concrete Research, 37,* 131–138.

Černý, R., & Rovnaníková, P. (2002). *Transport processes in concrete*. Abingdon: Spon press.

Červenka, V., Červenka, J., Jendele, L., & Šmilauer, V. (2014). ATENA simulation of crack propagation in CONCRACK benchmark. *European Journal of Environmental and Civil Engineering, 18*(7), 828–844.

Cervera, M., & Chiumenti, M. (2006). Mesh objective tensile cracking via a local continuum damage model and a crack tracking technique. *Computer Methods in Applied Mechanics and Engineering, 196,* 304–320.

Cervera, M., Prato, T., & Oliver, J. (1999a). Thermo-chemo-mechanical model for concrete. I: Hydration and aging. *Journal of Engineering Mechanics, 127,* 1018–1027.

Cervera, M., Olivier, J., & Prato, T. (1999b). A thermo-chemo-mechanical model for concrete. II: damage and creep. *Journal of Engineering Mechanics (ASCE), 125*(9), 1028–1039.

Chen, W.-F. (1982). *Plasticity in reinforced concrete*. New York: McGraw-Hill.

Chen, Y., Huang, R., Huang, Z., & Sun, L. (2012). Effective specific heats of multi-phase thermoelastic composites. *Acta Mechanica Solida Sinica, 25,* 262–276. https://doi.org/10.1016/S0894-9166(12)60024-X.

ConCrack. (2011). International benchmark for control of cracking in R.C. *Structures*. https://www.concrack.org.

Craeye, B., De Schutter, G., Van Humbeeck, H., & Van Cotthem, A. (2009). Early age behaviour of concrete supercontainers for radioactive waste disposal. *Nuclear Engineering and Design, 239,* 23–35. https://doi.org/10.1016/j.nucengdes.2008.10.006.

De Borst, R., Heeres, O. M., & Suiker, A. S. (2001). Some recent issues in computational plasticity. In *Proceedings of European Conference on Computational Mechanics, Kraków 2001*.

de Montaignac de Chauvance, R. (2011). Analyse du comportement d'éléments fléchis en béton renforcé de fibes métalliques. Du matériau à la structure. Dissertation (in french), Thesis of'Ecole Polytechnique de Montréal, Canada (in french).

De Sa, C., & Benboudjema, F. (2012). Modeling of concrete nonlinear mechanical behavior at high temperatures with different damage-based approaches. *Materials and Structures, 44,* 1411–1429.

De Sa, C., Benboudjema, F., Thiery, M., & Sicard, J. (2008). Analysis of microcracking induced by differential drying shrinkage. *Cement & Concrete Composites, 30,* 947–956.

De Schutter, G. (1999). Degree of hydration based Kelvin model for the basic creep of early age concrete. *Materials and Structures, 32,* 260–265.

De Schutter, G. (2002a). Finite element simulation of thermal cracking in massive hardening concrete elements using degree of hydration based material laws. *Computers & Structures, 80,* 2035–2042.

De Schutter, G. (2002b). Influence of hydration reaction on engineering properties of hardening concrete. *Materials and Structures, 35,* 447–452.

De Schutter, G., & Taerwe, L. (1996). Degree of hydration based description of mechanical properties of early-age concrete. *Materials and Structures, 29*(6), 335–344.

De Schutter, G., & Taerwe, L. (1997). Fracture energy of concrete at early ages. *Materials and Structures, 30,* 67–71.

England, G., & Khoylou, N. (1995). Moisture flow in concrete under steady state non-uniform temperature states: experimental observations and theoretical modeling. *Nuclear Engineering and Design, 156,* 83–107.

Fairbairn, E. M. R., Silvoso, M. M., Toledo Filho, R. D., Alves, J. L. D., & Ebecken, N. F. F. (2004). Optimization of mass concrete construction using genetic algorithms. *Computers & Structures, 82,* 281–299. https://doi.org/10.1016/j.compstruc.2003.08.008.

Faria, R., Azenha, M., & Figueiras, J. A. (2006). Modelling of concrete at early ages: application to an externally restrained slab. *Cement & Concrete Composites, 28,* 572–585.

Feldman, R. F., & Sereda, P. J. (1968). The model for hydrated Portland cement as deduced from sorption-length change and mechanical properties. *Materials and Construction, 1,* 509–520.

Fib. (2010). *Model Code for concrete structures 2010*. International Federation for Structural Concrete (fib).

Gawin, D., Pesavento, F., & Schrefler, B. A. (2002). Modelling of hygro-thermal behaviour and damage of concrete at temperature above critical point of water. *International Journal of Numerical and Analytical Methods in Geomechanics, 26*(6), 537–562.

Gawin, D., Pesavento, F., & Schrefler, B. A. (2003). Modelling of thermo-chemical and mechanical damage of concrete at high temperature. *Computer Methods in Applied Mechanics and Engineering, 192,* 1731–1771. https://doi.org/10.1016/S0045-7825(03)00200-7.

Gawin, D., Pesavento, F., & Schrefler, B. A. (2004). Modelling of deformations of high strength concrete at elevated temperatures. *Materials and Structures, 37*(268), 218–236.

Gawin, D., Pesavento, F., & Schrefler, B. A. (2006a). Hygro-thermo-chemo-mechanical modelling of concrete at early ages and beyond. Part I: Hydration and hygro-thermal phenomena. *International Journal for Numerical Methods in Engineering*, *67*(3), 299–331. https://doi.org/10.1002/nme.1615.

Gawin, D., Pesavento, F., & Schrefler, B. A. (2006b). Hygro-thermo-chemo-mechanical modelling of concrete at early ages and beyond. Part II: Shrinkage and creep of concrete. *International Journal for Numerical Methods in Engineering*, *67*(3), 332–363. https://doi.org/10.1002/nme.1636.

Gawin, D., Pesavento, F., & Schrefler, B. A. (2006c). Towards prediction of the thermal spalling risk through a multi-phase porous media model of concrete. *Computer Methods in Applied Mechanics and Engineering, 195*(41–43), 5707–5729.

Gawin, D., Pesavento, F., & Schrefler, B. A. (2008). Modeling of cementitious materials exposed to isothermal calcium leaching, with considering process kinetics and advective water flow. Part 1: Theoretical model. *Solids and Structures, 45,* 6221–6240. https://doi.org/10.1016/j.ijsolstr.2008.07.010.

Gawin, D., Pesavento, F., & Schrefler, B. A. (2009). Modeling deterioration of cementitious materials exposed to calcium leaching in non-isothermal conditions. *Computer Methods in Applied Mechanics and Engineering, 198,* 3051–3083. https://doi.org/10.1016/j.cma.2009.05.005.

Gray, W. G., & Miller, C. T. (2005). Thermodynamically constrained averaging theory approach for modeling flow and transport phenomena in porous medium systems: 1. Motivation and overview. *Advances in Water Resources, 28,* 161–180.

Gray, W. G., & Schrefler, B. A. (2007). Analysis of the solid phase stress tensor in multiphase porous media. *International Journal for Numerical and Analytical Methods in Geomechanics, 31*(4), 541–581.

Gray, W. G., Schrefler, B. A., & Pesavento, F. (2009). The solid phase stress tensor in porous media mechanics and the Hill-Mandel condition. *Journal of the Mechanics and Physics of Solids, 57,* 539–554. https://doi.org/10.1016/j.jmps.2008.11.005.

Gutsch, A., & Rostásy, F. S. (1994). Young concrete under high tensile stresses—creep, relaxation and cracking. In *Proceedings of the International RILEM Conference on Thermal Cracking in Concrete at Early Ages*, London.

Hansen, K. K. (1986). *Sorption isotherms: A catalogue. Kgs*. Lyngby, Denmark: Technical University of Denmark.

Hansen, P. F., Hansen, J. H., Kjaer, V., & Pedersen, E. J. (1982). Thermal properties of hardeing cement pastes. In *Proceedings of RILEM International Conference on Concrete at Early-Ages*. Paris.

Hanson, J. A. (1968). Effects of curing and drying environments on splitting tensile strength. *American Concrete Institute Journal, 65,* 535–543.

Hassanizadeh, S. M., & Gray, W. G. (1979a). General conservation equations for multi-phase systems: 1. Averaging procedure. *Advances in Water Resources, 2,* 131–144.

Hassanizadeh, S. M., & Gray, W. G. (1979b). General conservation equations for multi-phase systems: 2. Mass, momenta, energy and entropy equations. *Advances in Water Resources, 2,* 191–203.

Hassanizadeh, S. M., & Gray, W. G. (1980). General conservation equations for multi-phase systems: 3. constitutive theory for porous media flow. *Advances in Water Resources, 3,* 25–40.

Hilaire, A. (2014). Etude des déformations différées des bétons en compression et en traction, du jeune au long terme: Application aux enceintes de confinement. Dissertation (in french), École normale supérieure de Cachan - ENS Cachan, Paris.

Hillerborg, A., Modeer, M., & Petersson, P. (1976). Analysis of crack formation and crack growth in concrete by means of fracture mechanics and finite elements. *Cement and Concrete Research, 6,* 773–782.

Hofstetter, G., & Mang, H. A. (1995). *Computational mechanics of reinforced concrete structures*. Wiesbaden, Germany: Vieweg.

Honorio, T., Bary, B., & Benboudjema, F. (2014). Evaluation of the contribution of boundary and initial conditions in the chemo-thermal analysis of a massive concrete structure. *Engineering Structures, 80,* 173–188. https://doi.org/10.1016/j.engstruct.2014.08.050.

Jendele, L., Šmilauer, V., & Cervenka, J. (2014). Multiscale hydro–thermo–mechanical model for early-age and mature concrete structures. *Advances in Engineering Software, 72,* 134–146.

Ji, G. (2008). Cracking risk of concrete structures in the hardening phase: Experiments, material modeling and finite element analysis. Ph.D. thesis, Trondheim, Norway.

Klemczak, B. (2007). Adapting of the Willam-Warnke failure criteria for young concrete. *Archives of Civil Engineering, 53*(2), 323–339.

Klemczak, B. (2011). Prediction of coupled heat and moisture transfer in early-age massive concrete structures. *Numerical Heat Transfer, Part A: Applications, 60*(3), 212–233.

Künzel, H. (1995). *Simultaneous heat and moisture transport in building components*. Stutgart: IRB.

Kwak, H.-G., Ha, S.-J., & Kim, J.-K. (2006). Non-structural cracking in RC walls: Part I. *Finite Element Formulation, Cement and Concrete Research, 36*(4), 749–760.

Lackner, R., & Mang, H. A. (2004). Chemoplastic material model for the simulation of early-age cracking: From the constitutive law to numerical analyses of massive concrete structures. *Cement & Concrete Composites, 26,* 551–562.

Ladeveze, P. (1983). *Sur une theorie de l'endomagement anisotrope*. Internal Report no 34 Laboratoire de Mecanique et Technologie, Cachan, France.

Laplante, P. (1993). Propriétés mécaniques des bétons durcissants: Analyse comparée des bétons classiques et à très hautes performances. Dissertation (in french), ENPC.

Leal da Silva, W. R., Šmilauer, V., & Štemberk, P. (2015). Upscaling semi-adiabatic measurements for simulating temperature evolution of mass concrete structures. *Materials and Structures, 48*(4), 188–197.

Leblond, J. B., Perrin, G., & Devaux, J. (1992). Bifurcation effects in ductile metals with damage delocalisation. ASME Journal of Applied Mechanics

Lewis, R. W., & Schrefler, B. A. (1998). *The finite element method in the static and dynamic deformation and consolidation of porous media* (2nd ed.). Chichester: Wiley.

Liu, B. Y. H., & Jordan, R. C. (1963). A rational procedure for predicting the long-term average performance of flat-plate solar energy collectors. *Solar Energy, 7*(2), 53–74.

Lothenbach, B., Matschei, T., Möschner, G., & Glasser, F. P. (2008). Thermodynamic modelling of the effect of temperature on the hydration and porosity of Portland cement. *Cement and Concrete Research, 38,* 1–18. https://doi.org/10.1016/j.cemconres.2007.08.017.

Loukili, A., Chopin, D., Khelidj, A., & Le Touzo, J. Y. (2000). A new approach to determine autogenous shrinkage of mortar at an early age considering temperature history. *Cement and Concrete Research, 30,* 915–922.

Lura, P., & Van Breugel, K. (2001). Thermal properties of concrete. Sensitivity studies. In *IPACS (Improved Production of Advanced Concrete Structures) Project*, *Luleå*

Majewski, S. (2003). *Mechanika betonu konstrukcyjnego w ujeciu sprężysto–plastycznym. Monograph 45*. Gliwice, Poland: Silesian University of Technology.

Majewski, S. (2004). MWW3–Elasto–plastic model for concrete. *Archives of Civil Engineering, 50*(1), 11–43.

Mazars, J. (1984). Application de la mecanique de l'endommagement au comportement non lineaire et a la rupture du beton de structure. Dissertation, Universite Paris VI.

Mazars, J. (1986). A description of micro and macroscale damage of concrete structures. *Engineering Fracture Mechanics, 25*(5–6), 729–737.

Mazars, J. (2014). Control of cracking, a major issue for reinforced concrete structures. *European Journal of Environmental and Civil Engineering, 18*(7), 721–723.

Mazars, J., & Bournazel, J. P. (1996). Modelling of damage processes due to volumic variations for maturing and matured concrete. In *Proceedings of the International RILEM Conference on Concrete: from Material to Structure*, Arles, France.

Mazzotti, C., & Savoia, M. (2003). Nonlinear creep damage model for concrete under uniaxial compression. *Journal of Engineering Mechanics, 129*(9), 1065–1075.

Morabito, P. (2001). Thermal properties of concrete. Variations with the temperature and during the hydration phase. In *Project IPACS, Luleå*.

Mounanga, P. (2004). Étude expérimentale du comportement de pâtes de ciment au très jeune âge: Hydratation, retraits, propriétés thermophysiques. Dissertation (in French), Université de Nantes, Nantes.

Mounanga, P., Baroghel-Bouny, V., Loukili, A., & Khelidj, A. (2006). Autogenous deformations of cement pastes: Part I. Temperature effects at early age and micro–macro correlations. *Cement and Concrete Research, 36,* 110–122.

Neville, A. M., Dilger, W. H., & Brooks, J. J. (1983). *Creep of plain and structural concrete*. Longman Group Construction Press.

Park, K.-B., Jee, N.-Y., Yoon, I.-S., & Lee, H.-S. (2008). Prediction of temperature distribution in high-strength concrete using hydration model. *ACI Materials Journal, 105*(2), 180–186.

Patzák, B., & Rypl, D. (2012). Object-oriented, parallel finite element framework with dynamic load balancing. *Advances in Engineering Software, 47*(1), 35–50.

Perzyna, P. (1966). Fundamental problems in viscoplasticity. *Advances in Applied Mechanics, 9,* 243–377.

Pesavento, F. (2000). Non-linear modeling of concrete as multiphase porous material in high temperature conditions. Dissertation, University of Padova.

Pesavento, F., Gawin, D., & Schrefler, B. A. (2008). Modeling cementitious materials as multiphase porous media: theoretical framework and applications. *Acta Mechanica, 201,* 313–339. https://doi.org/10.1007/s00707-008-0065-z.

Pesavento, F., Gawin, D., Wyrzykowski, M., Schrefler, B. A., & Simoni, L. (2012). Modeling alkali-silica reaction in non-isothermal, partially saturated cement based materials. *Computer Methods in Applied Mechanics and Engineering (CMAME), 225–228,* 95–115. https://doi.org/10.1016/j.cma.2012.02.019.

Phan, T. S., et al. (2013a). Numerical modeling of the rebar/concrete interface: Case of the flat steel rebars. *Materials and Structures, 46*(6), 1011–1025.

Phan, T. S., Tailhan, J.-L., & Rossi, P. (2013b). 3D numerical modelling of concrete structural element reinforced with ribbed flat steel rebars. *Structural Concrete, 14*(4), 378–388.

Phan, T. S., Rossi, P., & Tailhan, J.-L. (2015). Numerical modelling of the concrete/rebar bond. *Cement & Concrete Composites, 59,* 1–9.

Pichler, B., & Hellmich, C. (2011). Upscaling quasi-brittle strength of cement paste and mortar: A multi-scale engineering mechanics model. *Cement and Concrete Research, 41,* 467–476.

Pickett, G. (1942). The effect of change in moisture-content of the creep of concrete under a sustained load. *Journal of the American Concrete Institute, 13,* 333–355.

Pijaudier-Cabot, G., & Bažant, Z. P. (1987). Nonlocal Damage Theory. *Journal of Engineering Mechanics*, *113*(10), 1512–1533.

Pijaudier-Cabot, G. (1995). Non local damage. In H.-B. Mühlhaus (Ed.), *Continuum models for materials with microstructure*. London: Wiley.

Pijaudier-Cabot, G., La Borderie, C., & Fichant, S. (1994). Damage mechanics for concrete modelling: applications and comparisons with plasticity and fracture mechanics. In N. Bicanic, et al. (Eds.) *Proceedings of EURO-C*. Pineridge Press Pubs.

Regourd, M., & Gauthier, E. (1980). Behavior of cement under accelerated hardening. *Annales de l'ITBTP (in French)* (Vol. 179, pp. 65–96).

Rossi, P. (1993). *Comportement dynamique des bétons: du matériau à la structure. Annales de l'Institut technique du bâtiment et des travaux publics* (Vol. 511). Institut technique du bâtiment et des travaux publics (in french).

Rossi, P. (2012). Experimental study of scaling effect related to post-cracking behaviours of metal fibres reinforced concretes. *European Journal of Environmental and Civil Engineering, 16*(10), 1261–1268.

Rossi, P., et al. (1994). Scale effect on concrete in tension. *Materials and Structures, 27,* 437–444.

Rossi, P., Daviau-Desnoyers, D., & Tailhan, J.-L. (2015). Analysis of cracking in steel fibre reinforced concrete (SFRC) structures in bending using probabilistic modelling. *Structural Concrete, 3,* 381–388.

Rossi, P., & Richer, S. (1987). Numerical modelling of concrete cracking based on a stochastic approach. *Materials and Structures, 20*(119), 334–337.

Rossi, P., Ulm, F. J., & Hachi, F. (1996). Compressive behaviour of concrete: physical mechanisms and modelling. *ASCE Engineering Mechanics, 122*(11), 1038–1043.

Rossi, P., & Wu, X. (1992). Probabilistic model for material behaviour analysis and appraisement of concrete. *Magazine of Concrete Research, 44*(161), 271–280.

Rots, J. G. (1988). Computational modeling of concrete fracture. Dissertation, Delft University of Technology, Delft (Netherlands).

Ruiz, J., Schindler, A., Rasmussen, R., Kim, P., Chang, G. (2001). Concrete temperature modeling and strength prediction using maturity concepts in the FHWA HIPERPAV software. In: *Proceedings of 7th International Conference on Concrete Pavements, Orlando, USA*.

Schrefler, B. A. (2002). Mechanics and thermodynamics of saturated-unsaturated porous materials and quantitative solutions. *Applied Mechanics Review, 55*(4), 351–388.

Sciumè, G., Benboudjema, F., De Sa, C., Pesavento, F., Berthaud, Y., & Schrefler, B. A. (2013). A multiphysics model for concrete at early age applied to repairs problems. *Engineering Structures, 57,* 374–387.

Sciumè, G., Schrefler, B.A., & Pesavento, F. (2012). Thermo-hygro-chemo-mechanical modelling of the behaviour of a massive beam with restrained shrinkage. In *Proceedings of CONCRACK 3, International Workshop on Crack Control of Mass Concrete and Related Issues Concerning Early-Age Concrete Structures*. Paris, France: RILEM, JCI.

Simoni, L., & Schrefler, B. A. (2014). Multi field simulation of fracture. In S. P. A. Bordas (Ed.), *Advances in applied mechanics—AAMS* (Vol. 47, pp. 367–519). UK: Academic Press.

Šmilauer, V., Baquerizo, L., Matschei, T., Havlásek, P., Leal da Silva, W. R., & Hájková, K. (2016). ConTemp—A virtual thermo-mechanical simulator for hydrating reinforced concrete blocks with extension to service life. *Service life of cement-based materials and structures* (pp. 463–472). Bagneux: Rilem Publications s.a.r.l.

Stefan, L., Benboudjema, F., Torrenti, J. M., & Bissonnette, B. (2010). Prediction of elastic properties of cement pastes at early ages. *Computational Materials Science, 47,* 775–784.

Tailhan, J.-L., et al. (2010). From Local to Global Probabilistic Modeling of Concrete Cracking. *Annals of Solid and Structural Mechanics, 1,* 103–115.

Thelandersson, S. (1987). Modelling of combined thermal and mechanical action in concrete. *ASCE Engineering Mechanics, 113*(6), 893–906.

Thomas, J. J., Biernacki, J. J., Bullard, J. W., Bishnoi, S., Dolado, J. S., Scherer, G. W., et al. (2011). Modeling and simulation of cement hydration kinetics and microstructure development. *Cement and Concrete Research, 41*(12), 1257–1278.

Torrenti, J. M., & Benboudjema, F. (2005). Mechanical threshold of concrete at an early age. *Materials and Structures, 38,* 299–304.

Ulm, F.-J., & Coussy, O. (1998). Couplings in early-age concrete: From material modeling to structural design. *International Journal of Solids and Structures, 35,* 4295–4311. https://doi.org/10.1016/S0020-7683(97)00317-X.

Ulm, F.-J., & Coussy, O. (2001). What is a "massive" concrete structure at early ages? Some dimensional arguments. *Journal of Engineering Mechanics, 127,* 512–522.

Valanis, K. C. (1991). A global damage theory and the hyperbolicity of the wave problem. *ASME Journal of Applied Mechanics, 58,* 311–316.

van Genuchten, M. T. (1980). A closed-form equation for predicting the hydraulic conductivity of unsaturated soils. *Soil Science Society of America Journal, 44*(5), 892–898.

Waller, V. (2000). Relations entre composition des bétons, exothermie en cours de prise et résistance en compression. Dissertation (in French), Ecole Nationale des Ponts et Chaussées, Marne-La-Vallée.

Whitaker, S. (1980). Heat and mass transfer in granular porous media. *Advances in Drying*, *1*.

Winnicki, A. (2001). Viscoplastic consistency model—basic features. In *Proceedings of European Conference on Computational Mechanics*, Kraków, 2001.

Wu, T., Temizer, I., & Wriggers, P. (2014). Multiscale hydro-thermo-chemo-mechanical coupling: Application to alkali-silica reaction. *Journal of Computational Material Science, 84,* 381–395.

Xi, Y., Bažant, Z. P., Molina, L., & Jennings, H. M. (1994). Moisture diffusion in cementitious materials. Moisture capacity and diffusion. *Advanced Cement Based Materials, 1*(6), 258–266.

Zienkiewicz, O. C., & Taylor, R. L. (2000). *The finite element method, The basis* (Vol. 1). Oxford: Butterworth-Heinemann.

Chapter 8
Cracking Risk and Regulations

Agnieszka Knoppik, Jean-Michel Torrenti, Shingo Asamoto, Eduardus Koenders, Dirk Schlicke and Luis Ebensperger

Abstract This chapter is focused on the cracking risk at early ages. After general considerations about cracking, the cracking risk prediction is discussed. Two main ways to assess this risk are considered: through an evaluation of the tensile stresses and through an evaluation of the strains. Finally, the evaluation of crack opening at early ages and the reinforcement design in regulations are presented.

8.1 Introduction—Significance of Cracking

Cracking is a normal phenomenon in reinforced concrete structures. Indeed, to obtain a good use of the reinforcement (i.e. a high stress in the reinforcement), cracking should occur. But of course the crack opening should be limited (see Sect. 8.1.2).

To evaluate the crack opening (and the crack spacing), three levels of model could be used:

- **Level I**: In the reinforced concrete codes, safety factors affecting the materials and the loadings are considered. Assuming simple behaviour (generally a constant

A. Knoppik (✉)
Silesian University of Technology, Gliwice, Poland
e-mail: agnieszka.jedrzejewska@polsl.pl

J.-M. Torrenti
IFSTTAR, University Paris-Est, Champs-Sur-Marne, France

S. Asamoto
Saitama University, Saitama, Japan

E. Koenders
Technische Universität Darmstadt, Darmstadt, Germany

D. Schlicke
Graz University of Technology, Graz, Austria

L. Ebensperger
Construtechnik Ltda., Santiago, Chile

© RILEM 2019

E. M. R. Fairbairn and M. Azenha (eds.), *Thermal Cracking of Massive Concrete Structures*, RILEM State-of-the-Art Reports 27,
https://doi.org/10.1007/978-3-319-76617-1_8

bond stress), the crack spacing, the stresses in the reinforcement and finally the crack opening could be calculated—see Sect. 8.2.4.

- **Level II**: The first-order second-moment method (FOSM) (Koenders et al. 2007) is a probabilistic approach for early-age cracking. It considers the probability of failure P_f as the probability of the tensile stress exceeding the tensile strength. This approach is presented in Sect. 8.3.
- **Level III**: A Monte Carlo approach can also be used. With this calculation procedure, all probability density functions of all strength and load variables are considered (Koenders et al. 2007)—see Sect. 8.3.

8.1.1 General Considerations About Crack Width

In the recent Model Code 2010 (CEB-FIP *fib* 2012), it is indicated that "*the phenomena of cracking are of highly probabilistic nature. Therefore, the comparison of calculated crack widths with nominal crack widths limits may only serve as an approximate means to satisfy the design criteria. High accuracy may not be expected*". Figure 8.1 shows an example of the distribution of maximal crack openings (ECP 2008).

The crack width w_k estimated by means of the Eurocode 2 (EN 1992-1-1 2004) corresponds indeed to a conventional crack width (or a design crack width), in a steady state.[1] In Eurocode 2, the index k means that it is a characteristic value.[2] The fractile is not defined in the text (like, for instance, it is for the compressive strength). In the 1978 version of the Model Code, a relation between the characteristic value and the mean value was proposed: $w_k = 1.7w_m$. This relation is coming from results of tests performed by Beeby (1972) and was used to elaborate the relations used in order to estimate the crack width (ECP 2008). Actually, the coefficient 1.7 is included in the coefficients that are used to estimate the maximum crack spacing $s_{r,\max}$ of Eurocode 2 and Model Code 2010.

Also, it should be noted that the crack width w_k corresponds to an opening measured at the concrete surface (this is not indicated in Eurocode 2 but it is in Model Code 2010; also the comparison between the proposed equations and tests is clearly made using surface measurements ECP 2008). And experimental results show that the larger the concrete cover the larger the crack width at concrete surface (cf. Figs. 8.2 and 8.3). This effect is taken into account in Eurocode 2 and Model Code 2010 in the estimation of the maximum crack spacing (and consequently in the crack width).

[1]The steady state corresponds to the moment where all the possible cracks are created. An increase of the loading will induct a larger crack opening. Before this steady state, the number and the spacing between cracks could be very different. Especially under imposed strains, the steady state is generally not obtained.

[2]In the MC2010, the crack width is clearly a design value and noted w_d

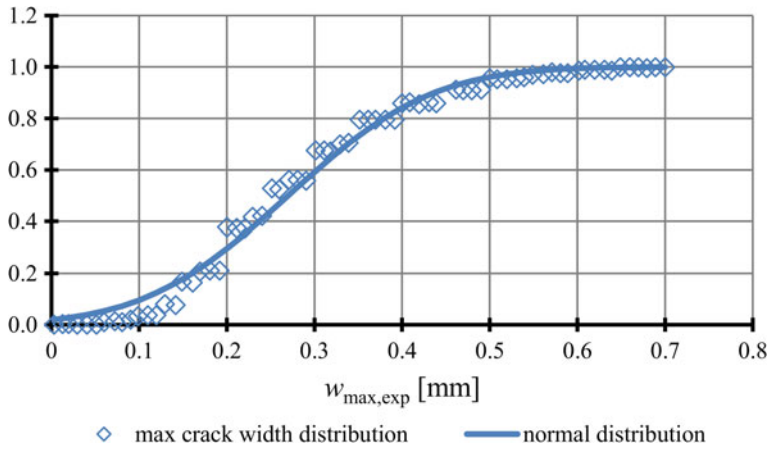

Fig. 8.1 Maximum experimental crack width distribution; after (ECP 2008)

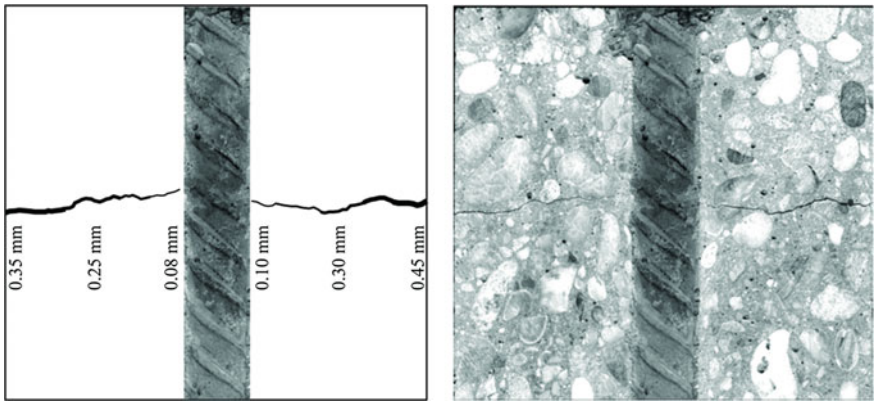

Fig. 8.2 Variation of crack width for specimen with concentric steel reinforcement (concrete cover of 50 mm); after (Borosnyoi and Snobli 2010). Cracking is obtained by means of direct tension. A resin is injected within cracks of the widths of 0.05–0.50 mm under sustained loading. The load was released only after the resin was allowed to set. Then, the samples were sawn. So, the crack width corresponds to a service state

8.1.2 Crack Width and Performance

For classical reinforced or prestressed structures, leakage is irrelevant or a limited leakage is accepted, and the control of cracking mainly aims at limiting the stress variations in the reinforcement and ensuring durability, aspect preservation, and

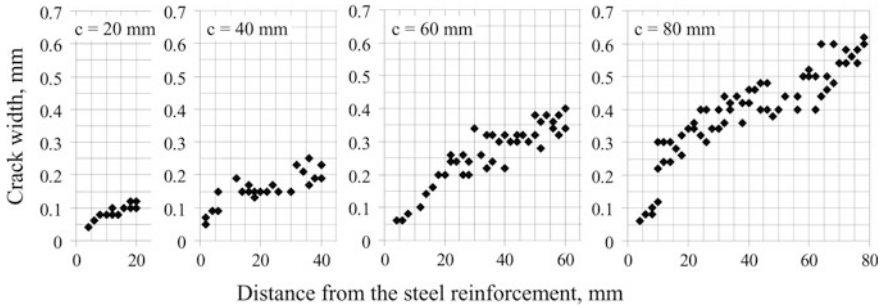

Fig. 8.3 Variation of crack width for specimens with eccentric steel reinforcement (concrete covers of 20, 40, 60, 80 mm); after (Borosnyoi and Snobli 2010)

continuity in the structural behaviour. In these structures, the crack opening is limited for durability reasons. Indeed, the cracking affects the transport properties of aggressive agents such as CO_2 and chloride ions. The admissible crack opening depends on environmental exposure according to the location and type of the structure. For instance, for Eurocode 2, if corrosion due to carbonation is the main risk, the crack opening should be limited to 0.3 mm. This limitation of the crack width ensures that the structural performance is not affected. Table 8.1 gives an example for the maximum allowable crack widths for reinforced concrete under service loads (ACI 224 2001).

In case of structures where tightness is an explicit operational requirement, the crack width should be lower, especially if the cracks are due to restrained shrinkage. This could be explained by the fact that—in the first approximation—permeability and diffusivity are proportional to the power of 3 of the crack opening and to the crack opening, respectively. In this case, the opening of possible cracks produced at early age due to restrained thermal or desiccation shrinkage, mechanical loadings during the execution phases, as well as the crack opening due to further service loading(s) associated to the tightness verification scenarios shall be considered and compared to the maximum design crack opening (Barre et al. 2016).

Note that due to possible self-healing, the crack width could be reduced with time (in a natural manner or with the use of permeability-reducing admixtures).

Table 8.1 Maximum allowable crack width in (ACI 224 2001)

Exposure condition	Crack width [mm]
Dry air or protective membrane	0.41
Humidity, moist air, soil	0.30
De-icing chemicals	0.18
Seawater and seawater spray, wetting and drying	0.15
Water-retaining structures	0.10

Fig. 8.4 Water treatment plant showing cracking due to the restrained shrinkage at early age and some self-healed cracks (photograph: A. Darquennes)

That is why the recent CEB-FIP *fib* Model Code 2010 (CEB-FIP *fib* 2012) indicates that "*with regard to crack width limitation for fluid-tightness […] if leakage should be limited to a small amount and some surface staining is acceptable* w_{lim} *= 0.20 mm may be used as a limit for self-healing cracks. Otherwise 0.1 mm may be more appropriate.*" Model Code 2010 specifies that "*whether self-healing of cracks can occur depends on the chemical composition of the fluid, type of cement, water pressure, time after subjecting to water pressure,* etc." Figure 8.4 gives an example of a water tank where some self-healing has closed some of the cracks.

8.2 Crack Risk Prediction

8.2.1 Role of Boundary Conditions

Concrete elements are subjected to early-age volume changes due to temperature and moisture variations which characterise the process of concrete hardening. These volume changes induce stresses in concrete elements. In massive concrete elements, such as foundation slabs or blocks, the stresses are induced mainly by significant temperature gradients developing between the interior and the surface of the element (the so-called self-induced stresses, self-balanced stresses or *Eigenstresses*). In externally restrained elements, such as walls, thermal–shrinkage stresses result from a coupled action of self-induced and restraint stresses. The restraint in these

elements is exerted by the bond between the new concrete of the element and the older concrete of the foundation or previous lift.

Stresses in the internally restrained elements result from volume changes due to temperature and moisture gradients. In such case, an internal restraint is induced and it is caused by a temperature and moisture difference within the section. In such elements, random crack maps on surfaces can be usually observed. Stresses in the externally restrained elements are caused by bond forces generated in the joint between the element and the restraining body. The main causes of the bond force generation are unbalanced thermal–shrinkage strains in the element and the restraining body if the two are executed separately one after another. In a typical externally restrained element, restraint stresses play a predominant role because volumetric strains caused by the temperature and humidity gradients are relatively small in comparison to the linear strains caused by the contraction of the element along the line of the restraint joint. Nevertheless, it must be remembered that with the increasing massiveness the share of the self-induced stresses increases. Surface tensile stresses occurring in thick walls (thermal gradients) and formed by early formwork removal (both thermal and moisture gradients) may lead to surface cracking which can further develop into through cracking in superposition with external restraint.

A typical pattern of cracking due to the edge restraint is shown in Fig. 8.5a. Without a restraint, the section would contract along the line of the base, and so with the restraint a horizontal force develops along the construction joint. The occurring cracks are vertical in the central part of the wall and splay towards the ends of the element where a vertical tensile force is required to balance the tendency of the horizontal force to warp the wall. A horizontal crack may occur at the construction joint at the ends of the walls due to this warping restraint. Figure 8.5b presents the cracking of the wall with end restraint. The external restraint might be a combination of a base and a side restraint (Fig. 8.5c, d). Usually, the first crack occurs at the construction joint as the strength of the bond between the new and mature concrete is less than the tensile strength of the element. Such a crack is therefore less likely to be fully developed. If the overall contraction of the wall can be satisfied by fully developed cracks at one or both construction joints, then the intermediate cracks shown in Fig. 8.5c, d may not occur.

In a typical base-restrained element, the occurring cracks have vertical alignment and may reach a significant height. The greatest height of the crack is observed in the middle of the element and it declines towards the side edges or towards the expansion joints. The maximum width of the crack occurs at some level above the joint (Flaga and Furtak 2009; Nilsson 2000). The extent and size of cracking depend on the amount and distribution of the applied reinforcement: When sufficient reinforcement is provided, the widths of the primary cracks are controlled but secondary cracks may be induced (ACI 207.1 2005; Mihashi and Leite 2004; RILEM TC 119-TCE 1997; RILEM TC 181-EAS 2002). Design of reinforcement and its influence on cracking pattern is further discussed in Sect. 8.4.

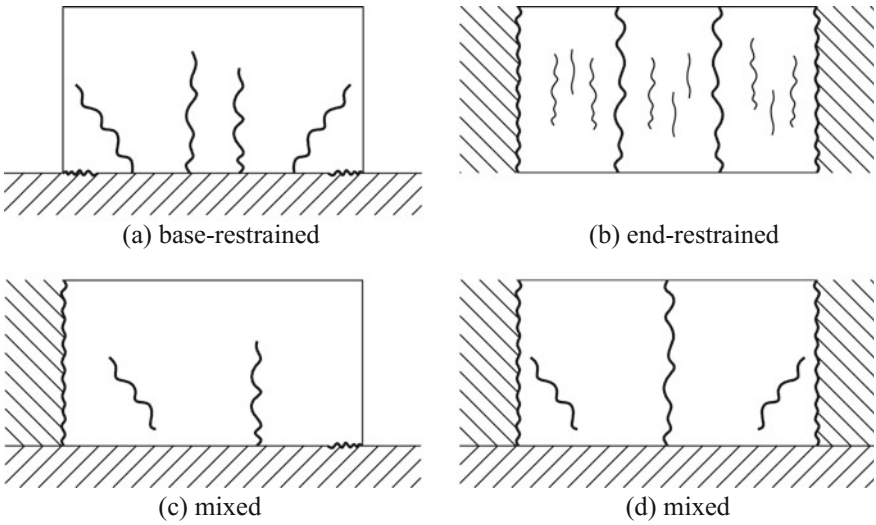

Fig. 8.5 Cracking pattern in restrained elements after (Knoppik-Wróbel 2015)

8.2.2 *Stress Approach Versus Strain Approach*

There are two basic approaches in crack risk prediction. The stress approach postulates that the crack is formed when the stress in a given point determined under the assumption of uncracked sections exceeds the actual tensile strength in that point. The maximum tensile stress σ_{ct} is compared with tensile strength f_t. If $\sigma_{ct} > f_t$, a crack is formed.

In the strain approach, the restrained strain is determined taking into account the effect of restraint, creep and sustained loading:

$$\varepsilon(x, y, z, t) = R(x, y, z) \cdot \varepsilon_{\text{free}}(x, y, z, t) \cdot \varphi \tag{8.1}$$

where

$\varepsilon_{\text{free}}(x, y, z, t)$ free strain in a given location (x, y, z) at time t,
$R(x, y, z)$ restraint coefficient in a given location (x, y, z),
φ creep coefficient (≤ 1).

This strain is then compared with the strain capacity, which relates tensile strength $f_t(t)$ and Young's modulus $E_c(t)$:

$$\varepsilon_{ctu}(t) = \frac{f_t(t)}{E_c(t)} \tag{8.2}$$

The crack is formed when $\varepsilon > \varepsilon_{ctu}$.

Comparing the two approaches, it can be concluded that conceptually stress and strain approaches can be used interchangeably. The approaches differ in detailed methods for determination of the subsequent components, i.e. strains, restraint coefficients and mechanical properties. Section 8.2.3 discusses the methods based on the stress approach while Sect. 8.2.4 discusses the strain approach.

8.2.3 Stress Approach and Cracking Index

8.2.3.1 Compensation Plane Method (JSCE 2011)

The compensation plane method (CPM) was developed by the Technical Committee of the Japan Concrete Institute in 1985 (JCI 1985) and is recommended in the JSCE Guideline no. 15. The method is based on the fact that the early-age stresses in hardening concrete elements result from a coupled action of internal and external restraints of strain. The total strain results from thermal strain (usually a gradient is considered) and shrinkage strain (usually limited to autogenous shrinkage which is assumed uniform). The method had been used mainly for slab and wall structures as the most practical method in Japan. Recently, the thermal cracking for various massive structures has been assessed based on 3D finite element method proposed by JCI guideline (JCI 2008) and AIJ Guideline (AIJ 2008)—please refer to Sect. 8.2.3.2.

The stress exerted due to the internal restraint is caused by a differential strain in the cross section resulting from the temperature (and moisture) gradients. The increment of stress $\Delta\sigma_{\text{int\_}i}$ between ages of t_{i-1} and t_i due to the internal restraint can be determined from the difference between the strain value at a point of the compensation line, $\varepsilon_{\text{comp}}$, and the thermal–shrinkage strain distribution curve, ε_0, by the equation (see Fig. 8.6):

$$\Delta\sigma_{\text{int\_}i}(x,z) = E_c(t_i) \cdot \left(\varepsilon_0(x,z) - \varepsilon_{\text{comp}}\right) \tag{8.3}$$

$$\varepsilon_0(x,z) = CTE \cdot \Delta T_i(x,z) \tag{8.4}$$

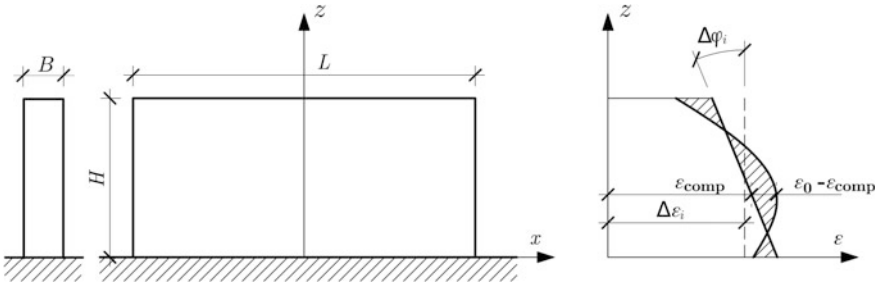

Fig. 8.6 Determination of stresses in a wall-on-slab structure caused by internal restraint according to compensation plane method according to (JSCE 2011)

where

$E_c(t_i)$ Young's modulus of concrete at the age of t_i,
CTE coefficient of thermal expansion of concrete,
$\Delta T_i(x, z)$ temperature difference between ages of t_{i-1} and t_i at point (x, z).

To determine the location of the compensation plane (zero-stress plane), equilibrium of stress block must be determined. For section stability, the sum of tensile stress induced by the temperature or moisture gradient in a cross section should be balanced by an equal compressive force. This approach allows obtaining the increment of the free axial strain $\Delta\varepsilon_i$, and the increment of curvature $\Delta\phi_i$.

$$\Delta\varepsilon_i = \frac{1}{A}\int \varepsilon_0(x,z)\mathrm{d}A \tag{8.5}$$

$$\Delta\phi_i = \frac{\int (\varepsilon_0(x,z) - \Delta\varepsilon_i)(z - z_{\mathrm{cen}})\mathrm{d}A}{I} \tag{8.6}$$

$$\varepsilon_{\mathrm{comp}} = \Delta\varepsilon_i + \Delta\phi_i(z - z_{\mathrm{cen}}) \tag{8.7}$$

where

A area of concrete cross section,
z_{cen} centre of gravity of concrete cross section,
I moment of inertia of area of concrete cross section.

The internal forces due to the external restraint are generated in the element trying to return the plane after deformation to the original restrained position—axial force ΔN_R and bending moment ΔM_R from the age of t_{i-1} to the age of t_i. The increment of stress due to the external restraint $\Delta\sigma_{\mathrm{ext\_}i}$ is determined by the coupled action of the axial force and bending moment, as presented in Fig. 8.7, according to the equation:

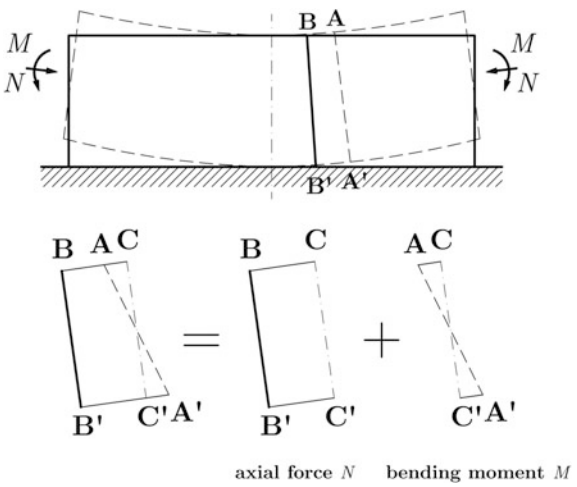

Fig. 8.7 Determination of stresses in a concrete element caused by external restraint according to compensation plane method according to (JSCE 2011)

$$\Delta\sigma_{\text{ext\_}i}(x,z) = \frac{\Delta N_R}{A} + \frac{\Delta M_R}{I}(z - z_{\text{cen}}) \tag{8.8}$$

The internal forces can be defined as follows:

$$\begin{aligned} \Delta N_R &= R_N \cdot E_c(t_i) \cdot A \cdot \Delta\varepsilon_i \\ \Delta M_R &= R_M \cdot E_c(t_i) \cdot I \cdot \Delta\phi_i \end{aligned} \tag{8.9}$$

where

R_N external restraint coefficient for the degree of axial deformation restraint,
R_M external restraint coefficient for the degree of flexural deformation restraint.

The external restraint coefficients are introduced to represent the degree of restraint of the element by the restraining body. Equation 8.8 gets a form:

$$\Delta\sigma_{\text{ext\_}i}(x,z) = R_N \cdot E_c(t_i) \cdot \Delta\varepsilon_i + R_M \cdot E_c(t_i) \cdot \Delta\phi_i \cdot (z - z_{\text{cen}}) \tag{8.10}$$

and the total thermal–shrinkage stress at any position (x, z) can be calculated as:

$$\sigma_{\text{tot}}(x,z) = \sum\nolimits_i \{\Delta\sigma_{\text{int\_}i}(x,z) + \Delta\sigma_{\text{ext\_}i}(x,z)\} \tag{8.11}$$

The values of the restraint coefficients vary within the element according to the degree of restraint. They depend on the difference in stiffness between the restraining body and the early-age concrete element as well as the ratio of the length to the height of the element (L/H). For that purpose the functions of the restraining factors need to be defined. JSCE Guideline no. 15 (JSCE 2011) proposes diagrams of restraining factors, determined with 3D numerical calculations.

Methods based on similar approach can be found in other standards worldwide. Eurocode 2 in Part 3 (EN 1992-3 2008) proposes to determine stress distribution due to translational and rotational restraint of the element based on the known imposed strain from the equation:

$$\sigma(z) = E_c(t_i) \cdot (\varepsilon_i(z) - \varepsilon_a(z)) \tag{8.12}$$

in which the actual strain at level z, $\varepsilon_a(z)$, is given by:

$$\varepsilon_a(z) = (1 - R_N) \cdot \Delta\varepsilon_i + (1 - R_M) \cdot \Delta\phi_i \cdot (z - z_{\text{cen}}) \tag{8.13}$$

where

R_N coefficient defining the degree of the external axial restraint; practical axial restraint factors for common situations may be taken from Fig. 8.8,

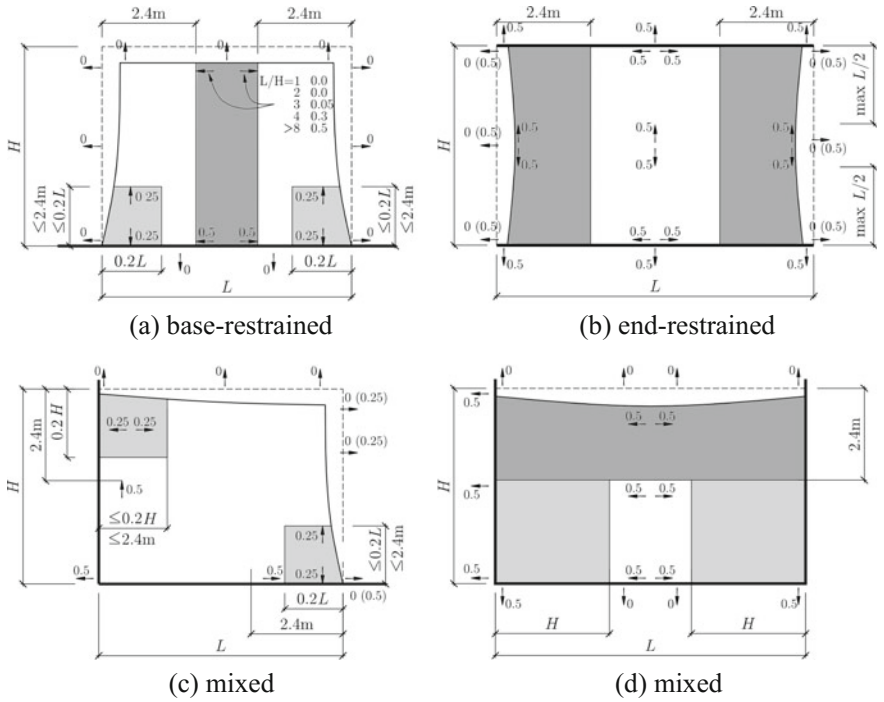

Fig. 8.8 Restraint coefficients in typical situations according to (EN 1992-3 2008)

R_M coefficient defining the degree of the moment restraint (EN 1992-3 2008) states that in a lot of cases the value of $R_M = 1$ can be assumed,
$\varepsilon_a(z)$ actual strain at level z,
$\varepsilon_i(z)$ imposed strain at level z,
$(z - z_{\text{cen}})$ distance to the section centroid, m.

ACI Committee 207 in (ACI 207.2 2007) proposed a simplified approach, allowing for determination of stresses at the centreline of the element, assuming pure translation (no flexure) of the element. The rotational restraint coefficient is assumed as equal to 1. The translational restraint coefficient is defined as a product of the structural shape restraint coefficient, K_R, and the foundation restraint coefficient, K_F:

$$R_N(z) = K_R(z) \cdot K_F \tag{8.14}$$

The tensile stress at any point on the centreline due to a decrease in length, $\bar{\varepsilon}$, can be calculated from the equation:

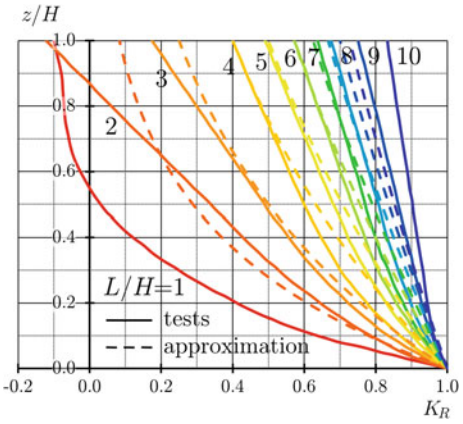

Fig. 8.9 Structural shape restraint coefficient according to (ACI 207.2 2007) after (Knoppik-Wróbel 2015)

$$\sigma(z) = R_N(z) \cdot \overline{\varepsilon} \cdot E_{c,\text{eff}} \tag{8.15}$$

where

$E_{c,\text{eff}}$ effective value of Young's modulus considering creep

The structural shape restraint coefficient, K_R, describes the variation of the restraint with the L/H of the element. The following approximation of K_R distribution is proposed:

$$K_R(z) = \begin{cases} \left[\frac{L/H-2}{L/H+1}\right]^{z/H_W} & \text{for} \quad L/H \geq 2.5 \\ \left[\frac{L/H-1}{L/H+10}\right]^{z/H_W} & \text{for} \quad L/H < 2.5 \end{cases} \tag{8.16}$$

where z signifies the location above the construction joint. The tensile restraint distribution at the centre section is shown in Fig. 8.9.

The restraint stresses decrease in direct proportion to the decrease in stiffness of the restraining foundation material. The foundation restraint coefficient, K_F, was introduced to account for the influence of the foundation stiffness on the restraint of the concrete element:

$$K_F = \frac{1}{1 + \frac{A_W E_W}{A_F E_F}} \tag{8.17}$$

where

$A_W E_W$ axial stiffness of early-age concrete element,

$A_F E_F$ axial stiffness of foundation or other restraining body. For the restraint by the rock, (ACI 207.2 2007) suggests to take $A_F = 2.5A_W$.

(ACI 207.2 2007) elaborates also on the effect of the internal restraint which adds to this of the external restraint. Stress due to the internal restraint is induced by the temperature and moisture difference in cross section and tensile stresses are due to occur at the surface of the element. The value of these stresses can be determined with the equation previously proposed, analogically as for the external restraint, except that the effective restraining plane is the plane of zero stress in the internal stress block (compensation plane). Internal restraint coefficient is introduced; however, no proposal for determination of its value is made.

When the stresses generated at the joint exceed the bond strength, a horizontal crack at the joint is formed and the bond between the two is limited—a slip of the element is observed. This has an influence on further development of stresses in the element. This effect was taken into consideration by Nilsson (2000, 2003). The approach based on CPM introduces a single restraint factor, R, to determine the restraint stress, σ, based on the stress at the total restraint, σ_{fix}:

$$\sigma = R\left(R_0, \delta_{\text{res}}, \delta_{\text{slip}}\right) \cdot \sigma_{\text{fix}} \tag{8.18}$$

with

$$\sigma_{\text{fix}} = E_{c,\text{eff}} \cdot \varepsilon_0 \tag{8.19}$$

where

R_0 plane-section restraint coefficient, which depends on the geometry of the structure as well as the rotational R_{Mz}, R_{My} and translational R_N boundary restraints,

δ_{res} resilience coefficient considering the nonlinear effects,

δ_{slip} slip coefficient which depicts a restraint stresses reduction as a result of slip failure.

The value of δ_{res} changes at the height of the wall and depends on the boundary restraint. It is a product of the basic resilience coefficient and translational and rotational correction coefficients. To simplify, the resilience coefficient is taken as equivalent to the basic resilience coefficient, $\delta_{\text{res}} = \delta_{\text{res}}^0$, and the correction to account for the translational and rotational boundary influence is included by introduction of the effective width of the restraining body, $B_{F,\text{eff}}$, instead of the real width, B_F. The resilience coefficient is analogical to the structural shape restraint factor, K_R, given by (ACI 207.2 2007). The values of δ_{res} are given in diagrams in Fig. 8.10 or can be approximated with a polynomial function:

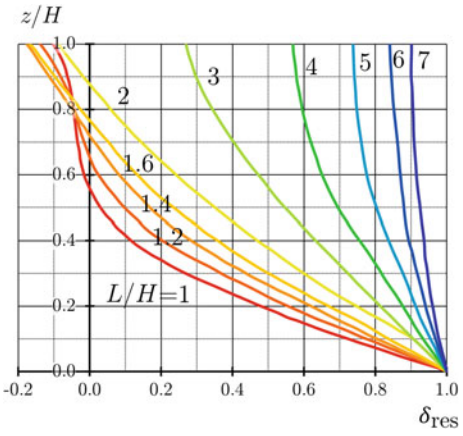

Fig. 8.10 Basic resilience coefficient according to (Nilsson 2000) after (Knoppik-Wróbel 2015)

$$\delta_{\text{res}}^{0} = \sum_{i=1}^{n} a_i \left(\frac{z}{H_W} \right)^i \tag{8.20}$$

where

a_i coefficients of a polynomial function describing resilience coefficient distribution.

The slip coefficient depends on the free length, the width and the height of the casting section. It can be determined experimentally or numerically. The values of δ_{slip} proposed by (Nilsson 2000) are given in diagrams in Fig. 8.11.

The decisive restraint coefficient distribution at height z in the central section of a wall can be calculated according to the following equation:

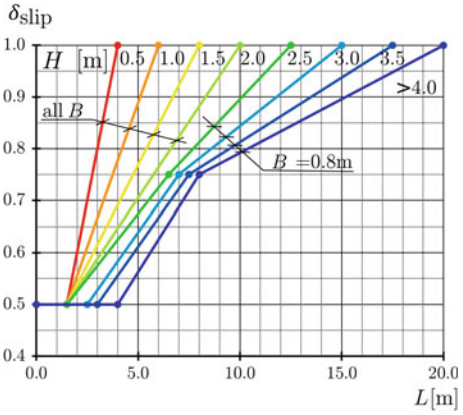

Fig. 8.11 Slip coefficient according to (Nilsson 2000) after (Knoppik-Wróbel 2015)

$$R(z) = \delta_{\text{res}} \cdot \delta_{\text{slip}} - R_0 = \delta_{\text{res}} \cdot \delta_{\text{slip}} - \left(R_N + R_{Mz} + R_{My}\right) \tag{8.21}$$

When the plane-section hypothesis applies, no slip occurs (for the walls with $L/H > 5$), no volume change in the restraining body occurs and there are no translational or rotational boundaries, and the restraint factor can be expressed with an analytic expression (Nilsson 2003):

$$R(z) = 1 - R_0 = 1 - \left(R_N(z) + R_{Mz}(z) + R_{My}(z)\right) \tag{8.22}$$

where R_N, R_{Mz} and R_{My} are given as follows:

$$\begin{aligned}
R_N(z) &= \frac{1}{1 + \frac{E_F}{E_W}\frac{H_F B_{F,\text{eff}}}{H_W B_W}} \\
R_{Mz}(z) &= \frac{(z_{\text{cen}} - z)(z_{\text{cen}} - 0.5H_W)}{\frac{{H_W}^2}{12} + \left(z_{\text{cen}} - \frac{H_W}{2}\right)^2 + \frac{E_F}{E_W}\frac{H_F B_{F,\text{eff}}}{H_W B_W}\left(\frac{{H_F}^2}{12} + \left(z_{\text{cen}} - \frac{H_F}{2}\right)^2\right)} \\
R_{My}(z) &= \frac{\left(y_{\text{cen}} - \omega 0.5\left(B_{F,\text{eff}} - B_W\right)\right)^2}{\frac{{B_W}^2}{12} + \left(y_{\text{cen}} - \omega\frac{B_{F,\text{eff}} - B_W}{2}\right)^2 + \frac{E_F}{E_W}\frac{H_F B_{F,\text{eff}}}{H_W B_W}\left(\frac{{B_{F,\text{eff}}}^2}{12} + {y_{cen}}^2\right)}
\end{aligned} \tag{8.23}$$

When slip failure in the joint is possible and if sections do not remain plane under deformation (high-wall effect), the restraint in the wall is defined as:

$$R(z) = \delta_{\text{slip}} \cdot \left(\delta_{\text{res}}(z) - \left(R_N(z) + R_{Mz}(z) + R_{My}(z)\right)\right) \tag{8.24}$$

where R_N, R_{Mz} and R_{My} are given as follows:

$$\begin{aligned}
R_N(z) &= \frac{\sum_{i=1}^{n}\frac{a_i}{i+1}}{1 + \frac{E_F}{E_W}\frac{H_F B_{F,\text{eff}}}{H_W B_W}} \\
R_{Mz}(z) &= \frac{(z_{\text{cen}} - z)\left(z_{\text{cen}}\sum_{i=1}^{n}\frac{a_i}{i+1} - H_W\sum_{i=1}^{n}\frac{a_i}{i+2}\right)}{\frac{{H_W}^2}{12} + \left(z_{\text{cen}} - \frac{H_W}{2}\right)^2 + \frac{E_F}{E_W}\frac{H_F B_{F,\text{eff}}}{H_W B_W}\left(\frac{{H_F}^2}{12} + \left(z_{\text{cen}} - \frac{H_F}{2}\right)^2\right)} \\
R_{My}(z) &= \frac{\left(y_{\text{cen}} - \omega 0.5\left(B_{F,\text{eff}} - B_W\right)\right)^2}{\frac{{B_W}^2}{12} + \left(y_{\text{cen}} - \omega\frac{B_{F,\text{eff}} - B_W}{2}\right)^2 + \frac{E_F}{E_W}\frac{H_F B_{F,\text{eff}}}{H_W B_W}\left(\frac{{B_{F,\text{eff}}}^2}{12} + {y_{cen}}^2\right)}
\end{aligned} \tag{8.25}$$

The restraint factor can be used as a measure to characterise the stresses induced in the walls; however, the degree of restraint obtained with the numerical and analytic model complies only to some extent. Generally, analytical formulations assume that the degree of restraint increases with an increasing *L/H* ratio. Nevertheless, actually for the same *L/H* ratios, it is not equal but has lower values in walls with larger *L* and *H* dimensions. Also, in case of walls of foundations where the centre of gravity of the combined cross section is located above the wall bottom,

restraint degree can decrease at the bottom. Hence, in determination of the degree of restraint not only the *L/H* ratio but also the individual dimensions of the wall and the restraining body must be taken into account (Knoppik-Wróbel and Klemczak 2015).

8.2.3.2 Simple Prediction of Thermal Stresses in Massive Structures (AIJ 2008)

Recent Japanese guidelines for massive concrete structures: Japanese Concrete Institute (JCI) Guideline (JCI 2008) and Architectural Institute of Japan (AIJ) Guideline (AIJ 2008) suggest that thermal stress analysis in massive concrete structures should be performed with 3D finite element method. The risk of cracking is then assessed with the cracking index (see Sect. 8.2.3.4) where stresses are compared with the actual strength (stress-to-strength ratio). The stress-to-strength ratio (inverse of cracking index) is limited to be less than 0.8 for thermal cracking assessment to avoid the penetration cracks.

The AIJ Guideline proposes also a simple method for prediction of the stress-to-strength ratio for relatively small slab elements (thickness ≤ 3.5 m and length ≤ 40 m) and wall elements (height ≤ 4 m, width ≤ 3.5 m and length 40 m) on the slab with less than 1.0 m thickness. The stress-to-strength ratio can be determined with the charts for a given cement type as shown in Fig. 8.12. According to the slab thickness or wall width and type of cement, the temperature rise (T_{up}) can be estimated (graph I). Then, the cross point between the ratio of the Young's modulus of concrete and soil or rock foundation (E_F/E_c) and length-to-height ratio of the element (L/H_c) in graph II-1 can be extended to the cross point with the foundation's Young's modulus (E_G) in graph II-2. Finally, the point in graph II-2 and the obtained T_{up} are connected to determine the stress-to-strength ratio in graph II-3.

The charts for this graphical method proposed by AIJ Guideline are based on more than 1000 cases and it has been proven that this simple fitting is reasonable for thermal stress cracking risk assessment.

8.2.3.3 An Example of a Simplified Approach

Knowing the evolution of the temperature of concrete, of the Young's modulus, of the relaxation function and of the tensile strength (see Chap. 4), and applying the superposition principle, it is possible to evaluate the stress in case of a uniaxial restrained section from the following equation (see Fig. 8.12):

$$\sigma_t = \sum_{t'=1}^{t' \leq t} CTE \cdot \Delta T(t') \cdot E_c(t') \cdot \psi(t, t') \cdot \gamma_R \tag{8.26}$$

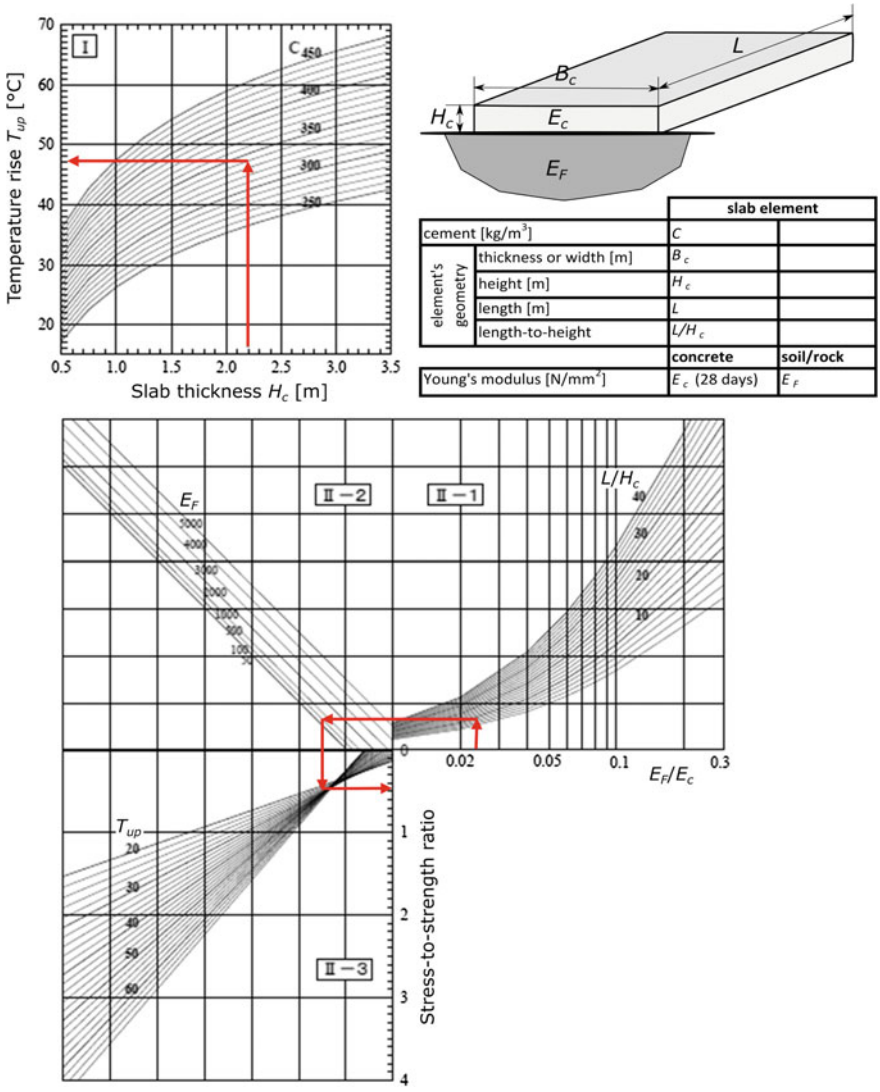

		slab element	
cement [kg/m^3]		C	
element's geometry	thickness or width [m]	B_c	
	height [m]	H_c	
	length [m]	L	
	length-to-height	L/H_c	
		concrete	soil/rock
Young's modulus [N/mm^2]		E_c (28 days)	E_F

Fig. 8.12 Charts for graphical prediction of stress-to-strength ratio for ordinary portland cement massive concrete structures according to AIJ Guideline (AIJ 2008). Example of red line: C = 340 kg/m^3, H_c = 2.2 m, E_F = 500 N/mm^2, E_c = 24400 N/mm^2, L = 20 m → T_{up} = 47 °C, E_F/E_c = 0.02, stress-to-strength ratio = 0.47

where

t concrete age,
t' the age where load/stress is applied,
$\psi(t,t')$ relaxation function,
γ_R restraint factor (1.0 for fully restrained).

For each time step, these parameters are considered constant.

The variation of concrete stress relaxation function during the first hours after mixing of concrete is very high. Van Breugel (1982) has proposed a relaxation function based on the degree of hydration, which permits to calculate stresses for each incremental increase or decrease of stresses at time t'. The author considered instead of the degree of hydration, due to the complexity in its determination, the Young's modulus of concrete, defining the estimated relaxation that would occur after a time t:

$$\psi(t,t') = \exp - \left[\left(\frac{E_c(t)}{E_c(t')} - 1 \right) + v \cdot t'^{-d} \cdot (t-t')^n \cdot \frac{E_c(t)}{E_c(t')} \right] \tag{8.27}$$

where

v a parameter equal to $0.44w/c$,
d parameter depending on the type of hydration (slow $d = 0.30$, fast $d = 0.40$),
n parameter depending on the type of load (compression $n = 0.30$, tension $n = 0.60$). Equation 8.27 does not consider the effect of autogenous shrinkage and recently the author has proposed to set the n parameter to a single value of 0.30 for both load types.

Figure 8.13 shows examples of the effect of relaxation on the stresses considering different times t_1–t_3 when compared to the elastic evolution (dashed line). The red curve gives the evolution of the stress when all the cumulative stress variations due to relaxation are taken into account.

Figure 8.14 shows an example of the stresses calculated with such an approach till an age of 7 days with a variable daily temperature variation. The red curve

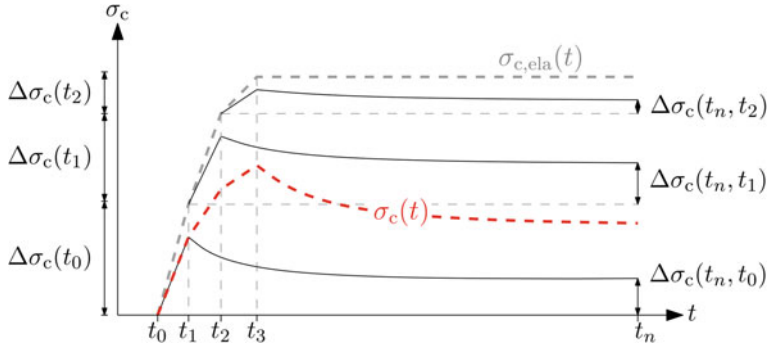

Fig. 8.13 Principle of evaluation of stresses (Schlicke 2014)

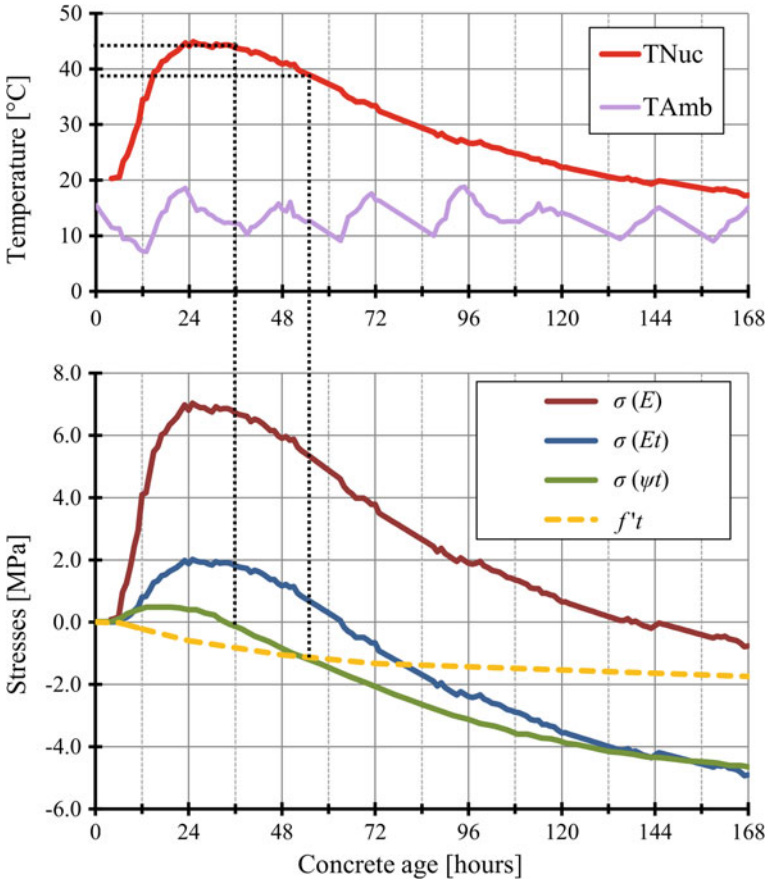

Fig. 8.14 Evolution of measured temperature and calculated stresses with different assumptions. Results by L. Ebensperger (unpublished)

corresponds to the measured concrete core temperature ($T_{max} = 45\,°C$ after 25 h). The green curve is the expected stresses when considering a constant E-modulus for concrete. The blue curve presents the expected stresses when considering an E-modulus for concrete variable in time. And finally, the brown curve is the expected stresses when considering stress relaxation using the incremental equation on a step-by-step calculation. These stresses are compared to the yellow dotted line which corresponds to the expected concrete tensile strength.

Two important temperatures could be noticed:

1. A temperature that corresponds to a stress is equal to zero (second zero temperature). It was reached when concrete showed a temperature of 44 °C after 34 h, just 9 h after reaching the maximal temperature. Each temperature decrease after this moment would generate tensile stresses in the concrete, and the moment of cracking would depend on one hand on how fast the concrete

gains tensile strength, and on the other hand on how fast the concrete loses temperature to the ambient.
2. The moment of the expected occurrence of cracking is achieved after 57 h with a concrete temperature of 38.2 °C, much higher than the ambient temperature.

Note that in case of temperature gradients, additional stresses should be considered and added at the surface level to the stresses that where calculated in this section in order to evaluate the cracking risk.

The theoretical background was gain through different doctoral thesis done at the Baustoffinstitut der TU München (Springenschmid 1987; Breitenbücher 1989; Ebensperger 1990; Schöppel 1993; Mangold 1994) using the 100% restrained cracking frame. The effect of restraint conditions (different than 100%) constant throughout the section may be estimated considering a restraint factor γ_R in Eq. 8.26, and in case of variable restraint conditions in the section, Fig. 8.9 may be used for determination of the tensile stresses. The restraint factor γ_R varies between 0 (free) and 1.0 (fully restrained).

8.2.3.4 Cracking Index

Level I: Cracking criterion based on average values

Cracking criteria are used to evaluate the moment of cracking of a hardening concrete element in time. The cracking index is a general description that uses the average values of the actual stress and strength level as a basis for evaluation, running between 0 and 1. A way to use this cracking index, for example proposed in the JSCE guidelines, is to relate the uniaxial tensile stress $\sigma_{ct}(t)$ to the mean concrete tensile splitting strength $f_{ctm}(t)$. In this way, the cracking index changes into:

$$I_{\mathrm{cr}} = \frac{\sigma_{ct}(t)}{f_{ctm}(t)} \tag{8.28}$$

For the mean tensile splitting strength of a normal strength concrete, (Lokhorst 2001; Czerny et al. 2005) developed an experimentally based refined formulation. For this, the ratio between the mean uniaxial tensile strength and the mean tensile splitting strength is explicitly considered with a factor 0.9, yielding into:

$$f_{ctm} = 0.9 \cdot f_{ctm,sp} \tag{8.29}$$

where

f_{ctm} mean uniaxial tensile strength,
$f_{ctm,sp}$ mean concrete tensile splitting strength.

Tensile splitting strength experiments on regular concretes (Lokhorst 2001) have shown cracking index at failure that ranges between 0.75 for a moderate and 0.88

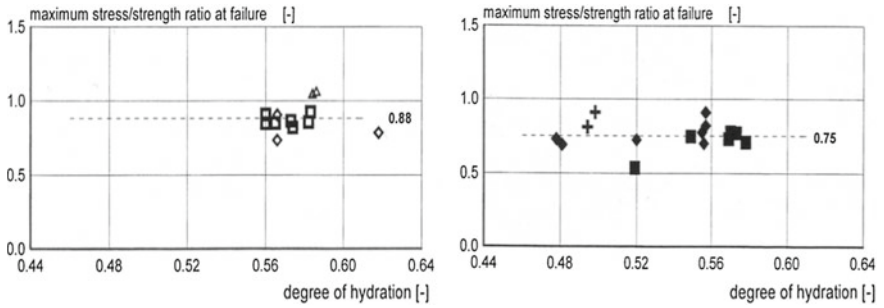

(a) maximum cracking index representing in-situ conditions (restraint deformations)

(b) maximum cracking indexof regular concretes specimens loaded in a laboratory

Fig. 8.15 Maximum cracking index (stress/strength ratio) in different conditions after (Lokhorst 2001)

for a faster loading rate, representing in situ and laboratory conditions, respectively (Fig. 8.15).

Taking this rate effect also into account, representing the difference in loading rates occurring in real-life in situ early-age concretes and rates commonly applied for laboratory testing tensile splitting strength specimens, a value of 0.85 is proposed, leading to the following criterion:

$$\sigma_{ct}(t) \leq 0.9 \cdot f_{ctm,sp,\text{long}} = 0.9 \cdot 0.85 \cdot f_{ctm,sp,\text{short}} \approx 0.75 \cdot f_{ctm,sp} \tag{8.30}$$

where

$f_{ctm,sp,\text{long}}$ mean concrete tensile splitting strength measured at slow loading rates representing loading rates that develop during early-age stress development in hardening concrete structures,

$f_{ctm,sp,\text{short}}$ mean concrete tensile splitting strength measured at high loading rates representing normal laboratory test loading rate conditions.

For high-strength reinforced concrete, (Sule 2003) developed a cracking criterion, where the effect of the materials ductility on the sensitivity towards the rate of loading has been accounted for. Taking this influence into consideration, the following cracking criterion for high-strength concrete was proposed:

$$\sigma_{ct}(t) \leq 0.6 \cdot f_{ctm,sp} \tag{8.31}$$

In the daily construction practise, where the cracking risk has to be defined in the design stage of a project, it is quite common that the tensile stresses should not exceed half of the tensile strength capacity. This general rule is implicitly representing a cracking index of 0.5. Reformulating this design rule for the mean tensile splitting strength leads to the following cracking criterion for the practice:

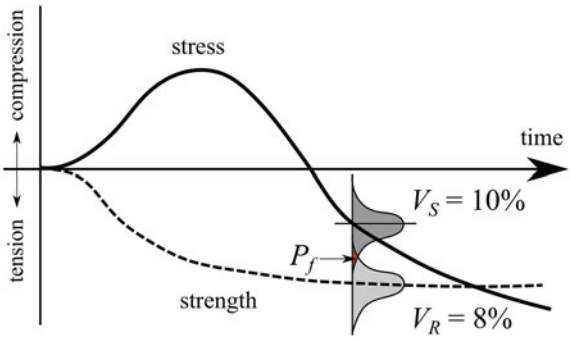

Fig. 8.16 Typical example of mean stress and strength development with time, showing the associated uncertainties expressed in terms of variation coefficients of 10% and 8%, respectively

$$\sigma_{ct}(t) \leq 0.5 \cdot f_{ctm} = 0.45 \cdot f_{ctm,sp} \tag{8.32}$$

In order to take into account the uncertainties on the materials heterogeneity and stress calculations, partial safety factors for both tensile strength and stress have to be applied.

Level II: First-Order Second-Moment Method (FOSM)

Whenever taking into account undetermined influences causing different uncertainties in the actual strength and/or stress level, a more advanced formulation of the cracking criterion is necessary. In this respect, a more detailed probabilistic analysis is required that may follow the Level II approach. Such method is called the first-order second-moment method (FOSM). An indicative example of the tensile stress and tensile strength development over time, in a fresh concrete wall cast on an already hardened floor slab (Fig. 8.6), is provided in Fig. 8.16.

The results also show the uncertainties that go along with both the stress and strength development expressed in terms of statistical variation coefficients with common values of 10% and 8%, respectively. The results show first an increase of the stresses in compression followed by a decrease in tension, following the temperature and autogenous shrinkage developments over time. The strength development follows the properties associated with the mix design.

This so-called first-order second-moment method is a very frequently used method for calculating the cracking risk of hardening massive concrete structures. The method uses the first two statistical moments, i.e. mean value and standard deviation, which represent the stress and strength that develop during a hardening process. When considering the concrete strength to be the resistance R and the stress to be the load S, a general statistical formulation can be derived for the cracking risk, indicated by the overlapping part of the Gauss curves in Fig. 8.16. In this general statistical approach, the uncertainties are assumed to follow a regular Gaussian normal distribution with coefficients of variation for the strength and stress of 10% and 8%, respectively. Cracking occurs whenever the cracking index

has reached a certain critical level, representing equilibrium between the actual tensile strength and tensile stress. Whenever considering the maximum allowable average tensile stress level not to exceed at an average stress level of 75% of the actual mean tensile splitting strength, the probability of failure, representing the event of first crack occurrence, can be defined. After a successful stress and strength computation, the risk of cracking can to be determined from the mean values, σ_S and σ_R, and standard deviations of μ_S and μ_R, respectively. The coefficients of variation are assumed to be $V_S = 10\%$ and $V_R = 10\%$. For the probability of failure, it holds (Koenders et al. 2005, 2007):

$$P_f\{Z = R - S = 0.75 \cdot f_{ctm,sp} - \sigma_{ct} < 0\} = P_f\left\{u < \frac{Z - \mu_Z}{\sigma_Z}\right\} = P_f\left\{u < -\frac{\mu_Z}{\sigma_Z}\right\} \tag{8.33}$$

with

$$\mu_Z = \mu_R - \mu_S \tag{8.34}$$

$$\sigma_Z = \sqrt{\sigma_R^2 + \sigma_S^2} \tag{8.35}$$

where

$$\sigma_R = \mu_R \cdot V_R = \left(0.75 \cdot f_{ctm,sp}\right) \cdot V_R \tag{8.36}$$

and

$$\sigma_S = \sigma_{ct} \cdot V_S \tag{8.37}$$

From this, the risk of cracking of the combined stress-strength system can be calculated from the combined mean value and standard deviation μ_Z and σ_Z, respectively. The cracking uncertainties of the combined system can also be expressed in terms of a so-called safety factor. The safety factor is defined as the ratio between the characteristic strength and the characteristic stress. The characteristic values are determined with a 5% reliability ($\beta = 1.64$). Herewith the safety factor can be calculated, leading to the following equation:

$$\gamma = \frac{R_{\text{char}}}{S_{\text{char}}} = \frac{\mu_R - 1.64 \cdot \sigma_R}{\mu_S + 1.64 \cdot \sigma_S} = \frac{(1 - 1.64 \cdot V_R)}{(1 + 1.64 \cdot V_S)} \cdot \frac{\mu_R}{\mu_S} \tag{8.38}$$

For early-age concrete, R_{char} can be replaced by the characteristic tensile failure strength, which is in this case the tensile splitting strength, and S_{char} by the characteristic stress. Elaboration leads to the following formula for the safety factor:

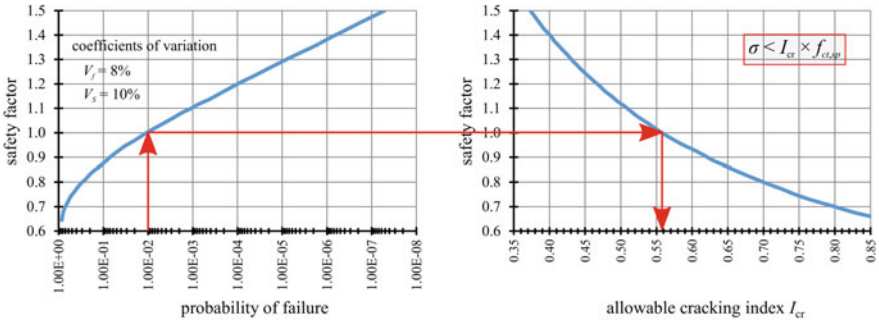

Fig. 8.17 Design graph for determination of the allowable cracking index (stress/strength ratio)

$$\gamma = \frac{f_{\text{char}}}{\sigma_{\text{char}}} = \frac{\left(1 - 1.64 \cdot V_f\right) \cdot 0.75 \cdot f_{ctm,sp}}{\left(1 + 1.64 \cdot V_\sigma\right) \cdot \sigma_{ct}} \tag{8.39}$$

where

V_f variation coefficient of the strength,
V_σ variation coefficient of the stress.

In order to avoid "complex" statistical calculations to calculate the cracking index, a design graph was developed. With this design graph, for a chosen probability of failure a corresponding safety factor and allowable cracking index can be determined that is representing the cracking risk of a massive concrete structure. Or, vice versa, for a calculated cracking index, the corresponding probability of cracking can be obtained. In Fig. 8.17, an example is shown for a probability of failure of $P_f = 10^{-2}$. Via this design graph the related safety factor turns out to be $\gamma = 1.0$ and the maximum allowable cracking index $I_{\text{cr}} = 0.56$. According to the results of this design graph, it is allowed that the cracking index, representing the cracking index, has a maximum value of $I_{\text{cr}} = 0.56$, which is the point where cracking is expected with a probability of occurrence of $P_f = 10^{-2}$. As already mentioned before, in practice, an allowable cracking index of $I_{\text{cr}} = 0.50$ is commonly used for mass concrete structures. This value for I_{cr}, thus, corresponds to a safety factor of $\gamma = 1.12$ and a probability of failure of $P_f = 10^{-3}$.

Level III

A Level III approach is a full probabilistic analysis where the statistical uncertainties of all parameters are taken into account by means of their probability density function, represented by a mean value and standard deviation. Most frequently used calculation method is the so-called Monte Carlo approach, where the variation in the parameters is taken into account by random selection of the parameters from their probability density functions while using this as input data for the analysis. With this calculation procedure, all probability density functions of all

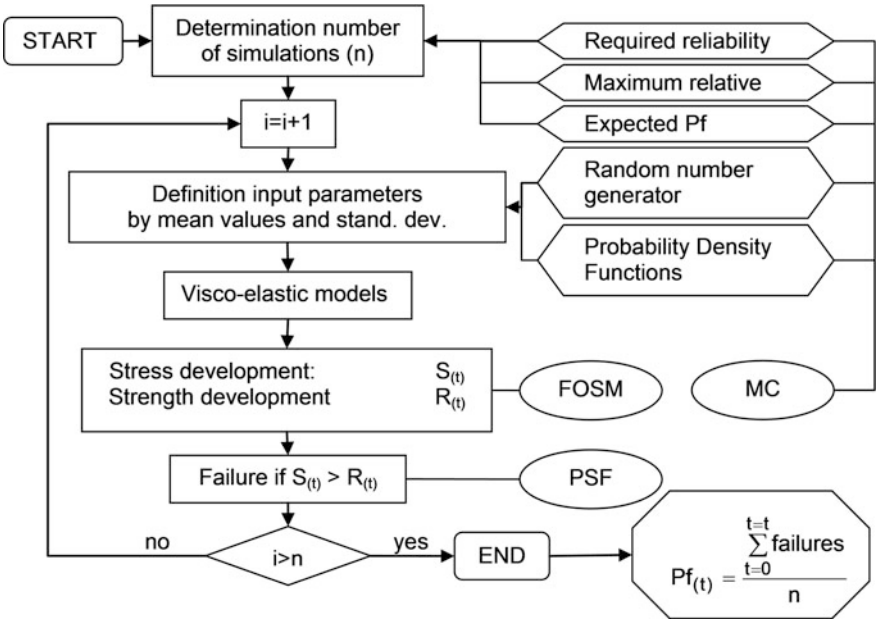

Fig. 8.18 General flowchart of the Monte Carlo approach (MC—Monte Carlo, PSF—partial safety factor and FOSM—first-order second-moment), according to (van der Ham et al. 2006a)

strength and load variables are taken into account. It links the cracking reliability of an element directly to the probability density functions of the stochastic input parameters, which can be either normal or lognormal. Results of laboratory tests or literature data can be used to establish the probability density functions of the input parameters of the early-age cracking problem. This stochastic data can then be used as input for the probabilistic analysis, where different sets of input parameters are generated for each new calculation event, following a Monte Carlo approach. A general flow chart of a Crude Monte Carlo (MC) analysis is shown in Fig. 8.18. The flowchart also indicates the possibility to calculate the level of the partial safety factor (PSF) and the level of the first-order second-moment (FOSM), from the same input data.

The simulation results are used to estimate a probability of failure of a massive concrete system while taking into account all parameter uncertainties. Since all input parameters are considered as random variables, the calculated probability function itself can be treated as a stochastic variable. The uncertainty in the estimation of the system probability will decrease with an increasing total number of simulations (events). For a required system reliability of 95% and a maximum relative error of 0.1, the required number of simulations n should exceed a minimum number of [5, 6]:

Table 8.2 Input data for the Monte Carlo approach, taken from (van der Ham et al. 2006a, b)

Variable	Mean value	CoV [%]	Variable	Mean value	CoV [%]
Material parameters			*External parameters*		
Density—gravel [kg/m^3]	2650	1	Wind speed [m/s]	2	10
Density—sand [kg/m^3]	2650	1	Mean surr. temp [°C]	20	10
Density—cement [kg/m^3]	3150	1	Ampl. surr. temp [°C]	10	20
E_a [kJ/mol]	45.7	10	Initial concrete temp [°C]	20	10
CTE [1/K]	1.2×10^{-5}	5	Construction width [m]	1.00	5
Q_{max} [kJ/kg cement]	440	2.5	Construction height	3.00	2.5
Density—concrete [kg/m^3]	2500	1	Restraint [-]	1.0	10
λ formwork [W/mK]	0.17	10	Formwork thickness [m]	0.02	5
Mix parameters			*Calculation parameters*		
			d age [-]	0.35	10
Air content [%]	1	10	*n* tension [-]	0.30	10
Gravel [kg]	695	10	*n* compression [-]	0.30	10
Sand [kg]	1236	1	E_a—aggregate [MPa]	55000	10
Cement [kg]	350	1	E_p—cement particle [MPa]	55000	10
Water [kg]	150	1	E_c—concrete [MPa]	31000	10

$$n > 400 \cdot \left(\frac{1}{P_f} - 1\right) \tag{8.40}$$

For an arbitrary estimated system probability failure of 0.5, the number of simulations required for this calculation should be at least $n > 400$, which is considered a reasonable number for common analyses on massive concretes.

In Table 8.2, an indicative overview of the most relevant parameters that play a role in the accuracy of the crack risk analysis are presented. In this example, 28 randomly distributed variables are considered, showing their mean value and assumed coefficient of variation (CoV = standard deviation/mean value), and represent their probability density function. All parameters are generated new, following a random likelihood, and used as input for the cracking analysis. This

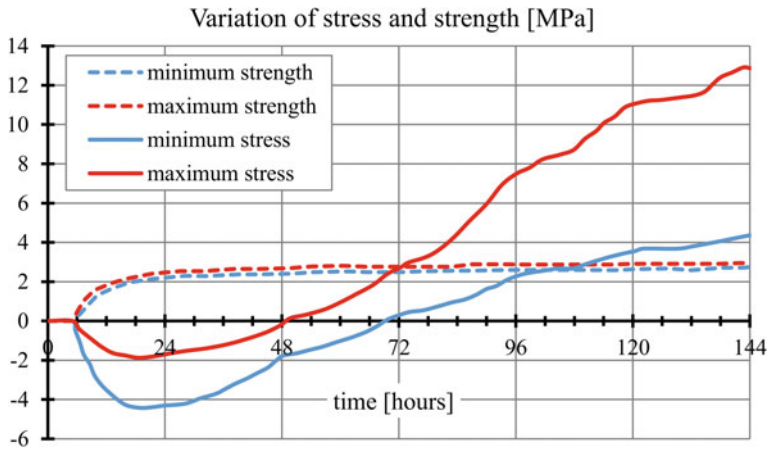

Fig. 8.19 Maximum and minimum stress/strength development from a full probabilistic analysis

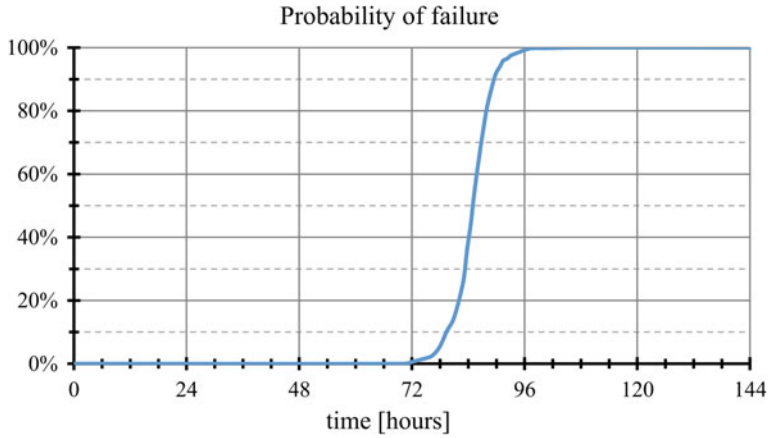

Fig. 8.20 System probability density function calculated with a Level III analysis

procedure will be repeated 400 times and will lead to a system probability function with time calculated from the various stress-strength calculations.

Figure 8.19 shows the results of a regular wall-on-slab structure (Fig. 8.6) assessed according to the Level III full probabilistic analysis. The results show the highest and lowest stress and strength developments with time, being the result of the randomly selected set of input parameters from Table 8.2. From the analysis, it can be seen that the tensile stress exceeds the actual tensile strength somewhere between 72 h (most unfavourable randomly selected parameter combination) and 108 h (most favourable randomly selected parameter combination). These

differences are the result of variations in the input values of the crack risk analysis. Between the 72 and 108 h, the system probability will increase from 0% to 100%, representing a so-called S-curve (see Fig. 8.20). This curve is indicative for all variations in the probabilistic system and shows the pace at which these variation affect the stress-strength development. Whenever comparing this method with the Level I or II methods, it can be observed that those methods consider a probability of failure of 50%, which shows that the Level III method also provides valuable data of the cracking risk already before this value has been reached.

8.2.4 Strain Approach and Strain Capacity

This approach is based on the assumption that cracking is caused by exceeding tensile strain capacity of hardening concrete. The effect of creep and sustained loading is taken into account by introduction of relevant coefficients. CIRIA C660 (Bamforth 2007) is an example of this approach.

The restrained strain due to internal restraint is said to be caused by solely thermal gradient and calculated by introduction of the internal restraint factor:

$$\varepsilon_{\text{int}} = K_1 \cdot CTE \cdot \Delta T \cdot R_i \tag{8.41}$$

where

K_1 coefficient for the effect of stress relaxation due to creep under sustained loading ($K_1 = 0.65$),
ΔT temperature gradient, °C,
R_i internal restraint factor; for the condition of internal restraint, it has been estimated that $R_i = 0.42$.

The restrained strain due to external restraint is calculated by taking into account the long-term thermal and shrinkage deformations as:

$$\varepsilon_{\text{ext}} = K_1 \left[(CTE \cdot T_1 + \varepsilon_{au}) \cdot R_1 + CTE \cdot T_2 \cdot R_2 + \varepsilon_{d,sh} \cdot R_3 \right] \tag{8.42}$$

where

T_1 difference between the peak temperature, $T_{\max}$, and the mean ambient temperature T_a, °C,
T_2 long-term decrease of temperature which takes into account the time of year at which the concrete was cast, °C,
ε_{au} autogenous shrinkage,
$\varepsilon_{d,sh}$ drying shrinkage,
R_1 restraint factor that applies during the early thermal cycle,
R_2, R_3 restraint factors applying to long-term thermal movement and drying shrinkage, respectively.

CIRIA C660 provides a detailed comparison of restraint coefficients in different restraint conditions given by various European standards. It is also commented that the values of restraint coefficient for long-term loads, R_2 and R_3, can be lower than R_1, so application of a single restraint coefficient as proposed by EC2-3 is a conservative approach: assuming that $R_1 = R_2 = R_3 = R$, the maximum value of $K_1 R = 0.5$.

In the strain criterion postulated by CIRIA C660, the expected strain in the hardening element accounting for the restraint, ε/R, is compared with the strain capacity of concrete, ε_{ctu}, calculated as the ratio between the mean tensile strength and the mean Young's modulus, $f_{ctm}(t)/E_{cm}(t)$, which is a lower bound limit value. Nevertheless, given the positive effects of creep on stress and strain relaxation, which can be expressed with a coefficient $K_1 = 0.65$, and sustained loading on tensile properties, which can be expressed with coefficient $K_2 = 0.8$, the actual tensile strain capacity can be increased by $K_2/K_1 = 1.23$.

8.2.5 Simplified Method for Macrocrack Assessment

A simplified method to assess the risk of hardening-induced macrocracks is the comparison of restraint forces with cracking forces. In contrast to the common approach in crack assessment, which is usually based on the overall stresses and failure in material points of a cross section, such procedure concentrates only on the stress resultants in a cross section, whereby the effects of *Eigenstresses* are not pursued. In the context of macrocrack assessment, this simplification is conservative since beneficial influences of the compressive part of *Eigenstresses* were neglected in the uncracked state. At the same time, the tensile part of *Eigenstresses* causes local tensile stress maxima in the cross section; however, *Eigenstresses* begin to disappear to a certain extent as soon as the failure criterion will be reached. The reason is the formation of microcracks or small, locally restricted cracks. Concluding: *Eigenstresses* are beneficial as long as a uncracked state can be presumed—but if cracking cannot be excluded, *Eigenstresses* have only minor importance for the location and width of macrocracks. The underlying model conception is illustrated in Fig. 8.21. For further details, see e.g. (Schlicke and Tue 2015) or (Knoppik-Wróbel and Schlicke 2016).

On basis of these conclusions and with regard to the aimed practicability, the simplified macrocrack assessment is based on an analytical solution. In particular, this will be enabled since only uniformly and linearly in the cross-section distributed deformation impacts need to be considered, whereas nonlinear effects due to temperature and moisture field changes in the cross section can be neglected. Of course, the absolute size of the restraint forces and moments still depends on a complex interaction of thermal and mechanical influences with strict respect to timely variations; however, this can be considered by equivalent temperature impacts with respect to the stiffness of the hardened member. The size of these

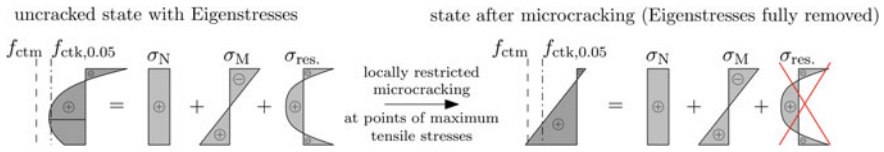

Fig. 8.21 Role of *Eigenstresses* on the process of macrocracking (Schlicke 2014)

equivalent temperature impacts has to be determined beforehand taking into account the hardening behaviour of the concrete as well as thickness of the cross section. But if they are once known, they can easily be provided for practical design, as implemented in related national guidelines of Germany and Austria (BAW 2011; OeBV 2018).

The analytical solution is derived from the equilibrium as well as the deformation compatibility of the present member. The mechanical consistence in such procedure enables both (i) a suitable consideration of the structural response of the member according to the material behaviour and member type and (ii) a realistic consideration of the restraint situation in the individual case. The most common member types affected by the outlined effects are ground slabs and walls on foundations for which the determination of restraint forces and moments is given in the following.

8.2.5.1 Decisive Restraint Forces and Moments in Ground Slabs

The decisive restraint stresses of ground slabs are subject to a superposition of bending restraint and external restraint. In detail, two critical states can be identified: (i) almost pure bending stresses with tension at the top surface at the time of maximum temperature at the bottom surface and (ii) a superposition of bending stresses and centric tensile stresses at the time of temperature equalisation. The according restraint situations are illustrated in Fig. 8.22.

The restraint moment with maximum tension at the top surface occurs shortly after the time of maximum temperature in the interior. At this time, the restraint force is still compression or almost zero and can be neglected. The restraint moment with maximum tension at the bottom surface occurs at temperature equalization. At the same time, the restraint force due to horizontal restraint of the soil is fully developed. Altogether, it holds:

$$M_{F,\text{top}} = -\frac{CTE \cdot \Delta T_{M,\text{eq},F,o}}{h_F} \cdot E_F I_F \leq \frac{\gamma_c \cdot A_F \cdot {L_{F,\text{eff}}}^2}{2} \quad \text{with} \quad N_{F,\text{acc}} = 0 \quad (8.43)$$

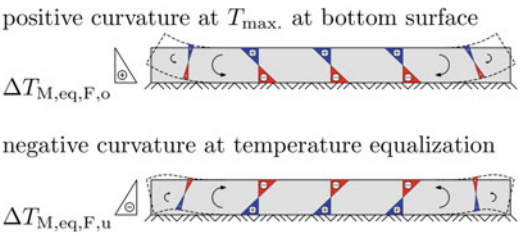

(a) Moments due to temperature gradients

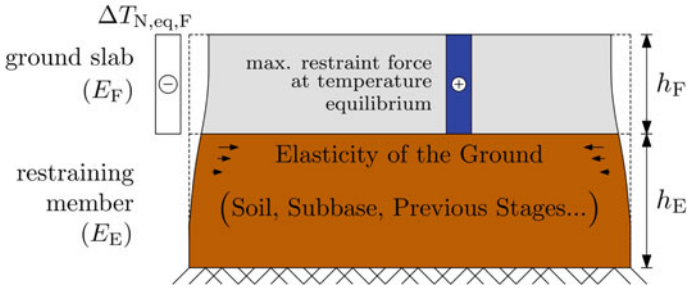

(b) Restraint force due to soil-structure interaction

Fig. 8.22 Equilibrium and stress resultants of ground slabs (Schlicke 2014)

and

$$M_{F,\text{bottom}} = \frac{CTE \cdot \Delta T_{M,\text{eq},F,u}}{h_F} \cdot E_F I_F \leq \frac{\gamma_c \cdot A_F \cdot L_{F,\text{eff}}{}^2}{2} \quad \text{with}$$
$$N_{F,\text{acc}} = -CTE \cdot \Delta T_{N,\text{eq},F} \cdot E_F A_F \cdot R_N \tag{8.44}$$

where

$\Delta T_{M,\text{eq},F,o}$	equivalent temperature gradient in the slab representing a positive curvature (usually at time of maximum temperature at the bottom),
$\Delta T_{M,\text{eq},F,u}$	equivalent temperature gradient in the slab representing a negative curvature (usually at time of temperature equalisation),
$E_F I_F$	bending stiffness of the foundation,
$E_F A_F$	axial stiffness of the foundation,
h_F	thickness of the slab,
γ_c	specific weight of concrete,
$L_{F,\text{eff}}$	distance between free edge of the slab and point of zero deformation,
A_F	cross-sectional area of the ground slab,
R_N	axial restraint degree of ground slab.

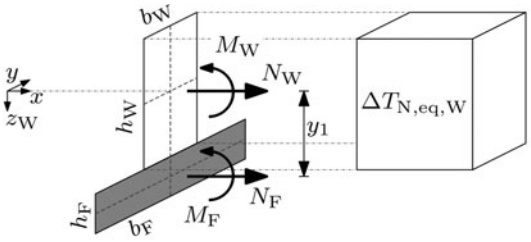

(a) Internal restraint forces

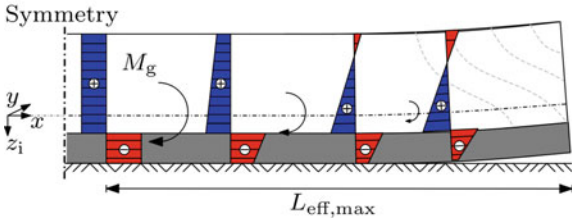

(b) External moment due to self-weight activation

Fig. 8.23 Equilibrium and stress resultants in walls on foundations (Schlicke 2014)

In case of ground slabs, critical stress states may occur on the top surface as well as on the bottom surface. Their size can be determined with:

$$\sigma_{F,\text{top}} = CTE \cdot \frac{\Delta T_{M,\text{eq},F,o}}{2} \cdot E_F \leq 3 \cdot \frac{\gamma_c \cdot {L_{F,\text{eff}}}^2}{h_F}$$

$$\sigma_{F,\text{bottom}} = -CTE \cdot \Delta T_{N,\text{eq},F} \cdot R_N \cdot E_F + \min\left\{ CTE \cdot \frac{-\Delta T_{M,\text{eq},F,u}}{2} \cdot E_F; 3 \cdot \frac{\gamma_c \cdot {L_{F,\text{eff}}}^2}{h_F} \right\} \tag{8.45}$$

8.2.5.2 Decisive Restraint Forces and Moments in Walls on Foundations

The restraint forces and moments of walls restrained by a foundation are subject to the inner deformation compatibility of the cross sections of wall and foundation as well as the activation of self-weight following the curvature of the cross-section compatibility. Figure 8.23 illustrates both with a shortening wall, which is symmetrically located on a foundation.

The internal forces can be determined with:

$$N_W = -CTE \cdot \Delta T_{N,\mathrm{eq},W} \cdot \left(\frac{1}{E_F A_F} + \frac{1}{E_W A_W} + \frac{{y_1}^2}{E_F I_F + E_W I_W} \right)^{-1}$$
$$M_W = N_W \cdot y_1 \cdot \frac{1}{1 + \frac{E_F I_F}{E_W I_W}} \tag{8.46}$$

where

$\Delta T_{N,\mathrm{eq},W}$ equivalent temperature impact in the wall representing the predominant of uniformly in the cross-section-distributed cooling
y_1 inner level arm, usually $(h_W + h_F)/2$.

And the additionally occurring external moment M_g can be determined according to the real member length L by:

$$M_g = \frac{\gamma_c \cdot A_{\mathrm{tot}} \cdot {L_{\mathrm{eff,max}}}^2}{2} \text{ with : } L_{\mathrm{eff,max}} = \sqrt{\frac{2 \cdot M_W}{\gamma_c \cdot A_{\mathrm{tot}}} \cdot \frac{I_i}{I_W}} \leq \frac{L}{2} \tag{8.47}$$

where

A_{tot} area of whole cross section (wall + foundation),
M_W inner moment due to cross-section compatibility,
I_i moment of inertia of whole cross section,
I_W moment of inertia of wall cross section,
L real length of the wall.

The correct consideration of the self-weight activation is of great importance. It is limited to a certain length $L_{\mathrm{eff,max}}$, which depends on geometrical conditions of the cross section as well as the height of the deformation impact. In systems with smaller lengths—which is often the case—there is only a partial activation of the self-weight possible. Finally, the stress distribution without *Eigenstresses* can be determined with:

$$\sigma_{W,\mathrm{bottom/top}} = \frac{N_W}{A_W} + \frac{M_W}{I_W} \cdot z_{W,\mathrm{bottom/top}} + \frac{M_g}{I_i} \cdot z_{i,\mathrm{bottom/top}} \tag{8.48}$$

where

$z_{W,\mathrm{bottom/top}}$ distance between point of gravity in the wall and bottom, respectively, top of the wall,
$z_{i,\mathrm{bottom/top}}$ distance between point of gravity of the whole cross section and bottom, respectively, top of the wall.

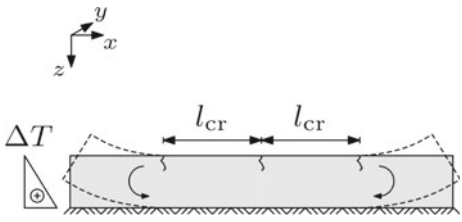

(a) bending cracks due to self-weight activation of a ground slab

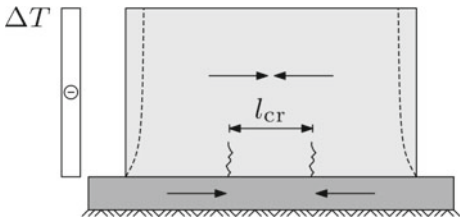

(b) separating cracks due to external restraint of a wall on a foundation

Fig. 8.24 Geometric set crack patterns of typical members which are predominantly restrained (Schlicke 2014)

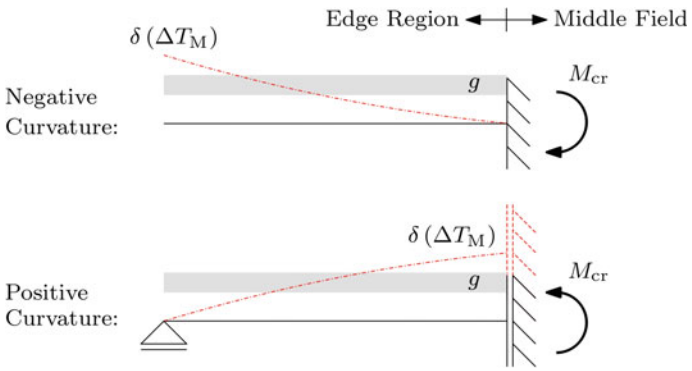

Fig. 8.25 Conceptual model for the distance between primary bending cracks of a ground slab (Schlicke 2014)

8.2.5.3 Crack Risk and Macrocrack Patterns to Be Expected

If the finally determined stresses exceed the present tensile strength $f_{ctm}(t)$, the formation of macrocracks should be assumed. In case of ground slabs, the most likely scenario is bending cracks at the top surface. Pure bending cracks at the bottom surface are almost impossible; however, if the superimpose with additional uniformly over the height distributed stresses according to N_F, the occurrence of

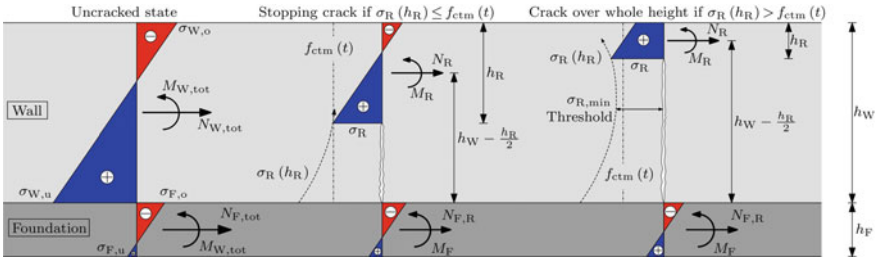

Fig. 8.26 Conceptual model for determination of the crack height in walls restrained by a foundation, based on the stress distribution in the uncracked state (Schlicke 2014)

separating cracks starting from the bottom surface cannot be excluded safely. But this requires unusual high stiffness of the ground in horizontal direction and is thus to be seen as a rare scenario. In case of walls on foundations, the highest stresses occur always at the bottom of the wall and would lead to separating cracks starting from the bottom and proceeding over the height of the wall.

A conservative estimate of the macrocrack pattern to be expected can be derived geometrical considerations, as illustrated in Fig. 8.24. This concentrates only on primary cracks which occur predominantly according to the restraining condition. Additional secondary cracks, which can be created in the surrounding of the primary cracks by activation of reinforcement, were addressed in Sect. 8.4.

In case of ground slabs, the distance between primary cracks predominantly depends on the bending moment according to self-weight activation, whereby the formation of a new crack can be assumed as soon as the cracking moment will be reached. The required length can be estimated using the conceptual model shown in Fig. 8.25.

The length needed to build up the cracking moment holds in both cases:

$$l_{\mathrm{cr}} = \sqrt{\frac{1}{3} \cdot \frac{f_{ctm}(t_{\mathrm{cr}}) \cdot h_F}{\gamma_c}} \tag{8.49}$$

where

$f_{ctm}(t_{cr})$ mean tensile strength of concrete at time of macrocrack formation,
h_F thickness of the slab.

The distance between primary cracks in walls restrained by a foundation is subject to the length needed to build up the axial restraint stresses again. But this length strongly correlates with the height the primary crack reaches. With the assumption of a plane cross section during the whole process of crack formation, the stress redistribution while cracking can be described as illustrated in Fig. 8.26. It should be mentioned that the final restraint force and restraint moment in the wall is to be determined from the results in Eq. 8.48.

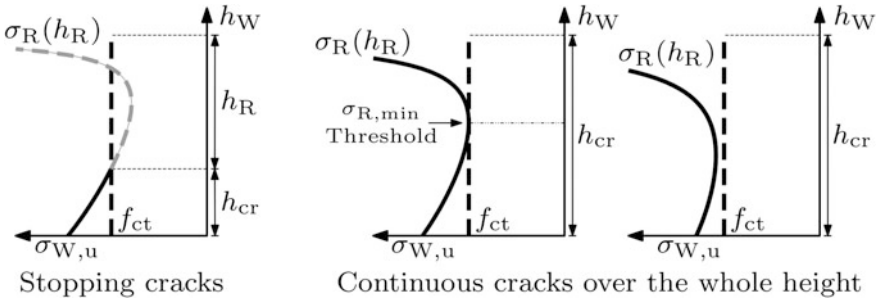

Fig. 8.27 Possible results of the graphically determined crack height in the wall

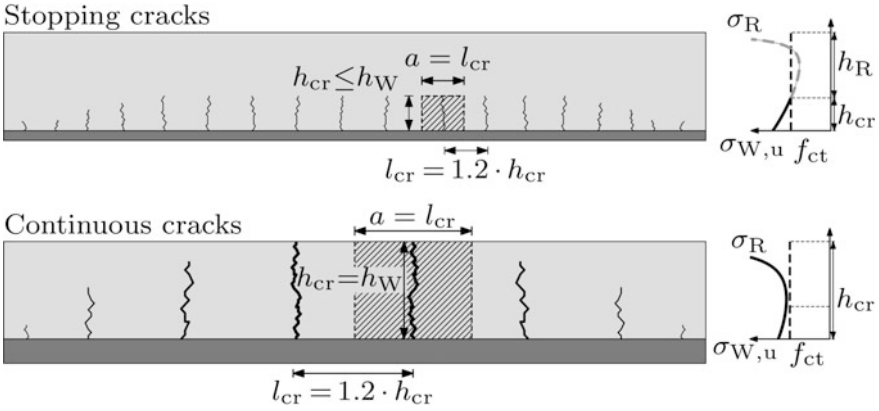

Fig. 8.28 Conceptual model to determine the distance between primary cracks in walls restrained by a foundation depending on the crack height (Schlicke 2014)

The stress at the top of the crack σ_R is of major interest. Its size depends on the remaining concrete height h_R, while the forces of the uncracked state are transferred through the remaining cross section until the crack proceeds over the whole height of the wall. Beginning with crack formation at the wall bottom, σ_R first decreases until a threshold is reached. From this point onwards, the constriction of the concrete area is decisive and σ_R is steadily increasing. Its development can be described with:

$$\sigma_R(h_R) = \frac{\kappa_R \cdot E_W \cdot b_W \cdot \left(h_R{}^3 - h_W{}^3\right) + 6 \cdot N_{W,\text{tot}} \cdot (h_W + h_F)}{6 \cdot b_W \cdot h_R \cdot (2 \cdot h_W - h_R + h_F)} + \frac{\kappa_R \cdot E_W \cdot h_R}{2} \tag{8.50}$$

where

$$\kappa_R = \frac{\sigma_{W,\text{bottom}} - \sigma_{W,\text{top}}}{E_W \cdot h_W} \text{ and } N_{W,\text{tot}} = \left(\sigma_{W,\text{bottom}} - \frac{\sigma_{W,\text{bottom}} - \sigma_{W,\text{top}}}{2}\right) \cdot b_W \cdot h_W$$

If σ_R falls below the tensile strength, the growth of the primary crack can be assumed to stop. The solution of whether or not the growth stops has to be found graphically. Figure 8.27 gives an impression of this approach by introducing the three possible types of solutions, indicating stopping cracks or continuous cracks over the whole height of the wall.

Finally, the distance between the primary cracks in the wall can be estimated according to the illustrations in Fig. 8.28 (Schlicke 2014).

8.3 Crack Width Estimation

To estimate the crack width, the spacing between cracks should be determined. Note that at early age, very often the cracking is not in a stabilised stage. In this case, the length between two cracks is larger and to evaluate the crack width one should use the transfer length over which slip between concrete and steel occurs. Indeed, within this length, steel and concrete strains contribute to the width of the crack. Generally, the equation for the evaluation of the crack width w_k is:

$$w_k = 2 \cdot l_{s,\max} \cdot (\varepsilon_{sm} - \varepsilon_{cm} - \varepsilon_{sh}) \tag{8.51}$$

with

$l_{s,\max}$ transfer length (maximum crack spacing in the stabilised cracking stage),
ε_{sm} mean tensile strain of reinforcement,
ε_{cm} mean tensile strain of concrete,
ε_{sh} shrinkage strain (negative in case of shrinkage).

8.3.1 Model Code 2010

The transfer length is a function of the ratio between $\emptyset$ of the rebars and the reinforcement ratio $\emptyset/\rho_{\text{eff}}$ on one hand and on the concrete cover c on the other hand (Perez Caldentey et al. 2013). The first term can be obtained with a classical bond theory. The second was introduced because of experimental evidences (Beeby 2004). In Model Code 2010, the transfer length is evaluated by means of the following relation:

$$l_{s,\max} = k_2 \frac{\emptyset}{\rho_{\text{eff}}} + k_1 c \tag{8.52}$$

The parameters k_1 and k_2 proposed by Model Code 2010 are fitted on experimental results. The term $(\varepsilon_{sm} - \varepsilon_{cm})$ could be evaluated like in Eurocode 2 (see next section).

8.3.2 Eurocode 2-3

In Eurocode 2 Part 3 (EN 1992-3 2008), two main cases are considered. In the first one, volume changes are restrained along two opposite faces—end-restrained case (Fig. 8.8). In this case, the difference between steel and concrete strains is estimated by the following relation:

$$(\varepsilon_{sm} - \varepsilon_{cm}) = 0.5 \cdot \alpha_e \cdot k_c \cdot k \cdot f_{ct,\text{eff}} \cdot \frac{\left(1 + \frac{1}{\alpha_e \cdot \rho}\right)}{E_s} \tag{8.53}$$

with

α_e the ratio E_s/E_{cm} with E_s the Young modulus of steel and E_{cm} the mean Young modulus of concrete,

k_c and k defined in EN 1992-1-1 as follows: $k = 1$ in the case of webs or flanges, where $h \leq 300\,\text{mm}$, and $k = 0.65$ for webs or flanges where $h > 800\,\text{mm}$, and $k_c = 1$ in direct tension only, $f_{ct,\text{eff}}$ is the mean value of the tensile strength of the concrete effective at the time when the cracks may first be expected to occur,

ρ the ratio between A_s the area of reinforcing steel and A_{ct} the area of concrete within tensile zone just before formation of the first crack.

The second case considers restraint on a base face. In this case, the difference between steel and concrete strains is:

$$(\varepsilon_{sm} - \varepsilon_{cm}) = R_N \cdot \varepsilon_0 \tag{8.54}$$

where

R_N the degree of restraint estimated using methods presented in Sect. 8.2.3.1,

ε_0 the imposed deformation.

8.3.3 ACI 224

In ACI 318 (ACI 318 2014), Chap. 24 Serviceability Requirements, 2014 version, crack control is provided by calculating the probable crack width and proportioning structural elements so that the computed width is less than a predefined value (see Table 8.1). Most equations predict the probable maximum crack width, which usually means that about 90% of the crack widths in the member are below the calculated value.

For one-way slabs (beams), (ACI 224 2001) proposes the following equation to estimate crack width:

$$w = 0.01102 \cdot \beta \cdot f_s \cdot \sqrt[3]{d_c \cdot A} \cdot 10^{-3} \tag{8.55}$$

where

w most probable maximum crack width, mm,
β ratio of distance between neutral axis and tension face to distance between neutral axis and reinforcement steel,
f_s reinforcing steel stress, MPa,
d_c thickness of cover from the extreme tension fibre to the closest bar, mm,
A area of concrete symmetric with reinforcing steel divided by number of bars, mm^2.

8.3.4 JCI Guidelines

In case of JCI Guidelines (JCI 2008), the verification for controlling the crack widths is implemented with the following equation:

$$\gamma_i \frac{w_c}{w_a} \leq 1.0 \tag{8.56}$$

where

γ_i safety factor for verification, generally allowed to be 1.0,
w_a allowable value of crack width,
w_c predicted value of thermal crack width.

The allowable crack width shall be defined based on the application, required performance, surrounding environmental conditions and the concrete cover.

In the guideline, the following equation to predict thermal crack widths is proposed using the thermal cracking index I_{cr}, which was introduced in Sect. 8.2.3.3.

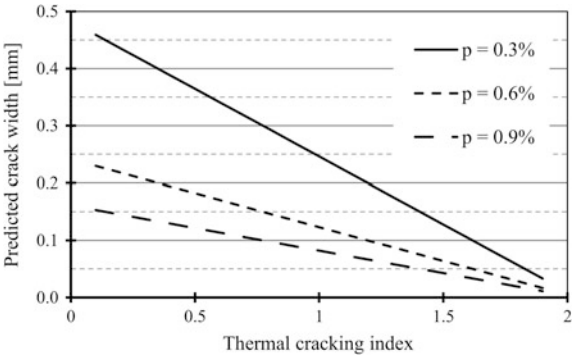

Fig. 8.29 Relation between thermal cracking indices and thermal crack

$$w_c = \gamma_a \left(\frac{-0.071}{\rho} \right) \cdot (I_{\mathrm{cr}} - 2.04) \tag{8.57}$$

$$I_{\mathrm{cr}} = \frac{\sigma(t)}{f_t(t)} \tag{8.58}$$

where

γ_a safety factor to evaluate the thermal crack widths, which shall be 1.0–1.7 depending on the performance requirements,

ρ reinforcement ratio (%, the ratio of the reinforcement area perpendicular the crack direction to the intended concrete area), the applicable range of which is 0.25–0.93%,

$\sigma(t)$ the maximum principal tensile stress at temperature adjusted age of t,

$f_t(t)$ tensile strength at temperature adjusted age of t.

The equation is formulated based on the experimental results of full-size wall specimens subjected to the predominant external restraint at the bottom while assuming insignificant influence of internal restraint and drying. Figure 8.29 gives an example of the relation between thermal cracking indices and thermal crack widths when γ_a is 1.0.

The thermal cracking index is calculated based on thermal and stress analyses, and the thermal crack widths can be derived by Eq. 8.56. Then, it is assessed that the obtained crack widths are less than the allowable crack widths.

The thermal crack index can vary with aging depending on the variation of hydration heat, autogenous shrinkage, restraint conditions and others, but may not be always getting smaller with aging. The thermal crack widths can increase with aging to be convergent gradually. The maximum thermal crack width, however, is not always dependent on the thermal crack index. In the guideline, it is recommended that the maximum thermal crack width obtained by the minimum thermal crack index during the target period can be used to compare with the allowable

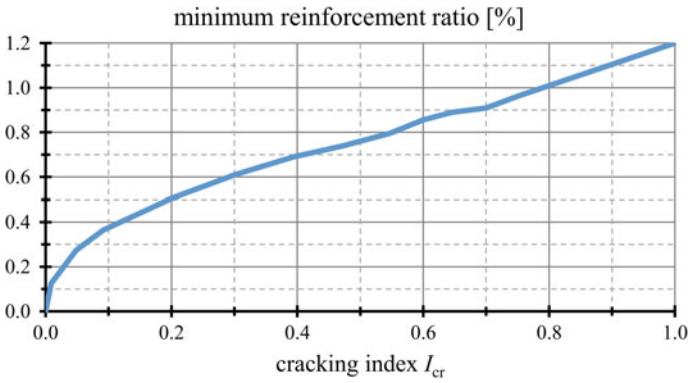

Fig. 8.30 Minimum reinforcement ratios necessary to comply a maximum crack width of 0.2 mm, for various cracking criteria after (van der Ham et al. 2006a)

crack width because it is confirmed that the minimum crack index in the members except the surface and corner is dependent on the maximum crack width.

8.3.5 Return on the Probabilistic Aspects of Cracking

The cracking width that occurs after the tensile stress has exceeded the actual tensile strength may also be considered from a probabilistic point of view. Most advanced method that can link the crack width to the probability of cracking is the Level III method, which is a full probabilistic approach that takes into account all uncertainties of the concrete materials, boundary conditions, geometry, etc., in terms of a probability density function for each individual parameter (see Sect. 8.2.3.4). This so-called stochastic approach considers the cracking risk of hardening concretes from a very detailed and associated uncertainties point of view while considering the influence of uncertainties of all individual parameters into a system probability function that represents all uncertainties in one result. This calculated system probability can also be used to assess the crack width and the most likely crack width, depending on the reinforcement ratio.

Using a method presented before (EN 1992-3 2008 in Sect. 8.3.2 for instance), the crack width can be calculated. For example, for an actual concrete tensile strength of 2.5 MPa and an actual Young's modulus at the moment of cracking of 37 GPa, the reinforcement ratio, needed to control the maximum crack width at 0.20 mm, is 0.97%, when using reinforcement bars of Ø12 mm. Whenever taking the probabilistic aspects into account, uncertainties expressed by the cracking index have to be considered explicitly. As an example, for a representative range of

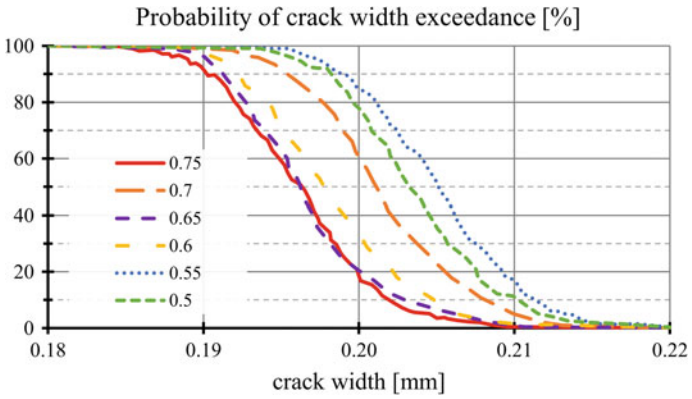

Fig. 8.31 Probability of crack exceedance for different crack criteria after (van der Ham et al. 2006a)

cracking criteria, i.e. ranging from 0.5 to 0.8, the necessary amount of reinforcement has been calculated to comply with the maximum crack width of 0.2 mm. Results are presented in Fig. 8.30, showing the minimum reinforcement versus various cracking criteria. The figure shows a square root type of relationship between the amount of reinforcement necessary and the cracking criterion ($I_{cr} = 0.75 \cdot f_{ctm,sp}/\sigma$), to obey the ultimate crack width of 0.20 mm. In the case of the lower values of I_{cr}, due to the lower tensile strength and Young's modulus at younger ages of the concrete, a relatively higher percentage of reinforcement is needed.

Simulations performed with a Level III calculation result in sets of data, which consist of a cracking time, tensile strength and elastic modulus of the assessed concrete at the moment of cracking, and other relevant data. This information can be used to calculate the crack width for each run. With these crack widths, a probability density function has been constructed, while using various cracking criteria (I_{cr}), i.e. from 0.5 to 0.75, representing probabilities of failure of 10^{-3} and 0.5, respectively (see Fig. 8.17). Results of the probabilities of crack exceedance are provided in Fig. 8.31. The figure shows that for an arbitrary maximum crack width of 0.2 mm, the probability of crack width exceedance is still substantial, and larger cracks are likely to occur in a massive concrete structure. Especially for the lower stress/strength ratios, i.e. 0.5 (cracking index I_{cr}), the probability of larger crack width occurrence is substantial. This shows that in case of critical structures, viz. watertight structures, the cracking criterion in relation to the desired maximum crack width should be considered carefully.

8.4 Reinforcement Design

8.4.1 *Crack Width Control on the Basis of Force Equilibrium*

The characteristically occurring crack width w_k can be derived from the difference of steel strain ε_s and concrete strain ε_c along the crack spacing s_r. By simplifying the real strain distribution along s_r with the introduction of average values, the following correlation can be constituted:

$$w_k = \int_{x=0}^{s_r} (\varepsilon_s - \varepsilon_c)\mathrm{d}x = s_r \cdot (\varepsilon_{sm} - \varepsilon_{cm}) \tag{8.59}$$

In the crack state of single cracks (not all possible cracks have been created along the member length), the difference of steel and concrete strain occurs only in the transfer lengths to both sides of the cracks, whereas stabilised crack patterns (all possible cracks have been created along the member length) are characterised by a difference between steel and concrete strain along the whole member length. On the safe side, the crack spacing can be determined by taking into account the cracking force F_{cr} of the effective concrete area $A_{c,\mathrm{eff}}$ ($F_{\mathrm{cr}} = A_{c,\mathrm{eff}} \cdot f_{ct,\mathrm{eff}}$), the average bond strength and the reinforcement diameter d_s. It holds:

$$s_r = 2 \cdot \frac{F_{\mathrm{cr}}}{\tau_{sm} \cdot \pi \cdot d_s} \tag{8.60}$$

where τ_{sm} is bond stress between reinforcement and concrete.

With respect to the influence of the load duration on the strain distribution in the crack spacing ($k_t = 0.6$ for short term and 0.4 for long term) and the force to be taken by the reinforcement after cracking (F_s), the crack width can be estimated for a given reinforcement (d_s, provided area A_s, elastic modulus E_s) by transformation of Eqs. 8.59 and 8.60 in a form of:

$$w_k = \frac{F_{\mathrm{cr}} \cdot (F_s - k_t \cdot F_{\mathrm{cr}}) \cdot d_s}{2 \cdot \tau_{sm} \cdot E_s \cdot {A_s}^2} \tag{8.61}$$

As long as $F_s \leq F_{\mathrm{cr}}$, only single crack patterns are to be expected and F_s is to set as F_{cr} in Eq. 8.61. If $F_s > F_{\mathrm{cr}}$, all possible cracks will form along the member and a stabilised crack pattern exists. Equation 8.61 considers for both crack states an undisturbed transfer length to both sides of the crack. Strictly seen, this is only correct in case of single cracks. As soon as a stabilised crack pattern has developed, the crack width might be overestimated by Eq. 8.61. The reason is that new cracks may form between neighbouring single cracks so that s_r decreases. Keeping in mind the transition between both crack states and statistical uncertainties of the distance

between cracks in stabilised crack patterns, Eq. 8.61 can be seen as justifiable for both cases. Another crucial point is consideration of the bond stresses between reinforcement and concrete which is usually simplified for conventional reinforcement with an average bond strength along the transfer lengths of $\tau_{sm} = 1.8 \cdot f_{ctm}(t)$. Further details are given in e.g. (König and Tue 2008; König and Tue 1996) or (Tue and Pierson 2001). Finally, the required reinforcement can be determined by transformation of Eq. 8.61 in a form of:

$$A_{s,\text{req}} = \sqrt{\frac{F_{\text{cr}} \cdot (F_s - k_t \cdot F_{\text{cr}}) \cdot d_s}{2 \cdot \tau_{sm} \cdot E_s \cdot w_k}} \tag{8.62}$$

Although several differences can be found in detail, Eqs. 8.61 and 8.62 represent in general the Eurocode 2 regulations for crack width control. The direct determination of the crack width in Eurocode 2 (Sect. 7.3.4) differs only in terms of the empirical determination of the crack spacing, whereas the indirect crack width verification (Sect. 7.3.3, Table 7.2N) can be directly derived from Eq. 8.62. For the relation between crack width, rebar diameter and steel stress can be written according to the same assumptions in Eurocode 2 ($F_s = F_{\text{cr}}$, $k_t = 0.4$, $\tau_{sm} = 1.8 \cdot f_{ctm}(t)$):

$$\sigma_s(w_k) = \sqrt{6 \cdot \frac{w_k \cdot f_{ctm}(t) \cdot E_s}{d_s}} \tag{8.63}$$

The EC2 regulation for the minimum reinforcement (Sect. 7.3.2) bases on the same assumptions and takes up the cracking force respectively the cracking moment. The decisive stress distribution just before cracking is considered by a factor k_c (pure centric restraint $k_c = 1.0$, pure bending restraint $k_c = 0.4$), whereby the absolute size of stresses to be taken up while cracking can be modified empirically for the benefit of an efficient design. These modifications concern positively assumed influences of pre-damage due to residual stresses (factor k) and reduced stresses in case of early-age cracking ($f_{ct,\text{eff}} < f_{ctm}$). Finally, it holds:

$$A_{s,\text{min}} = k_c \cdot k \cdot f_{ct,\text{eff}} \cdot \frac{A_{ct}}{\sigma_s(w_k)} \tag{8.64}$$

The application of Eqs. 8.62–8.64 takes place in the context of a verification of the force equilibrium without further respect to the type of stressing, as outlined in (Schlicke and Tue 2016). While this is very suitable for cases with external loads, such strategy has to be seen critically in cases with significant restraints. The main reason is that the restraint force depends strongly on the deformation compatibility and this includes also its decreasing by formation of any new crack. Furthermore, the crack pattern due to imposed deformations depends predominantly on the

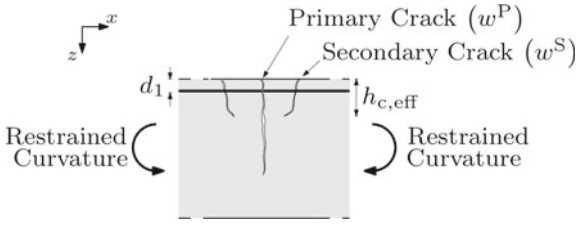

(a) bending cracks
(bending restraint over the thickness)

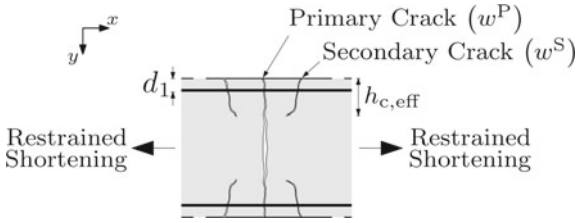

(b) separating cracks
(centric restraint over the thickness)

Fig. 8.32 Crack systems consisting of a primary crack and secondary cracks, here $A_{c,\text{eff}} < A_c$ (Schlicke and Tue 2015)

restraining condition which leads to geometrically set patterns of cracks, as exemplified in Fig. 8.22. Only exception is to systems in which the steel force in the reinforcement is in complete equilibrium with the restraint force, e.g. end-restrained tension rods.

Common reinforcement amounts have no influence on the occurrence of these geometric set crack patterns. Increasing reinforcement degrees would slightly reduce l_{cr}; however, the steel stress in the primary cracks is not affected by the formation of a new primary crack. Thus, these primary cracks can be assumed to be independent from each other, or in other words, the geometric set cracks separate the member in parts with a length of l_{cr} for which crack width control can be carried out independently.

The size of l_{cr} depends predominantly on the member type and restraining situation, whereby two principal cases can be distinguished for practical design. One is the restraining of a curvature due to self-weight activation (e.g. ground slab with temperature gradient over the height), the other one is the interaction with an rigidly connected, restraining component (e.g. shortening of a wall on a foundation). For these typical member types, robust engineering models were presented in Sect. 8.2.5. However, a generally valid model considering the present reinforcement would require further investigations, see (Knoppik-Wróbel and Schlicke 2016).

Besides, it needs to be said that the anchorage of the reinforcement will create secondary cracks next to the primary cracks, as shown in Fig. 8.32 for all cases with significant smaller effective concrete area ($A_{c,\text{eff}} < A_c$).

8.4.2 Crack Width Control on the Basis of Deformation Compatibility

Deformation compatibility is the comparison of deformation impacts in the material with the deformation response of the system. Predominant impacts are thermal expansion ($CTE \cdot \Delta T$), shrinkage due to hydration and drying ($\varepsilon_{au} + \varepsilon_{d,sh}$) as well as creep ($\varepsilon_{cr}$), whereas the system response mainly consists of free deformation ($\Delta l/l$) and restrained deformation in a form of restraint stresses (σ_{rest}/E_c). If the ratio between restraint stresses and real length changes is expressed by a so-called restraint degree R, it can be written in the uncracked state:

$$\left(CTE \cdot \Delta T + \varepsilon_{au} + \varepsilon_{d,sh} + \varepsilon_{cr}\right) \cdot R = -\frac{\sigma_{\text{rest}}}{E_{\text{c}}} \tag{8.65}$$

If restraint stresses exceed a certain limit value of the tensile strength, cracking is to be expected. After cracking, the deformation compatibility has to take into account the cracks with their certain width as well. As explained before, the geometric set cracks separate the member in independent parts with a length of l_{cr}, so that the deformation compatibility can be verified representatively for one primary crack in the length of l_{cr}. Besides, the stiffness of the restrained member decreases due to cracking, so that the restraint degree increases in all cases where the restraining condition is the same after cracking. With regard to the restrained deformation in the transfer length, it can be written for the cracked state:

$$\left(CTE \cdot \Delta T + \varepsilon_{au} + \varepsilon_{d,sh} + \varepsilon_{cc}\right) \cdot R^{\text{II}} \cdot l_{\text{cr}} = -\left[\frac{\sigma_{\text{rest}}^{\text{II}}}{E_{\text{c}}} \cdot \left(l_{\text{cr}} - s_r \cdot (1 - k_t)\right) + w\right] \tag{8.66}$$

and on the basis of the equilibrium between steel force in the primary crack and concrete force in the uncracked part between the primary cracks, the crack width amounts:

$$w = -\left(CTE \cdot \Delta T + \varepsilon_{au} + \varepsilon_{d,sh} + \varepsilon_{cc}\right) \cdot R^{\text{II}} \cdot l_{\text{cr}} - \frac{\sigma_{\text{s}} \cdot A_{\text{s}}}{E_{\text{c}} \cdot A_{\text{c}}} \cdot \left(l_{\text{cr}} - s_r \cdot (1 - k_t)\right) \tag{8.67}$$

Finally, the required reinforcement to limit the crack width under consideration of the deformation compatibility amounts:

$$A_{\text{s}} = \frac{w_{\text{k}} + \left(CTE \cdot \Delta T + \varepsilon_{au} + \varepsilon_{d,sh} + \varepsilon_{cc}\right) \cdot R^{\text{II}} \cdot l_{\text{cr}}}{\left(l_{\text{cr}} - s_r \cdot (1 - k_t)\right)} \cdot \frac{E_c A_c}{\sigma_s(w_k)} \tag{8.68}$$

The solution of Eq. 8.68 is not trivial, and challenging tasks are especially:

- determination of the restraint degree after cracking, in particular if present reinforcement has significant influence,

- consideration of remaining concrete stresses in the uncracked part between two primary cracks, especially if these stresses vary over the height of the cross section and along the member length as in case of bottom-restrained members (e.g. walls on foundations) and
- consideration of secondary cracking.

A possible simplification is that the primary crack, respectively the crack system consisting of primary crack and secondary cracks, will have to absorb the entire restrained deformation of the uncracked state. In practical cases, this assumption is conservative because the restrained deformation in the concrete between primary cracks after cracking is neglected, even though it is bigger than the influence of any possible increase of the restraint degree after cracking. But it is also appropriate because demanding iterations due to the above-listed points can be avoided. It holds:

$$w^P + \sum_{i=1}^{n} w_i^S = \frac{\sigma_{\text{rest}}}{E_{\text{c}}} \cdot l_{\text{cr}} \tag{8.69}$$

The basic idea of Eq. 8.69 is to create as many secondary cracks in the surrounding of the primary crack as needed to limit the crack width in the primary crack. The required number of secondary cracks can be determined with regard to the crack width criteria w_k and the simplification behind Eq. 8.69 by:

$$n = \left(\frac{\sigma_{\text{rest}}}{E_{\text{c}}} \cdot l_{cr} \cdot \frac{1}{w_k} - 1 \right) \cdot 1.1 \tag{8.70}$$

The decreasing width of subsequently occurring secondary cracks in comparison to the width of the primary crack is expressed by the factor 1.1 which covers relevant practical situations.

The minimum reinforcement required can be derived from the number of secondary cracks n, where n is rounded up to the next integer. If $n \leq 0$, the deformation compatibility is already fulfilled with the width of the primary crack and reinforcement for crack width control is not needed. Only a skin reinforcement taking up the cracking force of the effective concrete area would be recommended. All other cases require active crack width control and the required minimum reinforcement can be determined according to Bödefeld (2010). Altogether, it holds:

$$n \leq 0: \quad A_{s,\text{req}} = \frac{f_{ctm}}{f_{yk}} \cdot A_{c,\text{eff}} \tag{8.71}$$

with

f_{ctm} average tensile strength,
f_{yk} yield strength of reinforcement,
$A_{c,\text{eff}}$ effective concrete area (usually $2.5 \cdot d_1 \cdot b$).

$$n > 0: \quad A_{s,\text{req}} = \sqrt{\frac{d_s \cdot b^2 \cdot {d_1}^2 \cdot f_{ctm}(t_{\text{cr}}) \cdot (0.69 + 0.34 \cdot n)}{w_k \cdot E_s}} \tag{8.72}$$

with

d_s	reinforcement diameter,
b	width in direction viewed (normally 1 m),
d_1	edge-distance of the reinforcement,
$f_{ctm}(t_{cr})$	mean tensile strength of concrete at time of macrocrack formation,
n	mean number of required secondary cracks,
w_k	characteristic crack width or crack width criterion,
E_s	Young's modulus of reinforcing steel.

The restraint stresses to be considered in Eqs. 8.69 and 8.70 should represent the maximum stresses due to restraint forces and restraint moments without the effect of *Eigenstresses*. As explained in Sect. 8.2.5, *Eigenstresses* may have a significant influence on the risk of cracking but their effect on the resulting width of macrocracks is negligible.

References

ACI Committee 207. (2005). ACI 207.1R-05: Guide to mass concrete.

ACI Committee 207. (2007). ACI 207.2R-07: Report on thermal and volume change effects on cracking of mass concrete.

ACI Committee 224. (2001). ACI 224R-01: Control of cracking in concrete structures.

ACI Committee 318. (2014). ACI 318–14: Building code requirements for reinforced concrete.

Architectural Institute of Japan. (2008). *Recommendations for practice of thermal cracking control of massive concrete in buildings*. Maruzen Co., Ltd. (in Japanese).

Bamforth, P. B. (2007). *CIRIA C660: Early-age thermal crack control in concrete*. London: CIRIA.

Barre, F., Bisch, P., Chauvel, D., Cortade, J., Coste, J.-F., Dubois, J.-P. et al. (2016). *Control of cracking in reinforced concrete structures: Research project CEOS.fr*. Hoboken, NJ: Wiley.

BAW—German Federal Waterways Engineering and Research Institute. (2011). *BAW Code of Practice: MFZ—Limitation of crack widths resulting from thermal restraint due to hydration heat in solid structural elements*.

Beeby, A. W. (1972). *A study of cracking in reinforced concrete members subjected to pure tension.* Technical report, Cement and Concrete Association, London.

Beeby, A. W. (2004). The influence of the parameter $\emptyset/\rho_{\text{eff}}$. On crack widths. *Structural Concrete*, *5*(2), 71–85.

Bödefeld, J. (2010). *Rissmechanik in dicken Stahlbetonbauteilen bei abfließender Hydratationswärme*. Ph.D. Thesis, University of Leipzig (in German).

Borosnyoi, A., & Snobli, I. (2010). Crack width variation within the concrete cover of reinforced concrete members. *Journal of Hungarian Scientific Society of the Silicate Industry, 3,* 70–74.

Breitenbücher, R. (1989). *Zwangsspannungen und Riβbildung infolge Hydratationswärme*. Ph.D. Thesis, Technical University of Munich (in German).

CEB-FIP *fib*. (2012). Bulletin 65. *Model code 2010: Final draft* (Vol. 1).

Czerny, F., Koenders, E. A. B., & van Breugel, K. (2005). On the reliability of crack predictions for hardening concrete structures. In *Proceedings of 6th International Global Construction Conference, Dundee*.

Ebensperger, L. (1990). *Wirksamkeit von Quellzusätzen im Beton zur Kompensation von Zwangsspannungen infolge Hydratationswärme*. Ph.D. Thesis, Technical University of Munich (in German).

European Concrete Platform. (2008). Eurocode 2 commentary. Brussels.

EN 1992-1-1. (2004). Eurocode 2—Design of concrete structures. Part 1-1: General rules and rules for buildings.

EN 1992-3. (2008). Eurocode 2—Design of concrete structures. Part 3: Liquid retaining and containment structures.

Flaga, K., & Furtak, K. (2009). Problem of thermal and shrinkage cracking in tanks vertical walls and retaining walls near their contact with solid foundation slabs. *Architecture–Civil Engineering–Environment*, *2*(2), 23–30.

Japanese Concrete Institute. (1985). Technical committee report of thermal stress in massive concrete structures (in Japanese).

Japanese Concrete Institute. (2008). Guidelines for control of cracking of mass concrete.

JSCE. (2011). Guidelines for Concrete. No. 15: Standard Specifications for Concrete Structures. Design.

Knoppik-Wróbel, A. (2015). *Analysis of early-age thermal–shrinkage stresses in reinforced concrete walls*. Ph.D. Thesis. Silesian University of Technology, Gliwice, Poland.

Knoppik-Wróbel, A., & Klemczak, B. (2015). Degree of restraint concept in analysis of stresses in early age concrete walls. *Engineering Structures, 102,* 369–386.

Knoppik-Wróbel, A., & Schlicke, D. (2016). Computational prediction of restraint-induced crack patterns in reinforced concrete walls. In *Proceedings of MSSCE2016/Service Life Segment, Lyngby, Denmark* (Vol. 1, pp. 49–58).

Koenders, E. A. B., Czerny, F., & van Breugel, K. (2005). A design concept for crack predictions in hardening concrete structures. In N. Banthia, T. Uomoto, A. Bentur, & S. P. Shah (Eds.), *Proceedings of ConMat '05*, *Vancouver* (pp. 1–10) 2005.

Koenders, E. A. B., van der Ham, H., & van Breugel, K. (2007). Modern statistical methods for accessing the hardening process of concrete. In *Advances in construction materials 2007, part VI* (pp. 471–477).

König, G., & Tue, N. V. (2008). *Grundlagen des Stahlbetonbaus* (3 Auflage). Vieweg + Teubner Verlag (in German).

König, G., & Tue, N. V. (1996). *Grundlagen und Bemessungshilfen für die Rissbreitenbeschränkung im Stahlbeton und Spannbeton*. (DAfStb Heft 466). Berlin: Beuth-Verlag (in German).

Lokhorst, S. J. (2001). *Deformational behavior of concrete influenced by hydration related changes of the microstructures*. Technical University of Delft.

Mangold, M. (1994). *Die Entwicklung von Zwang- und Eigenspannungen im Betonbauteilen während der Hydratation*. Ph.D. Thesis, Technical University of Munich.

Mihashi, H., & Leite, J. P. (2004). State-of-the-art report on control cracking in early age concrete. *Journal of Advanced Concrete Technology, 2*(2), 141–154.

Nilsson, M. (2000). *Thermal cracking of young concrete. Partial coefficients, restraint effects and influence of casting joints*. Licentiate thesis, Luleå University of Technology.

Nilsson, M. (2003). *Restraint factors and partial coefficients for crack risk analyses of early age concrete structures*. Ph.D. Thesis, Luleå University of Technology.

OeBV Österreichische Bautechnik Vereinigung. (2018). Analytisches Bemessungsverfahren für die Weiße Wanne optimiert, Merkblatt (in German).

Pérez Caldentey, A., Corres Peiretti, H., Peset Iribarren, J., & Giraldo Soto, A. (2013). Cracking of RC members revisited: influence of cover, $\emptyset/\rho_{s,ef}$ and stirrup spacing—an experimental and theoretical study. *Structural Concrete*, *14*(1), 69–78.

RILEM TC 119-TCE. (1997). Avoidance of thermal cracking in concrete at early ages. *Materials and Structures*, *30*, 451–464.

RILEM TC 181-EAS. (2002). Early age cracking in cementitious systems—Report of RILEM Technical Committee TC 181-EAS.

Schlicke, D., & Tue, N. V. (2015). Minimum reinforcement for crack width control in restrained concrete members considering the deformation compatibility. *Structural Concrete, 16*(2), 221–232.

Schlicke, D. (2014). *Mindestbewehrung für zwangbeanspruchten Beton*. Ph.D. Thesis, Graz University of Technology (in German).

Schlicke, D., & Tue, N. V. (2016). Crack width control—verification of the deformation compatibility versus covering the cracking force. In *Proceedings of MSSCE2016/Service Life Segment*, Lyngby, Denmark (Vol. 2, pp. 563–572).

Schöppel, K. (1993). *Entwicklung der Zwangsspannungen im Beton während der Hydratation*. Ph.D. Thesis, Technical University of Munich (in German).

Springenschmid, R. (1987). Betontechnologie im Wasserbau. Chapter 1, Wasserbauten aus Beton, Handbuch für Beton-, Stahlbeton- und Spannbetonbau, Hans Blind (in German).

Sule, M. S. (2003). *Effect of reinforcement on early-age cracking in high strength concrete*. Ph.D. Thesis, Delft University of Technology.

Tue, N. V., & Pierson, R. (2001). Ermittlung der Rißbreite und Nachweiskonzept nach DIN 1045. *Beton- und Stahlbetonbau*, *96*, 365–372 (in German).

van Breugel, K. (1982). Development of temperature and properties of concrete as a function of the degree of hydration. In *RILEM International Conference on Concrete at Early Ages*, *Paris* (Vol. 1).

van der Ham, H. W. M., Koenders, E. A. B., & van Breugel, K. (2006a). Level III calculations for hardening concrete elements. In *Proceedings of Integrating Structural Analysis, Risk & Reliability*, *Glasgow* (pp. 1–8).

van der Ham, H. W. M., Koenders, E. A. B., & van Breugel, K. (2006b). Monte Carlo calculations for hardening concrete. In *Proceedings of the European Symposium on Service Life and Serviceability of Concrete Structures ESCS-2006*, *Helsinki* (pp. 189–194).

Chapter 9
On-site Monitoring of Mass Concrete

Dirk Schlicke, Fragkoulis Kanavaris, Rodrigo Lameiras and Miguel Azenha

Abstract On-site monitoring of mass concrete offers several benefits. It may comprise a wide range of objectives from (i) the maintaining of adequate temperature conditions for the evolution of the desired concrete properties and to (ii) the determination of thermal and mechanical parameters for verification of the calculation models and assumptions applied for crack assessment of the considered structure. Next to very general information on monitoring of mass concrete, this chapter presents different levels of measures with regard to the purpose and expected insights into each level, available instruments and least requirements on practical application, as well as possibilities for result verification. The chapter focuses on both established techniques with comprehensive experiences in many applications and comparably new techniques available on the market. Finally, the presented techniques and approaches were exemplified on three different application examples with regard to different measurement systems as well as types of structures.

D. Schlicke (✉)
Graz University of Technology, Graz, Austria
e-mail: dirk.schlicke@tugraz.at

F. Kanavaris
Queen's University of Belfast, Belfast, UK

R. Lameiras
University of Brasília (UnB), Brasília, Brazil

M. Azenha
ISISE, University of Minho, Guimarães, Portugal

© RILEM 2019

E. M. R. Fairbairn and M. Azenha (eds.), *Thermal Cracking of Massive Concrete Structures*, RILEM State-of-the-Art Reports 27,
https://doi.org/10.1007/978-3-319-76617-1_9

9.1 General Basics

9.1.1 Opportunities and Limitations of On-site Monitoring of Mass Concrete

An important outcome of mass concrete monitoring is the confirmation that adequate conditions for the evolution of the desired concrete properties were maintained. This refers to both the assurance of a correct hydration process within the limits of acceptable maximum concrete temperature as well as the avoidance of harmful temperature-induced cracking. The latter results from high temperature gradients between interior and surface of a lift as well as high temperature differences between the lift and neighbouring construction stages. Next to temperature measurements, monitoring of mechanical parameters provides also insights into strains or even stresses in the concrete. This enables, in combination with temperature measurements, a reliable database for further considerations. Besides, the measurement results provide important data to verify the calculation models and assumptions applied for crack assessment of the considered structure, as well as to improve these calculation models and assumptions for future projects.

Providing an appropriate measurement as well as correct analysis, it can be said that precision and reliability of the drawn conclusions correlate with the extent of monitoring measures applied. This means, e.g., solely measuring the temperature in a single point of the cross section requires further assumptions to draw conclusions on the temperature field of the member and solely measuring temperature—even with adequate number of measuring points in the cross section—requires further assumptions to quantify strains or even stresses and crack risk of the structure.

In general, the extent of monitoring measures should always be determined according to the intended insight. Of course, cutbacks are possible and often reasonable as well. Realistic assumptions and experience can also ensure meaningful and correct conclusions; however, it should always be kept in mind that such conclusions rely on the quality of the assumptions and might therefore be defective.

At this point, it should also be mentioned that measurement results and conclusions drawn are always subject to uncertainties. The main reasons are: (i) measurement uncertainties of the applied method, (ii) the influence of the presence of a sensor in the measurement environment and (iii) the need of additional assumptions to relate the measurement value correctly to the real concrete behaviour. These aspects will be addressed accordingly in the following presentation of available monitoring techniques.

9.1.2 Set-up of an On-site Monitoring

On-site monitoring of mass concrete aims to obtain maximum values of a given parameter, e.g. temperature, strain, but also to determine the distribution of such parameter within the monitored member and its evolution throughout time. Common sampling rates according to recently reported monitoring programmes are at least one sampling per hour or more (e.g. RILEM 1998; Morabito 2001; Azenha 2009; Schlicke 2014; Soutsos et al. 2016; Kanavaris 2017). Besides, it is of crucial importance to adequately record the relevant environmental conditions, which will be discussed in Sect. 9.2.

The positioning of sensors within the member should enable the prior mentioned aims: knowing peak values and their distribution in space. This can be achieved by sensor arrangement along the main axes of changes, e.g. over height and width of the member. According to Schlicke (2014), the number of required sensors along those axes should be determined with respect to the shape of the parameter distribution to be observed. Parabolic shapes, for instance, would require a minimum of three sensors over the width, whereas shapes of higher order require more sensors.

Besides, the positioning of sensors needs to respect least requirements of each sensor type in terms of minimum concrete cover as well as minimum distances between sensors. In general, this refers to a possible affecting of the concrete behaviour due to the presence of too many sensors in a too small area, mainly in regard to the disturbance of the strain field due to the presence of concrete embedment strain gauges or stressmeters with even higher influence on the surrounding. If in doubt, preliminary studies of the disturbed strain field can provide further information to find an optimal solution. Although specific reports of such procedure could not be found in the literature, a possible approach applied in the preparation of several on-site monitoring in the context of Schlicke (2014) should be outlined here. In these studies, the effect on the strain field was determined with FE studies by putting a representative void in a volume and shortening the volume. The conclusion was drawn from the change of the strain field since the sensor works are also strain-based. For low stiffness concrete embedment strain gauges with an inner diameter of the connection pipe of <2 mm, such FE studies showed that the influence of the presence of the sensor on the strain field of the cross section is smaller than 1% as long as the cover is >5 cm or the minimum distance between concrete embedment strain gauges is >10 cm.

For illustrative purposes, Fig. 9.1 summarizes the above-discussed points regarding the positioning of sensors in a general manner.

The illustration in Fig. 9.1 shows a proposal for sensor positioning in a more block-shaped member without a clear length direction. In these types of members, the parameters to be monitored show usually a volumetric distribution so that sensor arrangement is required in all three dimensions. One simplification could be the usage of symmetry over the depth if front and backside show comparable conditions. On the contrary, if the member to be monitored can be categorized as

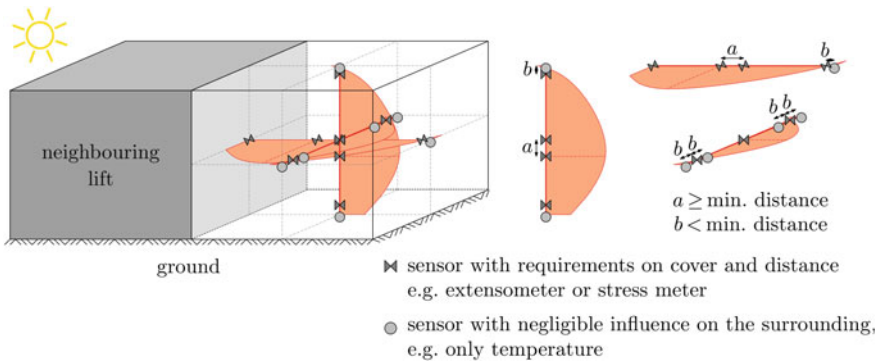

Fig. 9.1 Requirements on sensor positioning

slab or as wall, the number of sensors can be reduced further. As outlined in Schlicke (2014), slabs can be adequately monitored by a measurement chain over the height in a single point, whereas walls can be adequately monitored by a sensor arrangement in the decisive cross section in length direction. The reason is that parameters to be monitored are almost constant over the member length and in case of slabs also over the width, as exemplified in Fig. 9.2.

Other important aspects are cable routing and data logging. Common temperature monitoring can be seen as state of the art. There are numerous loggers designed to record temperature data, providing a variety in logger capabilities, such as power or battery operation, battery life, stand-alone or computer controlled thermocouple compatibility. Some examples were shown in Fig. 9.3.

With increasing extent of the monitoring programme, extensive cable routing and demanding data logging can become a challenging task and need to be handled with care. In case of electronic sensors, an increasing number of sensors cause significant cable bundles which could affect the measurement environment. Besides, professional data loggers with multiplexing properties are needed. Figure 9.4 shows the cable bundles of the monitoring programme of a 4.0-m-thick power plant slab as well as the installation of the data logger on the top surface of

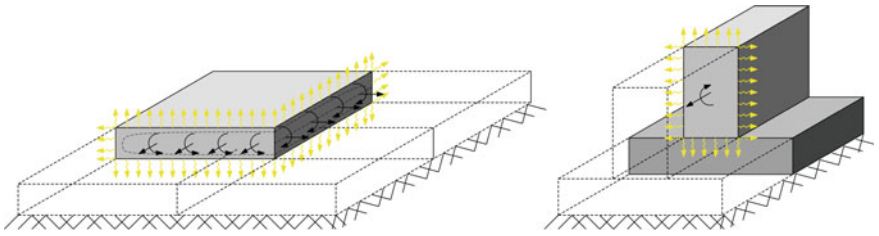

(a) ground slab *(b) wall on foundation*

Fig. 9.2 Member types with areal distribution of parameters to be monitored (Schlicke 2014)

(a) dataTaker DT85M
(photo: M. Azenha)

(b) Pico TC-8
(photo: F. Kanavaris)

(c) Ahlborn ALMEMO 3290 V5
(photo: D. Schlicke)

(d) Gant Squirrel OQ610-S
(photo: F. Kanavaris)

Fig. 9.3 Example of temperature data loggers

Fig. 9.4 Cable routing and arrangement of the data logger in the monitoring programme of the 4.0-m-thick power plant slab Boxberg (*Photos* D. Schlicke)

the slab. To protect the cable bundles from damage during casting, the cables were routed along the reinforcement mesh and finally guided in the inside of a steel pipe. Another important aspect is the sensitivity of electrical measurements against electrical disturbances due to welding on-site. Thus, especially construction sites with excessive arc welding activities require an independent grounding of the measurement installation.

Fibre optical measurements have advantages in regard to both insensitivity against electrical disturbances due to welding on-site as well as cable routing since

sensors can be connected serially. In the best case only one wire is needed (e.g. Humar et al. 2016; Bao and Chen 2012), but it should be noted that serially connected sensors cannot be controlled absolutely simultaneously. Depending on the scanning speed of the chosen system, a certain delay of measuring times between the sensors has to be accepted (Delsys 2017; Emilio 2013). Besides, an application with several independent wires which are controlled by only one interrogator causes time shifts between the exact measuring times of the sensors. The reason is the required time for signal processing before switching to the next cable; however, if measurement results are required at exactly the same, time this circumstance may be overcome by fitting of the result curves.

Recent advancements in concrete temperature monitoring also include wireless systems. Several efforts have been made to develop wireless systems based on various operating principles to enable the wireless evaluation of temperature history of concrete; see Kim et al. (2015), Lee et al. (2014), Barroca et al. (2013), Chang and Hung (2012), Noris et al. (2008). In addition to that, such systems have been recently commercialized and offer remote evaluation of the temperature and strength development in concrete structures, with their potential limitations described in Soutsos et al. (2016, 2017), Kanavaris (2017), Vollpracht et al. (2018).

It is also important to take into account the need to host the data logger in the vicinity of the actual construction. Mass concrete structures are frequently built-in remote areas or areas where there are no adjacent buildings, at least. Special care needs to be taken in regard to four main situations: (i) risk of theft or vandalism; (ii) need to shield the data logger from environmental action; (iii) ensuring a stable source of electricity; and (iv) usual need for a stand-alone solution that does not depend on a computer, which is bulky and an additional attractor for potential theft situations. The solution found by the team at the University of Minho (Costa 2011; Azenha et al. 2014) counteracts the four above-mentioned threats with a set of combined actions:

(i) In order to counteract theft/vandalism issues, or even damages due to curiosity of people passing by, the data logger and all connection hubs are hosted inside a robust electrician box. The box is screwed through the inside to a wall and closed with a key and external locker. This makes it very hard for anyone without the key to open the box or even remove it from the wall into which it is fixed. Care must also be taken to ensuring some fixing devices in between the data logger and the cables accessible from the outside: if someone pulls the cables from the outside (either on purpose or by chance), the corresponding force should not be exerted directly on the wiring connections of the data logger. On the contrary, it ends up being absorbed by the fixing device inside the box. No vandalism acts were recorded even in areas that are easily accessible by general public. However, there are cases in which wires can be incidentally cut.

(ii) In order to shield the data logger from outer environmental action, such as rain/snow, the electrician box (or similar) should be water tight, as shown in the door/opening of Fig. 9.5, which interpenetrate with a sealant rubber. In

(a) Data logger and battery inside the box *(b) Impermeable electric box with data logger inside*

Fig. 9.5 Data logger positioning and sheltering (Costa 2011; Azenha et al. 2014)

the event of heavy rain, there were no leakage events observed. Furthermore, the holes for the cabling are always made from the bottom surface of the bounding box, as to make sure that no entry of rain/snow happens. The hole should also be as tight as possible to the cables, as to avoid mice or other small animals or insects from coming in. In spite of such care, regular inspections should be done to the state of cables, data logger and bounding box.

(iii) Experience of the team at the University of Minho (Costa 2011; Azenha et al. 2014) has shown that power outages and surges are frequent in construction sites. Therefore, the system should be made independent of such type of problems that may cause disturbances on measurements, or even interruptions of measurement and ultimately damages to the data logger. To circumvent such problem, batteries are normally used to power the data logger; see the black box in Fig. 9.5. Even though this brings great advantages to the stability of electricity signals, it carries the downside of requiring regular replacement of the battery by a newly charged one. In the context of monitoring of mass concrete in few weeks processes, this is normally not a problem, as the consumption of the data logger tends to be small, and battery may withstand for several weeks without needing to be recharged.

(iv) Data loggers with stand-alone operation mode at low electricity consumption and large capacity to store data (USB flash drives) are normally desirable in this type of application. There are several options in the market that satisfy

these criteria. This extends the life of the battery, eliminates the need to extract data to avoid "full memory problems" and removes the need for a highly consuming computer, which is simultaneously the type of item that is rather prone to induce thefts.

Another important matter pertains to the support of sensors in the context of mass concrete structures. Indeed, there are many regions of mass concrete that are totally unreinforced (core, for example). In such cases, when measurements are intended, the support of sensors at predefined locations becomes an issue. As reported by Azenha (2009), this may be overcome by placing specific supports for this matter. Such do not have any special requirements, except for: (i) they must not induce fragilities or compatibility/durability issues in the mass concrete element; (ii) they must be stiff enough to ensure adequate location and direction of the sensors themselves throughout the operations of casting; and (iii) they must not significantly affect the temperature field. An example of such type of system can be seen in Fig. 9.6, where measurement of temperature and strain is illustrated with vibrating wire strain gauges in a core region of mass concrete. In such example, a staged construction dam is shown, with casting heights of 1.2 m. The PVC pipes were embedded by 1.2 m in the previous casting stage (present during the casting itself) and extended further 1.2 m in correspondence with the subsequent casting stage. Before the subsequent casting stage, the pipes were connected to each other by steel bars that simultaneously braced the pipes to each other and allowed the support of the sensors themselves at the desired heights of monitoring. Besides, the pipes were prefilled with mortar in order to reduce thermal influences due to the voids.

After completion of the monitoring, the embedded sensors remain in the concrete, whereas all external parts of the installation were usually dismantled. However, it might be recommended that the monitoring set-up provides also proper preservation of the cable ends during service life, rather than just being cut-off from

(a) vertical supports *(b) horizontal supports*

Fig. 9.6 Supports tailored for allowing vertical profiling of temperatures and strain in unreinforced regions of mass concrete (Azenha 2009; Azenha et al. 2014)

hardened concrete and sealed. This enables future assessments of the structure at later ages, even if long-term monitoring is not being considered at the moment.

9.1.3 Calibration of Sensors

Adequate calibration of the sensors is important and should be handled with care to ensure technically reliable measurements. Usually, sensors were calibrated against reference values, e.g. calibrating temperature sensors using 0 °C as reference point by inserting the sensor into an ice bath, as depicted in Meanset (2009). Further information can be found in ASTM (1993, 2015), EURAMET (2011) as well as in the individual specifications of the applied sensors.

9.1.4 Analysis of Results

Basically, the measurement results represent the state or course in time of the determined parameter (temperature, humidity, strain, stress, etc.) in single points of the cross section. With respect to the whole cross section, each parameter is distributed with a certain shape (e.g. temperature field or strain field). As outlined in Schlicke (2014) and shown in Schlicke (2015), detailed conclusions on structural behaviour require both to derive the field from the punctual measurement results and to identify characteristic parts in the field for further conclusions. In accordance with the common understanding, these characteristic parts are: (i) constantly in the whole cross-sectional distributed part; (ii) linearly over width and height of the cross-sectional distributed parts as well as (iii) the residual part, which is usually nonlinearly distributed and self-balanced within the cross section. Figure 9.7 illustrates this context; further information is given in, e.g., Schlicke and Tue (2015), Heinrich and Schlicke (2016), Eierle and Schikora (2000), Rostásy and Hennig (1990) or Reinhardt (2014).

Besides spatial aspects, the interpretation and further processing of measurement results can require time discrete and incremental analysis as well. One example is

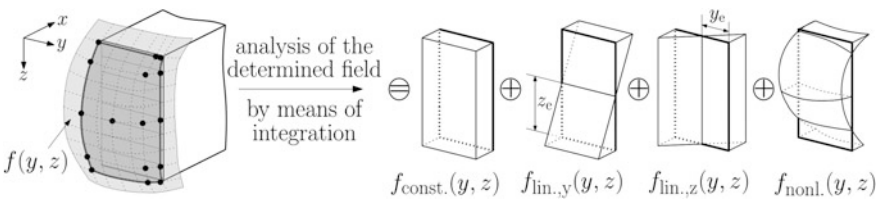

Fig. 9.7 Determination of the cross-sectional distribution $f(y, z)$ of the measurand out of punctual measurement results (•) and analysis of the determined field

the conclusion from measured strains to stresses, whereby several simultaneously evolving concrete properties in the course of time as well as the superposition with viscoelastic effects occurring by time need to be considered. As shown in Schlicke (2014), this can be achieved by splitting the course of time into time steps and adding up the changes of each time step to a course over time. Figure 8.12 in Chap. 8 gives an impression of such procedure.

The beginning of the monitoring is usually determined by the placement of concrete. In terms of temperature monitoring, this is usually witnessed by the person responsible for the monitoring. However, strain measurements require a clear definition of the beginning of reliable results with respect to the setting time, as reported in Azenha et al. (2014).

9.1.5 Verification

In the literature, different ways for the verification of monitoring results can be found. This refers mainly to:

1. Comparison of monitoring results with independently obtained measurements,
2. Comparison of monitoring results with results of computational simulations and
3. Compatibility check of monitoring results among each other.

The first point, comparison of monitoring results with independently obtained measurements, refers either to all cases in which third-party data is applied for verification, e.g. comparison of recorded environmental conditions on-site with data of nearby weather stations, or to all cases in which redundant measurement results within the monitoring were compared to each other. The latter is typical for verification of novel monitoring techniques, such as sensing of temperature in the concrete along optical fibres verified with conventional measurements of concrete temperature with sensors at single points.

The second point, comparison of monitoring results with results of computational simulations, refers to all kinds of monitoring results ranging from temperature development, overstrain histories up to stress development in the concrete. Such procedure is often applied, e.g. Azenha et al. (2009, 2017), Lawrence et al. (2012), Rostásy et al. (2007), Schlicke (2014, 2015), Kanavaris (2017). For illustrative purposes, Fig. 9.8 shows the results of the computational simulation of monitored temperature, strains and stresses of the prior mentioned power plant slab Boxberg.

Computational simulations, however, are always subject to the reliability of the material model and the calculation assumptions. Of course, the computational simulation of concrete temperature by means of analytical equations, e.g. Bamforth (2007), Riding et al. (2006), or by application of time discrete thermodynamic models, as presented in Chap. 7 of this report, provides usually reliable proof. The computational simulation of monitored strains and stresses, however, underlies a complex interplay between the thermomechanical material behaviour including

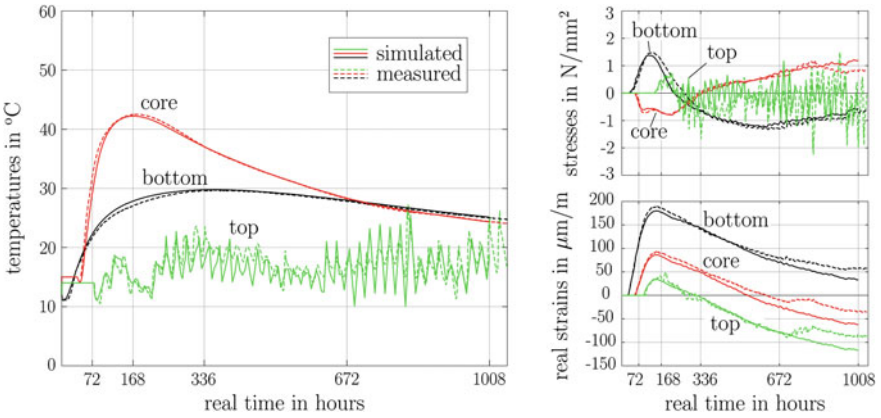

Fig. 9.8 Example of computational simulation of measurement results in the 4.0–m-thick power plant slab Boxberg (Schlicke 2014)

viscoelastic effects as well as the calculation assumptions. According to Schlicke (2014), unequivocal verification is therefore only provided if calculation results agree satisfactorily with the determined real deformation and stress history at the same time, as shown in Fig. 9.8.

The third point, compatibility check of monitoring results among each other, refers to check whether monitored temperature, strains as well as stresses are compatible with each other in the course of time. A mandatory requirement of this procedure is therefore the monitoring of all three parameters in comparable points of the structure, and it is usually limited to the uncracked state. Basically, such procedure was already proposed by Raphael and Carlson (1965) with the "combination of stressmeters and strain metres for completely independent check". A recent report of such procedure can be found in Schlicke (2014), whereby the verification was considered as successful if the monitored stress history could be retraced quantitatively over the course of time by the monitored strain history. For the purpose of illustration, Fig. 9.9 depicts the result of the compatibility check of the above-mentioned monitoring of the ground slab Boxberg.

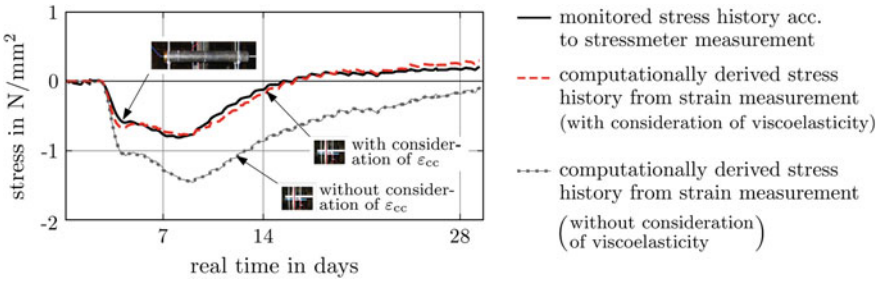

Fig. 9.9 Determined stresses on half height of the slab: comparison between stressmeter results and computational derivation from strain measurement (Schlicke 2014)

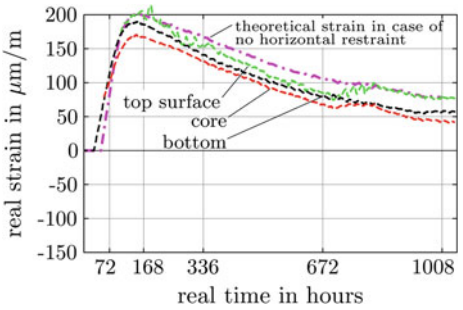

Fig. 9.10 Determined strains over the height of the slab (shifted at setting time to the present strain of the slab) and comparison with constant part of temperature field (Schlicke 2014)

Besides, the analysis of the obtained real strains enables a broader checking of the coherence of the monitoring. For instance, the theoretical axial elongation or shortening of the member according to thermal expansion and shrinkage can be compared with the real strain in each measuring point, whereby the difference between them should be in line with the expected restraint degree in axial direction (Austin et al. 2006; Schlicke 2014, 2015). Besides, the analysis of real strain measurements over the member height provides insights into the extent of self-weight activation due to temperature and/or moist gradients over the member height and whether the cross section remains even or not (Schlicke 2014, 2015). Figure 9.10 depicts such comparison for the above-mentioned monitoring of the ground slab Boxberg. In this example, the layerwise casting of the slab required the consideration of accordingly delayed setting of each casting layer. The strain history of each measuring point was therefore shifted on the y-axis until its initial value at setting complies with the present strain of the layer below. Altogether, the comparison with the theoretical strain of the whole member in case of no external restraint shows that the slab can deform in axial direction almost freely. On the contrary, the strains over the height are running almost parallel, which indicates a plane cross section as well as full restraint of any curvature.

9.2 Recording of External Conditions

9.2.1 Preliminary Remarks

Monitoring of the environmental conditions on-site refers predominantly to recording of ambient temperature, solar radiation, relative humidity and wind velocity. When it comes to mass concrete pouring and curing, this can provide improvements for three main reasons: (i) obtain the anticipated external conditions prior to concrete pouring in order to avoid critical pouring times regarding risk of cracking occurrence; (ii) monitor the external conditions during concrete pouring and curing to enable taking control measures in situ to mitigate cracking;

and (iii) incorporate the obtained ambient conditions in finite element modelling as input parameters in order to numerically estimate the thermal- and shrinkage-induced stresses in the concrete (e.g. Azenha 2009; Schlicke 2014).

A peculiarity of monitoring on-site is the determination of correct environmental conditions to which the member is exposed to reality. In contrast to meteorological observations, which comply with observation standards, e.g. WMO (2008), the decisive conditions of a member are significantly affected by microclimatic influences as outlined in Nilsson (1996).

Omitting explicit monitoring of on-site conditions and relying solely on meteorological weather data, which is e.g. provided comprehensively in several online weather databases, has to be seen with respect to its limitations. On the one hand, the available meteorological weather data is usually much less detailed over time and solely provided in form of average and min./max. values per day, and on the other hand, the aforementioned microclimatic effects can lead to significant differences between real on-site conditions and external conditions recorded with the nearby weather station. On the contrary, an objective comparison of measurements with meteorological weather data can provide an appropriate opportunity for the verification of the monitoring.

9.2.2 Ambient Temperature

The ambient temperature is usually measured using simple but robust sensors such as thermocouples as these are inexpensive options providing suitable accuracy for the purpose of the monitoring.

With respect to microclimatic effects, special attention is to be given to the location and shielding of the sensor. Regarding the location, two general possibilities exist: (i) the sensor is located very close to the concrete surface recording the temperature of the air which is in direct contact with the concrete, or (ii) the sensor is located away from the concrete surface where the ambient temperature is not affected by surface effects from the concrete, for example, following the placement guidelines outlined in WMO (2008). Both cases are illustrated in Fig. 9.11.

The first possibility provides results which can be used directly as boundary condition for computational simulations but cannot directly be compared with the air temperature as defined by meteorological standards. The second possibility provides an air temperature which could be compared to the air temperature according to meteorological standards, but requires corrections in order for it to be applied as a boundary condition in computational simulations. Both cases, however, need adequate protection of the sensor against radiation and moisture to avoid that solar radiation and/or evaporation on the sensor itself may influence the measurement. Solar radiation will result in an increase of the recorded temperature, whereas moisture (or the presence of fog) can reduce the recorded temperature.

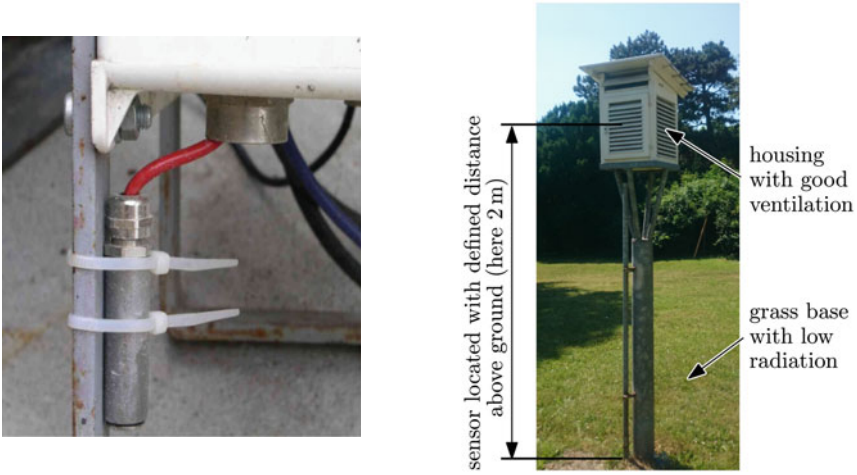

(i) placement close to the concrete surface with shielded sensor

(ii) placement according to meteorological standards, e.g. (WMO 2008)

Fig. 9.11 Measurement of ambient air temperature (*Photographs* D. Schlicke)

9.2.3 Solar Radiation

Solar radiation affects the temperature field of mass concrete in different ways. As outlined in Honorio (2015), Riding et al. (2009), van Breugel (1998), or Bernander (1998), the solar radiation on the final surface induces higher thermal gradients. Next to this, additional heat can also be included during the pouring when concrete is placed in large layers which remain open for a couple of hours (Schlicke 2014). Besides, the knowledge of occurring solar radiation improves the accuracy of calculation models in terms of considered heat transfer by irradiation (Bofang 2014; Riding et al. 2006).

The solar radiation in a horizontal surface is often measured on-site using high-precision sensors known as pyranometers (TGES 2008). There are different types of pyranometers, designed for different purposes, however, for the purpose of measuring the solar radiation on the surface of concrete; a low-cost silicon pyranometer as shown in Fig. 9.12a is usually accurate enough (Azenha 2009). Alternatively, solar radiation can be also measured with the so-called photovoltaic pyranometers, also known as reference cells, which implement a solar (photovoltaic) cell to convert energy of light directly into electricity (Meydbray et al. 2012). An example of a self-built device on basis of a solar cell is shown in Fig. 9.12b. Another opportunity is the application of thermopile pyranometers according to the standard of metrological monitoring, whilst all types of pyranometers are classified into categories in the relevant ISO standard (ISO 1990) in terms of their performance (Paulescu et al. 2013).

(a) commercial silicon pyranometer (Delta Ohm 2017)

(b) self-built device on basis of a solar cell (photo: D. Schlicke)

Fig. 9.12 Measurement instruments for the monitoring of solar radiation

9.2.4 Wind Speed

Wind speed usually fluctuates significantly with time and location, increases with distance from the ground and is affected by the surrounding environment (Burton et al. 2011). Complex fluctuations in wind speed on a fast timescale can also occur as a result of a phenomenon known as turbulence, whilst the effects of turbulence become more pronounced as the height above ground decreases (Burton et al. 2011).

With respect to mass concrete, wind could have a detrimental effect on its performance, as evaporation and cooling of exposed surfaces will rapidly increase due to increased convective and evaporative heat loss (Wojcik et al. 2003; Wojcik 2001), potentially leading to surface cracks from thermal shock or drying, depending on ambient temperature and relative humidity (van Breugel 1998).

In general, wind speed can be measured with anemometers. Among several types of anemometers, see Langreder (2010), Johnston (2005), a simple, robust and appropriate wind speed monitoring can be provided with so-called three- or four-cup anemometers. Relevant details regarding their use, installation and interpretation of results have been reported by Hunter (2003). However, as mentioned earlier there are very complex microclimatic interactions making the precise monitoring of wind at different locations difficult. A reasonable approach for determination of convection coefficients is to refer to simplified mean values or

wind strength scales. The most frequently adopted approach to quantify the wind intensity is the Beaufort wind force scale which is an empirical measure relating wind speed to observed land and sea conditions (Met Office 2010; Mather 2005).

9.2.5 Relative Humidity

It is common understanding that relative humidity is an important parameter of the curing process since moisture loss of the concrete surface is significantly influenced by the value of relative humidity (ACI 2007). However, the on-site monitoring of relative humidity is usually not essential for mass concrete applications. The drying depends predominantly on average conditions of relative humidity (Neville 2011), which can be gathered adequately from nearby weather stations. Nevertheless, if such measurements would be required for special purposes, hygrometers could be applied closely to the concrete surface whilst more detailed information is given elsewhere (Barnes 2016; Simpson 2016; Kanare 2005).

9.2.6 Integrated Monitoring with Weather Stations

In the cases in which a comprehensive gathering of meteorological on-site characteristics is required, weather stations may be also considered. These devices normally comprise of a thermometer for measuring air temperature, a hygrometer for measuring humidity, an anemometer for measuring wind speed, a pyranometer for measuring solar radiation and a rain gauge for measuring liquid precipitation (Davis 2016; WMO 2008). A weather station can be considered as an affordable option which provides a set of useful information, with respect to environmental conditions on-site, and it is particularly convenient as it combines different sensors and instruments in one device.

9.3 Temperature Measurements in the Concrete

9.3.1 Preliminary Remarks

Temperature monitoring within mass concrete provides fundamental information related to concrete performance. Besides the aforementioned detection of temperature maxima as well as temperature gradients, temperature monitoring is nowadays also applied to indirectly conclude on the evolution of strength in order to optimize stripping times or thermal insulation (e.g. Carino and Lew 2001).

There are several temperature sensors available on the market which are suitable for measuring the temperature of hardening concrete, having different operation principles and accuracy. The most commonly used are thermocouples, resistance temperature detectors and thermistors. In case of a longitudinal shape of the sensors or their housing, it is recommended to place near-surface sensors parallel to the exposed surface/formwork. This ensures that the sensor stays perpendicular to the main direction of thermal flux and has therefore a well-known position of measurement. Besides established sensors, novel techniques incorporating fibre optic sensors or thermographic methods for surface temperature monitoring have started to gain popularity.

9.3.2 Common Sensors and Their Peculiarities

9.3.2.1 Thermocouples

Thermocouples are commonly used sensors when it comes to in situ temperature monitoring of concrete, especially due to their comparably low cost, robustness and practicability (ASCE 2000).

The operating principle of the thermocouples is based on what has become known as the thermoelectric effect or "Seebeck effect" (discovered in 1821 by Thomas Johann Seebeck). In this phenomenon, voltage difference between two dissimilar electrical conductors or semiconductors is induced by temperature differences. This temperature-dependent voltage resulting from the thermoelectric effect is then interpreted to measure temperature (Morris and Langari 2016; Hagart-Alexander 2010).

There are different types of thermocouples, i.e. nickel alloy, platinum/rhodium alloy, tungsten/rhenium alloy, etc., and every particular type is denoted by a capital letter, i.e. Type E, Type K, Type T, Type R, etc., offering a variety of temperature ranges that can be measured and measurement accuracy (Tong 2001). The types which are commonly used in concrete temperature monitoring are Type K thermocouples (chromel–alumel) and Type T (copper–constantan) ensuring an accuracy of approximately 1.5–2 °C and 0.5–1 °C, respectively, which is adequate for the purpose of the measurement. Prior to the installation of the thermocouples, the ends of the two conductors have to be in direct contact which is usually accomplished by simply twisting them together or join them together through soldering or even welding (Omega Engineering 2000). A thermocouple connector is often required at the other end of the cable to enable connection between the thermocouple and the logger. An illustration of Type K and Type T thermocouples is shown in Fig. 9.13.

Once the thermocouples are prepared, the joined end of the wires is fixed to the desired locations, as exemplarily shown in Fig. 9.14.

(a) Type K thermocouple wire *(b) Type T thermocouple wire*

Fig. 9.13 Example of thermocouple wires (*Photographs* F. Kanavaris)

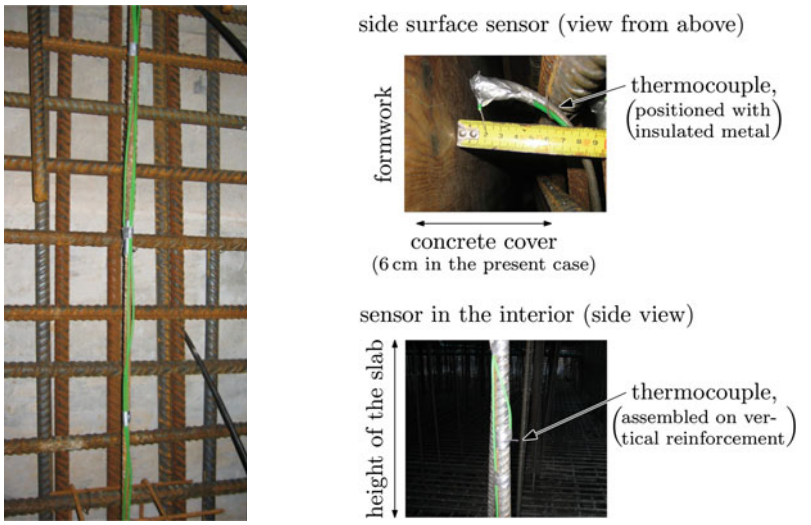

(a) Routing along the reinforcement *(b) Example of fixed measuring ends of thermocouples*

Fig. 9.14 Example of application of thermocouples in a concrete slab (*Photographs* D. Schlicke)

9.3.2.2 Resistance Temperature Detectors

Resistance temperature detectors (RTDs) are the temperature sensors which detect temperature through changes in resistance of a metallic material. The majority of RTD sensors are composed by a portion of fine wire wrapped around a ceramic or glass core, whilst the RTD wire is typically made of nickel, platinum or copper

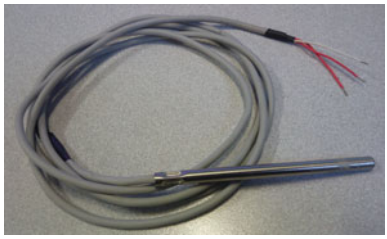

Fig. 9.15 Example of a commercially available RTD probe with PT100 (*Photograph* F. Kanavaris)

(Morris and Langari 2016; Hagart-Alexander 2010). In contrast to thermocouples, which measure temperature through changes in voltage, RTDs provide the higher accuracy, stability and repeatability. In detail, the accuracy of RTDs, such as PT100 (see Fig. 9.15), can be designed to fall below 0.2 °C.

Since RTDs operate at relatively low resistance, the influence of the lead wire resistance is not negligible (ASCE 2000). However, this is usually factored out by the manufacturer; otherwise, measurement distortions can occur. Although RTDs provide the highest measurement accuracy, they are generally among the most expensive temperature sensors.

9.3.2.3 Thermistors

Thermistors are electric resistors which also detect temperature through changes in resistance; however, thermistors differ from RTDs in terms of composing materials (Hagart-Alexander 2010) as well as their comparably high temperature coefficient of resistance (Nakra and Chaudhry 2016).

Thermistors are usually made of ceramic or polymer, whereby two principally different types of thermistors can be distinguished: PTC with positive temperature coefficient due to which resistance increases as temperature rises and NTC with negative temperature coefficient with decreasing resistance as temperature rises.

The high resistance coefficient contributes to measurement simplicity and minimization of potential errors arising from leading wires (ASCE 2000; Harris and Sabnis 1999), yielding slightly better accuracy than thermocouples, i.e. between 0.2 and 0.4 °C, whilst not being as cheap as the latter. An example of a pure thermistor as well as a ruggedized one specifically designed for measuring temperature of concrete is depicted in Fig. 9.16.

9.3.2.4 Sensing Along Optical Fibre Cables

Another opportunity of measuring temperatures is using optical fibre cable directly as sensing element by sensing along the cable length. So-called distributed temperature sensing systems (DTS) measure temperature along the optical sensor cable and provide a continuous temperature profile along the cable (e.g. Shi et al. 2016;

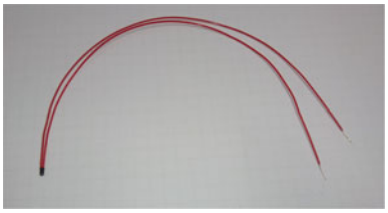

(a) "pure" thermistor (NTC)

(b) ruggedized thermistor placed with aramid sticks between reinforcement.

Fig. 9.16 Examples of thermistors (*Photographs* D. Schlicke)

Bao and Chen 2012; Ukil et al. 2011; Beck et al. 2010; Inaudi and Glisic 2006; Lee 2003). The provided accuracy of min. ±0.1 °C is sufficient for measurements in hardening concrete (Glisic and Inaudi 2007). The spatial resolution of such measurements, however, ranges commonly in the magnitude of decimetres (e.g. Glisic 2000; Lee 2003) and has been reported to be inversely proportional to the maximal distance range (Henault et al. 2011; Lee 2003).

9.3.2.5 Thermal Camera/Infrared Thermometers

Another technique for measuring the temperature history of hardening concrete that gains popularity is the infrared thermography or thermal imaging. With this technique, which has been previously used to detect defects in reinforced concrete (Milovanovic and Pecur 2016; Bagavathiappan et al. 2013), one can evaluate the surface temperature of objects using a thermal camera on the basis that all bodies emit thermal energy within the infrared wavelength band (Azenha et al. 2011; Childs 2001). The advantage of this method is that it can produce instantaneous real-time images (or videos) of the temperature distribution in the concrete surface, as well as its surroundings (Domski and Katzer 2015; Azenha et al. 2011; Weil 2004). Similarly to thermal cameras, infrared thermometers can be also used to provide an indication of the surface temperature of a concrete unit (Snell 2015); however, the spectrum of the infrared thermometers is narrowed down to a specific point and might not provide the capability of continuously recording the temperature. Additionally, some infrared thermometers also come with a thermocouple port enabling the simultaneous temperature measurement from the thermocouple and from the laser. One can fix several thermocouples in different locations of a mass concrete member and frequently evaluate the temperature differences between the concrete core and exposed surfaces for quality control purposes. An example of an image taken from a thermal camera and an infrared thermometer is shown in Fig. 9.17a and Fig. 9.17b, respectively.

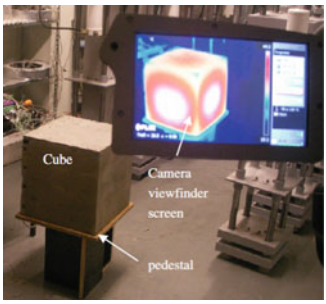

(a) Thermal image of concrete cube using a thermal camera (Azenha et al., 2011)

(b) Surface temperature measurement of a concrete slab with infrared thermometer (photo: F. Kanavaris)

Fig. 9.17 Examples of thermal camera and infrared thermometer

9.4 Monitoring of Strain Histories

9.4.1 Preliminary Remarks

Monitoring of strain history in mass concrete provides insights into the real deformation behaviour of the material. This includes concrete strains within the member but also the globally resulting deformation of the member. Next to further insights into the structural behaviour of hardening mass concrete, monitored strain histories provide also a strain-based opportunity to assess the resistance against cracking (Jung et al. 2017; Lawrence et al. 2014). In detail, this can be achieved by derivation of mechanical concrete strains out of the measurements (restrained part of thermal strains and shrinkage as well as additional viscoelastic strains) and their comparison with strain-based crack criteria. Of course, cracking itself would be determined directly by the measurement as soon as it occurs (Rostásy et al. 2007; Schlicke 2014).

With respect to strain monitoring in mass concrete, the literature review shows mainly the installation of so-called concrete embedment strain gauges as well as Carlson strain gauges. In general, concrete embedment strain gauges are characterized by an embeddable body which will deform together with the concrete and whose deformation is measured using different measuring principles. Usually, this procedure requires different post-processing, e.g. meaningful determination of the beginning of the monitoring (Azenha et al. 2009, 2014) and temperature compensation. In contrast to this, Carlson strain gauges combine different measuring principles in order to obtain the real concrete strain directly.

9.4.2 Common Measurement Equipment and Peculiarities

9.4.2.1 Electrical Resistance Strain Gauges

Electrical resistance strain gauges are sensors which measure induced deformation (strain) in a certain direction through a change in electric resistance and are used to detect relatively small displacements, i.e. 0–50 με (Morris and Langari 2016). Such sensors come at different sizes, where the selection of the appropriate size depends on the type of application and expected magnitude of strain (MM 2014a). These sensors are considered to be an efficient solution when it comes to strain monitoring in hardening concrete as they are relatively inexpensive, are available in different sizes and offer compatibility with numerous data loggers. Nonetheless, there are technical parameters that need to be taken into consideration when setting up a strain monitoring process, such as type of bridge (full, half and quarter), temperature compensation, gauge factor. More detailed information regarding the above is available in the existing literature (Nakra and Chaudhry 2016; Dally and Riley 2005; Harris and Sabnis 1999; Omega Engineering 1999).

The application of electrical resistance strain gauges in hardening mass concrete, however, is to be handled with caution because of their sensitivity to humidity as well as limited long-term stability (e.g. Rocha 1965). Bearing this in mind, two general types for application inside concrete have asserted: (i) electrical resistance strain gauges in specific devices for concrete embedment and (ii) electrical resistance strain gauges attached to reinforcement. With respect to monitoring of hardening mass concrete, specific examples were not obtained in the available literature. One reason for this could be found in the explanations of Azenha et al. (2009) indicating problems with the temperature compensation as well as vulnerabilities against interference with electrical apparatus in the sensors vicinity.

The second case, attaching the strain gauge on the reinforcement bars, is reported, e.g., in Kanavaris (2017), Faria et al. (2006), Bekowich (1968), Morabito (2001). Specific measures for providing an adequate steel surface in terms of smoothening and cleaning are required (e.g. Nakra and Chaudry 2016). The strain gauge is then adhered to the steel surface using a high strength glue/epoxy. It has to be noted that if the lead wires connected with the strain gauge are exposed, then they must not come in contact with the steel surface; otherwise, this will result in short-circuit occurrence. The protection of the strain gauge from water is then accomplished through application of a layer of a moisture protection coating in the strain gauge after it has been successfully attached to the desired location of the bar. Further information and details with respect to strain gauge installation can be found in MM (2014b, c, 2015). Finally, due to the fact the electrical resistance strain gauges are considerably sensitive and fragile sensors, protection against mechanical damaging, the gauge must be provided in order to ensure that the gauge will survive the rebar transportation (if the rebar is not in place) and concrete pouring process. Examples of the above processes are depicted in Fig. 9.18.

(a) strain gauge glued on smoothed steel re-bar

(b) moisture protection coating applied on strain gauge

(c) strain gauge protected against mechanical damage

Fig. 9.18 Example of strain gauge installation on a steel rebar (Kanavaris 2017)

Although it becomes rather obvious, it has to be pointed out that the strain measured from attaching strain gauges on the reinforcement bars is not the real strain induced in concrete. Apart from this, since the reinforcement ratio is kept relatively low in mass concrete applications and the reinforcement is predominately concentrated close to concrete surfaces, assessment of the strains in concrete core requires the application of additional reinforcement bars. Besides, such measurement is affected by a disproportionate slip between young concrete and reinforcement until concrete is stiff enough to ensure bonded deformations to steel. Up to such instant, which is difficult to ascertain, the measurements taken by strain gauges glued into reinforcement cannot be considered as representative of concrete deformations (Azenha et al. 2014).

9.4.2.2 Vibrating Wire Sensor

The application of vibrating wires in hardening mass concrete has a considerable history going back several decades (e.g. Mainstone 1953; Rocha 1965; Geymayer 1967). Nowadays, vibrating wires can be seen as the most established type of concrete embedment strain gauges (Jung et al. 2017; Lawrence et al. 2012, 2014; Yeon et al. 2013; Chu et al. 2013; Choi and Won 2010; Azenha et al. 2009, 2014, 2017; Zreiki et al. 2010; Sellers 2003; Morabito 2001 and Heimdal et al. 2001a, b). These sensors usually consist of a wire and a coil within a pipe which spans between two head plates. The basic measurement principle is the acquisition of the vibrating resonance frequency of the wire when excited by the coil. Due to the embedment in the concrete, the head plates will move apart or to each other when the concrete deforms, and by this the force in the wire changes. The according change of the vibrating resonance frequency of the wire enables to infer on the deformation of the concrete. For illustrative purposes, Fig. 9.19 shows an example

(a) "pure" vibrating wire sensor according to (Geokon, 2017)

(b) vibrating wire sensor applied in the reinforcement layer (photo: D. Schlicke)

Fig. 9.19 Vibrating wire sensor for embedment in concrete

of a pure vibrating wire sensor as well as its application on-site for measuring concrete strain within the reinforcement layer.

In general, vibrating wires record any real deformation along the measuring length, e.g. unrestrained thermal deformation, unrestrained shrinkage and creep (unrestrained viscoelastic behaviour).

However, vibrating wires require temperature compensation procedures that strictly depend on the coefficient of thermal dilation of the wire placed internally, which is constant and known (Azenha 2009). The temperature change in the measuring point is generally simultaneously monitored with a built-in thermistor inside the gauge body of vibrating wire sensors. Altogether, the real deformation in the measuring point can be derived from the vibrating wire measurement by:

$$\Delta\varepsilon_{\text{real}} = \Delta\varepsilon_{\text{meas}} + CTE_{\text{W}} \cdot \Delta T \tag{9.1}$$

where:

$\Delta\varepsilon_{\text{real}}$ Real strain in the measuring point,
$\Delta\varepsilon_{\text{meas}}$ Uncompensated recorded strain in the measuring point,
CTE_{W} Coefficient of thermal dilation of the wire,
ΔT Temperature change in the measuring point.

For profound understanding of the basic functionality of a vibrating wire, Fig. 9.20 illustrates the relation between concrete strain and wire deformation with respect to thermal dilation and shrinkage under different restraint situations. Besides, the effect of different coefficients of thermal dilation of the wire (CTE_{W}) and the concrete (CTE_{c}) is regarded as well.

In unrestrained conditions, the uncompensated strain of the vibrating wire corresponds to shrinkage as well as the difference in thermal dilation of wire and concrete. In restrained conditions, however, the vibrating wire displays the restrained part of thermal dilation of the concrete plus the difference in thermal dilation of wire and concrete as well as the unrestrained parts of shrinkage and viscoelastic strains. With respect to viscoelastic behaviour of concrete, it should be emphasized again that the vibrating wire records only unrestrained deformation so that restrained viscoelastic strains (recognizable as relaxation) are not recorded.

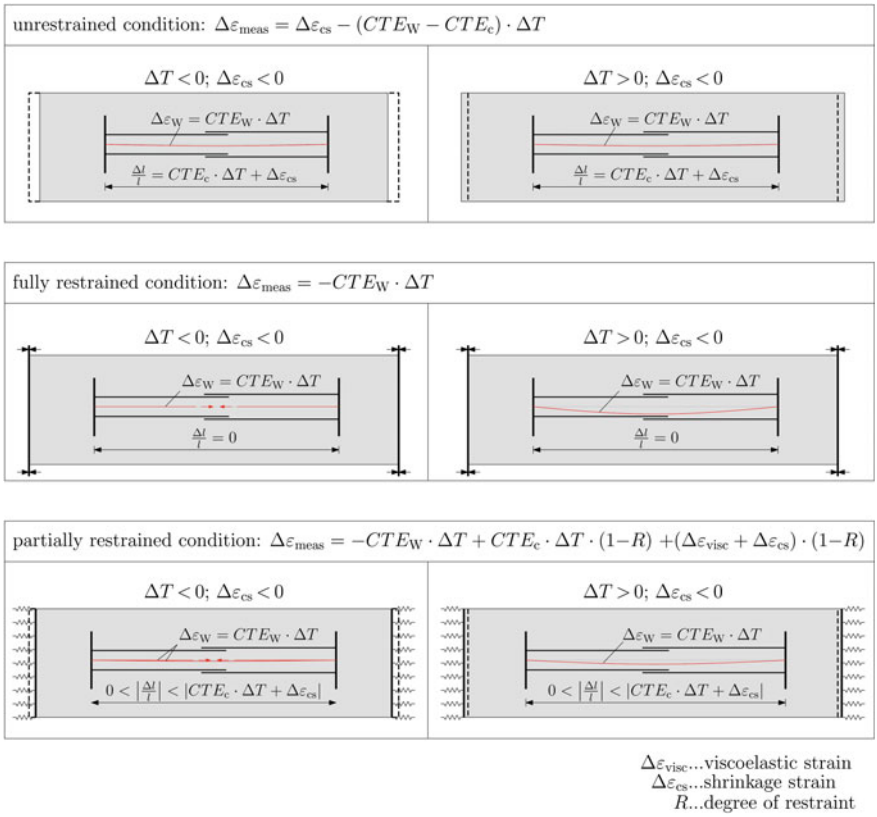

Fig. 9.20 General functionality of vibrating wire according to Schlicke (2014)

9.4.2.3 Concrete Embedment Strain Gauge on Basis of Fibre Optic Sensors

The application of concrete embedment strain gauges on basis of fibre optic sensors (explicit fibre optic sensor connected and controlled with a fibre optic cable), however, increases recently, especially in case of comprehensive programmes in which additional costs of the optical measuring device (interrogator) can be amortized by a considerable reduction of cabling efforts due to the serial connectivity of fibre optical sensors. Such sensors work on basis of fibre Bragg technique with a specific Bragg grating of the fibre in the measuring length. Similarly to vibrating wires, these sensors record an average strain in the measuring length. Figure 9.21 shows such a sensor.

Fig. 9.21 Fibre optical concrete embedment strain gauge on basis of fibre Bragg technique (*Photograph* D. Schlicke)

9.4.2.4 Carlson Type Strain Gauge

One of the most widely used sensors to monitor internal strains of mass concrete structures is the Carlson type strain gauge (Bekowich 1968; Nagataki 1970; Poblete et al. 1988; Shahawy and Arockiasamy 1996; Myrvoll et al. 2003; Conceição et al. 2014). This sensor contains a set of electrical strain gauges. The sensing element of Carlson type strain gauge includes two coils of carbon steel wire (elastic material), one of which increases in length and consequently in electrical resistance when a strain occurs, whilst the other decreases. One important aspect is that the ratio of the two registered resistances is independent of temperature and, therefore, the change in resistance ratio can be used to indicate strain. Besides that, the total resistance is independent of strain since one coil increases the same amount as the other decreases due to the change in length of the sensor. Hence, the total resistance can therefore be used to indicate temperature. This is one of the main advantages of using Carlson type strain gauges: the same instrument is capable to make both strain and temperature measurements, allowing the reduction of temperature sensors in the structure and the number of channels required for the data acquisition system. Further details on Carlson type strain gauges are given in Torrent and Fucaraccio (1982).

Carlson type strain gauges' body is usually shaped like a cylinder with a metallic flange at either extremity. The cylinder cover is usually made with PVC sleeving to break the bond with the concrete. The role of these flanges is to promote the bonding to the surrounding concrete. The PVC cover has a hollow section with the steel rods connected to either end. The elastic wire coils are mounted on these rods such that when the end flanges are pulled apart, one coil increases in length whilst the other decreases. The coils of steel wire are immersed in oil; the housing is hermetically sealed. This procedure results in a strain gauge with good stability and reliability. A schematic representation and a picture of Carlson strain gauges and application examples are shown in Fig. 9.22.

In the same way as with strain gauges on basis of electrical resistance, Carlson strain gauges are usually connected to a measuring three-wire, quarter-bridge wiring scheme in order to minimize cable effects (Myrvoll et al. 2003).

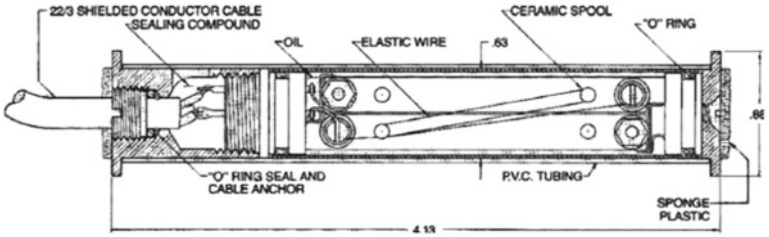

(a) Scheme of Carlson strain gauge taken from Myrvoll (2003)

(b) Carlson strain gauge (RST Instruments 2017)

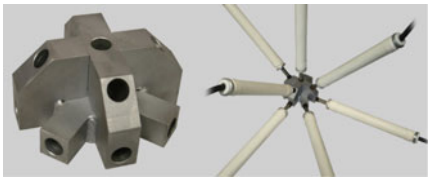

(c) Spider and Carlson strain gauges shown in a spider (RST Instruments 2017)

(d) Carlson strain gauges being grouped by a spider (Mata et al. 2015)

Fig. 9.22 Carlson type strain gauge and application opportunities

The installation procedure of Carlson type strain gauges requires a previous calibration in situ. This procedure is usually performed using a calibration device, e.g. micrometre screw or other displacement transducer.

9.4.2.5 Sensing of Concrete Strains with an Optical Fibre Cable Directly

This section refers to strain monitoring using the optical fibre cable directly as sensing element. In detail, two different methods can be distinguished: (i) fibres with fibre Bragg grating (FBG) and (ii) continuous sensing along the fibre without FBG. Regarding the general functioning of this technique, reference is made to Rogers (1999), Hill and Meltz (1997), Lee (2003), Henault (2013), Billon et al. (2014) or Delepine-Lesoille et al. (2017).

One of the main challenges of applying this technique to hardening concrete is the protection of the fibre and ensuring at the same time a meaningful connection between fibre and concrete (Delepine-Lesoille et al. 2006). The pure fibre is usually

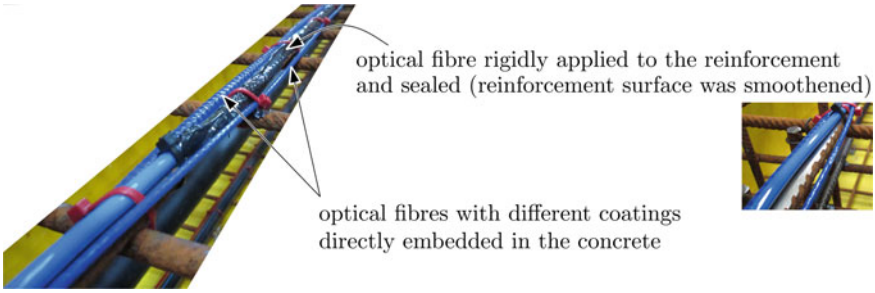

Fig. 9.23 Sensing of concrete strains with optical fibre cables directly (*Photograph* D. Schlicke)

too fragile to survive the pouring. But a helpful protection coating is also to be seen critical since it is expected to be too weak and thus the strain of the fibre is only presenting the smeared concrete strain over an undefined length. A ruggedized fibre optical sensor developed in EPFL known as SOFO has been also used in several monitoring programmes reportedly offering resolution in the micrometre range, long-term stability and insensitivity to temperature (Glisic and Inaudi 2007; Glisic and Simon 2000). Recent activities concentrate on application of the fibre on specifically prepared reinforcement surface but as mentioned before, this refers to a measurement of steel strain changes and requires again additional assumptions to draw conclusions on the real concrete strain. Figure 9.23 depicts different fibre applications for a comparative study; however, a report on these particular measurements was not available at this time.

Another challenge is the required strain resolution. Different specifications can be found in the literature indicating a resolution of *a few micrometres over one metre* (Bao and Chen 2012) up to 20 µm/m (Lee 2003) and higher. The required resolution for strain monitoring in hardening concrete ranges in the same order of magnitude. For example, the depicted strain monitoring of power plant slab Boxberg showed a real deformation to be monitored in the cooling phase of ca. −150 µm/m within ∼840 h, whereby the desired resolution for monitoring the strain evolution over time would range in the magnitude of ±3 µm/m per time step.

In case of cracking, the absolute size of strains increases locally in the surrounding of the crack; however, the associated increase of inhomogeneity of the strain field influences the measurement signal considerably. But at the same time, the local disturbance enables also the recognition of crack formation at a very early stage, even before cracks would be visible (Lee 2003; Bao and Chen 2012).

9.4.3 Experiences and Observations from Application

Nowadays, the most established technique is the embedment of 15–20-cm-long concrete embedment strain gauges in measuring direction (Jung et al. 2017;

Lawrence et al. 2012, 2014; Yeon et al. 2013; Chu et al. 2013; Choi and Won 2010; Azenha et al. 2009, 2014, 2017; Zreiki et al. 2010; Sellers 2003). The required accuracy can be obtained independently from the measurement principle, e.g. vibrating wire-based, electrical strain gauge-based or fibre optic-based devices.

The application of Carlson type strain gauges, however, is declining (ASCE 2000). Vibrating wire and fibre optic-based sensors have largely superseded the Carlson type strain gauge because their signals can be transmitted over long cables without degradation with relative immunity to changes of cable or contact resistance. In addition, the vibrating wire and fibre optic-based strain gauges have excellent long-term stability.

9.5 Determination of Stress Histories

9.5.1 Preliminary Remarks

The determination of stress histories in mass concrete on basis of measurements provides insights into the real stressing in a material point and enables the assessment of resistance against cracking by comparison of the determined stresses with stress-based crack criteria. Of course, cracking itself would be determined directly by the measurement as soon as it occurs (Rostásy et al. 2007; Schlicke 2014). With respect to the reports in the literature, three basic procedures can be distinguished:

1. Computational derivation of stresses from pure strain measurements,
2. Application of "no-stress" enclosures for simplification of the analysis of pure strain measurements and
3. Determination of stresses with specific measuring devices.

The computational derivation of stresses from pure strain measurements can be achieved by a clear identification of all stress-relevant parts in the strain measurement and superimposing them with the evolution Young's modulus.

The application of "no-stress" enclosures can be seen as a supporting measure in order to simplify the identification of stress-relevant parts in the strain measurement; however, this solution still requires computational post-processing since the effects of viscoelasticity and evolution of Young's modulus are not included.

The determination of stresses with specific measuring devices basically refers to an exclusive measurement of all stress-relevant concrete strains so that the measured values can provide a good estimate on concrete stresses without the need of advanced post-processing as in the previous solutions. But this method should not be misinterpreted as a direct stress measurement since its basic measurement principle is usually also deformation-based (strain gauge in a load cell).

9.5.2 Derivation of Stresses from Pure Strain Measurements

Pure strain measurements in hardening mass concrete are significantly influenced by the present degree of restraint. The results consist of either restrained or unrestrained parts of thermal strains (depending on the measurement principle) as well as of unrestrained parts of shrinkage and viscoelastic strains in form of creep.

For the derivation of stresses from such results, several approaches can be found in the literature. These approaches basically differ in terms of time discretization and consideration of viscoelasticity (e.g. Richardson 1959; Yeon et al. 2013; Bazant 1972a, b; Acerbis et al. 2011; Choi et al. 2011 or Schlicke 2014).

Solutions with implicit consideration of viscoelastic strains by modification of Young's modulus, the so-called effective modulus method, are user-friendly and well-established in practice (Bazant 1972b). In detail, these approaches consider viscoelasticity by multiplication of stress-independent strains with an accordingly modified Young's modulus, so that the stress response includes viscoelastic effects. However, the implementation of such approaches in time step-based solutions should be seen critical since they can require factitious modifications in unloading phases within the stress history or at later ages with very small changes of the stress-independent strains (e.g. Tue et al. 2007; Nietner et al. 2011).

A desirable solution with respect to mechanical consistency is a time discrete approach with explicit consideration of shrinkage and viscoelasticity in the course of time. Given the case that the strain measurement consists solely of the real concrete strains, the general solution would hold:

$$\sigma_c(t) = \int_{t_0}^{t} [\Delta\varepsilon_{real}(t) - \Delta\varepsilon_{ct}(t) - \Delta\varepsilon_{cs}(t) - \Delta\varepsilon_{cc}(t)] \cdot E_c(t)\mathrm{d}t \tag{9.2}$$

where:

$\sigma_c(t)$ Stress history in the measuring point,
$\Delta\varepsilon_{real}(t)$ History of real strain increments in the measuring point (here it is assumed that the measurement result consists solely of the unrestrained parts of thermal strains, shrinkage and viscoelastic strains),
$\Delta\varepsilon_{ct}(t)$ History of temperature strain increments in the measuring point,
$\Delta\varepsilon_{cs}(t)$ History of total shrinkage strain increments in the measuring point,
$\Delta\varepsilon_{cc}(t)$ History of total viscoelastic strain increments in the measuring point,
$E_c(t)$ Evolution of Young's modulus.

9.5.3 Derivation of Stress History with Strain Gauges in "No-Stress" Enclosures

A technique used to measure and compensate for shrinkage and thermal strains from the total or apparent strain measured by the sensors is the use of strain gauges

in "no-stress" enclosures (Rocha 1965; Choi et al. 2011; Chu et al. 2013; Yeon et al. 2013; Azenha et al. 2014). The "no-stress"-induced strain gauges are "dummy" strain gauges that are installed in a manner which isolates them from the effects of stress changes but under the same environment as the active strain gauges. Thus, this "dummy" sensor is subjected to the same history of temperature and humidity (if the enclosure is porous) suffered by the other strain gauges, being able to respond to and measure the unrestrained volume change of surrounding concrete.

In practice, the "no-stress" strain gauge consists of one regular concrete embedment strain gauge, e.g. electrical resistance, Carlson type, vibrating wire or fibre optic-based, that is embedded in a cylinder of concrete which is set in a foam-padded box (Figs. 9.24 and 9.25). The foam is attached to alleviate the friction between the concrete and the inner surface of box and to allow the volume changes of concrete inside the box without restraints, ensuring a stress-free condition in concrete. This box is filled with the same concrete, and at the same time the concrete of monitored structure around it is poured. Then, the box is installed inside the concrete structure, near the other active strain gauges.

The enclosure box to install the strain gauge is generally provided by the concrete embedment strain gauges' manufacturers (e.g. Geokon 2017; RST Instruments 2017). Nonetheless, some works have already reported the successful use of handmade produced enclosures to obtain the "no-stress" strain gauge (Yeon et al. 2013; Azenha et al. 2014).

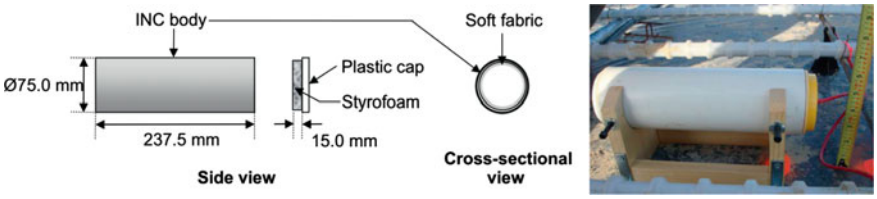

Fig. 9.24 Scheme and photograph of the enclosure used by Yeon et al. (2013)

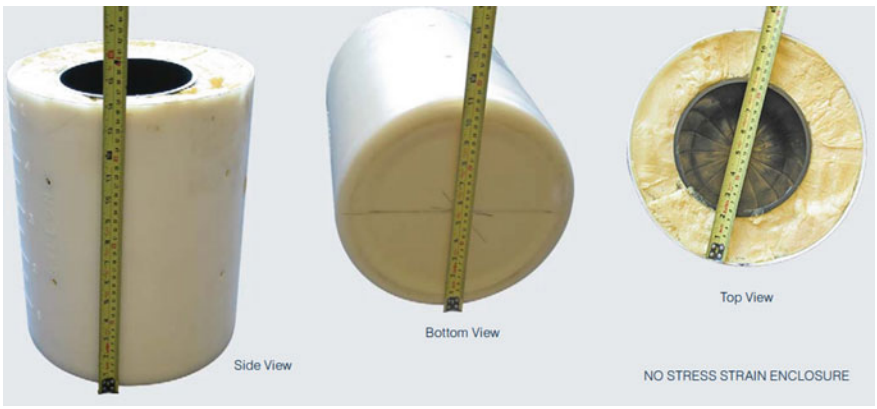

Fig. 9.25 Details of "No-stress" strain enclosure provided by RST Instruments (2017)

The stress history can be derived using Eq. 9.2, considering that the measurement made by the "no-stress" strain gauge corresponds to stress-independent parcel of the total measured strain. Thus, the measurement registered by the "no-stress" strain gauge represents the sum of terms $\Delta\varepsilon_{cs}(t)$ and $\Delta\varepsilon_{ct}(t)$ that stands for, respectively, the increment of the unrestrained shrinkage (autogenous and, possibly, drying shrinkages) and thermal strains between the time $t - 1$ and t.

9.5.4 *Determination of Stresses with Specific Measuring Devices*

As aforementioned, the determination of stresses with specific measuring devices aims at the measurement of concrete stresses without the need of any post-processing. A basic requirement of this technique is to provide thinnest possible sensors in order to reduce factitious stress concentrations in the vicinity of the sensor (Rocha 1965; Raphael and Carlson 1965; Carlson 1966). According to this requirement, a very flat sensor connected with a Carlson strain gauge, a so-called Carlson stressmeter, was developed and applied in several dam projects in the early second half of the last century. One mandatory requirement of these sensors was the application on a stiff surface which led to primary applications in construction joints.

With respect to recent reports in the literature, the more established technique of today appears to be a longer rod-shaped device encapsulating a cylinder of concrete within the poured concrete and coupling this in series with a load cell (e.g. Kawaguschi and Nakane 1996; Tanabe 1998; Rostásy et al. 2007; Tue et al. 2007, 2009; Kurata et al. 2009; Choi and Oh 2010; Choi et al. 2011; Schlicke 2014, 2015). The load cell is also thin; however, the encapsulated cylinder enables the installation of the sensor away from the construction joint and at the same time, the comparably equal properties of the concrete in the tube ensure a suitable consideration of evolution of Young's modulus. Figure 9.26 shows a scheme of the Geokon stressmeter based on Geokon (2015).

In the shown solution of Fig. 9.26, the concrete cylinder is approximately 0.5 m long and has a diameter of ca. 6.5 cm. Its encapsulation is achieved by a permeable tube which ensures the same concrete properties inside the tube as in the surrounding of it. At the same time, this encapsulation allows the concrete cylinder to interact with the stiffness of the load cell in the longitudinal direction of the sensor.

The orientation of the sensor controls the direction of stresses to be monitored. Another important detail of this measuring principle is the prevention of friction on the inside of the tube by a very smooth surface.

Sufficient filling of the tube and compacting of the concrete inside is achieved by the following procedure: (1) taking sensor out of its final position when the pouring process reaches this level, (2) filling the tube with the same fresh concrete, (3) compacting and closing the tube, (4) assembling the sensor in the final position and (5) setting in concrete by continuation of pouring. Figure 9.27 illustrates this procedure.

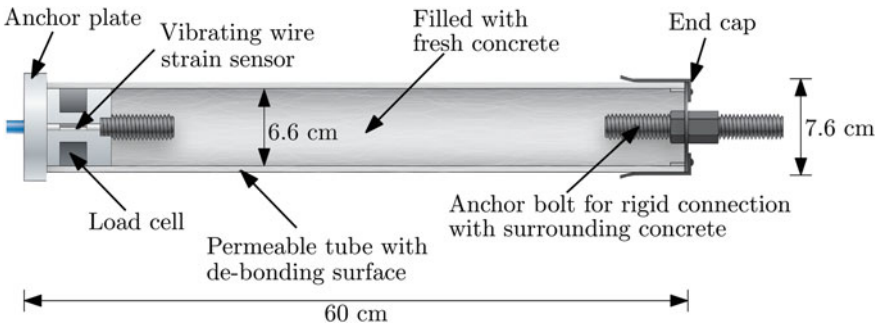

Fig. 9.26 Scheme of Geokon stressmeter, according to Geokon (2015)

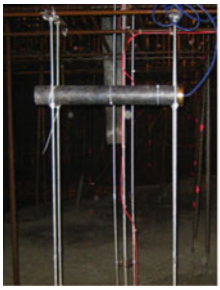

(a) preparation of stressmeter application before casting

(b) filling and compacting of the tube with fresh concrete when casting reaches the measurement point

(c) final application of the filled and closed stressmeter and continuation of casting

Fig. 9.27 Application of stressmeter (*Photographs* D. Schlicke)

The stress in the surrounding concrete can finally be derived from the recorded load divided by the cross-sectional area of the encapsulated cylinder. Typical, results are shown in Fig. 9.9.

9.6 Selected Application Examples

9.6.1 Wall of the Entrance of Paradela's Dam Spillway

Between the years of 2010 and 2012, a new spillway was built for the Paradela's dam, Portugal. A part of this building is a thick wall that pertains to the entrance of the dam spillway. The wall is 27.5 m long, with a maximum width of 2.8 m and height of 15.0 m. The constructors and owners were worried about a construction

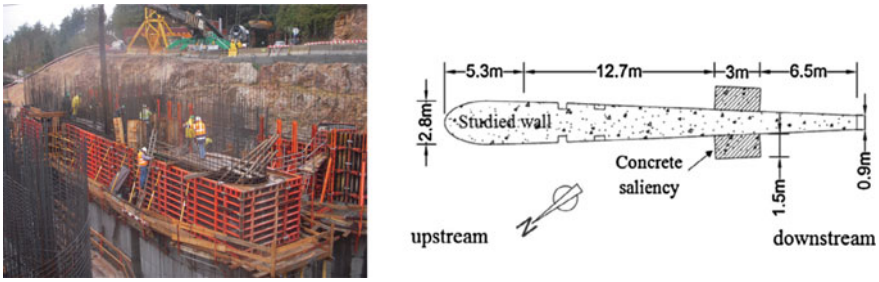

Fig. 9.28 Wall of entrance of Paradela's dam spillway: construction phase studied (*Photograph* M. Azenha; *Drawing* Azenha et al. 2014)

phase in which a 2.5-m-tall batch was poured (total of 150 m^3 of concrete); see Fig. 9.28.

Because of the thermal crack risk involved, an in-depth consulting work was contracted so that the cracking risk was assessed. The study encompassed laboratory thermal and mechanical characterization of concrete, thermomechanical simulation with finite element method as well as in situ monitoring of temperatures and strains. The solution implemented to control the temperature elevation and, consequently, high stresses in the structure was the use of a post-cooling system based on the used air-cooled prestressing ducts placed longitudinally along the wall. Details about this case study can be found elsewhere (Costa 2011; Azenha et al. 2014).

The monitoring programme has been carried out in situ to better understand the effectiveness of the cooling system, its influence on the cracking risk and assess the capabilities of the adopted numerical simulation strategy. The programme involved the use of 27 temperature sensors (20 Type K thermocouples and 7 resistive temperature sensors) and 7 vibrating wire strain gauges embedded in concrete. Particular attention was given to the evaluation of the effectiveness of the cooling system, with temperatures being measured at several points along the prestressing ducts, and with air velocity measurements taken with hand-held anemometers. Figure 9.29. illustrates the internal temperature and strain measuring points.

The sensors were positioned aiming particularly at assessing temperature profiles in a region near the maximum width of the wall. The placement of sensors in this section is depicted in the scheme of Fig. 9.29a, where thermocouples are identified by the prefix TC and vibrating wires and resistive temperature sensors are labelled as VW. The internal air temperature of prestressing ducts has been monitored in the same section and in neighbouring areas. Environmental temperature (dry-bulb) has been also assessed with a thermocouple.

Monitoring was carried out since the instant of casting during a period of 10 days, and the measurement frequency was set to 1 reading per each 30 min. The internally monitored temperatures in concrete are shown in Fig. 9.30 for a vertical and a horizontal alignment of sensors that passes through sensor VW3. From this figure, it can be seen that the initial temperature of concrete was $\sim$ 15 °C and the

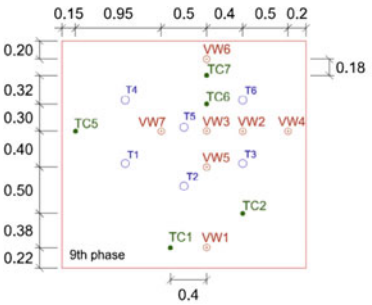

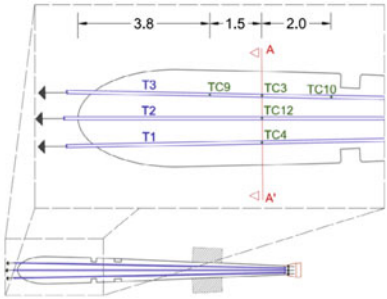

(a) measuring points (TC: thermocouples; VW: resistive thermistors and vibrating wire strain gauges; T1 to T6: air cooled prestressing ducts, units: m)

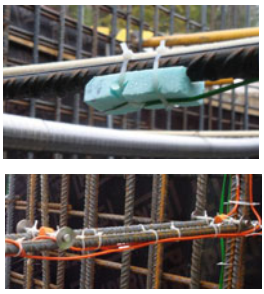

(b) detail of type K thermocouples and vibrating wire strain gauges

(c) detail of "no-stress" strain enclosure

Fig. 9.29 Monitoring programme in a wall of Paradela's dam spillway (*Drawings* Azenha et al. 2014; *Photographs* R. Lameiras)

peak temperature was approximately 42 °C in the core regions (VW3 and VW5). Furthermore, it can be observed that the ascending branch of temperature development is clearly affected at the age of 14 h, when the cooling system is activated. In specific regard to the vertical profile of temperatures shown in Fig. 9.30, the expectable behaviour was captured: the core region has the highest peak temperatures (VW3, VW5), whereas a decreasing trend is seen towards the top surface. In fact, sensors TC6 and TC7 exhibit maximum temperatures of ∼36 °C, whilst VW6 (near the top surface) has the lowest peak temperature (∼27 °C). Near the bottom surface of this construction phase, sensor VW1 highlights the importance of the heat storage effect caused by the previously cast concrete: in fact, even though the temperature peak is lower than that of the core regions, it occurs later and the heat loss rate observed afterwards is lower than in other regions. It should also be remarked that all sensors are almost in equilibrium with environmental temperature by the age of 8 days.

Strain measurement was carried out with vibrating wire strain gauges of metallic casing with 14 cm reference length. The strain gauges were placed at the locations

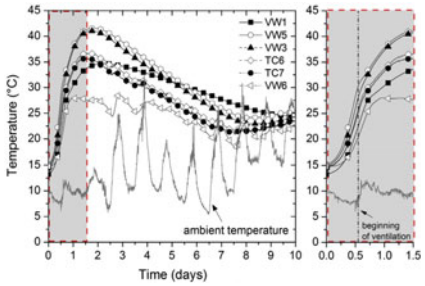

(a) monitored temperatures – vertical alignment

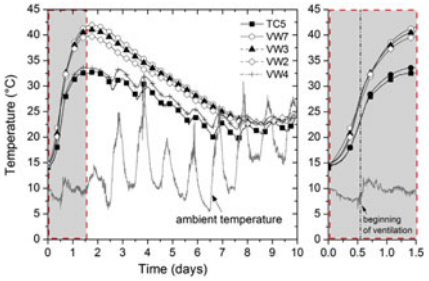

(b) monitored temperatures – horizontal alignment

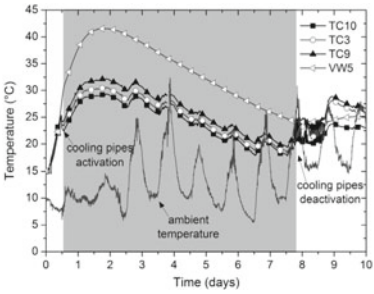

(c) temperature profile along the prestressing duct

Fig. 9.30 Temperature results in the monitored construction phase of Paradela's dam spillway (Azenha et al. 2014)

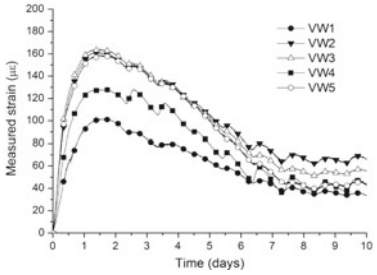

(a) measured strains

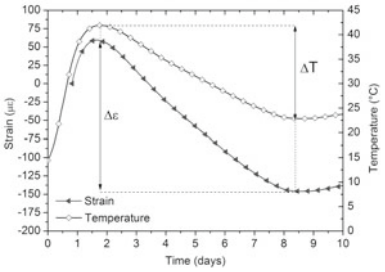

(b) temperature and strains in the "no stress" enclosure

Fig. 9.31 Strain results in the monitored construction phase of Paradela's dam spillway (Azenha et al. 2014)

dully positioned in order to measure strains in the longitudinal direction of the wall. Measurements were taken with the same data logger and at the same sampling rate as it was the case for temperature sensors. The measured strains in sensors VW1 to VW5 are shown in Fig. 9.31a.

In order to assess free deformations of the concrete used in the construction (associated with unrestrained autogenous shrinkage and thermal deformations), strain was measured in a "no-stress" enclosure at position VW 7. The concrete cylinder in this "no-stress" enclosure had dimensions of 150 mm diameter and 300 mm length and was prepared simultaneously with the studied construction phase. In detail, the concrete was cast into the mould right before the casting progress reached the location VW7 and then the mould was placed horizontally at the targeted position before continuing and finishing of the casting.

Reliable results were obtained by using the same concrete and a special mould which was internally coated with a soft membrane (with lids also coated with such material). The longitudinal strains in this specimen were measured with a strain gauge inside the mould, as shown in the photograph of the open mould in Fig. 9.29c. The results are given in Fig. 9.31b. Unfortunately, due to undetermined causes, the output of the sensor could not be read during the first 0.8 days, and thus the reported data only starts at such age.

9.6.2 Ground Slab Boxberg

The ground slab Boxberg is a 3.80-m-thick slab for a coal-fired power plant in Germany. It has aerial dimensions of $\sim 100 \times 100$ m and was poured in 5 construction stages. One construction stage with $\sim 10{,}000$ m^3 was comprehensively equipped with temperature sensors, vibrating wires and stressmeters in order to quantify the hardening-induced stress history of this construction stage. Measurements were carried out at two locations in this construction stage with ~ 15 sensors over the height at each location. Figure 9.32 illustrates the monitoring programme. Details about this case study can be found elsewhere (Tue et al. 2009; Schlicke 2014, 2015).

The following explanations concentrate on the measurement results and derived conclusions for the measuring location in the inner part of the slab. As illustrated in Fig. 9.33a, the measuring results at this location can be characterized by:

- Significant temperature differences over the height of the cross section,
- Significant stress differences over the height of the cross section and
- Absolutely shifted but parallel to each other running deformations.

As illustrated in Fig. 9.33b, the analysis of these results with respect to the characteristic parts in the cross section shows:

For temperatures:

- High uniformly distributed temperature field changes over time (ΔT_N) and

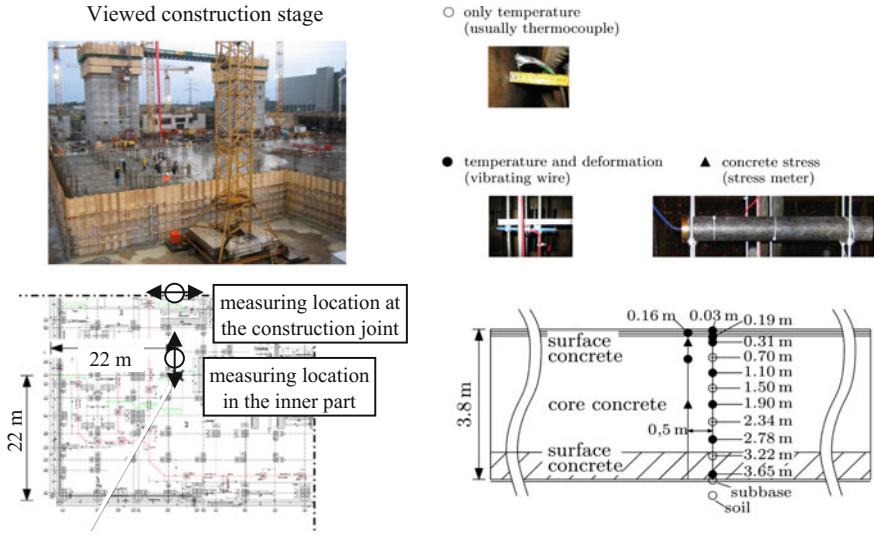

(a) construction stage and position of measuring points and measuring direction

(b) sensors arrangement over the height in a measuring point

Fig. 9.32 Monitoring programme ground slab Boxberg, measuring point "inner part of the slab" (*Photographs* D. Schlicke; *Drawings* Schlicke 2014)

- A high temperature gradient ΔT_M at very early ages resulting from an accelerated warming of the upper layers during the construction process meanwhile the bottom layer is still influenced by heat loss to the ground;

For stresses:

- Disproportional small centric restraint,
- Disappearing bending restraint at time of temperature equalization (bending is only significant during the construction progress) and
- Considerable eigenstresses;

For deformations:

- Almost congruent results at bottom, in the core and on top if the temporal offset due to retarded construction process with layers is considered.

The results of these observations are very consistent and can even be verified by themselves. Namely:

- The free deformation of all measuring points over the height reaches almost $\alpha_T \cdot \Delta T_N$ which confirms the very small centric restraint.

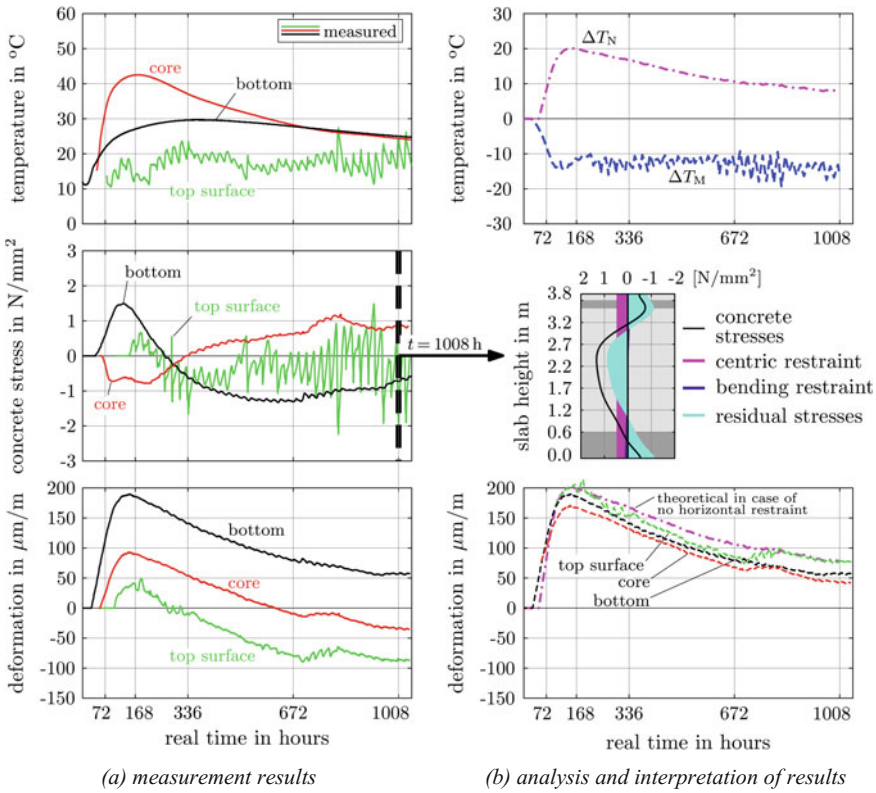

Fig. 9.33 Monitoring results for measuring point in the inner part of the construction stage (Schlicke 2015)

- The free deformation of all measuring points over the height shows almost no curvature which confirms the results of bending restraint.
- The free deformation of all measuring points over the height indicates an almost even cross section which confirms the almost perfect restraint of nonlinear parts of $\Delta T(z)$ causing the determined eigenstresses.

The above shown stresses were computationally derived from the strain measurements with vibrating wires. The reliability of their determination was verified by the compatibility check against the results of a stressmeter measurement in specific points of the cross section. In particular, stressmeters were positioned redundantly next to the vibrating wires at two selected heights of each measuring point (on half height as well as in the upper part of the slab, as shown in Fig. 9.32).

The results of the compatibility check on half height of the slab were already given in Fig. 9.9 for illustrative purpose of the compatibility check in general. Altogether, the compatibility check was considered as successful in the present case since the monitored stress history could be retraced quantitatively over the course of

time from the monitored strain history. Of course, this compatibility check refers rather to a verification of the material model than to a verification of the measurement technique itself. But with respect to a limited number of possible stressmeters in a cross section, a verification of the material model provides an appropriate basis for the derivation of stress histories in other points of the cross section.

In case of the monitoring programme ground slab Boxberg, the most important conclusion was the derivation of reasonable assumptions for efficient minimum reinforcement design of massive ground slabs, namely:

- Centric restraint can be neglected meanwhile.
- Bending restraint has to be taken into account.

Further results and conclusions of this monitoring programme as well as of similar monitoring of other member types are given in Schlicke (2014).

9.6.3 VeRCoRS (Focus on Fibre Optics)

VeRCoRs is a comprehensive project co-ordinated by Électricité de France (EDF) in which a mock-up of a reactor containment building was constructed with comprehensive monitoring of both early age as well as long-term behaviour. The mock-up, which is shown in its almost final stage in Fig. 9.34, consists of double

Fig. 9.34 VeRCoRS mock-up of a reactor containment building (Corbin and Garcia 2016)

containment walls made of reinforced concrete with a thickness varying between 0.7 m at the bottom of the inner wall and 0.4 m at the top of both containment walls.

More than 500 sensors were installed in the building in order to enable continuous monitoring of the behaviour of concrete, including temperature and humidity sensors, electrical resistance and vibrating wire strain gauges as well as 2 km of fibre optic cable sensors. With respect to the overall context of the present report, the following section concentrates on the monitoring of temperature and strain development in the hardening phase of the first lift of the inner wall, i.e. the "gusset", with a comparably thick cross-sectional dimension of 0.7 and 0.4 m thick and 1.20 m high.

Focus will be given on the application of innovative fibre optic techniques for the recording of temperature and strain development in the hardening concrete. In the present case, the fibre optic cables were placed across the circumference of the inner containment wall, as shown in Fig. 9.35b, measuring temperature and strain on an hourly basis.

The installation of fibre optic sensors under construction site conditions requires special care, especially to secure the cables during the pouring process. Reportedly, 80% of the fibre optic sensors survived the concrete pouring process, underlining the sensitivity of this type of sensor. Figure 9.36 gives an optical impression of the installation.

The advantage of the continuous measurement of temperature and strain using fibre optic sensors in the nuclear containment building is also shown in Beck et al. (2016), where sensor positioning and obtained strain histories across the circumference of the structure are demonstrated. The potential of obtaining continuous real-time measurements of temperature and strain evolution over considerably long distances undoubtedly contributes to a more comprehensive monitoring of mass concrete behaviour.

(a) sensor and their cables distributed in the circumference of the vessel

(b) fibre optic cable sensor running parallel to the reinforcement

Fig. 9.35 Monitoring sensors in the VeRCoRs project (Oukhemanou 2016)

(a) fibre optic cable sensors secured in place and grouped together

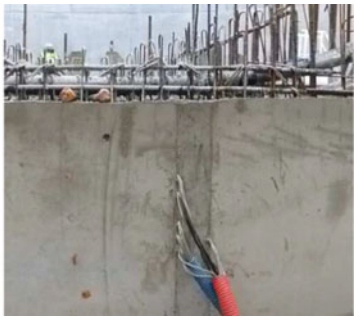

(b) residual sensor cables after concrete pouring and hardening

Fig. 9.36 Fibre optic sensors installed in the VeRCoRs project (Oukhemanou 2016; Oukhemanou et al. 2016)

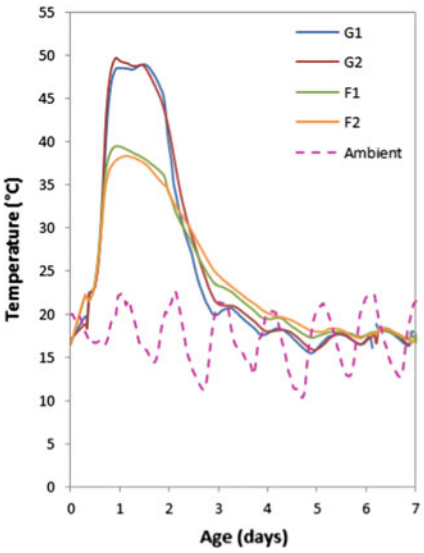

(a) Recorded temperatures in various locations in the "gusset"

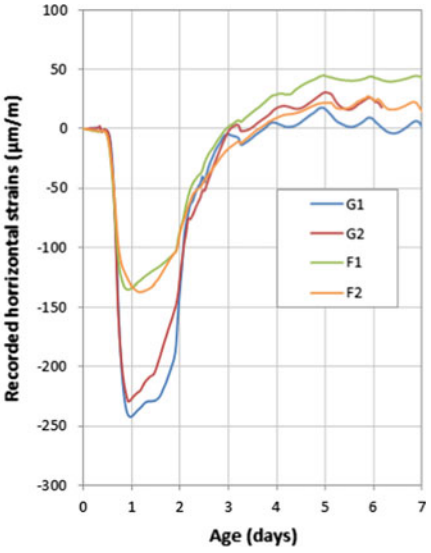

(b) Recorded horizontal strain histories in various locations in the "gusset"

Fig. 9.37 Example of results obtained from early-age monitoring in VeRCoRs project ("gusset"), adopted from Corbin and Garcia (2016)

Temperature and strain profiles obtained, see Fig. 9.37, are particularly useful in validating developed models in a more global manner (Kanavaris et al. 2016) and evaluating the effect of discontinuities in construction lifts and external loads on the concrete behaviour. Nevertheless, the early-age behaviour of the so-called gusset, which refers to the first construction stage after the raft foundation which also had an increased wall thickness compared to the rest of the inner containment wall, was

of particular interest. The corresponding locations of the designated sensors were as follows: G1 and F1 were top and bottom of the "gusset", respectively, and close to inner concrete surface, whilst G2 and F2 were top and bottom of the "gusset", respectively, and at mid-thickness of the section.

Acknowledgements The kind contribution of Benoit Masson, Alexis Courtois and François Martinot from EDF France for sharing their experience on VeRCoRS is gratefully acknowledged. Regarding the monitoring programme "ground slab Boxberg", we wish to thank MPA Braunschweig for the very professional technical support in the installation of the monitoring programme on-site as well as Vattenfall for the financial assistance.

Other work was partially supported by: project POCI-01-0145-FEDER-007633 (ISISE), funded by FEDER funds through COMPETE2020-Programa Operacional Competitividade e Internacionalização (POCI) and by Portuguese funds through FCT—Fundação para a Ciência e a Tecnologia. FCT and FEDER (COMPETE2020) are also acknowledged for the funding of the research project IntegraCrete PTDC/ECM-EST/1056/2014 (POCI-01-0145-FEDER-016841).

References

ASCE. (2000). Guidelines for instrumentation and measurements for monitoring dam performance. Report by the ASCE Task Committee on instrumentation and monitoring dam performance, USA.

Acerbis, R., Asche, H., Barbieri, G., & Collotta, T. (2011). Recommendations for converting strain measured in concrete to stress. *Geotechnical Instrumentation News, 65,* 29–33.

ACI Committee 305. (2007). *Specifications for hot weather concreting*. U.S.A.: The American Concrete Institute.

ASTM. (1993). Manual on the use of thermocouples in temperature measurement. ASTM Committee E20 on temperature measurement (4th ed.), ASTM manual series MNL 12. U.S.A.: ASTM International.

ASTM. (2015). ASTM G167-15, Standard test method for calibration of a pyranometer using a pyrheliometer. U.S.A.: ASTM International.

Austin S. A., Robins P. J., & Bishop, W. J. (2006). Instrumentation and early-age monitoring of concrete slabs. *Proceedings of the Institution of Civil Engineers – Structures and Buildings*, *159*(SB4), 187–195.

Azenha, M. (2009). Numerical simulation of structural behaviour of concrete since its early ages. Ph.D. thesis, Faculdade de Engenharia da Universidade do Porto.

Azenha, M., Faria, R., & Ferreira, D. (2009). Identification of early-age concrete temperatures and strains: Monitoring and numerical simulation. *Cement & Concrete Composites, 31,* 369–378.

Azenha, M., Faria, R., & Figueiras, H. (2011). Thermography as a technique for monitoring early age temperatures of hardening concrete. *Constructions and Building Materials, 25*(11), 4232–4240.

Azenha, M., Lameiras, R., de Sousa, C., & Barros, J. (2014). Application of air cooled pipes for reduction of early age cracking risk in a massive RC wall. *Engineering Structures, 62–63,* 148–163.

Azenha, M., Leitao, L., Granja, J. L., de Sousa, C., Faria, R., & Barros, J. A. O. (2017). Experimental validation of a framework for hygro-mechanical simulation of self-induced stresses. *Cement and Concrete Composites, 80*, 41–54.

Bagavathiappan, S., Lahiri, B. B., Saravanan, T., Philip, J., & Jayakumar, T. (2013). Infrared thermography for condition monitoring—A review. *Infrared Physics & Technology, 60*, 35–55.

Bamforth, P. B. (2007). *CIRIA660: Early-age thermal crack control in concrete*. London: CIRIA.

Bao, X., & Chen, L. (2012). Recent progress in distributed fiber optic sensors. *Sensors, 2012*(12), 8601–8639. https://doi.org/10.3390/s120708601.

Barnes, R. (2016). *Interpretation of hygrometer readings for moisture in concrete floors*. Concrete Advice No. 29. Camberley, U.K.: The Concrete Society.

Barroca, N., Borges, L. M., Velez, F. J., Monteiro, F., Gorski, M., & Castro-Gomes, J. (2013). Wireless sensor networks for temperature and humidity monitoring within concrete structures. *Construction and Building Materials, 40*, 1156–1166.

Bazant, Z. P. (1972a). Numerical determination of long-range stress history from strain history in concrete. *Material and Structures, 5*, 135–141.

Bazant, Z. P. (1972b). Prediction of concrete creep effects using age-adjusted effective modulus method. *American Concrete Institute, 69,* 212–217.

Beck, Y. L., Kah, A. A., Cunat, P., Guidoux, C., Artieres, O., Mars, J., et al. (2010). Thermal monitoring of embankment dams by fiber optics. In *8th ICOLD European Club Symposium on Dam Safety*, Innsbruck, Austria.

Beck, Y. L., Martonot, F., Desforges, S., Buchoud, E., & Henault, J. M. (2016). Distributed measurements with optical sensors in the EDF group: experience feedback and perspectives. In R. J. Mair, K. Soga, Y. Jin, A. K. Parlikad & J. M. Schooling (Eds.), *Proceedings of the International Conference on Smart Infrastructure and Construction*, June, Cambridge, UK (pp. 3–8).

Bekowich, R. S. (1968). Instrumentation in prestressed concrete containment structures. *Nuclear Engineering and Design, 8*(4), 500–512.

Bernander, S. (1998). Practical measures to avoiding early age thermal cracking in concrete structures. In R. Springenschmid (Ed.), *Prevention of thermal cracking in concrete at early ages, RILEM Report 15* (pp. 255–314). London, U.K.: E & FN Spon.

Billon, A., Henault, J. M., Quiertant, M., Taillade, F., Khadour, A., Martin, R. P., et al. (2014). Quantitative strain measurement with distributed fibre optic systems: Qualification of a sensing cable bonded to the surface of a concrete structure. In *Proceedings of the EWSHM-7th European Workshop on Structural Health Monitoring*, Nantes, France, July 8–11.

Bofang, Z. (2014). *Thermal stresses and temperature control of mass concrete*. Oxford, UK: Elsevier/Butterworth-Heinemann.

Burton, T., Jenkins, N., Sharpe, D., & Bossanyi, E. (2011). *Wind energy handbook* (2nd ed.). West Sussex, U.K.: Wiley.

Carino, N. J., & Lew, H. S. (2001). The maturity method: From theory to application. In C. Chang (Ed.), *Proceedings of the Structures Congress and Exposition* (19 pp.), May 21–23, Washington D.C.: American Society of Civil Engineers.

Carlson, R. W. (1966). *Manual for the use of stress meters, strain meters, and joint meters in mass concrete* (3rd ed.). Berkeley, California, U.S.A.: Gillick & Co.

Chang, C. Y., & Hung, S. S. (2012). Implementation RFIC and sensor technology to measure temperature and humidity inside concrete structures. *Construction and Building Materials, 26,* 628–637.

Childs, P. R. N. (2001). *Practical temperature measurement*. Oxford, U.K.: Butterworth-Heinemann.

Choi, S., & Won, M. C. (2010). Thermal strain and drying shrinkage of concrete structures in the field. *ACI Materials Journal, 107*(5), 498–507.

Choi, S., Cha, S. W., & Oh, B. H. (2011). Thermo-hygro-mechanical behavior of early-age concrete deck in composite bridge under environmental loadings. Part 2: Strain and stress. *Materials and Structures, 44*(7), 1347–1367.

Choi, S. C., & Oh, B. H. (2010). New viscoelastic model for early-age concrete based on measured strains and stresses. *ACI Materials Journal, 107*(3), 239–247.

Chu, I., Lee, Y., Amin, M. N., Jang, B.-S., & Kim, J.-K. (2013). Application of a thermal stress device for the prediction of stresses due to hydration heat in mass concrete structure. *Construction and Building Materials, 45*, 192–198.

Conceição, J., Faria, R., Azenha, M., Mamede, F., & Souza, F. (2014). Early-age behaviour of the concrete surrounding a turbine spiral case: Monitoring and thermo-mechanical modelling. *Engineering Structures, 81,* 327–340.

Corbin, M., & Garcia, M. (2016). *International benchmark VeRCoRs 2015—Overview, synthesis and lessons learnt*. Villeurbanne, France: EDF SEPTEN.

Costa, Â. M. V. (2011). *Thermo-mechanical analysis of self-induced stresses in concrete associated to heat of hydration: A case study of the spillway of Paradela dam*. Guimarães: University of Minho. (in Portuguese).

Dally, W. J., & Riley, F. W. (2005). *Experimental stress analysis* (4th ed.). USA: College House Enterprises.

Davis. (2016). *Precision weather instruments*. California, U.S.A.: Davis Instruments, Hayward.

Delepine-Lesoille, S., Merliot, E., Boulay, C., Quetel, L., Delaveau, M., & Courteville, A. (2006). Quasi-distributed optical fibre extensometers for continuous embedding into concrete: design and realization. *Smart Materials and Structures, 15,* 931–938.

Delepine-Lesoille, S., Girard, S., Landolt, M., et al. (2017). France state of the art distributed optical fibre sensors qualified for the monitoring of the French underground repository for high level and intermediate level long lived radioactive wastes. *Sensors, 17*(6).

Delsys. (2017). Technical note 301: Synchronisation and triggering, Boston, U.S.A.

Delta Ohm. (2017). LP Silicon-Pyro 03. Environmental Analysis 18, Ceselle di Selvazzano, Italy (2 pp.).

Domski, J., & Katzer, J. (2015). An example of monitoring of early-age concrete temperatures in a massive concrete slab. In I. Major & M. Major (Eds.), *Selected practical and theoretical aspects of contemporary mechanics* (pp. 94–105). Czestochowa University of Technology.

Eierle, B., & Schikora, K. (2000). Zwang und Rissbildung infolge Hydratationswärme - Grundlagen, Berechnungsmodelle und Tragverhalten, Heft 512. Deutscher Ausschuss für Stahlbeton (in German).

Emilio, M. D. P. (2013). *Data acquisition systems—From fundamentals to applied design*. New York, U.S.A.: Springer.

EURAMET. (2011). Calibration of thermocouples, Version 2.1, EURAMET cg-8, Germany.

Faria, R., Azenha, M., & Figueiras, A. (2006). Modelling of concrete at early ages. Application to an externally restrained slab. *Cement & Concrete Composites, 28,* 572–585.

Geokon. (2015). Instruction manual—Model 4370 concrete stressmeter. Retrieved July 12, 2017, from http://www.geokon.com/content/datasheets/4370_Concrete_Stressmeter.pdf.

Geokon. (2017). Instruction Manual—Model 4200 series vibrating wire strain gages. Retrieved May 29, 2017, from http://www.geokon.com/content/manuals/4200-4202-4204-4210_Strain_Gages.pdf.

Geymayer, H. G. (1967). Strain meters and stress meters for embedment in models of mass concrete structures. Technical Report No. 6-811 US Army Corps of Engineers, Vicksburg, Mississippi, U.S.A.

Glisic, B. (2000). Fibre optic sensors and behaviour in concrete at early age. Ph.D. thesis, Ecole Polytechnique Federale de Lausanne, Switzerland.

Glisic, B., & Inaudi, D. (2007). *Fibre optic methods for structural health monitoring*. West Sussex, England, U.K.: Wiley.

Glisic, B., & Simon, N. (2000). Monitoring of concrete at very early age using stiff SOFO sensor. *Cement & Concrete Composites, 22,* 115–119.

Hagart-Alexander, C. (2010). Part III: Measurement of temperature and chemical composition—Temperature measurements. In W. Boyes (Ed.), *Instrumentation reference book* (4th ed.) (pp. 269–326). Oxford, U.K.: Elsevier/Butterworth-Heinemann.

Harris, G. H., & Sabnis, G. M. (1999). *Structural modelling and experimental techniques* (2nd ed.). USA: CRC Press.

Heimdal, E., Kanstad, T., & Kompen, R. (2001a). Maridal Culvert, Norway - field test I. Luleå Sweden: Luleå university of technology, department of civil and mining engineering. IPACS-report BE96-3843/2001:73-7. pp. 69. ISBN 91-89580-73-7.

Heimdal, E., Kanstad, T., & Kompen, R. (2001b). Maridal culvert, Norway - field test II. Luleå Sweden: Luleå university of technology, department of civil and mining engineering. IPACS-report BE96-3843/2001:74-5. pp. 20. ISBN 91-89580-74-5.

Heinrich, J. P., & Schlicke, D. (2016). Hardening-induced stresses in very thick concrete members—Insights from comprehensive FE-Studies. In *MSSCE2016* (*Service Life Segment*), Lyngby, Denmark.

Henault, J.-M. (2013). Methodological approach for performance and durability assessment of distributed fiber optic sensors: Application to a specific fiber optic cable embedded in concrete. Ph.D. thesis, Universite de Paris-Est, France.

Henault, J.-M., Salin, J., Moreau, G., Delepine-Lesoille, S., Bertand, J., Taillade, F., et al. (2011). Qualification of a truly distributed fiber optic technique for strain and temperature measurements in concrete structures. In *EPJ Web of Conferences, 12, AMP 2010—International Workshop on Ageing Management of Nuclear Power Plants and Waste Disposal Structures* (EFC Event 334 – Ontario, Canada) (8 pp.).

Hill, K. O., & Meltz, G. (1997). Fiber Bragg grating technology fundamentals and overview. *Journal of Lightwave Technology, 15*(8), 1263–1276.

Honorio, T. (2015). Modelling concrete behaviour at early-age: Multiscale analysis and simulation of a massive disposal structure. Ph.D. thesis, Ecole normale superieure de Cachan, France.

Humar, N., Zupan, D., & Kryzanowski, A. (2016). Fiber optic measurement of mass concrete at an early age—Case study. In M. M. Ali & P. Platko (Eds.), *Advances and Tends in Engineering Sciences and Technologies II, Proceedings of the 2nd International Conference on Engineering Sciences and Technologies*, July. High Tatras Mountains, Slovak Republic: CRC Press – Taylor & Francis Group (pp. 433–440).

Hunter, S. R. (2003). Wind speed measurement and use of cup anemometry, Recommended practices for wind turbine testing, International Energy Agency (IEA) programme for research and development on wind energy conversion systems, Paris, France.

Inaudi, D., & Glisic, B. (2006). Distributed fiber optic strain and temperature sensing for structural health monitoring. In P. J. S. Cruz, D. M. Frangopol & L. C. C. Neves (Eds.), *Proceedings of the 3rd International Conference on Advances in Bridge Maintenance, Safety Management and Life-Cycle Performance*, July, Porto, Portugal (8 pp.).

ISO. (1990). ISO 9060:1990: Solar energy—Specification and classification of instruments for measuring hemispherical solar and direct solar radiation.

Johnston, L. G. (2005). *Wind energy systems, electronic edition*. Manhattan, KS, U.S.A.

Jung, S. H., Choi, Y. C., & Coi, S. (2017). Use of ternary blended concrete to mitigate thermal cracking in massive concrete structures—A field feasibility and monitoring case study. *Construction and Building Materials, 137*, 208–215.

Kanare, H. M. (2005). *Concrete floors and moisture*. Illinois, U.S.A.: Portland Cement Association, Engineering Bulleting 119.

Kanavaris, F. (2017). Early age behaviour and cracking risk of concretes containing GGBS. Ph.D. thesis, Queen's University of Belfast, UK.

Kanavaris, F., Robinson, D., Soutsos, M., & Chen, J.-F. (2016). Prediction of the early age behaviour of the gusset of the nuclear containment vessel. In *1st International Workshop on the EDF Benchmark VeRCoRs*, March, Paris, France.

Kawaguchi, T., & Nakane, S. (1996). Investigations on determining thermal stress in massive concrete structures. *ACI Materials Journal, 93*(1), 96–101.

Kim, J., Luis, R., Smith, S. M., Figueroa, J. A., Malocha, D. C., & Nam, B. H. (2015). Concrete temperature monitoring using passive wireless surface acoustic wave sensor system. *Sensors and Actuators A: Physical, 224*, 131–139.

Kurata, Y., Shionaga, R., Takase, K., & Shimomura, T. (2009). Study on measurement of concrete stress in structural members by effective stress meter. In Tanabe et al. (Eds.), *Creep, shrinkage and durability mechanics of concrete and concrete structures* (Vol. 1, pp. 293–297). CRC Press.

Langreder, W. (2010). Wind resource and site assessment. In W. Tong (Ed.), *Wind power generation and wind turbine design* (pp. 49–88). Southampton, U.K.: WIT Press.

Lawrence, A. M., Tia, M., Ferraro, C. C., & Bergin, M. (2012). Effect of early age strength on cracking in mass concrete containing different supplementary cementitious materials:

Experimental and finite-element investigation. *Journal of Materials in Civil Engineering, 24*, 362–372.
Lawrence, A. M., Tia, M., & Bergin, M. (2014). Consideration for handling of mass concrete: Control of internal restraint. *ACI Materials Journal, 111*(1), 3–11.
Lee, B. (2003). Review of the present status of optic fiber sensors. *Optical fiber Technology, 9,* 57–79.
Lee, H.-S., Cho, M.-W., Yang, H.-M., Lee, S.-B., & Park, W.-J. (2014). Curing management of early-age concrete at construction site using integrated wireless sensors. *Journal of Advanced Concrete Technology, 12,* 91–100.
Mainstone, R. J. (1953). Vibrating Wire Strain Gauge for USe in longterm test on structures. *Engineering, 176,* 153–156.
Mata, J., Lajes Martins, L., Silva Ribeiro, A., Tavares de Castro, A., & Serra, C. (2015). Contributions of applied metrology for concrete dam monitoring. In *Hydropower'15*, Stavanger, Norway.
Mather, R. J. (2005). Beaufort wind scale. In E. J. Oliver (Ed.), *Encyclopedia of world climatology* (pp. 156–157). Dordrecht, The Netherlands: Springer.
Meanset. (2009). Anemometer calibration procedure, Version 2, Spain.
Met Office. (2010). Beaufort: National meteorological library and archive fact sheet 6—The Beaufort scale, Version 01, Exeter, Devon, U.K.
Meydbray, J., Emery, K., & Kurtz, S. (2012). Pyranometers, reference cells: the difference. *PC Magazine*, (04), 108–110.
Milovanovic, B., & Pecur, I. B. (2016). Review of active IR thermography for detection and characterization of defects in reinforced concrete. *Journal of Imaging, 2*(11), 27 pp.
MM (Micro-Measurements). (2014a). Strain gage selection: Criteria, procedures, recommendations, strain gages and instruments, Tech Note TN-505-4, August, Wendell, U.S.A.
MM (Micro-Measurements). (2014b). Surface preparation for strain gage bonding. Instruction Bulletin B-129-8, August, Wendell, U.S.A.
MM (Micro-Measurements). (2014c). Strain gage installations with M-Bond 200 Adhesive. Instruction Bulletin B-127-14, December, Wendell, U.S.A.
MM (Micro-Measurements). (2015). Strain gage installations for concrete structures, strain gages and instruments, Tech Tip TT-611, July, Wendell, U.S.A.
Morabito, P. (2001). Sluice gate—Brembo river—Italy—Field test. IPACS report BE96-3843/2001:76-1.
Morris, A. S., & Langari, R. (2016). *Measurement and instrumentation—Theory and application* (2nd ed.). Oxford, U.S.A.: Academic Press/Elsevier.
Myrvoll, F., Hansen, S. B., Roti, J. A., & Halvorsen, A. (2003). *Field measurements in geomechanics*. Lisse (UK): Taylor Francis.
Nagataki, S. (1970). Shrinkage and shrinkage restraints in concrete pavements. *ASCE Structural Journal, ST7*, 1333–1358.
Nakra, B. C., & Chaudhry, K. K. (2016). *Instrumentation, measurement and analysis* (4th ed.). New Delhi, India: McGraw-Hill.
Neville, A. (2011). *Properties of concrete* (5th ed.). Harlow, England, UK: Pearson Education Limited.
Nietner, L., Schlicke, D., & Tue, N. V. (2011). Berücksichtigung von Viskoelastizität bei der Beurteilung von Zwangbeanspruchungen erhärtender Massenbetonbauteile. *Beton- und Stahlbetonbau, 106*, 169–177. https://doi.org/10.1002/best.201000051 (in German).
Nilsson, L. O. (1996). Interaction between microclimate and concrete—A prerequisite for deterioration. *Construction and Building Materials, 10*(5 Spec. Issue), 301–308.
Norris, A., Saafi, M., & Romine, P. (2008). Temperature and moisture monitoring in concrete structures using embedded nanotechnology/microelectromechanical systems (MEMS) sensors. *Construction and Building Materials, 22,* 111–120.
Omega Engineering. (1999). Practical strain gage measurements. Application note 290-1, U.S.A.
Omega Engineering. (2000). Practical temperature measurements. Application note, Agilent Technolgies, U.S.A.

Oukhemanou, E. (2016). Monitoring system. In *1st International Workshop on the EDF Benchmark VeRCoRs*, March, Paris, France.

Oukhemanou, E., Desforges, S., Buchoud, E., Michel-Ponnelle, S., & Courtois, A. (2016). VeRCoRs Mock-Up: Comprehensive monitoring system for reduced scale containment model. In *3rd Conference on Techonological Innovation in Nuclear Civil Engineering (TINCE-2016)*, September, Paris, France.

Paulescu, M., Paulescu, E., Gravila, P., & Badescu, V. (2013). *Weather modelling and forecasting of PV systems operation*. London, U.K.: Springer.

Poblete, M., Salshilli, R., Valenzuela, R., Bull, A., & Spratz, P. (1988). Field evaluation of thermal deformations in undowelled PCC pavement slabs. *Transportation Research Record, N., 1207,* 217–228.

Raphael, J. M., & Carlson, R. W. (1965). *Measurement of structural actions in dams* (3rd ed.). Berkeley, California, U.S.A.: Gillick & Co.

Reinhardt, H.-W. (2014). Aspects of imposed deformation in concrete structures—A condensed overview. *Structural Concrete, 15,* 454–460. https://doi.org/10.1002/suco.201400014.

Richardson, J. T. (1959). The structural behavior of Hungry Horse Dam. Engineering Monographs No. 24, US Department of the Interior Bureau of Reclamation, Denver, Colorado.

Riding, K. A., Poole, J. L., Schindler, A. K., Juenger, M. C. G., & Folliard, K. J. (2006). Evaluation of temperature prediction methods for mass concrete members. *ACI Materials Journal, 103*(25), 357–365.

Riding, K. A., Poole, J. L., Schindler, A. K., Juenger, M. C. G., & Folliard, K. J. (2009). Effects of construction time and coarse aggregate on bridge deck cracking. *ACI Materials Journal, 106* (5), 448–454.

RILEM Report 15. (1998). Prevention of thermal cracking in concrete at early ages (R. Springenschmid Ed.). RILEM Report 15. E & FN Spon, London, UK. ISBN 0 419 22310 X.

Rocha, M. (1965). In situ strain and stress measurements. In *Stress analysis, recent developments in numerical and experimental analysis*, Chapter 17 (pp. 425–461). London: Wiley.

Rogers, A. (1999). Review article: Distributed optical-fibre sensing. *Measurement Science Technology, 10*(8), R75–R99.

Rostásy, F. S., & Henning, W. (1990). Zwang und Rissbildung in Wänden auf Fundamenten, Heft 407. Deutscher Ausschuss für Stahlbeton (in German).

Rostásy, F. S., Krauß, M., Laube, M., Rusack, T., & Budelmann, H. (2007). Online-Monitoring und Berechnung der Betonspannungen infolge thermischen Zwangs für ein Trogbauwerk am Hauptbahnhof Berlin. *Bautechnik, 84*, 235–242. https://doi.org/10.1002/bate.200710020 (in German).

RST Instruments. (2017). Carlson strain meter. Retrieved May 29, 2017, from http://www.rstinstruments.com/Carlson-Strain-Meter.html.

Schlicke, D. (2014). Mindestbewehrung für zwangbeanspruchten Beton. Dissertation, 2. Aufl., Graz University of Technology (in German).

Schlicke, D. (2015). Lessons learned from in-situ measurements in hardening concrete members. In *2nd Workshop of COST Action TU1404 with Focus on Modelling of Cement-based Materials and Structures* (pp. 372–386). Presentations e-Book. https://doi.org/10.5281/zenodo.46070.

Schlicke, D., & Tue, N. V. (2015). Minimum reinforcement for crack width control in restrained concrete members considering the deformation compatibility. *Structural Concrete, 16,* 221–232. https://doi.org/10.1002/suco.201400058.

Sellers, B. (2003). The measurement of stress in concrete. In F. Myrvoll (Ed.), *Proceedings of 6th International Symposium in Field Measurements in Geomechanics* (pp. 643–656). Oslo, Norway.

Shahawy, M. A., & Arockiasamy, M. (1996). Field instrumentation to study the time-dependent behavior in sunshine skyway bridge. *Journal of Bridge Engineering. ASCE, 1*(2), 76–86.

Shi, N., Chen, Y., & Li, Z. (2016). Crack risk evaluation of early age concrete based on the distributed optical fiber temperature sensing. In *Advances in materials science and engineering* (Vol. 2016, 13 pp.).

Simpson, D. (2016). *Moisture in concrete floors*. Concrete Advice No. 22. Camberley, U.K.: The Concrete Society.

Snell, L. M. (2015). Monitoring temperatures in concrete construction using IR thermometers. *Concrete International, 37*(1), 57–63.

Soutsos, M., Hatzitheodorou, A., Kwasny, J., & Kanavaris, F. (2016). Effect of in situ temperature on the early age strength development of concretes with supplementary cementitious materials. *Construction and Building Materials, 103,* 105–116.

Soutsos, M., Hatzitheodorou, A., Kanavaris, F., & Kwasny, J. (2017). Effect of temperature on the strength development of mortar mixes with GGBS and fly ash. *Magazine of Concrete Research, 69*(15), 787–801.

Tanabe, T. (1998). Measurement of thermal stresses in situ. In R. Springenschmid (Ed.), *RILEM Report 15—Prevention of thermal cracking in concrete at early ages* (pp. 251–254). London: E & FN Spon.

TGES (The German Energy Society). (2008). *Planning and installing photovoltaic systems—A guide for installers, architects and engineers* (2nd ed.). Berlin, Germany: Earthscan.

Tong, A. (2001). Improving the accuracy of temperature measurements. *Sensor Review, 21*(3), 193–198.

Torrent, R. J., & Fucaraccio, J. R. (1982). Appropriate experimental techniques for the control of thermal cracking in large concrete masses. In *International Conference on Temperature Effect on Concrete and Asphaltic Concrete*, Baghdad.

Tue, N. V., Schlicke, D., & Bödefeld, J. (2007). Beanspruchungen in dicken Bodenplatten infolge des Abfließens der Hydratationswärme. *Bautechnik, 84*, 702–710. https://doi.org/10.1002/bate.200710060 (in German).

Tue, N. V., Schlicke, D., & Schneider, H. (2009). Zwangbeanspruchung massiver Kraftwerks-Bodenplatten infolge der Hydratationswärme. *Bautechnik, 86*, 142–149. https://doi.org/10.1002/bate.200910013 (in German).

Ukil, A., Braendle, H., & Krippner, P. (2011). Distributed temperature sensing: Review of technology and applications. *IEEE Sensors Journal, 12*(5), 885–892.

van Breugel, K. (1998). Prediction of temperature development in hardening concrete. In R. Springenschmid (Ed.), *RILEM Report 15 – Prevention of thermal cracking in concrete at early ages* (pp. 51–75). London, UK.

Vollpracht, A., Soutsos, M., & Kanavaris, F. (2018). Strength development of GGBS and fly ash concretes and applicability of fib model code's maturity function—A critical review. *Construction and Building Materials, 162,* 830–846.

Weil, J. G. (2004). Infrared thermographic techniques. In V. M. Malhotra & N. J. Carino (Eds.), *Nondestructive testing of concrete* (2nd ed.) (pp. 15/1–15/14). CRC Press.

WMO. (2008). *Guide to meteorological instruments and methods for observation* (No. 8, 7th ed.).

Wojcik, G. S., Fitzjarrald, D. R., & Plawsky, L. J. (2003). Modelling the interaction between the atmosphere and curing concrete bridge decks with the SLABS model. *Meteorological Applications, 10*(2), 165–186.

Wojcik, G. S. (2001). The interaction between the atmosphere and curing concrete bridge decks. Ph.D. thesis, State University of New York at Albany, U.S.A.

Yeon, J. H., Choi, S., & Won, M. C. (2013). In situ measurement of coefficient of thermal expansion in hardening concrete and its effect on thermal stress development. *Construction and Building Materials, 38,* 306–315.

Zreiki, J., Bouchelaghem, F., & Chaouche, M. (2010). Early-age behaviour of concrete in massive structures, experimentation and modelling. *Nuclear Engineering and Design, 240,* 2643–2654.

Chapter 10
Sustainability Aspects in Mass Concrete

Neven Ukrainczyk and Eduardus A. B. Koenders

Abstract This chapter addresses potential alternatives for base raw materials as well as potential solutions for sustainability in mass concrete. Issues like material selection and environment, material properties and mix design, durability, carbon footprint and life cycle analysis (LCA) of mass concretes are reviewed. The focus is put on recycling. Besides the use of conventional SCMs, non-conventional biomass pozzolans, based on combustion of renewable source of energy, like woody ashes, sugarcane bagasse ash and rice husk ash are covered. The synergic use of several mineral SCMs as a partial substituent of Portland cement is addressed. Furthermore, reuse of aggregates from construction–demolition waste as well as natural fiber alternatives to steel and synthetic reinforcements is discussed in detail. Materials selections and the consequence of it on the properties that affect the mix design and material properties specifically related to durability are summarized. An introduction on life cycle assessment (LCA) is given with its pros and cons, followed by its review on different mass concrete mixtures, separately addressing LCA of binders, aggregates, concretes and reinforced concrete structures with placement technologies. Limitations and further research directions are highlighted.

10.1 Introduction

Sustainability in mass concrete deals with designing of a sustainable concrete structure. Relevant issues in this respect are the environmental impacts occurred from raw materials extraction, through material production, transportation, construction, use, to the stages of disposal and recycling. All these elements together

N. Ukrainczyk (✉) · E. A. B. Koenders (✉)
Institute of Construction and Building Materials, Technische Universität Darmstadt, Darmstadt, Germany
e-mail: ukrainczyk@wib.tu-darmstadt.de

E. A. B. Koenders
e-mail: koenders@wib.tu-darmstadt.de

© RILEM 2019

E. M. R. Fairbairn and M. Azenha (eds.), *Thermal Cracking of Massive Concrete Structures*, RILEM State-of-the-Art Reports 27,
https://doi.org/10.1007/978-3-319-76617-1_10

determine that the impact mass concrete has on the environmental footprint, including CO_2 emissions, energy use and generated waste.

Materials in view of sustainability in mass concrete are given in first section. The Materials section starts with a plain overview of potential materials that can be used for mass concrete with their purpose. Next, mass concrete properties are discussed considering different mix design possibilities using possible alternative materials. Lastly, a review on LCA is given covering typical scenarios occurring during a production of mass concrete structures.

10.2 Materials Selection

The current materials used in mass concretes and the potential more sustainable alternatives are reported in this section.

Supplementary cementitious materials (SCMs) are used to partly replace traditional Portland cement in concrete. By-products from industrial processes, such as steel slag, silica fume or fly ashes, have latent hydraulic characteristics; however, the development of green ecological concretes asks for SCMs originating from renewable base materials. A great deal of research has been conducted to examine the potential use of biomass pozzolans, based on combustion of renewable source of energy, like woody ash, sugarcane bagasse ash, rice husk ash, but also marble and granite residues are considered to act as a sustainable replacement in concrete. These efforts have generated lots of knowledge in the field of using sustainable SCMs as a replacement material. When combining this knowledge with the application of recycled aggregates originating from construction–demolition wastes (CDW), as well as natural fiber alternatives to steel and synthetic reinforcements the ingredients are available to develop the framework of an ecological concrete.

As concrete is one of the most widely employed construction materials, the use of recycled constituents, such as binders, aggregates, reinforcement and even water, to partially replace the 'natural' raw materials is of particular interest as a possible solution for the reduction of the environmental footprint of the mass concrete production.

10.2.1 Binders: Cement, Pozzolans and Filers

The major negative environmental impact of concrete is caused by cement clinker production that results in around 5–7% of anthropogenic global CO_2-emissions (Schneider et al. 2011; Lothenbach et al. 2008; Fennis 2011). Blending supplementary cementitious materials (SCMs) (Schneider et al. 2011; Lothenbach et al. 2008), as well as fillers like limestone, micronized sand or, marble and granite residues (Bacarji et al. 2013) to replace cement clinker is the most promising route towards sustainable construction materials. Replacing large quantities of Portland

cement by pozzolans or fillers is a strategy that contributes largely to the reduction of traditional Portland cement in concrete, and with this, to reduced hydration heat development as well as reduced environmental footprint. Environmental impacts, such as CO_2 emission, natural resource usage, energy consumption and others, will all be positively influenced when replacing Portland cement by either a SCMs or non-reactive fillers. The challenge is to maintain equal performances for the cementitious composite as well as to minimize the environmental footprint by a maximum reuse of waste-like residuals.

An overview of SCMs and fillers is provided in Table 10.1. The main industrial SCMs are blast furnace slags, fly ash (FA, from coal combustion and co-fired with biomass), silica fume and ashes from combustion of biomass renewable energy sources like wood ash, sugar cane bagasse ash (SCBA) and rice husk ash (RHA).

Fly ash (FA) is fine particles that are collected in power plants running on combustion of coal or lignite, as well as co-fired by biomass, and are discussed in detail in Chap. 5.

Table 10.1 Overview of pozzolanic binders and fillers originating from primary waste streams

Type	Waste stream	Reactivity
Sugarcane bagasse ash	By-product of the sugar/ethanol agro-industry and is the microporous matter that remains after burning the sugarcane	Pozzolanic reactivity from amorphous SiO_2 and Al_2O_3
Rice husk ash	By-product of rice production and remains after burning the hard protecting coverings of rice grains	Pozzolanic reactivity from amorphous SiO_2
Sewage sludge ash	Residual, by drying and burning the semi-solid material left from industrial wastewater, or sewage treatment processes	Pozzolanic reactivity from partially crystalline SiO_2 and Al_2O_3
Fly ash (coal and biomass origin)	Fine residues generated in coal and/or biomass (co-)combustion of electricity plants	Pozzolanic reactivity from silicate glass containing Al_2O_3, Fe_2O_3 and alkali
Granulated blast furnace slag	Obtained by quenching molten iron slag (a by-product of iron and steel-making) from a blast furnace in water or steam	Cementitious material from silicate glass containing mainly CaO, MgO, Al_2O_3 and SiO_2
Silica fume	By-product of the induction arc furnaces in the silicon metal and ferrosilicon alloy industries	Pozzolanic reactivity from amorphous SiO_2
Metakaolin	Calcination of kaolinite clay	Reactivity from Al_2O_3 and SiO_2 dehydroxalated (amorphous nine parts)
Marble and granite residues	Residual waste product of the marble and granite industrial production plants	Non-reactive, acting as a filler material

The **biomass ashes** with the highest potential for use in mass concrete are the ones obtained by combustion of residues from timber industry and forest activities, the wastes from farms and agro-business and other plants deliberately grown for energetic purposes. The ash obtained by combustion of organic fraction of municipal solid wastes is not considered here.

Woody and agricultural biomass classes are among the highest biomass potentials for energy production in the EU and are considered as a CO_2 neutral and renewable source of energy as it releases less CO_2 by burning than it absorbs while growing. Therefore, biomass is increasingly being used as a sustainable fuel. The timber manufacturing and power generation industry is increasingly shifting towards the use of biomass waste from timber and forest processing for heat and electrical energy co-production. The use of energy from these renewable sources (Directive 2009/28/EC 'Promotion of the use of energy from renewable resources') will lead to the annual production of a foreseeable amount of 15.5 million tons of biomass ash in the EU-28 by 2020 (Carrasco-Hurtado et al. 2014; Obernberger and Supancic 2009). This will double the current annual amount. Presently, most ashes in Europe are landfilled, causing financial and material losses as well as an environmental burden. A possible application for biomass ash could be the replacement of cement and/or sand in cementitious materials (Carrasco-Hurtado et al. 2014; Obernberger and Supancic 2009; van Eijk et al. 2012; de la Grée et al. 2016; Berra et al. 2015; Cheah and Ramli 2011; Barbosa et al. 2013). Biomass is a renewable resource for raw materials and energy, so there is no concern over depleting limited supplies.

In general, biomass ash composition and properties are highly variable depending on:

(1) type of base-biomass feedstock (e.g. a spectrum of woody or agricultural biomass; different co-combustion combinations with peat, coal and/or another biomass type),
(2) geographical location (collection and handling process)
(3) combustion technology (e.g. fixed bed (grate), pulverized fuel or fluidized bed boilers).

Moreover, further classification of ashes is done by type of collection from a boiler:

(1) Bottom ash collected from the bottom of a combustion chamber,
(2) Relatively coarse fly ash collected from cyclones or boilers and
(3) Fine fly ash collected from electrostatic precipitators or bag house filters.

Particle size distribution of fly ash and cement is presented in Fig. 10.1. Results by Ukrainczyk et al. (2016) show that the ash is widening the particle size distribution of cement as it comprises particles smaller than 1 μm and larger than 100 μm. This shows to be a great potential of the biomass ash and may improve the packing density of the blends. Chemical composition of wood ash typically indicates a relative high level of CaO, MgO and alkali. Alkali oxides ($Na_2O + K_2O$)

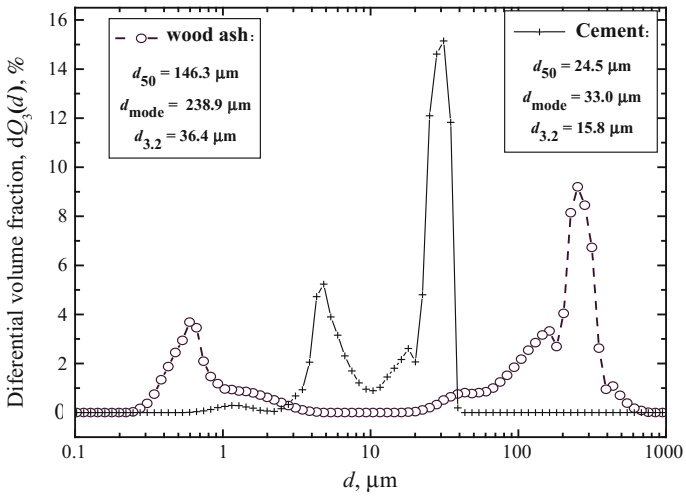

Fig. 10.1 Particle (volume) size distribution of woody ash and cement (adapted from Ukrainczyk et al. 2016)

may be considered acceptable in amounts up to 2% in cement and up to 5% in fly ash (EN 450-1). Alkali content in woody ash is around 5–10% which contributes with 0.75–1.5% for 15% replacement of the cement. This is then 1.75–2.5% of absolute (0.75–1.5% from ash + 1% from cement), which may thus become above the upper limit value for blended cements (2%).

Qualitative analysis of wood ash X-ray diffraction data (Fig. 10.2, Ukrainczyk et al. 2016) determined the main mineral phases of the sample as being lime (free CaO), MgO, larnite ($2CaO\ SiO_2$), calcium carbonate ($CaCO_3$), quartz (SiO_2), Brownmillerite ($4CaO_4\ Al_2Fe_2O_6$) and calcium aluminosilicate ($2CaO\ Al_2O_3\ SiO_2$).

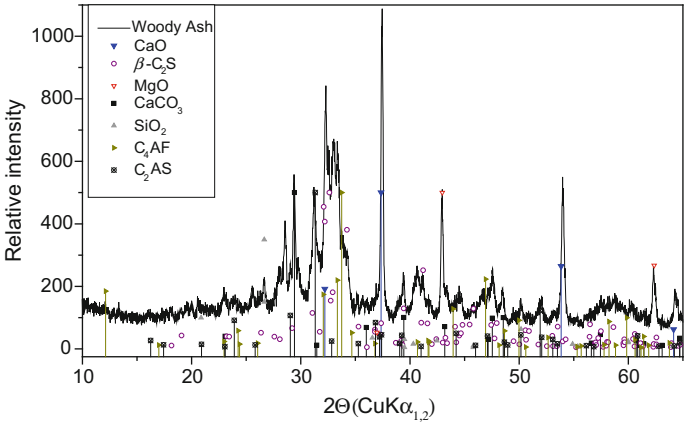

Fig. 10.2 Powder X-ray diffraction analysis of woody ash (adapted from Ukrainczyk et al. 2016)

When considering the properties of sugar cane bagasse ash (**SCBA**), which is a by-product of the sugar/ethanol agro-industry, its pozzolanic reactivity has shown great potential to act as a SCM in cement. With its base material used for ethanol production to replace petrol for cars (Cordeiro 2006; Fairbairn et al. 2010a, b), the burned remainings of sugarcane plant turned out to be suitable to act as a pozzolanic material that can partially replace cement.

RHA is obtained by combustion of an agricultural by-product material, which on burning, decompose cellulose and lignin to leave silica ash. The sensitivity of burning conditions is the primary reason that prevents the widespread use of this material as pozzolan (Hewlett 1998; Real et al. 1996). The X-ray data and chemical analyses of RHA produced under different burning conditions given by Hwang and Wu (1989) showed that the higher the burning temperature, the greater the percentage of silica in the ash. K, S, Ca, Mg as well as several other components were found to be volatile. Reactivity of RHA is attributed to its high content of amorphous silica and to its very large surface area governed by the porous structure of the particles (Cook 1984; Mehta 1992). Rice is the principal production in many developing countries where the cement needs are drastically increasing, it is probably the most promising vegetable ash. Note that 20 Mt annual generation of RHA is similar to GBFS and can absolutely not be compared to the 4000 Mt of cement that will be needed in 2050.

Non-renewable SCMs, i.e. with natural origin, are pyroclastic rocks rich in siliceous or siliceous and aluminous volcanic glass. Common silicate minerals are feldspar, mica, hornblende, pyroxene and quartz or olivine depending on the volcanic rock's chemical composition, but most of these minerals are easily alterable to form clays, zeolites, calcite and various amphiboles. Good natural pozzolan has in general low quantities of clays and zeolites (Habert et al. 2008). Natural SCMs may need a pre-treatment to enhance their pozzolanic activity, namely various mechano-chemical treatments (Habert et al. 2008) of volcanic rocks or calcined clays (Habert et al. 2009).

Huge amounts of mud and other residues are yearly being produced by various countries as a waste product by the **marble and granite** industry, causing serious threats to the environment, polluting soil and water, and when dry, turning into a fine dust that is harmful to the population. Most of the marble and granite residues are landfilled, and alternative solutions are being explored in many countries with the aim to turn this waste into a sustainable material. Bacarji et al. (2013) investigated the applicability of marble and granite residues as a sustainable alternative for cement replacement in production of concrete. Chemical analysis and particle size distribution showed that marble and granite residues (from three different sources) exhibit non-reactive properties but act as a filler. Replacement level of 5% (from only one source) showed only minor impact on the mechanical properties and rheology and could be considered as a promising sustainable alternative for cement.

10.2.2 Water

Water is a key ingredient needed not only to disperse and gradually dissolve cement particles but also is a reactant which is consumed in cement hydration reactions. The shortage of drinkable water resources forces concrete industry to find alternative water sources. The two main strategies for this are (1) recycling of wastewater produced in several human activities and (2) utilizing sources of water, derived by natural processes, which are not suitable for other uses.

Quality of water used in concrete must comply with the current norms, such as EN 1008:2002 (CEN 2002). Most common limitations deal with the content of the following species:

- Chlorides, maximum concentration is 1000 mg/l for concrete with metal reinforcement;
- Sulphates, maximum concentration of SO_4^{2-} ions is 2000 mg/l;
- Alkalis, maximum concentration of equivalent Na_2O is 1500 mg/l;
- Sugar (inhibits cement hydration process);
- Harmful pollutants, e.g. phosphates, nitrates, zinc and heavy metals.

The same norm makes the following classification of water:

- Potable water is suitable for use in concrete and needs no testing;
- Water recovered from processes in the concrete industry is usually suitable for use in concrete, but shall be tested;
- Water from underground sources may be suitable for use in concrete (shall be tested);
- Natural surface water and industrial wastewater may be suitable for use in concrete (shall be tested);
- Sea water or brackish water may be used for concrete without metal reinforcement but is in general not suitable for the production of reinforced or prestressed concrete: the permitted total chloride content in the concrete is the determining factor;
- Sewage water is not suitable for use in concrete.

10.2.3 Aggregates

Usage of natural aggregates is discussed in Chap. 5, and here the focus is put on its recycling. Reusing aggregates from construction–demolition waste (Fig. 10.3) asks for the development of an innovative mix design that deals with grading, with the properties in terms of hydration, strength and durability, and with the replacement procedure, affecting the workability of the mixtures. The question here is how to develop a mix design and an associated mix procedure for concretes with a partial replacement of natural aggregates by recycled aggregates. Recycled aggregates

Fig. 10.3 (Up) Demolition of hospital section, Ilha do Fundão, Rio de Janeiro, Brazil; (down left to right) homogenization process, grinding process with a crusher and autogenous cleaning

(RA) can only be considered as a serious sustainable alternative for natural aggregates (NA) if it leads to a concrete with predictable mechanical and durability properties, similar to those of ordinary concrete mixtures with natural aggregates. A controllable and predictable performance of RA, therefore, should be considered as a major issue that brings the use of recycled aggregates in the construction industry a step closer. Adding RA to the concrete matrix may affect the bearing capacity of the aggregate grain structure, and it may affect the morphological nature of the cementitious microstructure as well. RA, in general, consists of construction–demolition waste, i.e. of crushed concrete, which implicitly means that it contains both natural aggregate fractions, but also remainings of the former cement paste microstructure. This can be either fully hydrated C–S–H gel or anhydrous cement grains. These cement paste remainings are also partly responsible for the increased adsorption capacity of RA, which can be attributed to the relatively higher porosity of RA and the existence of surface and micro-cracks that have the ability to accumulate water. Saturation of these aggregates with water would increase their heat (absorption) capacity, which may be advantageously used in controlling the temperature gradients of mass concrete.

10.2.4 Fiber Reinforcement

Conventional design of steel reinforcement is detailed in Chap. 5, and here the focus is put on sustainable reinforcement alternatives with fibers. The micro- and macro-fracturing processes can be favourably modified by adding short, randomly distributed fibers of various suitable materials such as steel, carbon, cellulose, polypropylene, polyester, glass and nylon. Fibers not only suppress the formation of cracks due to early age self-heating problems, and loading but also abate their propagation and growth (Banthia et al. 2014).

An overview on properties of different types of fiber materials used as reinforcement is presented in Table 10.2. Although **asbestos** is an almost ideal fiber, it

Table 10.2 Physical and mechanical properties of synthetic and natural fibers (adapted from Sierra Beltran 2011 and Odler 2000)

Fibers	Properties					
	Length (l, mm)	Diameter (d, μm)	Aspect ratio (l/d)	Tensile strength (MPa)	Modulus of elasticity (GPa)	Elongation at break (%)
PE	12.7	38	335	2700	120	3–80
PVA	8–12	39	255	1620	42.8	6
PP	6	12	500	770–880	11.2–13.2	17.6–25.7
Asbestos	1–5	0.02–20		700–3000	170–200	2–3
Flax	10–40	11–33	1060	345–1035	28–45	1.3–3.3
Hemp	8.2–28	15–50	560	310–1000	30–60	1–4
Jute	2–5	16–200	75	250–750	25–30	1.5–2
Ramie	60–250	40–80	2310	400–1050	60	2–4
Hibiscus, Kenaf	2–6	200	10	930	53	1.6
Sugarcane	0.8–2.8	6.6–26	115	170–290	15–19	
Bamboo	2.8	10–40	280	350–500	7.3	11.3
Hardwood	0.3–2.5	10–60	35	200–1300	5–45	
Softwood	1.0–9.0	15–60	110	200–1500	40	15–40
Cotton	10–65	12–20	2040	300–600	4.5–12.6	7–9
Coir	0.9–1.2	16.2–19.5	60	130–175	4–6	10–25
Sisal	1–5	10–200	65	250–640	9–26	2–2.5
Banana	2.7–5.5	18–30	165	530–750	20–51	5–2
Cement paste				3–7		
Steel				3000–4000	200	
E-glass		10–20		1100–3900	70–80	
AR-Glass		10–20		3700	75	
Graphite PAN-based		7–8		3000–4000	250–400	
Graphite pitch-based		14–18		600–2000	30–200	
PAN		10–50		800		

is no more used due to health hazard. **Steel fibers** exhibit good composite properties, but only with binders that protect the fibers from corrosion (pore solution pH > 11). **Glass fibers** seem to be the main candidate to replace asbestos. Alkali resistant fibers with a high ZrO_2 content have been developed (AR-glass) as ordinary E-glass undergoes alkali corrosion and the tensile strengths decrease over time (Bentur 1989; Serbin et al. 1992). To improve poor bond of graphite fibers to cement matrix, and thus increase the composite tensile strength, micro-silica, methylcellulose, a SBR latex or a combination of these may be added (Fu et al. 1996), or even more effective is fiber pre-treatment by ozone (Fu et al. 1998).

Synthetic fibers like PE, PP, polyacrylamide (except polyester) fibers, generally have a sufficiently high resistance to the high pH values of the cement pore solution. However, they exhibit a poor fiber–paste bond, which does not improve distinctly with added micro-silica (Dyczek and Petri 1992). The fracture process is usually characterized by pull-out of the fibers. The bond is improved if fibrillated instead of straight fibers are used (such as PP) (Rice et al. 1988). Polyacrylonitrile (PAN) fibers have a significantly higher Young's modulus than conventional plastic fibers, providing a significant increase of the maximum strength (Odler 2000).

Cellulosic (e.g. wood and non-wood vegetable) fibers are being studied as reinforcement for cement-based materials because they are non-hazardous, renewable, low-cost alternative to synthetic fibers (Ardanuy et al. 2015; Sierra Beltran 2011). The development of new environmentally friendly materials to replace steel reinforcement for concrete structure applications is a good step to achieve sustainable concrete and structures. In the last few years, because of the increasing environmental concern, the utilization of fibers from natural resources (i.e. vegetable fibers) to replace synthetic carbon/glass fibers for fiber-reinforced polymer (FRP) composite application has gained popularity. Cellulose fibers exhibit a set of important advantages (Ardanuy et al. 2015), such as wide availability at relatively low cost, bio-renewability, ability to be recycled, biodegradability, non-hazardous nature, zero carbon footprint and interesting physical and mechanical properties, e.g. low density and well-balanced stiffness, toughness and strength. A combination of interesting mechanical and physical properties and their environmental benefits has been the main driver for their use as alternatives for conventional reinforcements. Compared to synthetic fibers, natural fibers are more easily available worldwide and they are friendlier to the environment since less energy is needed to produce them. They are also a renewable resource. Natural fibers, e.g. flax, hemp, jute, coir and sisal, are cost-effective, have good specific strength and specific stiffness and are readily available (Yan and Chouw 2013). However, the properties of natural fibers are not as constant as those of synthetic fibers and natural fibers have a lower tensile strength (Table 10.2). The main chemical components that form the physical fiber structure of wood cells are cellulose, hemicellulose and lignin. Wood fibers have high tensile strength and relatively high modulus of elasticity compared to other natural fibers, as can be seen in Table 10.2. In many occasions, published literature does not clearly specify if a natural fiber is a single cell fiber or a bundle of cell fibers. Therefore, a wide spectrum of properties for the same type of fiber can be found. A limited number of

wood species are suitable as a reinforcing material, due to the negative interaction of the water-soluble oligosaccharides from the wood with the cement hydration process (Sierra Beltran 2011).

According to their origin and composition, cellulosic fibers are classified as non-wood and wood (lignocellulosic) fibers (Ardanuy et al. 2015). The main chemical components that form the physical fiber structure of wood cells are cellulose, hemicellulose and lignin. The two main groups of wood fibers are

(1) softwood fibers (obtained from pines, firs, etc.) and
(2) hardwood fibers (from the birch tree, eucalyptus, beech, etc.).

Non-wood fibers are grouped into four main groups depending on the part of the plant used to extract the fibers:

(1) bast fibers (hemp, jute, kenaf, flax, ramie and others),
(2) leaf fibers (sisal, henequen, pineapple, oil palm, banana or others),
(3) stalk fibers (straws—as rice, wheat and barley; reeds—as bamboo and grass—as esparto and elephant grass) and
(4) seed fibers (cotton, coir and others).

Stem or bast fibers come from the stalks of plants, and these fibers are usually obtained following a retting process that involves bacteria and moisture. These types of natural fibers are commonly not used as single fibers but in the form of bundles or strands, usually long ones.

Forms of the reinforcements based on cellulose fibers (Ardanuy et al. 2015) are

(1) strands (long fibers with lengths between around 20 and 100 cm),
(2) staple fibers (short length fibers which can be spun into yarns) or
(3) pulp (very short fibers of lengths around 1–10 mm which should be dispersed into water to separate them).

Recently, Ardanuy et al. (2015) presented a review on the research done in the last few years in the field of cement-based composites reinforced with cellulose fibers, focusing on their composition, preparation methods, mechanical properties and strategies to improve fiber–matrix bonding and composite durability. They concluded the following. Softwood and sisal pulps and sisal strands were the most commonly studied fibers for preparing fiber cementitious composites (FCCs). Adequate dispersion of the fibers in the matrix is crucial for obtaining FCC with good mechanical performance. This can be achieved by various production methods like various improvements of the traditional Hatscheck method (Ardanuy et al. 2015) or newer methods such as extrusion of pulp cement mixtures and laminates with long fibers or sheet-like structures. Different treatments used to improve the durability of cellulose cement composites include (1) pozzolanic additions, either directly introduced into the mass of cement or applied to the fibers and (2) refining the pulps, with hornification treatments or chemical surface treatments, like silanes.

10.3 Mix Design and Material Properties

The design of a suitable mass concrete composition is detailed in Chap. 5 and here extended to address it from sustainability (durability) point of view. Various chemical and physical processes involved in mass concrete placement affect not only the fresh concrete workability, i.e. rheology, hydration kinetics and mechanical properties but also development of porosity and thus the durability of hardened concrete in service.

At present, there are two principal standards to define the eligibility of pozzolans including ASTM C618 (ASTM, 2012) and EN 196 (BS-EN, 2013). Some standards prohibit use of biomass ash in concrete. Technical regulations and standards for coal and ashes obtained by co-firing of coal with up to 50% biomass share are used as a reference framework for ash producers and building industry customers. An example is the NEN 450-1: Fly ash in Concrete (2012) (Saraber et al. 2009), which gives a set of requirements to assess the quality of coal fly ash (co-firing percentages up to 50 mass% of clean wood) for use in concrete. These standards, however, do not apply to pure (non-coal) biomass ashes. On the one hand, this results in rising costs for biomass ash waste managers that force power plant owners to search for new opportunities how to recycle these ashes. On the other hand, blending cement with biomass ash could anticipate further improvements in concrete material performance while resulting in a lower environmental impact of the cement production as well as the biomass combustion. Vassilev and Vassileva (2007) proposed an unbiased method to define the eligibility of pozzolans which relies on the amorphous (glassy) content in ash to classify as high pozzolanic activity (PA, 82–100% of glass), medium PA (65–82%) and low PA (30–65%).

The use of high-volume SCMs (e.g. with a FA content of at least 50%) is general not directly allowed for more aggressive exposure environments, but only after its equivalent performance is proved in comparison to the eligible reference concrete (van den Heede and de Belie 2012).

Materials selections and the consequence of it on the properties that affect the mix design such as rheological, heat development, mechanical and durability properties are summarized in Table 10.3 and discussed further in this section. Here the focus is more on sustainability aspects, i.e. durability, while the mechanical properties e.g. elastic modulus are detailed in Chap. 5.

The rate and total amount of evolved heat in concrete generally decrease with decreasing C_3S and C_3A contents of cement. On the other hand, the pozzolanic reaction is slower than C_3S hydration and it produces less total potential heat than does cement hydration (Nili and Salehi 2010). Concrete containing SCMs generally exhibits low rate of hydration heat development and thus a small increase in material temperature due to self-heating. Schindler and Folliard (2003) showed that the use of FA and GGBFS retards the hydration process and reduces the amount of heat generated during the acceleration stage. Wang and Lee (2010) demonstrated

Table 10.3 General trend effects of SCMs and recycled aggregates (100% RAC) on concrete properties (adapted from Paris et al. 2016)

Concrete property		GBFS		FA class F		SF	
		Replacement (%)	Effect	Replacement (%)	Effect	Replacement (%)	Effect
Early age	Workability	30–50	Increased	10–40	Increased	>5	Decreased
	Bleeding and segregation	40–70	Increased	10–40	Increased	–	–
	Setting time	10–70	Increased		Increased	5–20	Increased
	Hydration enthalpy		Decreased		Decreased	10	Decreased
Mechanical	Compressive strength	30–50	28d Increased	10–50 (and sand replacement)	Increased	5–20	28d Increased
	Tensile strength	30	Increased	10–50	Increased	5–30	Increased
	Flexural strength	30–60	Increased	40–75	Increased	5–25	Increased
Durability	Permeability	33–50	Decreased	10–100	Increased	>5	Decreased
	SO_4/Cl^- resistance	10–50	Increased	<50	Increased	5–15	Increased
	Corrosion resistance	40	Increased	10–30	Increased	<20	Increased
	ASR resistance	30–60	Increased	20–40	Increased	4–20	Increased
	Freeze/Thaw resistance	10–60	Decreased	40–60	Increased	10–20	Increased

Concrete property		RHA		SCBA		RAC	
		Replacement (%)	Effect	Replacement (%)	Effect	Replacement (%)	Effect
Early age	Workability	10–40	Decreased	10–30	Decreased	100%	Decreased
	Bleeding and segregation		–	–	–		
	Initial set Final set	5–30 5–35	Increased Decreased	–	–		
	Hydration enthalpy			10–30	Decreased		
Mechanical	Compressive strength	5–30	Increased	10–30	Increased		Decreased 5–20%
	Tensile strength	5–30	Increased	5–15	Increased		Decreased 0–30%
	Flexural strength	5–20	Increased	–	–		
Durability	Permeability	7.5–40	Decreased	10–30	Decreased		Increased 40–50%
	SO_4/Cl^- resistance	7.5–40	Increased	5–30	Increased		Increased-Cl^- 50–70%
	Corrosion resistance	5–30	Increased	20	Increased		
	ASR resistance	4–15	Increased	–	–		
	Freeze/Thaw resistance	10	Increased	–	–		Decreased 0–10%

that FA is more effective in reducing the heat of hydration in concrete than GGBFS. Atis (2002) showed that 50% FA reduces the peak temperature of concrete by 23% as compared with OPC, indicating that the moderate levels (10–30%) of FA currently used in cement production may not provide sufficient reduction in the heat evolution of concrete. The use of large amounts of SCMs also significantly contributes to the sustainability of mass concrete (Yang et al. 2014, 2016) in terms of low CO_2 emissions, recycling of by-products and conservation of natural resources as well as the enhancement of workability and durability of concrete (Zhao et al. 2015).

An accurate model to simulate the heating process is essential for thermal stress analysis in mass concrete (Chap. 2). A reliable heat evolution kinetic model is still lacking in high-volume SCM concrete (Yang et al. 2016).

10.3.1 Ground Granulated Blast Furnace Slag (GGBFS)

The use of GGBFS as a substitute for cement clinker can improve technical properties, including workability, strength and durability (Shi and Qian 2000; Song and Saraswathy 2006).

GGBFS used in concrete can effectively reduce the pore sizes and cumulative pore volume (Basheer et al. 2002). Increased GGBFS replacement shows denser structure which prevents concrete from capillary water absorption. Densification of microstructure (lower porosity) comes from higher 'pozzolanic' C–S–H content related to higher GGBFS replacement which represents a higher durability of concrete. Luo et al. (2003) studied the pore structure of three types of concretes (mix ratios 1:1.7:3.29, w/b of 0.34) made with plain OPC and 70% GGBFS and 65% GGBFS/5% gypsum replacements. They demonstrated a great improvement in pore structure for 70% slag replacement, especially after 60 days. However, sulphates did not improve the pore structure of GGBFS. Gao et al. (2005) investigated the effect of slag on interface zone between aggregate–cement paste using XRD, SEM and micro-hardness measurements. They concluded that (a) the pozzolanic reaction rate was in direct proportion to the specific surface area of GGBFS, (b) GGBFS significantly decreased the content and the mean size of $Ca(OH)_2$ crystals in the aggregate–mortar ITZ, which made the microstructure of ITZ more dense, and (c) the ITZ weak zone almost vanished in concrete with 40% slag of 425 m^2/kg specific surface area, and completely vanished in concrete with 20% slag with 600 m^2/kg surface area, strengthening the cementitious matrix. The improvement in strength of concrete containing 20–60% GGBFS occurs only after 28 days of curing, where similar or higher long-term strength was obtained as compared with that of normal PC concrete (Aldea et al. 2000; Miura and Iwaki 2000). Babu and Kumar (2000) reported that 28-day compressive strength of concretes containing GGBFS up to 30% replacement was all slightly above that of normal concretes, and all other replacements (up to 80%) were below. Also, they

observed that the variations due to the different percentages of slag replacement were smaller than the corresponding variations in the case of fly ash.

Cheng et al. (2005) also reported the beneficial influence of GGBFS on the rapid chloride permeability (RCPT) and water permeability of concrete. Khatib and Hibbert (2005) investigated the influence of incorporating GGBFS and metakaolin (MK) on the compressive strength of concrete.

Dhir et al. (1996) investigated the effect of GGBFS on chloride-binding capacity. With the increase in GGBFS percentage, the chloride-binding capacity increased for all chloride concentrations. For a GGBFS replacement level of 66.7%, the chloride-binding capacity was around five times that of the PC control for the case of 5 mol/L exposure chloride concentrations. At 28 days, despite the lower compressive strengths of the GGBFS concrete, the intrinsic permeability was similar. But, at 90 days when the strengths equalized, the intrinsic permeability of the GGBFS concrete was much better than PC reference. Moreover, with the increase in GGBFS replacement level, the coefficient of chloride diffusion steeply decreased. Luo et al. (2003) found that GGBFS increased the chloride-binding capability greatly, although sulphates and alkalinity also decreased it due to competing binding.

Carbonation rate of low fineness GGBFS (4500 cm^2/g) concrete increased with an increase in OPC replacement level (Sulapha et al. 2003). The reduction in portlandite content seemed to have more influence over pore morphology refinement and hence led to faster rates of carbonation. On the other hand, GGBFS of higher fineness (6.000 and 8.000 cm^2/g) reduced the carbonation rates compared to plain OPC concrete. The pore morphology modification, being more dominant than the change in portlandite content, appeared to control the carbonation rate. Ternary blended concrete containing 35% OPC, 55% GGBFS and 10% SF showed a higher carbonation rate than the plain OPC mixture and 10% SF concrete, but lower than 65% GGBFS concrete.

GGBFS at a level of 50% OPC replacement is effective in controlling ASR expansion (Hester et al. 2005). This is because (1) GGBFS reduces the alkalinity of the concrete and thus the alkali–silica ratio; (2) GGBFS reduces mobility (diffusivity) of alkalis in the concrete; and (3) GGBFS reduces free lime in the concrete which is regarded as an important factor for alkali–silica reaction. Yeau and Kim (2005) showed that the corroded areas of steel embedded in control concrete mixtures were about two times and three times larger than those of steel involved in 40% GGBFS concrete mixture and 55% GGBFS concrete mixture, respectively.

10.3.2 Coal Fly Ash (FA)

FA addition improved the corrosion resistance properties even up to 50% replacement level. The reduction in the water content and the good dispersing and the filler effect of the fly ash may contribute to the relatively good strength and permeability development of the fly ash concrete (Chindaprasirt et al. 2007).

With the use of finer fly ash, by sieve separation, the water content can be further reduced and the strength and durability of concrete enhanced. Shafiq and Cabrera (2004) showed that FA addition lowers porosity, oxygen gas and water permeability and investigated the influence of curing conditions on the porosity. For PC reference concrete (0%), 40% and 50% FA cement replaced concrete total porosity of dry-cured samples was 5–10%, 9–20% and 23–40% higher, respectively, than that of their corresponding wet cured samples. Oxygen and water permeability were 2–19 times higher for dry cured reference concrete, whereas 16–210 times greater for FA concretes. Inadequate (dry) curing of a 20 and 40% fly ash (cement replacement) concrete resulted in an increase of 20 and 60% in concrete sorptivity, respectively (Gopalan 1996).

Chloride diffusion value for paste with fly ash Portland cement was 14.7×10^{-9} cm^2/s compared to 44.7×10^{-9} cm^2/s for normal Portland cement paste (Short and Page 1982). Concrete mixtures were made with 15, 30 and 50% fly ash as cement replacements, exhibited reduction in the permeability values by 50, 60 and 86%, respectively (Thomas and Matthews 1992). Up to about seven days, the extent of concrete carbonation was higher for fly ash than the control concrete. However, after 90 days curing, the trend reversed in that the fly ash concrete exhibited less carbonation. The addition of fly ash (20–50%) seemed to improve the sulphate resistance of concretes when they are exposed to sulphates at 20 °C, while no effect at 8 °C was related to the retardation of pozzolanic reaction (Mulenga et al. 2003). Perry et al. (1987) found reduction in ASR expansion after one year in 5 to 81% at 20% replacement level, 34–89% at 30% replacement level and 47–92% at 40% replacement level. The alkalis present in fly ashes were less susceptible for reaction with aggregate, unlike the free and water-soluble alkalis of Portland cement. The chloride penetration was comparatively low and decreased with the increase of fly ash replacement (Chalee et al. 2007)

10.3.3 Woody Ash

High dosages of high calcium wood ash (>20%) may result in expansions which rapidly increases with further ash dosage (Ukrainczyk et al. 2016). This expansion is due to a delayed hydration of free and dead (hard) burned CaO and MgO. The potential of woody ash as an expansive additive to mitigate autogenous and thermal shrinkage problems of mass concretes represents a new research line worth investigating.

Regarding the pozzolanic reaction, Ukrainczyk et al. (2016) showed (Fig. 10.4) that plain ash hydration (no blending with cement) produces a maximal $Ca(OH)_2$ quantity at three days and decreases with further hydration demonstrating the pozzolanic activity of the ash. With increasing ash content, more $Ca(OH)_2$ is produced initially (at early ages) than for plain cement due to hydraulic properties

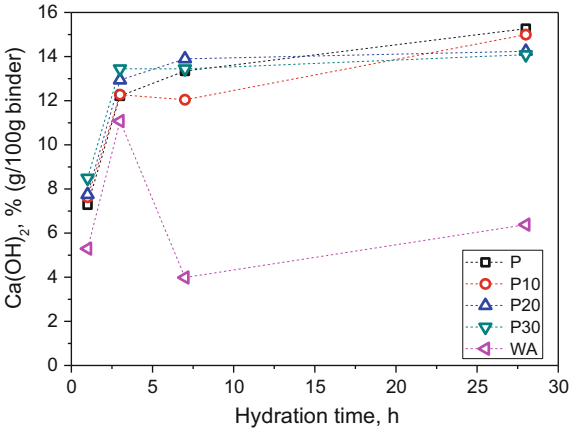

Fig. 10.4 Evolution of Ca $(OH)_2$ during hydration obtained from TG analysis: only 27 mass% of the woody ash (WA, with particles below 80 μm) was considered as a binder (adapted from Ukrainczyk et al. 2016)

of the ash with a relatively high content of reactive CaO, but at 28 days, inversely, there is less $Ca(OH)_2$ due to activated pozzolanic reaction. With increase in the cement replacement level, the hydration kinetics, workability, compressive and flexural strength reduced. Ukrainczyk et al. (2016) also found an optimum dosage of 15% woody ash, which replaces 5% of cement and 3.33% of the sand, still producing a structural grade mortar with acceptable workability and mechanical properties. Thus, potential reuse of woody ash could reduce landfilling and at the same time improve the sustainability perspective of cement production, reducing its energy needs, cutting back in CO_2 emissions and preserving natural resources (i.e. limestone) with no concern for depletion of biomass ash supplies.

Chowdhury et al. (2015) gave a review on the work done on the reuse of wood ash in concrete from 1991 to 2012. Work on ashes obtained from the combustion of forest waste wood and agricultural waste escalated (de la Grée et al. 2016; Cheah and Ramli 2011; Berra et al. 2015; Rajamma et al. 2012, 2015). de la Grée et al. (2016) indicated that a more contaminated biomass fly ash is obtained by combustion of treated waste wood rather than when forestry or agricultural waste is used as fuel. They investigated various treatment methods, at laboratory and pilot scale, for lowering the level of contaminants.

Review of the research results indicates that wood waste ash has potential for effective utilization as a cement replacement for production of blended cements (Cheah and Ramli 2011; Chowdhury et al. 2015). The inclusion of wood ash as partial cement replacement in blended cements has the following effects:

- longer setting times, but still within the standard limits.
- tend to have more soundness, i.e. volume changes after setting (due to excessive amounts of free lime or magnesia). However, the maximal soundness observed at 30% replacement level was still much lower than the maximum allowable soundness limit.
- a higher water requirement for a given level of mix workability of binder pastes.

- beneficial effects on microstructure.
- reduction in bulk density of the hardened binder.

Wood waste ash has high potential for effective utilization as a cement replacement for production of structural grade concretes and mortars of acceptable strength and durability performances (Cheah and Ramli 2011; Chowdhury et al. 2015). The inclusion of wood ash as partial cement replacement has the following effects on concrete properties:

- a higher water requirement for a given level of mix workability of mortars and concretes. However, at the same time there is a significant contribution towards the reduction of drying shrinkage induced micro-cracking of concrete, which could be attributed to a high porosity of ash particles that result in the beneficial internal curing effects (Naik et al. 2002).
- at replacement levels up to 10% by total binder weight can produce structural grade concrete or mortar with acceptable strength properties.
- generally increased magnitudes of concrete water absorption properties, but still far below maximum values allowed for construction material.
- no adverse effects on the resistance of concrete against deterioration by freeze–thaw action (Naik et al. 2002). However, there is a higher demand of air-entraining agents in order to achieve a specified volume of entrained air within the concrete mix.
- no adverse effects on the resistance of concrete against chloride penetration (at replacement levels up to 25% by total binder weight). Blends of 20% wood ash and 80% coal fly ash significantly enhances the resistance to chloride penetration (at cement replacement level of 25%).
- improved durability when exposed to the corrosive actions of monobasic acid solutions, but adverse effects under dibasic acid solutions.
- Mitigation of delirious expansion reaction in cement mortars due to ASR and sulphate attack.

High calcium wood ash (HCWA) can be effectively used in combination with other pozzolanic (SCM) binders to enhance the mechanical and durability performance of concrete (Cheah and Ramli 2014).

10.3.4 Sugarcane Bagasse Ash (SCBA)

At the UFRJ, extended research has been done to examine the properties of this class of SCMs in terms of grinding, burning, reactivity, morphology, chemistry and mechanical properties (Fig. 10.5) and also to evaluate its applicability in concrete (Cordeiro 2006; Cordeiro et al. 2008, 2009a; Fairbairn et al. 2010a, b). The morphological structure of such ashes is investigated directly after burning and after 4 h of grinding. The chemical results showed a SiO_2 content of about 78% (24% of

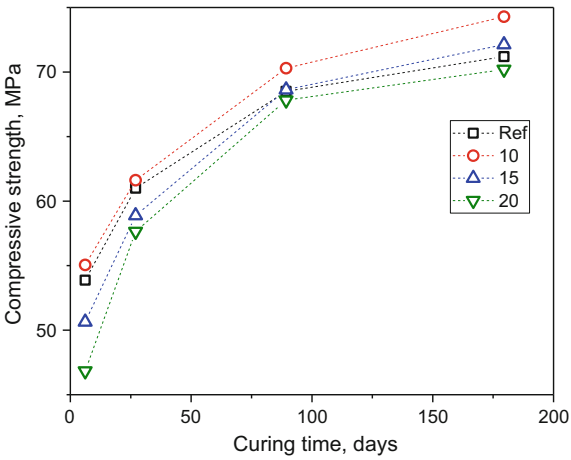

Fig. 10.5 Time evolution of compressive strength for concrete with cement replaced by SCBA (adapted from Cordeiro et al. 2008)

amorphous SiO_2), a density of 2530 kg/m^3 and a specific surface (Blaine) of 196 m^2/kg (Cordeiro et al. 2008). These properties show the potential of sugarcane bagasse ash to act as a sustainable replacement material for cement.

The pozzolanic activity tested by strength index is defined as the ratio between the compressive strengths of mortars with mineral admixture and a reference mortar. On the other hand, the pozzolanic activity Chapelle test measures consumption of CaO in diluted lime-pozzolanic dispersion. Cordeiro et al. (2008) systematically investigated the correlation among the grinding time, median particle size, Blaine fineness, by pozzolanic activity strengthen activity test and Ca^{2+} consumption capacity of SCBA (Fig. 10.6). A finer particle size (from 76.3 to 1.7 μm) consistently resulted in better pozzolanic activity (49–103%). The improvement of pozzolanic activity enhanced the strength of mortars via promoting CH consumption in the pozzolanic reaction (36–298 mg CaO/g).

Compressive strength tests (Fig. 10.5) have confirmed this, showing a high-performance concrete with a w/c ratio of 0.35 and a SCBA replacing ratio of 10, 15 and 20% (Cordeiro et al. 2009a). The results show that the replacement of cement by different percentages of SCBA leads to a similar strength capacity as the reference mixture. The addition of the SCBA also resulted in improvements in rheology of concrete in the fresh state (Cordeiro et al. 2009b). In relation to durability, the results of chloride-ion penetrability based on ASTM C1202-05 indicated that SCBA decreases by about 30% of passed charges for both conventional and high-performance concretes. It was also proven, by a case study for the south-eastern region of Brazil, that SCBA could be used at industrial scale, significantly reducing CO_2 emissions (Fairbairn et al. 2010a, b). The material can, therefore, be considered as a valuable substitute for the development of green and ecological mass concretes.

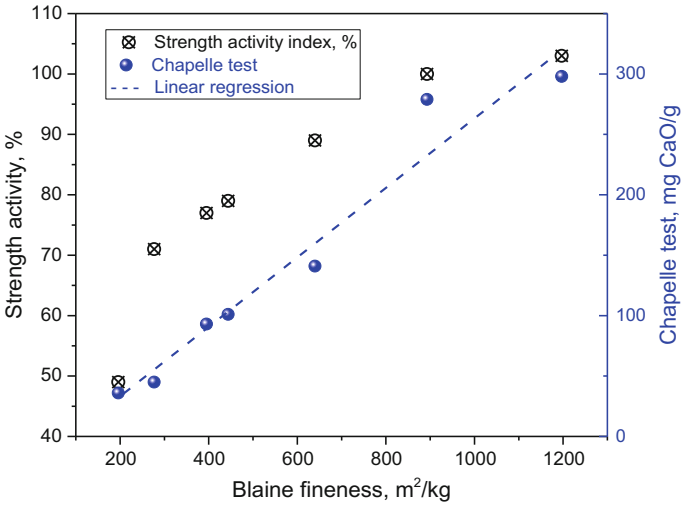

Fig. 10.6 Pozzolanic activity as quantified by Chapelle activity of consumed CaO in diluted lime-SCBA dispersion (right axis) and mortar strength index tests (left axis) as a function of Blaine fineness of SCBA (adapted from Cordeiro et al. 2008)

10.3.5 Rice Husk Ash (RHA)

Increase in RHA content in the paste results in higher water requirement to maintain the same normal consistency (Singh et al. 2002; Jaturapitakkul and Roongreung 2003). Zhang and Malhotra (1996) indicated that RHA concrete had a drying shrinkage of 638×10^{-6} after 448 days, which was similar to the strains for the control and silica fume concretes. Slump decreased with the increase in RHA content for same level of superplasticizer (Bui et al. 2005).

Bui et al. (2005) investigated the compressive strength of concrete mixtures made with two types of PC (Blain 2700 and 3759 cm^2/g) using w/c of 0.30, 0.32 and 0.34 with a cement replacement ratio of 10, 15 and 20%. They demonstrated that RHA can be used as a highly reactive pozzolanic material to improve the microstructure of the interfacial transition zone (ITZ) between the cement paste and the aggregate in high-performance concrete. Relative strength increase was higher for coarser cement (i.e. the gap-graded binder) due to improved particle packing structure accompanied by a decrease in porosity and particularly in particle spacing. Saraswathy and Song (2007) showed that cement replacements with 0, 5, 10, 15, 20, 25 and 30% RHA improved rapid chloride permeability (charge passed) through concretes: 1161, 1108, 653, 309, 265, 213 and 273 coulombs, respectively. Non-ground RHA did not significantly change the rapid chloride penetrability of concrete, whereas finely ground RHA, depending on the type and addition level, improved the RCM results (Nehdi et al. 2003) comparably to those achieved by SF. The results of air permeability by de Sensale (2006) revealed the significance of the filler and pozzolanic effect for the concretes with RHA. On the one hand, for the

RHA obtained by controlled burning (98.5% reactive SiO_2) the results are consistent with the compressive strength development at 28 days. On the other hand, in the concretes with RHA with 39.55% reactive SiO_2, lower air permeability was observed, which was attributed to the higher filler effect than the pozzolanic effect. Inclusion of RHA (0–15%) was very effective in controlling the ASR expansion of mortar (with quartzite and basalt reactive aggregates) at the age of 16 and 30 days.

Chindaprasirt et al. (2007) showed that sulphate resistance of mortars made with 20 and 40% PC (2900 cm^2/g) replacement levels by FA (6000 cm^2/g) and RHA (14,000 cm^2/g) is significantly improved compared to reference.

10.3.6 Synergy Effect of Multi-component Binder Blends

Yang et al. (2016) investigated the high volume (40, 80 and 90%, Table 10.4) use of varying combinations of fly ash, GGBFS and PC in order to control the hydration heat development in mass concrete and enhance its sustainability. The cumulatively evolved heat obtained by adiabatic hydration tests of the concrete was 370 (OPC), 280 (T4), 202 (T8) and 145 J/g (T9) (expressed per gram of binder), which were close to the values obtained by isothermal calorimeter: 350, 251, 198, 185 J/g, respectively. The theoretically calculated values were 507, 425, 369, 364 J/g binder. Isothermal heating rates show (Fig. 10.7 left) a significant decrease. The maximal heat rate (W/g) values decreased by 40% 69% and 67% for the T4, T8 and T9 paste, respectively, as compared with that of the OPC paste. These reductions were only minimally affected by temperature (13–33 °C). The heating rate curves (Fig. 10.7 left) also indicate to a relative increase in the second peak occurring due to the sequential reaction schemes of the aluminate phases ($C_3A \rightarrow$ etringite $\rightarrow$ monosulphate). This is probably due to a relative increase in aluminate content of the blended system. Typical Al_2O_3 mass fractions for fly ash, slag and OPC are 23, 12 and 7%. The compressive strength development of very high-volume SCM concrete (Fig. 10.7 right) could be reasonably correlated to the degree of hydration function determined from the calorimetry hydration tests (both isothermal and adiabatic).

Fairbairn et al. (2010a, b) performed experimental and numerical analyses based on a thermo-chemo-mechanical model. The model considered the coupling of hydration reactions of blended cements, exothermicity, thermo-activation, chemo-plasticity, with the evolution of thermal and mechanical properties, including also creep and relaxation. The authors emphasized the importance of high-performance finite element numerical models to simulate and predict such thermo-chemo-mechanical behaviour in real case scenarios. Sugar cane bagasse ash and rice husk ash are considered as potential mineral additions for constructing dams. The SCBA/RHA blended mixture had 60% of cement, 20% SCBA and 20% RHA while the reference concrete contains 100% of cement as cementitious materials. It was shown that besides the reduction of CO_2 emissions, the multi-component blended material had a thermo-chemo-mechanical behaviour more suitable for mass concrete than the reference material, yielding lower thermal and stress fields.

Table 10.4 Details of concrete mixture proportions and results for LCA studies (Yang et al. 2016; Crossin 2015) with the functional unit of 1 m^3 30 MPa concrete for 50 years (detailed strength development for concrete II-series is plotted in Fig. 10.7 left)

Concrete name	Source	Cement (kg/m^3)	FA (kg/m^3)	GGBFS (kg/m^3)	Water (kg/m^3)	Sand (kg/m^3)	Gravel aggregate	Slump (mm)	Global warming
II	Yang et al. (2016)	350	0	0	175	873	873	185	100%
II-T4		240	100	60	165	814	886	210	65%
II-T8		78	156	156	140	802	945	220	22%
II-T9		40	164	206	140	792	933	225	14%
R	Crossin (2015)	374	0	0	157.6	685	1092	–	378.5 kg eq. CO_2/m^3
R-S7		112	0	262	149.5	703	1056	–	198.6 kg eq. CO_2/m^3

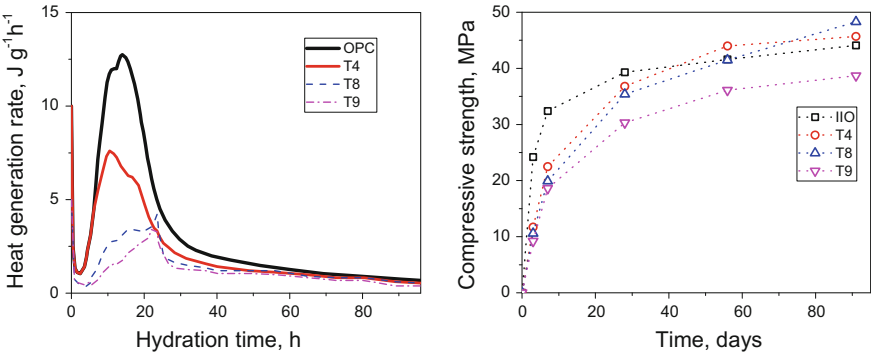

Fig. 10.7 High volume (40, 80 and 90%) use of fly ash and GGBFS (Table 10.4: Left) heat generation rate of paste samples with w/b = 0.50 at 23 °C; Right) concrete compressive strength development (adapted from Yang et al. 2016)

10.3.7 Recycled Aggregate Concrete (RAC)

Controlling the compressive strength of RAC boils down to the control of the mechanical properties, the adsorption capacity, the grading and morphology of the RA (Figs. 10.8, 10.9 and 10.10). Koenders et al. (2014) proposed a model to predict the hydration kinetics and the mechanical behaviour of recycled aggregate concrete (RAC). Particularly, it reports the possible influence of two key parameters, such as w/c ratio and moisture conditions of recycled concrete aggregates (RCAs), on the hydration reactions and on the time evolution of the compressive strength for four different mixtures with recycled aggregates (Table 10.5). The time monitoring of the temperature developed inside the hardening concrete has led to the indirect identification of a model with which the hydration processes for various mixes considered in that study can be described. The simulation of the setting and hardening process in the concrete samples tested in compression showed clear linear correlation between degree of hydration and compressive strength. Such a correlation is strongly affected by both w/c ratio (as already known for ordinary concrete mixes) and moisture conditions of recycled aggregates. The linear correlation emerged between degree of hydration and compressive strength indicates a possible design approach for the type of concrete under consideration.

The RCA can fully or partially replace NA, however, the high water absorption of the fine material smaller than 150 μm, lowers the strength and increases the concrete shrinkage significantly. As higher water demand significantly complicates concrete quality control, some standards do not allow the use of fine RCA in recycled aggregate concrete for structural use (DAfStb 2004; En 206-1 2006). As the origin of RCA is usually unknown, care should take about RAC chemical

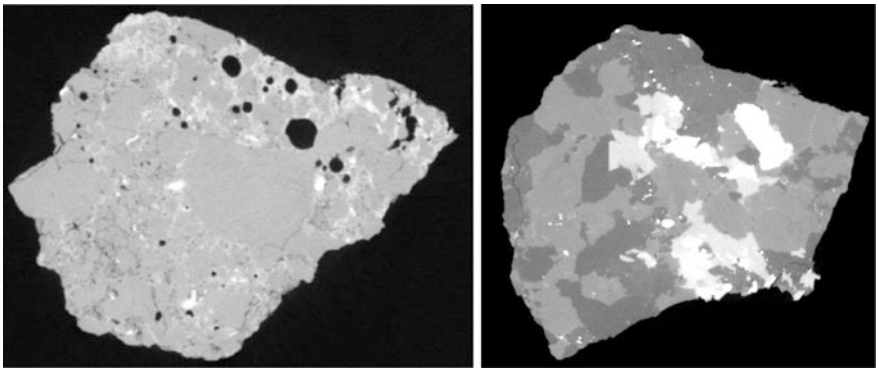

Fig. 10.8 Cross-section of 3D computerized tomography micro-scans for the recycled (left) and natural aggregates (right)

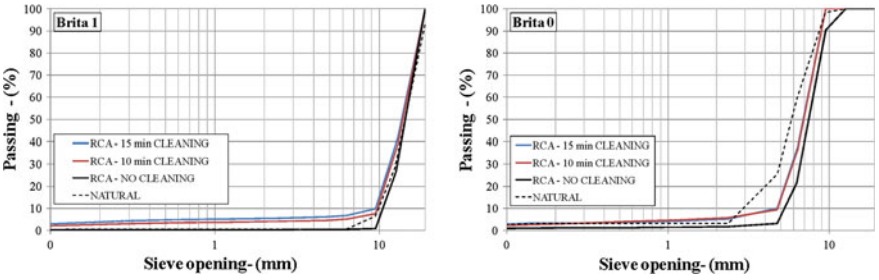

Fig. 10.9 Grain size distribution comparison for natural and recycled aggregates (adapted from Koenders et al. 2014)

Fig. 10.10 Compressive strength development for the five mixtures as presented in Table 10.5 (adapted from Koenders et al. 2014)

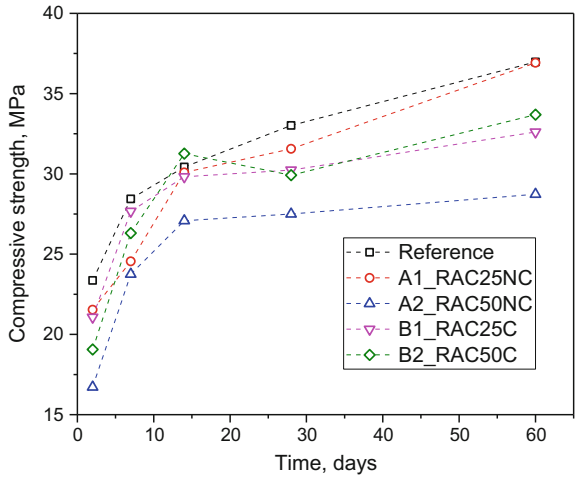

Table 10.5 Mix design prepared for ecological concrete with recycled aggregates (kg/m^3) (adapted from Koenders et al. 2014)

Concrete type	Cem	Water	Superplast	Natural components			RCA without cleaning		RCA with cleaning		Slump (mm)
				Sand	Brita 0	Brita 1	Brita 0	Brita 1	Brita 0	Brita 1	
Reference	300	191	4.02	9523	439.9	470.2	–	–	–	–	160
A1_RAC25NC	300	205	4.02	952	439.5	–	–	404.5	–	–	160
A2_RAC50NC	300	232	4.02	950	–	–	346.6	404.0	–	–	240
B1_RAC25C	300	202	4.02	952	439.8	–	–	–	–	415.3	190
B2_RAC50C	300	110	4.02	951	–	–	–	–	403.1	415.1	220

properties, like the content of chlorides, sulphates and alkali–silica reactivity. Pryce-Jenkins (2011) performed a comparative analysis of 103 studies on RAC (100% coarse aggregate replacement) use in structural concrete and showed following typical effects. Compressive and tensile strength is 5–20% and 0–30% lower, respectively, with little effect below 30% and 50% replacement level. Modulus of elasticity is 15–30% lower, little effect below 20% replacement. Shrinkage is increased by 10–20%, creep +25–50%, water absorption +40–50%, no effect or improved resistance to carbonation, 0–10% decreased freezing and thawing resistance, 50–70% increased chloride penetration resistance. This typical reduction in concrete properties shows that RCA has a good potential to replace natural aggregates in low-to-medium strength structural concrete.

Although the Revised Waste Framework Directive (WFD) 2008/98/EC (EU 2008) established that by 2020, the minimum recycling percentage of 'non-hazardous' construction and demolition wastes should be at least 70% by weight (Pacheco-Torgal et al. 2013), it is still not clearly defined to whom the benefits of recycling should be credited: to the primary producer or to the user of recycled materials (Chen et al. 2010).

10.3.8 Fiber Reinforcement

The tensile strength of the fiber-reinforced concrete is determined by the strength properties of the matrix and the fibers, the amount and the geometry (and aliment) of the fibers and amount of the fiber–matrix bond. There is an optimum fiber–matrix bond strength at which the fracture energy (for complete failure) of the material attains its maximum value, and the material's behaviour is the least brittle. One of the main reasons to add fibers to cement-based materials is the possibility of improving the toughness and ductility of the composite and therefore overcomes the inherent disadvantages of brittle cementitious materials. Both ductility and toughness are concepts that describe the mechanical behaviour of concrete composite in the post-cracking stage.

10.3.8.1 Wood Fibers

Adding fibers to a cement-based mixture increases the surface area and therefore decreases the workability. In praxis, all fiber-reinforced concretes have a higher water/cement ratio, lower coarse aggregate content and smaller size of aggregates compared with conventional concretes (Sierra Beltran 2011). Sugar is a main inhibitor of cement setting, and it is present in the chemical components of fibers, mainly in lignin and in hemicellulose. Because of its chemical composition and extractives hardwood is therefore more an inhibitor to cement setting than softwood fibers (Blankenhorn et al. 2001).

The addition of fibers can reduce plastic shrinkage because they stop the spread of micro-cracks and increase the tensile strength of concrete (Soroushian and Marikunte 1991). Because of their hygroscopic properties wood fibers keep concrete moist for a longer time so that drying of the concrete surface starts later (Sierra Beltran 2011).

Following Rapoport and Shah (2005) in a cementitious matrix, fibers can be distributed in three fundamental modes: uniform, random or clumped. A uniform distribution is ideal while in cast-in-place concrete a random distribution is the best that one can obtain. In their study, cellulose fibers do disperse well under normal mixing circumstances. Processing the secondary fibers into fibrous form improves their dispersion in the cement matrix (Blankenhorn et al. 1999). Pulp fibers have the tendency to clump together in water and fiber clumps become weak spots in concrete.

Wood-reinforced cement composites have lower compressive strength than fiberless mortar or concrete (Sierra Beltran 2011; Blankenhorn et al. 2001; Pehanich et al. 2004), consistent with the higher water/cement ratio of the fiber composites.

Pulp fibers significantly increase the fracture toughness. Wood fiber-reinforced composites have higher values of flexural strength and toughness than fiberless cement samples (Blankenhorn et al. 2001; Pehanich et al. 2004). The authors consider that the origin of fracture toughness comes mainly from the work dissipated in pulling out the cellulose fibers from the cement mortar matrix. Long fibers enhance even more the toughness of the composites because they have a bigger surface area in contact with the cement matrix enabling them to resist fiber pull-out. Additionally, it can also make a more effective bridge of the micro-cracks. Fiber and cement matrix bond depends on many factors like the physical characteristics of the fibers: geometry, type, surface characteristics, orientation, volume and distribution, the chemical composition of the fiber, but also the treatment of the fiber and additives in the cement mixture.

Tonoli et al. (2009) reported decrease of flexural toughness, deflection and modulus of rupture after 200 wet/dry ageing cycles. The decrease of final deflection was bigger for untreated cellulose fibers than for treated ones.

10.3.8.2 Non-wood Natural Fibers

As with wood fibers, the addition of other natural fibers to cementitious matrices decreases the compressive strength. In concrete reinforced with palm trees fibers, the compressive strength decreases with increasing fiber percentage and with increasing fiber length (Kriker et al. 2005). Mortar samples prepared with coir, sisal, jute and hibiscus cannabinus also exhibit lower compressive strengths than mortar without fibers (Ramakrishna and Sundararajan 2005).

Fibers from agave sisalana (sisal) benefit the flexural behaviour if the composite is prepared by slurry de-watering instead of cast-in-place (Savastano et al. 2003, 2005).

Natural fibers enhance the flexural toughness of cement-based materials, even in cases where the bending strength was lower than samples without fibers (Kriker et al. 2005). Savastano et al. (2003) report higher values of fracture toughness for

composites with kraft banana (Musa cavendishii) and composites with sisal fibers that were obtained through different pulping processes. The toughening in the natural fiber-reinforced composites occurs as a result of crack bridging. When comparing the behaviour of the different sisal fibers, it is evident that the pulping process affects the fiber failure mechanism. Mechanical pulp fibers tend to pull-out and have little fracture. As a consequence, the mortar samples with these fibers develop higher toughness.

The flexural toughness increased with increasing fiber content of curaua fibers (D'Almeida et al. 2010). For the same fiber content, samples with longer fibers exhibited higher toughness.

Cement composites reinforced with some natural fibers show loss of bending strength after either accelerated weather tests or natural weathering. Samples prepared using a slurry vacuum de-watering technique and reinforced with 8 wt% of sisal were tested after two years of external exposure to tropical weather. They exhibited a considerable reduction in bending strength since the modulus of rupture of the composite decreased to 70% (Savastano et al. 2009). Likewise, the toughness reduced from 0.85 kJ/m^2 at 28 days to 0.62 kJ/m^2 after two years of external exposure. The loss in mechanical strength of the composites was attributed to the degradation of both the vegetable fibers and the cementitious matrix.

10.4 Life Cycle Assessment (LCA)

First an introduction on life cycle assessment (LCA) is given, followed by its review on different mass concrete mixtures and placement technologies.

10.4.1 LCA Background

Life cycle assessment (LCA) is a systematic approach to evaluate the environmental impacts and other sustainability indicators (Fig. 10.11) (Schau et al. 2011; Gencturk et al. 2016) of processes and products during their life cycle. According to ISO standards 14040 (2006a) and 14044 (2006b), this is performed in four steps (explained in more details latter): (1) planning: goal and scope definition which describes the product system boundaries and the functional unit; (2) life cycle inventory (LCI): compiling an inventory of relevant energy and material inputs with corresponding environmental releases; (3) evaluating the potential environmental impacts associated with identified inputs and releases; and (4) interpreting the results leading to more informed decisions. LCA includes various stages of producing a product (Fig. 10.11), from raw materials extraction, through material production, transportation, construction, use, to the stages of disposal and recycling. A life cycle approach identifies energy use, material inputs and waste generated from the time raw materials are obtained to the final disposal of the product. This provides a global

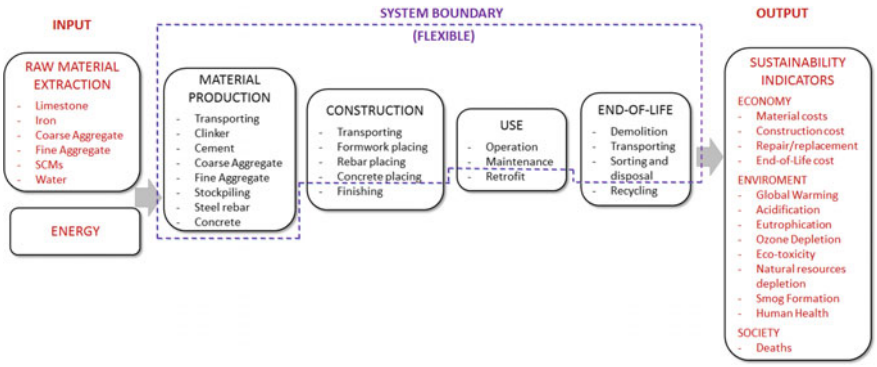

Fig. 10.11 Life cycle assessment (LCA) system for reinforced concrete structure defined by a flexible system boundary with input and output flows of materials, energy, pollutants and economic values

and objective basis for comparisons. Capital goods, including plant and infrastructure, are usually excluded from the system boundary. Although LCA originally aimed at considering every stage of the product's life cycle, known as *cradle-to-grave*, many studies narrow the system boundary. For example, the LCA system boundary usually comprises the raw materials production and the construction only, known as *cradle-to-gate*, where the effects of the concrete structure use and it's end-of-life processes are not included.

When comparing different concrete mix designs, the calculated environmental impact depends on the adopted functional unit, which should incorporate differences in strength, durability and service life. How the concrete service life influences the results of most LCA studies have seldom been included. To consider both strength and durability of concrete structure, the functional unit should contain the amount of concrete needed to produce a structural element designed to carry a particular mechanical load over a particular service lifetime. To evaluate the concrete structure, service life requires employment of service life (probabilistic) prediction models based on experimental durability tests corresponding to specific exposure conditions.

Once the functional unit and system boundary are defined, the second step is the inventory analysis. This means time-intensive collecting and validating the data, calculating and allocating the inputs and outputs. The data quality depends on the access to manufacturer data, regional inventory databases, literature, estimates and judgments of the researchers. At the world level the *Ecoinvent* proprietary database is the largest and most complete database for life cycle inventory. Furthermore, a growing number of regional and national databases are emerging that can facilitate data collection (Finnveden et al. 2009). Very careful attention must be paid when combining databases (Lasvaux et al. 2014).

The third step is the impact assessment which provides quantified information on the environmental impact of the studied products or processes. In LCA, when a process produces more than one product (i.e. a by-product such as fly ash or slag), the environmental impact of this process needs to be allocated between the product and the

by-product. If the by-product can be considered as waste, all impacts are allocated to the main product, but if this by-product can be considered a co-product of the process, then environmental impacts have to be shared between the main and co-products.

The last step is the interpretation and conclusion of the implications of the life cycle assessment that involves the evaluation of principal issues, limitations and recommendations. In relation to the interpretation, the focus is on uncertainty analysis. Explicit description of the uncertainties should be of great importance here, however, only few LCA studies report it. The uncertainty in an LCA can be obtained by various statistical methods, e.g. parameter variation and scenario analysis, Monte Carlo simulations, analytical methods based on first-order propagation and qualitative uncertainty methods based on quality indicators (Finnveden et al. 2009).

The LCA standard ISO 14040-44 is quite generalized and non-specific in its requirements and offers little help to the LCA practitioner in making choices. There are various tools for performing LCA or for supporting the different phases and applications of LCA. Most tools include databases, some more comprehensive than others. Table 10.6 shows a list of existing LCA tools with some main characteristics. Most tools are designed for experts, and only few for non-specialists (Lehtinen et al. 2011).

Table 10.6 List of some LCA tools

Name	Developer	Main database	Application	Open source	Web page
BEES 4.0	National Institute of Standards and Technology (NIST)	Bees	Construction industry	Yes	http://www.nist.gov/el/economics/BEESSoftware.cfm
CCaLC Tool	The University of Manchester	CCaLC and EcoInvent	General	Yes	http://www.ccalc.org.uk/index.php
Eco-Bat 2.1	Haute Ecole d'Ingénierie et de Gestion du Canton de Vaud	Eco-Bat	Construction industry	No	http://www.eco-bat.ch/index.php?option=com_content&view=frontpage&Itemid=1&lang=en
Environmental Impact Estimator V3.0.2	Athena Sustainable Materials Institute	Own	Construction industry	No	http://www.athenasmi.org/
GaBi 4	PE International GmbH University of Stuttgart, LBP-GaBi	Gabi	General	No	http://www.gabi-software.com/index.php?id=85&L=0&redirect=1
LEGEP 1.4	LEGEP Software GmbH		Construction industry	No	http://www.legep.de/index.php?AktivId=1125
OpenLCA	GreenDeltaTC GmbH		General	Yes	http://www.openlca.org
SimaPro 7	PRé Consultants B.V.	SimaPro	General	No	http://www.pre.nl/

10.4.2 LCA Limitations

The broad scope of analysing the complete life cycle of a product can only be achieved at the expense of simplifying other aspects (Guinée et al. 2004). A core challenge of LCA is the comparability of different concrete studies, due to different methods and assumptions. Currently, available indicators for assessing resource consumption are generally based on global scale and are thus not fully adapted to the concrete industry (Habert et al. 2010; van den Heede and de Belie 2012), where the resource availability and accessibility should account regional specific conditions. The inventories and results are based on supply chain and time specific data. Databases are being developed in various countries, and although the format for databases is being standardized, in practice data are frequently obsolete, incomparable, or of unknown quality (Guinée et al. 2004). LCA case studies on commonly used concretes have been carried out in developed countries but there are insufficient studies in developing countries using local data. Furthermore, LCA is typically a steady state, rather than a dynamic approach. However, improvements are increasingly being taken into account in more detailed LCA studies. Although LCA is a tool based on linear modelling (Guinée et al. 2004), some progress is being made in reducing this limitation. The results of available concrete studies are not fully comparable due to different study scopes and system boundaries. Great caution needs to be taken in generalizing any LCA findings or transferring it to different cases.

10.4.3 LCA of Binders

The environmental impact related to the class of potential binders that can be used for mass concretes will be discussed in this section.

Some indicative LCA data sources for embodied carbon in typical binders used for making concrete are shown in Table 10.7. Embodied carbon for cement production can be split to raw material (chemical) decarbonation contribution (mainly $CaCO_3$), which amounts about 47%, and energy use which amounts 53% of the total CO_2 emissions. It is important to note that significant differences exist between cement plants which should be considered to improve accuracy of environmental evaluation (van den Heede and de Belie 2012). Table 10.7 indicates that the CO_2 emissions range from 930 kg per tonne of CEM I to 230 kg per tonne of CEM III/B comprising 80% GGBFS content. The embodied CO_2 values for blended cements taken from (MPA 2011) (Table 10.7) are based on the CEM I and SCM ingredients and the range of supplemented proportion. The calculations consider CEM I with supplement combined at concrete plant. For such combinations, the CO_2 value for CEM I is used together with the values for limestone, fly ash and GGBFS (shown in Table 10.8, MPA 2011) in the appropriate proportions. Therefore, the values can be interpolated for proportions between the minimum and maximum SCM addition.

Table 10.7 Some indicative LCA data sources for embodied carbon in typical binders used for making concrete

Material	Type	kg CO_2/tonne	Source (and comments)
Cement	Raw material decarbonation	425	Gartner (2004)
	Energy use	470	
	Total	895	
	OPC	844	Ecoinvent database v2, Frischknecht and Jungblut (2001)
Blended cement	CEM I (95% clinker, 5% gypsum)	930	MPA (2011)
	CEM II: 6–20% limestone	880–750	MPA (2011) (CO_2 values for blends can be interpolated between the min and max SCM addition)
	CEM II: 6–20% fly ash	870–750	
	CEM II: 21–35% fly ash	730–610	
	CEM II: 21–35% GGBFS	740–620	
	CEM III: 36–65% GGBFS	610–360	
	CEM III: 66–80% GGBFS	340–230	
	CEM IV: 36–55% Siliceous fly ash	590–420	

For example, using values for the end member components, namely CEM I has 930 kg CO_2/t while GGBFS 52 kg CO_2/t, then linear interpolation for CEM III in the range of 36–65% GGBFS gives CO_2 impacts of 610–360 kg CO_2/t. More specifically, 360 = 0.65 * 52 + 930 * (1 − 0.65). Likewise, any interpolated value can be used to estimate the impact for any blend.

Some relevant environmental impact factors from proprietary Ecoinvent database v2 (Frischknecht and Jungbluth 2001) are given in Table 10.8. There the ground blast furnace slag, fly ash and silica fume were considered as reused waste from other industries, thus without consideration of allocation and treatment (as detailed in Chen et al. 2010). Usual practice is to assume SCMs as waste, i.e. to assign them a null environmental impact. However, industrial sectors may have to share these environmental loads. This is very relevant to the use of SCMs such as blast furnace slags and fly ash, which now has to be regarded as a by-product because they fulfil three conditions specified by European Union Directive (EU 2008). Regarding to the first condition, they are used entirely, e.g. in Europe. Secondly, both SCMs are produced as an integral part of a production process,

Table 10.8 Some indicative LCA data sources for embodied carbon in typical SCMs and other additions used for making concrete

Material	kg CO_2/tonne	Source (and comments)
GGBFS	16.9	Ecoinvent database v2, Frischknecht and Jungblut (2001)
Fly ash	5.3	
Limestone filler	35.1	
Silica fume	0.313	
Metakaolin	92.4	
Kaolinite	2.93	
Superplasticizer	750	
Water	0.155	
GGBFS	52	MPA (2011)
Fly ash	4	
Limestone filler	32	

Table 10.9 Mass and economic allocation coefficients for FA and GGBFS (van den Heede and de Belie 2012)

Product	Produced amount	Market price	Mass allocation (%)	Economic allocation (%)
Electricity	2.7 kW h/ (kg of hard coal)	0.1 €/ (kW h)	87.6	99.0
FA	0.14 kg	20 €/t	12.4	1.0
Steel	1 kg	400 €/t	80.6	97.7
GGBFS	0.24 kg	40 €/t	19.4	2.3

and thirdly, they can be used directly without any further processing other than normal industrial practice. GBFS and FA used in the cement industry fulfil existing standards that consider their suitability in terms of mechanical performance, risk for concrete durability and risk for the environment, e.g. according to EN 450-1 standard for FA (EN 2007) and EN 197-1 for GBFS (EN 2001). When mass allocation is applied (Table 10.9), the FA and GGBFS environmental burdens become higher than for OPC. Therefore, an economic allocation (Table 10.9) is recommended, which results in an order of magnitude lower impacts of FA and BFS (van den Heede and de Belie 2012). The main problem with the economic allocation is the question of price variability (van den Heede and de Belie 2012). The allocation method, based on the European Union GHG emission trading system (EU-ETS), is calculated so that the economic gains and losses are the same for all of the industries involved in the trading of by-products, which underlines the overall environmental benefit of the exchanges (Habert et al. 2013). For natural SCMs, e.g. volcanic rocks or (calcined) clays, there is no allocation problem and their environmental impact results only from the energy used during their processing, which is always much lower than cement.

Table 10.10 Normalized values describing the sustainability profile of concretes incorporating coal and/or biomass-based fly ash (adapted from Teixeira et al. 2016)

	FA0	CFA60	BFA60	CBFA60
Material input (kg/m^3 of concrete)				
Portland cement	350	140	140	140
Gravel	1100	1100	1100	1100
Sand	750	750	750	750
Water	175	175	175	175
Superplasticizer	8.8	8.8	8.8	8.8
Coal fly ash		210		105
Biomass fly ash			210	105
Transportation (tkm)				
Portland cement	14.4	5.7	5.7	5.7
Sand and gravel	577.2	577.2	577.2	577.2
Superplasticizer	2.9	2.9	2.9	2.9
Coal fly ash		34.7		17.3
Biomass fly ash			30.2	15.1
Global warming (kg CO_2 eq.)	784	416	413	415
Relative overall sustainability index	0	0.98	1.00	0.99

Yang et al. (2016) investigated the high volume (40, 80 and 90%) use of varying combinations of fly ash, slag and PC in order to control the hydration heat development in mass concrete and enhance its sustainability. The studied system boundary included the following phases: (1) procurement of all constituents in a materials inventory (Korean LCI database, Yang et al. 2014) taken from cradle-to-gate, (2) transportation of the constituents to a ready-mixed concrete plant and (3) in-plant mixing of concrete. The reduction percentage in the global warming, photochemical oxidation and abiotic depletion categories, as compared with the reference OPC concrete, was 35%, 36% and 34%, respectively, for the T4 (25%FA + 15%GGBFS) concrete, 75%, 80% and 73% for the T8 (40%FA + 40% GGBFS) concrete and 86%, 89% and 82% for the T9 (40%FA + 50%GGBFS) concrete.

Use of biomass ash as a binder shows a capability to reduce the environmental impacts of conventional concrete (Table 10.10). Using LCA analysis Teixeira et al. (2016) showed that the most sustainable concrete was the one in which 60% of cement is replaced by biomass fly ashes. Nevertheless, with such a concrete it was possible to achieve satisfactory mechanical properties. The incorporation of biomass fly ashes could solve a problem of ash disposal while contributing to the development of concretes with improved environmental performance. However, these results should be complemented by experimental studies aimed at assessing both strength and durability of concretes affected by variability in biomass ash quality. If biomass fly ashes are considered as a waste product without economic value (true in most EU countries, Berra et al. 2015; de la Grée et al. 2016;

Ukrainczyk et al. 2016), then there are no flows from the biomass power plant allocated to its production. On the other hand, coal fly ashes have a market value and consequently a percentage of the power plant's flows are allocated to their productions (García-Gusano et al. 2015).

The amount of superplasticizer used in concrete is almost negligible, thus its emissions, which are approaching cement values (shown in Table 10.8), do not contribute significantly to the overall environmental impact. On the other hand, application of superplasticizer can even reduce the overall concrete CO_2 emissions by 26% (Purnell and Black 2012) due to reduced cement content while achieving same targeted workability and strength.

10.4.4 LCA of Aggregates

Aggregates are the major component of concrete and are inherently a low carbon product (Table 10.11). Most are naturally occurring materials requiring little processing. Besides the type of aggregate, its regional availability and accessibility are of importance. They are generally local sourced, due to the associated impact of transport costs and CO_2 emissions. For example, the transport of aggregates doubles its price (per t) every 30 km. Table 10.11 shows that the CO_2 impact for crushed (virgin) aggregates increases from 6.6 kg CO_2/t for cradle-to-gate system boundary (extraction and production only), for additional 2.7 kg CO_2/t due to transportation delivery and return distance of 58.5 km by road. Reported GHG emissions, including production and average transport values, for crushed aggregates are 45.9 kg CO_2 equivalents/t of granite/hornfels and 35.7 kg CO_2 equivalents/t of basalt, while for sand it is lower, 13.9 kg CO_2 equivalents/t of sand (Flower and Sanjayan 2007) as it does not involve crushing process. Emissions and energy consumption per metric ton of glacier rock produced by a Nordberg HP400 SX rock crusher (55 de Belie) are 0.6465 kg CO_2/t and 9.8192 MJ/t, respectively.

CO_2 emissions for recycled aggregates are compared with virgin aggregate in Table 10.11. It can be seen that for transport distances longer than about 15 km, the CO_2 emissions may become higher than for virgin aggregates with 58.5 km transportation distance (Table 10.11). For the same transport distance of 58.5 km, contributing for 2.7 kg CO_2/t, the resulting total value for RA is 15% higher than for virgin (crushed) aggregate. Therefore, recycled aggregates should only be used if they are locally available and can be demonstrated to reduce overall CO_2 impact. However, to estimate the overall CO_2 impact, benefits in preservation of natural bulk resources and reduction of landfill space as well as CO_2 uptake of crushed concrete should also be considered. This is discussed further in next section (concrete).

Table 10.11 Some indicative LCA data sources for embodied energy and carbon in aggregates, including transportation, used for making concrete

Material	Type	Energy, MJ/tonne	kg CO_2/ tonne	Source (and comments)
Sand, fine aggregates			2.4	Ecoinvent database v2, Frischknecht and Jungblut (2001)
Coarse aggregates			4.3	
Aggregate	Virgin (gravel)	23.8	4	MPA (2011)
	Virgin (crushed)	30.2	6.6	
	+58.5 km delivery by road		9.3	
Recycled aggregate from concrete demolition	0 km transport by road	62.1	7.9	MPA (2011)
	+15 km transport		9.3	
	+58.5 km transport		10.6	

10.4.5 LCA of Concrete

Absolute contributions of CO_2 emissions for each of the individual materials and processes relevant for placement of 40 MPa grade concrete are shown in Table 10.12 (Turner and Collins 2013) which in descending relative terms amounts: 76% for cement, 14.4% coarse agg., 3.1% sand, 2.5% transport, 2.5% placement, 0.85% batching, 0.3% admixtures and 0.3% curing. The contribution of the cement production phase varied from 75% to 94% of the total impact, depending on the category indicator and the concrete type. This result is in agreement with Braunschweig et al. (2011).

Although GGBFS has higher material emission factor than fly ash (about 13 times, Table 10.8), it can generally replace more cement (40%) than fly ash (25%) due to its self-cementing properties, which may lead to better reductions in total emissions, 22% for GGBFS instead of 13–15% for FA, respectively, for typical 25 and 32 MPa concrete mixes (Flower and Sanjayan 2007). Some typical CO_2 impacts for OPC and GGBFS and FA concretes are shown in Table 10.12. Baseline GHG emission reductions of between 22 and 40% (Crossin 2015; Flower and Sanjayan 2007) have been reported, while Blankendaal et al. (2014) suggest a total environmental impact reduction of up to 39%.

In different life cycle studies on GGBFS, Flower and Sanjayan (2007), Lee and Park (2005), Kellenberger et al. (2007) and Heidrich et al. (2005) include the emissions associated with processing and transport of GGBFS, but excluded emissions associated with the blast furnace operation.

Table 10.12 Some indicative LCA data sources for embodied energy and carbon in materials and processes for building concrete structures

Material	Type	Energy (MJ/tonne)	kg CO_2/tonne	Source (and comments)
OPC concrete	40 MPa, Coarse agg. 1242 kg/m^3, sand 781 kg/m^3, OPC 328 kg/m^3, water 190 kg/m^3		112(Cement) + 21.3 (coarse agg.) + 4.6(sand) + 0.4(admix.) + 1.3 (Batching) + 3.8 (Transport) + 3.8 (Placement) + 0.4 (Curing) = 147.5	Turner and Collins (2013) (concrete density 2400 kg/m^3 assumed)
Concrete	Structural	1111	159	Hammond and Jones (2011) (density of 2400 kg/m^3 assumed for unit conversion)
	RC40 with 25% PFA	970	132	
	RC40 with 50% GGBFS	880	101	
Concrete	30 MPa (Table 10.4) PC		164	Crossin (2015)
	70% slag (Table 10.4)		87	
Reinforcement			427	MPA (2011)
Reinforced concrete	C28/35 unreinforced (w:c:a = 0.55:1:6.4)		95	(density of 2380 kg/m^3 assumed for unit conversion)
	C28/35 (w:c:a = 0.55:1:6.4) with steel bars 110 kg/m^3		110	
	Mass foundation GEN1 d_{agg} < 70 mm, unreinforced	CEM I	75	MPA (2011) (concrete density of 2300 kg/m^3 assumed for unit conversion)
		30% FA	54	
		50% slag	43	
	Trench foundation GEN1 d_{agg} < 120 mm, with steel bars 25 kg/m^3	CEM I	80	
		30% FA	62	
		50% slag	47	
	Reinforced foundation RC30 d_{agg} < 70 mm, with 100 steel bars kg/m^3	CEM I	138	
		30% FA	116	
		50% slag	87	
	Ground floors RC35 d_{agg} < 70 mm, with steel bars 30 kg/m^3	CEM I	137	
		30% FA	113	
		50% slag	81	
	Structural walls RC40 d_{agg} < 70 mm, with 100 kg/m^3 steel bars	CEM I	162	
		30% FA	138	
		50% slag	103	
	High strength RC50 d_{agg} < 70 mm, with steel bars 100 kg/m^3	CEM I	190	
		30% FA	155	
		50% slag	120	
	N. agg. (Table 10.13)	668	142 (CO_2 eq.)	Marinkovic et al. (2014) (excluding agg. transportation)
	Natural crushed aggregate (NCA, Table 10.13)	752	160 (CO_2 eq.)	
	Recycled agg. replacing 50% NCA (Table 10.13)	666	142 (CO_2 eq.)	
	Recycled agg. fully replacing NCA (Table 10.13)	724	152 (CO_2 eq.)	

(continued)

Table 10.12 (continued)

Material	Type	Energy (MJ/tonne)	kg CO_2/tonne	Source (and comments)
Concrete batching and pumping			2.35 (CO_2 eq.)	Crossin (2015) (concrete density of 2300 kg/m^3 assumed for unit conversion)
Transport of concrete to site			0.3 per km	
Concrete mixer truck	12 tonne	2.06 (per km)	0.154 (CO_2 eq. per km)	Hong et al. (2014), Akbarnezhad and Nadoushani (2014)
Truck	16.5 tonne	0.94 (per km)	0.065 (CO_2 eq. per km)	
Excavator	0.2 m^3	107.5 (per h)	13.12 (CO_2 eq. per h)	
Truck crane	25 tonne	215.3 (per h)	16.01 (CO_2 eq. per h)	
Loader	1.77 tonne	899.6 (per h)	35.07 (CO_2 eq. per h)	
Crawler crane	50–80 tonne	607.2 (per h)	45.23 (CO_2 eq. per h)	
Concrete pump	80 m^3/h	1094.3 (per h)	81.37 (CO_2 eq. per h)	
Concrete vibrator	2.5 m^3/h	34.9 (per h)	2.59 (CO_2 eq. per h)	
Air compressor	425 m^3/h	968.8 (per h)	37.77 (CO_2 eq. per h)	
Concrete structure	15 stories building, 3375 m^2 of total floor area, 30 MPa concrete 985 kg/m^2 and rebar 57 kg/m^2		189(Material extraction) + 13.4(Transport) + 14.2 (Construction) = 216.4	Nadoushani et al. (2015) (unit adapted from per m^2 of floor area to per tonne of concrete structure)

Crossin (2015) investigated two utilization scenarios: (1) GGBFS is readily available in the marketplace and is not fully utilized and (2) the supply of GGBFS is constrained. Life cycle modelling was undertaken using SimaPro 7.2.4, with background datasets taken from ecoinvent 2.2 (Frischknecht and Jungblut 2001) and the Australasian Unit Process Life Cycle Inventory. In the assessment, they included the full fuel cycle for all energy consumption processes, but excluded the steel reinforcement. The results showed that the impacts of concrete were dominated by GHG emissions from the production of cement and blended cement, contributing to 85% and 73%, respectively of the total impact. The use of GGBFS as a cement substitute in concrete resulted in a 47.5% reduction of GHG emissions provided that the supply of GGBFS is not constrained. Conclusive determinations of supply constraints, and subsequently the establishment of potential environmental benefits, require the better provision and access to market data, including price information. GGBFS prices have increased from 2005 to 2011, while cement prices peaked in 2008. The unit price for GGBFS is higher from CEM I cement from 2009 to 2011 (van Oss USGS Mineral info 2006–2011 cited in Crossin 2015).

In order to achieve the same strength characteristics, the total cementitious content of GGBFS concrete mixes needs to be higher than for concrete mixes without GGBFS (Richardson 2006; Shariq et al. 2008; Babu and Kumar 2000). GGBFS concretes typically require increase in binder content of about 5–10 kg/m^3 up to replacement levels of 50% to achieve equivalent 28-day strength (MPA 2011). These changes would likely result in a minor increase in the greenhouse gas impacts reported in that study. For concrete containing 40% fly ash, the total binder content may be around 15% higher than a reference concrete containing CEM I only.

10.4.5.1 Recycled Aggregates Concrete (RAC)

Replacing natural aggregates with recycled concrete aggregates can decrease concrete environmental impact by preserving natural resources and minimizing waste disposals. LCA benefits of concrete with replaced NA by RAC are given in FIB TG3.6 (2008), Hájek et al. (2011) and Marinkovic (2013, 2014). Braunschweig et al. (2011) showed that environmental impacts of NAC and concrete with 25% recycled aggregate are similar, considering the increase of cement amount in RAC is below few per cent. Blankendaal et al. (2014) concluded that the recycling of concrete does neither contribute nor harm the environmental impact. Weil et al. (2006) compared NAC to RAC with 35 and 50% of recycled concrete aggregate and different cement content. Marinkovic et al. (2014) investigated the effect of three different types of aggregate: natural gravel, natural crushed and recycled concrete aggregate (Table 10.13) on the transport phase and CO_2 uptake during the life cycle of concrete. Within the limits of that case study, based on Serbian LCI data and typical conditions, brought the conclusion that RCA application in structural concrete can bring environmental benefits over gravel aggregate, and certainly over crushed aggregate, but this depends on transport conditions and types of natural and recycled aggregate.

The impairment in sustainability of NCA relative to NA ranged from 12% to 18% in all category indicators (namely energy use, global warming, eutrophication, acidification, photochemical oxidant creation) due to 9% higher cement content, needed to maintain workability and strength in NAC and different transportation types: truck and ship, respectively. The 50% and 100% replacement ratio of NCA, i.e. RA50 and RA100, relative to NA (Table 10.13) showed a negligible effect of below 2 and 3%, respectively, on the indicators for all impact categories of the concrete. However, for RA concretes there is a clear benefit in avoiding the landfilling of 1071 kg of concrete waste and extraction of 1071 kg of natural aggregate per 1 m^3 of RAC100. This indicates that additional special indicators should be developed to quantify benefits in (a) preservation of natural bulk resources (e.g. natural resource depletion indicator as shown in Fig. 10.11) and (b) reduction of landfill space.

Table 10.13 Mix proportions and properties of concretes made by NA and RA (adapted from Marinkovic et al. 2014)

Concrete short name	Concrete with	Cement (kg/m^3)	Water (kg/m^3)	Aggregate			Slump (cm)	Comp. strength at 28 days (MPa)	CO_2 eq. (kg/m^3)	Energy (MJ/m^3)
				Fine (kg/m^3)	Coarse (kg/m^3)					
					Natural	Recycled				
NA	Natural aggregate	354	185	600	1164	0	8.0	43.7	328	1538
NCA	Natural crushed aggregate	384	201	592	1165	0	8.8	41.5	356	1677
RA50	Recycled agg. replacing 50% NCA	354	178	598	555	555	9.7	44.2	333	1559
RA100	Recycled agg. fully replacing NCA	365	218	576	0	1071	9.7	42.5	356	1623

The contribution of the aggregate production phase is very small, ranging between 0.8 and 5.4%. Therein, RCA concretes have higher contribution than NA concretes due to higher energy requirement for the production of RCA (62.1 MJ/t) than NA (23.8 MJ/t) or NCA (30.2 MJ/t). However, the different energy requirement for production of different aggregate types affects the total impacts by up to a few per cent only. The contribution of the concrete production phase is also small and varies from 0.1 to 5.1%, depending primarily on the category indicator. The transport phase contributed from 3 to 20%, wherein was largest for NCA due to the case assumption that 100 km transport was made by a truck, a much more polluting means than by a ship. This emphases that the results of the concrete LCA studies depend primarily on the concrete mix design, i.e. the amount of cement used, and secondly on the assumed transportation means and distances. For transport distances longer than about 15 km, CO_2 emissions for recycled aggregates may become higher than for virgin aggregates (Table 10.11).

Another benefit of concrete recycling is CO_2 uptake of crushed concrete. During its stockpiling for a certain period of time, a revealed surface area, and thus CO_2 uptake, is much greater than for landfilled concrete waste which is not that finely crushed. Literature results show that CO_2 uptake in post-use phase can be significant, depending on the concrete structure, namely concrete CO_2 uptake normalized to CO_2 emission from calcination during service life is 8.6% (Gajda 2001), which is much smaller than CO_2 uptake during secondary life when demolished concrete is crushed into RCA and reused in the construction: 33–57% (Kjellsen et al. 2005) or 86% (Collins 2010). Dodoo et al. (2009) showed that the uptake of CO_2 during the concrete building service life for 100 years was 23% of the clinker calcination emissions. However, when the concrete was crushed, after demolition, and exposed to air for four months, the CO_2 uptake was 43% of the calcination emissions. Collins (2010) indicated that during the concrete building service life for 100 years CO_2 uptake was only 3% of the calcination emissions, while when the concrete was crushed, after demolition, into RCA and used in the construction of a new bridge for another 30 years, CO_2 absorption is as high as 55 and 86% of the clinker calcination emissions, depending on RCA application. The amount of this CO_2 uptake should then be allocated between the product that generates waste and the product which receives it.

Beside partial replacement of cement with SCMs, or recycling of aggregates, another option to improve sustainability in mass concrete would be to reduce the concrete volume or decrease maintenance burdens by enhancing the concrete performance. Habert et al. (2013, 2014) highlighted that significant saving can be achieved with high-performance concretes, which are at the same time less environmental friendly than conventional concrete. However, the gain prevails when concrete is designed to be used in much smaller amounts (lower cross sections) or for much longer time.

10.4.6 LCA of Reinforced Concrete Structure

The composite combination of concrete and rebar employs tensile and compressive qualities, respectively. Steel reinforcement is used to deliver tensile capacity, a week property of concrete alone needed (1) to minimize the thermal induced cracking problems and/or ensure tensile loadings during structural use. Efficient use of reinforcing steel is dependent on good structural design and on the material's chemical composition, mechanical properties and rib geometry, as well as accurate cutting, bending and fixing.

Rebar contents in reinforced concrete may vary, and this will affect the embodied CO_2. Rebar amount of 110 kg per m^3 of concrete will increase CO_2 emissions by 16%, as shown in Table 10.12 for C28/35 concrete (MPA 2011). Rebars can be recovered, recycled and reused at the end of a structure's service life.

Nadoushani and Akbarnezhad (2015) investigated concrete structural systems designed for 3, 10 and 15 stories buildings including moment resisting frames, braced frames and shear walls systems. The CO_2 footprint of each individual design is estimated by considering the emissions incurred in: (1) material extraction, (2) transportation, (3) construction, (4) operation and (5) end-of-life phases. The cradle-to-gate embodied CO_2 was estimated for per square metre of different structural systems, which was converted into per tonne of concrete structure and shown in Table 10.12. This unit conversion was done by averaging the amount of concrete and rebar used in the whole building. The results show that the cradle-to-gate for reinforced concrete materials extraction embodied majority (87.3%) of the total CO_2 for the whole structure. Transportation of the high amount of the materials accounted for 6.2% of the total CO_2 impact. The use of energy consuming vehicles and equipment such as concrete truck mixers and concrete pumps in construction process, to complete concrete frames, resulted in 6.6% of total CO_2 embodiment. Table 10.12 includes also the energy consumption and GHG emission factor for transportation vehicles and construction equipment. This also gives a rough estimate on the specific technologies applied for mass concrete, namely occurred for additional construction processes for (1) controlling the lift thickness and the time intervals between lifts placing, to allow hydration heat to dissipate and (2) reducing the temperature of concrete, either by pre-cooling the mix and/or its ingredients or by post-cooling the mix after placement.

10.4.6.1 Fibers

Currently, there are insufficient efforts in applying LCA to fiber-reinforced concrete composites. To provide an even starting point for environmental comparisons, functional units should be developed to consider an appropriated lifespan and similar mechanical responses.

Natural fiber production has superior environmental impacts compared to glass fiber production (Joshi et al 2004). However, this is compromised by a lower

operating service life compared to glass fiber components (Beltran, Romildo). Significant environmental savings, of about 48%, can be achieved compared to steel reinforced concrete, when using only 3 vol% of bamboo (Zea Escamilla and Wallbaum 2011). The replacement of traditional reinforcements brings both a significant environmental and economical saving for the production of concrete.

10.5 Conclusion

Based on this review, chapter on sustainability in mass concrete following points may be recommended and/or summarized.

(1) LCA should be performed when improving mass concrete mix design and placement technology, following the outlined approach and recent studies. An objective functional comparison criteria should be used, for example the equivalent mechanical strength, volume of binder paste and/or replaced aggregate, but also it is crucial to consider durability criteria. A more advanced rational approach is required to include durability and service life of mass concrete in the LCA assessment. Further research on the compromise between longer concrete service life and increase in initial input value of raw materials is recommended, as it is crucial to find optimal environmental solutions over the entire life cycle of mass concrete structure. However, the broad scope of analysing the complete life cycle of a product can only be achieved at the expense of simplifying other aspects. A core challenge of LCA is the comparability of different concrete sustainability studies, due to different methods and simplifying assumptions. At least the extended cradle-to-gate system boundary conditions should be performed, which define the amount of mass concrete needed to maintain the structure during well-specified service life, with required repairs and maintenance.

(1.1) The quality of LCA results depends significantly on the quality of life cycle inventory input data. An LCA should be performed locally, to include the local conditions and impact of transport, and make it comparable to the result with other studies.

(2) Contributions of CO_2 emissions relevant for placement of conventional (40 MPa) concrete in descending relative terms amounts: 76% for cement (varies from 75 to 94% depending on the concrete type), 14.4% coarse agg., 3.1% sand, 2.5% transport, 2.5% placement, 0.85% batching, 0.3% admixtures and 0.3% curing. The cradle-to-gate LCA for reinforced concrete structure indicates following CO_2 contributions for typical stages: 87.3% for materials extraction, 6.2% for transportation and 6.6% for the use of energy consuming vehicles and equipment (Table 10.12). This also gives an order of magnitude estimate ($\sim$<5%) for the possible contribution of the specific technologies

applied for mass concrete, namely for controlling the lift thickness and the time intervals between lifts placing and for pre-cooling or post-cooling the mix.

(3) The use of non-conventional wastes and/or a high volume of conventional SCMs is general not directly allowed to be used in concrete, but only after its equivalent performance is proved in comparison to the eligible reference concrete.
The SCMs with the highest potential for improving the sustainability in mass concrete are the biomass ash obtained by combustion of residues from timber industry and forest activities (woody ash), the wastes from farms and agro-business (sugar cane bagasse and rice husk ash), and other plants grown for energetic purposes. The utilization of biomass ash in production of mass concrete is an environmentally motivated choice. It will save costs for ash disposal, decrease energy requirement mainly related to cement clinker production, preserve natural resources, i.e. quarried limestone, sand and natural aggregates which consume also huge amounts of non-renewable and pre-treated natural raw materials and decrease greenhouse gas emissions by cement clinker substitution. The challenge is to maintain equal performances of the produced mass concrete while minimizing the environmental footprint by a maximum reuse of waste-like residuals.

(4) Using of recycled aggregates in mass concrete can make a big contribution to accomplish the Revised Waste Framework Directive (WFD) 2008/98/EC (EU 2008) which established that by 2020, the minimum recycling percentage of 'non-hazardous' construction, and demolition wastes should be at least 70% by weight. Indeed, RCA has a good potential to replace natural aggregates in low-to-medium strength structural concrete. However, recycled aggregates should only be used when they are locally available and can be demonstrated to reduce overall CO_2 impact. For impact estimation, benefits in preservation of natural bulk resources and reduction of landfill space as well as CO_2 uptake of crushed concrete should be included.

(5) To derive value from various wastes, namely various ashes from biomass (wood, sugar cane bagasse and rice husks) combustion and/or construction and demolition wastes, capable of satisfying the technical needs of mass concrete manufacture industry within the framework of sustainable development, still several requirements need to be fulfilled. Currently, there are limitations in technical and regulatory (standard) specifications as well as logistics. The main reasons for this situation relate to waste quality variations, environment and sustainability. To overcome these barriers for a more widespread waste utilization in the mass concrete production, a quality control systems and demonstrations from both different locations and on the various mass concrete application options are needed. These actions will also stimulate cooperation between producers and end-users and increase awareness among market actors.

(6) Natural fibers present several advantages such as lower environmental impact, production costs and weight as well as the higher sustainability of the materials, although the bending strength and ductility by reinforcing concrete with natural

fibers is lower than some other fiber reinforcements. Despite all these advantages, the industrial production of natural fiber-reinforced concrete composites is currently limited by the long-term durability of these materials, which needs to be evaluated in detail. In general, the durability problem is associated with an increase in fiber–matrix performance due to a combination of the weakening of the fibers by alkali attack, fiber mineralization by diffusion of hydration products to lumens and volume variation due to their high water absorption. This causes the material to have a reduction in post-cracking strength and toughness.

(7) Alternative option to improve sustainability in mass concrete, beside reuse of wastes or natural fibers, would be to design mass concretes with smaller volumes, i.e. concretes with lower cross sections and/or for much longer service time, i.e. more durable.

References

Akbarnezhad, A., & Nadoushani, M. Z. S. (2014). A computational method for selection of optimal concrete recycling strategy. *Magazine of Concrete Research, 67*, 543–558. http://dx.doi.org/10.1680/macr.14.00211

Aldea, C., Young, F., Wang, K., & Shah, S. P. (2000). Effect of curing conditions on properties of concrete using slag replacement. *Cement Concrete Research, 30*, 465–472. http://dx.doi.org/10.1016/S0008-8846(00)00200-3.

Ardanuy, M., Claramunt, J., & Filho, R. D. T. (2015). Cellulosic fiber reinforced cement-based composites: A review of recent research. *Construction and Building Materials, 79,* 115–128. https://doi.org/10.1016/j.conbuildmat.2015.01.035.

Atis, C. D. (2002). Heat evolution of high-volume fly ash concrete. *Cement and Concrete Research, 32*(5), 751–756. https://doi.org/10.1016/S0008-8846(01)00755-4.

Babu, K. G., & Kumar, V. S. R. (2000). Efficiency of GGBS in concrete. *Cement and Concrete Research, 30,* 1031–1036. https://doi.org/10.1016/S0008-8846(00)00271-4.

Bacarji, E., Toledo Filho, R. D., Koenders, E. A. B., Figueiredo, E. P., & Lopes, J. L. M. P. (2013). Sustainability perspective of marble and granite residues as concrete fillers. *Construction and Building Materials, 45,* 1–10. https://doi.org/10.1016/j.conbuildmat.2013.03.032.

Banthia, N., Zanotti, C., & Sappakittipakorn, M. (2014). Sustainable fiber reinforced concrete for repair applications. *Construction and Building Materials, Concrete Sustainability, 67*, 405–412. http://dx.doi.org/10.1016/j.conbuildmat.2013.12.073.

Barbosa, R., Lapa, N., Dias, D., & Mendes, B. (2013). Concretes containing biomass ashes: Mechanical, chemical, and ecotoxic performances. *Construction and Building Materials, 48,* 457. https://doi.org/10.1016/j.conbuildmat.2013.07.031.

Basheer, P. A. M., Gilleece, P. R. V., Long, A. E., & McCarter, W. J. (2002). Monitoring electrical resistance of concretes containing alternative cementitious materials to assess their resistance to chloride penetration. *Cement & Concrete Composites, 24,* 437–449. https://doi.org/10.1016/S0958-9465(01)00075-0.

Bentur, A. (1989). Fiber reinforced cementitious materials. In J. P. Skalny (Ed.), *Materials science of concrete I* (pp. 223–284). American Ceramic Society.

Berra, M., Mangialardi, T., & Paolini, A. E. (2015). Reuse of woody biomass fly ash in cement-based materials. *Construction and Building Materials, 76,* 286. https://doi.org/10.1016/j.conbuildmat.2014.11.052.

Blankendaal, T., Schuur, P., & Voordijk, H. (2014). Reducing the environmental impact of concrete and asphalt: A scenario approach. *Journal of Cleaner Production, 66,* 27–36. https://doi.org/10.1016/j.jclepro.2013.10.012.

Blankenhorn, P. R., Blankenhorn, B. D., Silsbee, M. R., & DiCola, M. (2001). Effects of fiber surface treatments on mechanical properties of wood fiber-cement composites. *Cement and Concrete Research, 31,* 1049–1055. https://doi.org/10.1016/S0008-8846(01)00528-2.

Blankenhorn, P. R., Silsbee, M. R., Blankenhorn, B. D., DiCola, M., & Kessler, K. (1999). Temperature and moisture effects on selected properties of wood fiber-cement composites. *Cement and Concrete Research, 29,* 737–741. https://doi.org/10.1016/S0008-8846(99)00046-0.

Braunschweig, A., Kytzia, S., & Bischof, S. (2011). Recycled concrete: Environmentally beneficial over virgin concrete? http://www.lcm2011.org/papers.html.

Bui, D. D., Hu, J., & Stroeven, P. (2005). Particle size effect on the strength of rice husk ash blended gap-graded Portland cement concrete. *Cement & Concrete Composites, 27,* 357–366. https://doi.org/10.1016/j.cemconcomp.2004.05.002.

Carrasco-Hurtado, B., Corpas-Iglesias, F. A., Cruz-Perez, N., Terrados-Cepeda, J., & Perez-Villarejo, L. (2014). Addition of bottom ash from biomass in calcium silicate masonry units for use as construction material with thermal insulating properties. *Construction and Building Materials, 52,* 155. https://doi.org/10.1016/j.conbuildmat.2013.11.018.

CEN. (2002). *Mixing water for concrete—Specification for sampling, testing and assessing the suitability of water, including water recovered from processes in the concrete industry, as mixing water for concrete, EN 1008:2002*. Bruxelles (BE): Comité Européen de Normalisation.

Chalee, W., Teekavanit, M., Kiattikomol, K., Siripanichgorn, A., & Jaturapitakkul, C. (2007). Effect of W/C ratio on covering depth of fly ash concrete in marine environment. *Construction and Building Materials, 21,* 965–971. https://doi.org/10.1016/j.conbuildmat.2006.03.002.

Cheah, B. C., & Ramli, M. (2011). The implementation of wood waste ash as a partial cement replacement material in the production of structural grade concrete and mortar: An overview. *Resources, Conservation and Recycling, 55,* 669. https://doi.org/10.1016/j.resconrec.2011.02.002.

Cheah, C. B., & Ramli, M. (2014). The fluid transport properties of HCWA–DSF hybrid supplementary binder mortar. *Composites: Part B, 56,* 681–690. https://doi.org/10.1016/j.compositesb.2013.09.021.

Chen, C., Habert, G., Bouzidi, Y., Jullien, A., & Ventura, A. (2010). LCA allocation procedure used as an initiative method for waste recycling: An application to mineral additions in concrete. *Resources, Conservation and Recycling, 54*(12), 1231–1240. https://doi.org/10.1016/j.resconrec.2010.04.001.

Cheng, A., Huang, R., Wu, J. K., & Chen, C. H. (2005). Influence of GGBS on durability and corrosion behavior of reinforced concrete. *Materials Chemistry and Physics, 93,* 404–411. https://doi.org/10.1016/j.matchemphys.2005.03.043.

Chindaprasirt, P., Kanchanda, P., Sathonsaowaphak, A., & Cao, H. T. (2007). Sulfate resistance of blended cements containing fly ash and rice husk ash. *Construction and Building Materials, 21* (6), 1356–1361. https://doi.org/10.1016/j.conbuildmat.2005.10.005.

Chowdhury, S., Mishra, M., & Suganya, O. (2015). The incorporation of wood waste ash as a partial cement replacement material for making structural grade concrete: An overview. *Ain Shams Engineering Journal, 6,* 429–437. https://doi.org/10.1016/j.asej.2014.11.005.

Collins, F. (2010). Inclusion of carbonation during the life cycle of built and recycled concrete: influence on their carbon footprint. *International Journal of Life Cycle Assessment, 15,* 549–556. https://doi.org/10.1007/s11367-010-0191-4.

Cook, D. J. (1984). Development of microstructure and other properties in rice husk ash—OPC systems. In *Proceedings of the 9th Australasian Conference on the Mechanics of Structures and Materials*, University of Sydney, Sydney (pp. 355–360).

Cordeiro, G. C. (2006). Ph.D. thesis, Universidade Federal do Rio de Janeiro, Brasil. http://www.coc.ufrj.br/index.php/teses-de-doutorado/150-2006.

Cordeiro, G. C., Toledo Filho, R. D., Fairbairn, E. M. R. (2008). Use of ultra-fine sugar cane bagasse ash as mineral admixture for concrete. *ACI Materials Journal, 105*, 487–493.

Cordeiro, G. C., Toledo-Filho, R. D., Fairbairn, E. M. R. (2009a). Effect of calcination temperature on the pozzolanic activity of sugar cane bagasse ash. *Construction and Building Materials, 23*, 3301–3303. https://doi.org/10.1016/j.conbuildmat.2009.02.013.

Cordeiro, G. C., Toledo Filho, R. D., Tavares, L. M., Fairbairn, E. M. R. (2009b). Ultrafine grinding of sugar cane bagasse ash for application as pozzolanic admixture in concrete. *Cement and Concrete Research, 39*, 110–115. https://doi.org/10.1016/j.cemconres.2008.11.005.

Crossin, E. (2015). The greenhouse gas implications of using ground granulated blast furnace slag as a cement substitute. *Journal of Cleaner Production, 95,* 101–108. https://doi.org/10.1016/j.jclepro.2015.02.082.

D'Almeida, A., Toledo Filho, R., & Melo Filho, J. (2010). Cement composites reinforced by short curaua fibers. *Revista Materia, 15*(2), 153–159. http://dx.doi.org/10.1590/S1517-70762010000200010.

DAfStb. (2004). DAfStb-Richtlinie: Beton nach DIN EN 206-1 und DIN 1045-2 mit rezyklierten Gesteinskörnungen nach DIN 4226-100. Berlin: DAfStb (in German).

de la Grée, D. G. C. H., Florea, M. V. A., Keulen, A., & Brouwers, H. J. H. (2016). Contaminated biomass fly ashes—Characterization and treatment optimization for reuse as building materials. *Waste Management, 49,* 96–109. https://doi.org/10.1016/j.wasman.2015.12.023.

de Sensale, R. G. (2006). Strength development of concrete with rice-husk ash. *Cement & Concrete Composites, 28,* 158–160. https://doi.org/10.1016/j.cemconcomp.2005.09.005.

Dhir, R. K., El-Mohr, M. A. K., & Dyer, T. D. (1996). Chloride binding in GGBS concrete. *Cement and Concrete Research, 26*(12), 1767–1773. https://doi.org/10.1016/S0008-8846(96)00180-9.

Dodoo, A., Gustavsson, L., & Sathre, R. (2009). Carbon implications of end-of-life management of building materials. *Resources, Conservation and Recycling, 53,* 276–286. https://doi.org/10.1016/j.resconrec.2008.12.007.

Dyczek and Petri. (1992). FRC reinforced with short polypropylene fibers fracture process. In *Proceedings 9th ICCC*, New Delhi (Vol. 5, pp. 485–491).

EN 206-1. (2006). Part 2: Specification for constituent materials and concrete.

EN, European Committee for Standardization. (2001). EN 197-1. Cement—Part 1: Composition, specifications and conformity criteria for common cements.

EN, European Committee for Standardization. (2007). EN 450-1. Fly ash for concrete—Part 1: Definition, specifications and conformity criteria.

European Union (EU). (2008). Directive 2008/98/EC of the European Parliament and of the Council on waste and repealing certain directives. Official Journal of the European Union, European Parliament, Brussels. L312, 3–30. http://eurlex.europa.eu/LexUricerv/LexUricerv.do?uri=OJ:L:2008:312:0003:0030:en:PDF.

Fairbairn, E. M. R., Ferreira, I. A., Cordeiro, G. C., Silvoso, M. M., Toledo Filho, R. D., & Ribeiro, F. L. B. (2010a). Numerical simulation of dam construction using low-CO_2-emission concrete. *Materials and Structures, 43,* 1061–1074. https://doi.org/10.1617/s11527-009-9566-z.

Fairbairn, E. M. R., Americano, B. B., Cordeiro, G. C., Paula, T. P., Toledo Filho, R. D., & Silvoso, M. M. (2010b). Cement replacement by sugarcane bagasse ash: CO_2 emissions reduction and potential for carbon credits. *Journal of Environmental Management, 91,* 1864–1871. https://doi.org/10.1016/j.jenvman.2010.04.008.

Fennis, S. A. A. M. (2011). Design of ecological concrete by particle packing optimization. Ph.D. thesis. Delft: Delft University of Technology. http://repository.tudelft.nl/view/ir/uuid%3A5a1e445b-36a7-4f27-a89a-d48372d2a45c/.

FIB TG3.6. (2008). Environmental design of concrete structures—General principles, fib bulletin 47. Lausanne, International Federation for Structural Concrete (fib).

Finnveden, G., Hauschild, M. Z., Ekvall, T., Guinée, J., Heijungs, R., Hellweg, S., et al. (2009). Recent developments in life cycle assessment. *Journal of Environmental Management, 91*(1), 1–21. https://doi.org/10.1016/j.jenvman.2009.06.018.

Flower, D. J. M., & Sanjayan, J. G. (2007). Green house gas emissions due to concrete manufacture. *International Journal Life Cycle Assesment, 12*(5), 282–288. https://doi.org/10.1065/lca2007.05.327.

Fu, X., Lu, W., & Chung, D. L. L. (1996). Improving the bond strength between carbon fiber and cement by fiber surface treatment of fibers. *Cement and Concrete Research, 26,* 1007–1012. https://doi.org/10.1016/0008-8846(96)00084-1.

Fu, X., Lu, W., & Chung, D. L. L. (1998). Improving the strain-sensing ability of carbon fiber-reinforced cement by ozone treatment of the fibers. *Cement and Concrete Research, 28,* 138–186. https://doi.org/10.1016/S0008-8846(97)00265-2.

Frischknecht, R., Jungbluth, N. (eds.). (2001). *Overview and methodology*. Final Report ecoinvent v2.0 No. 1. St-Gallen: Swiss Centre for Life Cycle Inventories; 2007. 40p Gajda J. Absorption of Atmospheric Carbon Dioxide by Portland Cement, R&D, Serial no. 2255a, Chicago: PCA.

Gao, J. M., Qian, C. X., Liu, H. F., Wang, B., & Li, L. (2005). ITZ microstructure of concrete containing GGBS. *Cement and Concrete Research, 35*(7), 1299–1304. https://doi.org/10.1016/j.cemconres.2004.06.042.

García-Gusano, D., Garraín, D., Herrera, I., Cabal, H., & Lechon, Y. (2015). Life cycle assessment of applying CO_2 post-combustion capture to the Spanish cement production. *Journal of Cleaner Production, 104,* 328–338. https://doi.org/10.1016/j.jclepro.2013.11.056.

Gartner, E. (2004). Industrially interesting approaches to low-CO_2 cements. *Cement Concrete Research, 34*(9), 1489–1498. https://doi.org/10.1016/j.cemconres.2004.01.021.

Gajda, J. (2001). Absorption of Atmospheric Carbon Dioxide by Portland Cement, R&D, Serial no. 2255a. Chicago: PCA.

Gencturk, B., Hossain, K., & Lahourpour, S. (2016). Life cycle sustainability assessment of RC buildings in seismic regions. *Engineering Structures, 110,* 347–362. https://doi.org/10.1016/j.engstruct.2015.11.037.

Gopalan, M. K. (1996). Sorptivity of fly ash concretes. *Cement and Concrete Research, 26*(8), 1189–1197. https://doi.org/10.1016/0008-8846(96)00105-6.

Guinée, J., Gorrée, M., Heijungs, R., Huppes, G., Kleijn, R., de Koning, A., et al. (2004). *Handbook on life cycle assessment. Operational guide to the ISO Standards*. Dordrecht: Kluwer Academic Publishers.

Habert, G. (2014). Assessing the environmental impact of conventional and 'green' cement production, chapter 10. In F. Pacheco-Torgal, L. F. Cabeza, J. Labrincha and A. de Magalhães (Eds.), *Eco-efficient construction and building materials, life cycle assessment (LCA), eco-labelling and case studies* (Vol. 49, pp. 119–238). Woodhead Publishing Series in Civil and Structural Engineering.

Habert, G., Bouzidi, Y., Chen, C., & Jullien, A. (2010). Development of a depletion indicator for natural resources used in concrete. *Resources, Conservation and Recycling, 54*(6), 364–376. https://doi.org/10.1016/j.resconrec.2009.09.002.

Habert, G., Choupay, N., Escadeillas, G., Guillaume, D., & Montel, J. M. (2009). Clay content of argillites: Influence on cement based mortars. *Applied Clay Science, 43,* 322–330. https://doi.org/10.1016/j.clay.2008.09.009.

Habert, G., Choupay, N., Montel, J. M., Guillaume, D., & Escadeillas, G. (2008). Effects of the secondary minerals of the natural pozzolans on their pozzolanic activitym. *Cement and Concrete Research, 38,* 963–975. https://doi.org/10.1016/j.cemconres.2008.02.005.

Habert, G., Denarié, E., Šajna, A., & Rossi, P. (2013). Lowering the global warming impact of bridge rehabilitations by using ultra high performance fiber reinforced concretes. *Cement & Concrete Composites, 38,* 1–11. https://doi.org/10.1016/j.cemconcomp.2012.11.008.

Hammond, G., & Jones, C. (2011). Inventory of Carbon and Energy (ICE) V2.0, Sustainable Energy Research Team (SERT) University of Bath, UK.

Hájek, P., Fiala, C., & Kynclová, M. (2011). Life cycle assessments of concrete structures—A step towards environmental savings. *Structural Concrete Journal of the fib, 1,* 13–22. https://doi.org/10.1002/suco.201000026.

Heidrich, C., Hinczak, I., & Ryan, B. (2005). SCM's potential to lower Australia's greenhouse gas emissions profile. In *Australasian Slag Association Conference*, Sydney.

Hester, D., McNally, C., & Richardson, M. (2005). A study of the influence of slag alkali level on the alkali–silica reactivity of slag concrete. *Construction and Building Materials, 19,* 661–665. https://doi.org/10.1016/j.conbuildmat.2005.02.016.

Hewlett, P. C. (1998). *Chemistry of cement and concrete* (pp. 471–601). New York: Wiley.

Hong, T., et al. (2014). Assessment model for energy consumption and greenhouse gasemissions during building construction. *Journal of Management in Engineering, 30*(2), 226–235. https://doi.org/10.1061/(ASCE)ME.1943-5479.0000199.

Hwang, C. L., & Wu, D. S. (1989). Properties of cement paste containing rice husk ash. *American Concrete Institute, SP, 114,* 733–765.

ISO, International Standardisation Organisation. (2006a). ISO 14040: Environmental management-life cycle assessment—Principles and framework. International Standardisation Organisation.

ISO, International Standardisation Organisation. (2006b). ISO 14044: Environmental management-life cycle assessment—Requirements and guidelines. International Standardisation Organisation.

Joshi, S. V., Drzal, L. T., Mohanty, S. K., & Aror, S. (2004). Are natural fiber composites environmentally superior to glass fiber reinforced composites? *Composites: Part A, 35,* 371–376. https://doi.org/10.1016/j.compositesa.2003.09.016.

Jaturapitakkul, C., & Roongreung, B. (2003). Cementing material from calcium carbide residue-rice husk ash. *Journal of Materials in Civil Engineering, 15*(5), 470–475. https://doi.org/10.1061/(ASCE)0899-1561(2003)15:5(470).

Kellenberger, D., Althaus, H.-J., Jungbluth, N., Künniger, R., Lehmann, M., & Thalmann, P. (2007). *Life cycle inventories of building products*. Final Report Ecoinvent Data v. 2.0 No. 7. EMPA Dübendorf, Swiss Centre for Life Cycle Inventories, Dübendorf.

Khatib, J. M., Hibbert, J. J. (2005). Selected engineering properties of concrete incorporating slag and metakaolin. *Construction and Building Materials, 19*, 460–472. http://dx.doi.org/10.1016/j.conbuildmat.2004.07.017.

Kjellsen, K. O., Guimaraes, M., & Nilsson A. (2005). *The CO_2 balance of concrete in a life cycle perspective*. Danish Technological Institute (DTI). http://www.nordicinnovation.org/Publications/co2-uptake-during-the-concretelifecycle/.

Koenders, E. A. B., Pepe, M., & Martinelli, E. (2014). Compressive strength and hydration processes of concrete with recycled aggregates. *Cement and Concrete Research, 56,* 203–212. https://doi.org/10.1016/j.cemconres.2013.11.012.

Kriker, A., Debicki, G., Bali, A., Khenfer, M. M., & Chabannet, M. (2005). Mechanical properties of date palm fibers and concrete reinforced with date palm fibers in hot-dry climate. *Cement & Concrete and Composites, 27,* 554–564. https://doi.org/10.1016/j.cemconcomp.2004.09.015.

Lasvaux, S., Habert, G., Schiopu, N., Chevalier, J., & Peuportier, B. (2014). Influence of simplification of life cycle inventories on the accuracy of impact assessment: Application to construction products. *Journal of Cleaner Production, 79*(15), 142–151. https://doi.org/10.1016/j.jclepro.2014.06.003.

Lee, K.-M., & Park, P.-J. (2005). Estimation of the environmental credit for the recycling of granulated blast furnace slag based on LCA. *Resources, Conservation and Recycling, 44,* 139–151. https://doi.org/10.1016/j.resconrec.2004.11.004.

Lehtinen, H., Saarentaus, A., Rouhiainen, J., Pitts, M., & Azapagic, A. (2011). A Review of LCA Methods and Tools and their Suitability for SMEs.

Lothenbach, B., Le Saout, G., Gallucci, E., & Scrivener, K. (2008). Influence of limestone on the hydration of Portland cements. *Cement and Concrete Research, 38,* 848–860. https://doi.org/10.1016/j.cemconres.2008.01.002.

Luo, R., Cai, Y., Wang, C., & Huang, X. (2003). Study of chloride binding and diffusion in GGBS concrete. *Cement and Concrete Research, 33,* 1–7. https://doi.org/10.1016/S0008-8846(02)00712-3.

Marinkovic, S. (2013). LCA aspects of concrete. In F. P. Torgal, S. Jalali, J. Labrincha, & V. M. John (Eds.), *Eco-efficient concrete*. Cambridge: Woodhead Publishing Limited.

Marinkovic, S. B., Malesev, N., & Ignjatovic, I. (2014). Life cycle assessment (LCA) of concrete made using recycled concrete or natural aggregates, Ch 11 in Eco-efficient construction and building materials. In F. Pacheco-Torgal, L. F. Cabeza, J. Labrincha and A. de Magalhães (Eds.), *Life cycle assessment (LCA), eco-labelling and case studies* (Vol. 49, pp. 239–266). Woodhead Publishing Series in Civil and Structural Engineering.

Mehta, P. K. (1992). Rice husk ash—A unique supplementary cementing material. In *Proceedings of the International Symposium on Advances in Concrete Technology*, Athens, Greece (pp. 407–430).

Miura, T., & Iwaki, I. (2000). Strength development of concrete incorporating high levels of ground granulated blast-furnace slag at low temperatures. *ACI Materials Journal, 97*(1), 66–70.

MPA—The Concrete Centre. (2011). Specifying sustainable concrete; Understanding the role of constituent materials. www.concretecentre.com/publications.

Mulenga, D. M., Stark, J., & Nobst, P. (2003). Thaumasite formation in concrete and mortars containing fly ash. *Cement & Concrete Composites, 25,* 907–912. https://doi.org/10.1016/S0958-9465(03)00136-7.

Nadoushani, M. Z. S., & Akbarnezhad, A. (2015). Effects of structural system on the life cycle carbon footprint of buildings. *Energy and Buildings, 102,* 337–346. https://doi.org/10.1016/j.enbuild.2015.05.044.

Naik, T. R., Kraus, R. N., & Siddique, R. (2002). Demonstration of manufacturing technology for concrete and CLSM utilizing wood ash from Wisconsin, Report No. CBU-2002-30, for Project # 01-06 UWM Center for By-Products Utilization Milwaukee: Department of Civil Engineering and Mechanics, University of Wisconsin-Milwaukee, 124. https://www4.uwm.edu/cbu/Papers/2002%20CBU%20Reports/REP-485.pdf.

Nehdi, M., Duquette, J., & El Damatty, A. (2003). Performance of rice husk ash produced using a new technology as a mineral admixture in concrete. *Cement and Concrete Research, 33,* 1203–1210. https://doi.org/10.1016/S0008-8846(03)00038-3.

Nili, M., & Salehi, A. M. (2010). Assessing the effectiveness of pozzolans in massive high strength concrete. *Construction and Building Materials, 24*(11), 2108–2116. https://doi.org/10.1016/j.conbuildmat.2010.04.049.

Obernberger, I., & Supancic, K. (2009). Possibilities of ash utilization from biomass combustion plants. In *Proceedings of the 17th European Biomass Conference & Exhibition*, Hamburg, Germany.

Odler, I. (2000). Special inorganic cements, E & FN Spon 2000. ISBN 0-419-22790-3.

Pacheco-Torgal, F., et al. (2013). *Handbook of recycled concrete and other demolition waste*. Woodhead Publishing Limited.

Paris, J. M., Roessler, J. G., Ferraro, C. C., De Ford, H. D., & Townsend, T. G. (2016). A review of waste products utilized as supplements to Portland cement in concrete. *Journal of Cleaner Production, 121,* 1–18. https://doi.org/10.1016/j.jclepro.2016.02.013.

Pehanich, J. L., Blankenhorn, P. R., & Silsbee, M. R. (2004). Wood fiber surface treatment level effects on selected mechanical properties of wood fiber-cement composites. *Cement and Concrete Research, 34,* 59–65. https://doi.org/10.1016/S0008-8846(03)00193-5.

Perry, C., Day, R. L., Joshi, R. C., Langan, B. W., & Gillot, J. E. (1987). The effectiveness of twelve Canadian fly ashes in suppressing expansion due to alkali-silica reaction. In *Proceedings of the 7th International Conference on Alkali-Aggregate Reaction*, Ottawa (pp. 93–97).

Pryce-Jenkins, V. (2011). A comparative review of the latest experimental research on the use of recycled concrete aggregate in structural concretes. Masters thesis, Department of Civil, Environmental and Geomatic Engineering, University College London.

Purnell, P., & Black, L. (2012). Embodied carbon dioxide in concrete: Variation with common mix design parameters. *Cement and Concrete Research, 42,* 874–877. https://doi.org/10.1016/j.cemconres.2012.02.005.

Rajamma, R., Labrincha, J. A., & Ferreira, V. M. (2012). Alkali activation of biomass fly ash–metakaolin blends. *Fuel, 98,* 265–271. https://doi.org/10.1016/j.fuel.2012.04.006.

Rajamma, R., Senff, L., Ribeiro, M. J., Labrincha, J. A., Ball, R. J., Allen, G. C., et al. (2015). Biomass fly ash effect on fresh and hardened state properties of cement based materials. *Composites Part B: Engineering, 77,* 1–9. https://doi.org/10.1016/j.compositesb.2015.03.019.

Ramakrishna, G., & Sundararajan, T. (2005). Studies on the durability of natural fibers and the effect of corroded fibers on the strength of mortar. *Cement & Concrete Composites, 27,* 575–582. https://doi.org/10.1016/j.compositesb.2015.03.019.

Rapoport, J. R., & Shah, S. P. (2005). Cast-in-place cellulose fiber-reinforced cement paste, mortar, and concrete. *ACI Materials Journal, 102*(5), 299–306.

Real, C., Alcala, M. D., & Criado, J. M. (1996). Preparation of silica from rice husks. *Journal of American Ceramic Society, 79*(8), 2012–2016. https://doi.org/10.1111/j.1151-2916.1996.tb08931.x.

Rice, E. K., Vondran, G. L., & Kundbargi, H. (1988). Bonding of fibrillated polypropylene fibers to cementitious materials. *Materials Research Society Symposium Proceedings, 114,* 145–152. https://doi.org/10.1557/PROC-114-145.

Richardson, D. N. (2006). *Strength and durability of a 70% ground granulated blast furnace slag concrete mix*. Rolla, Missouri: University of Missouri-Rolla.

Saraber, A. J., Feuerborn, H. J., van den Berg, J. W. (2009). Fly ash for concrete, CEN TC 104MIG 4 DOC 83-2009. Backgrounds to the revision of EN 450-1: 2005/A1:2007 and EN 450-2:2005.

Saraswathy, V., & Song, H.-W. (2007). Corrosion performance of rice husk ash blended concrete. *Construction and Building Materials, 21*(8), 1779–1784. https://doi.org/10.1016/j.conbuildmat.2006.05.037.

Savastano Jr., H., Warden, P. G., & Coutts, R. S. P. (2003). Mechanically pulped sisal as reinforcement in cementitious matrices. *Cement and Concrete Composites, 25*, 311–319. http://dx.doi.org/10.1016/S0958-9465(02)00055-0.

Savastano Jr., H., Warden, P. G., & Coutts, R. S. P. (2005). Microstructure and mechanical properties of waste fiber-cement composites. *Cement and Concrete Composites, 27*, 583–592. http://dx.doi.org/10.1016/j.cemconcomp.2004.09.009.

Savastano, H., Santos, S. F., Radonjic, M., Soboyejo, W. O. (2009). Fracture and fatigue of natural fibre-reinforced cementitious composites. *Cement and Concrete Composites, 31*, 232–243. https://doi.org/10.1016/j.cemconcomp.2009.02.006

Schau, E., Traverso, M., Lehmann, A., & Finkbeiner, M. (2011). Life cycle costing in sustainability assessment—A case study of remanufactures alternators. *Sustainability, 3,* 2268–2288. https://doi.org/10.3390/su3112268.

Schindler, A. K., & Folliard, K. J. (2003). Influence of supplementary cementing materials on the heat of hydration of concrete. In *Advances in Cement and Concrete IX Conference*. Oopper Mountain Conference Resort, Colorado, USA.

Schneider, M., Romer, M., Tschudin, M., & Bolio, H. (2011). Sustainable cement production—Present and future. *Cement and Concrete Research, 41,* 642–650. https://doi.org/10.1016/j.cemconres.2011.03.019.

Serbin, V. P., Glukovskiy, V. V., & Serbina, R. V. (1992). Composites: Cement and glass fibers. In *Proceedings 9th ICCC*, New Delhi (Vol. 5, pp. 479–484).

Shafiq, N., & Cabrera, J. G. (2004). Effects of initial curing condition on the fluid transport properties in OPC and fly ash blended cement concrete. *Cement & Concrete Composites, 26,* 381–387. https://doi.org/10.1016/S0958-9465(03)00033-7.

Shariq, M., Prasad, J., & Ahuja, A. K. (2008). Strength development of cement mortar and concrete incorporating GGBFS. *Asian Journal of Civil Engineering (Building and Housing), 9,* 61–74.

Shi, C., & Qian, J. (2000). High performance cementing materials from industrial slags a review. *Resources, Conservation and Recycling, 29,* 195–207. https://doi.org/10.1016/S0921-3449(99)00060-9.

Short, N. R., & Page, C. L. (1982). The diffusion of chloride ions through Portland and blended cement pastes. *Silicate Industrials* 237–240.

Sierra Beltran, M. G. (2011). Ductile cement-based composites with wood fibers. Ph.D. thesis, TU Delft, Delft, The Netherlands.

Singh, N. B., Singh, V. D., Rai, S., & Chaturvedi, S. (2002). Effect of lignosulfonate, calcium chloride and their mixture on the hydration of RHA-blended Portland cement. *Cement and Concrete Research, 32,* 387–392. https://doi.org/10.1016/S0008-8846(01)00688-3.

Song, H.-W., & Saraswathy, V. (2006). Studies on the corrosion resistance of reinforced steel in concrete with ground granulated blast-furnace slagdan overview. *Journal of Hazardous Materials, 138,* 226–233. https://doi.org/10.1016/j.jhazmat.2006.07.022.

Soroushian, P., & Marikunte, S. (1991). Moisture sensitivity of cellulose fiber reinforced cement. In *Durability of Concrete V. 2, SP-126* (pp. 821–835). American Concrete Institute, Detroit.

Sulapha, P., Wong, S. F., Wee, T. H., & Swaddiwudhipong, S. (2003). Carbonation of concrete containing mineral admixtures. *Journal of Materials in Civil Engineering, 15,* 134–143. https://doi.org/10.1061/(ASCE)0899-1561(2003)15:2(134).

Teixeira, E. R., Mateus, R., Camoes, A. F., Bragança, L., & Branco, F. G. (2016). Comparative environmental life-cycle analysis of concretes using biomass and coal fly ashes as partial cement replacement material. *Journal of Cleaner Production, 112,* 2221–2230. https://doi.org/10.1016/j.jclepro.2015.09.124.

Thomas, M. D. A., & Matthews, J. D. (1992). The permeability of fly ash concrete. *Materials and Structures, 25*(151), 388–396. https://doi.org/10.1007/BF02472254.

Tonoli, G. H. D., Rodrigues Filho, U. P., Savastano, H., Jr., Bras, J., Belgacem, M. N., & Rocco Lahr, F. A. (2009). Cellulose modified fibers in cement based composites. *Composites: Part A, Applied Science and Manufacturing, 40,* 2046–2053. https://doi.org/10.1016/j.compositesa.2009.09.016.

Turner, L. K., & Collins, F. G. (2013). Carbon dioxide equivalent (CO_2-e) emissions: A comparison between geopolymer and OPC cement concrete. *Construction and Building Materials, 43,* 125–130. https://doi.org/10.1016/j.conbuildmat.2013.01.023.

Ukrainczyk, N., Vrbos, N., & Koenders, E. A. B. (2016). Reuse of woody biomass ash waste in cementitious materials. *Chemical and Biochemical Engineering Quarterly, 30,* 2. https://doi.org/10.15255/CABEQ.2015.2231.

van den Heede, P., & de Belie, N. (2012). Environmental impact and life cycle assessment (LCA) of traditional and 'green' concretes: Literature review and theoretical calculations. *Cement & Concrete Composites, 34,* 431–442. https://doi.org/10.1016/j.cemconcomp.2012.01.004.

van Eijk, R. J., Obernberger, I., & Supancic, K. (2012). *Options for increased utilization of ash from biomass combustion and co-firing*. IEA Bioenergy Task 32: Biomass combustion and co-firing. Arnhem, Netherlands.

Vassilev, S. V., & Vassileva, C. G. (2007). A new approach for the classification of coal fly ashes based on their origin, composition, properties, and behaviour. *Fuel, 86*(10–11), 1490–1512. https://doi.org/10.1016/j.fuel.2006.11.020.

Wang, X. Y., & Lee, H. S. (2010). Modeling the hydration of concrete incorporating fly ash or slag. *Cement and Concrete Research, 40*(7), 984–996. https://doi.org/10.1016/j.cemconres.2010.03.001.

Weil, M., Jeske, U., & Schebek, L. (2006). Closed-loop recycling of construction and demolition waste in Germany in view of stricter environmental threshold values. *Waste Management and Research, 24,* 197–206. https://doi.org/10.1177/0734242X06063686.

Yan, L., & Chouw, N. (2013). Sustainable concrete and structures with natural fiber reinforcements. In L. Yang (Ed.), *Infrastructure corrosion and durability—A sustainability study*. OMICS Group Incorporation.

Yang, K. H., Moon, G. D., & Jeon, Y. S. (2016). Implementing ternary supplementary cementing binder for reduction of the heat of hydration of concrete. *Journal of Cleaner Production, 112,* 845–852. https://doi.org/10.1016/j.jclepro.2015.06.022.

Yang, K. H., Jung, Y. B., Cho, M. S., & Tae, S. H. (2014). Effect of supplementary cementitious materials on reduction of CO_2 emissions from concrete. *Journal of Cleaner Production, 103,* 774–783. https://doi.org/10.1016/j.jclepro.2014.03.018.

Yeau, K. Y., & Kim, E. K. (2005). An experimental study on corrosion resistance of concrete with ground granulate blast-furnace slag. *Cement and Concrete Research, 35,* 1391–1399. https://doi.org/10.1016/j.cemconres.2004.11.010.

Zea Escamilla, E. B. B., & Wallbaum, H. (2011). Environmental savings from the use of vegetable fibers as concrete reinforcement. In *ISEC-6*, Zürich, June. https://www.researchgate.net/publication/269082837.

Zhao, H., Sun, W., Wu, X., & Gao, B. (2015). The properties of the self-compacting concrete with fly ash and ground granulated blast furnace slag mineral admixtures. *Journal of Cleaner Production, 95,* 66–74. https://doi.org/10.1016/j.jclepro.2015.02.050.

Zhang, M. H., & Malhotra, V. M. (1996). High-performance concrete incorporating rice husk ash as a supplementary cementing material. *ACI Materials Journal, 93*(6), 629–636.